

NOVEMBER 2017

AJNR

VOLUME 38 • PP 2033–2217

AJNR

AMERICAN JOURNAL OF NEURORADIOLOGY

NOVEMBER 2017
VOLUME 38
NUMBER 11
WWW.AJNR.ORG

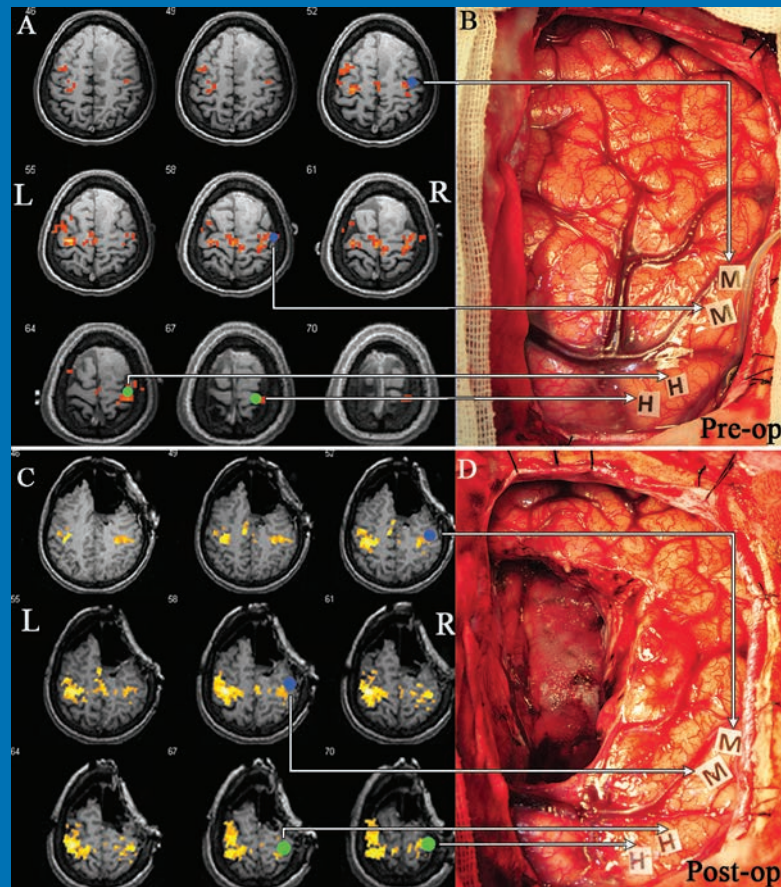
THE JOURNAL OF DIAGNOSTIC AND
INTERVENTIONAL NEURORADIOLOGY

Real-time motor cortex mapping of glioma resection using
resting-state fMRI

ADC histograms of human papillomavirus–positive head and neck
squamous cell carcinoma

ASL perfusion MR imaging in NPH

Official Journal ASNR • ASFNR • ASHNR • ASPNR • ASSR



A 360-Degree Approach to Neuroendovascular Therapy



Aneurysm Therapy Solutions



LVIS® | LVIS® Jr.
Intraluminal Support Device

Braided Coil Assist Stents with High
Neck Coverage, Excellent Opening,
and Improved Radial Force*

*Humanitarian Device: Authorized by Federal Law for use with bare platinum embolic coils for the treatment of unruptured, wide neck (neck \geq 4 mm or dome to neck ratio $<$ 2), intracranial, saccular aneurysms arising from a parent vessel with a diameter \geq 2.5 mm and \leq 4.5 mm. The effectiveness of this device for this use has not been demonstrated.



Access Product Solutions



Headway® DUO
Microcatheter

Innovative Catheter Technology
and Construction in a Complete
Range of Sizes and Softness

For more information or a product demonstration,
contact your local MicroVention representative:



MicroVention, Inc.
Worldwide Headquarters
35 Enterprise
Aliso Viejo, CA 92656 USA
MicroVention UK Limited
MicroVention Europe, S.A.R.L.
MicroVention Deutschland GmbH
microvention.com

PH +1.714.247.8000

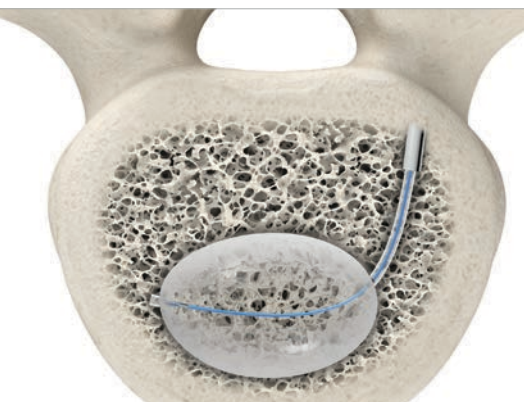
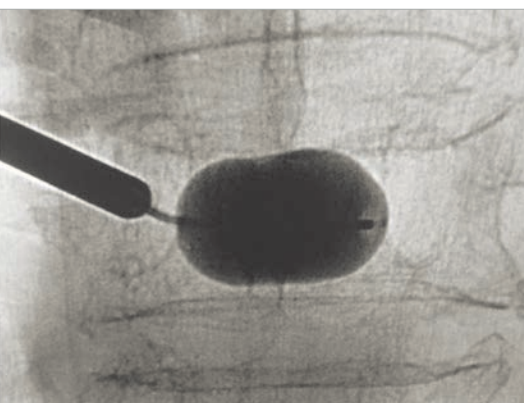
PH +44 (0) 191 258 6777

PH +33 (1) 39 21 77 46

PH +49 211 210 798-0



stryker



Unipedicular
approach.

**Bipedicular
results.***

AVAflex® Balloon System

Simplify your approach in treating vertebral compression fractures (VCFs) and create larger voids with a single incision. The AVAflex system's flexible, curved balloon is available up to 30mm, the longest balloon on the market today.[†] Our curved, coaxial needle achieves targeted cement placement. It's more than a minimally invasive approach with the potential for less risk of patient trauma. It's a powerful reminder that we're in this together.

Achieve precision with a single incision.

strykerIVS.com/avaflex

* Based on fill volume

† As of March 2017

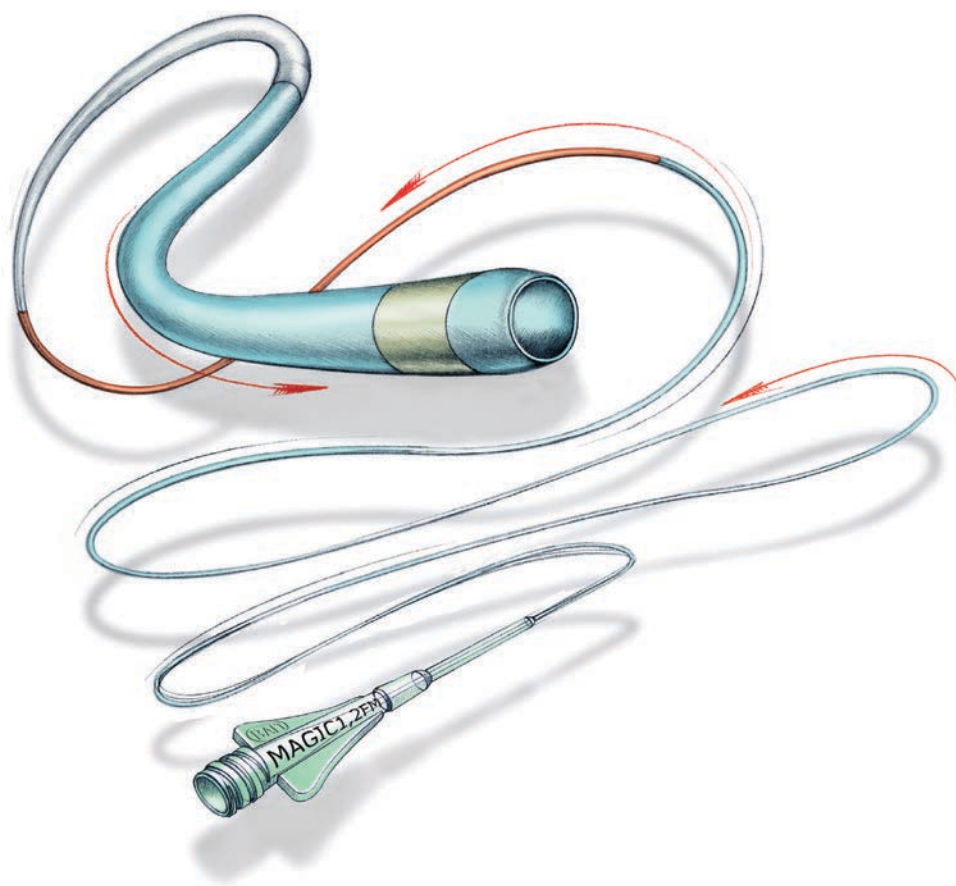
1000-025-577 Rev None

Magic[®]



FLOW-DEPENDENT MICROCATHETER SERIES

Now available through Balt USA



ordermagics@balt-usa.com

MAGIC catheters are designed for general intravascular use. They may be used for the controlled, selective regional infusion of therapeutic agents or embolic materials into vessels.¹

Federal (USA) law restricts this device to sale, distribution by or on the order of a physician. Indications, contraindications, warnings and instructions for use can be found in the product labeling supplied with each device.

1. Magic Catheters IFU – Ind 19



BALT USA
18 Technology Drive #169, Irvine, CA 92618
P 949.788.1443 F 949.788.1444

© 2017 BALT USA MKTG-068 Rev. B

Unleash Your Tiger



TIGERTRIEVER

 **RAPIDMEDICAL**
The brain at your fingertips

[//www.rapid-medical.com](http://www.rapid-medical.com)



ASNR 56th Annual Meeting & The Foundation of the ASNR Symposium 2018

June 2 - 7, 2018 | Vancouver, B.C., CANADA



The Vancouver Convention Centre East
© 2013 Vancouver Convention Centre

Welcome and Greetings

Please join us in Vancouver, CANADA for the **56th Annual Meeting of the American Society of Neuroradiology** on June 2–7, 2018 at the Vancouver Convention Centre East. Surrounded by the coastal mountains and located on the waterfront, you can enjoy these spectacular views in the heart of downtown Vancouver. With its undeniable charm and friendly atmosphere, Vancouver is known around the world as both a popular tourist attraction and one of the best places to live.

ASNR enthusiastically presents **Neuroradiology: Adding Value and Improving Healthcare** at the Symposium of the Foundation of the ASNR, as well as the common thread throughout the Annual Meeting. Implementing a value-based strategy in imaging has grasped the attention of nearly every healthcare provider; in particular with Radiologists understanding that the future will demand their imaging practices deliver better value. Value in healthcare is typically defined as those imaging strategies that yield improved outcomes, lower costs, or both. As payment transitions from a fee-for-service to a value-based system, thus creating a fundamentally different marketplace dynamic, measuring good outcomes are at the center of this changeover. At this time of uncertainty what little remains clear is that without a well-defined knowledge of their outcomes, no medical specialty will be able to succeed in the future value-based system. The Symposium will feature how Neuroradiology, in its many subspecialty areas, adds value to clinical care pathways by directing healthcare practice towards better outcomes. The annual meeting programming will continue on this theme emphasizing imaging that improves health outcomes, while considering costs, thus adding value. Our discussions will incorporate many innovative approaches to how neuroimaging currently does and will continue to improve overall healthcare performance.

As the Program Chair for ASNR 2018, it is my pleasure and honor to welcome you to Vancouver, CANADA for our annual meeting! Vancouver is known for being a very walkable city with a compact downtown core hosting many places to enjoy. So pack your comfortable walking shoes and let's tour together with our colleagues and friends!

Pina Sanelli

Pina C. Sanelli, MD, MPH, FACR
ASNR 2018 Program Chair/President-Elect



ASNR 2018 ■ VANCOUVER

ASFNR ASHNR ASPNR ASSR SNIS

THE FOUNDATION OF THE ASNR



Pina C. Sanelli, MD, MPH, FACR

ASNR 2018 Program Chair/President-Elect

Programming developed in cooperation with the...

American Society of Functional Neuroradiology (ASFNR)

Max Wintermark, MD

American Society of Head and Neck Radiology (ASHNR)

Deborah R. Shatzkes, MD

American Society of Pediatric Neuroradiology (ASPNR)

Ashok Panigrahy, MD

American Society of Spine Radiology (ASSR)

John D. Barr, MD, FACR, FSIR, FAHA

Society of NeuroInterventional Surgery (SNIS)

Maresh V. Jayaraman, MD

ASNR Health Policy (HPC) Committee

William D. Donovan, MD, MPH, FACR,

Gregory N. Nicola, MD, FACR

ASNR Computer Sciences & Informatics (CSI) Committee

John L. Go, MD, FACR

ASNR Research Scientist Programming Committee

Dikoma C. Shungu, PhD, Timothy P.L. Roberts, PhD

The International Hydrocephalus Imaging Working Group (IHIWG) / CSF Flow Group

William G. Bradley, Jr., MD, PhD, FACR, Harold L. Rekate, MD
and Bryn A. Martin, PhD

Abstract Deadline: Friday, December 15, 2017

Please visit 2018.asnr.org for more information



Fairmont Waterfront
© Copyright 2017 FRHI



Pan Pacific Vancouver
© 2017 Pan Pacific Hotels and Resorts

ASNR 56th Annual Meeting

c/o American Society of Neuroradiology
800 Enterprise Drive, Suite 205
Oak Brook, Illinois 60523-4216
Phone: 630-574-0220 + Fax: 630 574-0661
2018.asnr.org





Smooth and stable.

Target Detachable Coils deliver consistently smooth deployment and exceptional microcatheter stability. Designed to work seamlessly together for framing, filling and finishing. Target Coils deliver the high performance you demand.

For more information, please visit www.strykerneurovascular.com/Target or contact your local Stryker Neurovascular sales representative.



Target[®]
DETACHABLE COILS

Trevo® XP ProVue Retrievers

See package insert for complete indications, complications, warnings, and instructions for use.

INDICATIONS FOR USE

1. The Trevo Retriever is indicated for use to restore blood flow in the neurovasculature by removing thrombus for the treatment of acute ischemic stroke to reduce disability in patients with a persistent, proximal anterior circulation, large vessel occlusion, and smaller core infarcts who have first received intravenous tissue plasminogen activator (IV t-PA). Endovascular therapy with the device should start within 6 hours of symptom onset.
2. The Trevo Retriever is intended to restore blood flow in the neurovasculature by removing thrombus in patients experiencing ischemic stroke within 8 hours of symptom onset. Patients who are ineligible for intravenous tissue plasminogen activator (IV t-PA) or who fail IV t-PA therapy are candidates for treatment.

COMPLICATIONS

Procedures requiring percutaneous catheter introduction should not be attempted by physicians unfamiliar with possible complications which may occur during or after the procedure. Possible complications include, but are not limited to, the following: air embolism; hematoma or hemorrhage at puncture site; infection; distal embolization; pain/headache; vessel spasm, thrombosis, dissection, or perforation; emboli; acute occlusion; ischemia; intracranial hemorrhage; false aneurysm formation; neurological deficits including stroke; and death.

COMPATIBILITY

3x20mm retrievers are compatible with Trevo® Pro 14 Microcatheters (REF 90231) and Trevo® Pro 18 Microcatheters (REF 90238). 4x20mm retrievers are compatible with Trevo® Pro 18 Microcatheters (REF 90238). 4x30mm retrievers are compatible with Excelsior® XT-27® Microcatheters (150cm x 6cm straight REF 275081) and Trevo® Pro 18 Microcatheters (REF 90238). 6x25mm Retrievers are compatible with Excelsior® XT-27® Microcatheters (150cm x 6cm straight REF 275081). Compatibility of the Retriever with other microcatheters has not been established. Performance of the Retriever device may be impacted if a different microcatheter is used.

Balloon Guide Catheters (such as Merci® Balloon Guide Catheter and FlowGate® Balloon Guide Catheter) are recommended for use during thrombus removal procedures.

Retrievers are compatible with the Abbott Vascular DOC® Guide Wire Extension (REF 22260).

Retrievers are compatible with Boston Scientific RHV (Ref 421242).

SPECIFIC WARNINGS FOR INDICATION 1

- The safety and effectiveness of the Trevo Retrievers in reducing disability has not been established in patients with large core infarcts (i.e., ASPECTS ≤ 7). There may be increased risks, such as intracerebral hemorrhage, in these patients.
- The safety and effectiveness of the Trevo Retrievers in reducing disability has not been established or evaluated in patients with occlusions in the posterior circulation (e.g., basilar or vertebral arteries) or for more distal occlusions in the anterior circulation.

WARNINGS APPLIED TO BOTH INDICATIONS

- Administration of IV t-PA should be within the FDA-approved window (within 3 hours of stroke symptom onset).
- Contents supplied STERILE, using an ethylene oxide (EO) process. Nonpyrogenic.
- To reduce risk of vessel damage, adhere to the following recommendations:
 - Take care to appropriately size Retriever to vessel diameter at intended site of deployment.
 - Do not perform more than six (6) retrieval attempts in same vessel using Retriever devices.
 - Maintain Retriever position in vessel when removing or exchanging Microcatheter.
- To reduce risk of kinking/fracture, adhere to the following recommendations:
 - Immediately after unsheathing Retriever, position Microcatheter tip marker just proximal to shaped section. Maintain Microcatheter tip marker just proximal to shaped section of Retriever during manipulation and withdrawal.
 - Do not rotate or torque Retriever.
 - Use caution when passing Retriever through stented arteries.
- Do not resterilize and reuse. Structural integrity and/or function may be impaired by reuse or cleaning.
- The Retriever is a delicate instrument and should be handled carefully. Before use and when possible during procedure, inspect device carefully for damage. Do not use a device that shows signs of damage. Damage may prevent device from functioning and may cause complications.



Concentric Medical
301 East Evelyn Avenue
Mountain View, CA 94041

Stryker Neurovascular
47900 Bayside Parkway
Fremont, CA 94538

strykerneurovascular.com

Date of Release: SEP/2016

EX_EN_US

Copyright © 2016 Stryker
NV00018973.AB

Target® Detachable Coil

See package insert for complete indications, contraindications, warnings and instructions for use.

INTENDED USE / INDICATIONS FOR USE

Target Detachable Coils are intended to endovascularly obstruct or occlude blood flow in vascular abnormalities of the neurovascular and peripheral vessels.

Target Detachable Coils are indicated for endovascular embolization of:

- Intracranial aneurysms
- Other neurovascular abnormalities such as arteriovenous malformations and arteriovenous fistulae
- Arterial and venous embolizations in the peripheral vasculature

CONTRAINDICATIONS

None known.

POTENTIAL ADVERSE EVENTS

Potential complications include, but are not limited to: allergic reaction, aneurysm perforation and rupture, arrhythmia, death, edema, embolus, headache, hemorrhage, infection, ischemia, neurological/intracranial sequelae, post-embolization syndrome (fever, increased white blood cell count, discomfort), TIA/stroke, vasospasm, vessel occlusion or closure, vessel perforation, dissection, trauma or damage, vessel rupture, vessel thrombosis. Other procedural complications including but not limited to: anesthetic and contrast media risks, hypotension, hypertension, access site complications.

WARNINGS

- Contents supplied STERILE using an ethylene oxide (EO) process. Do not use if sterile barrier is damaged. If damage is found, call your Stryker Neurovascular representative.
- For single use only. Do not reuse, reprocess or resterilize. Reuse, reprocessing or resterilization may compromise the structural integrity of the device and/or lead to device failure which, in turn, may result in patient injury, illness or death. Reuse, reprocessing or resterilization may also create a risk of contamination of the device and/or cause patient infection or cross-infection, including, but not limited to, the transmission of infectious disease(s) from one patient to another. Contamination of the device may lead to injury, illness or death of the patient.

- After use, dispose of product and packaging in accordance with hospital, administrative and/or local government policy.
- **This device should only be used by physicians who have received appropriate training in interventional neuroradiology or interventional radiology and preclinical training on the use of this device as established by Stryker Neurovascular.**
- Patients with hypersensitivity to 316LVM stainless steel may suffer an allergic reaction to this implant.
- MR temperature testing was not conducted in peripheral vasculature, arteriovenous malformations or fistulae models.
- The safety and performance characteristics of the Target Detachable Coil System (Target Detachable Coils, InZone Detachment Systems, delivery systems and accessories) have not been demonstrated with other manufacturer's devices (whether coils, coil delivery devices, coil detachment systems, catheters, guidewires, and/or other accessories). Due to the potential incompatibility of non Stryker Neurovascular devices with the Target Detachable Coil System, the use of other manufacturer's device(s) with the Target Detachable Coil System is not recommended.
- To reduce risk of coil migration, the diameter of the first and second coil should never be less than the width of the ostium.
- In order to achieve optimal performance of the Target Detachable Coil System and to reduce the risk of thromboembolic complications, it is critical that a continuous infusion of appropriate flush solution be maintained between a) the femoral sheath and guiding catheter, b) the 2-tip microcatheter and guiding catheters, and c) the 2-tip microcatheter and Stryker Neurovascular guidewire and delivery wire. Continuous flush also reduces the potential for thrombus formation on, and crystallization of infusate around, the detachment zone of the Target Detachable Coil.
- Do not use the product after the "Use By" date specified on the package.
- Reuse of the flush port/dispenser coil or use with any coil other than the original coil may result in contamination of, or damage to, the coil.
- Utilization of damaged coils may affect coil delivery to, and stability inside, the vessel or aneurysm, possibly resulting in coil migration and/or stretching.
- The fluoro-saver marker is designed for use with a Rotating Hemostatic Valve (RHV). If used without an RHV, the distal end of the coil may be beyond the alignment marker when the fluoro-saver marker reaches the microcatheter hub.

- If the fluoro-saver marker is not visible, do not advance the coil without fluoroscopy.
- Do not rotate delivery wire during or after delivery of the coil. Rotating the Target Detachable Coil delivery wire may result in a stretched coil or premature detachment of the coil from the delivery wire, which could result in coil migration.
- Verify there is no coil loop protrusion into the parent vessel after coil placement and prior to coil detachment. Coil loop protrusion after coil placement may result in thromboembolic events if the coil is detached.
- Verify there is no movement of the coil after coil placement and prior to coil detachment. Movement of the coil after coil placement may indicate that the coil could migrate once it is detached.
- Failure to properly close the RHV compression fitting over the delivery wire before attaching the InZone® Detachment System could result in coil movement, aneurysm rupture or vessel perforation.
- Verify repeatedly that the distal shaft of the catheter is not under stress before detaching the Target Detachable Coil. Axial compression or tension forces could be stored in the 2-tip microcatheter causing the tip to move during coil delivery. Microcatheter tip movement could cause the aneurysm or vessel to rupture.
- Advancing the delivery wire beyond the microcatheter tip once the coil has been detached involves risk of aneurysm or vessel perforation.
- The long term effect of this product on extravascular tissues has not been established so care should be taken to retain this device in the intravascular space.

Damaged delivery wires may cause detachment failures, vessel injury or unpredictable distal tip response during coil deployment. If a delivery wire is damaged at any point during the procedure, do not attempt to straighten or otherwise repair it. Do not proceed with deployment or detachment. Remove the entire coil and replace with undamaged product.

- After use, dispose of product and packaging in accordance with hospital, administrative and/or local government policy.

CAUTIONS / PRECAUTIONS

- Federal Law (USA) restricts this device to sale by or on the order of a physician.
- Besides the number of InZone Detachment System units needed to complete the case, there must be an extra InZone Detachment System unit as back up.

- Removing the delivery wire without grasping the introducer sheath and delivery wire together may result in the detachable coil sliding out of the introducer sheath.
- Failure to remove the introducer sheath after inserting the delivery wire into the RHV of the microcatheter will interrupt normal infusion of flush solution and allow back flow of blood into the microcatheter.
- Some low level overhead light near or adjacent to the patient is required to visualize the fluoro-saver marker; monitor light alone will not allow sufficient visualization of the fluoro-saver marker.
- Advance and retract the Target Detachable Coil carefully and smoothly without excessive force. If unusual friction is noticed, slowly withdraw the Target Detachable Coil and examine for damage. If damage is present, remove and use a new Target Detachable Coil. If friction or resistance is still noted, carefully remove the Target Detachable Coil and microcatheter and examine the microcatheter for damage.
- If it is necessary to reposition the Target Detachable Coil, verify under fluoroscopy that the coil moves with a one-to-one motion. If the coil does not move with a one-to-one motion or movement is difficult, the coil may have stretched and could possibly migrate or break. Gently remove both the coil and microcatheter and replace with new devices.
- Increased detachment times may occur when:
 - Other embolic agents are present.
 - Delivery wire and microcatheter markers are not properly aligned.
 - Thrombus is present on the coil detachment zone.
- Do not use detachment systems other than the InZone Detachment System.
- Increased detachment times may occur when delivery wire and microcatheter markers are not properly aligned.
- Do not use detachment systems other than the InZone Detachment System.



Stryker Neurovascular
47900 Bayside Parkway
Fremont, CA 94538

strykerneurovascular.com

Date of Release: MAR/2016

EX_EN_US

Copyright © 2016 Stryker
NV00018669.AB

NEW

Indication for Trevor[®] Retrievers

A New Standard of Care in Stroke



FIRST

mechanical thrombectomy device
indicated to reduce disability in stroke.*

FIRST

new treatment indication for
stroke in 20 years.

Trevo XP

PROVUE RETRIEVER

Success accelerated.

*The Trevo Retriever is indicated for use to restore blood flow in the neurovasculature by removing thrombus for the treatment of acute ischemic stroke to reduce disability in patients with a persistent, proximal anterior circulation, large vessel occlusion, and smaller core infarcts who have first received intravenous tissue plasminogen activator (IV t-PA). Endovascular therapy with the device should start within 6 hours of symptom onset.

CALL FOR AJNR EDITORIAL FELLOWSHIP CANDIDATES

ASNR and AJNR are pleased once again to join efforts with other imaging-related journals that have training programs on editorial aspects of publishing for trainees or junior staff (3–5 years after training), including Radiology (Olmsted fellowship), AJR (Figley and Rogers fellowships), JACR (Bruce J. Hillman fellowship), and Radiologia.

2018 Candidate Information and Requirements

GOALS

- Increase interest in “editorial” and publication-related activities in younger individuals.
- Increase understanding and participation in the AJNR review process.
- Incorporate into AJNR's Editorial Board younger individuals who have previous experience in the review and publication process.
- Fill a specific need in neuroradiology not offered by other similar fellowships.
- Increase the relationship between “new” generation of neuroradiologists and more established individuals.
- Increase visibility of AJNR among younger neuroradiologists.

ACTIVITIES OF THE FELLOWSHIP

- Serve as Editorial Fellow for one year. This individual will be listed on the masthead as such.
- Review at least one manuscript per month for 12 months. Evaluate all review articles submitted to AJNR.
- Learn how electronic manuscript review systems work.
- Be involved in the final decision of selected manuscripts together with the Editor-in-Chief.
- Participate in all monthly Senior Editor telephone conference calls.
- Participate in all meetings of the Editors and Publications Committee during the annual meetings of ASNR and RSNA as per candidate's availability. The Foundation of the ASNR will provide \$2000 funding for this activity.
- Evaluate progress and adjust program to specific needs in annual meeting or telephone conference with the Editor-in-Chief.
- Embark on an editorial scientific or bibliometric project that will lead to the submission of an article to AJNR or another appropriate journal as determined by the Editor-in-Chief. This project will be presented by the Editorial Fellow at the ASNR annual meeting.
- Serve as liaison between AJNR and ASNR's Young Professionals Network and the 3 YPs appointed to AJNR as special consultants. Participate in meetings and telephone calls with this group. Design one electronic survey/year, polling the group regarding readership attitudes and wishes.
- Recruit trainees as reviewers as determined by the Editor-in-Chief.
- Organize and host a Fellows' Journal Club podcast.
- Serve as Guest Editor for an issue of AJNR's News Digest with a timely topic.

QUALIFICATIONS

- Be a fellow in neuroradiology from North America, including Canada (this may be extended to include other countries).
- Be a junior faculty neuroradiology member (< 3 years) in either an academic or private environment.
- Be an “in-training” or member of ASNR in any other category.

APPLICATION

- Include a short letter of intent with statement of goals and desired research project. CV must be included.
- Include a letter of recommendation from the Division Chief or fellowship program director. A statement of protected time to perform the functions outlined is desirable.
- Applications will be evaluated by AJNR's Senior Editors and the Chair of the Publications Committee prior to the ASNR meeting. The name of the selected individual will be announced at the meeting.
- Applications should be received by March 1, 2018 and sent to Ms. Karen Halm, AJNR Managing Editor, electronically at khalm@asn.org.



Simplify the MOC Process



Manage your CME Credits Online

Available to Members of Participating Societies

American Board of Radiology (ABR) Radiological Society of North America (RSNA)
 American College of Radiology (ACR) Society of Interventional Radiology (SIR)
 American Roentgen Ray Society (ARRS) SNM
 American Society of Neuroradiology (ASNR) The Society for Pediatric Radiology (SPR)
 Commission on Accreditation of Medical
 Physics Educational Programs, Inc. (CAMPEP)

CMEgateway.org

It's Easy and Free!

Log on to CME Gateway to:

- View or print reports of your CME credits from multiple societies from a single access point.
- Print an aggregated report or certificate from each participating organization.
- Link to SAMs and other tools to help with maintenance of certification.

American Board of Radiology (ABR) participation!

By activating ABR in your organizational profile, your MOC-fulfilling CME and SAM credits can be transferred to your own personalized database on the ABR Web site.

Sign Up Today!

go to CMEgateway.org



Statement of Ownership, Management, and Circulation (All Periodicals Publications Except Requester Publications)

1. Publication Title American Journal of Neuroradiology	2. Publication Number 5 3 2 - 6 3 0	3. Filing Date 9/15/2017
4. Issue Frequency Monthly	5. Number of Issues Published Annually 12	6. Annual Subscription Price \$390-Individual-US
7. Complete Mailing Address of Known Office of Publication (Not printer) (Street, city, county, state, and ZIP+4®) 800 Enterprise Drive, Suite 205, Oakbrook, IL 60523		Contact Person Karen Halm Telephone (Include area code) 630/574-1487 x238
8. Complete Mailing Address of Headquarters or General Business Office of Publisher (Not printer) 800 Enterprise Drive, Suite 205, Oakbrook, IL 60523		
9. Full Names and Complete Mailing Addresses of Publisher, Editor, and Managing Editor (Do not leave blank) Publisher (Name and complete mailing address) American Society of Neuroradiology, 800 Enterprise Drive, Suite 205, Oakbrook, IL 60523 Editor (Name and complete mailing address) Jeffrey Ross, AJNR, 800 Enterprise Drive, Suite 205, Oakbrook, IL 60523 Managing Editor (Name and complete mailing address) Karen Halm, AJNR, 800 Enterprise Drive, Suite 205, Oakbrook, IL 60523		
10. Owner (Do not leave blank. If the publication is owned by a corporation, give the name and address of the corporation immediately followed by the names and addresses of all stockholders owning or holding 1 percent or more of the total amount of stock. If not owned by a corporation, give the names and addresses of the individual owners. If owned by a partnership or other unincorporated firm, give its name and address as well as those of each individual owner. If the publication is published by a nonprofit organization, give its name and address.) Full Name Complete Mailing Address American Society of Neuroradiology 800 Enterprise Drive, Oakbrook, IL 60523		
11. Known Bondholders, Mortgagees, and Other Security Holders Owning or Holding 1 Percent or More of Total Amount of Bonds, Mortgages, or Other Securities. If none, check box <input checked="" type="checkbox"/> None Full Name Complete Mailing Address		
12. Tax Status (For completion by nonprofit organizations authorized to mail at nonprofit rates) (Check one) The purpose, function, and nonprofit status of this organization and the exempt status for federal income tax purposes: <input checked="" type="checkbox"/> Has Not Changed During Preceding 12 Months <input type="checkbox"/> Has Changed During Preceding 12 Months (Publisher must submit explanation of change with this statement)		

13. Publication Title American Journal of Neuroradiology	14. Issue Date for Circulation Data Below September 2017
15. Extent and Nature of Circulation	Average No. Copies Each Issue During Preceding 12 Months
a. Total Number of Copies (Net press run)	3591
(1) Mailed Outside-County Paid Subscriptions Stated on PS Form 3541 (Include paid distribution above nominal rate, advertiser's proof copies, and exchange copies)	2809
(2) Mailed In-County Paid Subscriptions Stated on PS Form 3541 (Include paid distribution above nominal rate, advertiser's proof copies, and exchange copies)	0
(3) Paid Distribution Outside the Mails Including Sales Through Dealers and Carriers, Street Vendors, Counter Sales, and Other Paid Distribution Outside USPS®	471
(4) Paid Distribution by Other Classes of Mail Through the USPS (e.g., First-Class Mail®)	0
c. Total Paid Distribution (Sum of 15b (1), (2), (3), and (4))	3280
d. Free or Nominal Rate Distribution (By Mail and Outside the Mail)	0
(1) Free or Nominal Rate Outside-County Copies included on PS Form 3541	0
(2) Free or Nominal Rate In-County Copies included on PS Form 3541	0
(3) Free or Nominal Rate Copies Mailed at Other Classes Through the USPS (e.g., First-Class Mail)	0
(4) Free or Nominal Rate Distribution Outside the Mail (Carriers or other means)	33
e. Total Free or Nominal Rate Distribution (Sum of 15d (1), (2), (3), and (4))	33
f. Total Distribution (Sum of 15c and 15e)	3313
g. Copies not Distributed (See Instructions to Publishers #4 (page #3))	278
h. Total (Sum of 15f and g)	3591
i. Percent Paid (15c divided by 15f times 100)	99
16. Electronic Copy Circulation	No. Copies of Single Issue Published Nearest to Filing Date
a. Paid Electronic Copies	0
b. Total Paid Print Copies (Line 15c) + Paid Electronic Copies (Line 16a)	3280
c. Total Print Distribution (Line 15f) + Paid Electronic Copies (Line 16a)	3313
d. Percent Paid (Both Print & Electronic Copies) (16b divided by 16c × 100)	99
<input checked="" type="checkbox"/> I certify that 50% of all my distributed copies (electronic and print) are paid above a nominal price.	
17. Publication of Statement of Ownership <input checked="" type="checkbox"/> If the publication is a general publication, publication of this statement is required. Will be printed in the <u>November</u> issue of this publication. <input type="checkbox"/> Publication not required.	
18. Signature and Title of Editor, Publisher, Business Manager, or Owner <i>Karen Halm</i>	Date 9/15/2017

DOTAREM[®]

(gadoterate meglumine) Injection

NOW
AVAILABLE
IN 5mL
VIALS

**Trusted for high
molecular stability^{1,2}**

Now approved for pediatric patients less than
two years of age including term neonates

Macrocyclic
and Ionic...

DOTAREM
...There is only One.³

**Following repeated administration:
No visible T1 signal intensity detected on non-contrast images within
the brain.*⁴⁻⁸**

- ⦿ NEW indication for pediatric patients less than two years of age including term neonates
- ⦿ The only imaging contrast with macrocyclic and ionic structure for high thermodynamic and kinetic stability^{1,2}
- ⦿ Many pediatric hospitals have or plan to switch to Dotarem, a stable macrocyclic GBCA⁹
- ⦿ Available in a wide variety of dosing options, now including 5mL vials
- ⦿ Trusted for proven global clinical experience, with over 70 million doses administered worldwide¹⁰

Guerbet | 
Contrast for Life

For more information on Dotarem,
visit guerbet.com or call your
local representative.

See opposite page for Important
Safety Information on Dotarem.

*Supporting data
based on ages 5 and up



Access Product Solutions



Sofia® Plus
Distal Access Catheter

Soft Torqueable Catheter Optimized
for Intracranial Access with
Excellent Navigation and Trackability



Neurovascular Malformation Solutions



Scepter® XC
Occlusion Balloon Catheter

Clinical Applications in Four Key
Areas: Balloon Remodeling, Stent
Delivery, Liquid Embolic Injection,
and Balloon-Test Occlusion

INDICATIONS FOR USE:

The SOFIA® Catheter is indicated for general intravascular use, including the neuro and peripheral vasculature. The SOFIA® Catheter can be used to facilitate introduction of diagnostic or therapeutic agents. The SOFIA® Catheter is not intended for use in coronary arteries.

The Scepter C® and Scepter XC® Occlusion Balloon Catheters are intended for use in the peripheral and neuro vasculature where temporary occlusion is desired. The balloon catheters provide temporary vascular occlusion which is useful in selectively stopping or controlling blood flow. The balloon catheters also offer balloon assisted embolization of intracranial aneurysms. For use in the peripheral vasculature for the infusion of diagnostic agents, such as contrast media, and therapeutic agents such as embolization materials. For neurovascular use for the infusion of diagnostic agents such as contrast media, and therapeutic agents, such as embolization materials, that have been approved or cleared for use in the neurovasculature and are compatible with the inner diameter of the Scepter C/XC Balloon Catheter.

The LVIS® Device is intended for use with bare platinum embolic coils for the treatment of unruptured, wide neck (neck \geq 4 mm or dome to neck ratio $<$ 2), intracranial, saccular aneurysms arising from a parent vessel with a diameter \geq 2.5 mm and \leq 4.5 mm.

The Headway® Duo Microcatheter is intended for general intravascular use, including the peripheral and coronary vasculature for the infusion of diagnostic agents, such as contrast media, and therapeutic agents, such as embolization materials. The Headway® Duo Microcatheter is intended for neurovascular use, for the infusion of diagnostic agents, such as contrast media, and therapeutic agents that have been cleared or approved for use in the neurovasculature and are compatible with the inner diameter of the Headway® Duo Microcatheter.



IMPORTANT SAFETY INFORMATION³

WARNING: NEPHROGENIC SYSTEMIC FIBROSIS (NSF)

Gadolinium-based contrast agents (GBCAs) increase the risk for NSF among patients with impaired elimination of the drugs. Avoid use of GBCAs in these patients unless the diagnostic information is essential and not available with non-contrasted MRI or other modalities. NSF may result in fatal or debilitating fibrosis affecting the skin, muscle and internal organs.

- The risk for NSF appears highest among patients with:
 - Chronic, severe kidney disease (GFR < 30 mL/min/1.73m²), or
 - Acute kidney injury.
- Screen patients for acute kidney injury and other conditions that may reduce renal function. For patients at risk for chronically reduced renal function (e.g. age > 60 years, hypertension, diabetes), estimate the glomerular filtration rate (GFR) through laboratory testing.
- For patients at highest risk for NSF, do not exceed the recommended DOTAREM dose and allow a sufficient period of time for elimination of the drug from the body prior to any re-administration.

INDICATIONS AND USAGE

DOTAREM® (gadoterate meglumine) injection is a prescription gadolinium-based contrast agent indicated for intravenous use with magnetic resonance imaging (MRI) in brain (intracranial), spine and associated tissues in adult and pediatric patients (including term neonates) to detect and visualize areas with disruption of the blood brain barrier (BBB) and/or abnormal vascularity.

CONTRAINDICATIONS

History of clinically important hypersensitivity reactions to DOTAREM.

WARNINGS AND PRECAUTIONS

- Anaphylactic and anaphylactoid reactions have been reported with DOTAREM, involving cardiovascular, respiratory, and/or cutaneous manifestations. Some patients experienced circulatory collapse and died. In most cases, initial symptoms occurred within minutes of DOTAREM administration and resolved with prompt emergency treatment.
- Before DOTAREM administration, assess all patients for any history of a reaction to contrast media, bronchial asthma and/or allergic disorders. These patients may have an increased risk for a hypersensitivity reaction to DOTAREM.
- Administer DOTAREM only in situations where trained personnel and therapies are promptly available for the treatment of hypersensitivity reactions, including personnel trained in resuscitation.
- In patients with chronically reduced renal function, acute kidney injury requiring dialysis has occurred with the use of GBCAs. The risk of acute kidney injury may increase with increasing dose of the contrast agent; administer the lowest dose necessary for adequate imaging.
- Ensure catheter and venous patency before the injection of DOTAREM. Extravasation into tissues during DOTAREM administration may result in tissue irritation.

ADVERSE REACTIONS

- The most common adverse reactions associated with DOTAREM in clinical trials were nausea, headache, injection site pain, injection site coldness and rash.
- Serious adverse reactions in the Postmarketing experience have been reported with DOTAREM. These serious adverse reactions include but are not limited to: arrhythmia, cardiac arrest, respiratory arrest, pharyngeal edema, laryngospasm, bronchospasm, coma and convulsion.

USE IN SPECIFIC POPULATIONS

- **Pregnancy:** There are no available data with DOTAREM use in pregnant women to inform a drug-associated risk of adverse developmental outcomes. While it is unknown if gadoterate crosses the placenta, other GBCAs have been shown to cross the human placenta and result in fetal exposure. Advise pregnant women of the potential risk of fetal exposure to GBCAs.
- **Lactation:** There are no data on the presence of gadoterate in human milk, the effects on the breastfed infant, or the effects on milk production. However, published lactation data on other GBCAs indicate that 0.01 to 0.04% of the maternal gadolinium dose is present in breast milk.
- **Pediatric Use:** The safety and efficacy of DOTAREM at a single dose of 0.1 mmol/kg has been established in pediatric patients from birth (term neonates ≥ 37 weeks gestational age) to 17 years of age based on clinical data. The safety of DOTAREM has not been established in preterm neonates. No cases of NSF associated with DOTAREM or any other GBCA have been identified in pediatric patients age 6 years and younger.

You are encouraged to report negative side effects of prescription drugs to the FDA. Visit www.fda.gov/medwatch or call 1-800-FDA-1088.

References: 1. Port M et al. Efficiency, thermodynamic and kinetic stability of marketed gadolinium chelates and their possible clinical consequences: a critical review. *Biometals*. 2008;21:469-90. 2. Frenzel T et al. Stability of gadolinium-based magnetic resonance imaging contrast agents in human serum at 37°C. *Invest Radiol*. 2008;43:817-828. 3. Dotarem [package insert]. Princeton, NJ: Guerbet LLC; Aug 2017. 4. Radbruch A et al. Gadolinium retention in the dentate nucleus and globus pallidus is dependent on the class of contrast agent. *Radiology*. 2015 Jun;275(3):783-91. 5. Radbruch A et al. Intraindividual analysis of signal intensity changes in the dentate nucleus after consecutive serial applications of linear and macrocyclic gadolinium-based contrast agents. *Invest Radiol*. 2016 Nov;51(11):683-690. 6. Eisele P et al. Lack of increased signal intensity in the dentate nucleus after repeated administration of a macrocyclic contrast agent in multiple sclerosis: An observational study. *Medicine (Baltimore)*. 2016 Sep;95(39):e4624. 7. Radbruch A et al. Pediatric brain: no increased signal intensity in the dentate nucleus on unenhanced T1-weighted MR images after consecutive exposure to a macrocyclic gadolinium-based contrast agent. *Radiology*. 2017 Mar 8;162980. [Epub ahead of print]. 8. Tibussek D et al. Gadolinium Brain Deposition after Macrocyclic Gadolinium Administration: A Pediatric Case-Control Study. *Radiology*. 2017 161151 [Epub ahead of print]. 9. Mithal LB, Patel PS, Mithal D, Palac HL, Rozenfeld MN. Use of gadolinium-based magnetic resonance imaging contrast agents and awareness of brain gadolinium deposition among pediatric providers in North America. *Pediatr Radiol*. 2017 Mar 10. doi: 10.1007/s00247-017-3810-4. [Epub ahead of print]. 10. Data on file, Guerbet LLC.



Not for sale within the territory of the United States

VISIBLE ADAPTABILITY

DERIVO® Embolisation Device

Advanced flow diverter with outstanding visibility and balanced mechanical properties for excellent clinical performance in the treatment of intracranial aneurysms.

SMOOTH. RELIABLE. PRECISE.

www.acandis.com

acandis®

ENGINEERING STROKE SOLUTIONS

Official Journal:

American Society of Neuroradiology
American Society of Functional Neuroradiology
American Society of Head and Neck Radiology
American Society of Pediatric Neuroradiology
American Society of Spine Radiology

EDITOR-IN-CHIEF

Jeffrey S. Ross, MD

*Professor of Radiology, Department of Radiology,
Mayo Clinic College of Medicine, Phoenix, AZ*

SENIOR EDITORS

Harry J. Cloft, MD, PhD

*Professor of Radiology and Neurosurgery,
Department of Radiology, Mayo Clinic College of
Medicine, Rochester, MN*

Thierry A.G.M. Huisman, MD

*Professor of Radiology, Pediatrics, Neurology, and
Neurosurgery, Chairman, Department of Imaging
and Imaging Science, Johns Hopkins Bayview,
Director, Pediatric Radiology and Pediatric
Neuroradiology, Johns Hopkins Hospital,
Baltimore, MD*

Yvonne W. Lui, MD

*Associate Professor of Radiology,
Chief of Neuroradiology,
New York University School of Medicine,
New York, NY*

C.D. Phillips, MD, FACR

*Professor of Radiology, Weill Cornell Medical
College, Director of Head and Neck Imaging,
New York-Presbyterian Hospital, New York, NY*

Pamela W. Schaefer, MD

*Clinical Director of MRI and Associate Director of
Neuroradiology, Massachusetts General Hospital,
Boston, Massachusetts, Associate Professor,
Radiology, Harvard Medical School, Cambridge, MA*

Charles M. Strother, MD

*Professor of Radiology, Emeritus, University of
Wisconsin, Madison, WI*

STATISTICAL SENIOR EDITOR

Bryan A. Comstock, MS

*Senior Biostatistician,
Department of Biostatistics,
University of Washington, Seattle, WA*

EDITORIAL BOARD

Ashley H. Aiken, *Atlanta, GA*
Lea M. Alhilali, *Phoenix, AZ*
John D. Barr, *Dallas, TX*
Ari Blitz, *Baltimore, MD*
Barton F. Branstetter IV, *Pittsburgh, PA*
Jonathan L. Brisman, *Lake Success, NY*
Julie Bykowski, *San Diego, CA*
Keith Cauley, *Danville, PA*
Asim F. Choudhri, *Memphis, TN*
Alessandro Cianfoni, *Lugano, Switzerland*
J. Matthew Debnam, *Houston, TX*
Seena Dehkharghani, *New York, NY*
Colin Derdeyn, *Iowa City, IA*
Rahul S. Desikan, *San Francisco, CA*
Yonghong Ding, *Rochester, MN*
Clifford J. Eskey, *Hanover, NH*
Saeed Fakhran, *Phoenix, AZ*
Massimo Filippi, *Milan, Italy*
Allan J. Fox, *Toronto, Ontario, Canada*
Wende N. Gibbs, *Los Angeles, CA*
Christine M. Glastonbury, *San Francisco, CA*
John L. Go, *Los Angeles, CA*
Allison Grayev, *Madison, WI*
Brent Griffith, *Detroit, MI*
Wan-Yuo Guo, *Taipei, Taiwan*
Ajay Gupta, *New York, NY*
Rakesh K. Gupta, *Lucknow, India*
Lotfi Hachein-Bey, *Sacramento, CA*
Christopher P. Hess, *San Francisco, CA*
Andrei Holodny, *New York, NY*
Benjamin Huang, *Chapel Hill, NC*
George J. Hunter, *Boston, MA*
Mahesh V. Jayaraman, *Providence, RI*
Valerie Jewells, *Chapel Hill, NC*
Christof Karmonik, *Houston, TX*
Timothy J. Kaufmann, *Rochester, MN*
Hillary R. Kelly, *Boston, MA*
Toshibumi Kinoshita, *Akita, Japan*
Kenneth F. Layton, *Dallas, TX*
Michael M. Lell, *Nürnberg, Germany*
Michael Lev, *Boston, MA*
Karl-Olof Lovblad, *Geneva, Switzerland*
Franklin A. Marden, *Chicago, IL*
M. Gisele Matheus, *Charleston, SC*
Joseph C. McGowan, *Merion Station, PA*
Stephan Meckel, *Freiburg, Germany*
Christopher J. Moran, *St. Louis, MO*
Takahisa Mori, *Kamakura City, Japan*
Suresh Mukherji, *Ann Arbor, MI*
Amanda Murphy, *Toronto, Ontario, Canada*
Alexander J. Nemeth, *Chicago, IL*
Sasan Partovi, *Cleveland, OH*
Laurent Pierot, *Reims, France*
Jay J. Pillai, *Baltimore, MD*

Whitney B. Pope, *Los Angeles, CA*
M. Judith Donovan Post, *Miami, FL*
Tina Young Poussaint, *Boston, MA*
Joana Ramalho, *Lisbon, Portugal*
Otto Rapalino, *Boston, MA*
Álex Rovira-Cañellas, *Barcelona, Spain*
Paul M. Ruggieri, *Cleveland, OH*
Zoran Rumboldt, *Rovinj-Rovigno, Croatia*
Amit M. Saindane, *Atlanta, GA*
Erin Simon Schwartz, *Philadelphia, PA*
Lubdhra M. Shah, *Salt Lake City, UT*
Aseem Sharma, *St. Louis, MO*
J. Keith Smith, *Chapel Hill, NC*
Maria Vittoria Spampinato, *Charleston, SC*
Gordon K. Sze, *New Haven, CT*
Krishnamoorthy Thamburaj, *Hershey, PA*
Cheng Hong Toh, *Taipei, Taiwan*
Thomas A. Tomsick, *Cincinnati, OH*
Aquila S. Turk, *Charleston, SC*
Willem Jan van Rooij, *Tilburg, Netherlands*
Arastoo Vossough, *Philadelphia, PA*
Elysa Widjaja, *Toronto, Ontario, Canada*
Max Wintermark, *Stanford, CA*
Ronald L. Wolf, *Philadelphia, PA*
Kei Yamada, *Kyoto, Japan*
Carlos Zamora, *Chapel Hill, NC*

EDITORIAL FELLOW

Vahe Zohrabian, *New Haven, CT*

SPECIAL CONSULTANTS TO THE EDITOR

AJNR Blog Editor

Neil Lall, *Denver, CO*

Case of the Month Editor

Nicholas Stence, *Aurora, CO*

Case of the Week Editors

Juan Pablo Cruz, *Santiago, Chile*

Sapna Rawal, *Toronto, Ontario, Canada*

Classic Case Editor

Sandy Cheng-Yu Chen, *Taipei, Taiwan*

Facebook Editor

Peter Yi Shen, *Sacramento, CA*

Health Care and Socioeconomics Editor

Pina C. Sanelli, *New York, NY*

Physics Editor

Greg Zaharchuk, *Stanford, CA*

Podcast Editor

Wende N. Gibbs, *Los Angeles, CA*

Twitter Editor

Jennifer McCarty, *Atlanta, Georgia*

YOUNG PROFESSIONALS ADVISORY COMMITTEE

Asim K. Bag, *Birmingham, AL*
Anna E. Nidecker, *Sacramento, CA*
Peter Yi Shen, *Sacramento, CA*

Founding Editor
Juan M. Taveras

Editors Emeriti
**Mauricio Castillo, Robert I. Grossman,
Michael S. Huckman, Robert M. Quencer**

Managing Editor
Karen Halm

Assistant Managing Editor
Laura Wilhelm

Digital Publications and Social Media Coordinator
Kylie Mason

Executive Director, ASNR

Mary Beth Hepp

Director of Communications, ASNR

Angelo Artemakis

AJNR

AMERICAN JOURNAL OF NEURORADIOLOGY

NOVEMBER 2017
VOLUME 38
NUMBER 11
WWW.AJNR.ORG

Publication Preview at www.ajnr.org features articles released in advance of print. Visit www.ajnrblog.org to comment on AJNR content and chat with colleagues and AJNR's News Digest at <http://ajnrdigest.org> to read the stories behind the latest research in neuroimaging.

2033 **PERSPECTIVES** *J.H. Rees*

REVIEW ARTICLE

🔑 2034 **The Management and Imaging of Vestibular Schwannomas** *E.P. Lin, et al.* **HEAD & NECK**

GENERAL CONTENTS

★ 🔑 2044 **The Brain Thermal Response as a Potential Neuroimaging Biomarker of Cerebrovascular Impairment** *C.C. Fleischer, et al.* **ADULT BRAIN**

🔑 📄 2052 **Added Value of Arterial Spin-Labeling MR Imaging for the Differentiation of Cerebellar Hemangioblastoma from Metastasis** *K.M. Kang, et al.* **ADULT BRAIN**

2059 **Detection of Volume-Changing Metastatic Brain Tumors on Longitudinal MRI Using a Semiautomated Algorithm Based on the Jacobian Operator Field** *O. Shearkhani, et al.* **ADULT BRAIN**

📄 2067 **Pituitary Macroadenoma and Visual Impairment: Postoperative Outcome Prediction with Contrast-Enhanced FIESTA** *S. Hisanaga, et al.* **ADULT BRAIN**

📄 2073 **Topographic Diagnosis of Craniopharyngiomas: The Accuracy of MRI Findings Observed on Conventional T1 and T2 Images** *R. Prieto, et al.* **ADULT BRAIN**

📄 📄 2081 **Arterial Spin-Labeling Perfusion MR Imaging Demonstrates Regional CBF Decrease in Idiopathic Normal Pressure Hydrocephalus** *J. Virhammar, et al.* **ADULT BRAIN**

🔑 2089 **Prevalence of Intracranial Aneurysms in Patients with Aortic Dissection** *W.S. Jung, et al.* **ADULT BRAIN**

🔑 📄 2094 **Reaction Time Is Negatively Associated with Corpus Callosum Area in the Early Stages of CADASIL** *S. Delorme, et al.* **ADULT BRAIN**

2100 **MR Imaging Features of the Cerebellum in Adult-Onset Neuronal Intranuclear Inclusion Disease: 8 Cases** *A. Sugiyama, et al.* **ADULT BRAIN**

🔑 2105 **Differences in Morphologic and Hemodynamic Characteristics for "PHASES-Based" Intracranial Aneurysm Locations** *N. Varble, et al.* **INTERVENTIONAL**

★ 🔑 📄 2111 **Angioarchitectures and Hemodynamic Characteristics of Posterior Communicating Artery Aneurysms and Their Association with Rupture Status** *B.J. Chung, et al.* **INTERVENTIONAL**

📄 📄 2119 **Patient Outcomes and Cerebral Infarction after Ruptured Anterior Communicating Artery Aneurysm Treatment** *J.J. Heit, et al.* **INTERVENTIONAL**

AJNR (Am J Neuroradiol ISSN 0195-6108) is a journal published monthly, owned and published by the American Society of Neuroradiology (ASNR), 800 Enterprise Drive, Suite 205, Oak Brook, IL 60523. Annual dues for the ASNR include \$170.00 for journal subscription. The journal is printed by Cadmus Journal Services, 5457 Twin Knolls Road, Suite 200, Columbia, MD 21045; Periodicals postage paid at Oak Brook, IL and additional mailing offices. Printed in the U.S.A. POSTMASTER: Please send address changes to American Journal of Neuroradiology, P.O. Box 3000, Denville, NJ 07834, U.S.A. Subscription rates: nonmember \$400 (\$470 foreign) print and online, \$320 online only; institutions \$460 (\$530 foreign) print and basic online, \$915 (\$980 foreign) print and extended online, \$380 online only (basic), extended online \$825; single copies are \$35 each (\$40 foreign). Indexed by PubMed/Medline, BIOSIS Previews, Current Contents (Clinical Medicine and Life Sciences), EMBASE, Google Scholar, HighWire Press, Q-Sensei, RefSeek, Science Citation Index, and SCI Expanded. Copyright © American Society of Neuroradiology.

-  **2126** Comparison of Clinical Outcomes of Intracranial Aneurysms: Procedural Rupture versus Spontaneous Rupture *H.H. Choi, et al.* **INTERVENTIONAL**
-  **2131** Flow Diversion with Low-Profile Braided Stents for the Treatment of Very Small or Uncoilable Intracranial Aneurysms at or Distal to the Circle of Willis *K. Aydin, et al.* **INTERVENTIONAL**
-   **2138** Anterior Circulation Acute Ischemic Stroke Associated with Atherosclerotic Lesions of the Cervical ICA: A Nosologic Entity Apart *O.F. Eker, et al.* **INTERVENTIONAL**
ADULT BRAIN
-     **2146** Real-Time Motor Cortex Mapping for the Safe Resection of Glioma: An Intraoperative Resting-State fMRI Study *T.-m. Qiu, et al.* **FUNCTIONAL**
-     **2153** Apparent Diffusion Coefficient Histograms of Human Papillomavirus–Positive and Human Papillomavirus–Negative Head and Neck Squamous Cell Carcinoma: Assessment of Tumor Heterogeneity and Comparison with Histopathology *T. de Perrot, et al.* **HEAD & NECK**
- 2161** The Diagnostic Accuracy of Contrast-Enhanced CT of the Neck for the Investigation of Sialolithiasis *Y.M. Purcell, et al.* **HEAD & NECK**
- 2167** Prevalence of Internal Auditory Canal Diverticulum and Its Association with Hearing Loss and Otosclerosis *K.J. Pippin, et al.* **HEAD & NECK**
-   **2172** Clinical and Imaging Characteristics of Arteriopathy Subtypes in Children with Arterial Ischemic Stroke: Results of the VIPS Study *M. Wintermark, et al.* **PEDIATRICS**
-  **2180** Brain Temperature Is Increased During the First Days of Life in Asphyxiated Newborns: Developing Brain Injury Despite Hypothermia Treatment *Z.P. Owji, et al.* **PEDIATRICS**
- 2187** Does the Addition of a “Black Bone” Sequence to a Fast Multisequence Trauma MR Protocol Allow MRI to Replace CT after Traumatic Brain Injury in Children? *M.H.G. Dremmen, et al.* **PEDIATRICS**
-   **2193** Volume of Structures in the Fetal Brain Measured with a New Semiautomated Method *R. Ber, et al.* **PEDIATRICS**
- 2199** Transient Focal Neurologic Symptoms Correspond to Regional Cerebral Hypoperfusion by MRI: A Stroke Mimic in Children *L.L. Lehman, et al.* **PEDIATRICS**
- 2203** MR Neurography of Greater Occipital Nerve Neuropathy: Initial Experience in Patients with Migraine *L. Hwang, et al.* **PERIPHERAL NERVOUS SYSTEM**
-   **2210** T1-Weighted Dynamic Contrast-Enhanced MR Perfusion Imaging Characterizes Tumor Response to Radiation Therapy in Chordoma *P. Santos, et al.* **SPINE**
- 2217** **35 YEARS AGO IN AJNR**

ONLINE FEATURES

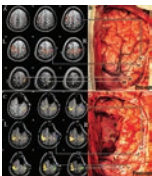
LETTERS

- E88** Emergency Department MR Imaging Scanner: Supportive Data *D.M. Yousem, et al.*
- E89** *Reply* *M. Buller, et al.*
- E90** Cerebral Microbleeds: A Call for Standardized Advanced Neuroimaging *A. Rauscher, et al.*
- E92** Radiomics Approach Fails to Outperform Null Classifier on Test Data *J.B. Colby*
- E94** *Reply* *P. Tiwari, et al.*

- E95** **Imaging Findings of Benign Enhancing Foramen Magnum Lesions**
M.U. Antonucci, et al.
- E97** **Selective Poststent Balloon Angioplasty for Carotid Stenting**
D.M. Pelz, et al.
- E98** **Reply** *O. Petr, et al.*
- E99** **Open Globe Injury: Ultrasound First!** *A. Lecler, et al.*
- E101** **Reply** *U.K. Bodanapally, et al.*

BOOK REVIEWS *R.M. Quencer, Section Editor*

Please visit www.ajnrblog.org to read and comment on Book Reviews.



Validation of intraoperative resting state-fMRI with direct cortical stimulation (DCS). *A.* Preoperative resting state-fMRI shows the motor cortex located posterior to the tumor. *B.* DCS locates positive sites in the hand area (H) and positive sites in the mouth area (M). Green and blue dots in *A* represent positive sites in the hand and mouth areas, respectively (located by intraoperative DCS). *C.* Intraoperative resting state-fMRI shows the motor cortex behind the tumor cavity. *D.* Motor cortex is intact after tumor resection.



Indicates Editor's Choices selection



Indicates Fellows' Journal Club selection



Indicates open access to non-subscribers at www.ajnr.org



Indicates article with supplemental on-line table



Indicates article with supplemental on-line photo



Indicates article with supplemental on-line video



Evidence-Based Medicine Level 1



Evidence-Based Medicine Level 2



Title: Monument Valley Utah, viewed from Hunts Mesa. As the sun sets, the shadows of the monuments lengthen, creating a beautiful otherworldly perspective. Over 200 million years ago, this area and most of the American West was covered by a large shallow sea. These monuments were created by water currents within that sea. The Rocky Mountains thrust upward, and the sea receded into swamp and eventually became desert. Fossilized dinosaur footprints are found on the tops of the monuments. This is Navajo land and Native Americans, Navajo and before them Anasazi, have lived here for thousands of years.

On October 16, 1984, a USAF B-52 on a low altitude training run between Fairchild AFB in Spokane, Washington and Lovelace AFB in Albuquerque, New Mexico crashed into Hunts Mesa very near where this photo was taken more than 20 years later. I was EMS Director for this area and though not on duty, I was called in. Assisted by a local Search and Rescue 4-wheel drive team, my EMTs and I made our way to the crash site in a heavy snow storm and rescued 5 of 7 airmen who were subsequently flown out by helicopter. The strength and endurance displayed by the injured airmen that night cannot be underestimated and we were very glad when all 5 returned a year later for a more peaceful visit to Hunts Mesa.

John H. Rees, MD, Assistant Professor of Radiology, University of Florida, Shands Hospital, Gainesville, Florida

The Management and Imaging of Vestibular Schwannomas

 E.P. Lin and  B.T. Crane



ABSTRACT

SUMMARY: Vestibular schwannomas are the most common cerebellopontine angle tumor. During the past century, the management goals of vestibular schwannomas have shifted from total resection to functional preservation. Current treatment options include surgical resection, stereotactic radiosurgery, and observation. Imaging has become a crucial part of the initial screening, evaluation, and follow-up assessment of vestibular schwannomas. Recognizing and understanding the management objectives, various treatment modalities, expected posttreatment findings, and complications allows the radiologist to play an essential role in a multidisciplinary team by providing key findings relevant to treatment planning and outcome assessment. The authors provide a comprehensive discussion of the surgical management, role of radiation therapy and observation, imaging differential, and pre- and posttreatment imaging findings of vestibular schwannomas.

ABBREVIATIONS: AAO-HNS = American Academy of Otolaryngology-Head and Neck Surgery; CN = cranial nerve; CPA = cerebellopontine angle; 3D SS-GRE = volumetrically acquired steady-state gradient-echo; IAC = internal auditory canal; MF = middle fossa craniotomy; PF = posterior fossa; RS = retrosigmoid craniotomy; SRS = stereotactic radiosurgery; TL = translabyrinthine craniotomy; VS = vestibular schwannoma

Vestibular schwannomas (VSs) are benign neoplasms of the nerve sheath and account for 6%–8% of all intracranial tumors and 80% of cerebellopontine angle (CPA) tumors.¹ VSs may remain within the internal auditory canal (IAC) or extend into the CPA. Symptoms are typically related to compression of adjacent cranial nerves (CNs), brain stem, or posterior fossa (PF) structures.

Imaging plays a central role in the screening and initial and follow-up assessment of VSs. Imaging can often differentiate VS from other entities such as facial nerve schwannoma, meningioma, epidermoid cyst, arachnoid cyst, aneurysm, and metastasis.² MR imaging is the preferred technique and can provide exquisite tumor characterization, surgical planning, and posttherapeutic evaluation.^{3–5} Contrast-enhanced CT of the temporal bones can serve as an alternative if the patient cannot undergo MR imaging.

The goals of VS management have shifted from total resection to functional preservation, particularly when the entire tumor cannot be safely resected with respect to cranial nerve preservation.^{6,7} Studies have revealed suboptimal postsurgical facial nerve function in gross total resection of large VSs.^{8,9} Depending on many factors, including patient age, tumor size and growth, and symptomatology, patients can choose surgery, radiation, or conservative management. Patients with neurofibromatosis type 2, which is characterized by bilateral VSs, other schwannomas, meningiomas, ependymomas, and ocular abnormalities, are managed differently than those with sporadic unilateral VSs¹⁰ and will not be further discussed due to the scope of this topic.

Advances in surgical management of VS during the past century have defined lateral skull base approaches that are now applied in the management of other PF and skull base pathologies. Each approach offers different surgical exposures, benefits, and disadvantages. Stereotactic radiosurgery (SRS) is an acceptable option, with similar rates of tumor control and a low risk for permanent facial nerve palsy. Observation is a reasonable option for smaller tumors, older patients, and those with major comorbidities.


This article will review the treatment objectives, surgical approaches, and expected posttreatment findings and complications of VS management. Knowledge of these advances enhances the radiologist's ability to participate in a multidisciplinary team

From the Departments of Imaging Sciences (E.P.L.) and Otolaryngology (B.T.C.), University of Rochester Medical Center, Rochester, New York.

During preparation of this article, B.T.C. was supported by National Institute on Deafness and Other Communication Disorders grant R01 DC013580.

Paper previously presented in part at: Annual Midwest Head and Neck Imaging Meeting, March 5–6, 2016; Madison, Wisconsin, entitled “The Lateral Skull Base: Historical, Surgical and Radiologic Perspectives.”

Please address correspondence to Edward P. Lin, MD, University of Rochester Medical Center, Department of Imaging Sciences, 601 Elmwood Ave, Box 648, Rochester, NY 14642; e-mail: Edward_Lin@URMC.rochester.edu

 Indicates open access to non-subscribers at www.ajnr.org

<http://dx.doi.org/10.3174/ajnr.A5213>

by providing key information relevant to the treatment planning and outcome.

Background

VS, often referred to as “acoustic neuroma,” most commonly originates from the vestibular division of the vestibulocochlear nerve sheath, often at the transition from central to peripheral myelin near the vestibular ganglion at the IAC fundus.

Inactivation of the neurofibromin 2 gene has been implicated in sporadic and neurofibromatosis type 2 VS.¹¹ This gene is located on chromosome 22 and produces schwannomin (merlin), a tumor-suppressor cell membrane-related protein. Perineural elements of Schwann cells, with areas of dense (Antoni A) and sparse (Antoni B) cellularity, are found histopathologically. Immunohistochemical staining is typically positive for S-100 protein.

VS presents at a median age of 50 years and is unilateral in >90% of patients, with an equal incidence on the left and right. Symptomatology is often related to cranial neuropathies. Patients more often present with chronic asymmetric sensorineural hearing loss than tinnitus or unsteadiness. True vertigo, sudden hearing loss, facial pain, numbness, and weakness are uncommon due to slow tumor growth. Sensorineural hearing loss is confirmed by audiometry and brain stem–evoked response audiometry, with findings that are abnormal in >90%–95% of patients with VS.¹²

Historical Perspective

Charles McBurney performed the first suboccipital plate removal in 1891,¹³ though the patient died soon after. A few years later, Sir Charles Ballance in England was the first to successfully remove a VS via a suboccipital plate and blunt dissection of a CPA mass.¹⁴ Surgical outcome, in general, remained poor in the late 1800s, with a surgical mortality rate of 80% and high postoperative morbidity.¹⁵

By observing the radiographic properties of bowel gas, Walter Dandy injected air into the subarachnoid spaces, creating the first pneumoencephalographic images in the early 1900s.¹⁶ Pneumoencephalography allowed the localization of intracranial masses by observing the mass effect on the ventricles and the direction of the midline shift.¹⁷

Advances in neurosurgery in the early 1900s led to a decrease in surgical mortality to 20%. Harvey Cushing promoted a bilateral suboccipital approach and removal of the tumor core while leaving the tumor capsule in place to improve CN preservation.¹⁸

In 1961, William House introduced the operative microscope in temporal bone surgeries, allowing exquisite visualization and improved preservation of the facial nerve.¹⁹ William House fostered collaboration with the neurosurgeon William Hitselberger, establishing a multidisciplinary approach to VS resections. William House re-introduced the translabyrinthine approach as an option for patients with unserviceable hearing.²⁰ In 1979, Tomas Delgado performed the first intraoperative CN monitoring, which improved CN preservation.²¹

During the same period, Lars Leksell in Sweden invented the gamma knife in 1968 and performed the first SRS on a VS in 1969.^{22,23} SRS was later confirmed as an effective alternative to surgery in the treatment of VS.²⁴

Radiographically, positive-contrast cisternography in the 1960s improved delineation of PF structures.²⁵ Polytome-pan-topaque allowed depiction of even smaller intracanalicular VSs.²⁶ The advent of cross-sectional imaging in the 1970s now provides noninvasive means of detecting and evaluating small VSs.

Natural History of VS

More than half of all VSs grow at an average of 2–4 mm/year, whereas <10% regress.²⁷ One study revealed that extrameatal tumors (28.9%) were more likely to grow compared with intrameatal tumors (17%) and a larger percentage of tumors grew early on after detection.²⁸ A VS of >2 cm is more likely to grow compared with a smaller VS.^{29,30} Growth rates of >2 mm/year are associated with decreased rates of hearing preservation compared with slower growth rates.³¹

Surgical Management of VS

Surgical objectives have shifted from total resection to long-term functional preservation.^{6,7} Subtotal resection followed by observation or SRS, particularly for a large VS, can achieve long-term tumor control with improved CN preservation.^{6,7,32} In general, a small-to-medium VS of <3 cm is managed differently from a large VS because surgery is often favored over SRS for a large VS. While some investigators have experience in successfully treating large VSs with SRS,³³ others believe that SRS may risk compressive ischemia of CN VII and brain stem compression in the treatment of a large VS.^{34,35} The optimal treatment of a VS, particularly a small-to-medium one, remains controversial, and treatment technique preference will vary from center to center.

Gross total resection is offered to younger patients with persistent dizziness, patients with small anatomically favorable tumors and good hearing, cystic tumors, and larger tumors with symptoms related to mass effect.³⁵ Surgery, as opposed to SRS, provides a definitive histopathologic diagnosis. Due to the post-radiation effects on tissue, SRS following surgical resection is more favorable than surgical resection following SRS. Surgery, however, is associated with a greater risk of permanent facial nerve palsy compared with SRS.³⁵ Other risks of surgical resection include iatrogenic hearing loss, CSF leak, meningitis, headache, and anesthesia-related complications. Following gross total resection, the 5-year recurrence rate of VS has been reported as up to 10%.⁷ The 10-year tumor control rates for gross total and subtotal resection are 78% and 82%, respectively.⁷

Surgical Approaches

VS may be approached by a translabyrinthine (TL), retrosigmoid (RS), or middle fossa (MF) craniotomy. The indications, advantages, and disadvantages of each are summarized in Table 1.

Translabyrinthine Craniotomy

The TL is a posterior approach through the mastoid temporal bone, anterior to the sigmoid sinus (Fig 1). Following a simple mastoidectomy, the vertical facial nerve canal is skeletonized and a labyrinthectomy is performed, allowing access to the IAC behind the vestibule (Fig 1).³⁶ Access to the CPA can be gained by removing bone posterior to the porus acusticus. While one performs facial nerve monitoring, the tumor is debulked and micro-

Table 1: Indications, benefits, and disadvantages of lateral skull base approaches for VS resection

	Translabyrinthine	Retrosigmoid	Middle Fossa
Indications	Unserviceable hearing; any IAC or CPA VS	VS with large CPA component; medial IAC VS	Small lateral IAC VS (<0.5 cm); small medial IAC VS with <1 cm CPA component
Advantages	Minimal brain retraction	Panoramic CPA exposure; better facial nerve and hearing preservation for medial VS	Better exposure, lateral IAC
Disadvantages	Complete hearing loss; difficult approach for CPA VS ventral to porus acusticus; risk for facial nerve injury	Limited access to lateral IAC; potential for cerebellar and brain stem injury	Limited PF access; temporal lobe retraction; risk for facial nerve injury

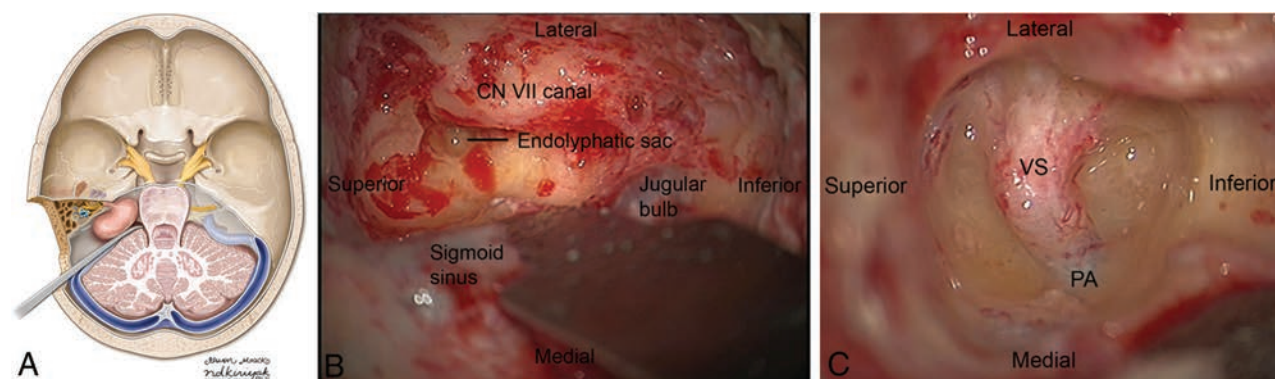


FIG 1. Axial illustration (A) of a translabyrinthine craniotomy demonstrates exposure of the IAC and CPA, and it may be performed with or without cerebellar retraction. Intraoperative images just before (B) and following (C) the labyrinthectomy demonstrate exposure to the intracanalicular vestibular schwannoma. PA indicates porus acusticus. A is reproduced with permission from the University of Rochester.

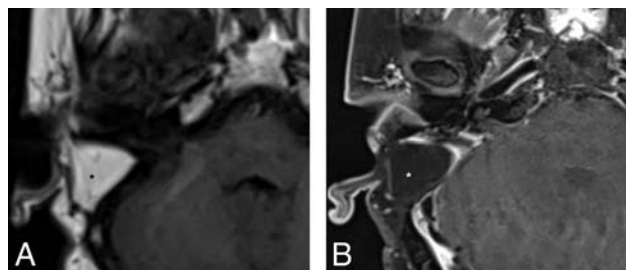


FIG 2. Precontrast axial T1WI (A) and postcontrast axial T1WI with fat-suppression (B) demonstrate typical postoperative findings following a translabyrinthine craniotomy, with abdominal fat packing within the mastoidectomy defect (*asterisk*). Linear enhancement along the mastoidectomy bed reflects postsurgical changes without evidence of recurrent tumor within the IAC.

dissected. The craniotomy is closed by placing the temporalis fascia at the aditus ad antrum and abdominal fat packing within the mastoidectomy defect. Fat is preferred to muscle because fat is easily obtainable and associated with less morbidity. The fat signal can be advantageously suppressed on follow-up contrast-enhanced MR imaging (Fig 2).

The TL allows adequate exposure of the IAC and PF with minimal brain retraction. The RS approach may be preferred if a large PF component is present. Due to the complete loss of hearing, TL is reserved only for patients with unserviceable hearing or poor hearing prognosis.

Retrosigmoid Craniotomy

RS is a posterior approach that allows panoramic visualization of the CPA (Fig 3). Following a suboccipital craniotomy posterior to

the sigmoid sinus, the cerebellum is retracted medially, exposing the CPA mass and neurovascular structures (Fig 3). The facial nerve is identified, and the CPA component is dissected. The intrameatal component can then be accessed and removed by drilling the posterior meatal lip (Fig 3). Tumor infiltration of the cochlear nerve, poor preoperative hearing, and larger tumor size decrease the likelihood of hearing preservation.³⁶

RS permits resection of large extrameatal and small medial intrameatal tumors while allowing hearing preservation.^{37–39} The RS approach to intrameatal VS can be limited by a high-riding jugular bulb or obstructed by the labyrinth.³⁹ Cerebellum retraction may lead to parenchymal injury. Early postoperative headaches following RS may be higher than in TL,⁴⁰ possibly secondary to subarachnoid bone dust dissemination or the use of a titanium plate.

Middle Fossa Approach

The MF is a lateral approach to the IAC (Fig 4). A temporal craniotomy is performed above the external auditory canal (Fig 4). The dura is elevated off the skull base, and the temporal lobe is retracted superiorly. Landmarks for this approach include the arcuate eminence and the greater superficial petrosal nerve. The IAC can then be accessed from above (Fig 4), and the tumor can be resected following microdissection of the facial and cochlear nerves. Bone wax is used to fill exposed mastoid air cells.

The MF is best for small lateral IAC tumors, particularly those that extend to the IAC fundus, when hearing preservation is a treatment objective. MF is not typically attempted on tumors with a >1-cm CPA component due to limited exposure to the PF,³⁶ though some surgeons have had success with larger tumors via

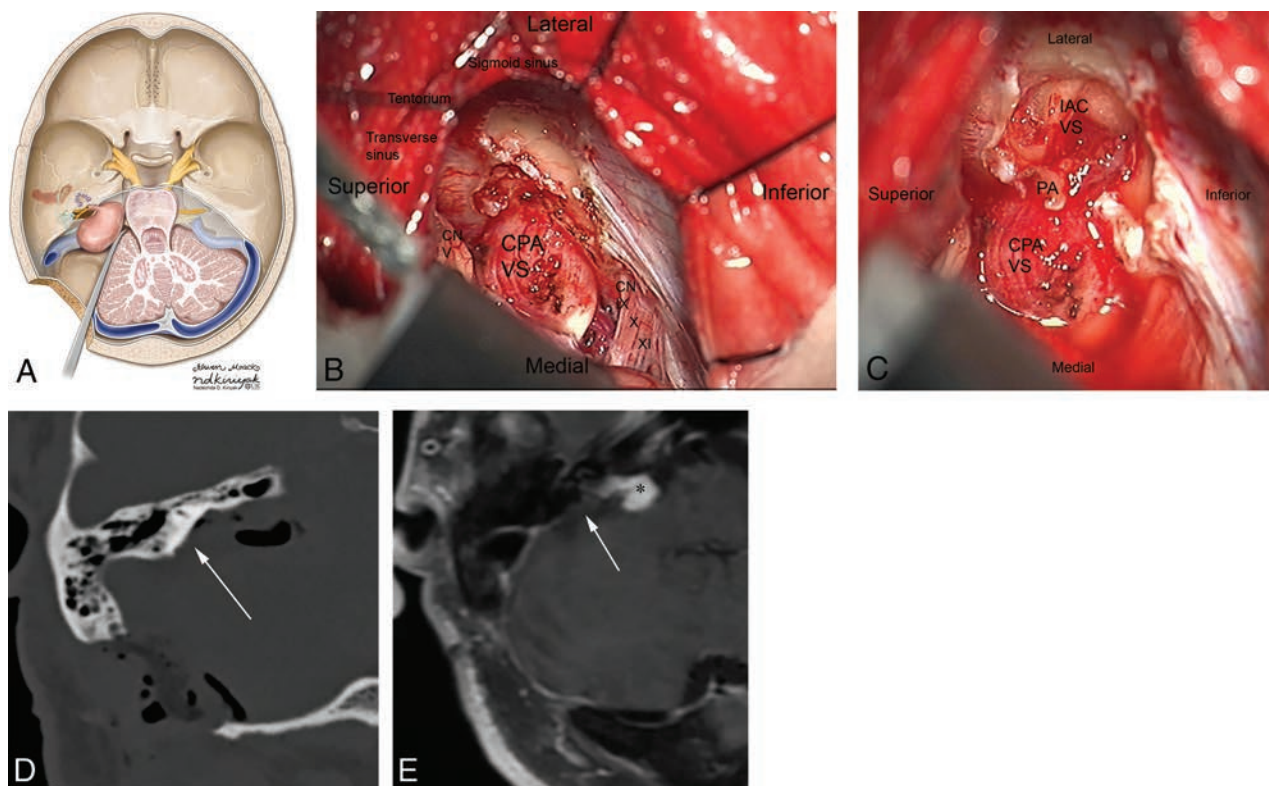


FIG 3. Axial illustration (A) of a retrosigmoid craniotomy reveals a typical exposure of the CPA and lateral IAC by drilling through the posterior meatal lip. Intraoperative image (B) reveals excellent exposure of the CPA VS and adjacent cranial nerves (CNs V, IX–XI). A second intraoperative image (C) following removal of the posterior face of the IAC wall exposes the intrameatal component of the VS (IAC VS). Immediate postoperative noncontrast axial CT (D) and a contrast-enhanced T1WI with fat-suppression (E) demonstrate a retrosigmoid craniectomy with a defect in the posterior meatal lip (arrow) and a residual extrameatal enhancing VS on the contrast-enhanced T1WI. A is reproduced with permission from the University of Rochester.

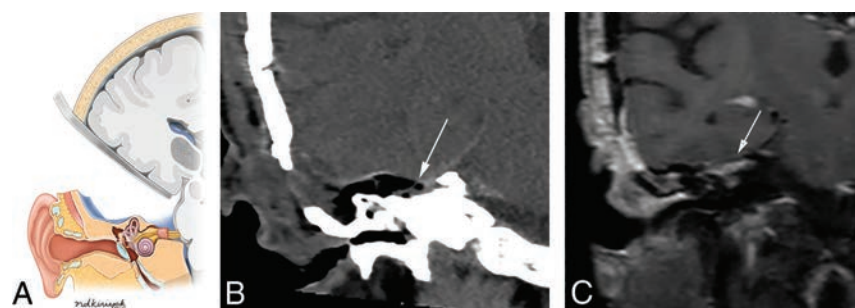


FIG 4. Coronal illustration (A) of a middle fossa craniotomy demonstrates retraction of the temporal lobe and drilling of the petrous apex over the superior semicircular canal to provide access to the IAC. Postoperative coronal reformation of noncontrast CT (B) and coronal T1WI with fat suppression (C) reveal a temporal craniotomy and absence of the IAC roof (arrows), through which the VS was accessed, and linear enhancement within the IAC, which reflects expected postsurgical changes without evidence of residual tumor. A is reproduced with permission from the University of Rochester.

this approach. Temporal lobe retraction is associated with a small risk of seizures, aphasia, and stroke. MF is optimal for a VS arising from the superior division, which displaces the facial nerve anteriorly.

Radiation Therapy

Radiation can be performed by using SRS, stereotactic radiation therapy, and conventional fractionated radiation therapy. SRS is the most commonly used technique and converges multiple beams onto a delineated volume by using cross-sectional imaging

to minimize injury to adjacent tissues. An initial SRS dosage of a 16- to 20-Gy marginal dose achieved a 98% tumor control rate but resulted in unacceptably high rates of early hearing loss (60%) and facial and trigeminal neuropathies (33%).^{24,41–43}

SRS dose reductions from 13–14 to 11–12 Gy in more recent years have resulted in >90% tumor control rates and <1% risk for permanent facial nerve palsies.^{44,45} Slightly lower doses of 12–13 Gy can be preferentially given to patients with serviceable hearing, and slightly higher doses of 13–14 Gy, to patients with poor hearing prognosis.⁴³

While hearing preservation rates of 60%–70% were initially reported, longer term follow-up studies of up to 10 years revealed progressive hearing deterioration in most patients. Serviceable hearing was preserved in only 23%–24% patients at 10 years.^{46–48} Older age, larger tumors, and poorer pretreatment hearing were found to be risk factors for progressive posttreatment hearing loss.^{46,48,49} Reducing the cochlear dose to improve hearing preservation continues to be controversial and has not been confirmed to reduce long-term hearing deterioration.⁵⁰

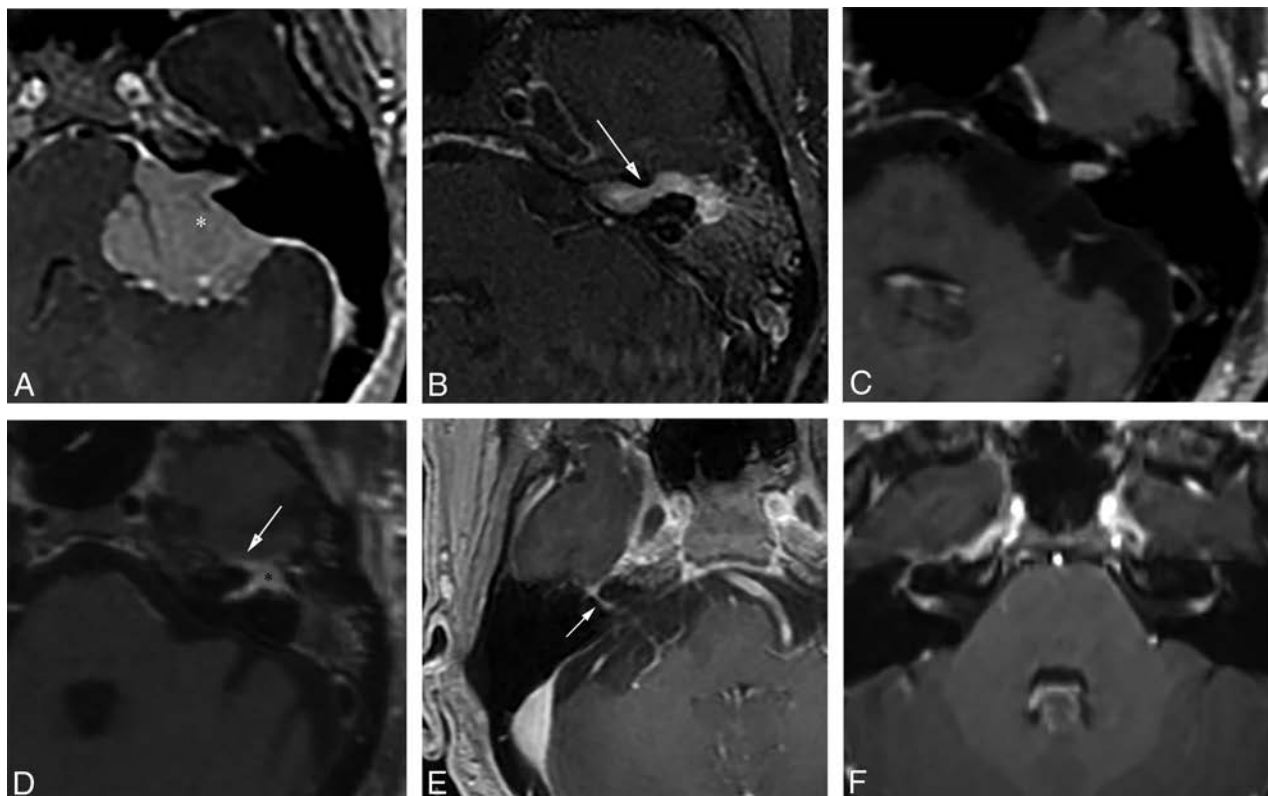


FIG 5. Examples of various enhancing IAC and CPA masses on contrast-enhanced T1WI with fat-suppression (*B–D*, and *F*) and 3D echo-spoiled gradient-echo images (*A* and *E*). *A*, A large CPA meningioma, located eccentric to the porus acusticus (the *asterisk* denotes the tumor midline), extends into the IAC without the associated bony expansion often seen with VS (see Fig 6). *B*, An enhancing facial nerve schwannoma within the IAC extends into the labyrinthine segment (*arrow*), which differentiates a facial nerve from a vestibular schwannoma, as well as into the anterior genu and tympanic segments. *C*, A small enhancing metastatic lesion within the IAC in a patient with non-small cell lung cancer extends into the IAC fundus, labyrinthine, anterior genu, and tympanic segments. *D*, Perineural spread along the intratemporal and intracranial segments of the facial nerve in a patient with squamous cell carcinoma of the periauricular skin (the *asterisk* indicates the anterior genu; *arrow*, the greater superficial petrosal nerve). *E*, An ill-defined tuft of enhancement within the IAC fundus extending into the labyrinthine segment (*arrow*) and anterior genu of the facial nerve in a patient with right Bell palsy. *F*, Bilateral ill-defined enhancement of the distal IAC bilaterally extending into the labyrinthine segment and anterior genu of the facial nerve canal in a patient with neurosarcoidosis.

Observation

Observation is offered to select patients who are typically followed with serial MR imaging every 6–12 months. Indications include patients older than 60 years of age with significant comorbidity, small tumor size, and absence of symptoms. Patients who are at risk for hearing loss from other causes or prefer observation may also be offered conservative management. Observation, however, is associated with progressive hearing loss, due to the slow growth of most of these tumors. Tumor growth of >2.5 mm/year is associated with higher rates of hearing deterioration compared with slower growing tumors.³¹ If hearing preservation remains a treatment objective, earlier intervention may lead to a better outcome.⁵¹

Imaging

Differential. VS is the most common extra-axial CPA mass (70%–80%), followed by meningiomas (10%–15%) and epidermoid cysts (5%).⁵² CPA meningiomas are dural-based enhancing masses that grow along the petrous ridge and can extend into the IAC. Large meningiomas are often located asymmetrically relative to the IAC (Fig 5). Meningiomas may contain intralesional calcifications, and a dural tail and can result in changes of the under-

lying bone, as well as peritumoral vasogenic edema if mass effect is present.

Other enhancing lesions of the IAC and CPA include neoplastic etiologies, such as leptomeningeal metastasis, lymphoma, meningeal melanocytoma, or malignant melanoma; facial nerve perineural spread; inflammatory processes, such as Bell palsy and neurosarcoidosis; and aneurysms (Fig 5). Identifying enhancement of the labyrinthine facial nerve can distinguish CN VII pathologies from a VS (Fig 5). Aneurysms demonstrate nodular enhancement but are contiguous with vascular structures and often exhibit flow voids, eccentric peripheral enhancement, and pulsation artifacts on MR imaging.

Because a VS can contain cystic components, the radiologist should also be aware of other cystic lesions of the CPA. The characteristic MR signal and enhancement patterns of these lesions, however, should not lead to any confusion among these entities. Epidermoid cysts are nonenhancing cysts of congenital ectodermal elements that encase or displace neurovascular structures and extend into the cerebellar fissures with ill-defined margins. Relative to CSF, these cysts demonstrate similar attenuation on CT, isointense-to-slightly hyperintense signal to CSF on T1WI and T2WI, and incomplete suppression on T2 FLAIR. The presence of

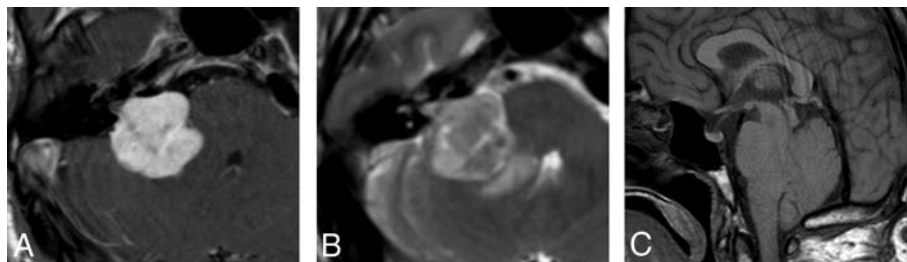


FIG 6. Contrast-enhanced axial T1WI (A), axial T2WI (B), and sagittal T1WI (C) reveal a large right CPA VS with asymmetric enlargement of the IAC, brain stem and cerebellar compression, peritumoral edema, and tonsillar herniation.

Table 2: A sample MR imaging protocol for the evaluation of VS^a

Sequence	FOV (cm)	Thickness and Spacing (mm)	TR (ms) (or Flip Angle)	TE (ms)	Matrix	Comments
Sag T1 FLAIR	24	5 × 1	2800	9	320 × 224	(TI 858 ms)
Ax DTI	26	3 × 0	8000	Min	128 × 128	
Sag 3D T2 FLAIR FS	27	1.4	7600	120	256 × 256	With Ax and Cor reformations
Ax T2 FLAIR	24	5 × 1	9500	125	352 × 224	Alternative to 3D T2 FLAIR (TI = 2250 ms)
Ax T2 FS	18	3 × 0.5	4917	87	320 × 320	Through PF only
Ax FIESTA	18	0.8	(45°)	Min	300 × 300	With Ax and Sag oblique reformations
Ax SWAN or SWI	25	2	Min (15°)	25	320 × 224	Optional
Sag 3D T1 FS+C	25	1.2	600	Min	288 × 288	With Ax and Cor reformations
Ax 3D SPGR+C	25	1.5	(20°)	Min	320 × 224	For treatment planning; nonangled orthogonal Ax
Ax T1 FS+C	18	3 × 0.5	2723.5	22	320 × 320	Alternative to 3D T1 FS + C (TI = 111 ms)
Cor T1 FS+C	18	3 × 0.5	2475	Min	383 × 224	Alternative to 3D T1 FS + C (TI = 111 ms)

Note:—SPGR indicates echo-spoiled gradient echo; FS, fat suppression; C, contrast; Sag, sagittal; Ax, axial; Cor, coronal; SWAN, T2 star-weighted angiography; Min, minimum.

^a Except for the axial 3D SPGR+C, all sequences are referenced to the anterior/posterior commissure line. An axial T2 FLAIR can be performed instead of the sagittal 3D T2 FLAIR. An axial and coronal T1 FS+C can be performed in lieu of a sagittal 3D T1 FS+C.

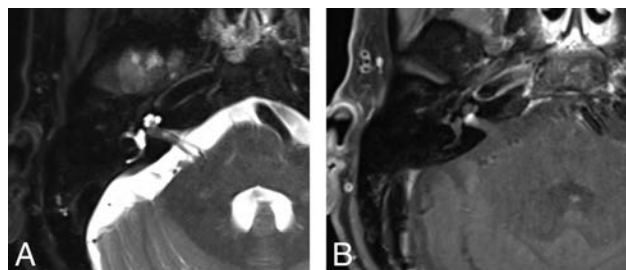


FIG 7. Precontrast axial T2WI (A) and postcontrast axial T1WI (B) demonstrate a small intracanalicular VS with lateral extension into the IAC fundus and the modiolus, which is associated with a decreased rate of hearing preservation.

diffusion restriction differentiates epidermoid from arachnoid cysts, which follow CSF signal on all sequences. Arachnoid cysts do not enhance, and they displace rather than engulf adjacent structures. Other uncommon cysts include dermoid cysts, neurocysticercosis, and neuroenteric cysts.

Initial Assessment. CT can detect moderate-large VSs, though small intracanalicular tumors can be missed. On CT, a solid VS is isoattenuating relative to the cerebellar parenchyma and typically enhances. Unlike a meningioma, a VS does not have calcifications.

CT is advantageous in assessing bony anatomy and pathologic changes. Unlike meningiomas, a moderate-large VS tends to expand the IAC (Fig 6), which may reflect tumor aggressiveness.⁵³ IAC expansion is associated with poorer preoperative hearing and postoperative hearing function.⁵³ Because the cochlear nerve is often located anterior or inferior to the tumor, larger tumors extending in this direction may encapsulate, infiltrate, or stretch the

nerve.^{37,53} The facial nerve can be affected by anterior extension of the tumor, though it appears to be more resilient than the cochlear nerve.⁵³

Due to superior contrast resolution, MR imaging is now the standard of care in evaluating VS. A sample MR imaging protocol used in the evaluation of CPA masses is included in Table 2. VS is typically T1 isointense relative to the cerebellar parenchyma and demonstrates avid enhancement on postcontrast T1WI (Fig 6). A VS may contain intralesional hemorrhage, which may exhibit T1 hyperintense signal and susceptibility artifacts on T2* gradient-echo sequences. A larger VS often demonstrates inhomogeneous enhancement secondary to intralesional hemorrhage and cysts. Concerning features include larger size, brain stem or cerebellar compression, peritumoral edema, hydrocephalus, and tonsillar herniation (Fig 6). Enhancement may extend into the modiolus secondary to cochlear infiltration (Fig 7), which decreases the rate of hearing preservation.

Cystic VSs are a subtype that accounts for approximately 10% of all VSs and are associated with higher degrees of hearing loss.⁵⁴ VS cysts are thought to arise from recurrent microbleeding or osmosis-induced expansion of CSF trapped in arachnoid tissue,⁵⁴ leading to T2 hyperintense signal and variable T1 signal (Fig 7). Enhancement of the cyst wall differentiates a cystic VS from an arachnoid or epidermoid cyst, the latter of which demonstrates diffusion restriction. Cystic VS may rapidly expand, leading to brain stem and cerebellar compression, edema, and hydrocephalus.⁵⁵ Surgical intervention is favored over SRS in the management of cystic VS because cystic VSs may respond poorly and unpredictably to SRS.^{56,57} In 1 study, 6.4% of cystic VSs initially treated with radiation therapy required surgical intervention.⁵⁷

Cystic VSs are considered more aggressive, with shorter symptomatic periods before presentation. They may surround and adhere to neurovascular structures as well as the more hypervascular solid component of the mass, leading to a less favorable surgical outcome.⁵⁵ Subtotal resection of cystic VS is sometimes advocated, particularly if there are peripherally located thin-walled cysts,⁵⁵ which should be emphasized in radiologic reporting (Fig 8).

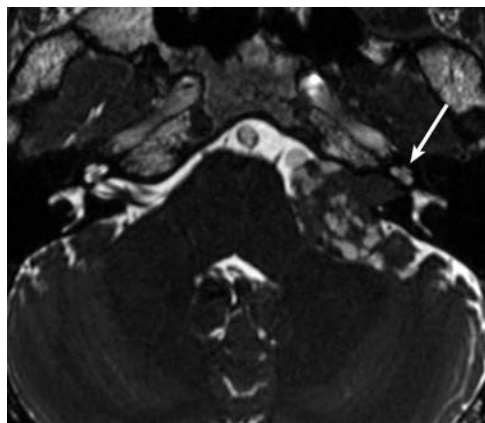


FIG 8. Axial FIESTA reveals a large left CPA VS with multiple superficial cysts, which may indicate increased adherence to neurovascular structures and lead to a more difficult surgical resection. Note asymmetric decreased T2 signal within the left cochlea (arrow) compared with the right.

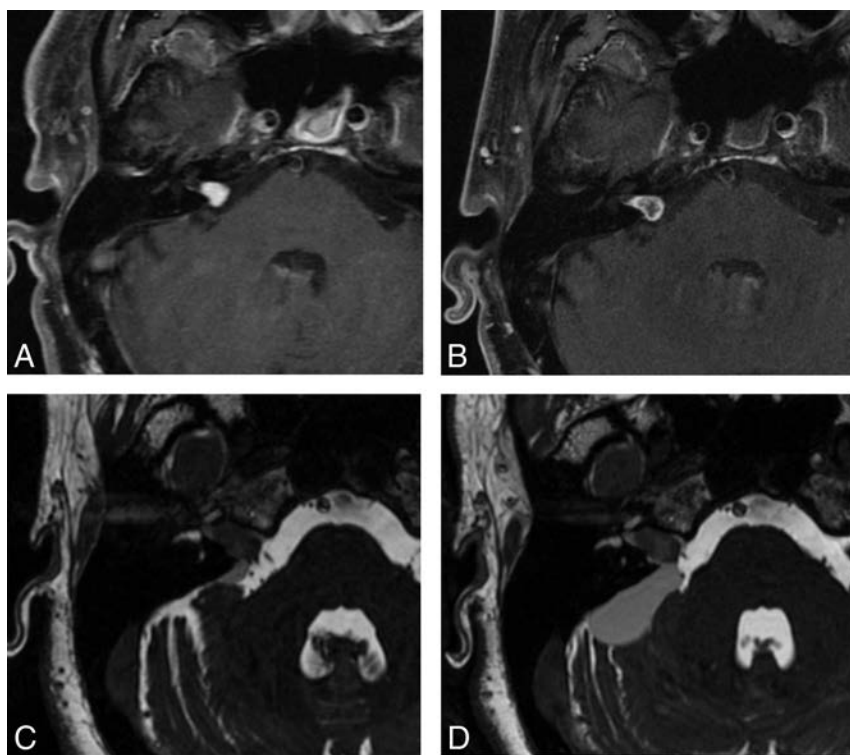


FIG 9. Two examples of post-SRS imaging. Postcontrast axial T1WI with fat suppression in a patient before (A) and following (B) SRS reveals decreased enhancement centrally within the tumor on posttherapeutic imaging (B), confirming a positive response to SRS. Two axial FIESTA images (C and D) obtained during 2 consecutive follow-up examinations in a 2-year period demonstrate interval enlargement of the cystic component within the right CPA associated with a predominantly intrameatal VS following radiation therapy. The cystic component was later resected (not shown).

High-resolution volumetrically acquired steady-state gradient-echo (3D SS-GRE) sequences with heavily T2-weighted signal provide exquisite detail of the location and morphology of the mass, the presence of decreased labyrinthine signal, the course of neighboring CNs in relation to the mass, and the relationship of the labyrinth to the posterior meatal lip. Identifying CSF lateral to an intracanalicular mass near the IAC fundus on 3D SS-GRE or contrast-enhanced T1WI is a favorable prognostic finding because involvement of the IAC fundus is associated with decreased rates of hearing preservation (Fig 7).⁵⁸ Decreased labyrinthine signal of 3D SS-GRE on initial imaging is associated with lower rates of posttreatment hearing preservation (Fig 8).⁵⁹

Sagittal-oblique reformations of 3D SS-GRE sequences allow detailed assessment of the facial nerve course relative to a mass. A VS arising from the superior division of the vestibular nerve will often displace the facial nerve anteriorly, whereas one arising from the inferior division will displace the facial nerve more superiorly. The location of the facial nerve in relation to the VS influences the surgical approach chosen. Facial nerves that are displaced superiorly by the VS may be more easily injured with a TL or MF approach, leading the surgeon to favor the RS.

Because the posterior meatal lip is drilled to access the IAC in the RS approach, this region is carefully evaluated preoperatively by either CT or MR imaging. Pneumatized air cells in this region may lead to a postsurgical CSF fistula.⁵³ A high-riding jugular bulb or jugular bulb diverticulum within the posterior meatal lip may potentially lead to vascular injury. Portions of the labyrinthine lying medial to the fundus-sinus line (the line from the sigmoid sinus to the IAC fundus) pose a higher risk for fenestration than those located laterally.⁵³

An abbreviated noncontrast MR imaging with 3D SS-GRE has been proposed as an inexpensive screening examination to exclude an IAC mass.⁶⁰ This study reported 100% sensitivity with high specificity and advocated adding a coronal T2WI to reduce false-positive/-negative examination findings secondary to volume averaging and banding artifacts, which could occur if relying solely on 3D SS-GRE.⁶⁰ An abbreviated non-contrast screening MR imaging, however, may not identify etiologies that are better depicted with contrast-enhanced MR imaging, such as other neoplastic and inflammatory conditions discussed above.

Increased labyrinthine T2 FLAIR hyperintense signal has been detected in patients with various pathologies, including VS, meningiomas, Menière disease, Ramsay Hunt syndrome, otosclerosis, and sudden idiopathic sensorineural hearing loss.⁶¹⁻⁶³ The T2 FLAIR hyperintense cochlear signal in patients with VS is attributed to increased pro-

tein content within the perilymph,^{61,64} which may be secondary to tumor compression of the cochlear nerve, resulting in interference with neuroaxonal transport of proteins.⁶¹ 3D-FLAIR sequences can optimally detect cochlear T2 FLAIR hyperintense signal.^{63,65,66} Kim et al⁶⁵ reported a significant correlation between the T2 FLAIR hyperintense cochlear signal and the degree of hearing impairment in patients with intracanalicular VS. This retrospective study, however, did not specify whether the 3D-FLAIR sequence was performed consistently before or following intravenous contrast administration. Two smaller retrospective studies reported no correlation and a weak correlation between postcontrast T2 FLAIR hyperintense signal and the level of hearing impairment in patients with VS.^{63,66} Additional studies should be performed to further clarify the significance of the T2 FLAIR hyperintense cochlear signal in VS.

Follow-Up Assessment

Objectives of follow-up imaging include identification of residual/recurrent tumor, assessment of tumor size, response to radiation therapy, and the presence of posttherapeutic complications. Residual tumor is best assessed with a fat-suppressed contrast-enhanced T1WI, because the signal from fat packing can be nullified (Fig 2). Because the goals of therapy have shifted from total resection to functional preservation, residual tumor is often intentionally left behind in areas near the facial nerve. The presence of residual enhancing tumor is not uncommon and may be followed with serial imaging and further treated with SRS (Fig 3). A residual mass tends to contract and become more rounded within 6–12 months of completion of SRS.

Standardized methods of tumor reporting and measurements have been promoted by national organizations, such as the American Academy of Otolaryngology-Head and Neck Surgery (AAO-HNS) in 1995⁶⁷ and the Consensus Meeting on Systems for Reporting Results in Acoustic Neuroma in 2003,⁶⁸ though no single method has been clearly adopted. VS should be described as intracanalicular, extrameatal, or intrameatal and extrameatal, and cross-sectional measurements should be specific for each component. Growth tends to be the greatest in the extrameatal component, and recommendations have focused on the extrameatal measurements. The AAO-HNS has recommended the square root product of the extrameatal anteroposterior \times medial lateral diameters, with the anteroposterior diameter measured parallel to the petrous ridge.⁶⁷ The Consensus Meeting in 2003 favored using the maximum extrameatal diameter, which, by itself, sufficiently reflected growth of the tumor.⁶⁸ One study has found the AAO-HNS methodology to be preferable because tumors tend to grow in both anteroposterior and ML directions.⁶⁹

Immediately following SRS, the tumor may increase in size due to intralesional edema, which rarely indicates treatment failure.⁷⁰ In 1 study, 5% of tumors enlarged following SRS but remained stable on subsequent imaging.⁷¹ Most VSs treated with SRS will subsequently decrease or remain stable in size, reflecting adequate tumor control.⁴³ Decreased enhancement centrally within the tumor is considered a positive response to therapy and is typically seen within 6 months following SRS (Fig 9).⁴³ Radiation therapy may uncommonly induce cystic degeneration that may be secondary to microbleeding, increased vascular permea-

bility, or scarring of arachnoid adhesions (Fig 9).⁷² The potential for postradiation cystic degeneration is one rationale for treating cystic VS initially with surgical resection.

While uncommon, dural sinus thrombus may be seen following an RS or TL approach secondary to injury of the sigmoid sinus and may result in venous congestion or infarction. Brain retraction during an RS or MF approach may result in edema or ischemia of the cerebellum or temporal lobe, respectively. Postoperative infection may result in meningitis or, if severe, cerebritis. CSF leak can sometimes be detected by identifying the presence of a fluid collection within or subjacent to the craniotomy site. Other complications such as CN deficits are better assessed by clinical examination.

Labyrinthine fenestration may present with postoperative hearing loss and can be evaluated with a dedicated CT of the temporal bones. Bony labyrinthine dehiscence, however, may not always correlate with hearing loss or vestibular symptoms.⁷³ Decreased T2 signal within the vestibulocochlear complex on 3D SS-GRE imaging postsurgically may reflect membranous fenestration, microvascular injury to the cochlea, or labyrinthitis ossificans. The decrease in T2 signal has been correlated with postoperative hearing loss.⁷³

CONCLUSIONS

VSs are benign neoplasms of the vestibulocochlear nerve sheath and are the most common CPA tumor. VS can be managed by surgical resection, radiation therapy, and observation, though only select patients are followed conservatively due to its association with hearing loss. The treatment objectives of VS have shifted from total resection to long-term tumor control with maximum functional preservation. Larger tumors of >3 cm are generally surgically resected because radiation poses a risk of brain stem compression due to posttreatment edema. Smaller tumors may be treated with surgery or radiation. Lateral skull base approaches include the TL, RS, and MF and have been applied to other skull base and PF pathologies. Knowledge of the management options and objectives allows the radiologist to provide imaging findings pertinent to initial management and to recognize expected posttherapeutic findings and unexpected complications.

ACKNOWLEDGMENTS

We thank Nadezhda Kiriya and Gwen Mack for their illustrations in this article.

Disclosures: Benjamin T. Crane—**RELATED:** Grant: National Institute on Deafness and Other Communication Disorders, Comments: R01 DC013580, K23 DC011298*; **UNRELATED:** Patents (Planned, Pending, or Issued): University of Rochester, Comments: B.T. Crane, "Methods and Systems for Rehabilitation of Vestibular Disorders," US Patent 9,167,998. Filed February 24, 2012. Issued October 27, 2015. Assignee University of Rochester.* *Money paid to the institution.

REFERENCES

1. Mahaley MS Jr, Mettlin C, Natarajan N, et al. Analysis of patterns of care of brain tumor patients in the United States: a study of the Brain Tumor Section of the AANS and the CNS and the Commission on Cancer of the ACS. *Clin Neurosurg* 1990;36:347–52 Medline
2. Gentry LR, Jacoby CG, Turski PA, et al. Cerebellopontine angle-petromastoid mass lesions: comparative study of diagnosis with MR imaging and CT. *Radiology* 1987;162:513–20 CrossRef Medline
3. House JW, Waluch V, Jackler RK. Magnetic resonance imaging in

- acoustic neuroma diagnosis. *Ann Otol Rhinol Laryngol* 1986;95:16–20 CrossRef Medline
4. Curati WL, Graif M, Kingsley DPE, et al. MRI in acoustic neuroma: a review of 35 patients. *Neuroradiology* 1986;28:208–14 CrossRef Medline
5. Jackler RK, Shapiro MS, Dillon WP, et al. Gadolinium-DTPA enhanced magnetic resonance imaging in acoustic neuroma diagnosis and management. *Otolaryngol Head Neck Surg* 1990;102:670–77 CrossRef Medline
6. Kemink JL, Langman AW, Niparko JK, et al. Operative management of acoustic neuromas: the priority of neurologic function over complete resection. *Otolaryngol Head Neck Surg* 1991;104:96–99 CrossRef Medline
7. Sughrue ME, Kaur R, Rutkowski MJ, et al. Extent of resection and the long-term durability of vestibular schwannoma surgery. *J Neurosurg* 2011;114:1218–23 CrossRef Medline
8. Samii M, Gerganov VM, Samii A. Functional outcome after complete surgical removal of giant vestibular schwannomas. *J Neurosurg* 2010;112:860–67 CrossRef Medline
9. Bloch O, Sughrue ME, Kaur R, et al. Factors associated with preservation of facial nerve function after surgical resection of vestibular schwannoma. *J Neurooncol* 2011;102:281–86 CrossRef Medline
10. Slatery WH. Neurofibromatosis type 2. *Otolaryngol Clin North Am* 2015;48:443–60 CrossRef
11. Sughrue ME, Yeung AH, Rutkowski MJ, et al. Molecular biology of familial and sporadic vestibular schwannomas: implications for novel therapeutics. *J Neurosurg* 2011;114:359–66 CrossRef Medline
12. Doyle KJ. Is there still a role for auditory brainstem response audiometry in the diagnosis of acoustic neuroma? *Arch Otolaryngol Head Neck Surg* 1999;125:232 CrossRef Medline
13. McBurney C, Starr MA. A contribution to cerebral surgery: diagnosis, localization and operation for removal of three tumors of the brain: with some comments upon the surgical treatment of brain tumors. *Am J Med Sci* 1893;55:361–87
14. Ballance C. *Some Points in the Surgery of the Brain and Its Membranes*. London: Macmillan; 1907
15. Van Eiselsberg A. Über die chirurgische Behandlung der Hirntumoren. *Trans Intl Cong Med* 1913;7:209–17
16. Dandy WE. Ventriculography following the injection of air into the cerebral ventricles. *Ann Surg* 1918;68:5–11 CrossRef Medline
17. Beller AJ, Schwartz A. Pneumoencephalographic studies following complete removal of supratentorial lesions. *Radiology* 1953;61:200–07 CrossRef Medline
18. Cushing H. The acoustic tumors. In: *Intracranial Tumors*. Springfield, Illinois: Charles C. Thomas; 1932:85–92
19. House WF. Surgical exposure of the internal auditory canal and its contents through the middle cranial fossa. *Laryngoscope* 1961;71:1363–85 Medline
20. House WF. Transtemporal bone microsurgical removal of acoustic neuromas: evolution of transtemporal bone removal of acoustic tumors. *Arch Otolaryngol* 1964;80:731–42 CrossRef Medline
21. Delgado TE, Bucheit WA, Rosenholtz HR, et al. Intraoperative monitoring of facial muscle evoked responses obtained by intracranial stimulation of the facial nerve: a more accurate technique for facial nerve dissection. *Neurosurgery* 1979;4:418–21 CrossRef Medline
22. Leksell L. The stereotactic method and radiosurgery of the brain. *Acta Chir Scand* 1951;102:316–19 Medline
23. Leksell L. A note on the treatment of acoustic tumours. *Acta Chir Scand* 1971;137:763–65 Medline
24. Kondziolka D, Lunsford LD, McLaughlin MR, et al. Long-term outcomes after radiosurgery for acoustic neuromas. *N Engl J Med* 1998;339:1426–33 CrossRef Medline
25. Burrows EH. Positive contrast examination (cerebellopontine cisternography) in extrameatal acoustic neurofibromas. *Br J Radiol* 1969;42:902–13 CrossRef Medline
26. Hitselberger WE, House WF. Polytome-pantopaque: a technique for the diagnosis of small acoustic tumors: technical note. *J Neurosurg* 1968;29:214–17 CrossRef Medline
27. Smouha EE, Yoo M, Mohr K, et al. Conservative management of acoustic neuroma: a meta-analysis and proposed treatment algorithm. *Laryngoscope* 2005;115:450–54 CrossRef Medline
28. Stangerup SE, Caye-Thomasen P, Tos M, et al. Natural history of vestibular schwannoma. *Otol Neurotol* 2006;27:547–52 CrossRef Medline
29. Nikolopoulos TP, Fortnum H, O'Donoghue G, et al. Acoustic neuroma growth: systematic review of the evidence. *Otol Neurotol* 2010;31:478–85 CrossRef Medline
30. Fucci MJ, Buchman CA, Brackmann DE, et al. Acoustic tumor growth: implications for treatment choices. *Am J Otol* 1999;20:495–99 Medline
31. Sughrue ME, Yang I, Aranda D, et al. The natural history of untreated sporadic vestibular schwannomas: comprehensive review of hearing outcomes. *J Neurosurg* 2010;112:163–67 CrossRef Medline
32. Huang MJ, Kano H, Mousavi SH, et al. Stereotactic radiosurgery for recurrent vestibular schwannoma after previous resection. *J Neurosurg* 2016 Jul 29. [Epub ahead of print] CrossRef Medline
33. Chung WY, Pan DH, Lee CC, et al. Large vestibular schwannomas treated by gamma knife surgery: long-term outcomes. *J Neurosurg* 2010;113(suppl):112–21 CrossRef Medline
34. Mandl ES, Meijer OW, Slotman BJ, et al. Stereotactic radiation therapy for large vestibular schwannomas. *Radiother Oncol* 2010;95:94–98 CrossRef Medline
35. Carlson M, Tveiten OV, Driscoll C, et al. Long-term quality of life in patients with vestibular schwannoma: an international multicenter, cross-sectional study comparing microsurgery, stereotactic radiosurgery, observation, and nontumor controls. *J Neurosurg* 2015;122:833–42 CrossRef Medline
36. Oghalai JS, Driscoll CL. *Atlas of Neurotologic and Lateral Skull Base Surgery*. Berlin: Springer; 2016:19–103
37. Madjid S, Cordula M. Management of 1000 vestibular schwannomas (acoustic neuromas): hearing function in 1000 tumor resections. *Neurosurgery* 1997;40:248–62 CrossRef Medline
38. Samii M, Gerganov V, Samil A. Improved preservation of hearing and facial nerve function in vestibular schwannoma surgery via the retrosigmoid approach in a series of 200 patients. *J Neurosurg* 2006;105:527–35 CrossRef Medline
39. Blevins NH, Jackler RK. Exposure of the lateral extremity of the internal auditory canal through the retrosigmoid approach: a radioanatomic study. *Otolaryngol Head Neck Surg* 1994;111:81–90 CrossRef Medline
40. Ruckenstein MJ, Harris JP, Cueva RA, et al. Pain subsequent to resection of acoustic neuromas via suboccipital and translabyrinthine approaches. *Am J Otol* 1996;17:620–24 Medline
41. Flickinger JC, Lunsford LD, Linskey ME, et al. Gamma knife radiosurgery for acoustic tumors: multivariate analysis of four year results. *Radiother Oncol* 1993;27:91–98 CrossRef Medline
42. Foote RL, Coffey RJ, Swanson JW, et al. Stereotactic radiosurgery using the gamma knife for acoustic neuromas. *J Radiat Oncol Biol Phys* 1995;32:1153–60 CrossRef Medline
43. Jacob JT, Pollock BE, Carlson ML, et al. Stereotactic radiosurgery in the management of vestibular schwannoma and glomus jugulare: indications, techniques and results. *Otolaryngol Clin North Am* 2015;48:515–26 CrossRef Medline
44. Flickinger JC, Kondziolka D, Lunsford LD. Dose and diameter relationships for facial, trigeminal, and acoustic neuropathies following acoustic neuroma radiosurgery. *Radiother Oncol* 1996;41:215–19 CrossRef Medline
45. Lunsford LD, Niranjan A, Flickinger JC, et al. Radiosurgery of vestibular schwannomas: summary of experience in 829 cases. *J Neurosurg* 2013;119:195–99 Medline
46. Roos DE, Potter AE, Zacest AC. Hearing preservation after low dose linac radiosurgery for acoustic neuroma depends on initial hearing and time. *Radiother Oncol* 2011;101:420–24 CrossRef Medline
47. Hasegawa T, Kida Y, Kato T, et al. Long-term safety and efficacy of stereotactic radiosurgery for vestibular schwannomas: evaluation

- of 440 patients more than 10 years after treatment with gamma knife surgery. *J Neurosurg* 2013;118:557–65 CrossRef Medline
48. Carlson ML, Jacob JT, Pollock BE, et al. Long-term hearing outcomes following stereotactic radiosurgery for vestibular schwannoma: patterns of hearing loss and variables influencing audiometric decline. *J Neurosurg* 2013;118:579–87 CrossRef Medline
 49. Mousavi SH, Niranjana A, Akpinar B, et al. Hearing subclassification may predict long-term auditory outcomes after radiosurgery for vestibular schwannoma patients with good hearing. *J Neurosurg* 2016;125:845–52 CrossRef Medline
 50. Jacob JT, Carlson ML, Schiefer TK, et al. Significance of cochlear dose in the radiosurgical treatment of vestibular schwannoma: controversies and unanswered questions. *Neurosurgery* 2014;74:466–74; discussion 474 CrossRef Medline
 51. Akpinar B, Mousavi SH, McDowell MM, et al. Early radiosurgery improves hearing preservation in vestibular schwannoma patients with normal hearing at the time of diagnosis. *Int J Radiat Oncol Biol Phys* 2016;95:729 CrossRef Medline
 52. Sarrazin JL. Infra tentorial tumors [in French]. *J Radiol* 2006;87:748–63 Medline
 53. Matthies C, Samii M, Krebs S. Management of vestibular schwannomas: radiological features in 202 cases. *Neurosurgery* 1997;40:469–81; discussion 481–82 Medline
 54. Piccirillo E, Wiet MR, Flanagan S, et al. Cystic vestibular schwannoma: classification, management and facial nerve outcomes. *Otol Neurotol* 2009;30:826–34 CrossRef Medline
 55. Pendt G, Ganz JC, Kitz K, et al. Acoustic neurinomas with macrocysts treated with gamma knife radiosurgery. *Stereotact Funct Neurosurg* 1996;66:103–11 Medline
 56. Benech F, Perez R, Fontanella MM, et al. Cystic versus solid vestibular schwannomas: a series of 80 grade III-IV patients. *Neurosurg Rev* 2005;28:209–13 CrossRef Medline
 57. Delsanti C, Régis J. Cystic vestibular schwannomas [in French]. *Neurochirurgie* 2004;50:401–06 Medline
 58. Goddard J, Schwartz M, Friedman R. Fundal fluid as a predictor of hearing preservation in the middle cranial fossa approach for vestibular schwannoma. *Otol Neurotol* 2010;31:1128–34 CrossRef Medline
 59. Somers T, Casselman J, de Ceulaer G, et al. Prognostic value of magnetic resonance imaging findings in hearing preservation surgery for vestibular schwannoma. *Otol Neurotol* 2001;22:87–94 CrossRef Medline
 60. Abele TA, Besachio DA, Quigley EP, et al. Diagnostic accuracy of screening MR imaging using unenhanced axial CISS and coronal T2WI for detection of small internal auditory canal lesions. *AJNR Am J Neuroradiol* 2014;35:2366–70 CrossRef Medline
 61. Bhadelia RA, Tedesco KL, Hwang S, et al. Increased cochlear fluid-attenuation inversion recovery signal in patients with vestibular schwannomas. *AJNR Am J Neuroradiol* 2008;29:720–23 CrossRef Medline
 62. Lee IH, Kim HJ, Chung WH, et al. Signal intensity change of the labyrinth in patients with surgically confirmed or radiologically diagnosed vestibular schwannoma on isotropic 3D fluid-attenuated inversion recovery MR imaging at 3 T. *Eur Radiol* 2010;20:949–57 CrossRef Medline
 63. Yoshida T, Sugiura M, Naganawa S, et al. Three-dimensional fluid-attenuated inversion recovery magnetic resonance imaging findings and prognosis in sudden sensorineural hearing loss. *Laryngoscope* 2008;118:1433–37 CrossRef Medline
 64. O'Connor AF, France MW, Morrison AW. Perilymph total protein levels associated with cerebellopontine angle lesions. *Am J Otol* 1981;2:193–95 Medline
 65. Kim DY, Lee JH, Sung YS, et al. Clinical significance of an increased cochlear 3D fluid-attenuated inversion recovery signal intensity on an MR imaging examination in patients with acoustic neuroma. *AJNR Am J Neuroradiol* 2014;35:1825–29 CrossRef Medline
 66. Yamazaki M, Naganawa S, Kawai H, et al. Increased signal intensity of the cochlea on pre- and post-contrast enhanced 3D-FLAIR in patients with vestibular schwannoma. *Neuroradiology* 2009;51:855–63 CrossRef Medline
 67. Committee on Hearing and Equilibrium guidelines for the evaluation of hearing preservation in acoustic neuroma. *Otol Head Neck Surg* 1995;113:179–80 CrossRef Medline
 68. Kanzaki J, Tos M, Sanna M, et al. New and modified reporting systems from the consensus meeting on systems for reporting results in vestibular schwannomas. *Otol Neurotol* 2003;24:42–48; discussion 648–49 Medline
 69. Walsh RM, Bath AP, Bance ML, et al. Comparison of two radiologic methods for measuring the size and growth rate of extracanalicular vestibular schwannomas. *Am J Otol* 2000;21:716–21 Medline
 70. Nagano O, Higuchi Y, Serizawa T, et al. Transient expansion of vestibular schwannoma following stereotactic radiosurgery. *J Neurosurg* 2008;109:811–16 CrossRef Medline
 71. Delsanti C, Roche PH, Thomassin JM, et al. Morphological changes of vestibular schwannomas after radiosurgical treatment: pitfalls and diagnosis of failure. *Prog Neurol Surg* 2008;21:93–97 CrossRef Medline
 72. Park CK, Kim DC, Park SH, et al. Microhemorrhage, a possible mechanism for cyst formation in vestibular schwannomas. *J Neurosurg* 2006;105:576–80 CrossRef Medline
 73. Warren FM 3rd, Kaylie DM, Aulino JM, et al. Magnetic resonance appearance of the inner ear after hearing-preservation surgery. *Otol Neurotol* 2006;27:393–97 CrossRef Medline

The Brain Thermal Response as a Potential Neuroimaging Biomarker of Cerebrovascular Impairment

C.C. Fleischer, J. Wu, D. Qiu, S.-E. Park, F. Nahab, and S. Dehkharghani



ABSTRACT

BACKGROUND AND PURPOSE: Brain temperature is critical for homeostasis, relating intimately to cerebral perfusion and metabolism. Cerebral thermometry is historically challenged by the cost and invasiveness of clinical and laboratory methodologies. We propose the use of noninvasive MR thermometry in patients with cerebrovascular disease, hypothesizing the presence of a measurable brain thermal response reflecting the tissue hemodynamic state.

MATERIALS AND METHODS: Contemporaneous imaging and MR thermometry were performed in 10 patients (32–68 years of age) undergoing acetazolamide challenge for chronic, anterior circulation steno-occlusive disease. Cerebrovascular reactivity was calculated with blood oxygen level–dependent imaging and arterial spin-labeling methods. Brain temperature was calculated pre- and post-acetazolamide using previously established chemical shift thermometry. Mixed-effects models of the voxelwise relationships between the brain thermal response and cerebrovascular reactivity were computed, and the significance of model coefficients was determined with an *F* test ($P < .05$).

RESULTS: We observed significant, voxelwise quadratic relationships between cerebrovascular reactivity from blood oxygen level–dependent imaging and the brain thermal response (x coefficient = 0.052, $P < .001$; x^2 coefficient = 0.0068, $P < .001$) and baseline brain temperatures (x coefficient = 0.59, $P = .008$; x^2 coefficient = -0.13 , $P < .001$). A significant linear relationship was observed for the brain thermal response with cerebrovascular reactivity from arterial spin-labeling ($P = .001$).

CONCLUSIONS: The findings support the presence of a brain thermal response exhibiting complex but significant interactions with tissue hemodynamics, which we posit to reflect a relative balance of heat-producing versus heat-dissipating tissue states. The brain thermal response is a potential noninvasive biomarker for cerebrovascular impairment.

ABBREVIATIONS: ACZ = acetazolamide; ASL = arterial spin-labeling; BOLD = blood oxygen level–dependent; BTR = brain thermal response; CMRO₂ = cerebral metabolic rate of oxygen; CVR = cerebrovascular reactivity; MRSI = MR spectroscopic imaging; OEF = oxygen extraction fraction

Chronic cerebrovascular disease remains a common cause of death and disability. While treatment advances have reduced stroke rates in such individuals, there exists a subset of patients at heightened ongoing risk linked to a tenuous state of so-called misery perfusion and characterized by exhaustion of hemodynamic compensatory mechanisms.^{1–4} Although individual pa-

tients may deviate from the proposed paradigm of decompensation, misery perfusion confers an increased risk for future ischemic injury, and refined characterization of the pathophysiologic underpinnings may allow improved prognostication or therapy selection in such patients.^{1,2}

Historically, ¹⁵O-PET has been used to identify misery perfusion as defined by disturbances in CBF, CBV, oxygen extraction fraction (OEF), and the cerebral metabolic rate of oxygen (CMRO₂).^{5–7} Challenges inherent to ¹⁵O-PET, including reliance on short half-life radioisotope tracers and radiation exposure, compel the development of pragmatic, ideally noninvasive and noncontrast, MR imaging biomarkers to identify and characterize misery perfusion. Such approaches would enable safe and repeat-

Received January 17, 2017; accepted after revision July 9.

From the Department of Biomedical Engineering (C.C.F., S.-E.P.), Emory University and Georgia Institute of Technology, Atlanta, Georgia; and the Departments of Radiology and Imaging Sciences (C.C.F., J.W., D.Q., S.D.), Neurology (F.N., S.D.), and Pediatrics (F.N.), Emory University School of Medicine, Atlanta, Georgia.

Dr Dehkharghani is currently affiliated with the Department of Radiology, Neuro-radiology Section, New York University, New York, New York.

Deqiang Qiu is supported by National Institutes of Health grants AG25688, AG42127, AG49752, and AG51633.

Abstract previously presented at: Annual Meeting and Exhibition of the International Society for Magnetic Resonance in Medicine, May 7–13, 2016; Singapore; and the Annual Meeting of the American Society of Neuroradiology, May 21–26, 2016; Washington, DC.

Please address correspondence to Seena Dehkharghani, MD, Department of Radiology, Neuroradiology Section, New York University, 660 First Ave, New York, New York 10016; e-mail: seena.dehkharghani@nyumc.org

Indicates open access to non-subscribers at www.ajnr.org

<http://dx.doi.org/10.3174/ajnr.A5380>

able imaging, allowing structural and functional characterization of the tissue state.⁸ Among MR imaging techniques, cerebrovascular reactivity (CVR) measured from blood oxygen level–dependent (BOLD) imaging or calculated from arterial spin-labeling (ASL) has been proposed using hemodynamic augmentation such as induced hypercapnia or acetazolamide (ACZ) administration.^{8–10} Impaired CVR is strongly associated with ischemic risk in patients with carotid steno-occlusive disease, suggesting that early identification combined with appropriate intervention may improve outcomes.^{11,12}

Under-represented in such studies is the role of brain temperature, a homeostatic variable inextricably linked to CBF and cerebral metabolism.^{13,14} Increased brain and systemic temperatures strongly potentiate ischemic injury due to the high sensitivity of neuronal substrate to even small temperature fluctuations.^{15–19} Cerebral thermoregulation remains poorly understood, owing to historically limited methodologies consisting of highly invasive and costly implantable probes. Past study has thus relied primarily on animal models or used systemic temperature as a surrogate for brain temperature, with limited empirical exploration of the effect of hemodynamic impairment on thermal dynamics.^{15,17,20–22}

Our goal was to explore the feasibility of a “brain thermal response” (BTR) as a potential MR neuroimaging biomarker for hemodynamic impairment by characterizing the relationship between BTR and CVR. We propose BTR as a measurement of dynamic brain temperature fluctuations in response to a hemodynamic maneuver, hypothesizing the presence of detectable, coherent temperature response differences paralleling tissue-level hemodynamic impairment.

MATERIALS AND METHODS

Experimental Design

Retrospective analysis was performed on data acquired in patients undergoing treatment for chronic, unilateral anterior circulation steno-occlusive disease and recurring neurovascular events (minor stroke or transient ischemic attack), referred by a vascular neurologist to undergo a standardized institutional protocol in our chronic neurovascular disease patient population. A waiver of Health Insurance Portability and Accountability Act authorization and informed consent was approved by the institutional review board. Exclusion criteria included contraindications to MR imaging, renal impairment, sensitivity to sulfa derivatives, extreme head motion during the scan, or inability to comply with the study protocol for 2-day multiphasic MR imaging (3 subjects excluded). After exclusion, 10 subjects between 32 and 68 years of age (mean, 46 ± 13 years) were included in the study (8 women, 32–68 years of age; mean, 41 ± 12 years; 2 men, 56 and 61 years of age).

MR Imaging and Spectroscopy

Subjects completed a standardized, 2-day MR imaging protocol with ACZ challenge (Fig 1). Multivoxel MR spectroscopic imaging (MRSI), ASL, and BOLD data were acquired both pre- and post-ACZ. All scanning was performed on a Tim Trio 3T whole-body MR imaging scanner (Siemens, Erlangen, Germany) with a 32-channel head-array coil. A 3D T1-weighted MPRAGE (TR/TE = 1900/3.5 ms, T1 = 900 ms, flip angle = 9°, 1 mm isotropic resolution) anatomic image was used to guide MRSI grid place-

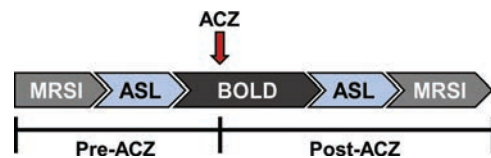


FIG 1. Schematic of MR imaging scan protocol. ACZ was injected 5 minutes after the start of the BOLD sequence and data were acquired for ~10 minutes post-injection. ASL and MRSI were acquired pre- and post-ACZ.

ment and to plan the ASL and BOLD experiments. A 6-minute multi-TI ASL sequence with background suppression was acquired with a multidelay single-shot 3D gradient- and spin-echo readout and flow-sensitive alternating inversion recovery tagging with the following parameters: TR/TE = 3600/19.3 ms, FOV = 320×160 mm, section thickness = 3.5 mm, 32 sections, 5 averages, and 10 postlabel delays: first TI = 300 ms, increment = 300 ms. A 20-minute continuous BOLD study was performed, beginning with 5 minutes of baseline acquisition, after which ACZ (Diamox, 1 g dissolved in 10 mL of normal saline) was administered without scan interruption or patient repositioning. ACZ was delivered via slow, manual IV infusion for 3–5 minutes in aliquots of approximately 2 mL per minute, followed by a normal saline flush, after which the remaining ~10 minutes of continuous and uninterrupted BOLD imaging was performed. BOLD data were acquired with a gradient-echo echo-planar imaging sequence (TR/TE = 2000/30 ms, FOV = 220 mm, matrix = 64×64 , section thickness = 4 mm, 30 sections).

MRSI scans for thermometry were acquired pre- and post-ACZ injection with the semi-localized by adiabatic selective refocusing sequence^{23–25} with an 8×8 voxel ROI with the center of the grid aligned over the midline of the brain (TR/TE = 1700/35 ms, 3 averages, $10 \times 10 \times 15$ mm³ nominal voxel size, 16×16 voxel acquisition matrix with lipid saturation outside the ROI, 50-Hz water-suppression bandwidth).

For each subject, the diseased hemisphere was identified on contemporaneous 3D time-of-flight brain MRA, as well as on conventional DSA or CTA when available. All imaging was evaluated by a dedicated neuroradiologist with subspecialty certification and 8 years of experience in advanced stroke imaging (S.D.), and a vascular neurologist with >10 years of experience in stroke and neurovascular imaging (F.N.).

Cerebrovascular Reactivity

CVR pre- versus post-ACZ administration was calculated using both relative CBF from ASL data (CVR_{ASL}) and BOLD signal augmentation (CVR_{BOLD}). For CVR_{ASL}, the CBF map from the post-ACZ ASL acquisition (CBF_{post}) was coregistered to the pre-ACZ CBF (CBF_{pre}) map to correct for motion effects and smoothed with a Gaussian kernel (full width at half maximum = 8 mm). The raw data were fit with a kinetic model reported elsewhere using the inline vendor-supplied processing output.^{26,27} CVR_{ASL} was calculated from Equation 1.

$$1) \quad \text{CVR}_{\text{ASL}} = \frac{\text{CBF}_{\text{post}} - \text{CBF}_{\text{pre}}}{\text{CBF}_{\text{pre}}} \times 100\%$$

CVR_{BOLD} was calculated from BOLD images following realignment to correct for motion and smoothed with a Gaussian kernel

(full width at half maximum = 8 mm). The voxelwise mean intensity values from 30 BOLD volumes acquired before ACZ injection ($BOLD_{pre}$) and the mean intensity values from the final 30 BOLD volumes ($BOLD_{post}$) were calculated. CVR_{BOLD} was then computed with Equation 2.

$$2) \quad CVR_{BOLD} = \frac{BOLD_{post} - BOLD_{pre}}{BOLD_{pre}} \times 100\%$$

The final CVR maps were coregistered to the T1-weighted images in the patient coordinate system, to facilitate voxelwise analysis with the MRSI data, and were resampled to a nominal 1 mm isotropic resolution. For CVR_{ASL} values, augmentation of <30% was used as a threshold to identify regions of hemodynamic impairment as previously reported.^{10,28-30} For CVR_{BOLD} , 70% of the subject-wise mean contralateral CVR value was used as a threshold. The use of an individual cutoff value was chosen to minimize variation from intersubject BOLD fluctuations. To generate the CVR maps for display, a brain mask was generated using the T1-weighted image with the FSL Brain Extraction Tool (<http://fsl.fmrib.ox.ac.uk/fsl/fslwiki/BET>),³¹ and masked CVR color maps were generated in Matlab (Version 2015a; MathWorks, Natick, Massachusetts).

Thermometry and Brain Thermal Response

MRSI data for thermometry were processed using LCModel (<http://www.lcmodel.com>)³² as reported previously.^{19,24,25} Temperature analysis and localization of the grid onto CVR maps were performed using in-house software written in Matlab. Specifically, absolute temperature was calculated using the difference between water and NAA proton resonance frequencies and the relationship $-0.01 \text{ ppm}/^{\circ}\text{C}$.^{33,34} Voxelwise temperature changes were calculated as a difference between post- and pre-ACZ absolute temperatures ($T_{post} - T_{pre}$). The unitless parameter, BTR, was defined as the temperature change normalized to the pre-ACZ temperature (Equation 3). Temperature maps were calculated on a voxelwise basis and interpolated using bicubic interpolation for visualization purposes.

$$3) \quad BTR = \frac{T_{post} - T_{pre}}{T_{pre}}$$

To facilitate the voxelwise analysis between BTR and CVR, the MRSI grid was localized onto the CVR images. Because the MRSI grid was planned using the T1-weighted image in the patient coordinate system, the data for both MRSI and CVR use the same coordinate system. The MRSI grid was first rotated parallel to the axial plane of the patient coordinate system, followed by a linear translation of the center of the MRSI grid to the origin (0,0,0 mm). These same transformations were also applied to the CVR data, which were then resliced using the trilinear interpolation method while retaining the nominal 1-mm isotropic resolution. The same transformation and reslicing were also applied to the T1-weighted image to visually confirm the location of the MRSI grid onto the CVR map and to overlay the temperature grid onto the anatomic image. The final CVR data were interpolated to an 8×8 grid ($10 \times 10 \times 15 \text{ mm}^3$ voxel resolution), identical to the MRSI grid, and an average CVR value was calculated for each MRSI voxel.

Statistical Analysis

Statistical analysis was performed with SPSS (Version 22.0; IBM, Armonk, New York). Hemispheric comparisons (ipsilateral versus contralateral) of baseline brain temperature and BTR were performed for both random and fixed effects. However, most of the analysis was performed voxelwise to permit comparison of BTR, baseline brain temperature, and CVR and to explore localized impairment across the entire ROI. The voxelwise relationships among these parameters were determined with a mixed-effects model (Equation 4), in which \vec{y} is the vector of measured BTR or baseline temperature values; \vec{X} is a matrix of fixed effects (CVR, square of CVR, and intercept) and the corresponding vector of fixed-effect coefficients, $\vec{\beta}$; \vec{Z} is a matrix of random between-subject variations and the corresponding vector of random-effect coefficients, \vec{b} ; and $\vec{\epsilon}$ is a vector of random errors.

$$4) \quad \vec{y} = \vec{X}\vec{\beta} + \vec{Z}\vec{b} + \vec{\epsilon}$$

The restricted maximum likelihood estimation with 150 iterations was used to fit the model using either unstructured or first-order autoregressive covariance structures, along with a random intercept to account for multiple nonindependent measurements from voxels within each subject. The best fit models, comparing both linear and quadratic models along with different covariance structures for the random effects, were determined with the Schwarz Bayesian information criterion and a value of >10 to establish differences among models.³⁵ In the case in which the Schwarz Bayesian information criterion was <10, parsimony was applied for the final model selection. *df* for the mixed-models were determined with the Satterthwaite approximation. Exponential models were also explored but did not converge. The significance of the regression was determined with the mixed-model *F* statistic and $P < .05$.

RESULTS

Patient characteristics are presented in Table 1. Representative CVR_{BOLD} and CVR_{ASL} augmentation maps, the corresponding BTR map, and a diffusion-weighted image for a patient with unilateral left middle cerebral artery stenosis are presented in Fig 2. The position of the MRSI grid is shown in white.

Best-fit models and respective parameters for the voxelwise relationships are summarized in Table 2. We observed a significant, positive quadratic relationship for all voxels between BTR and CVR_{BOLD} (Fig 3; CVR coefficient, $P < .001$; CVR^2 coefficient, $P < .001$). A significant, negative quadratic relationship between baseline brain temperature and CVR_{BOLD} was also observed (CVR coefficient, $P = .008$; CVR^2 coefficient, $P < .001$). No significant global relationships were observed with CVR_{ASL} .

In the analysis of CVR_{ASL} , thresholded and dichotomized into voxels exhibiting either <30% augmentation (impaired) or $\geq 30\%$ augmentation (healthy), a significant linear relationship was observed for BTR with CVR_{ASL} of $\geq 30\%$ augmentation ($P = .001$). No significant relationships were observed for the thresholded CVR_{ASL} values with baseline brain temperature. Similarly, we used the CVR_{BOLD} values thresholded subject-wise at <70% (impaired) or $\geq 70\%$ (healthy) of the mean contralateral CVR augmentation. Significant relationships were observed between

BTR and CVR_{BOLD} of <70% (positive quadratic: CVR coefficient, $P < .001$; CVR^2 , coefficient, $P < .001$) and $\geq 70\%$ (linear, $P = .02$) of the mean contralateral hemisphere. Additionally, significant relationships for baseline brain temperature and CVR_{BOLD} of <70% (negative quadratic: CVR, $P < .001$; CVR^2 ,

$P < .001$) and $\geq 70\%$ (linear, $P = .001$) of the contralateral hemisphere were also observed.

We did not observe a significant difference in BTR ($P = .58$) or baseline temperature ($P = .38$) between the ipsilateral and contralateral hemispheres. However, within-subject variations (random-effects, Equation 4) were highly significant for both BTR ($P < .001$) and baseline brain temperature ($P < .001$).

DISCUSSION

The results support the presence of a BTR as a potential neuroimaging biomarker reflecting a hypothesized, convolved interaction of hemodynamic and metabolic tissue properties. The measurement of a BTR is feasible in routine clinical MR imaging implementations,

Table 1: Patient characteristics

Patient No.	Age (years)	Sex	Presentation and Diagnosis
1	41	F	Left-sided-predominate supraclinoid ICA stenosis
2	61	M	Left cervical ICA stenosis; aphasia
3	39	F	Right-sided-predominate ICA stenosis; recurrent minor stroke
4	32	F	Left MI stenosis; left monocular vision loss and recurrent right hemiparesis
5	56	M	Intracranial ICA stenosis; recurrent TIA
6	68	F	Left ICA stenosis; recurrent left hemispheric TIA and borderzone ischemia
7	33	F	Right-sided-predominate supraclinoid ICA stenosis; Moyamoya disease following STA-MCA bypass and recurrent TIA
8	36	F	Left MI stenosis; recurrent left deep borderzone ischemia
9	38	F	Right-sided-predominate intracranial stenosis; recurrent MCA infarctions
10	51	F	Left ICA stenosis; recurrent TIA

Note:—STA indicates superficial temporal artery.

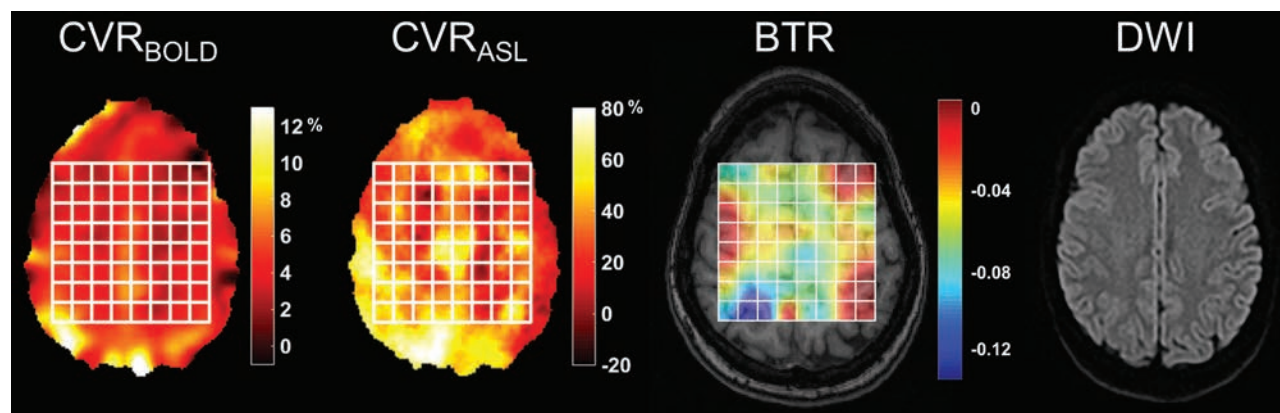


FIG 2. Representative CVR percentage augmentation maps calculated with BOLD and ASL, along with a BTR map overlaid on a T1-weighted image. Images are all from the same subject (a 32-year-old woman) with unilateral left MCA stenosis without infarction. The white grid overlay represents the MR thermometry grid derived from multivoxel spectroscopy analysis using the water-NAA chemical shift difference. Diffusion-weighted imaging demonstrates no evidence for acute infarction. Images are displayed in the radiologic convention. Impaired CVR in the left hemisphere is present in both BOLD and ASL, with a greater severity of impairment in ASL likely related to delay sensitivity and tag decay (see text). The BTR map demonstrates an asymmetric thermal response, with less brain cooling following vasodilatory stimulus in the diseased left hemisphere, indicated by lower and more positive BTR values and corresponding primarily to the areas of greatest impairment in the anterior and posterior MCA borderzone territories.

Table 2: Parameter estimates calculated with a mixed-effects model of BTR and baseline brain temperature as a function of CVR

	CVR				CVR ²				Intercept			
	Coefficient	F	df ^a	P Value	Coefficient	F	df ^a	P Value	Coefficient	F	df ^a	P Value ^b
BTR												
CVR _{BOLD}	−0.052	74.1	1, 513	<.001	0.0068	57.5	1, 619	<.001	0.031	6.0	1, 35	.02
CVR _{ASL}	0.0018	1.2	1, 8.0	.30	—	—	—	—	−0.069	205	1, 3.8	<.001
CVR _{BOLD} < 70 ^c	−0.096	59.7	1, 97	<.001	0.024	25.0	1, 128	<.001	0.031	2.8	1, 11	.12
CVR _{BOLD} ≥ 70 ^c	0.0070	5.5	1, 200	.02	—	—	—	—	−0.081	46.0	1, 51	<.001
CVR _{ASL} < 30 ^d	0.0018	1.1	1, 7.4	.33	—	—	—	—	−0.068	183.2	1, 69	<.001
CVR _{ASL} ≥ 30 ^d	0.0014	12.1	1, 47	.001	—	—	—	—	−0.10	33.5	1, 44	<.001
T _{pre} ^e (°C)												
CVR _{BOLD}	0.59	7.0	1, 598	.008	−0.13	14.8	1, 630	<.001	37.5	4871	1, 27	<.001
CVR _{ASL}	−0.039	0.9	1, 7.3	.39	—	—	—	—	38.4	8655	1, 6.0	<.001
CVR _{BOLD} < 70 ^c	2.1	19.5	1, 139	<.001	−0.65	12.9	1, 150	<.001	37.1	1810	1, 17	<.001
CVR _{BOLD} ≥ 70 ^c	−0.38	10.7	1, 429	.001	—	—	—	—	39.0	4575	1, 28	<.001
CVR _{ASL} < 30 ^d	−0.049	1.1	1, 6.8	.34	—	—	—	—	38.5	12,953	1, 6.5	<.001
CVR _{ASL} ≥ 30 ^d	0.0026	0.01	1, 198	.91	—	—	—	—	37.5	1094	1, 27	<.001

^a df calculated with the Satterthwaite approximation are reported as numerator, denominator.

^b P value represents the significance of a nonzero intercept.

^c CVR_{BOLD} values thresholded to 70% of the subject-wise mean contralateral value.

^d CVR_{ASL} values thresholded to 30% augmentation.

^e T_{pre} is the baseline brain temperature.

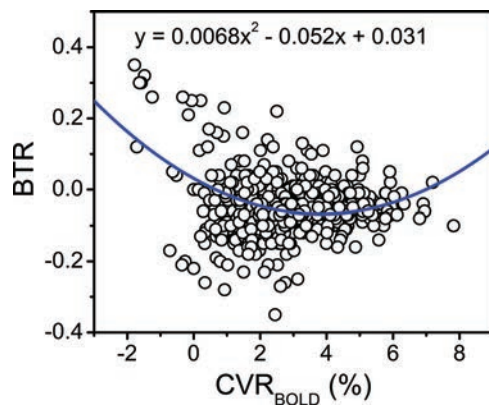


FIG 3. Voxelwise relationship of the BTR versus BOLD MR imaging signal augmentation following ACZ administration. The blue line and corresponding equation represent the fit of the raw data (circles) calculated with a mixed-effects model. A significant quadratic relationship between BTR and CVR_{BOLD} was identified for all voxels, wherein an initially negative slope is observed at low CVR_{BOLD} but a positive trend is observed for CVR_{BOLD} augmentation upward of approximately 4% (see “Results” and “Discussion”; F , $x^2 = 57.5$, $P < .001$; F , $x = 74.1$, $P < .001$).

with significant relationships identified between both BTR and baseline brain temperature relative to CVR, supporting further exploration of BTR as a fully noninvasive and dynamic biomarker. The use of voxelwise measurements facilitated a nuanced description of local hemodynamics and temperature, allowing contemporaneous, multiparametric classification of the diseased hemisphere, all potentially achievable in a single imaging session. MR chemical shift thermometry, exploiting the temperature-dependent difference between water and the methyl proton resonance of NAA, was chosen to approximate temperature using our previously reported protocol for phantom as well as human and nonhuman primate in vivo thermometry.^{19,24,25,33} The present study takes advantage of the unique pathophysiologic attributes of chronic cerebrovascular ischemia, in a cohort allowing multiphasic interrogation of a flow-temperature relationship, which may not be pragmatic in the clinical acute stroke setting. Ishigaki et al³⁶ previously reported the use of PET combined with localized, single-voxel MR spectroscopy-based thermometry to explore the relationship of brain temperature in steno-occlusive disease, observing positive correlations between the brain temperature difference (ipsilateral-contralateral hemisphere) with both CBV and OEF. A limited number of additional studies using single-voxel MR spectroscopy thermometry have observed higher temperatures in ischemic brain tissues, further supporting the investigation of brain temperature in the development of a pathophysiologic framework defining cerebral energetics.^{16,36-38}

Our analysis of the relationship between BTR and baseline brain temperature with CVR was performed voxelwise to examine whole-brain effects in patients with steno-occlusive disease. CVR and flow augmentation are generally hypothesized to reduce brain temperature and might, therefore, have been expected to produce a negative BTR. Our results were, however, more complex, and the observed flow-temperature relationship may not be immediately intuitive but, on deeper examination, can be reconciled with prevailing theories regarding cerebral blood flow, temperature, oxygen metabolism, and BOLD signal evolution. Exist-

ing models of cerebral temperature homeostasis propose a dynamic modulation of heat-producing mechanisms (oxygen cleavage from hemoglobin, glycolysis, and generation of metabolic by-products) and heat dissipation through the inflow of cooler systemic blood with lesser contributions from conduction to the brain surface. This is predicated on the notion of heat sink/radiator effects of inflowing blood, cooling tissues through the removal of metabolic waste.

We would also anticipate relative heating among those tissues with insufficient blood flow to meet metabolic demands. Conceptually, a linear or at least monotonically changing thermal response as a function of flow might be expected. However, several factors could interfere with this conceptual framework: 1) the temperature-flow relationship may vary radially within the brain, whereby superficial structures closer to the surface CSF are cooler than arterial inflow, thus warming with increasing flow; and 2) oxygen extraction, a primary contributor to the production of thermal waste, may be variably upregulated depending on the depth of misery perfusion, ostensibly at its highest among tissues with the most impaired flow. However, as demonstrated in several past studies, the capacity for flow augmentation may remain even among tissues with OEF elevation. The downregulation of OEF among such tissues during hemodynamic augmentation may occur on a time scale shorter than the duration of the BOLD scan and therefore shorter than the separation in time between CBF or thermometry imaging. This may, in part, drive a component of time shifts observed in BOLD signal augmentation if, for instance, a very high OEF must be overcome before BOLD augmentation can be detectable (ie, for deoxyhemoglobin dilution to occur sufficiently).³⁹ Accordingly, CVR augmentation following ACZ was initially anticipated to produce negative BTR values as a result of the increased inflow of cooler arterial blood, acting as a heat sink for warmer cerebral temperatures and removing metabolic by-products, including thermal waste.

Such interactions could underlie the observed quadratic relationship between BTR with CVR_{BOLD} , wherein a negative BTR-CVR relationship was present at a low CVR but a positive trend was observed for CVR_{BOLD} augmentation upward of approximately 4%. The far left of the curve follows the expected relationship, with decreasing (ie, more negative) BTR accompanied by increasing CVR augmentation and, indirectly, CBF. The source of the observed positive correlation between BTR and CVR above 4% remains inconclusive within the limitations of this exploratory analysis, in the absence of concurrent OEF and CMRO₂ interrogation (see below).

An opposing relationship (positive-versus-negative quadratic curve) was observed between baseline brain temperature and CVR_{BOLD} , suggesting that resting brain temperature alone may not fully explain the dynamics of the brain temperature response to a hemodynamic maneuver. This difference may, in part, reflect that baseline brain temperature is inherently a known indicator of diseased tissue energetics, with higher temperature associated positively with hypoperfusion and ischemia.^{16,19,36-38} The benefit of BTR is the ability to quantify a maneuver response, thus producing a form of physiologic contrast with the potential for characterizing not only static tissue impairment, as with baseline brain temperatures, but also the dynamics of the hemodynamic re-

sponse in a manner similar to that of CVR. The overall quadratic relationships suggest the presence of multiple regimes of temperature regulation or dysregulation across the brain, determined by additional hemodynamic parameters such as OEF and CMRO₂.

In addition to the relationships observed among BTR, baseline temperature, and CVR_{BOLD} for all voxels, significant associations were also observed for the CVR_{BOLD} values thresholded to 70% of the contralateral hemispheres, demonstrating a robust interaction between BTR and CVR_{BOLD}. The use of thresholding to explore voxelwise relationships enabled discrimination between impaired and healthy voxels, given the absence of a healthy control cohort undergoing the MR imaging ACZ protocol for comparison in this study.

Using CVR_{ASL} to study the same relationships resulted in a single significant correlation for BTR with CVR_{ASL} of $\geq 30\%$. Inherent challenges to ASL perfusion in highly delayed or low-flow environments, such as expected even in compensated territories downstream from steno-occlusive disease, may impact its use in this context, even when using multi-TI approaches to the extent governed by tag decay. We suspect that several, potentially divergent errors in ASL quantitation in such patients may have confounded the BTR relationship with CVR_{ASL}, among them: 1) exaggerated hypoperfusion if tagged spins are undelivered to the vascular network at the selected TI; 2) exaggerated hyperperfusion if tagged spins are delivered but linger in the arterial network overlying the tissue of interest (particularly when crusher gradients are not used, or when partial volume effects preclude reliable segmentation of the cortical tissues from such overlying vessels, both of which exist in our protocol); or 3) exaggerated hypoperfusion due to excessive tag decay, which may affect our measurements, particularly at the longest TI of 3000 ms. An additional circumstance of negative CVR_{ASL}, which we have observed to occur despite preserved BOLD and dynamic susceptibility contrast augmentation, exists in tissues with large delays. Arterial transit artifacts at baseline that spuriously elevate perfusion are somewhat cleared following ACZ but appear not to increase the apparent tissue perfusion to the same extent that the arterial transit artifacts previously had, therefore leading to apparently negative CVR. While exploratory, we suspect that temperature dynamics, together with flow, blood volume, and oxygen use, may be better subsumed by CVR_{BOLD}, albeit in an entangled manner requiring deeper, multiparametric study. Taken together, the observed trends imply the presence of at least 2 distinct regimes for BTR as a function of CVR augmentation: 1) decreasing BTR in response to increasing CVR (negative relationship) as predicted from existing models of brain temperature regulation, which we hypothesize may be dominated by heat-dissipating CBF augmentation over metabolic heat production, with decreasing temperatures in response to ACZ^{13,14}; and 2) a positive BTR-CVR regime in which increasing CVR augmentation is accompanied by increasing, or more positive, BTR values.

In line with previous work examining hemispheric differences in the study of hemodynamics and brain temperature,³⁶ we compared BTR and baseline brain temperature across hemispheres. Our analysis, however, did not reveal differences in baseline brain temperature and BTR between the ipsilateral and contralateral hemispheres such as those previously observed following isch-

emic injury.^{16,36} However, the lack of hemispheric temperature differences is not surprising because even in cases of unilateral disease, consequential hemodynamic impairment may not be limited to the affected hemisphere and compromised function and tissue damage may exist bilaterally and heterogeneously.³ Consequently, temperature differences resulting from impaired cerebral perfusion and impaired autoregulation may be averaged out in coarse hemispheric comparisons. Nevertheless, the presence of significant random-effects differences in BTR and baseline brain temperature between hemispheres could suggest that in a larger sample size, a difference may exist.

We acknowledge several study limitations. While it was designed to test our hypothesis regarding the association between brain temperature changes and hemodynamic augmentation, the lengthy, multiparametric protocol necessitated a 2-day study, which limited the sample size. The findings nevertheless emphasize the feasibility of dynamic brain thermometry in this setting and compel more rigorous study of BTR as a prognostic biomarker. A challenge in the analysis was the observation of negative CVR values, suggesting the possibility of vascular steal and limitations in the measurement of CBF.^{10,29} As discussed above, several possible mechanisms may contribute to negative CVR values, particularly arterial transit artifacts, collateral rather than antero-grade flow after ACZ, and the time scale of ASL-based measures of CVR. These may also contribute to spuriously high CVR values. As a result, continuous BOLD measurements may be a more reliable surrogate for the hemodynamic response to ACZ. The temporal dynamics of the ACZ response are worth considering. To mitigate potential errors related to a rapidly changing baseline, the initial BOLD signal used for CVR_{BOLD} in our study was derived from a pre-ACZ phase of the examination spanning the initial 5 minutes of BOLD acquisition. A uniform protocol was prescribed in which a slow infusion of ACZ was then administered for 3–5 minutes without patient repositioning or scan interruption, followed by ~10 more minutes of uninterrupted BOLD signal acquisition. It was recently reported that CVR_{BOLD} increases continuously following ACZ administration, reaching a plateau at approximately 8.5 minutes, which continues through the remainder of the acquisition.⁴⁰ While CVR delays beyond 20 minutes are difficult to exclude, we expect that the window of maximal augmentation is likely captured within this study design.

While we cannot conclusively parcellate the competing hemodynamic effects from the technical challenges, further studies with MR-based methods to characterize functional activity, CBF, and metabolism in cerebrovascular disease would complement our results. While direct estimation of OEF and CMRO₂ with MR-based techniques remains challenging, ongoing efforts to optimize MR oximetry measurements will enable further studies into the relationship of BTR with these metabolic parameters.⁸ A more thorough description could be facilitated through study of a healthy control population; however, administration of intravenous vasodilatory stimuli is not common practice in our experience. Other approaches such as induced hypercapnia or breath-hold may be valuable in this regard, though the mechanism, depth, and magnitude of flow augmentation may differ. Last, the relatively small sample size and limited longitudinal follow-up information in this cohort of patients limit our characterization of

BTR as a prognostic tool to predict future stroke risk in such patients. Further study in a larger and, ideally, prospectively collected cohort is warranted to better assess the prognostic power of BTR in a clinical population.

CONCLUSIONS

These findings suggest the feasibility and potential utility of non-invasive brain thermometry during the dynamic modulation of CBF and CVR, supporting further exploration of BTR as a potential biomarker in patients with steno-occlusive cerebrovascular disease. These results compel further study into the mechanistic nature of cerebral temperature regulation and the potential use of noninvasive MR thermometry in the diagnosis, prognostication, and treatment selection in chronic steno-occlusive disease.

Disclosures: Candace C. Fleischer—UNRELATED: Grants/Grants Pending: National Institutes of Health, Comments: National Institutes of Health postdoctoral fellowship (F32CA199834); Support for Travel to Meetings for the Study or Other Purposes: International Society for Magnetic Resonance in Medicine, Comments: International Society for Magnetic Resonance in Medicine travel award to attend the annual meeting in Singapore to present this work. Deqiang Qiu—UNRELATED: Grants/Grants Pending: Medtronic and Siemens Healthcare, Comments: research support*. Fadi Nahab—UNRELATED: Expert Testimony: Grant Law Firm, Comments: pertains to cases of stroke treatment, not imaging of stroke; Payment for Lectures Including Service on Speakers Bureaus: Medtronic, American Heart Association/American Stroke Association, Genzyme, Comments: lectures on cryptogenic stroke, Fabry disease; Payment for Development of Educational Presentations: Imedex, Comments: education on cryptogenic stroke. Seena Dehkharghani—UNRELATED: Travel/Accommodations/Meeting Expenses Unrelated to Activities Listed: Society of Vascular and Interventional Neurology and All India Institute of Medical Sciences, Comments: travel expenses paid by the Society of Vascular and Interventional Neurology and All India Institute of Medical Sciences as an invited speaker. *Money paid to the institution.

REFERENCES

1. Yamauchi H, Higashi T, Kagawa S, et al. Is misery perfusion still a predictor of stroke in symptomatic major cerebral artery disease? *Brain* 2012;135:2515–26 [CrossRef Medline](#)
2. Powers WJ. Stroke: misery perfusion in cerebrovascular disease—is it important? *Nat Rev Neurol* 2012;8:479–80 [CrossRef Medline](#)
3. Derdeyn CP, Videen TO, Yundt KD, et al. Variability of cerebral blood volume and oxygen extraction: stages of cerebral haemodynamic impairment revisited. *Brain* 2002;125(pt 3):595–607 [Medline](#)
4. Powers WJ. Cerebral hemodynamics in ischemic cerebrovascular disease. *Ann Neurol* 1991;29:231–40 [CrossRef Medline](#)
5. Nemoto EM, Yonas H, Pindzola RR, et al. PET OEF reactivity for hemodynamic compromise in occlusive vascular disease. *J Neuroimaging* 2007;17:54–60 [CrossRef Medline](#)
6. Heiss WD, Podreka I. Role of PET and SPECT in the assessment of ischemic cerebrovascular disease. *Cerebrovasc Brain Metab Rev* 1993;5:235–63 [Medline](#)
7. Okazawa H, Yamauchi H, Toyoda H, et al. Relationship between vasodilatation and cerebral blood flow increase in impaired hemodynamics: a PET study with the acetazolamide test in cerebrovascular disease. *J Nucl Med* 2003;44:1875–83 [Medline](#)
8. Christen T, Bolar DS, Zaharchuk G. Imaging brain oxygenation with MRI using blood oxygenation approaches: methods, validation, and clinical applications. *AJNR Am J Neuroradiol* 2013;34:1113–23 [CrossRef Medline](#)
9. Mandell DM, Han JS, Poulblanc J, et al. Mapping cerebrovascular reactivity using blood oxygen level-dependent MRI in patients with arterial steno-occlusive disease: comparison with arterial spin labeling MRI. *Stroke* 2008;39:2021–28 [CrossRef Medline](#)
10. Rogg J, Rutigliano M, Yonas H, et al. The acetazolamide challenge: imaging techniques designed to evaluate cerebral blood flow reserve. *AJR Am J Roentgenol* 1989;153:605–12 [CrossRef Medline](#)
11. Markus H, Cullinane M. Severely impaired cerebrovascular reactivity predicts stroke and TIA risk in patients with carotid artery stenosis and occlusion. *Brain* 2001;124:457–67 [CrossRef Medline](#)
12. Gupta A, Chazen JL, Hartman M, et al. Cerebrovascular reserve and stroke risk in patients with carotid stenosis or occlusion: a systematic review and meta-analysis. *Stroke* 2012;43:2884–91 [CrossRef Medline](#)
13. Wang H, Wang B, Normoyle KP, et al. Brain temperature and its fundamental properties: a review for clinical neuroscientists. *Front Neurosci* 2014;8:307 [CrossRef Medline](#)
14. Sukstanskii AL, Yablonskiy DA. An analytical model of temperature regulation in human head. *J Therm Biol* 2004;29:583–87 [CrossRef](#)
15. Reith J, Jørgensen HS, Pedersen PM, et al. Body temperature in acute stroke: relation to stroke severity, infarct size, mortality, and outcome. *Lancet* 1996;347:422–25 [CrossRef Medline](#)
16. Karaszewski B, Wardlaw JM, Marshall I, et al. Measurement of brain temperature with magnetic resonance spectroscopy in acute ischemic stroke. *Ann Neurol* 2006;60:438–46 [CrossRef Medline](#)
17. Campos F, Blanco M, Barral D, et al. Influence of temperature on ischemic brain: basic and clinical principles. *Neurochem Int* 2012;60:495–505 [CrossRef Medline](#)
18. Dehkharghani S, Bowen M, Haussen DC, et al. Body temperature modulates infarction growth following endovascular reperfusion. *AJNR Am J Neuroradiol* 2017;38:46–51 [CrossRef Medline](#)
19. Dehkharghani S, Fleischer CC, Qiu D, et al. Cerebral temperature dysregulation: MR thermographic monitoring in a nonhuman primate study of acute ischemic stroke. *AJNR Am J Neuroradiol* 2017;38:712–20 [CrossRef Medline](#)
20. McDannold N. Quantitative MRI-based temperature mapping based on the proton resonant frequency shift: review of validation studies. *Int J Hyperthermia* 2005;21:533–46 [CrossRef Medline](#)
21. Corbett RJT, Purdy PD, Laptook AR, et al. Noninvasive measurement of brain temperature after stroke. *AJNR Am J Neuroradiol* 1999;20:1851–57 [Medline](#)
22. Castillo J, Martinez F, Leira R, et al. Mortality and morbidity of acute cerebral infarction related to temperature and basal analytic parameters. *Cerebrovasc Dis* 1994;4:66–71 [CrossRef](#)
23. Scheenen TW, Klomp DW, Wijnen JP, et al. Short echo time 1H-MRSI of the human brain at 3T with minimal chemical shift displacement errors using adiabatic refocusing pulses. *Magn Reson Imaging* 2008;24:1–6 [Medline](#)
24. Fleischer CC, Qiu D, Zhong X, et al. Multivoxel proton magnetic resonance spectroscopy for non-invasive thermometry: improvements in spectral quality using semiLASER with GRE shim. *Proc Int Soc Magn Reson Med* 2015;23:4062
25. Dehkharghani S, Fleischer CC, Qiu D, et al. Relationship between cerebrovascular reserve and brain temperature following acetazolamide challenge in patients with chronic steno-occlusive disease. *Proc Int Soc Magn Reson Med* 2016;24:0601
26. Chappell MA, MacIntosh BJ, Donahue MJ, et al. Separation of macrovascular signal in multi-inversion time arterial spin labeling MRI. *Magn Reson Med* 2010;63:1357–65 [CrossRef Medline](#)
27. Günther M, Oshio K, Feinberg DA. Single-shot 3D imaging techniques improve arterial spin labeling perfusion measurements. *Magn Reson Med* 2005;54:491–98 [CrossRef Medline](#)
28. Bonte FJ, Devous MD, Reisch JS, et al. The effect of acetazolamide on regional cerebral blood flow in patients with Alzheimer's disease or stroke as measured by single-photon emission computed tomography. *Invest Radiol* 1989;24:99–103 [CrossRef Medline](#)
29. Vagal AS, Leach JL, Fernandez-Ulloa M, et al. The acetazolamide challenge: techniques and applications in the evaluation of chronic cerebral ischemia. *AJNR Am J Neuroradiol* 2009;30:876–84 [Medline](#)
30. Okazawa H, Yamauchi H, Sugimoto K, et al. Effects of acetazolamide on cerebral blood flow, blood volume, and oxygen metabolism: a positron emission tomography study with healthy volunteers. *J Cereb Blood Flow Metab* 2001;21:1472–79 [CrossRef Medline](#)
31. Smith SM. Fast robust automated brain extraction. *Hum Brain Mapp* 2002;17:143–55 [CrossRef Medline](#)
32. Provencher SW. Automatic quantitation of localized in vivo 1H

- spectra with LCModel. *NMR Biomed* 2001;14:260–64 [CrossRef](#) [Medline](#)
33. Dehkharghani S, Mao H, Howell L, et al. **Proton resonance frequency chemical shift thermometry: experimental design and validation toward high-resolution noninvasive temperature monitoring and in vivo experience in a nonhuman primate model of acute ischemic stroke.** *AJNR Am J Neuroradiol* 2015;36:1128–35 [CrossRef](#) [Medline](#)
 34. Kuroda K. **Non-invasive MR thermography using the water proton chemical shift.** *Int J Hyperthermia* 2005;21:547–60 [CrossRef](#) [Medline](#)
 35. Kass RE, Raftery AE. **Bayes factors.** *J Am Stat Assoc* 1995;90:773–95 [CrossRef](#)
 36. Ishigaki D, Ogasawara K, Yoshioka Y, et al. **Brain temperature measured using proton MR spectroscopy detects cerebral hemodynamic impairment in patients with unilateral chronic major cerebral artery steno-occlusive disease: comparison with positron emission tomography.** *Stroke* 2009;40:3012–16 [CrossRef](#) [Medline](#)
 37. Marshall I, Karaszewski B, Wardlaw JM, et al. **Measurement of regional brain temperature using proton spectroscopic imaging: validation and application to acute ischemic stroke.** *Magn Reson Imaging* 2006;24:699–706 [CrossRef](#) [Medline](#)
 38. Murakami T, Ogasawara K, Yoshioka Y, et al. **Brain temperature measured by using proton MR spectroscopy predicts cerebral hyperperfusion after carotid endarterectomy.** *Radiology* 2010;256:924–31 [CrossRef](#) [Medline](#)
 39. Wu J, Dehkharghani S, Nahab F, et al. **The effects of acetazolamide on the evaluation of cerebral hemodynamics and functional connectivity using blood oxygen level–dependent MR imaging in patients with chronic steno-occlusive disease of the anterior circulation.** *AJNR Am J Neuroradiol* 2017;38:139–45 [CrossRef](#) [Medline](#)
 40. Wu J, Dehkharghani S, Nahab F, et al. **Acetazolamide-augmented dynamic bold (aczBOLD) imaging for assessing cerebrovascular reactivity in chronic steno-occlusive disease of the anterior circulation: an initial experience.** *Neuroimage Clin* 2017;13:116–22 [CrossRef](#) [Medline](#)

Added Value of Arterial Spin-Labeling MR Imaging for the Differentiation of Cerebellar Hemangioblastoma from Metastasis

K.M. Kang, C.-H. Sohn, S.-H. You, J.G. Nam, S.H. Choi, T.J. Yun, R.-E. Yoo, and J.-h. Kim



ABSTRACT

BACKGROUND AND PURPOSE: In adults with only cerebellar masses, hemangioblastoma and metastasis are the 2 most important differential diagnoses. Our aim was to investigate the added value of arterial spin-labeling MR imaging for differentiating hemangioblastoma from metastasis in patients with only cerebellar masses.

MATERIALS AND METHODS: This retrospective study included a homogeneous cohort comprising patients with only cerebellar masses, including 16 hemangioblastomas and 14 metastases. All patients underwent enhanced MR imaging, including arterial spin-labeling. First, the presence or absence of a hyperperfused mass was determined. Next, in the hyperperfused mass, relative tumor blood flow (mean blood flow in the tumor divided by blood flow measured in normal-appearing cerebellar tissue) and the size ratio (size in the arterial spin-labeling images divided by size in the postcontrast T1WI) were measured. To validate the arterial spin-labeling findings, 2 observers independently evaluated the conventional MR images and the combined set of arterial spin-labeling images.

RESULTS: All patients with hemangioblastomas and half of the patients with metastases presented with a hyperperfused mass ($P < .001$). The size ratio and relative tumor blood flow were significantly larger for hemangioblastomas than for metastases ($P < .001$ and $P = .039$, respectively). The size ratio revealed excellent diagnostic power (area under the curve = 0.991), and the relative tumor blood flow demonstrated moderate diagnostic power (area under the curve = 0.777). The diagnostic accuracy of both observers was significantly improved after the addition of arterial spin-labeling; the area under the curve improved from 0.574 to 0.969 ($P < .001$) for observer 2 and from 0.683 to 1 ($P < .001$) for observer 1.

CONCLUSIONS: Arterial spin-labeling imaging can aid in distinguishing hemangioblastoma from metastasis in patients with only cerebellar masses.

ABBREVIATIONS: ASL = arterial spin-labeling; AUC = area under the curve; ROC = receiver operating characteristic; rTBF = relative tumor blood flow

Hemangioblastoma and metastasis are the 2 most important differential diagnoses of cerebellar masses in adults. Hemangioblastomas are benign tumors of vascular origin and are the second most common infratentorial parenchymal tumor, ac-

counting for 7% of posterior fossa tumors in adults.¹ Metastases are the most common type of brain tumor, and posterior fossa metastases represent approximately 8.7%–10.9% of all brain metastases.^{2,3} Discriminating between hemangioblastoma and brain metastasis is important because their therapeutic approaches and prognoses are quite different. The standard treatment for hemangioblastoma is complete surgical resection. However, patients with a brain metastasis usually undergo surgery, stereotactic surgery, whole-brain radiation therapy, chemotherapy, or a combination of these. Furthermore, hemangioblastomas are associated with longer patient survival times,⁴ whereas brain metastases are associated with a poor prognosis.⁵ Because the frequency of metastasis increases with time, patient age is often helpful in distinguishing between these tumors but is not always reliable. In addition, although one-third of patients with cerebellar hemangioblastomas also have von Hippel-Lindau disease,⁶ a clinical history of von Hip-

Received April 20, 2017; accepted after revision June 30.

From the Department of Radiology (K.M.K., C.-H.S., J.G.N., S.H.C., T.J.Y., R.-E.Y., J.-h.K.), Seoul National University Hospital, Seoul, Korea; Department of Radiology (C.-H.S., S.H.C.), Seoul National University College of Medicine, Seoul, Korea; and Department of Radiology (S.-H.Y.), Korea University Hospital, Seoul, Korea.

This study was supported by a grant from the Ministry of Science, ICT and Future Planning (grant No. NRF-2014M3C7A1046042).

Paper previously presented at: Annual Meeting of the American Society of Neuroradiology, April 22–27, 2017; Long Beach, California.

Please address correspondences to Chul-Ho Sohn, MD, PhD, Department of Radiology, Seoul National University Hospital, 101, Daehangno, Jongno-gu, Seoul 110-744, Korea; e-mail: neurorad63@gmail.com

Indicates open access to non-subscribers at www.ajnr.org

Indicates article with supplemental on-line table.

<http://dx.doi.org/10.3174/ajnr.A5363>

pel-Lindau disease may not be available at the time of initial presentation.

Hemangioblastoma is characterized by markedly increased vascularity⁷; therefore, angiographically dense tumor staining may suggest hemangioblastoma rather than metastasis.⁸ However, cerebral angiography is invasive and involves risks of complications, such as stroke. MR perfusion imaging can provide useful information about vascularization in hemangioblastoma. Previous studies using dynamic susceptibility contrast and dynamic contrast-enhanced MR perfusion imaging have reported increased vascular perfusion in hemangioblastomas.^{9,10}

Arterial spin-labeling (ASL), unlike DSC and dynamic contrast-enhanced perfusion imaging, is a noninvasive MR perfusion technique that uses electromagnetic endogenous arterial water as a freely diffusible tracer instead of an exogenous MR imaging contrast agent. The utility of ASL perfusion imaging in the evaluation of the vascularity of brain tumors has been explored in several recent studies.^{11–14} One prior study differentiated hemangioblastomas from metastases on the basis of quantitative blood flow measurements using ASL.¹⁵ The authors reported that tumor blood flow was significantly higher in hemangioblastomas than in metastases. However, their study included a limited number of patients and examined metastatic tumors located primarily in the supratentorial region. Because metastasis usually presents with multiple enhancing supratentorial and infratentorial masses and 90%–95% of hemangioblastomas are in the posterior fossa, it is difficult to differentiate hemangioblastoma from metastasis in patients with only cerebellar masses in daily clinical practice.

Therefore, the aim of this study was to determine whether the addition of ASL imaging is useful for differentiating hemangioblastoma from metastasis in a homogeneous cohort of patients with only cerebellar masses and to validate the findings by investigating observer performance.

MATERIALS AND METHODS

This study was approved by our institutional review board, and informed consent was waived due to its retrospective nature.

Subjects

After a review of our radiology data base from October 2011 to October 2016, we identified 112 consecutive patients with cerebellar hemangioblastomas who satisfied the following inclusion criteria: 1) patients whose histopathologic diagnoses were confirmed as cerebellar hemangioblastomas or patients with von Hippel-Lindau disease having probable cerebellar hemangioblastomas, and 2) patients who did not have supratentorial mass lesions. For the patients with von Hippel-Lindau disease having probable cerebellar hemangioblastomas, the diagnosis of hemangioblastoma was made on the basis of radiologic evidence showing no other tumors with metastatic potential, including renal cell carcinomas, pheochromocytomas, or pancreatic neuroendocrine tumors. Of these patients, 96 were excluded for the following reasons: 1) lack of ASL images ($n = 95$), or 2) no contrast-enhanced MR imaging ($n = 1$). The remaining 16 patients were included in this study. Ten of the 16 patients had von Hippel-Lindau disease. Among the final 16 patients, 14 had pathologic confirmations of hemangioblastomas, and 2 had von Hippel-

Lindau disease; abdominal CT revealed 2 hemangiomas in the liver in 1 patient and multiple serous cystadenomas in the pancreas in the other.

We found 129 patients suspected of having cerebellar metastases who met the following inclusion criteria: 1) patients whose histopathologic diagnoses were confirmed as cerebellar metastases or patients whose diagnoses were made on the basis of their clinical history and follow-up imaging studies,¹⁶ and 2) patients who did not have supratentorial mass lesions. Of these patients, 115 were excluded on the basis of the following criteria: 1) the presence of leptomeningeal seeding ($n = 28$), 2) history of previous radiation therapy or gamma knife surgery ($n = 18$), 3) coexisting acute infarction ($n = 28$), 4) no contrast-enhanced MR imaging ($n = 1$), and 5) lack of ASL images ($n = 40$). Finally, 14 patients with cerebellar metastases confirmed by imaging follow-up ($n = 12$) or pathologic examination ($n = 2$) were included in the analysis.

MR Imaging Protocol

All patients underwent MR imaging with a 1.5T (Signa HDxt; GE Healthcare, Milwaukee, Wisconsin) or 3T (Discovery 750w; GE Healthcare) MR imaging scanner with an 8- or 32-channel head coil. Imaging sequences included FSE T2WI, contrast-enhanced spin-echo T1WI, and ASL images. MR imaging parameters were as follows: TR = 467–567 ms, TE = 8–9 ms, flip angle = 90°, and matrix = 320 × 192 for spin-echo T1WI; TR = 4850–5330 ms, TE = 92–127 ms, flip angle = 90°–142°, and matrix = 448 × 256 for FSE T2WI; and section thickness = 5 mm with a 1-mm gap, FOV = 240 × 240 mm for T1WI and T2WI. Contrast-enhanced T1WI was acquired after intravenous administration of gadobutrol (Gadovist; Bayer Schering Pharma, Berlin, Germany) at a dose of 0.1 mmol per kilogram of body weight.

ASL images were acquired before administration of the contrast agent. ASL perfusion imaging was performed with a pseudo-continuous ASL pulse sequence, which significantly increases the flow-labeling efficacy in a single-coil setting.^{17,18} ASL images were acquired for 1.5 seconds of labeling followed by 1.5 seconds of labeling delay. Saturation pulses were used to suppress the background.¹⁹ The image acquisition consisted of a stack of interleaved 3D fast spin-echo spiral readouts, each of which lasted 4 ms. Each spiral arm included 512 sampling points in k -space, and a total of 8 interleaves (arms) were acquired separately. The ASL parameters were as follows: TR = 4446–4564 ms, TE = 9.4–9.9 ms, echo-train length = 1, FOV = 240 × 240 mm, matrix = 128 × 128, number of excitations = 3, number of interleaved sections = 32, section thickness = 5–6 mm, intersection gap = 0 mm, and number of sections = 32–44. The signal intensity change between the labeled image and the control image was fitted to a model from which a quantitative perfusion map of cerebral blood flow was obtained.²⁰

Image Analysis

Two radiologists (a qualified neuroradiologist with 8 years of clinical experience and a third-year resident radiologist) who were blinded to the clinical and pathologic information independently reviewed the MR image sets in a random order. First, they reviewed the ASL images and determined the presence or absence of

Table 1: Results of intra- and interobserver reproducibility^a

	Hemangioblastomas		Metastases	
	Intraobserver	Interobserver	Intraobserver	Interobserver
Size of an enhancing mass on postcontrast T1WI (a)	0.900 (0.739–0.964)	0.975 (0.931–0.991)	0.987 (0.927–0.998)	0.983 (0.916–0.997)
Size of a hyperintense mass on ASL images (b)	0.786 (0.489–0.920)	0.958 (0.886–0.985)	0.973 (0.850–0.995)	0.935 (0.705–0.998)
Size ratio (b/a)	0.862 (0.649–0.949)	0.934 (0.825–0.976)	0.730 (0.049–0.948)	0.801 (–0.159–0.966)
rTBF	0.824 (0.567–0.935)	0.643 (0.246–0.858)	0.996 (0.979–0.999)	0.969 (0.853–0.995)

^a Data are intraclass correlation coefficient values, and the numbers in parentheses are 95% CIs.

a hyperperfused cerebellar mass in each patient. The hyperperfused mass was defined as a space-occupying hyperintense lesion compared with the appearance of normal gray matter on the CBF map from ASL imaging. In case of a hyperperfused mass, quantitative analyses were performed. The size of the mass was measured as the largest axial diameter on both the postcontrast T1WI and the CBF map from ASL imaging. The size ratio was calculated as the size on the CBF map divided by the size on the postcontrast T1WI.

Absolute tumor blood flow was calculated as the mean blood flow in an ROI, which was drawn over the hyperperfused mass on the section showing the largest cross-sectional area.¹⁵ Then, relative tumor blood flow (rTBF) was calculated by normalizing the absolute tumor blood flow to the blood flow measured in cortical gray matter with a normal appearance in the contralateral hemisphere based on methods in previous reports.^{15,21} An ROI of >100 mm² was selected in normal-appearing cortical gray matter. The reference ROI was placed in the same section as the one with the ROI for the tumor or the nearest section. In the case of tumors located across the midline, the reference ROI was placed in the cortical gray matter of the side in which the tumor was least present.

To assess the intraobserver reproducibility of the measurements, the qualified neuroradiologist with 8 years of clinical experience performed the size measurements and ROI placement twice at 2-week intervals. The mean value of the repeat measurements was used to determine the tumor size, size ratio, and rTBF. Mean ROI sizes were 83.3 ± 100 mm² for hemangioblastomas and 204.4 ± 75.6 mm² for their corresponding contralateral gray matter; and 68.8 ± 46.3 mm² for metastases and 267.2 ± 66.8 mm² for their corresponding contralateral gray matter.

Observer Performance

To investigate the added value of ASL imaging with conventional MR imaging for predicting hemangioblastomas, 2 qualified neuroradiologists (with 27 and 7 years of clinical experience, individually) who were blinded to the patients' histories and pathologic data independently reviewed 2 MR image sets—that is, the conventional image set including precontrast T1WI, T2WI, and postcontrast T1WI, and the combined ASL image set of the conventional image set and the CBF map derived from ASL perfusion imaging. For the conventional image set, hemangioblastoma diagnoses were made according to the following findings: a markedly enhancing mural nodule with a large surrounding cyst, a solid enhancing nodule, or the presence of large draining and feeding vessels within the periphery and a solid nodule.^{8,22} For the combined ASL image set, the observers were provided with the predictive findings, the measurement results (median and ranges) of each tumor, and the

Table 2: Results of the comparative analyses^a

	Hemangioblastomas (n = 16)	Metastases (n = 7)	P Value ^b
Size ratio ^b	1.4 (0.95–3.64)	0.80 (0.60–0.98)	<.001
rTBF ^b	8.18 (1.95–17.15)	2.44 (1.88–14.36)	.039

^a Size, rTBF, and size ratio data are presented as median values, and the numbers in parentheses are the lowest and highest values.

^b Mann-Whitney *U* test comparing the size ratio and rTBF between hemangioblastomas and metastases.

diagnostic performances of rTBF and the size ratio, which were acquired from the above image analyses.

For each set, the observers were asked to predict the presence of a hemangioblastoma according to the provided criteria, and they recorded their confidence levels with the following 5-point scale: 1, definitely metastasis; 2, probably metastasis; 3, indeterminate lesion; 4, probably hemangioblastoma; and 5, definitely hemangioblastoma.

Statistical Analysis

Intra- and interobserver reproducibility for the size, size ratio, and rTBF were assessed by calculating intraclass correlation coefficients.²³ The Fisher exact test was used to compare the frequencies of a hyperperfused mass between hemangioblastomas and metastases. The difference in sizes between the postcontrast T1WI and the CBF map was evaluated with the Wilcoxon signed rank test for hemangioblastomas and metastases. The size ratios and rTBF values were compared between hemangioblastomas and metastases with the Mann-Whitney test. A receiver operating characteristic (ROC) curve analysis was performed to evaluate the diagnostic performance of the size ratio and rTBF for differentiating hemangioblastoma from cerebellar metastasis. In addition, a pair-wise comparison of the ROC curves was performed to compare the diagnostic accuracies of the size ratio and rTBF.

For observer performance, interobserver variability regarding the confidence level for diagnosing hemangioblastoma was assessed with κ statistics. The diagnostic performance of each observer was assessed with an ROC curve analysis. To compare the diagnostic accuracy before and after evaluating the ASL images, we performed a pair-wise comparison of the ROC curves. We used 95% confidence intervals to express the statistical precision of the results. Sensitivity, specificity, and diagnostic accuracy were calculated for both observers on the assumption that a confidence level of 4 or higher was positive for the diagnosis of hemangioblastoma. Under this assumption, the McNemar test was used to compare the overall accuracy before and after evaluating additional ASL images.

Statistical analyses were performed with MedCalc for Windows (Version 9.3.0.0; MedCalc Software, Mariakerke, Belgium). *P* < .05 was considered statistically significant.

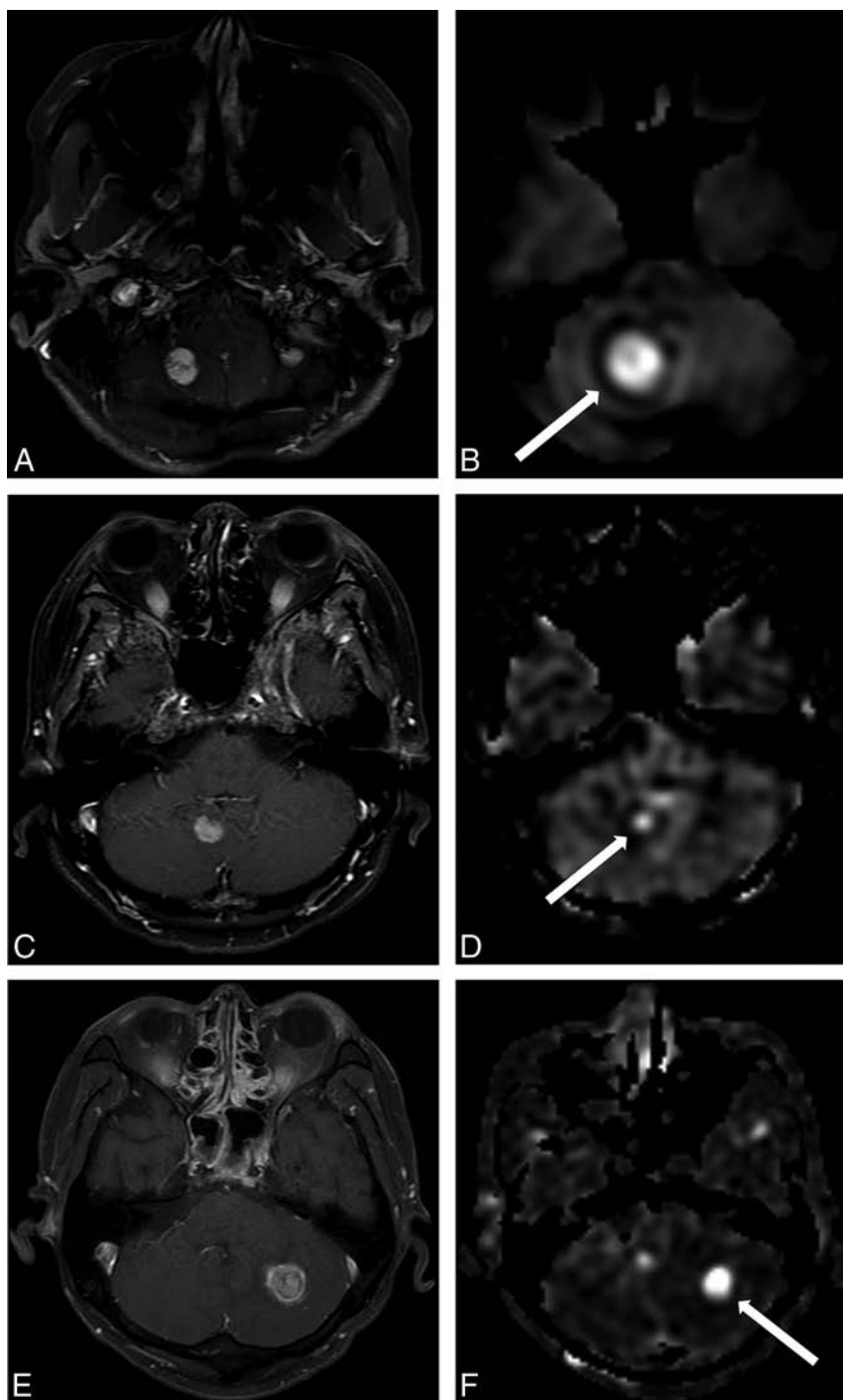


FIG 1. Contrast-enhanced TIWI (A and C) and CBF maps derived from ASL imaging (B and D) for 2 representative cases. A and B, A cerebellar hemangioblastoma in a 36-year-old woman with a high size ratio of 1.92 and rTBF of 6.16. C and D, A cerebellar metastasis in a 42-year-old woman with breast cancer with a relatively low size ratio of 0.71 and rTBF of 2.1. E and F, A cerebellar metastasis in a 56-year-old man with renal cell carcinoma with a size ratio of 0.82 and rTBF of 14.36.

RESULTS

Patients with cerebellar hemangioblastomas included 11 men (mean age, 41.8 years; range, 20–71 years) and 5 women (mean age, 44.2 years; range, 36–62 years). Patients with cerebellar metastases included 8 men (mean age, 60.6 years; range, 41–76 years) and 6 women (mean age, 47.3 years; range, 40–58 years). The primary types of cancer in these patients were as follows: lung cancer ($n = 6$), breast cancer ($n = 5$), gastric cancer ($n = 1$), colon

cancer ($n = 1$), and renal cell carcinoma ($n = 1$). Three of the 16 patients with hemangioblastomas and 2 of the 14 patients with metastases had >2 masses. In patients with multiple hyperperfused masses, the largest representative mass was included in the following quantitative analyses.

Image Analysis for Differentiating Hemangioblastoma from Metastasis

The presence of at least 1 hyperperfused mass in the cerebellum was observed in all 16 patients with hemangioblastomas and in 7 of the 14 (50%) patients with metastases by both reviewers, with 100% agreement. There was a significant difference in the frequency of hyperperfused cerebellar masses between patients with hemangioblastomas and those with metastases ($P = .0002$). Hyperperfused cerebellar metastases were observed in patients with lung cancer ($n = 2$), breast cancer ($n = 2$), gastric cancer ($n = 1$), colon cancer ($n = 1$), and renal cell carcinoma ($n = 1$). The other lung ($n = 4$) and breast cancer ($n = 3$) metastases did not demonstrate hyperperfusion. The analyses described below were performed on the hyperperfused masses (16 hemangioblastomas and 7 metastases).

The intraclass correlation coefficient values, with 95% CIs, were calculated for the size, size ratio, and rTBF data, as shown in Table 1. For both hemangioblastomas and metastases, the intra- and interobserver agreements were fair to excellent for the size, size ratio, and rTBF values.

The Wilcoxon signed rank test of the paired samples revealed that the measured size of hemangioblastomas was significantly larger on the CBF map (median, 16.04 mm; range, 6.75–46.27 mm) than on the postcontrast T1WI (median, 20.12 mm; range, 8.87–33.70 mm; $P < .001$). Conversely, the measured size of hyperperfused metastases was significantly larger on the postcontrast T1WI (median,

25.02 mm; range, 12.47–36.24 mm) than on the CBF map (median, 20.12 mm; range, 8.87–33.70 mm; $P = .016$). The Mann-Whitney test revealed that the size ratio of hemangioblastomas was significantly larger than that of metastases ($P < .001$). Furthermore, the rTBF of hemangioblastomas was significantly higher than that of metastases ($P = .039$). The results are summarized in Table 2. Representative images are shown in Fig 1.

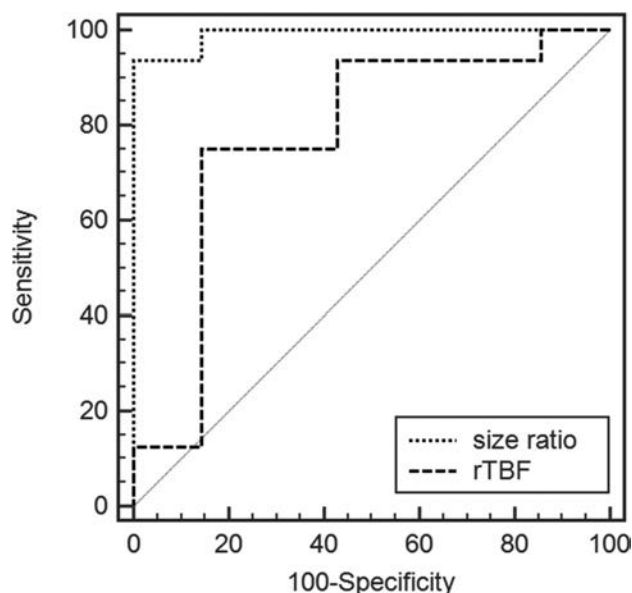


FIG 2. ROC curves used to differentiate hemangioblastomas from metastases by comparing size ratio and rTBF values. The AUC values for the rTBF and size ratio were 0.777 and 0.991, respectively.

According to the ROC analysis, the area under the curve (AUC) was 0.991 (95% CI, 0.83–1.000) for the size ratio and 0.777 (95% CI, 0.557–0.922) for the rTBF. A size ratio of >0.98 could differentiate hemangioblastomas from hyperperfused metastases with a sensitivity of 93.7% (15/16), a specificity of 100% (7/7), and an accuracy of 91% (40/44). A rTBF of >3.78 corresponded to a sensitivity of 75% (12/16), a specificity of 85.7% (6/7), and an accuracy of 78.3% (18/23) (Fig 2). Although the AUC value for the size ratio (0.991) was higher than for the rTBF (0.777), they were not significantly different in the comparison of ROC curves ($P = .062$).

There were no significant differences in the frequencies of hemangioblastomas and metastases between patients examined with 3T and 1.5T magnets ($P = .657$). Nine of the 16 patients with hemangioblastomas and 8 of the 14 patients with metastases underwent MR imaging at 1.5T, and the others underwent MR imaging at 3T. Among 7 patients with hyperperfused metastases, 5 underwent MR imaging at 1.5T. Detailed results for the size ratio and rTBF data regarding magnetic strength are summarized in the On-line Table.

Observer Performance

Interobserver agreement was improved from poor ($\kappa = 0.384$; 95% CI, 0.217–0.551) to excellent ($\kappa = 0.911$; 95% CI, 0.777–1) after the addition of ASL imaging to conventional image sets. The diagnostic accuracy in the differentiation of hemangioblastomas from metastases was significantly improved for both observers after they reviewed the ASL images: The AUC improved from 0.574 to 0.969 ($P < .001$) for observer 1 and from 0.683 to 1 ($P < .001$) for observer 2 (Table 3 and Fig 3). The McNemar test revealed that the overall accuracy significantly improved for both observers after the addition of the ASL images (observer 1, $P = .0005$; observer 2, $P = .022$). Additional ASL image interpretation enabled observers to correct several diagnostic errors (observer 1,

Table 3: Diagnostic predictive values for the differentiation of hemangioblastomas from metastases^a

Reading Session and Statistic	Observer 1	Observer 2
Conventional image set		
AUC ^b	0.594 (0.400–0.768)	0.683 (0.489–0.840)
Sensitivity (%)	18.8 (3/16)	43.7 (7/16)
Specificity (%)	100 (14/14)	92.9 (13/14)
Accuracy (%)	57 (17/30)	67 (20/30)
Combined ASL image set		
AUC ^b	0.969 (0.831–0.999)	1.000 (0.884–1.000)
Sensitivity (%)	93.7 (15/16)	100 (16/16)
Specificity (%)	100 (14/14)	100 (14/14)
Accuracy (%)	97 (29/30)	100 (30/30)
<i>P</i> value for pair-wise comparison of ROC curves	$< .001$	$< .0001$
<i>P</i> value calculated with the McNemar test for the comparison of accuracy	$< .001$.022

^a Unless otherwise indicated, the numbers in parentheses are raw data. Sensitivity, specificity, and accuracy were calculated under the assumption that a confidence score of 4 or higher was considered positive for the diagnosis of hemangioblastoma.

^b Data in parentheses are 95% CIs.

$n = 12$; observer 2, $n = 13$) made on the basis of conventional image interpretation alone.

DISCUSSION

Our study investigated the added diagnostic value of ASL imaging for the differentiation of hemangioblastomas from metastases in a homogeneous cohort of patients with only cerebellar masses. All patients with hemangioblastomas had at least 1 hyperperfused mass, while only half of the patients with metastases presented with a hyperperfused mass. The size ratios and rTBF of the masses were measured for differential diagnoses between hemangioblastomas and metastases for the hyperperfused cerebellar masses. The values of both variables were significantly higher in hemangioblastomas than in metastases. The size ratio revealed excellent diagnostic power (AUC = 0.991), and rTBF demonstrated moderate diagnostic power (AUC = 0.777). In addition, we investigated the 2 observers' performances to validate the use of ASL for distinguishing hemangioblastomas from metastases in patients with only cerebellar masses. Both the diagnostic accuracy of the observers and the interobserver agreement were significantly improved after the addition of ASL images.

A prior study with ASL reported that rTBF was significantly higher for hemangioblastomas than for metastases.¹⁵ However, the study included only 5 hemangioblastomas, and 10 of 14 (71%) metastases were in the supratentorial region. In addition, there was no information regarding visually assessed signal intensities—that is, the prevalence of a hyperperfused mass in the respective tumors. One of strengths of this study is that we included a homogeneous cohort of patients with only cerebellar masses for both hemangioblastomas and metastases. In addition, the frequency of the presence of hyperperfused masses in the 2 tumor types was assessed. In contrast to the patients with metastases, no patients with hemangioblastomas had hypo- or isointense cerebellar masses. Therefore, when a patient has an enhancing mass in the cerebellum that does not show hyperperfusion on ASL imaging, the diagnosis might not be hemangioblastoma.

The rTBF and size ratio of hyperperfused masses aided in differentiating hemangioblastomas and metastases. Our rTBF results are like those of a previous study.¹⁵ They reported that the

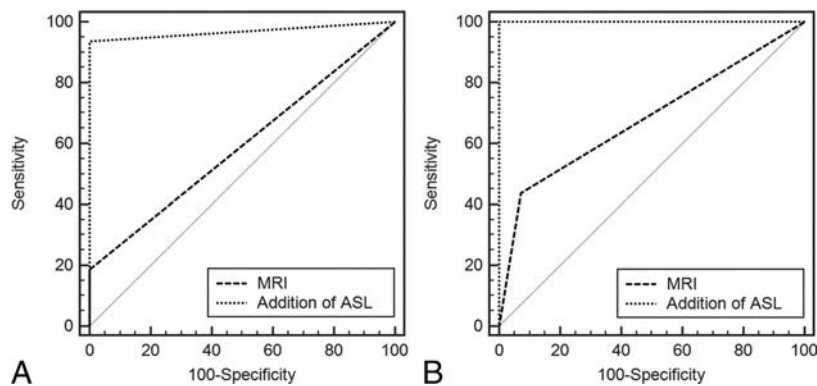


FIG 3. ROC curves used to differentiate hemangioblastomas from metastases before and after the addition of ASL MR images for both observers. *A*, For observer 1, the AUC was significantly improved after additional review of the ASL MR images (from 0.594 to 0.969). *B*, For observer 2, the AUC was also significantly improved after this review (from 0.683 to 1).

mean rTBF was 7.96 ± 3.12 in hemangioblastomas and 2.98 ± 3.91 in metastases, and its diagnostic accuracy was 84.2%, with a cutoff value of 3.3. In our study, the median rTBF was 8.18 (interquartile range, 4.10–12.19) in hemangioblastomas and 2.44 (interquartile range, 2.04–3.73) in metastases, and the diagnostic accuracy was 78.3%, with a cutoff value of 3.78.

However, we also investigated the diagnostic performance of size ratio, and it revealed a better accuracy of 91%, with a cutoff value of 0.98. In addition, the multivariable analysis revealed that size ratio was the only independent predictor of a differential diagnosis. Therefore, the size ratio seems to be useful for differentiating hemangioblastoma from metastasis. For example, a metastasis from renal cell carcinoma mimicked a hemangioblastoma due to its very high rTBF (16.2), like the findings for hemangioblastomas reported in the previous study.¹⁵ However, in our study, an accurate diagnosis of a metastasis from renal cell carcinoma was made when it was based on the low size ratio of 0.82, which took precedence over a high rTBF of 14.36 (Fig 1).

The size ratio determined by ASL imaging suggests that hemangioblastomas appear to become enlarged or “bloom” in ASL sequences. Because a hemangioblastoma is composed of a cluster of thin-walled, tightly packed blood vessels lined with endothelial cells, it may be identified as a dense tumor nodule or as a heterogeneous network of tangled vessels fed by dilated artery draining veins in angiographs.⁸ Therefore, we presumed that the “bloom” appearance represented the emphasized bright signal intensities, which might be attributed to delayed filling and flow stagnation in the tumor.

Observer performance was evaluated to validate the findings based on ASL imaging. The diagnostic accuracy for differentiating hemangioblastomas from metastases was significantly improved after additional review of the CBF map from ASL imaging for both observers. Observer 1 made 1 error after viewing the additional ASL images. On review, the size ratio had been overlooked in this case. The addition of ASL images increased the κ value between observer 1, who was an experienced radiologist with 28 years of clinical experience, and the other observer, who had 6 years of clinical experience. This finding suggests that not only diagnostic accuracy but also interobserver variation can be improved by the addition of ASL images.

When the clinical findings are non-contributory and hemangioblastomas appear as solid contrast-enhancing masses with peritumoral edema, conventional MR imaging cannot distinguish them from metastases.¹⁰ In such cases, markedly increased vascularity visible on cerebral angiographs may suggest hemangioblastoma rather than metastasis.⁸ However, a non-negligible neurologic complication rate of up to 1.3% has been reported.^{24–26} In addition, preoperative embolization is not generally used.²⁷ Therefore, better diagnostic accuracy with MR imaging is crucial. Our results suggest that the addition of ASL imaging could provide practical information to differentiate

hemangioblastoma from metastasis in patients with only enhancing cerebellar masses. When enhancing cerebellar masses do not show hyperperfusion on ASL imaging, the possibility of hemangioblastoma is minimal. When enhancing cerebellar masses reveal hyperperfusion, the size ratio can provide strong diagnostic power. If the masses appear larger on the contrast-enhanced T1WI than on the CBF map, then the possibility of hemangioblastoma is minimal. In patients with impaired renal function, rTBF alone may aid in differentiating hemangioblastoma from metastasis using noncontrast conventional MR imaging with additional ASL imaging.

There are several limitations of this study. First, this was a retrospective study, and the sample size was small. Therefore, the same population had to be used to validate the suggested ASL findings. In addition, because of the small sample size, the comparison of ROC curves did not reveal a significant difference between the AUC values for the size ratio and rTBF ($P = .062$). Despite this limitation, we included a relatively larger number of patients compared with several previous studies using MR perfusion imaging.^{9,10,15} Furthermore, we included a homogeneous cohort of patients with only cerebellar masses. Second, ASL imaging was performed with 2 different MR imaging scanners with different magnetic field strengths. However, we used the normalized rTBF values to minimize the influence of these differences. Although, statistical comparison could not be performed due to the small sample size, a subgroup analysis still revealed that the size ratio and rTBF values were larger for hemangioblastomas than for metastases.

CONCLUSIONS

The addition of ASL imaging to conventional MR imaging may be a reliable and noninvasive method to increase diagnostic accuracy and interobserver variation for the differentiation of hemangioblastoma from metastasis in patients with only cerebellar masses. Combining size ratio and rTBF data could aid in providing correct diagnoses.

ACKNOWLEDGMENTS

The authors appreciate the statistical advice from the Medical Research Collaborating Center at the Seoul National University Hospital.

REFERENCES

1. Chaudhry AP, Montes M, Cohn GA. **Ultrastructure of cerebellar hemangioblastoma.** *Cancer* 1978;42:1834–50 [Medline](#)
2. Yoshida S, Takahashi H. **Cerebellar metastases in patients with cancer.** *Surg Neurol* 2009;71:184–87; discussion 187 [CrossRef Medline](#)
3. Kanner AA, Suh JH, Siomin VE, et al. **Posterior fossa metastases: aggressive treatment improves survival.** *Stereotact Funct Neurosurg* 2003;81:18–23 [CrossRef Medline](#)
4. Catapano D, Muscarella LA, Guarnieri V, et al. **Hemangioblastomas of central nervous system: molecular genetic analysis and clinical management.** *Neurosurgery* 2005;56:1215–21; discussion 1221 [CrossRef Medline](#)
5. Alexandru D, Bota D, Linskey M. **Epidemiology of central nervous system metastases.** In: Kim DG, Lunsford LD, eds. *Current and Future Management of Brain Metastasis*. Basel: Karger Publishers; 2012:13–29
6. Richard S, Campello C, Taillandier L, et al. **Haemangioblastoma of the central nervous system in von Hippel-Lindau disease: French VHL Study Group.** *J Intern Med* 1998;243:547–53 [CrossRef Medline](#)
7. Berkman RA, Merrill MJ, Reinhold WC, et al. **Expression of the vascular permeability factor/vascular endothelial growth factor gene in central nervous system neoplasms.** *J Clin Invest* 1993;91:153–59 [CrossRef Medline](#)
8. Ho VB, Smirniotopoulos JG, Murphy FM, et al. **Radiologic-pathologic correlation: hemangioblastoma.** *AJNR Am J Neuroradiol* 1992;13:1343–52 [Medline](#)
9. Cha J, Kim ST, Nam D-H, et al. **Differentiation of hemangioblastoma from metastatic brain tumor using dynamic contrast-enhanced MR imaging.** *Clin Neuroradiol* 2016 Mar 7. [Epub ahead of print] [CrossRef Medline](#)
10. She D, Yang X, Xing Z, et al. **Differentiating hemangioblastomas from brain metastases using diffusion-weighted imaging and dynamic susceptibility contrast-enhanced perfusion-weighted MR imaging.** *AJNR Am J Neuroradiol* 2016;37:1844–50 [CrossRef Medline](#)
11. Yoo RE, Yun TJ, Cho YD, et al. **Utility of arterial spin labeling perfusion magnetic resonance imaging in prediction of angiographic vascularity of meningiomas.** *J Neurosurg* 2016;125:536–43 [CrossRef Medline](#)
12. Sunwoo L, Yun TJ, You S-H, et al. **Differentiation of glioblastoma from brain metastasis: qualitative and quantitative analysis using arterial spin labeling MR imaging.** *PLoS One* 2016;11:e0166662 [CrossRef Medline](#)
13. Warmuth C, Gunther M, Zimmer C. **Quantification of blood flow in brain tumors: comparison of arterial spin labeling and dynamic susceptibility-weighted contrast-enhanced MR imaging.** *Radiology* 2003;228:523–32 [CrossRef Medline](#)
14. Noguchi T, Yoshiura T, Hiwatashi A, et al. **Perfusion imaging of brain tumors using arterial spin-labeling: correlation with histopathologic vascular density.** *AJNR Am J Neuroradiol* 2008;29:688–93 [CrossRef Medline](#)
15. Yamashita K, Yoshiura T, Hiwatashi A, et al. **Arterial spin labeling of hemangioblastoma: differentiation from metastatic brain tumors based on quantitative blood flow measurement.** *Neuroradiology* 2012;54:809–13 [CrossRef Medline](#)
16. Jeon JY, Choi JW, Roh HG, et al. **Effect of imaging time in the magnetic resonance detection of intracerebral metastases using single dose gadobutrol.** *Korean J Radiol* 2014;15:145–50 [CrossRef Medline](#)
17. Dai W, Garcia D, de Bazelaire C, et al. **Continuous flow-driven inversion for arterial spin labeling using pulsed radio frequency and gradient fields.** *Magn Reson Med* 2008;60:1488–97 [CrossRef Medline](#)
18. Garcia D, De Bazelaire C, Alsop D. **Pseudo-continuous flow driven adiabatic inversion for arterial spin labeling.** In: *Proceedings of the International Society for Magnetic Resonance in Medicine*, Miami, Florida. May 7–13, 2005;13:37
19. Mani S, Pauly J, Conolly S, et al. **Background suppression with multiple inversion recovery nulling: applications to projective angiography.** *Magn Reson Med* 1997;37:898–905 [CrossRef Medline](#)
20. Yoo RE, Choi SH, Cho HR, et al. **Tumor blood flow from arterial spin labeling perfusion MRI: a key parameter in distinguishing high-grade gliomas from primary cerebral lymphomas, and in predicting genetic biomarkers in high-grade gliomas.** *J Magn Reson Imaging* 2013;38:852–60 [CrossRef Medline](#)
21. Lehmann P, Monet P, de Marco G, et al. **A comparative study of perfusion measurement in brain tumours at 3 Tesla MR: arterial spin labeling versus dynamic susceptibility contrast-enhanced MRI.** *Eur Neurol* 2010;64:21–26 [CrossRef Medline](#)
22. Leung RS, Biswas SV, Duncan M, et al. **Imaging features of von Hippel-Lindau disease.** *Radiographics* 2008;28:65–79 [CrossRef Medline](#)
23. Kang KM, Lee JM, Yoon JH, et al. **Intravoxel incoherent motion diffusion-weighted MR imaging for characterization of focal pancreatic lesions.** *Radiology* 2014;270:444–53 [CrossRef Medline](#)
24. Willinsky RA, Taylor SM, TerBrugge K, et al. **Neurologic complications of cerebral angiography: prospective analysis of 2,899 procedures and review of the literature.** *Radiology* 2003;227:522–28 [CrossRef Medline](#)
25. Dawkins A, Evans A, Wattam J, et al. **Complications of cerebral angiography: a prospective analysis of 2,924 consecutive procedures.** *Neuroradiology* 2007;49:753–59 [CrossRef Medline](#)
26. Thiex R, Norbash A, Frerichs K. **The safety of dedicated-team catheter-based diagnostic cerebral angiography in the era of advanced noninvasive imaging.** *AJNR Am J Neuroradiol* 2010;31:230–34 [CrossRef Medline](#)
27. Montano N, Doglietto F, Pedicelli A, et al. **Embolization of hemangioblastomas.** *J Neurosurg* 2008;108:1063–64; author reply 1064–65 [CrossRef Medline](#)

Detection of Volume-Changing Metastatic Brain Tumors on Longitudinal MRI Using a Semiautomated Algorithm Based on the Jacobian Operator Field

O. Shearkhani, A. Khademi, A. Eilaghi, S.-P. Hojjat, S.P. Symons, C. Heyn, M. Machnowska, A. Chan, A. Sahgal, and P.J. Maralani

ABSTRACT

BACKGROUND AND PURPOSE: Accurate follow-up of metastatic brain tumors has important implications for patient prognosis and management. The aim of this study was to develop and evaluate the accuracy of a semiautomated algorithm in detecting growing or shrinking metastatic brain tumors on longitudinal brain MRIs.

MATERIALS AND METHODS: We used 50 pairs of successive MR imaging datasets, 30 on 1.5T and 20 on 3T, containing contrast-enhanced 3D T1-weighted sequences. These yielded 150 growing or shrinking metastatic brain tumors. To detect them, we completed 2 major steps: 1) spatial normalization and calculation of the Jacobian operator field to quantify changes between scans, and 2) metastatic brain tumor candidate segmentation and detection of volume-changing metastatic brain tumors with the Jacobian operator field. Receiver operating characteristic analysis was used to assess the detection accuracy of the algorithm, and it was verified with jackknife resampling. The reference standard was based on detections by a neuroradiologist.

RESULTS: The areas under the receiver operating characteristic curves were 0.925 for 1.5T and 0.965 for 3T. Furthermore, at its optimal performance, the algorithm achieved a sensitivity of 85.1% and 92.1% and specificity of 86.7% and 91.3% for 1.5T and 3T, respectively. Vessels were responsible for most false-positives. Newly developed or resolved metastatic brain tumors were a major source of false-negatives.

CONCLUSIONS: The proposed algorithm could detect volume-changing metastatic brain tumors on longitudinal brain MRIs with statistically high accuracy, demonstrating its potential as a computer-aided change-detection tool for complementing the performance of radiologists, decreasing inter- and intraobserver variability, and improving efficacy.

ABBREVIATIONS: AUC = area under the curve; 3D-T1-Gad = contrast-enhanced 3D T1-weighted; Δ MBT = volume-changing MBT; Δ MBT_{os} = newly developed or resolved MBT; Δ MBT_{ts} = changing MBT present on both baseline and follow-up scans; FPR = false-positive rate; JOF = Jacobian operator field; MBT = metastatic brain tumor; ROC = receiver operating characteristic; VCR = volume change ratio

Metastatic brain tumors (MBTs) occur in 24%–45% of patients diagnosed with primary cancers outside the brain.¹ Accurate assessment of MBTs on follow-up imaging is critical for better prognosis and selecting the most appropriate treatment such as chemotherapy, surgery, and radiation therapy or a combination of the aforementioned.^{2–4} This is becoming more important with increasing use of stereotactic radiosurgery.⁵

Contrast-enhanced 3D T1-weighted (3D-T1-Gad) MR imaging is commonly used for detection and follow-up of MBTs and is the sequence of choice for stereotactic radiosurgery planning of MBTs.^{5,6} During follow-up of MBTs, longitudinal volumetric imaging is performed every 2–3 months.⁵ This results in a large amount of data to process and a demanding workload for radiologists.⁷ Moreover, the inherent limitations of viewing scans section by section, changes in head position from one scan to another, and user subjectivity result in the potential for increased inter- and intraobserver variability in both detection and volume assessment, especially with small MBTs or subtle volume changes.⁸

Although several studies have investigated the efficiency of computer-aided detection techniques in MBTs on a single MR scan,^{9–14} the literature is limited in studies evaluating the efficacy of computer algorithms in the follow-up of MBTs¹⁵ and detection of volume-changing MBTs (Δ MBTs) as an indicator of treatment response. Tracking volumetric changes is of high clinical value,

Received January 5, 2017; accepted after revision June 15.

From the Departments of Medical Imaging (O.S., S.-P.H., S.P.S., C.H., M.M., A.C., P.J.M.) and Radiation Oncology (A.S.), University of Toronto, Toronto, Ontario, Canada; Department of Biomedical Engineering (A.K.), Ryerson University, Toronto, Ontario, Canada; and Mechanical Engineering Department (A.E.), Australian College of Kuwait, Kuwait City, Kuwait.

This work was supported by the Radiological Society of North America (RMS1640 to O.S.) and the Brain Tumour Foundation of Canada (to O.S.).

Please address correspondence to Pejman Jabejdar Maralani, MD, 2075 Bayview Ave, Room AG270c, Toronto, ON, M4N 3M5; e-mail: pejman.maralani@sunnybrook.ca

<http://dx.doi.org/10.3174/ajnr.A5352>

and implementing computer-aided techniques in the follow-up of MBTs can improve diagnostic accuracy and efficiency¹⁶⁻¹⁹ and complement current single-scan detection algorithms.

While computer-aided detection tools are limited for MBTs, automated change-detection techniques in MS are an active area of research and development.²⁰ Like MBTs, in MS, quantitative analyses are important for assessing disease progression,²¹ activity,²² and treatment evaluation.²³ The literature on automatic change detection of MS lesions broadly divides existing approaches into deformation-based (analysis of deformation fields resulting from nonrigid registration of scans) and intensity-based (voxel-to-voxel comparison between scans) methods and suggests a potentially strong role for deformation field-based and combined techniques.^{20,23} Furthermore, techniques based on the deformation field have been proposed as promising in detecting structural changes on longitudinal brain MR imaging²⁴⁻²⁷ and encompass techniques based on vector displacement fields such as those centered around divergence²⁸ and Jacobian operator fields (JOFs).²⁹

To detect Δ MBTs on longitudinal brain MRIs, a semiautomated algorithm based on the JOF is proposed here. The JOF has certain advantages compared with other methods because it can be used independently to detect local volume changes²⁸ compared with divergence techniques³⁰ and is computationally less expensive than other deformation field morphometry approaches.²⁰

In conjunction with other image-processing methods, the JOF is used in this study to identify MBT candidates that have changed in size, independent of changes in intensity or contrast compared with surrounding structures. We hypothesized that our algorithm can detect Δ MBTs with statistically high accuracy compared with a reference standard, defined here as detection by a board-certified neuroradiologist with 5 years of experience.

MATERIALS AND METHODS

Dataset Extraction

This retrospective study was approved by the Research Ethics Board of our institution (Sunnybrook Health Sciences Centre, Toronto, Ontario, Canada) with a waiver of informed consent. Patient datasets from June 2014 to June 2015 were extracted from the PACS of our institution. All patients included in this study were adults (older than 18 years of age) with MBTs, who had undergone 2 consecutive 3D-T1-Gad scans at our institution. Patients with other brain pathologies—such as primary brain neoplasms, MS lesions, or stroke—or those who had undergone a brain operation for any reason were excluded. Datasets were divided into 2 groups based on magnetic field strength (1.5T versus 3T) to assess the performance of the algorithm in 2 different scenarios. The 1.5T group had MR images obtained on 2 identical 1.5T TwinSpeed Excite scanners (GE Healthcare, Milwaukee, Wisconsin) with a standard 8-channel head coil. The parameters for 3D-T1-Gad included the following: TR/TE/flip angle, 8.6 ms/4.2 ms/20°; FOV, 220 × 220 mm; and voxel size, 0.58 × 0.58 × 1.5 mm. The 3T group had MR images obtained on a 3T Achieva TX scanner (Philips Healthcare, Best, the Netherlands) with a standard 8-channel head coil. The parameters for 3D-T1-Gad included the following: TR/TE/flip angle, 9.5 ms/2.3 ms/8°; FOV,

312 × 206 mm; and voxel size, 0.67 × 0.67 × 1.5 mm. The parameters are part of the routine contrast-enhanced brain MR imaging protocol at our institution.

Image Analysis

Overview and Definitions. In this section, the image-processing pipeline used to detect Δ MBTs is described (Fig 1).

Δ MBTs were classified by the authors as either Δ MBT_{ts}, which represent Δ MBTs present on both baseline and follow-up scans, or Δ MBT_{os}, which only appear on 1 scan (ie, newly developed or resolved MBTs). The volume change ratio (VCR) of an object across 2 scans was defined as the ratio of its volume change across time over its initial volume. This metric was defined because it is accepted that the values of JOFs are directly associated with the VCR of the brain, and higher JOF values suggest higher VCR and vice-versa.²⁰

Concerning volume changes, “growing” MBTs refer to all MBTs that have grown in volume from baseline to follow-up scans, including newly developed MBTs. “Shrinking” MBTs refer to MBTs that shrank in size from baseline to follow-up, including resolved MBTs. Note that to detect growing MBTs in the forward direction (ie, from baseline to follow-up), our algorithm detected shrinking MBTs in the reverse direction (ie, from follow-up to baseline) because the JOF provides richer information in the shrinking field.³⁰ In addition, this approach allowed detection of newly developed MBTs that do not have a corresponding MBT on baseline, though the processes going in the forward and reverse directions are identical. While our algorithm identified growing MBTs by detecting shrinking MBTs in the reverse direction, for clarity, here we will describe the process going in the forward direction only. SPM12 (<http://www.fil.ion.ucl.ac.uk/spm/software/spm12>) and Matlab (MathWorks, Natick, Massachusetts) software packages were used for data processing. All average values are presented as mean ± SD.

Spatial Normalization. To ensure that longitudinal baseline and follow-up scans were comparable and could be registered to one another for analyzing changes, we spatially normalized both scans to the Montreal Neurological Institute template³¹ with the methods described by Ashburner et al³² (Fig 1A) on SPM12 software (Fig 2).³³

Deformation Field. Next, a nonrigid registration technique, based on joint diffeomorphic and rigid-body registration and proposed for intrasubject registration,³⁴ was used to align the images using SPM12.³³ This generated a 3D displacement field, which determined structural changes between the 2 scans (Fig 1A).

Calculation of the JOF. To determine whether a tumor shrank between time points, the JOF—which quantifies local volume changes—was computed from the displacement field (Fig 2C, -D), using SPM12.³³

Segmentation of MBT Candidates. To segment MBT candidates, we used a modified version of the approach proposed by Seghier et al³⁵ for lesion segmentation. First, a probabilistic segmentation of GM and WM was computed with the methods described by Ashburner and Friston.³² These 2 tissue maps were then added

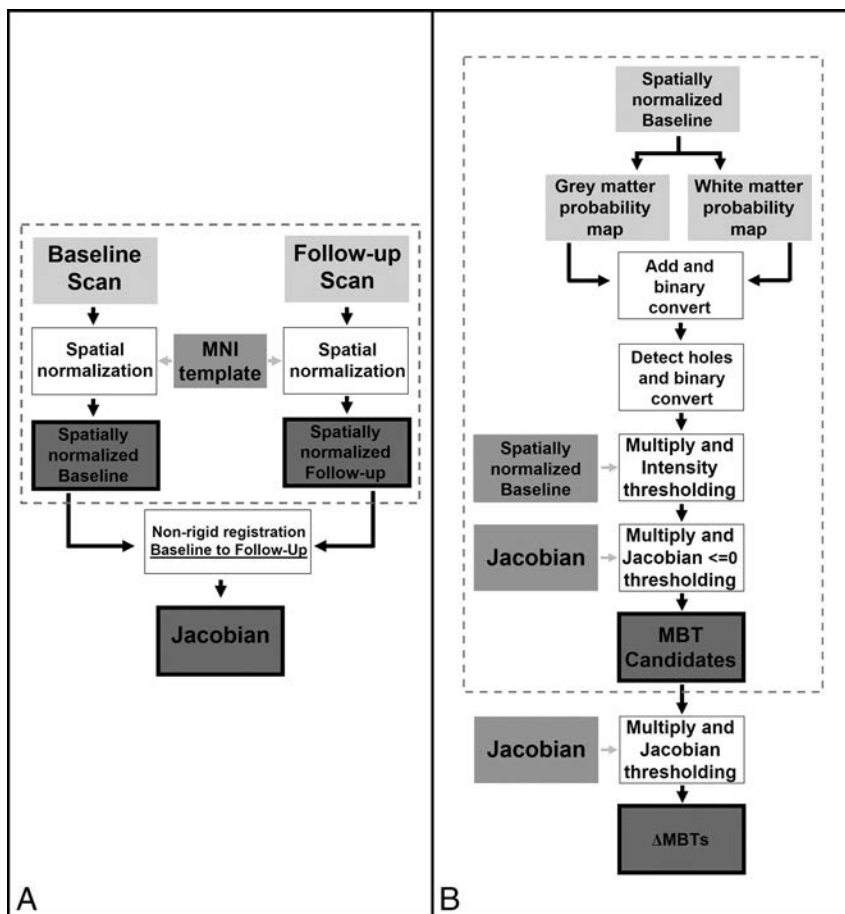


FIG 1. Steps summarizing the preprocessing of patient datasets (dotted box) and calculation of the Jacobian operator field in the forward direction (A) and for segmentation of metastatic brain tumor candidates (dotted box) and detection of shrinking MBTs in the forward direction (B).

together to create a brain mask, which was then converted to binary in which voxels of nonzero value were retained. Because MBTs generally appear on MR images as bright objects fully or partially confined within the brain matter, they are not detected during this step and are therefore excluded from the binary mask, leaving “holes” within the brain mask. To detect MBT candidates, we created a binary mask of the holes, and this mask was multiplied to the original intensity image to identify MBT candidates in the intensity domain. Automatic postprocessing, with no user interaction, was completed to remove irrelevant objects that had an intensity lower than the average intensity of GM and WM.

False-Positive Reduction and Detection of Δ MBTs. To limit MBT candidates to islands that shrank, we converted the MBT candidates to binary, multiplied to the JOF, and discarded 2D islands in the axial dimension with a positive median value, permitting false-positive reduction. To detect Δ MBTs, we then thresholded these MBT candidates using various JOF values. For each threshold value, 3D islands present on at least 1 section in the axial dimension with a median value of the threshold value or less were retained (Figs 1B and 2E, -F).

Statistical Analysis

The presence and location of Δ MBTs were confirmed and extracted by a board-certified neuroradiologist with 5 years of experience,

blinded to the technical details of our detection algorithm using Medical Image Processing, Analysis & Visualization (MIPAV; National Institutes of Health, Bethesda, Maryland); this defined our reference standard. To validate the algorithm, we considered its accuracy in detecting Δ MBTs in the 1.5T and 3T groups separately. For statistical analysis of the accuracy of our algorithm and to find the optimal threshold value of the JOF, we used receiver-operating characteristic (ROC) analysis.³⁶ At each threshold value, a detection was marked as a true-positive if it overlapped an Δ MBT identified by the neuroradiologist; the rest were marked as false-positives. The area under the curve (AUC) of the ROC curve was used to evaluate accuracy, for which an AUC > 0.9 corresponds to a technique with statistically high accuracy.³⁷ For verification of our results, in addition to assessing the algorithm using 2 independent datasets, we used the jackknife approach,³⁸ with evaluation of the AUC, sensitivity, specificity, and false-positive rate (FPR) at the optimal threshold value of each iteration. To assess the potential role of our algorithm in complementing the performance of radiologists and reducing interobserver variability, we compared the true-positives detected by our algorithm

against those detected by a different board-certified neuroradiologist with 3 years of experience, blinded to the technical details of our algorithm. The Mann-Whitney *U* test was used to compare the following: 1) the accuracy, sensitivity, specificity, and FPR of our algorithm at 1.5T and 3T; 2) the VCR of missed-versus-detected Δ MBTs; and 3) the VCR of Δ MBT_{os} versus the VCR of Δ MBT_{ts}. A *P* < .05 defined statistical significance.

RESULTS

Patient MR Imaging Datasets

The 1.5T group, comprising 30 patients, had 74 MBTs. The 3T group, comprising 20 patients, had 76 MBTs. Table 1 summarizes information about patient demographics, scan timeline, and MBT details.

Algorithm Performance

Detecting Δ MBTs. For the 1.5T group, an ROC curve with 233 points (0 to -0.232, separated by -0.001) and, for the 3T group, an ROC curve with 656 points (0 to -0.655, separated by -0.001) were constructed by thresholding MBT candidates using various values of the JOF (Fig 3 and Table 2). Both ROC curves showed statistically high accuracy with an AUC of 0.925 and 0.965 for the 1.5T and 3T groups, respectively. There was no significant difference in the VCR between the detected and missed Δ MBTs for either group (*P* > .05).

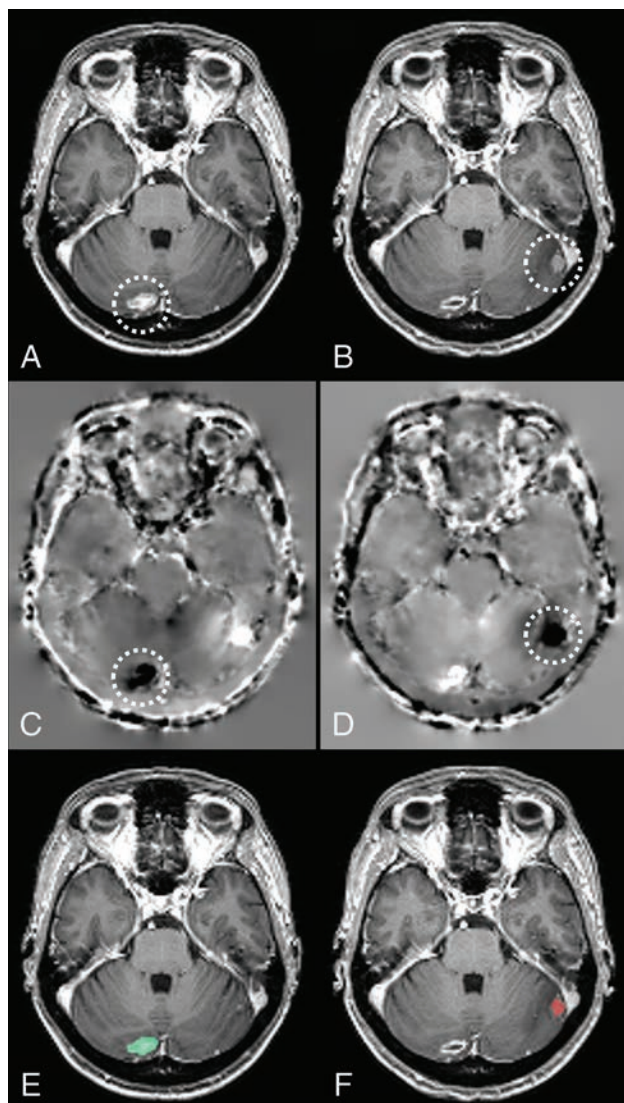


FIG 2. Axial sections of a patient's baseline (A) and follow-up (B) scans. The Jacobian operator field, calculated from the deformation field in the forward (C) and reverse (D) directions. The final output of our algorithm produced for baseline (E) and follow-up (F) scans, highlighting volume-changing metastatic brain tumors on each scan. Note that darker voxels on C and D correspond to negative JOF values and brighter voxels correspond to positive JOF values. The location of a metastatic brain tumor that has shrunk in size across the scans has been circled on A–D. The green on E indicates shrinkage, and the red on F indicates growth. Note that while this image is demonstrated in 2D, various operations as described here were performed in 3D.

False-Positives

False-positives detected by the algorithm were divided into 5 categories (Table 3): 1) arteries: branches of anterior and middle cerebral arteries and vertebrobasilar system; 2) veins: superficial cortical veins, deep veins including internal cerebral veins, and basal veins of Rosenthal; 3) dural venous sinuses; 4) dura, tentorium, and falx cerebelli; and 5) choroid plexus. Vessels, including arteries, veins, and dural venous sinuses, were responsible for $79.0\% \pm 24.0\%$ and $77.8\% \pm 18.5\%$ of false-positives in the 1.5T and 3T groups, respectively. Visual inspection of the datasets suggested that at times, subtle structural differences such as pulsation of vessels between scans resulted in high JOF values and, conse-

Table 1: Summary of information on patients, scans, and MBTs

Variable	1.5T	3T
Sex		
Male (total %)	15 (50%)	11 (55%)
Female (total %)	15 (50%)	9 (45%)
Age (yr)		
Average ^a	60.3 \pm 13.1	58.7 \pm 15.7
Range	23.4–91.0	27.3–84.5
Time between baseline and follow-up (days)		
Average ^a (per patient)	147 \pm 155	132 \pm 129
Range	26–676	17–532
Number of Δ MBTs		
Total	74	76
Δ MBT _{ts}	58	67
Δ MBT _{os}	16	9
Average ^a (per patient)	4.4 \pm 3.1	3.8 \pm 3.9
Δ MBT volume (mL)		
Average ^a	2.4 \pm 4.0	2.2 \pm 3.8
Range	4.0×10^{-3} – 1.9×10^1	2.0×10^{-2} – 3.0×10^1
Δ MBT volume change (mL)		
Average ^a	1.5 \pm 2.2	2.2 \pm 3.5
Range	3.4×10^{-3} – 3.5×10^1	9.1×10^{-2} – 2.0×10^1
Δ MBT VCR (%)		
Average ^a	$7.0 \times 10^1 \pm 29.5$	$7.6 \times 10^1 \pm 1.7 \times 10^1$
Range	7.8×10^{-1} – 1.0×10^2	4.2 – 1.0×10^2

^a Average \pm SD.

quently, detection as false-positives. However, these can easily be dismissed on visual inspection by a radiologist.

False-Negatives

At its optimal threshold value, the algorithm did not detect 11 Δ MBTs in the 1.5T group and 6 Δ MBTs in the 3T group. Δ MBT_{ts} false-negatives could subsequently be divided into the following (Table 4): 1) those that had a size of ≤ 2 voxels on one of the scans, or 2) those segmented poorly during the candidate segmentation portion of the algorithm, which consequently negatively affected the evaluation of their JOF values.

In the 1.5T group, the sensitivity of the algorithm in detecting Δ MBT_{os} showed inferior values compared with its sensitivity in detecting Δ MBT_{ts} (75% versus 87.9%, respectively). This is even though Δ MBT_{ts} had a significantly lower VCR than Δ MBT_{os} ($P < .0001$). These results suggested that Δ MBT_{os} may be a major source of false-negatives for our algorithm. To assess this, we evaluated the performance of the algorithm with Δ MBT_{os} omitted. This analysis was only performed in the 1.5T group because all instances of Δ MBT_{os} were detected in the 3T group. Like Δ MBT detection, an ROC curve with 302 points (0 to -0.301 , separated by -0.001) was generated with an AUC of 0.929. At its optimal performance (achieved at a threshold value of -0.035), the algorithm had a sensitivity of 87.9%, specificity of 86.6%, and FPR of 0.210 per section, equivalent to 25.4 per scan. Note that detected the Δ MBT_{os} was included in the calculation of specificity and FPR.

Verification

In addition to performing all analyses on 2 independent patient datasets, as demonstrated above, we conducted jackknifing for further verification of findings. Results from jackknifing were like the findings before the procedure, verifying initial results (Table 5). Furthermore, statistical analysis of the mean AUC of the algorithm and the sensitivity of the algorithm when applied to jackknifed 1.5T Δ MBT_{ts}-only data versus jackknifed 1.5T Δ MBT data

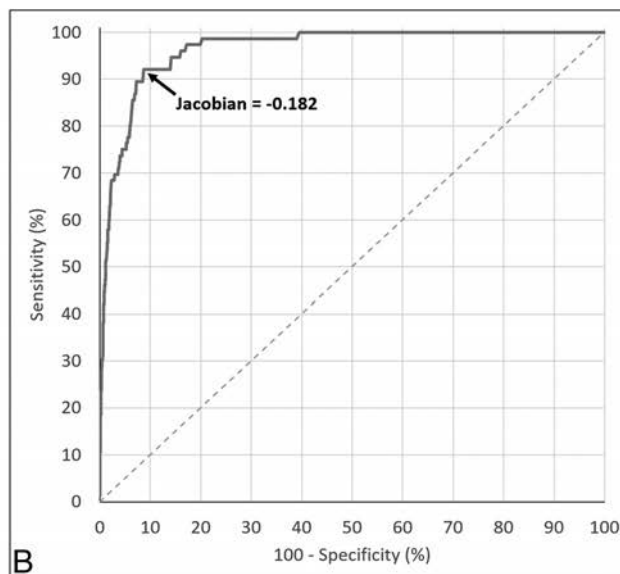
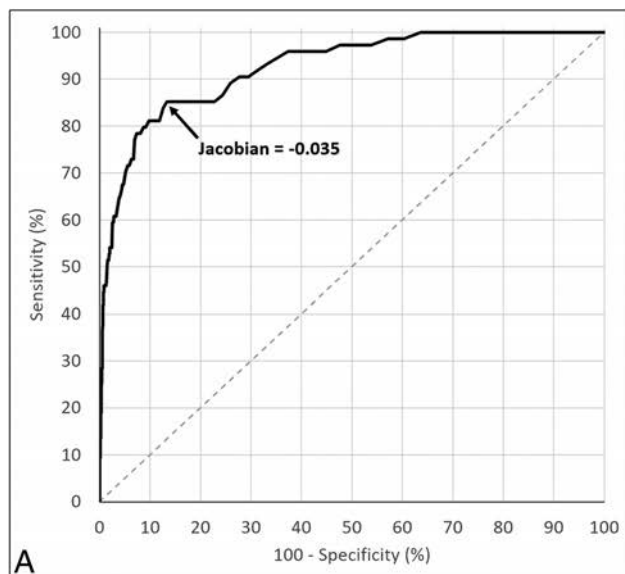


FIG 3. A, Illustration of the receiver operating characteristic curve of our algorithm for detecting volume-changing metastatic brain tumors at 1.5T, constructed from 233 different thresholding values of the Jacobian operator field (from 0 to -0.232 , separated by -0.001). The arrow shows the optimal point of balance. B, Illustration of the ROC curve of our algorithm for detecting Δ MBTs at 3T, constructed from 656 different thresholding values of the Jacobian operator field (from 0 to -0.655 , separated by -0.001). The arrow shows the optimal point of balance between sensitivity and specificity, which happens at the Jacobian value of -0.182 .

Table 2: Summary of ROC analysis, for detecting all 1.5T and 3T Δ MBTs and 1.5T Δ MBT_{ts} only, and the VCR of detected and missed Δ MBTs

Variable	1.5T	3T
ROC curve		
AUC	0.925	0.965
Optimal Jacobian threshold	-0.035	-0.182
Sensitivity ^a (%)	85.1	92.1
Specificity ^a (%)	86.7	91.3
FPR ^a (per section)	0.208	0.227
FPR ^a (per scan)	25.1	27.5
Detected ^a Δ MBT VCR (%)		
Average ^b	$7.1 \times 10^1 \pm 2.8 \times 10^1$	$7.7 \times 10^1 \pm 1.7 \times 10^1$
Median	7.9×10^1	7.5×10^1
Range	$7.8 \times 10^{-1} - 1.0 \times 10^2$	$4.2 - 1.0 \times 10^2$
Missed ^a Δ MBT VCR (%)		
Average ^b	$6.2 \times 10^1 \pm 3.8 \times 10^1$	$7.3 \times 10^1 \pm 1.9 \times 10^1$
Median	7.5×10^1	8.2×10^2
Range	$3.9 - 1.0 \times 10^2$	$4.3 \times 10^1 - 8.6 \times 10^1$

^a At the optimal Jacobian threshold.

^b Average \pm SD.

Table 3: Categories and distribution of false-positives at the optimal Jacobian threshold

False-Positive Categories	1.5T	3T
Arteries ^a (%)	49.8 ± 25.3	44.9 ± 22.9
Veins ^a (%)	16.0 ± 8.7	17.3 ± 12.8
Dural venous sinuses ^a (%)	13.2 ± 15.9	15.5 ± 14.4
Dura ^a (%)	16.6 ± 23.5	12.0 ± 12.3
Choroid plexus ^a (%)	4.4 ± 5.4	10.2 ± 12.5

^a Average \pm SD.

showed significant improvement ($P < .0001$ for both AUC and sensitivity).

Effect on Performance

Of the 150 Δ MBTs in our datasets, a second neuroradiologist could detect 144 Δ MBTs, equivalent to 96% sensitivity. Of the 6 Δ MBTs missed by the neuroradiologist, 2 Δ MBTs, consisting of 1 Δ MBT_{os} and 1 Δ MBT_{ts}, were missed by both the algorithm and

Table 4: Categories and distribution of false-negatives at the optimal Jacobian threshold

False-Negative Categories	1.5T	3T
Δ MBT _{os} (percentage of total)	4 (36.3%)	0 (0%)
Δ MBT _{ts} (percentage of total)	7 (63.7%)	6 (100%)
≤ 2 voxels	3 (27.3%)	1 (16.7%)
Poorly segmented	4 (36.4%)	5 (83.3%)

Table 5: Summary of ROC analysis after jackknifing datasets, for detecting all 1.5T and 3T Δ MBTs and 1.5T Δ MBT_{ts} only

Variable	1.5T	1.5T: Δ MBT _{ts} Only	3T
AUC of ROC curve			
Average ^a	0.925 ± 0.003	0.929 ± 0.003	0.965 ± 0.002
Median	0.924	0.928	0.965
Sensitivity ^b (%)			
Average ^a	85.1 ± 0.8	87.9 ± 0.8	92.2 ± 0.5
Median	84.9	87.7	92.0
Specificity ^b (%)			
Average ^a	86.7 ± 0.3	86.6 ± 0.3	91.3 ± 0.6
Median	86.7	86.6	91.1
FPR (per section)			
Average ^a	0.208 ± 0.005	0.210 ± 0.005	0.227 ± 0.02
Median	0.209	0.211	0.232

^a Average \pm SD.

^b At the optimal Jacobian threshold.

neuroradiologist. However, 1 Δ MBT_{os} and 3 instances of Δ MBT_{ts} were missed by the neuroradiologist but detected by the algorithm. Inspection of those 4 Δ MBTs revealed subtle volume changes, ranging from 9.1×10^{-2} to 2.5×10^{-1} mL. The addition of these detections would improve the neuroradiologist's sensitivity to 98.7%.

DISCUSSION

In this article, we have presented our semiautomated algorithm for detecting Δ MBTs in longitudinal brain MRIs with statistically

high accuracy at 1.5T and 3T ($AUC > 0.9$). Our approach uses the JOF—a vector displacement field operator—which quantifies longitudinal structural changes of the brain on the basis of the deformation field. At its optimal performance, our algorithm had a sensitivity of 85.1% and 92.1% and a specificity of 86.7% and 91.3% for the 1.5T and 3T groups, respectively. Although performances at the optimal thresholds were similar, the difference in optimal JOF threshold values for the 2 groups indicated the effect of scan parameters on optimal threshold values and the need to identify a unique optimal threshold value for each set of scan parameters. Moreover, missed and detected ΔMBT_s had a statistically similar VCR, suggesting that the detection ability of our algorithm is not dependent on VCR values. Compared with manual reading, this can be considered an advantage of our algorithm because manual reading of longitudinal brain MR images is biased against subtle changes.¹⁶ Thus, the findings in this study supported the potential of our algorithm to aid performance by identifying lesions with subtle volume change that could otherwise be missed by the user. Although it is accepted that the values of the Jacobian operator field are directly associated with the VCR of the brain,²⁰ we speculate that this association may not be the case for VCR values of individual brain regions because the missed and detected ΔMBT_s of our algorithm had statistically similar VCRs despite differences in JOF values. Although this difference may limit the information provided by the JOF about the amount of volume change, our results demonstrate the adequacy of the JOF in detecting ΔMBT_s , even for relatively small VCR values, and support its potential to serve as a diagnostic aid.

At present, the literature is limited in studies concerning the follow-up and volume-change detection of MBTs. Chitphakdithai et al¹⁵ proposed a method for tracking MBTs, relying on a 4-level label map to denote the intensity-correspondence relation between baseline and follow-up images. Although authors reported a sensitivity of 92% in detecting ΔMBT_s , this was verified on only a limited dataset comprising 3 patients. In addition, the authors did not report specificity or FPR; this omission prevented accurate comparison with our algorithm.

With our algorithm, nonlinear registration of baseline and follow-up scans was used to detect structural changes. One of its main limitations is the infinite number of displacement fields for a given pair of scans, depending on the registration technique used.¹⁶ More important, these techniques rely on the assumption that a lesion or tissue region exists on both scans with similar intensity.¹⁶ This assumption limits the detection of ΔMBT_s of negligible size on one of the scans and ΔMBT_{os} . Reviewing the detections of the algorithm showed that most false-negatives were of the aforementioned 2 categories. Moreover, although our algorithm could detect 75% of ΔMBT_{os} at 1.5T, this was inferior to the general sensitivity of our algorithm; however, this problem was not isolated to our algorithm.

A similar problem exists in MS, in which computer-aided detection tools are more developed and prevalent in the clinical environment. Although MS computer-aided detection tools focus more on the amount of volume change as opposed to mere detection of change, both techniques use automated quantitative analysis techniques that can be compared. A recent study by

Cabezas et al³⁹ combined subtraction and deformation field analyses to detect new MS lesions on T2-weighted images. Using this approach on 36 patient datasets, Cabezas et al reported a 70.8% sensitivity.³⁹ Comparatively, our 1.5T datasets consisted of 30 patients with 16 instances of ΔMBT_{os} . When these were omitted, the AUC and sensitivity of our algorithm improved; this change suggests that ΔMBT_{os} has a negative effect on its performance. However, because detecting ΔMBT_{os} is equivalent to detecting MBTs on a single scan, this limitation can be addressed by combining our algorithm with previously described MBT computer-aided detection tools.⁹⁻¹⁴

Further enhancement of the clinical utility of our algorithm rests on improving its FPR. Like other studies concerned with automatic MBT detection on 3D-T1-Gad,⁹⁻¹³ bright vessels were a major source of false-positives. Differentiating vessels and MBTs could be achieved by incorporating 3D template matching-based algorithms for MBT segmentation⁹⁻¹³ in place of our current method. This may also improve the sensitivity of our algorithm because some of the false-negatives of our technique were a direct result of poor MBT segmentation. Further false-positive reduction may be achieved with vessel filters^{40,41} or cerebrovascular atlases.⁴² The use of black-blood MR imaging can also address this problem¹⁴ because this technique has been shown to be superior in capturing smaller MBTs compared with other MR images.^{43,44} More recently, Pérez-Ramírez et al¹³ proposed the use of a degree of anisotropy to distinguish blood vessels and MBTs.

CONCLUSIONS

The proposed semiautomated algorithm presented in this article could detect volume-changing MBTs on longitudinal brain MR imaging with high accuracy. With the growing quantity and quality of automated techniques for MBT detection, implementation of some of these elements may further improve the sensitivity, specificity, and FPR of our algorithm. The clinical role of our technique lies in its potential to improve the high workload⁷ and ambiguity¹⁶ associated with manual reading, which is crucial for appropriate treatment.⁵ Through demonstrating the potential of deformation-based techniques and our algorithm, this study serves as an initial step in developing a computer-aided change-detection tool to complement the performance of radiologists.

Disclosures: Omid Shearkhani—RELATED: Grant: Brain Tumour Foundation of Canada Research Studentship, Radiological Society of North America Medical Student Grant. Arjun Sahgal—UNRELATED: Consultancy: Varian Medical Systems, Hoffmann-La Roche; Grants/Grants Pending: Elekta; Payment for Development of Educational Presentations: Medtronic, Elekta, Accuray Inc, Varian Medical Systems; Travel/Accommodations/Meeting Expenses Unrelated to Activities Listed: Medtronic, Elekta, Varian Medical Systems; OTHER RELATIONSHIPS: past educational seminars with Medtronic, Elekta, Accuray Inc, and Varian Medical Systems; consulting/advisory role with Varian Medical Systems, Hoffmann-La Roche; research grant with Elekta; travel accommodations/expenses by Medtronic, Elekta, and Varian Medical Systems. Dr Sahgal also belongs to the Elekta MR Linac Research Consortium. Pejman Jabehdar Maralani—UNRELATED: Grants/Grants Pending: grants from the Radiological Society of North American and the Brain Tumour Foundation of Canada. *Money paid to the institution.

REFERENCES

1. Nussbaum ES, Djalilian HR, Cho KH, et al. **Brain metastases: histology, multiplicity, surgery, and survival.** *Cancer* 1996;78:1781–88 Medline

2. Okunieff P, Schell MC, Ruo R, et al. **Long-term management of patients with multiple brain metastases after shaped beam radiosurgery: case report and review of the literature.** *J Neurosurg* 2004;101(suppl 3):46–12 CrossRef Medline
3. Patchell RA, Tibbs PA, Walsh JW, et al. **A randomized trial of surgery in the treatment of single metastases to the brain.** *N Engl J Med* 1990;322:494–500 CrossRef Medline
4. Smith ML, Lee JY. **Stereotactic radiosurgery in the management of brain metastasis.** *Neurosurg Focus* 2007;22:1–8 CrossRef Medline
5. Patel SH, Robbins JR, Gore EM, et al; Expert Panel on Radiation Oncology–Brain Metastases. **ACR Appropriateness Criteria® follow-up and retreatment of brain metastases.** *Am J Clin Oncol* 2012; 35:302–06 CrossRef Medline
6. Kakeda S, Korogi Y, Hiai Y, et al. **Detection of brain metastasis at 3T: comparison among SE, IR-FSE and 3D-GRE sequences.** *Eur Radiol* 2007;17:2345–51 CrossRef Medline
7. Prastawa M, Bullitt E, Moon N, et al. **Automatic brain tumor segmentation by subject specific modification of atlas priors.** *Acad Radiol* 2003;10:1341–48 CrossRef Medline
8. Loganathan AG, Chan MD, Alphonse N, et al. **Clinical outcomes of brain metastases treated with Gamma Knife radiosurgery with 3.0 T versus 1.5 T MRI-based treatment planning: have we finally optimised detection of occult brain metastases?** *J Med Imaging Radiat Oncol* 2012;56:554–60 CrossRef Medline
9. Ambrosini RD. *Automated Detection and Growth Rate Determination of Metastatic Tumors in the Brain and Lungs* [dissertation]. Rochester: University of Rochester; 2010:134
10. Ambrosini RD, Wang P, O'Dell WG. **Computer-aided detection of metastatic brain tumors using automated three-dimensional template matching.** *J Magn Reson Imaging* 2010;31:85–93 CrossRef Medline
11. Farjam R, Parmar HA, Noll DC, et al. **An approach for computer-aided detection of brain metastases in post-Gd T1-W MRI.** *Magn Reson Imaging* 2012;30:824–36 CrossRef Medline
12. Pérez-Ramírez Ú, Arana E, Moratal D. **Computer-aided detection of brain metastases using a three-dimensional template-based matching algorithm.** In: *Proceedings of the 36th Annual International Conference of the Institute of Electrical and Electronics Engineers Engineering in Medicine and Biology Society*, Chicago, Illinois. August 26–30, 2014:2384–87
13. Pérez-Ramírez Ú, Arana E, Moratal D. **Brain metastases detection on MR by means of three-dimensional tumor-appearance template matching.** *J Magn Reson Imaging* 2016;44:642–52 CrossRef Medline
14. Yang S, Nam Y, Kim MO, et al. **Computer-aided detection of metastatic brain tumors using magnetic resonance black-blood imaging.** *Invest Radiol* 2013;48:113–19 CrossRef Medline
15. Chitphakdithai N, Chiang VL, Duncan JS. **Tracking metastatic brain tumors in longitudinal scans via joint image registration and labeling.** In: Durrleman S, Fletcher T, Gerig G, Niethammer M, eds. *Spatio-temporal Image Analysis for Longitudinal and Time-Series Image Data: STIA 2012*. Berlin: Springer; 2012:124–36
16. Patriarche J, Erickson B. **A review of the automated detection of change in serial imaging studies of the brain.** *J Digit Imaging* 2004; 17:158–74 CrossRef Medline
17. Doi K. **Computer-aided diagnosis in medical imaging: historical review, current status and future potential.** *Comput Med Imaging Graph* 2007;31:198–211 CrossRef Medline
18. Doi K. **Diagnostic imaging over the last 50 years: research and development in medical imaging science and technology.** *Phys Med Biol* 2006;51:R5–27 CrossRef Medline
19. Takahashi R, Kajikawa Y. **Computer-aided diagnosis: a survey with bibliometric analysis.** *Int J Med Inform* 2017;101:58–67 CrossRef Medline
20. Lladó X, Ganiler O, Oliver A, et al. **Automated detection of multiple sclerosis lesions in serial brain MRI.** *Neuroradiology* 2012;54:787–807 CrossRef Medline
21. Martola J, Bergström J, Fredrikson S, et al. **A longitudinal observational study of brain atrophy rate reflecting four decades of multiple sclerosis: a comparison of serial 1D, 2D, and volumetric measurements from MRI images.** *Neuroradiology* 2010;52:109–17 CrossRef Medline
22. Tian W, Zhu T, Zhong J, et al. **Progressive decline in fractional anisotropy on serial DTI examinations of the corpus callosum: a putative marker of disease activity and progression in SPMS.** *Neuroradiology* 2012;54:287–97 CrossRef Medline
23. Calcagno G, Staiano A, Fortunato G, et al. **A multilayer perceptron neural network-based approach for the identification of responsiveness to interferon therapy in multiple sclerosis patients.** *Information Sciences* 2010;180:4153–63 CrossRef
24. Südmeyer M, Pieperhoff P, Ferrea S, et al. **Longitudinal deformation-based morphometry reveals spatio-temporal dynamics of brain volume changes in patients with corticobasal syndrome.** *PLoS One* 2012;7:e41873 CrossRef Medline
25. Durand-Dubief F, Belaroussi B, Armspach J, et al. **Reliability of longitudinal brain volume loss measurements between 2 sites in patients with multiple sclerosis: comparison of 7 quantification techniques.** *AJNR Am J Neuroradiol* 2012;33:1918–24 CrossRef Medline
26. Fuentes D, Contreras J, Yu J, et al. **Morphometry-based measurements of the structural response to whole-brain radiation.** *Int J Comput Assist Radiol Surg* 2015;10:393–401 CrossRef Medline
27. Unay D. **Local and global volume changes of subcortical brain structures from longitudinally varying neuroimaging data for dementia identification.** *Comput Med Imaging Graph* 2012;36:464–73 CrossRef Medline
28. Thirion JP, Calmon G. **Deformation analysis to detect and quantify active lesions in three-dimensional medical image sequences.** *IEEE Trans Med Imaging* 1999;18:429–41 CrossRef Medline
29. Davatzikos C, Vaillant M, Resnick S, et al. **Morphological analysis of brain structures using spatial normalization.** In: Höhne KH, Kinikis R. *Visualization in Biomedical Computing: 4th International Conference, VBC '96, Hamburg, Germany, September 22–25, 1996: Proceedings*. Berlin: Springer-Verlag; 1996:355–60
30. Rey D, Subsol G, Delingette H, et al. **Automatic detection and segmentation of evolving processes in 3D medical images: application to multiple sclerosis.** *Med Image Anal* 2002;6:163–79 CrossRef Medline
31. Evans AC, Collins DL, Mills S, et al. **3D statistical neuroanatomical models from 305 MRI volumes.** In: Institute of Electrical and Electronics Engineers. IEEE Nuclear and Plasma Sciences Society. *Nuclear Science Symposium and Medical Imaging Conference*, 1993; 1993 IEEE Conference Record. Piscataway: Institute of Electrical and Electronics Engineers; 1993:1813–17
32. Ashburner J, Friston KJ. **Unified segmentation.** *Neuroimage* 2005;26: 839–51 CrossRef Medline
33. Ashburner J, Barnes G, Chen C, et al. *SPM12 Manual*. London: Wellcome Trust Centre for Neuroimaging; 2016
34. Ashburner J, Ridgway GR. **Symmetric diffeomorphic modeling of longitudinal structural MRI.** *Front Neurosci* 2012;6:197 CrossRef Medline
35. Seghier ML, Ramlackhansingh A, Crinion J, et al. **Lesion identification using unified segmentation-normalisation models and fuzzy clustering.** *Neuroimage* 2008;41:1253–66 CrossRef Medline
36. Greiner M, Pfeiffer D, Smith R. **Principles and practical application of the receiver-operating characteristic analysis for diagnostic tests.** *Prev Vet Med* 2000;45:23–41 CrossRef Medline
37. Hanley JA, McNeil BJ. **The meaning and use of the area under a receiver operating characteristic (ROC) curve.** *Radiology* 1982;143: 29–36 CrossRef Medline
38. Miller RG. **The jackknife—a review.** *Biometrika* 1974;61:1–15
39. Cabezas M, Corral J, Oliver A, et al. **Improved automatic detection of new T2 lesions in multiple sclerosis using deformation**

- fields.** *AJNR Am J Neuroradiol* 2016 Jun 9. [Epub ahead of print] [CrossRef Medline](#)
40. Frangi AF, Niessen WJ, Vincken KL, et al. **Multiscale vessel enhancement filtering.** In: Wells WM, Colchester AC, Delp S. *Medical Image Computing and Computer-Assisted Intervention: MICCAI'99*. Berlin: Springer-Verlag; 1998:130–37
 41. Li Q, Sone S, Doi K. **Selective enhancement filters for nodules, vessels, and airway walls in two- and three-dimensional CT scans.** *Med Phys* 2003;30:2040–51 [CrossRef Medline](#)
 42. Forkert N, Fiehler J, Suniaga S, et al. **A statistical cerebroarterial atlas derived from 700 MRA datasets.** *Methods Inf Med* 2013;52:467–74 [CrossRef Medline](#)
 43. Park J, Kim EY. **Contrast-enhanced, three-dimensional, whole-brain, black-blood imaging: application to small brain metastases.** *Magn Reson Med* 2010;63:553–61 [CrossRef Medline](#)
 44. Park J, Kim J, Yoo E, et al. **Detection of small metastatic brain tumors: comparison of 3D contrast-enhanced whole-brain black-blood imaging and MP-RAGE imaging.** *Invest Radiol* 2012;47:136–41 [CrossRef Medline](#)

Pituitary Macroadenoma and Visual Impairment: Postoperative Outcome Prediction with Contrast-Enhanced FIESTA

 S. Hisanaga,  S. Kakeda,  J. Yamamoto,  K. Watanabe,  J. Moriya,  T. Nagata,  Y. Fujino,  H. Kondo,  S. Nishizawa, and  Y. Korogi



ABSTRACT

BACKGROUND AND PURPOSE: Contrast-enhanced FIESTA can depict anterior optic pathways in patients with large suprasellar tumors. We assessed whether the degree of kink in the optic nerve at the optic canal orifice on contrast-enhanced FIESTA correlates with the postoperative improvement of visual impairment in patients with pituitary macroadenoma.

MATERIALS AND METHODS: Thirty-one patients with pituitary macroadenoma who underwent preoperative MR imaging and an operation were evaluated. We measured the optic nerve kinking angle on sagittal oblique contrast-enhanced FIESTA parallel to the optic nerve; the optic nerve kinking angle was defined as the angle between a line parallel to the planum sphenoidale and a line parallel to the intracranial optic nerve at the optic canal orifice. We used logistic regression analyses to determine whether the clinical (sex, age, and duration of symptoms) and imaging (tumor height, chiasmal compression severity, hyperintense optic nerve on T2WI, and optic nerve kinking angle) characteristics were associated with the postoperative improvement (good-versus-little improvement) of visual acuity disturbance and visual field defect.

RESULTS: There were 53 impaired sides before the operation: 2 sides with visual acuity disturbance alone, 25 with visual field defect alone, and 26 with both. After the operation, good improvement was found in 17 of the 28 sides with visual acuity disturbance and in 32 of the 51 sides with visual field defects. Only the optic nerve kinking angle was significantly associated with good improvement of the visual acuity disturbance ($P = .011$) and visual field defect ($P = .002$).

CONCLUSIONS: The degree of the optic nerve kinking angle was an independent predictor of postoperative improvement, indicating that irreversible damage to the optic nerve may be associated with its kinking at the optic canal orifice.

ABBREVIATIONS: CE = contrast-enhanced; ON = optic nerve; ONKA = optic nerve kinking angle; VAD = visual acuity disturbance; VFD = visual field defect

In patients with pituitary macroadenoma, the presence of visual impairment, namely visual acuity disturbance (VAD) and visual field defect (VFD), is a major indication for surgical treatment.¹ Although several studies have reported that the VFD in some 10%–20% of cases was not improved with an operation,^{2–4} the predictors for the postoperative improvement of visual impairment are controversial. Furthermore, few studies have evaluated the ability of MR imaging to predict postoperative improvement in visual impairment. Watanabe et al⁵ reported that a hyperintense optic nerve (ON) on MR imaging predicted persistence of visual impairment after the

operation, but the group of patients in whom VAD and/or VFD persisted after an operation was quite small (only 4 patients).⁵


Bitemporal hemianopia is a well-known VFD associated with pituitary macroadenomas that compress the chiasm. However, a recent report revealed that complete bitemporal hemianopia associated with pituitary macroadenoma was rare.⁶ The authors also demonstrated that 44.9% of patients with VFDs had nontemporal defects, suggesting that it is not uncommon to have extrachiasmal optic pathway involvement rather than chiasmal compression alone. Furthermore, in large suprasellar tumors, such as tuberculum sellae meningiomas, the ONs are sometimes compressed at the optic canal orifice, and some investigators suggest that ON compression at the optic canal orifice may be the main cause of visual impairment and asymmetric visual loss.^{7,8}

Balanced steady-state free-precession techniques, such as fast imaging employing steady-state acquisition, constructive interference in steady state, fast imaging with steady-state free precession, and balanced fast-field echo, can provide strong T2 contrast, which emphasizes CSF signals.^{9–12} FIESTA also shows contrast enhancement due to T1 shortening caused by administration of

Received January 11, 2017; accepted after revision June 6.

From the Departments of Radiology (S.H., S.K., K.W., J.M., Y.K.), Neurosurgery (J.Y., S.N.), Ophthalmology (T.N., H.K.), and Preventive Medicine and Community (Y.F.), University of Occupational and Environmental Health School of Medicine, Kitakyushu, Japan.

Please address correspondence to Shingo Kakeda, MD, Department of Radiology, University of Occupational and Environmental Health, 1-1 Iseigaoka, Yahatanishi-ku, Kitakyushu 807-8555, Japan; e-mail: kakeda@med.uoeh-u.ac.jp

 Indicates article with supplemental on-line tables.

<http://dx.doi.org/10.3174/ajnr.A5394>

gadolinium-based contrast material, because signal intensity on FIESTA is partially T1-dependent.^{13,14} Therefore, in patients with skull base tumors, gadolinium-based contrast material can increase the relative contrast between the enhanced tumor and the cranial nerves using FIESTA. A previous study reported that contrast-enhanced FIESTA (CE-FIESTA) was a useful MR imaging method for performing preoperative evaluation of suprasellar tumors, because CE-FIESTA can depict segments of the optic pathways in patients with large suprasellar tumors.⁵

When using CE-FIESTA, we frequently observe kinking in the ON at the optic canal orifice because of compression by pituitary macroadenomas, prompting the hypothesis that this feature on CE-FIESTA might be useful for determining the postoperative prognosis of visual impairment. Thus, the aim of the current study was to determine whether the degree of ON kink at the optic canal orifice correlates with the postoperative improvement of visual impairment in patients with pituitary macroadenoma.

MATERIALS AND METHODS

Patient Selection

The institutional review board approved this retrospective study and waived informed consent. By searching and reviewing the operative records in our institution between May 2007 and May 2015, we selected 34 consecutive patients with pituitary adenomas who underwent an operation and received a pathologically proved diagnosis. A single radiologist (S.H., with 4 years' experience in radiology) included patients in this study provided they met all of the following: 1) They had a pituitary macroadenoma that tightly touched or compressed the optic pathways on MR imaging; 2) they had undergone preoperative brain MR imaging examinations with our standard brain MR imaging protocol, which included CE-FIESTA; 3) after an operation, the tumor reduction and compression of the optic chiasm resolved; and 4) formal ophthalmology consultations before and after the surgical treatment were available. Three of the 34 patients were excluded from analysis for the following reasons: One was diagnosed with a pituitary apoplexy, and one had a history of an operation due to a brain tumor. One patient with optic disc pallor and atrophy on ophthalmologic examinations before the operation was also excluded because it predicted poor outcome.¹⁵ In this patient, the VAD and/or VFD persisted after the operation. Thirty-one patients were ultimately included in the final analysis (16 women, 15 men; mean age, 54.6 ± 16.9 years; age range, 18–87 years). The surgical approach was transsphenoidal in all patients.

Before the operation, 29 (94%) of 31 patients had VAD and/or VFD. The ophthalmologic examinations showed VADs in 18 patients (bilateral in 10 patients and unilateral in 8). Regarding VFDs, the ophthalmologic examinations showed bilateral temporal hemianopia in 17 patients, unilateral temporal hemianopia in 5 patients, bilateral superior temporal defects in 3 patients, bilateral homonymous hemianopia in 2 patients, and bilateral central scotoma in 1 patient. There were 53 impaired sides in 29 patients: 2 sides (4%) with VAD alone, 25 (47%) with VFD alone, and 26 (49%) both with VAD and VFD. Two patients who had neither VAD nor VFD underwent surgical treatment for chiasmal compression due to pituitary macroadenoma; 1 patient also showed tumor progression during follow-up MR imaging.

MR Imaging Data Acquisition

All MR imaging studies were performed with a Signa Excite 3T scanner (GE Healthcare, Milwaukee, Wisconsin) using a dedicated 8-channel phased array coil (USA Instruments, Aurora, Ohio). Gadodiamide (Omniscan; GE Healthcare, Piscataway, New Jersey) or gadopentetate dimeglumine (Magnevist; Bayer HealthCare Pharmaceuticals, Wayne, New Jersey) was administered at 0.1 mmol/kg of body weight as the intravenous contrast agent. We used the following parameters for the FIESTA sequence: TR/TE, 5.4/2.4 ms; acquisition, 2 times; flip angle, 50°; bandwidth, ± 62.5 kHz; matrix, 224×224 ; 100% image; section thickness, 0.8 mm; FOV, 14×14 cm; resolution, $0.6 \times 0.6 \times 0.8$ mm; and imaging time, 5 minutes 6 seconds. All CE-FIESTA data were acquired in the coronal plane. In addition, all patients underwent our standard brain MR imaging protocol for suprasellar tumors, including coronal T2WI. We used the following imaging parameters for the coronal T2WI: TR/TE, 4000/85 ms; flip angle, 90°; bandwidth, 62.5 kHz; section thickness, 3 mm; matrix, 512×224 ; FOV, 18×18 cm; imaging time, 2 minutes 16 seconds.

Ophthalmologic Examination and Evaluation

Ophthalmologic examinations were performed by ophthalmologists and consisted of testing the patient's visual acuity with the best-corrected visual acuity for both eyes, funduscopy, and measuring intraocular pressure for the diagnosis of concomitant disorders, such as glaucoma or/and cataracts. VAD was positive when the visual acuity with the best-corrected visual acuity was $<20/50$ vision on the Snellen Eye Chart.¹⁶ The visual fields were determined with the Goldmann perimeter (isopters: V/4, III/4, I/4, I/3, I/2, and I/1).¹⁷

The pre- and postoperative VAD and/or VFD were compared, and the patients were divided into 2 subgroups based on the improvement between the 2 points: good improvement versus little improvement. For patients who had undergone an ophthalmologic examination after the operation, the results of the most recent examination were included in this analysis. For VADs, good postoperative improvement was defined when the postoperative visual acuity with the best-corrected visual acuity was 20/50 vision or better on the Snellen Eye Chart, whereas little improvement was defined when the postoperative visual acuity with the best-corrected visual acuity was $<20/50$ vision, despite the absence of any concomitant disorders. For VFDs, good postoperative improvement was defined as either the disappearance of the VFD or the persistence of the VFD with I/3, I/2, or I/1, whereas little improvement was defined as the persistence of the VFD with V/4, III/4, or I/4.

Image Interpretation

Two radiologists (radiologists A [J.M.] and B [K.W.], with 16 and 8 years' experience in neuroradiology, respectively), who were unaware of the clinical findings, independently evaluated the CE-FIESTA and coronal T2WI. To assess the CE-FIESTA findings, we used 3 cross-sectional images (coronal, axial, and sagittal) reconstructed with a section thickness of 1 mm without a gap. First, the 2 radiologists evaluated the CE-FIESTA data for depiction of the anterior optic pathways, and this was scored as either visible or invisible. Simultaneously, the radiologists also blindly reviewed

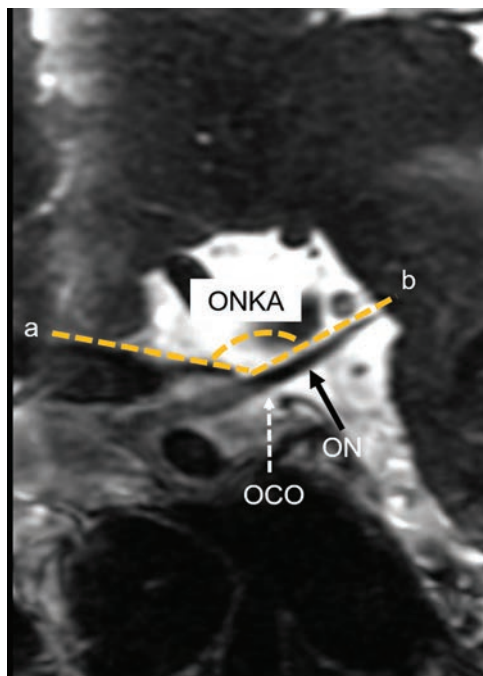


FIG 1. A sagittal oblique CE-FIESTA from a subject with normal brain MR imaging findings shows the optic nerve kinking angle. a = line extending across the anterior cranial fossa, b = line through the intracranial optic nerve. OCO indicates optic canal orifice.

abnormal signal intensity in the anterior optic pathways (bilateral ONs, optic chiasm, and bilateral optic tracts) on CE-FIESTA images. The signal intensity of the optic chiasm and tracts could not be sufficiently evaluated with T2WI because it could not depict the optic chiasm and tracts when they were markedly thinned and/or deviated due to tumor compression. Thus, for the T2WI, the radiologists reviewed the signal intensity only in the bilateral ONs. The radiologists also classified the degree of chiasmal compression on CE-FIESTA into 2 grades (mild or moderate compression, <5 mm of optic chiasm displacement; and severe compression, ≥ 5 mm of optic chiasm displacement).⁶ The cephalocaudal diameter of each tumor was also measured on sagittal CE-FIESTA images. According to the information above, for the analyses, we used the final judgments by 2 radiologists in consensus and the mean measurements by the radiologists.

Measurement of the Optic Nerve Kinking Angle at the Optic Canal Orifice

Two radiologists (J.M. and K.W.) measured the optic nerve kinking angle (ONKA) on sagittal oblique images parallel to the ON reconstructed from CE-FIESTA image data. The ONKA was defined as the angle between a line parallel to the planum sphenoidale and a line parallel to the intracranial ON at the optic canal (Fig 1). Although we found susceptibility artifacts on CE-FIESTA related to the skull base, no cases showed any degradation of the image quality for measuring the ONKA.

Statistical Analyses

All the statistical analyses were performed with the SPSS program (IBM, Armonk, New York). κ statistics were used to evaluate the level of interobserver agreement of scores from the 2 radiologists. The strength of agreement was considered fair for κ values of

Table 1: The evaluation of chiasmal compression by 2 radiologists

Radiologist B	Radiologist A		
	Mild or Moderate	Severe	Total
Mild or moderate	7	2	9
Severe	4	18	22
Total	11	20	31

Table 2: The evaluations of hyperintense ON at T2WI by 2 radiologists

Radiologist B	Radiologist A		
	Absent	Present	Total
Absent	35	5	40
Present	0	22	22
Total	35	27	62

0.21–0.40, moderate for κ values of 0.41–0.60, good for κ values of 0.61–0.80, and excellent for κ values of ≥ 0.81 .¹⁸ The percentage agreement between measurements (tumor height and ONKA) from the radiologists was also calculated by concordance correlation coefficients and 95% confidence intervals.¹⁹ To determine the variables associated with the visual impairment before the operation and postoperative improvement, we used a univariate binary logistic regression analysis using generalized estimating equations that adjusted for laterality of the optic pathway. The variables included the clinical (age, sex, and duration of symptoms) and imaging (tumor height, chiasmal compression, hyperintense ONs on T2WI, and ONKA) characteristics. P values $< .05$ indicated statistical significance. For the ONKA, we calculated the sensitivity, specificity, and accuracy for the prediction of postoperative improvement. For this analysis, we used cutoff values in a receiver operating characteristic curve analysis, which were determined with the Youden index.²⁰

RESULTS

In all cases, 1 radiologists could detect the optic pathway with CE-FIESTA. Radiologists A and B scored 20 (65%) and 22 (71%) of 31 optic chiasms as severe chiasmal compression, respectively (Table 1). On the basis of the ratings of radiologists A and B, hyperintense ONs on T2WI were seen in 27 (44%) of 62 sides and 22 (35%) sides, respectively (Table 2). On CE-FIESTA, the radiologists found an area of abnormal high signal intensity in the center of the right optic tract in only 1 patient, who had little improvement of visual impairment after the operation. Therefore, we excluded the finding of hyperintense ONs on CE-FIESTA from all analyses because it was thought to be of infrequent incidence.

The presence of chiasmal compression and hyperintense ONs on T2WI was shown to have moderate and excellent interobserver agreement, with κ values of 0.56 and 0.83, respectively. Interobserver reproducibility of measurements by the 2 radiologists demonstrated 99% agreement for tumor height (95% CI, 97%–99%) and 98% for ONKA (95% CI, 69%–99%).

The multivariate logistic regression analyses showed that hyperintense ON ($P = .020$) and ONKA ($P = .030$) were independently associated with the presence of VAD before the operation (On-line Table 1). The multivariate logistic regression analyses showed that the chiasmal compression severity ($P = .047$) was

independently associated with the presence of VFD before the operation (On-line Table 1).

The postoperative ophthalmologic examinations were obtained, on average, 14.8 days (range, 4–92 days) after the operation. Of the 29 sides with VAD and the 51 sides with VFD before the operation, we found good improvement after the operation in 17 (59%) and 32 (63%) sides, respectively. For VAD, the univariate and multivariate analyses revealed that only ONKA ($P = .009$ and $P = .011$, respectively) was significantly associated with postoperative improvement (On-line Table 2 and Figs 2 and 3). For VFD, the multivariate analysis revealed that only ONKA ($P = .002$) was significantly associated with postoperative improvement (On-line Table 2).

The receiver operating characteristic analysis suggested optimal cutoff levels for the ONKA ($\geq 102.5^\circ$ for VAD and $\geq 114.5^\circ$ for VFD) for prediction of the postoperative improvement. Therefore, the sensitivity, specificity, and accuracy for the prediction of postoperative improvement with ONKA were 88% (15/17), 92% (11/12), and 90% (26/29) for VAD and 72% (23/32), 89% (17/19), and 78% (40/51) for VFD, respectively (Table 3).

DISCUSSION

Multivariate and univariate analyses demonstrated that the degree of ONKA was the only independent predictor of postoperative improvement for VAD and VFDs. Other MR imaging findings were associated with visual impairment before the operation but not with its postoperative improvement.

The ONKA with an optimal cutoff level had a high specificity for the prediction of postoperative improvement of VAD and VFD. This result indicates that patients with ONKA of $<114.5^\circ$ may have potential irreversible damage to the ON. Regarding this irreversible damage to the ON at the optic canal orifice, we speculate 2 possible mechanisms: 1) direct damage due to ON compression from the falx ligaments, and 2) hemodynamic complications affecting the ON induced by the kink. In large suprasellar tumors, the ONs have been compressed by the falx ligament at the optic canal orifice.²¹ Therefore, the decompression procedure of the optic canal consists of extradural anterior clinoidectomy with falx lig-

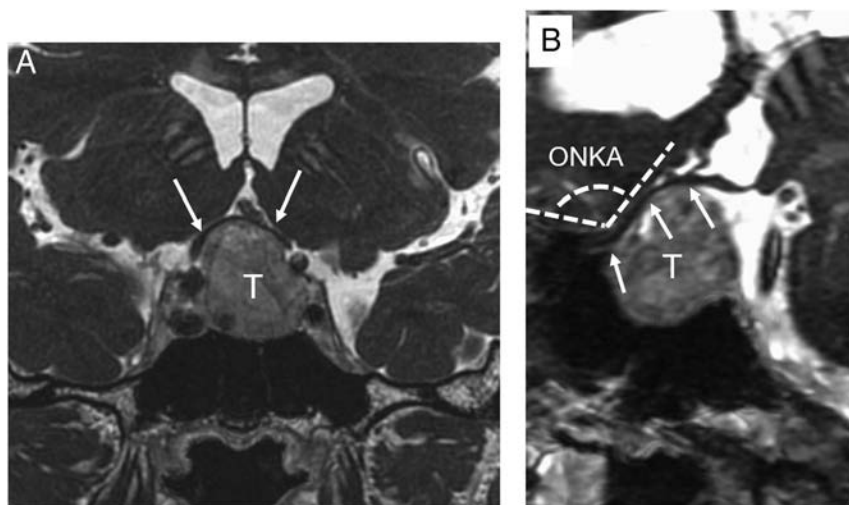


FIG 2. Images from a 53-year-old man with a pituitary macroadenoma who presented with left visual acuity disturbance (20/50 vision on the Snellen Eye Chart) before the operation. After the operation, the left visual acuity disturbance was improved (20/20 vision on the Snellen Eye Chart). A, A coronal CE-FIESTA image shows severe chiasmal compression (arrows) by the pituitary macroadenoma. B, A sagittal oblique CE-FIESTA image demonstrates a left optic nerve kinking angle of 120° . The arrows indicate the left optic nerve. T indicates pituitary macroadenoma.

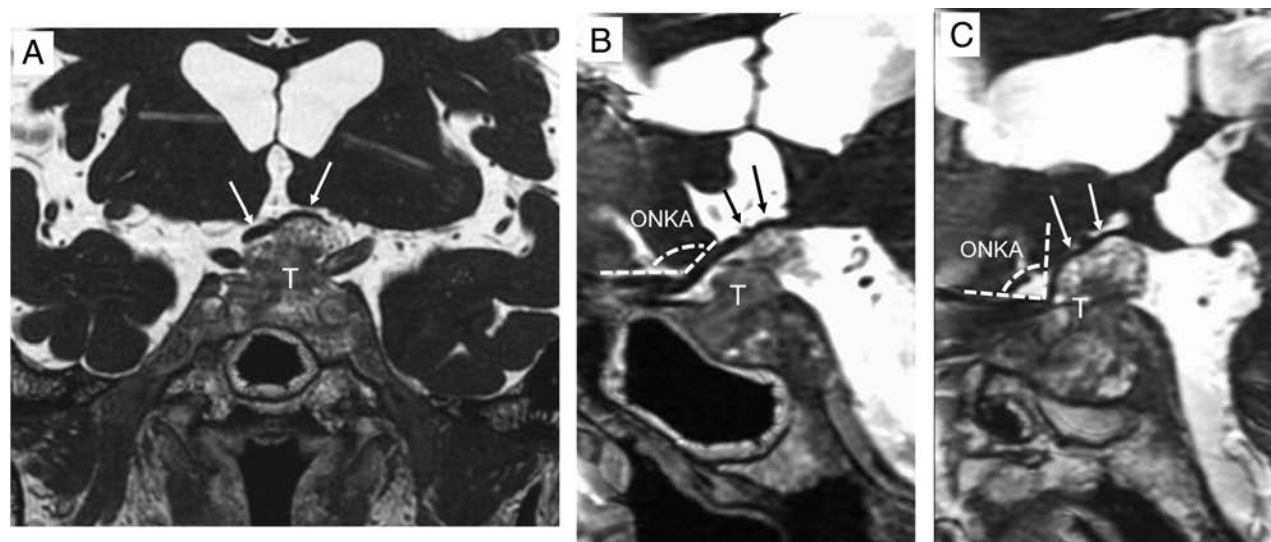


FIG 3. Images from a 75-year-old man with a pituitary macroadenoma who presented with a bilateral visual acuity disturbance (right: 20/50 and left: 20/70 vision on the Snellen Eye Chart, respectively) before the operation. After the operation, the left visual acuity disturbance was not improved (20/50 vision), though the right visual acuity disturbance was improved (20/30 vision). Left optic atrophy (disc pallor) was noted on a postoperative assessment by an ophthalmologist, but there were negative findings on the preoperative assessment. A, A coronal CE-FIESTA image shows moderate chiasmal compression by the pituitary macroadenoma. A sagittal oblique CE-FIESTA image demonstrates a right optic nerve (arrows) kinking angle of 133° (B) and a left optic nerve (arrows) kinking angle of 90° (C). T indicates pituitary macroadenoma.

Table 3: ONKA with CE-FIESTA—correlation with indicators of postoperative good improvement^a

	VAD	VFD
Cutoff values for the ONKA	≥102.5°	≥114.5°
Sensitivity	88 (15/17)	72 (23/32)
Specificity	92 (11/12)	89 (17/19)
Accuracy	90 (26/29)	78 (40/51)

^aData are percentages. Numbers in parentheses were used to calculate the percentages.

ament and optic nerve sheath opening.²¹ Regarding the hemodynamic complications, Hoyt²² reported that ON compression due to pituitary macroadenoma disrupts the arterial supply, and long-term compression of the arteries, veins, and capillary networks in the ON leads to stagnant anoxia. We believe that these mechanisms have resulted in a cumulative or additive effect for irreversible damage to the ON.

The ONKA measurement as a quantitative evaluation demonstrated excellent interobserver agreement, possibly due to the high accuracy of CE-FIESTA in depicting the anterior optic pathways. For ON depiction in patients with pituitary macroadenoma, CE-FIESTA has several advantages over conventional MR images—namely the high spatial resolution and defined contrast difference between the tumor and surrounding structures, such as the ON, CSF, and skull bone.⁵ The spatial resolution with CE-FIESTA is $0.6 \times 0.6 \times 0.8$ mm, and 3D CE-FIESTA data also allow radiologists to examine the entire optic pathway contiguously. Furthermore, CE FIESTA images provide good contrast of the optic pathway relative to enhanced tumor and CSF, because the optic pathway has a low signal intensity, whereas the enhanced tumor and CSF have high signal intensity. Conversely, the contrast difference between the ON and tumors with T2WI may decrease due to hyperintense ONs caused by compression by the tumor. For CE-T1WI, the poor visibility of the optic pathways may be due to poor contrast between the CSF and the optic pathways; both may be hypointense on CE-T1WI. Therefore, our assessment with CE-FIESTA has clinical importance in that it may provide a simple and reproducible method for evaluating the irreversible visual impairment in patients with a pituitary macroadenoma.

Regarding the association between the duration of symptoms and the postoperative improvement of VFD, the results from previous studies are inconsistent,^{2-4,23} and we found no association between them. One possible explanation for our result may be due to poor subjective symptoms caused by pituitary macroadenomas because of their slow growth. Hyperintensity of the ONs was also not associated with irreversible damage to the ON. Our results are supported by the findings of a previous report⁵; for the prediction of irreversible damage to the ONs after an operation in a large suprasellar tumor, hyperintense ONs on T2WI had good sensitivity (100%) but poor specificity (42%), suggesting the possibility of not only degeneration of the ONs but also reversible damage as an etiologic factor in the hyperintense ONs.

Although VFDs are well-known to be caused by chiasmal compression, we found that the degree of chiasmal compression was not associated with irreversible damage to the ONs. Our results indicate that for reflecting damage to the ONs, an ON kink at the optic canal orifice may be a more important factor than chiasmal compression. In a previous study, hyperintensity of the optic

pathways on CE-FIESTA had high accuracy in predicting irreversible damage to the ONs.⁵ Consistent with the findings from this previous report, we found 1 patient with hyperintensity on CE-FIESTA who had little improvement of visual impairment after the operation. However, this finding seems to be of infrequent incidence in patients with pituitary macroadenomas. The previous study also demonstrated that an optic nerve size on MR imaging is an important predictive factor for vision recovery.¹⁵ However, we excluded this finding from all analyses because there was no case with obvious optic nerve atrophy on MR imaging. The main reason seems to be that almost all our cases included patients with a relatively shorter duration of vision loss. Our data indicate that optic nerve atrophy on MR imaging may be a finding in advanced phases of compressive neuropathy.

Our study has several limitations. First, the postoperative ophthalmologic examinations were performed at various intervals after an operation. Moreover, in the current study, the mean time to postoperative ophthalmologic examinations was relatively short (14.9 days). One previous report showed that postoperative improvement of the VFD was progressive and apparent even at the 5-year follow-up.⁴ Therefore, this finding may lead to overestimation of the association between the ONKA and the postoperative improvement of visual impairment. Further prospective long-term follow-up studies, including thorough clinical investigations, are needed to determine the clinical impact of the finding of the ONKA. Second, we evaluated VFDs using the ophthalmologic examination, in which, however, false-positives and false-negatives can occur with the perimetry, depending on patient cooperation. Chouinard et al²⁴ demonstrated that longitudinal changes in visual field perimetry before and after the operation correlated with those in fMRI activation in a retinotopic manner. Because a retinotopic examination with fMRI is passive and more objective, in a further study, the use of fMRI may allow a more accurate evaluation of VFD.

CONCLUSIONS

In our logistic analyses, the only independent predictor of postoperative improvement of visual impairment in patients with pituitary macroadenomas was the degree of ONKA. Our results indicate that early irreversible damage to the ONs is associated with kinking at the optic canal orifice caused by compression of the pituitary macroadenomas. Our quantitative assessment with CE-FIESTA with high excellent interobserver agreement may provide useful information for managing patients with pituitary macroadenomas. This study suggests that CE-FIESTA is indeed a beneficial and practical MR imaging method for the preoperative evaluation of pituitary macroadenomas.

REFERENCES

1. Fahlbusch R, Honegger J, Buchfelder M. **Surgical management of acromegaly.** *Endocrinol Metabol Clin North Am* 1992;21:669–92 [Medline](#)
2. Powell M. **Recovery of vision following transsphenoidal surgery for pituitary adenomas.** *Br J Neurosurg* 1995;9:367–74 [Medline](#)
3. Peter M, De Tribolet N. **Visual outcome after transsphenoidal surgery for pituitary adenomas.** *Br J Neurosurg* 1995;9:151–57 [CrossRef Medline](#)
4. Gnanalingham K, Bhattacharjee S, Pennington R, et al. **The time**

- course of visual field recovery following transphenoidal surgery for pituitary adenomas: predictive factors for a good outcome. *J Neurol Neurosurg Psychiatry* 2005;76:415–19 [CrossRef Medline](#)
5. Watanabe K, Kakeda S, Yamamoto J, et al. Delineation of optic nerves and chiasm in close proximity to large suprasellar tumors with contrast-enhanced FIESTA MR imaging. *Radiology* 2012;264:852–58 [CrossRef Medline](#)
 6. Lee IH, Miller NR, Zan E, et al. Visual defects in patients with pituitary adenomas: the myth of bitemporal hemianopsia. *AJR Am J Roentgenol* 2015;205:W512–18 [CrossRef Medline](#)
 7. Margalit NS, Lesser JB, Moche J, et al. Meningiomas involving the optic nerve: technical aspects and outcomes for a series of 50 patients. *Neurosurgery* 2003;53:523–33; discussion 532–33 [CrossRef Medline](#)
 8. Liu JK, Christiano LD, Patel SK, et al. Surgical nuances for removal of tuberculum sellae meningiomas with optic canal involvement using the endoscopic endonasal extended transsphenoidal transplanum transtuberculum approach. *Neurosurg Focus* 2011;30:E2 [CrossRef Medline](#)
 9. Haacke EM, Wielopolski PA, Tkach JA, et al. Steady-state free precession imaging in the presence of motion: application for improved visualization of the cerebrospinal fluid. *Radiology* 1990;175:545–52 [CrossRef Medline](#)
 10. Tsuchiya K, Aoki C, Hachiya J. Evaluation of MR cisternography of the cerebellopontine angle using a balanced fast-field-echo sequence: preliminary findings. *Eur Radiol* 2004;14:239–42 [CrossRef Medline](#)
 11. Chung HW, Chen CY, Zimmerman RA, et al. T2-weighted fast MR imaging with true FISP versus HASTE: comparative efficacy in the evaluation of normal fetal brain maturation. *AJR Am J Roentgenol* 2000;175:1375–80 [CrossRef Medline](#)
 12. Jayakumar PN, Kovoov JM, Srikanth SG, et al. 3D steady-state MR cisternography in CSF rhinorrhoea. *Acta Radiol* 2001;42:582–84 [CrossRef Medline](#)
 13. Shigematsu Y, Korogi Y, Hirai T, et al. Contrast-enhanced CISS MRI of vestibular schwannomas: phantom and clinical studies. *J Comput Assist Tomogr* 1999;23:224–31 [CrossRef Medline](#)
 14. Davagnanam I, Chavda SV. Identification of the normal jugular foramen and lower cranial nerve anatomy: contrast-enhanced 3D fast imaging employing steady-state acquisition MR imaging. *AJNR Am J Neuroradiol* 2008;29:574–76 [CrossRef Medline](#)
 15. Carlson AP, Stippler M, Myers O. Predictive factors for vision recovery after optic nerve decompression for chronic compressive neuropathy: systematic review and meta-analysis. *J Neurol Surg B Skull Base* 2013;74:20–38 [CrossRef Medline](#)
 16. McGraw P, Winn B, Whitaker D. Reliability of the Snellen chart. *BMJ* 1995;310:1481–82 [CrossRef Medline](#)
 17. Levin LA. Topical diagnosis of chiasmal and retrochiasmal disorders. In: Miller NR, Walsh FB, Hoyt WF, eds. *Walsh and Hoyt Clinical Neuro-Ophthalmology*. 6th ed. Baltimore: Lippincott Williams & Wilkins; 2005:503–73
 18. Landis JR, Koch GG. The measurement of observer agreement for categorical data. *Biometrics* 1977;33:159–74 [CrossRef Medline](#)
 19. Bernard SA, Murphey MD, Flemming DJ, et al. Improved differentiation of benign osteochondromas from secondary chondrosarcomas with standardized measurement of cartilage cap at CT and MR imaging. *Radiology* 2010;255:857–65 [CrossRef Medline](#)
 20. Youden WJ. Index for rating diagnostic tests. *Cancer* 1950;3:32–35 [CrossRef Medline](#)
 21. Sade B, Lee JH. High incidence of optic canal involvement in tuberculum sellae meningiomas: rationale for aggressive skull base approach. *Surg Neurol* 2009;72:118–23; discussion 123 [CrossRef Medline](#)
 22. Hoyt W. Correlative functional anatomy of the optic chiasm. 1969. *Clin Neurosurg* 1970;17:189–208 [Medline](#)
 23. Cohen AR, Cooper PR, Kupersmith MJ, et al. Visual recovery after transsphenoidal removal of pituitary adenomas. *Neurosurgery* 1985;17:446–52 [CrossRef Medline](#)
 24. Chouinard PA, Striemer CL, Ryu WH, et al. Retinotopic organization of the visual cortex before and after decompression of the optic chiasm in a patient with pituitary macroadenoma: case report. *J Neurosurg* 2012;117:218–24 [CrossRef Medline](#)

Topographic Diagnosis of Craniopharyngiomas: The Accuracy of MRI Findings Observed on Conventional T1 and T2 Images

R. Prieto, J.M. Pascual, and L. Barrios



ABSTRACT

BACKGROUND AND PURPOSE: The topography of craniopharyngiomas has proved fundamental in predicting the involvement of vital brain structures and the possibility of achieving a safe radical resection. Beyond the imprecise term “suprasellar,” indiscriminately used for craniopharyngiomas, an accurate definition of craniopharyngioma topography should be assessed by preoperative MR imaging. The objective of this study was to investigate the MRI findings that help define craniopharyngioma topography.

MATERIALS AND METHODS: This study retrospectively investigated a cohort of 200 surgically treated craniopharyngiomas with their corresponding preoperative midsagittal and coronal conventional T1- and T2-weighted MR images, along with detailed descriptions of the surgical findings. Radiologic variables related to the occupation of the tumor of intracranial compartments and the distortions of anatomic structures along the sella turcica–third ventricle axis were analyzed and correlated with the definitive craniopharyngioma topography observed during the surgical procedures. A predictive model for craniopharyngioma topography was generated by multivariate analysis.

RESULTS: Five major craniopharyngioma topographies can be defined according to the degree of hypothalamic distortion caused by the tumor: sellar-suprasellar, pseudointraventricular, secondary intraventricular, not strictly intraventricular, and strictly intraventricular. Seven key radiologic variables identified on preoperative MRI allowed a correct overall prediction of craniopharyngioma topography in 86% of cases: 1) third ventricle occupation, 2) pituitary stalk distortion, 3) relative level of the hypothalamus in relation to the tumor, 4) chiasmatic cistern occupation, 5) mammillary body angle, 6) type of chiasm distortion, and 7) tumor shape.

CONCLUSIONS: Systematic assessment of these 7 variables on conventional preoperative T1 and T2 MRI is a useful and reliable method to ascertain individual craniopharyngioma topography.

ABBREVIATIONS: CP = craniopharyngioma; CRT = Classification and Regression Tree; LR = likelihood ratio; MBA = mammillary body angle; PS = pituitary stalk; 3V = third ventricle; TVF = third ventricle floor

Craniopharyngiomas (CPs) remain a neurosurgical challenge. This type of tumor is characterized by extreme heterogeneity regarding clinical expression, pathologic features, and topography. The vague, general description of CPs as “suprasellar” tumors has frequently led to imprecise topographic diagnoses.^{1,2} The use of the term “suprasellar” dates to the early 20th Century, when the presence of calcifications above the sella turcica on skull radiographs was the fundamental radiologic sign indicating CP

diagnosis. Currently, the incorrect assumption of a primary suprasellar position for most CPs might lead to improper surgical planning. Therefore, an accurate topographic classification of individual cases should be established preoperatively.²

The potential for CP development at any point along the vertical hypothalamic-hypophyseal axis, from the sella turcica to the third ventricle (3V), determines the wide range of topographies displayed. Certainly, current MR imaging technology provides a tool allowing an accurate definition of CP topography in most cases.^{2,3} The specific anatomic relationships between CPs and the 3V floor and walls, where the vital hypothalamic nuclei are located, are an essential factor for assessing the possibility of achieving a safe radical removal.^{1–5} Consequently, defining the topographic relationships between the tumor and the third ventricle floor (TVF) should be one major objective of preoperative MR imaging in patients with CP.

In 2004, our group developed a topographic classification system based on the types of TVF distortion caused by CPs.^{1–4} This

Received May 16, 2017; accepted June 30.

From the Department of Neurosurgery (R.P.), Puerta de Hierro University Hospital, Madrid, Spain; Department of Neurosurgery (J.M.P.), La Princesa University Hospital, Madrid Spain; and Statistics Department (L.B.), Computing Center, Consejo Superior de Investigaciones Científicas, Madrid, Spain.

Please address correspondence to Ruth Prieto, MD, PhD, Department of Neurosurgery, Puerta de Hierro University Hospital, C/Joaquín Rodrigo 2, Majadahonda, 28222, Madrid, Spain; e-mail: rprieto29@hotmail.com

Indicates article with supplemental on-line tables and appendix.

<http://dx.doi.org/10.3174/ajnr.A5361>

scheme has proved helpful to preoperatively ascertain the anatomic position of the hypothalamus and its degree of distortion, information that is correlated with surgical risks and patient outcome. In previous studies, we have been able to identify some specific MR imaging signs invaluable for defining the true CP-3V relationships, such as the mammillary body angle (MBA) and the type of optic chiasm distortion.^{6,7} The aim of the present study was to analyze the diagnostic power of conventional T1- and T2-weighted sequences for an accurate depiction of CP topography on midsagittal and transinfundibular-coronal MR images. Specifically, we have examined the preoperative MR imaging findings that best predict the type of CP-3V relationships present in each patient.

MATERIALS AND METHODS

Case Series

The cases included in this study were selected from a recent publication in which we analyzed CP topography in a series of 500 cases and correlated it with the patterns of tumor adhesion to the hypothalamus.⁵ A total of 200 CPs published in the MR imaging era (1990–2016) were selected from this cohort, all meeting the following inclusion criteria: 1) CP diagnosis was confirmed pathologically, 2) preoperative midsagittal and transinfundibular-coronal MR images were displayed in the reports, and 3) the patient was surgically treated, and a detailed description and photographic evidence of the tumor relationships with the TVF/hypothalamus was provided (On-line Table 1; On-line Appendix).

Topographic Classification of CPs

The tumors were classified into 5 major categories, according to our classification scheme of CP-3V relationships^{1–5}: 1) sellar-suprasellar CPs, which include tumors occupying exclusively the sellar and/or suprasellar compartments beneath an intact TVF; 2) suprasellar-pseudointraventricular CPs, suprasellar lesions causing an upward displacement of the TVF, mimicking an intraventricular position; 3) secondary intraventricular CPs, lesions developing initially beneath the 3V but invading the 3V after breaking through the TVF; 4) infundibulo-tuberal or not strictly intraventricular CPs, tumors developed originally within the nervous tissue of the TVF itself (within the infundibulum and/or tuber cinereum), which predominantly expand within the 3V at later stages; and 5) strictly intraventricular CPs, tumors primarily originating within the 3V, above an intact TVF (Fig 1). The final CP topographic categorization for the 200 cases constituting our cohort was established in a previous article that analyzed the correlation of intraoperative anatomic and pathologic findings with pre- and postoperative MR imaging studies.⁵ In the present study, we performed a “blinded” analysis of the MR imaging variables used to ascertain the CP topography—that is, in each case, we evaluated the different MR imaging variables without knowing the definitive topography confirmed in our previous article.

Surgical Treatment and Outcome

Surgical routes chosen for each case were recorded and postoperative outcome was classified into 4 categories: 1) good, long-term survival without new neurologic deficits; 2) fair, new but not disabling deficits, including panhypopituitarism or diabetes insipidus; 3) poor,

new neurologic symptoms that considerably impair the quality of life; and 4) death within the first month after surgery.

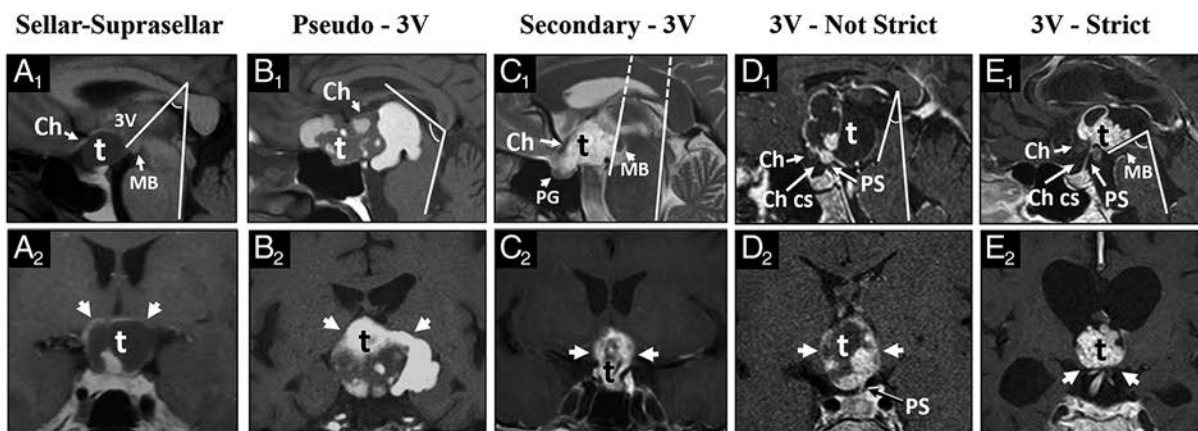
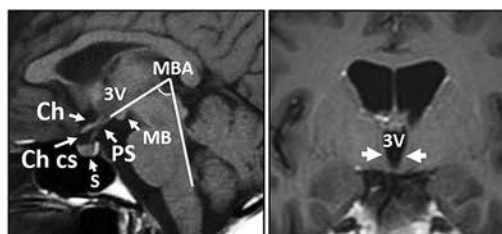
Selection and Categorization of Variables Analyzed on Preoperative MR Images

The size, shape, and consistency of the tumor, in addition to the occupation of intracranial compartments and distortion of anatomic structures along the sella-3V axis, were evaluated on midsagittal and coronal conventional T1- and T2-weighted MR images. Occupation of the sella turcica and chiasmatic cistern was classified into 3 categories (tumor-free, partially occupied, and wholly occupied), whereas only 2 groups were considered regarding the occupation of the 3V (tumor-free or occupied). The appearance of the pituitary stalk (PS) was categorized as follows: 1) wholly visible, intact PS; 2) infiltrated by tumor, thickened PS due to macroscopic tumor infiltration; 3) amputated, PS upper portion not visible due to tumor growth; and 4) not visible, unrecognizable PS due to tumor encroachment. The relative anatomic position between the hypothalamus and the CP, best assessed on coronal MR imaging sections, was classified into 3 groups: 1) below the lower tumor pole level, 2) around its midthird portion, and 3) above the upper third of the tumor. We measured the mammillary body angle, formed by the intersection of a plane tangential to the base of the mammillary bodies with the plane tangential to the fourth ventricle floor, on the midsagittal MR images.⁶

Finally, the chiasm distortion caused by the tumor was evaluated and classified according to the scheme published by our group in 2013: 1) not distorted, normal position and shape; 2) compressed downward, flattened chiasm at the anteroinferior margin of the tumor; 3) compressed forward, flattened chiasm between the tumor and the tuberculum sellae; 4) stretched forward, elongated along the anterior margin of the tumor; 5) stretched upward, elongated chiasm along the superior surface of the tumor; 6) stretched backward, elongated along the posterior margin of the tumor; and 7) not visible, completely unrecognizable.⁷

Statistical Analysis

Bilateral correlations between pairs of categorical variables were assessed with the asymptotic χ^2 , the Monte Carlo exact, or the linear-by-linear association tests. A multivariate Classification and Regression Tree (CRT) growing method was then applied to explain CP topography. This hierarchic stepwise procedure creates a decision tree by splitting the cohort into 2 branches at each step to maximize the homogeneity of case subgroups within each branch. At each step, the CRT chooses the nominal variable showing the strongest independent interaction with the topographic categories included in the previous step. Then, we used a multiple correspondence analysis to investigate the power of the radiologic variables selected in the first and second steps by the CRT method. Finally, we quantified the accuracy of the multivariate MR imaging model generated to discriminate among the 5 CP categories. For that purpose, we used the likelihood ratio (LR) for positive test results [$LR+ = \text{sensitivity}/(1-\text{specificity})$] and [$LR- = (1-\text{sensitivity})/\text{specificity}$] for negative test results. Statistical analyses



	Sellar-Suprasellar	Pseudo-3V	Secondary-3V	3V-Not Strict	3V-Strict
3V	Free	Occupied	Occupied	Occupied	Occupied
Ch cistern	Wholly occupied	Wholly occupied	Wholly occupied	Partially occupied	Free
Stalk	Not visible	Not visible	Not visible	Amputated, Infiltrated	Wholly visible
Hypothal.	Upper-third	Upper-third	Middle-third	Middle-third	Lower-third
MBA	60-89°	≥90°	30-59°	<30°	30-59°
Chiasm	Stretched upward	Stretched upward	Stretched forward	Compressed forward	Compressed downward
CP shape	Round, Pear-like, Dumbbell	Multilobulated, Pear-like	Multilobulated, Elliptical	Elliptical, Round	Round

FIG 1. Preoperative MR imaging assessment to accurately define the 5 major CP topographies. The upper images correspond to midsagittal and transinfundibular-coronal T1-weighted MR images from a healthy adult. Ch indicates chiasm; Ch cs, chiasm cistern; MB, mammillary body. The middle (1, sagittal) and lower (2, coronal) rows show MR images of the 5 CP topographic categories considered. A, Sellar-suprasellar CP: the Ch cistern is occupied by a round tumor, the PS is not visible, the chiasm is stretched upward, and the hypothalamus (arrows) is above the tumor. B, Pseudointraventricular CP: the sella, the Ch cistern, and the 3V are occupied by a multilobulated tumor. The PS is not visible, the MBA is obtuse, and the hypothalamus (arrows) is over the upper third of the tumor. C, Secondary intraventricular CP: the Ch cistern and the 3V are occupied by the tumor, the PS is not visible, the chiasm is stretched forward, and the hypothalamus (arrows) is around the midthird of the tumor. D, Infundibulo-tuberal or not strictly intraventricular CP: the Ch cistern is partially occupied by tumor, the PS is amputated, the chiasm is compressed forward, the MBA is hyperacute, and the hypothalamus (arrows) is around the midthird of the tumor. E, Strictly intraventricular CP: the Ch cistern is tumor-free, the PS is entirely visible, the chiasm is compressed downward, and the hypothalamus (arrows) is below the lower third of the tumor. The Table summarizes the most typical MR imaging characteristics for each topographic category. T indicates tumor.

were performed using SPSS software (Version 23; IBM, Armonk, New York).

RESULTS

Topographic Distribution and Surgical Outcome

On-line Table 2 shows the distribution of the topographic categories included in this cohort of 200 CPs. The infundibulo-tuberal or not strictly intraventricular category was the predominant one (32.5%, $n = 65$), followed by the strictly intraventricular (21%, $n = 42$). The remaining lesions originating from the pituitary gland–stalk complex beneath the TVF were categorized into the sellar-suprasellar ($n = 37$), pseudointraventricular ($n = 32$), and secondary intraventricular ($n = 24$) topographies.

All patients underwent surgical treatment. The most frequent surgical routes used were basal pterional/subfrontal (31%) and transsphenoidal (33%). Postoperative outcomes were available in 155 of 200 patients. Most cases had a satisfactory long-term outcome: good in 41% and fair, with minor disturbances, in 43% of

cases. Last, an overall 3% mortality ($n = 5$) was registered within the first month following the surgical procedure. Poor outcomes and deaths reported in our cohort were related to the hypothalamic injury inflicted by surgical maneuvers in all cases, a finding analogous to those reported in large surgical series published in the MR imaging era.⁸

Variables Analyzed on Conventional Midsagittal and Coronal MR Imaging

On-line Table 2 presents the distribution of the major radiologic features analyzed on preoperative T1- and T2-weighted MR images. The most common CP shape in this cohort was round (42%), followed by elliptical (22.5%) and multilobulated (22.5%). The sella turcica was tumor-free in almost 60% of the cases and wholly occupied in 25.5%. The chiasmatic cistern was tumor-free in 33% of the cases, showed a partial occupation in 23.5%, and was totally filled in 43.5%. In this cohort, the 3V was occupied by the tumor in almost 90% of cases.

Bivariate relationships between the variables analyzed on preoperative MRI and CP topography

MRI Variables ^a	P Value	Specific Relationships
3V occupation	<.001	Free: highest rate in Sellar-SS (57%) Occupied: in 100% of Pseudo-3V, Secondary, 3V-Not-Strict, and 3V-Strict cases
Stalk visualization	<.001	Visible (wholly identifiable): highest rate in 3V-Strict (79%) Infiltrated: highest rate in 3V-Not-Strict (23%) Amputated (lower half visible): highest rate in 3V-Not-Strict (68%) Not visible: highest rates in Sellar-SS (92%), Pseudo-3V (100%), and Secondary-3V (92%)
Hypothalamus level relative to the CP	<.001	Lower third: highest rate in 3V-Strict (82%) Middle: highest rates in 3V-Not-Strict (91%) and Secondary-3V (77%) Upper third: highest rates in Sellar-SS (100%) and Pseudo-3V (91%)
Chiasmatic cistern	<.001	Free: highest rate in 3V-Strict (98%) Partially occupied: highest rate in 3V-Not-Strict (54%) Wholly occupied: highest rates in Sellar-SS (86.5%), Pseudo-3V (97%), and Secondary-3V (75%)
MBA	<.001	<30°: highest rate in 3V-Not-Strict (43%) 30°–59°: highest rates in Secondary-3V (58%) and 3V-Strict (55%) 60°–89°: highest rate in Sellar-SS (64%) ≥90°: highest rate in Pseudo-3V (89%)
Chiasm distortion	<.001	Compressed downward: highest rates in 3V-Strict (66%) and 3V-Not-Strict (33%) Compressed forward: highest rate in 3V-Not-Strict (40%) Stretched forward: highest rate in Secondary-3V (50%) Stretched upward: highest rates in Sellar-SS (81%) and Pseudo-3V (70%)
Tumor shape	<.001	Round: highest rate in 3V-Strict (76%) Elliptical: highest rate in 3V-Not-Strict (37%) Multilobulated: highest rates in Pseudo-3V (62.5%) and Secondary-3V (62.5%) Pearlike: highest rates in Sellar-SS (30%) and Pseudo-3V (19%) Dumbbell: highest rates in Sellar-SS (13.5%)

Note:—SS indicates suprasellar; 3V-Not-Strict, not strictly intraventricular or infundibulo-tuberal; Pseudo-3V, suprasellar pseudointraventricular; Secondary-3V, secondary intraventricular category; 3V-Strict, strictly intraventricular.

^a Only the 7 variables included in the multivariate predictive model are shown.

The PS could not be identified in almost half of the cases (46.5%), owing to the occupation of the chiasmatic cistern by tumoral tissue. It had a normal appearance in only 18.5% of studies, whereas in 27%, its upper portion was not visible due to tumor growth (a sign we term “PS amputation”). In 8%, the PS appeared thickened due to macroscopic infiltration by the tumor. The position of the hypothalamus relative to the CP was observed around the lower pole of the CP in 19%, around the equator or middle third of the tumor in 42%, and above its upper third in 39% of cases. The MBA could be measured in 84.5% of the cases. This angle was hyperacute (<30°) in 18% of cases, moderately acute (30°–59°) in 31.5%, slightly acute (60°–89°) in 19.5%, and obtuse (≥90°) in 15.5%. Finally, the optic chiasm could be identified in 88.5% of midsagittal MR images and was grossly deformed in most cases. The 2 most common types of chiasm distortion were an upward stretching by CPs originating beneath the TVF (26%) and a downward compression by intraventricular CPs (24%).

Correlation between CP Topography and Surgical Outcome

A significant correlation between CP topography and surgical outcome was found in this cohort ($P < .034$), a fact related to the different degree of hypothalamic involvement associated with each topographic category.⁵ The most favorable outcomes were reported for the sellar-suprasellar and pseudointraventricular topographies (good or fair outcomes in >90%), both characterized by a meningeal layer interposed between the tumor and the TVF. Conversely, the worst outcomes were found among patients with CPs showing a secondary intraventricular location (poor outcome or death, ≈40%), characterized by their extensive attachments to the hypothalamus. CPs with an intraventricular topog-

raphy had moderate outcomes, more favorable for those tumors with a strictly intraventricular location (good outcome, 49%; poor, 11%) than for the not strictly intraventricular cases (good outcome 28%; poor 15%) due to the intimate relation of the latter category with the hypothalamic region.

Preoperative Definition of CP Topography: An MR Imaging Multivariate Model

The specific relationships between CP topography and the most important radiologic features analyzed on preoperative conventional MR images are shown in the Table. At the outset of this study, it was found that all CPs lacking occupation of the 3V ($n = 21$) corresponded to the sellar-suprasellar topography. Consequently, these cases were excluded from further analysis. The remaining 179 cases were included in a hierarchic multivariate analysis using the CRT growing method to explore the optimal combination of MR imaging variables providing the best discrimination model for the 5 topographic categories considered. PS appearance was identified as the variable showing the strongest relation to CP topography, followed by tumor occupation of the chiasmatic cistern and the level of the hypothalamus relative to the tumor. In further steps, the MBA, the type of chiasm distortion, and tumor shape were selected as additional independent variables to build a predictive model of CP topography (Fig 2). The predictive power of this model was 83.8%—that is, a correct overall preoperative classification can be achieved in almost 84% of cases by accurately defining these 6 radiologic variables on MR images.

After that, a multiple correspondence analysis including the whole cohort of 200 cases was performed to investigate the predictive accuracy of CP topography achieved with the 3 independent variables selected in the first and second steps by the CRT

CP Topography

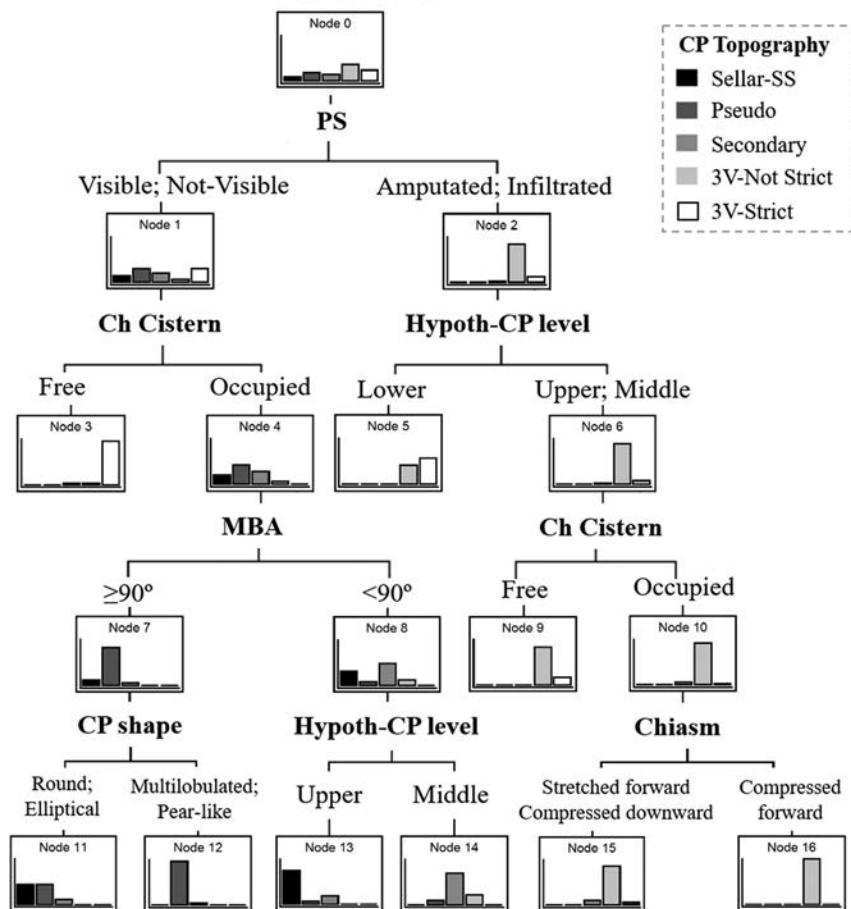


FIG 2. MR imaging predictors of CP topography. This growing decision tree shows the variables selected in a multivariate model to define the CP topography. The appearance of the pituitary stalk on preoperative MR imaging was chosen in the first step. The occupation of the chiasmatic cistern (Ch Cistern), the position of the hypothalamus regarding the tumor (Hypoth-CP level), the MBA, the tumor shape (CP shape), and the chiasm distortion (Chiasm) were selected in the following steps. Note that the probability for the not strictly intraventricular category (3V-Not Strict) significantly increased when the PS was either amputated or infiltrated, the Hypoth-CP level was not in the lower third of the tumor, the Ch cistern was occupied by tumor, and the Chiasm was compressed forward (nodes 2, 6, 10, 16). In contrast, the probability of the strictly intraventricular category (3V-Strict) significantly increased when the Ch cistern was free of tumor (node 3). The probability of the pseudointraventricular topography (Pseudo) significantly increased when the PS cistern was not visible, the Ch cistern was occupied by tumor, the MBA was obtuse ($>90^\circ$), and the tumor had a multilobulated or pearlike shape (nodes 1, 4, 7, 12). Among the cases with an MBA of $<90^\circ$ (node 8), the position of the hypothalamus above the upper third of the tumor indicated the sellar-suprasellar category (Sellar-SS), whereas its position around the middle portion of the tumor suggested a secondary intraventricular topography (Secondary, nodes 13, 14). Correct prediction of CP topography with this multivariate model, including 6 categoric variables studied on preoperative MR imaging, reached 83.8%.

method (PS appearance, hypothalamus level, and chiasmatic cistern occupation). We found that a correct preoperative topographic prediction was achieved in 76.3% of cases simply by considering these 3 MR imaging variables (Fig 3).

Finally, we assessed the diagnostic accuracy of a multivariate model that included the 7 MR imaging variables to define CP topography (tumor occupation of the 3V in addition to the 6 variables selected by the CRT method). Overall, the percentage of correct classification improved to 86%. The accuracy of this model for discriminating among the 5 topographic CP categories was quantified with positive (LR+) and negative (LR-) likeli-

hood ratios. The best discrimination power, characterized by a high LR+ along with a low LR-, was achieved for the sellar-suprasellar, pseudointraventricular, and strictly intraventricular categories. On the contrary, the worst identified category (lowest LR+ and highest LR- values) corresponded to the secondary intraventricular topography (Fig 4).

DISCUSSION

Craniopharyngioma Topography: The Importance of an Accurate Preoperative Definition

Neuroradiologists should recognize the extremely heterogeneous pathologic spectrum of CPs, particularly the huge influence that tumor topography pattern has on surgical outcome. The imprecise, generalized description of CPs as "suprasellar lesions" must be replaced by a comprehensive topographic characterization, one capable of predicting the surgical risks associated with each topographic category.² A detailed preoperative understanding of the anatomic relationships between a CP and the surrounding neurovascular structures is essential to maximize the likelihood of a radical excision while minimizing the risks of undue hypothalamic injury, which is the most devastating complication during CP surgery.^{5,8,9}

This study analyzes the MR imaging findings observed on conventional T1 and T2 images displayed in the CP reports included in our cohort. In most cases, only midsagittal and coronal scans through the infundibular region of the 3V (transinfundibular-coronal) were shown. The lack of a complete set of images obtained in each case can be judged as an obvious limitation of our analysis. However, in our topographic scheme, the fundamental criterion for categorizing CPs is the anatomic relationship between the tumor and the hypothalamus, the critical structure to be preserved in an operation.¹⁻⁶ CPs are predominately midline lesions developed from epithelial remnants of the Rathke pouch placed at any point of the pituitary-hypothalamic axis, usually within the pars tuberalis (a tongue of adenohypophyseal tissue enveloping the PS and infundibulum).⁴ The relative original position of these cells with regard to the meningeal layers covering the PS and infundibulum will determine the final CP topography.^{1,2} Consequently, the midsagittal and transinfundibular-coronal MR images represent the 2 basic sections to accurately elucidate the CP topography.

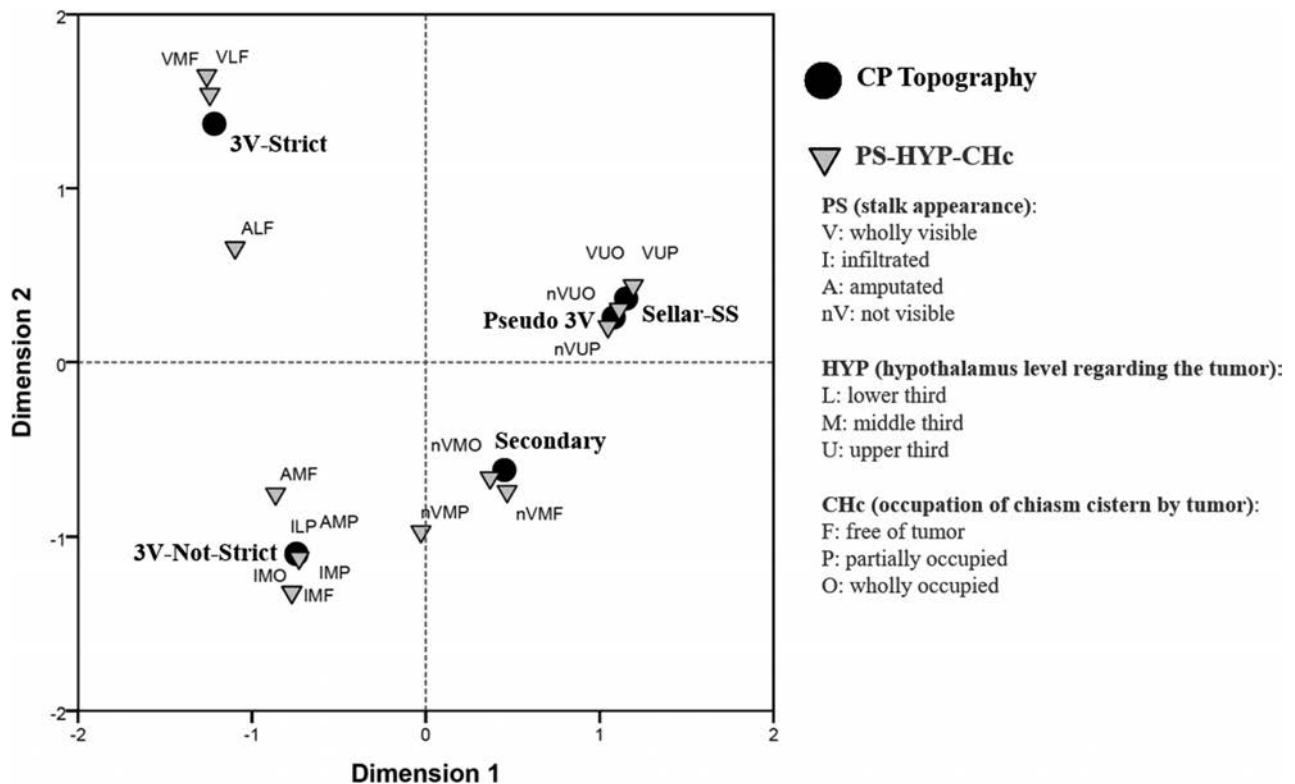


FIG 3. Multivariate model of CP topography for CPs: A 2D plot showing the multiple correspondence analysis between CP topographic categories (black circles) and the appearance of the pituitary stalk, the hypothalamus level in relation to the tumor (HYP), and the occupation of the chiasmatic cistern (CHC) (gray triangles). Dimension 1 separates the intraventricular topographies (strictly and not strictly) from the remaining variables, whereas dimension 2 mostly separates the strictly intraventricular CPs (3V-Strict) from the not strictly ones (3V-Not-Strict). Note that the position of the secondary intraventricular category (Secondary), the most difficult to define preoperatively, is in the trajectory between the 3V-Not-Strict and the sellar-suprasellar (SS) or pseudointraventricular (Pseudo-3V) categories, owing to the radiologic signs that these lesions share with the other topographies. A visible PS, a lower position of the hypothalamus, and a free chiasmatic cistern typically characterize the 3V-Strict group. In contrast, the 3V-Not-Strict category is defined by amputation or infiltration of the stalk, a position of the hypothalamus around the middle-third of the tumor, and a partial occupation of the chiasmatic cistern. Lack of visualization of the pituitary stalk was a sign common to the remaining 3 categories. However, the hypothalamus is typically observed at the upper third of the tumor in the sellar-SS and Pseudo-3V groups, whereas it is around the middle third in the Secondary-3V category. The variance of CP topography explained only by these 3 radiologic variables was 76.3%.

Our scheme has proved useful for an accurate characterization of the CP-TVf relationships, which can be properly observed on the midsagittal and transinfundibular-coronal MR imaging sections.^{1,5} Other topographic classifications are based on the relative position of alternative anatomic references such as the optic chiasm, the diaphragma sellae, or the infundibulum, as observed through a particular operational view.¹⁰ In contrast, our topographic scheme is the only one incorporating the dynamics of tumor growth by considering the original development site along the vertical pituitary-hypothalamic axis, a feature strongly related to the surgical risks and patient outcome.¹⁻⁵

MR Imaging Features Essential to Define CP Topography

The multivariate model generated in this study identified 7 MR imaging signs whose collective assessment allows an accurate prediction of CP topography in roughly 85% of cases:

1) CP Occupation of the Third Ventricle

Third ventricle involvement is a common feature of CPs, observed in 179 cases of this cohort. In each of the remaining 21 cases in which the 3V was tumor-free, the CP extended exclusively within the sellar and/or suprasellar compartments. Hence, we

propose that 3V occupation should be the first radiologic variable scrutinized on preoperative MR images to immediately identify a sellar-suprasellar location.

2) Type of Pituitary Stalk Distortion

The appearance of the PS on preoperative MR images is a fundamental variable to accurately predict CP topography. A not-visible PS suggests any of the 3 topographic categories that originate beneath the TVf (sellar-suprasellar, pseudointraventricular, and secondary intraventricular varieties), whereas a normal PS appearance points to the strictly intraventricular category. Alternatively, a PS whose upper infundibular edge has been amputated by the tumor or a PS wholly visible but infiltrated by the tumor represent 2 patterns strongly associated with the not-strictly intraventricular (infundibulo-tuberal) category, which is the most common topography.

3) Level of the Hypothalamus Relative to the Tumor

The position of the hypothalamus in relation to the tumor is best defined on transinfundibular-coronal scans. The position of this structure around the lower third of a CP strongly indicates a strictly intraventricular location, whereas a position of

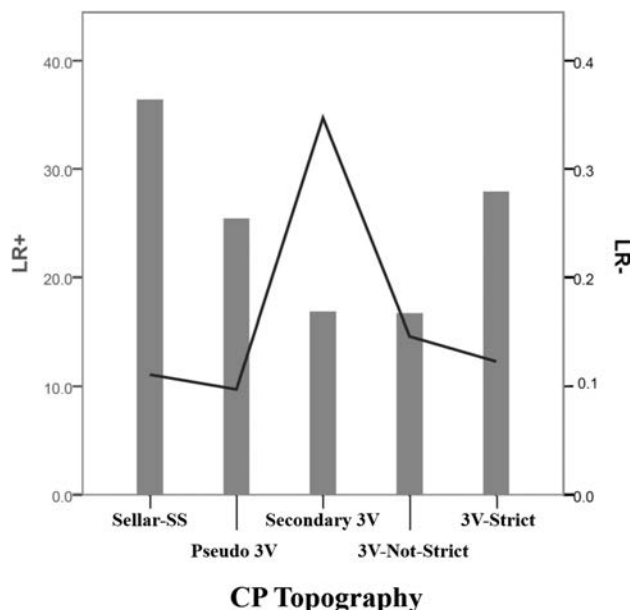


FIG 4. Diagnostic accuracy of CP topography quantified with likelihood ratios after using the 7 radiologic variables showing the strongest association (variables included in the Table). The higher the positive likelihood ratio (LR+, gray bars), the more reliable the topographic diagnosis is for the category considered. The lower the negative likelihood ratio (LR-, black line), the more reliable it is to rule out the category considered. Note that all topographic categories were associated with LR+ values higher than 10, though the highest figures were observed for the sellar-suprasellar (Sellar-SS), pseudointraventricular (Pseudo-3V), and strictly intraventricular (3V-Strict) categories. LR- was lower than 0.2 for all topographic categories except the secondary intraventricular one (Secondary-3V). Thus, the highest accuracy of the multivariate model of topographic diagnosis, including 7 MR imaging variables, was for the Sellar-SS, Pseudo3V, and 3V-Strict categories, and the lowest accuracy was for the Secondary-3V category.

the hypothalamus above the upper third of the tumor points to the topographic categories that develop below the TVF (the sellar-suprasellar and pseudointraventricular ones). In contrast, the hypothalamus is usually observed around the midthird portion or equator of the tumor, in infundibulo-tuberal CPs that originate within the TVF itself, or in some secondary intraventricular tumors.

4) Chiasmatic Cistern Occupation

CP extension into the arachnoid cistern beneath the chiasm and infundibulum is a useful variable to predict the tumor topography. The most valuable sign is a tumor-free patent cistern, which strongly indicates a strictly intraventricular position. In contrast, partial occupation of the cistern is frequently seen on the MRIs of patients with infundibulo-tuberal CPs. A cistern wholly obliterated by a tumor may be observed in any of the 3 topographic categories that originate in the sellar and/or suprasellar compartments.

5) Mammillary Body Angle

In an earlier study that included intraventricular CPs, we proved that the type of mammillary body displacement caused by these tumors was a useful sign for predicting their topography.⁶ The utility of this sign has been confirmed in this cohort. An obtuse angle ($\geq 90^\circ$), which is related to the upward displacement of

the TVF by the tumor, strongly indicates a pseudointraventricular topography. Conversely, none of the intraventricular CPs and only 10% of secondary intraventricular tumors had an obtuse deformation of the MBA. Among the intraventricular categories, hyperacute angles ($<30^\circ$) generally indicate an infundibulo-tuberal (not strictly intraventricular) topography (Table).

6) Type of Chiasm Distortion

In a previous study, we defined 6 major types of chiasm distortion caused by CPs that were found to be correlated with both the pattern of visual disturbances and the tumor topography.⁷ The present analysis substantiates the association between the chiasm deformation and CP topography. A compressed type of chiasm distortion was typically associated with tumors originating within the TVF. Specifically, a downwardly compressed chiasm indicates the strictly intraventricular topography, whereas a chiasm compressed forward suggests the not strictly intraventricular type. Conversely, a chiasm displaced upward and showing a stretched deformation by the tumor is usually observed with CPs originating beneath the chiasm at the sellar or suprasellar compartments. Another possible pattern is a forward-stretched distortion of the chiasm, frequently caused by the secondary intraventricular topography.

7) Tumor Shape

Our multivariate model selected tumor shape as the last variable that should be evaluated on preoperative MR images to improve the diagnostic accuracy of CP topography. A round, smooth tumor shape was most frequently observed in the strictly intraventricular category. A multilobulated tumor morphology was generally found among lesions expanding within the sellar and/or suprasellar area. CPs with a pearlike outline usually originated in the sellar compartment and pushed the diaphragma sellae upward into the chiasmatic cistern.

MR Imaging Accuracy to Discern CP Topography

This study shows that the methodic assessment of 7 MR imaging variables, easily identifiable on conventional T1- and T2-weighted midsagittal and coronal scans, permits a correct topographic diagnosis in 86% of cases. Nevertheless, the accuracy of our MR imaging multivariate model to preoperatively define the exact tumor location varies for each topographic category. The discriminative power of our model was dramatically increased for the sellar-suprasellar, pseudointraventricular, and strictly intraventricular categories. A correct topographic diagnosis was made in 90% of the tumors within these 3 categories. In contrast, the secondary intraventricular topography could be accurately predicted in $<70\%$ of cases. This lower accuracy rate can be explained by the highly variable range of anatomic distortions caused by this topographic subgroup (Fig 3). A secondary intraventricular category should be presumed when a preoperative MR imaging shows a CP extending from the sella turcica into the 3V and the PS is not visible (occurring in 92% of these cases). A hypothalamus positioned around the midthird portion of the lesion (in 77%) and a multilobulated shape (58%) are other signs usually shown by this category.

With the aim of achieving an optimal preoperative prediction

for CP topography, specific MR imaging sequences should be obtained, in addition to the conventional T1- and T2-weighted ones. The heavily T2-weighted and the fast-imaging employing steady-state acquisition MR imaging sequences represent the 2 methods that offer the finest resolution of the CP-brain contact surfaces, as well as the best definition of the distorted neurovascular structures.¹¹⁻¹⁴ In particular, the high-resolution 3D-FIESTA sequence has proved invaluable to ascertain the accurate anatomic relationship between a CP and the TVF.¹³ The resolution power of this technique to correctly define the displacement pattern of the mammillary bodies and optic chiasm, 2 structures not visible in around 15% of cases with routine T1- and T2-weighted MRI, should be further investigated in a large series. High-resolution 3D-FIESTA/CISS sequences could quite possibly improve the accuracy of diagnosis in large CPs presenting MR imaging features shared by several topographies.¹⁴

CONCLUSIONS

A precise description of CP topography is essential to guide a surgeon's judicious decision regarding the approach to the tumor and degree of removal suitable to avoid undue injury to the hypothalamus. Seven MR imaging variables should be analyzed to obtain an accurate preoperative definition of CP topography: third ventricle occupation by the tumor, pituitary stalk appearance, level of the hypothalamus relative to the tumor, chiasmatic cistern occupation, mammillary body angle, type of chiasm distortion, and tumor shape. The systematic assessment of these variables on midsagittal and coronal conventional T1- and T2-weighted MR images allows an accurate topographic classification in 86% of cases.

ACKNOWLEDGMENTS

The authors are grateful to George Hamilton for his critical review of the language and style of the manuscript.

REFERENCES

1. Pascual JM, González-Llanos F, Barrios L, et al. **Intraventricular craniopharyngiomas: topographical classification and surgical approach selection based on an extensive overview.** *Acta Neurochir (Wien)* 2004;146:785–802 Medline
2. Pascual JM, Prieto R, Castro-Dufourny I, et al. **Topographic diagnosis of papillary craniopharyngiomas: the need for an accurate MRI-surgical correlation.** *AJNR Am J Neuroradiol* 2015;36:E55–56 CrossRef Medline
3. Pascual JM, Carrasco R, Prieto R, et al. **Craniopharyngioma classification.** *J Neurosurg* 2008;109:1180–82; author reply 1182–83 CrossRef Medline
4. Pascual JM, Prieto R, Carrasco R. **Infundibulo-tuberal or not strictly intraventricular craniopharyngioma: evidence for a major topographical category.** *Acta Neurochir (Wien)* 2011;153:2403–25; discussion 2426 CrossRef Medline
5. Prieto R, Pascual JM, Rosdolsky M, et al. **Craniopharyngioma adherence: a comprehensive topographical categorization and outcome-related risk stratification model based on the methodical examination of 500 tumors.** *Neurosurg Focus* 2016;41:E13 CrossRef Medline
6. Pascual JM, Prieto R, Carrasco R, et al. **Displacement of mammillary bodies by craniopharyngiomas involving the third ventricle: surgical-MRI correlation and use in topographical diagnosis.** *J Neurosurg* 2013;119:381–405 CrossRef Medline
7. Prieto R, Pascual JM, Barrios L. **Optic chiasm distortions caused by craniopharyngiomas: clinical and magnetic resonance imaging correlation and influence on visual outcome.** *World Neurosurg* 2015; 83:500–29 CrossRef Medline
8. Prieto R, Pascual JM, Castro-Dufourny I, et al. **Craniopharyngioma: surgical outcome as related to the degree of hypothalamic involvement.** *World Neurosurg* 2017;104:1006–10 CrossRef Medline
9. Pascual JM, Prieto R, Castro-Dufourny I, et al. **Development of intracranial approaches for craniopharyngiomas: an analysis of the first 160 historical procedures.** *Neurosurg Focus* 2014;36:E13 CrossRef Medline
10. Lubuulwa J, Lei T. **Pathological and topographical classification of craniopharyngiomas: a literature review.** *J Neurol Surg Rep* 2016;77: e121–127 CrossRef Medline
11. Saeki N, Murai H, Kubota M, et al. **Heavily T2 weighted MR images of anterior optic pathways in patients with sellar and parasellar tumors: prediction of surgical anatomy.** *Acta Neurochir (Wien)* 2002;144:25–35 CrossRef Medline
12. Watanabe K, Kakeda S, Yamamoto J, et al. **Delineation of optic nerves and chiasm in close proximity to large suprasellar tumors with contrast-enhanced FIESTA MR imaging.** *Radiology* 2012;264: 852–58 CrossRef Medline
13. Xie T, Zhang XB, Yun H, et al. **3D-FIESTA MR images are useful in the evaluation of endoscopic expanded endonasal approach for midline skull-base lesions.** *Acta Neurochir (Wien)* 2011;153:12–18 CrossRef Medline
14. Gu Y, Zhang X. **Mamillary body angle and craniopharyngioma.** *J Neurosurg* 2014;120:1241–43; author reply 1243–45 CrossRef Medline

Arterial Spin-Labeling Perfusion MR Imaging Demonstrates Regional CBF Decrease in Idiopathic Normal Pressure Hydrocephalus

J. Virhammar, K. Laurell, A. Ahlgren, and E.-M. Larsson



ABSTRACT

BACKGROUND AND PURPOSE: Regional cerebral blood flow has previously been studied in patients with idiopathic normal pressure hydrocephalus with imaging methods that require an intravenous contrast agent or expose the patient to ionizing radiation. The purpose of this study was to assess regional CBF in patients with idiopathic normal pressure hydrocephalus compared with healthy controls using the noninvasive quantitative arterial spin-labeling MR imaging technique. A secondary aim was to compare the correlation between symptom severity and CBF.

MATERIALS AND METHODS: Differences in regional cerebral perfusion between patients with idiopathic normal pressure hydrocephalus and healthy controls were investigated with pseudocontinuous arterial spin-labeling perfusion MR imaging. Twenty-one consecutive patients with idiopathic normal pressure hydrocephalus and 21 age- and sex-matched randomly selected healthy controls from the population registry were prospectively included. The controls did not differ from patients with respect to selected vascular risk factors. Twelve different anatomic ROIs were manually drawn on coregistered FLAIR images. The Holm-Bonferroni correction was applied to statistical analyses.

RESULTS: In patients with idiopathic normal pressure hydrocephalus, perfusion was reduced in the periventricular white matter ($P < .001$), lentiform nucleus ($P < .001$), and thalamus ($P < .001$) compared with controls. Cognitive function in patients correlated with CBF in the periventricular white matter ($r = 0.60$, $P < .01$), cerebellum ($r = 0.63$, $P < .01$), and pons ($r = 0.71$, $P < .001$).

CONCLUSIONS: Using pseudocontinuous arterial spin-labeling, we could confirm findings of a reduced perfusion in the periventricular white matter, basal ganglia, and thalamus in patients with idiopathic normal pressure hydrocephalus previously observed with other imaging techniques.

ABBREVIATIONS: ASL = arterial spin-labeling; DWMH = deep white matter hyperintensities; iNPH = idiopathic normal pressure hydrocephalus; MMSE = Mini-Mental State Examination; QRAPMASTER = Quantification of Relaxation Times and Proton density by Multiecho acquisition of a saturation recovery with Turbo spin-echo Readout

Idiopathic normal pressure hydrocephalus (iNPH) is a condition with balance and gait disturbances, cognitive dysfunction, and urinary incontinence.¹ The symptoms can be reversed with

implantation of a shunt system, with improvement in 50%–80% of patients.^{2–4}

Regional CBF has been assessed in patients with iNPH to find explanations for the pathophysiology and in search of better methods to identify shunt responders. Several studies have shown reduced perfusion in the frontal cortex, periventricular WM, basal ganglia, thalamus, and cerebellum in patients with iNPH compared with controls, but the results have been divergent.^{5–11} In a recent study, reduced hippocampal CBF was reported as well.⁹

These previous studies have used different methods to estimate CBF: SPECT, PET, DSC MR imaging, and CT perfusion.^{8,9,12,13} These methods require administration of a radioactive tracer or a contrast agent, and SPECT, PET, and CT expose the patient to ionizing radiation.

Pseudocontinuous arterial spin-labeling (ASL) is an MR imaging technique with the advantage of allowing quantitative mea-

Received March 16, 2017; accepted after revision June 12.

From the Departments of Neuroscience, Neurology (J.V.) and Surgical Sciences, Radiology (E.-M.L.), Uppsala University, Uppsala, Sweden; Department of Pharmacology and Clinical Neuroscience (K.L.), Unit of Neurology, Östersund, Umeå University, Umeå, Sweden; and Department of Medical Radiation Physics (A.A.), Lund University, Lund, Sweden.

Johan Virhammar was supported by the independent Swedish foundation Erik, Karin och Gösta Selanders Stiftelse; Katarina Laurell received research grants from the Region Jämtland Härjedalen.

Please address correspondence to J. Virhammar, MD, PhD, Department of Neuroscience, Neurology, Uppsala University, Akademiska sjukhuset, ing 85, 751 85 Uppsala, Sweden; e-mail: johan.virhammar@neuro.uu.se; @johanvirhammar



Indicates article with supplemental on-line tables and appendix.



Indicates article with supplemental on-line photo.

<http://dx.doi.org/10.3174/ajnr.A5347>

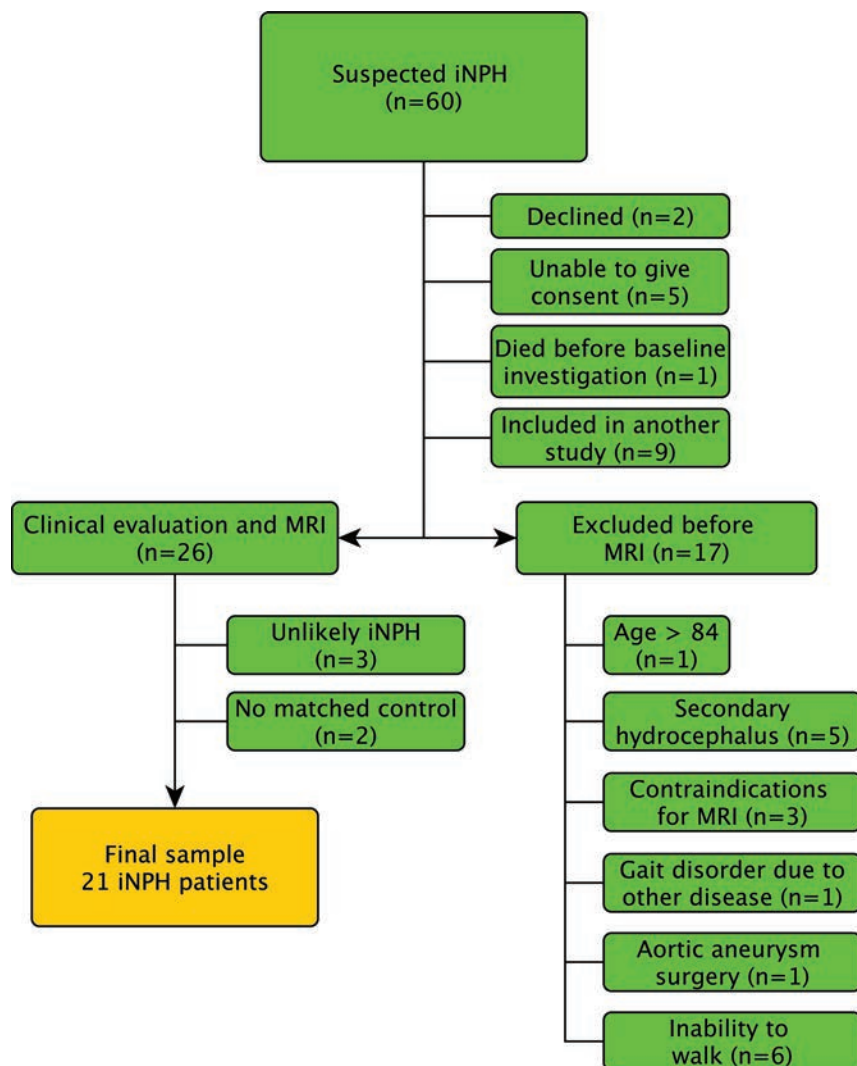


FIG 1. Flow chart describing the inclusion process of patients.

surements of CBF without injection of any contrast agent.¹⁴ The method is completely noninvasive, with a relatively short scan time (~5 minutes) and can therefore easily be added to a standard MR imaging protocol. To the best of our knowledge, no previous study has investigated differences in CBF between healthy controls and patients with iNPH with an ASL technique.

The purpose of this study was to use ASL to investigate whether regional cerebral perfusion is reduced in patients with iNPH compared with healthy controls and whether the level of clinical symptoms correlates with CBF.

MATERIALS AND METHODS

Patients and Healthy Controls

Sixty patients were prospectively and consecutively recruited from the waiting list of patients referred to Uppsala University Hospital for evaluation of suspected iNPH. Nine patients were excluded for participating in an ongoing multicenter study of the CSF tap test. Patients with complete inability to walk were excluded because of the intention to study the relationship between CBF and gait and balance function. Other exclusion criteria were secondary or congenital hydrocephalus, contraindications to MR

imaging, older than 84 years of age, severe cognitive dysfunction with an inability to give informed consent, refusal to undergo evaluation or shunt surgery, and gait problems that could be explained by other known diseases. The inclusion process is illustrated in the flow chart (Fig 1). Of the 26 patients examined clinically, 17 were classified as having probable iNPH according to the iNPH guidelines.¹⁵ Six patients were classified as having possible iNPH, 1 because of only 1 triad symptom (gait disturbance), 1 due to severe white matter changes, 1 because of a small cyst communicating with 1 of the lateral ventricles, and 3 due to a history of head trauma, probably unrelated to the hydrocephalus. Three patients were considered unlikely to have iNPH, 2 because of symptoms of Parkinson disease and 1 with an aqueductal stenosis. The patients examined in this study have been described in detail in a previous study.¹⁶

Controls were randomly recruited from the county of Uppsala using the Swedish population registry and were matched with patients with respect to age (± 2 years) and sex. Exclusion criteria were any known neurologic disease, stroke, diabetes mellitus, history of myocardial infarction that required acute treatment or resulted in persistent electrocardiogram changes, dependence on walking aids, or any terminal disease. Antihypertensive medication, aspirin, and common pain

medications were allowed. Information was sent to 105 potential elderly controls. Forty-nine did not reply; 31 responded that they did not want to participate or could not participate according to the exclusion criteria. The remaining 25 accepted participation and were examined clinically by a neurologist. MR imaging examination was not possible in 2 of the 25 controls because the MR imaging scanner was upgraded before those 2 controls were examined, and another 2 controls did not match any patient. Thus, a total of 21 matched pairs of patients (15 with probable iNPH and 6 with possible iNPH) and controls were available and included in the statistical analysis. The study was approved by the local ethics committee in Uppsala, Sweden.

Clinical Examination

Neurologists, especially trained physiotherapists, and occupational therapists performed the clinical examinations. Besides a standard neurologic examination, the tests included the modified Rankin Scale, Mini-Mental State Examination (MMSE), incontinence scale,¹⁷ Romberg test, and time and number of steps required to walk 10 m at a maximum pace. Tests of motor function were performed twice, and the mean result was used in the statistical analyses.

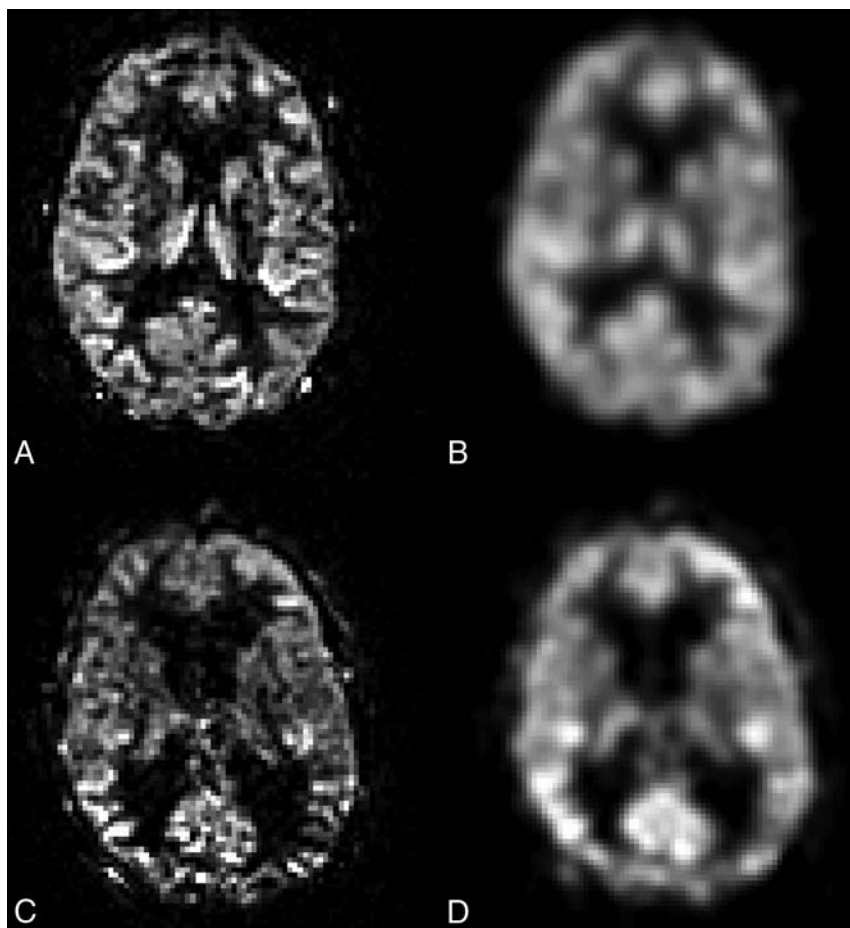


FIG 2. Example of ASL perfusion maps from a healthy control without (A) and with (B) smoothing, as well as from a patient with iNPH without (C) and with (D) smoothing.

Imaging

Details of the imaging method, scanner protocol, and postprocessing have been described previously.¹⁶ The first MR imaging was performed between 8:00 AM and 10:00 AM. The second MR imaging was performed 60 minutes after the first scan to assess the repeatability of the method. The patients left the scanner after the first investigation. Between the investigations, the patients rested in the supine position in a quiet, isolated room next to the scanner. The patients were not allowed to use caffeine on the day of the MR imaging, and all transportation was performed with the patient in bed or in a wheelchair to minimize variations in CBF. Healthy controls were only examined once with MR imaging.

Scanner and Imaging Protocol

Imaging was performed with a 3T MR imaging scanner (Achieva; Philips Healthcare, Best, the Netherlands) with a 32-channel head coil. A 3D T1-weighted gradient-echo and a T2-weighted FLAIR sequence were included in the protocol. Perfusion MR imaging was performed with a background-suppressed pseudocontinuous ASL sequence, with a single-shot echo planar imaging readout, with the following protocol: FOV = 264×264 mm², in-plane resolution = 2.75×2.75 mm², section thickness = 5 mm, number of sections = 20, TR = 4100 ms, TE = 14.5 ms, label duration = 1650 ms, postlabeling delay = 1600 ms, and 30 repetitions.

To allow quantitative CBF values, we obtained a fast reference scan.

Synthetic MR imaging data were acquired with the multisection, multi-echo, and multisaturation delay sequence Quantification of Relaxation Times and Proton density by Multiecho acquisition of a saturation recovery with Turbo spin-echo Readout (QRAPMASTER).¹⁸ Because of technical problems, synthetic MR imaging data were not acquired in 2 patients and in 1 control.

Perfusion MR Imaging

Postprocessing

For perfusion quantification, the compartment model proposed by Alsop and Detre was used.¹⁹ The magnetization difference (perfusion-weighted signal) is given by

$$\Delta M = 2 M_{0a} \alpha f T_{1a} (1 - e^{-\tau/T_{1a}}) e^{-w/T_{1a}},$$

where M_{0a} is the arterial blood magnetization, α is the labeling efficiency, f is the perfusion, T_{1a} is the T1 of arterial blood, τ is the labeling duration, and w is the postlabeling delay. Labeling efficiency was set to 70%, T_{1a} was set to 1664 ms, and M_{0a} was estimated with the signal intensity of CSF (see Alsop and Detre¹⁹ for more detail).

As an anatomic reference, the FLAIR images were coregistered to the perfusion maps by using a 12-degree affine transform (elastix; <http://elastix.isi.uu.nl/>).

To minimize the effect of nonideal image coregistration and to reduce the intrasubject variation caused by varying delineation of regions, we spatially smoothed the CBF maps (Gaussian kernel with 4-mm full width at half maximum, Fig 2).

ROIs and Morphologic Evaluations

Twelve different ROIs were drawn manually on transverse T2 FLAIR images using the in-house software Eval Gui (developed by Markus Nilsson, Lund University, Lund, Sweden). We covered the following regions: cerebellum, pons, high-convexity cortex, medial frontal cortex, lentiform nucleus, medial temporal lobe, supplementary motor area, thalamus, frontal WM, lateral WM, superior WM, and periventricular WM. The number of sections and voxels for all ROIs is listed in Table 1. Four different ROIs are illustrated in Fig 3, and all ROIs in both patients and controls are illustrated in the On-line Appendix. All sections of all scans were visually inspected, and care was taken not to include artifacts or large vessels in the ROIs. The ROIs were drawn by the first author (J.V., 4 years of experience) and reviewed by the last author (E.-M.L., >30 years of experience). When ROIs were drawn, the investigator was blinded to the patients' clinical data. CBF values were calculated for every voxel, and a mean CBF was provided in each ROI.

For descriptive purposes, we assessed the following morphologic

Table 1: Cerebral blood flow values in patients and controls^a

ROI	Sections	Voxels ^b	CBF, Repeatability ^c	CBF (Mean) (SD) (mL/100 g/min)		P Value ^d
				Patients	Controls	
Cerebellum	2	924 (144)	0.92	20.7 (9.3)	27.2 (7.0)	.006
MFC	3	133 (30)	0.90	24.9 (5.6)	27.4 (5.1)	.23
Lentiform nucleus	1	115 (15)	0.75	20.4 (2.7)	25.0 (4.0)	<.001 ^e
MTL	1	114 (15)	0.86	30.4 (5.6)	31.7 (3.8)	.86
HCC	2	1350 (459)	0.72	22.5 (5.5)	21.6 (3.0)	.47
Pons	3	68 (17)	0.90	22.0 (7.0)	24.1 (5.3)	.19
SMA	2	130 (18)	0.72	25.1 (5.1)	25.2 (3.7)	.93
Thalamus	2	116 (19)	0.92	26.8 (10.2)	34.1 (5.6)	<.001 ^e
Frontal WM	2	41 (8)	0.91	11.0 (5.0)	10.7 (2.2)	.76
Lateral WM	2	136 (33)	0.89	12.2 (3.0)	13.8 (1.7)	.014
Superior WM	2	67 (7)	0.88	14.2 (5.0)	12.6 (2.5)	.17
Periventricular WM	1	186 (15)	0.88	8.0 (2.5)	13.1 (3.1)	<.001 ^e

Note:—HCC indicates high-convexity cortex; MFC, medial frontal cortex; MTL, medial temporal lobe; SMA, supplementary motor area.

^a Data are mean with SD in parentheses unless otherwise indicated.

^b Mean (SD) voxels in each ROI in patients.

^c Repeatability of perfusion measurements between the 2 baseline investigations using the intraclass correlation coefficient.

^d Unadjusted *P* values tested with the paired-samples *t* test.

^e Significant after Holm-Bonferroni correction.

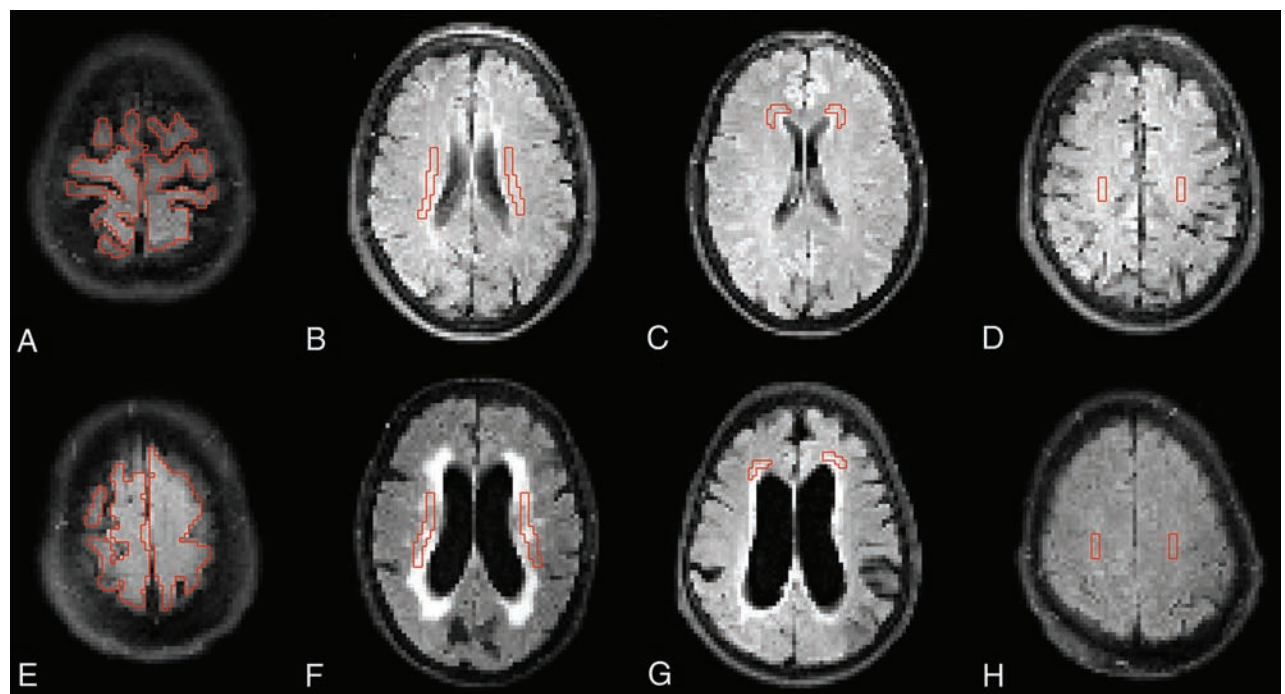


FIG 3. FLAIR images that were coregistered to the ASL images and used to draw ROIs. A–D, Healthy controls. E–H, Patients with iNPH. A and E, High-convexity cortex. B and F, Lateral periventricular WM. C and G, Frontal WM. D and H, Superior WM. All ROIs above were drawn in 2 adjacent sections, 1 of which is shown here.

MR imaging features: the Evans index,²⁰ the callosal angle,²¹ and deep white matter hyperintensities (DWMH) according to the visual grading scale of Fazekas et al.²² Disproportionately enlarged sub-arachnoid space hydrocephalus was defined as a combination of enlarged ventricles (Evans index of >0.3), narrow sulci at the high-convexity or parafalcine and dilated Sylvian fissures (Table 2).³ The measurements of morphologic features were performed by the last author (E.-M.L.). She was blinded to CBF data.

Volumetric Measurement

Measurements of CSF volumes were performed by using the QRAPMASTER sequence,¹⁸ which provides quantification of

longitudinal relaxation time (T1), transverse relaxation time (T2), and proton density. The software SyMRI Brain Studio (SyntheticMR, Linköping, Sweden) uses combinations of T1, T2, and proton density to estimate voxelwise partial volumes of GM, WM, and CSF, which allow volumetric estimation of these tissues. The volume of both lateral ventricles was calculated semiautomatically in both patients and controls after manual delineation on each section that included the lateral ventricles.

Statistical Analysis

The mean CBF in each ROI from the 2 scans of the patients was used in the statistical analyses. Each patient was paired with an

Table 2: Demographics and background data in patients and controls^a

	Patients (n = 21)	Controls (n = 21)	P Value
Age (median) (range)	74 (65–81)	74 (65–82)	NS ^b
No. of men (%)	11 (52%)	11 (52%)	NS ^c
MMSE	25 (22–27)	30 (29–30)	<.001 ^d
Urgency scale	3 (1–4)	1 (1–1)	<.001 ^d
Modified Rankin Scale score	2 (2–3)	0 (0–0)	<.001 ^d
Romberg test (sec)	18 (4–60)	60 (60–60)	<.001 ^d
10-m Walk time (sec)	12 (8–17)	5 (5–6)	<.001 ^d
10-m Walk (No. of steps)	22 (16–30)	12 (11–13)	<.001 ^d
Evans index score	0.35 (0.34–0.39)	0.28 (0.24–0.30)	<.001 ^d
DWMH	1 (1–3)	1 (1–2)	NS ^d
DESH (No.) (%)	14 (67%)	0 (0%)	<.001 ^c
Callosal angle	66° (60°–73°)	113° (104°–121°)	<.001 ^d
Lateral ventricular volume (mL)	130 (111–136)	31 (24–54)	<.001 ^d

Note:—DESH indicates disproportionately enlarged subarachnoid space hydrocephalus; NS, not significant.

^a Unless indicated otherwise, data are median, with interquartile range in parentheses.

^b Mann-Whitney *U* test.

^c McNemar test.

^d Wilcoxon signed rank test.

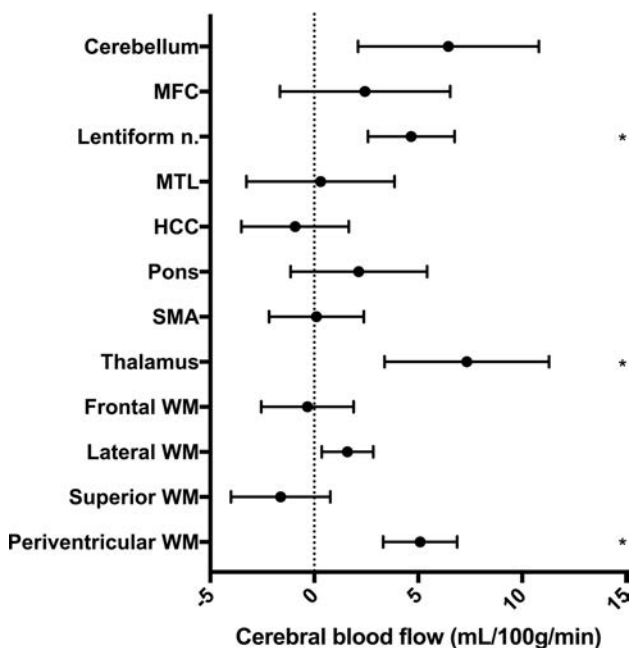


FIG 4. Mean difference with 95% CI between patients with iNPH and healthy controls. MFC indicates the medial frontal cortex; HCC, high-convexity cortex; MTL, medial temporal lobe; SMA, supplementary motor area. The asterisk indicates a significant difference after Holm-Bonferroni correction.

age- and sex-matched control. A paired-samples *t* test was used for the difference in CBF between patients and controls. Differences in descriptive data and comorbidity were analyzed with the Wilcoxon signed rank test or the McNemar test. Difference in age was tested with the Mann-Whitney *U* test. Correlations were assessed with the Spearman correlation. An intraclass correlation coefficient (2-way mixed, single measures) was used to calculate the repeatability of CBF between the 2 investigations in patients. For the analysis of CBF in patients and controls in the 12 ROIs, the Holm-Bonferroni correction for multiple comparisons was applied to reduce type I errors. Holm-Bonferroni correction works by sorting the *N* *P* values from the multiple tests and testing the smallest *P* value against α/N , the second smallest against $\alpha/(N-1)$, and so on. As soon as a null hypotheses is not rejected, all subse-

quent null hypotheses are also deemed not rejected, resulting in an effective significance threshold. With $\alpha = .05$, the effective significance threshold for ROI analysis in patients and controls was $P < .006$. Correlations were tested among all 12 ROIs, and the 4 clinical tests as well as the 4 morphologic imaging features. Only correlations with $r > 0.60$ were considered strong and included in the results section. All analyses were performed with SPSS Statistics for Macintosh, Version 22.0 (IBM, Armonk, New York).

RESULTS

Background Data

The radiologic morphologic measurements and the results of gait and balance tests, urgency, and MMSE differed markedly between patients and healthy controls (Table 2). However, there were no significant differences between patients and controls concerning age, the radiologic finding DWMH, and the use of antihypertensive drugs, acetylsalicylic acid, antidiabetic drugs, or statins, and there were no differences in the history of stroke, traumatic brain injury, meningitis, and previous or present smoking.

Cerebral Blood Flow

The CBF in all patients and controls is presented in Table 1. In patients, the CBF was significantly lower in the periventricular WM, lentiform nucleus, and thalamus after Holm-Bonferroni correction (Fig 4). In 3 patients with iNPH, the ASL maps contained vascular artifacts and apparent hypoperfusion in the brain parenchyma. If these 3 patients were excluded from statistical analyses, CBF was still significantly lower in patients in the periventricular WM, lentiform nucleus, and thalamus. There was no difference in age or symptom severity among the 3 patients with vascular artifacts compared with the other patients.

Morphologic Features and CBF

In controls, there were negative correlations between the Evans index and perfusion in frontal WM ($r = -0.75$, $P < .001$), lateral WM ($r = -0.73$, $P < .001$), and periventricular WM ($r = -0.66$, $P < .01$). In controls, there were also negative correlations between quantified lateral ventricular volume with Synthetic MR imaging and perfusion in the frontal WM ($r = -0.72$, $P < .001$), lateral WM ($r = -0.67$, $P < .01$), periventricular WM ($r = -0.65$, $P < .01$), and medial frontal cortex ($r = -0.61$, $P < .01$). There were no correlations between ventricular volume and CBF in patients.

Clinical Symptoms and CBF

In patients, the MMSE score correlated significantly with CBF in the pons ($r = 0.71$, $P < .001$), cerebellum ($r = 0.63$, $P < .01$), and periventricular WM ($r = 0.60$, $P < .01$), but not in controls. Neither in patients nor in controls did gait, balance, or urgency incontinence correlate with CBF values. See On-line Tables 1 and 2 for all correlation coefficients in patients.

Repeatability

Repeatability for the CBF values obtained in the 2 investigations in patients is presented in Table 1 as intraclass correlation coefficients. The intraclass correlation coefficients were in the range of 0.72–0.92.

Volumetric Measurement

The median lateral ventricular volume in patients was significantly larger than in controls, 130 mL (interquartile range = 111–136 mL) and 31 mL (interquartile range, 24–54 mL), respectively.

DISCUSSION

In this study, pseudocontinuous ASL, a noninvasive perfusion method without ionizing radiation or contrast agent, was used to compare cerebral perfusion between patients with iNPH and healthy controls. In agreement with previous studies using anatomic ROIs in patients with iNPH, CBF was reduced in the periventricular WM, basal ganglia, and thalamus.^{5,9} There was a trend indicating that CBF was also reduced in the cerebellum in patients with iNPH, but the difference was not significant after Holm-Bonferroni correction. In patients, MMSE correlated significantly with CBF in the pons, cerebellum, and periventricular WM. The repeatability of the CBF measurements was acceptable to high, which strengthens our findings.

In the present study, reduced CBF in patients with iNPH was found in the basal ganglia, thalamus, and periventricular WM, whereas previous studies also reported hypoperfusion in the frontal cortex, temporal lobes, and cerebellum.^{5,9,13} The more conservative correction for multiple analyses performed in our study could be one explanation for this difference, but another could be differences in the selection of healthy controls as well as the difference in imaging methods.

The mechanism of the reduced regional CBF in iNPH is likely multifactorial. One hypothesis is that transependymal passage of CSF into the parenchyma leads to reversal of interstitial fluid flow, initiating local CSF edema in the periventricular WM. The accumulation of interstitial fluid may cause local compression of small vessels and, more important, reduce elimination of vasoactive metabolites. The region mainly affected by hypoperfusion, according to this hypothesis, should be the periventricular WM, which is in line with our results and has also been reported by others.^{6,9} The reduced CBF in the thalamus and lentiform nucleus may be an indirect result of periventricular WM edema, by affecting the penetrating arteries that supply the thalamus and lentiform nucleus.

The supplementary motor area, basal ganglia, thalamus, mesencephalon, or the white matter tracts connecting these regions have been suggested as the most important anatomic structures behind gait and balance disturbances in patients with iNPH.^{23,24} There were no correlations between gait function and CBF in the present study. These findings indicate that the etiology of the gait disturbance in iNPH is complex and might be caused by factors other than reduced CBF.

However, there were correlations in the present study between impaired cognitive function measured with MMSE and reduced CBF in the pons, cerebellum, and periventricular WM. Perfusion in the brain stem has not been well-studied in iNPH, but Tullberg

et al²⁵ reported a relative CBF increase in the mesencephalon in patients with improved wakefulness after shunt surgery. Disturbances in cognitive function, especially in attention and executive ability, have been reported after insults to the pons,²⁶ and such symptoms are often seen in iNPH as well.²⁷ The connection between impaired cognitive function and reduced CBF in the cerebellum is harder to explain; however, there are reports that the cerebellum is involved in cognitive function.^{28,29}

Hypertension and vascular risk factors³⁰ and MR imaging evidence of vascular disease such as DWMH are overrepresented in patients with iNPH.³¹ These vascular risk factors are associated with reduced CBF³²; therefore, differences in CBF could be overestimated if controls are a highly selected sample of healthy elderly. In the present study, the controls were randomly selected from the population, with a limited number of exclusion criteria. There was no significant difference in the burden of DWMH or the use of acetylsalicylic acid or antihypertensive drugs between patients and controls, which strengthens our findings.

In controls, there were correlations between the size of the lateral ventricles and reduced CBF in WM regions. A potential reason may be asymptomatic small-vessel disease with reduction of WM volume and secondary dilation of the lateral ventricles, indicating that even moderately enlarged ventricles may not be considered a normal aging phenomenon.

The pseudocontinuous ASL technique has some advantages compared with other perfusion methods. The repeatability in healthy controls and in patients with Alzheimer disease is high, and CBF values have been validated against PET.³³ Like PET, perfusion values can be quantified. Therefore, no reference regions are needed to calculate relative perfusion values. In SPECT and DSC perfusion, relative values are used, with the risk that pathologic perfusion in the reference regions may affect the relative perfusion values. In a recent study, CT perfusion was evaluated in iNPH and may be a promising alternative because it is available in many sites and is not as sensitive to artifacts from the shunt valve after shunt implantation as with MR imaging.⁸

In the iNPH guidelines from 2005, the SPECT-acetazolamide challenge is the only perfusion method mentioned as a supportive diagnostic technique.¹⁵ A SPECT-acetazolamide challenge requires a separate imaging investigation, is time-consuming, and exposes the patient to ionizing radiation from the injected tracer. The ASL sequence is rapid and noninvasive; these features make it ideal for research studies in patients with iNPH, but the diagnostic value of the method is uncertain. Although CBF differences were found between patients and controls on a group level, the effect may not be large enough in individual cases to allow the use of ASL as a supportive diagnostic technique in clinical routine.

The strength of this study was that prospectively and consecutively included patients were compared with age- and sex-matched controls who were randomly selected from the population.

Some limitations need to be considered. Three patients had a high intravascular signal with low signal intensity in the brain parenchyma, probably due to a longer arterial transit time than postlabeling delay.³⁴ Statistical analysis with and without these 3 patients did not show any significant differences; therefore, we chose not to exclude them. Individually optimized postlabeling

delays would be preferable in elderly patients with pathologic CBF.

The CBF values in both our patients and controls were low compared with those reported in PET studies,^{5,35} but they were in line with other ASL studies in patients with iNPH.³⁶ Also, it has been reported that quantified perfusion values are underestimated in elderly individuals with ASL.³⁷ Our main results were probably not affected by this limitation because we compared patients with age-matched controls.

White matter perfusion estimation with ASL is challenging, due to a longer arterial transit time and lower blood volume compared with gray matter. Thus, the WM perfusion signal had a low signal-to-noise ratio, and the corresponding results should be treated with some caution. On the other hand, 2 recent studies suggest that though pixel-wise analysis is challenging, ROI-based analysis of WM perfusion is feasible in single subjects.^{38,39} This finding increases the credibility of our group-level results based on ROI analysis in 21 patients and 21 controls.

Spatial smoothing was applied to reduce the effects of nonideal coregistration but can potentially introduce partial volume effects on CBF measurements. This might have influenced the results of small ROIs with contamination of data from surrounding tissue.

The MMSE cognitive test used in this study may underestimate subcortical deficits that are very relevant in iNPH. More sophisticated neuropsychological tests could have revealed more information about the relationship between cognition and CBF in both patients and controls.⁴⁰

CONCLUSIONS

Pseudocontinuous ASL was used to compare perfusion of patients with iNPH versus healthy controls. In patients, perfusion values were reduced in the periventricular WM, basal ganglia, and thalamus, and there was a correlation between cognitive dysfunction and reduced CBF. Because ASL is a noninvasive quantitative perfusion method without ionizing radiation or contrast agent, it is a suitable perfusion method for research studies in patients with iNPH.

ACKNOWLEDGMENTS

The authors thank Markus Nilsson for the software Eval Gui, Markus Fahlström for technical assistance, and Emma Jansson for assistance with examinations of healthy controls. The authors also thank our normal pressure hydrocephalus team and the MR imaging staff at Uppsala University Hospital, especially Britt-Mari Bolinder. Finally, the authors thank Selanders Stiftelse for its support.

Disclosures: Johan Virhammar—RELATED: Grant: Selanders Foundations, Comments: Swedish independent foundation*; UNRELATED: Payment for Lectures Including Service on Speakers Bureaus: Medtronic, Comments: I have received 1 educational lecture honoraria from Medtronic for 1 lecture. André Ahlgren—UNRELATED: Grant: Swedish Research Council.* Money paid to the institution.

REFERENCES

- Adams RD, Fisher CM, Hakim S, et al. **Symptomatic occult hydrocephalus with "normal" cerebrospinal-fluid pressure: a treatable syndrome.** *N Engl J Med* 1965;273:117–26 CrossRef Medline
- Klinge P, Hellström P, Tans J, et al. **One-year outcome in the European multicentre study on iNPH.** *Acta Neurol Scand* 2012;126:145–53 CrossRef Medline
- Hashimoto M, Ishikawa M, Mori E, et al. **Study of INPH on neurological improvement (SINPHONI). Diagnosis of idiopathic normal pressure hydrocephalus is supported by MRI-based scheme: a prospective cohort study.** *Cerebrospinal Fluid Res* 2010;7:18 CrossRef Medline
- Sundström N, Malm J, Laurell K, et al. **Incidence and outcome of surgery for adult hydrocephalus patients in Sweden.** *Br J Neurosurg* 2017;31:21–27 CrossRef Medline
- Owler BK, Momjian S, Czosnyka Z, et al. **Normal pressure hydrocephalus and cerebral blood flow: a PET study of baseline values.** *J Cereb Blood Flow Metab* 2004;24:17–23 CrossRef Medline
- Momjian S, Owler BK, Czosnyka Z, et al. **Pattern of white matter regional cerebral blood flow and autoregulation in normal pressure hydrocephalus.** *Brain* 2004;127:965–72 CrossRef Medline
- Sasaki H, Ishii K, Kono AK, et al. **Cerebral perfusion pattern of idiopathic normal pressure hydrocephalus studied by SPECT and statistical brain mapping.** *Ann Nucl Med* 2007;21:39–45 CrossRef Medline
- Ziegelitz D, Arvidsson J, Hellström P, et al. **Pre-and postoperative cerebral blood flow changes in patients with idiopathic normal pressure hydrocephalus measured by computed tomography (CT) perfusion.** *J Cereb Blood Flow Metab* 2016;36:1755–66 CrossRef Medline
- Ziegelitz D, Starck G, Kristiansen D, et al. **Cerebral perfusion measured by dynamic susceptibility contrast MRI is reduced in patients with idiopathic normal pressure hydrocephalus.** *J Magn Reson Imaging* 2014;39:1533–42 CrossRef Medline
- Corkill RG, Garnett MR, Blamire AM, et al. **Multi-modal MRI in normal pressure hydrocephalus identifies pre-operative haemodynamic and diffusion coefficient changes in normal appearing white matter correlating with surgical outcome.** *Clin Neurol Neurosurg* 2003;105:193–202 CrossRef Medline
- Owler BK, Pena A, Momjian S, et al. **Changes in cerebral blood flow during cerebrospinal fluid pressure manipulation in patients with normal pressure hydrocephalus: a methodological study.** *J Cereb Blood Flow Metab* 2004;24:579–87 CrossRef Medline
- Owler BK, Pickard JD. **Normal pressure hydrocephalus and cerebral blood flow: a review.** *Acta Neurol Scand* 2001;104:325–42 CrossRef Medline
- Larsson A, Bergh AC, Bilting M, et al. **Regional cerebral blood flow in normal pressure hydrocephalus: diagnostic and prognostic aspects.** *Eur J Nucl Med* 1994;21:118–23 Medline
- Wu WC, Fernández-Seara M, Detre JA, et al. **A theoretical and experimental investigation of the tagging efficiency of pseudocontinuous arterial spin labeling.** *Magn Reson Med* 2007;58:1020–27 CrossRef Medline
- Relkin N, Marmarou A, Klinge P, et al. **Diagnosing idiopathic normal-pressure hydrocephalus.** *Neurosurgery* 2005;57:S4–16; discussion ii–v Medline
- Virhammar J, Laurell K, Ahlgren A, et al. **Idiopathic normal pressure hydrocephalus: cerebral perfusion measured with pCASL before and repeatedly after CSF removal.** *J Cereb Blood Flow Metab* 2014;34:1771–78 CrossRef Medline
- Hellström P, Klinge P, Tans J, et al. **A new scale for assessment of severity and outcome in iNPH.** *Acta Neurol Scand* 2012;126:229–37 CrossRef Medline
- Warntjes JB, Leinhard OD, West J, et al. **Rapid magnetic resonance quantification on the brain: optimization for clinical usage.** *Magn Reson Med* 2008;60:320–29 CrossRef Medline
- Alsop DC, Detre JA. **Reduced transit-time sensitivity in noninvasive magnetic resonance imaging of human cerebral blood flow.** *J Cereb Blood Flow Metab* 1996;16:1236–49 CrossRef Medline
- Evans W. **An encephalographic ratio for estimating ventricular enlargement and cerebral atrophy.** *Arch Neurol Psychiatry* 1942;47:931–37 CrossRef
- Virhammar J, Laurell K, Cesarini KG, et al. **The callosal angle** *AJNR Am J Neuroradiol* 38:2081–88 Nov 2017 www.ajnr.org 2087

- measured on MRI as a predictor of outcome in idiopathic normal-pressure hydrocephalus. *J Neurosurg* 2014;120:178–84 [CrossRef](#) [Medline](#)
22. Fazekas F, Chawluk JB, Alavi A, et al. MR signal abnormalities at 1.5 T in Alzheimer's dementia and normal aging. *AJR Am J Roentgenol* 1987;149:351–56 [CrossRef](#) [Medline](#)
23. Lundin F. *Idiopathic Normal Pressure Hydrocephalus, Aspects on Pathophysiology, Clinical Characteristics and Evaluation Methods* [PhD thesis]. Linköping: Linköping University; 2012
24. Hellstrom P. *The Neuropsychology of Idiopathic Normal Pressure Hydrocephalus* [PhD thesis]. Gothenburg: University of Gothenburg; 2011
25. Tullberg M, Hellström P, Piechnik SK, et al. Impaired wakefulness is associated with reduced anterior cingulate CBF in patients with normal pressure hydrocephalus. *Acta Neurol Scand* 2004;110:322–30 [CrossRef](#) [Medline](#)
26. Garrard P, Bradshaw D, Jäger HR, et al. Cognitive dysfunction after isolated brain stem insult: an underdiagnosed cause of long term morbidity. *J Neurol Neurosurg Psychiatry* 2002;73:191–94 [CrossRef](#) [Medline](#)
27. Ogino A, Kazui H, Miyoshi N, et al. Cognitive impairment in patients with idiopathic normal pressure hydrocephalus. *Dement Geriatr Cogn Disord* 2006;21:113–19 [CrossRef](#) [Medline](#)
28. E KH, Chen SH, Ho MH, et al. A meta-analysis of cerebellar contributions to higher cognition from PET and fMRI studies. *Hum Brain Mapp* 2014;35:593–615 [CrossRef](#) [Medline](#)
29. Moore DM, D'Mello AM, McGrath LM, et al. The developmental relationship between specific cognitive domains and grey matter in the cerebellum. *Dev Cogn Neurosci* 2017;24:1–11 [CrossRef](#) [Medline](#)
30. Malm J, Graff-Radford NR, Ishikawa M, et al. Influence of comorbidities in idiopathic normal pressure hydrocephalus: research and clinical care—a report of the ISHCSF task force on comorbidities in INPH. *Fluids Barriers CNS* 2013;10:22 [CrossRef](#) [Medline](#)
31. Krauss JK, Regel JP, Vach W, et al. White matter lesions in patients with idiopathic normal pressure hydrocephalus and in an age-matched control group: a comparative study. *Neurosurgery* 1997;40:491–95; discussion 495–96 [Medline](#)
32. Bastos-Leite AJ, Kuijter JP, Rombouts SA, et al. Cerebral blood flow by using pulsed arterial spin-labeling in elderly subjects with white matter hyperintensities. *AJNR Am J Neuroradiol* 2008;29:1296–301 [CrossRef](#) [Medline](#)
33. Xu G, Rowley HA, Wu G, et al. Reliability and precision of pseudo-continuous arterial spin labeling perfusion MRI on 3.0 T and comparison with 15O-water PET in elderly subjects at risk for Alzheimer's disease. *NMR Biomed* 2010;23:286–93 [CrossRef](#) [Medline](#)
34. Zaharchuk G, Bammer R, Straka M, et al. Arterial spin-label imaging in patients with normal bolus perfusion-weighted MR imaging findings: pilot identification of the borderzone sign. *Radiology* 2009;252:797–807 [CrossRef](#) [Medline](#)
35. Klinge PM, Berding G, Brinker T, et al. A positron emission tomography study of cerebrovascular reserve before and after shunt surgery in patients with idiopathic chronic hydrocephalus. *J Neurosurg* 1999;91:605–09 [CrossRef](#) [Medline](#)
36. Ivkovic M, Reiss-Zimmermann M, Katzen H, et al. MRI assessment of the effects of acetazolamide and external lumbar drainage in idiopathic normal pressure hydrocephalus. *Fluids Barriers CNS* 2015; 12:9 [CrossRef](#) [Medline](#)
37. Ambarki K, Wählin A, Zarrinkoob L, et al. Accuracy of parenchymal cerebral blood flow measurements using pseudocontinuous arterial spin-labeling in healthy volunteers. *AJNR Am J Neuroradiol* 2015;36:1816–21 [CrossRef](#) [Medline](#)
38. Wu WC, Lin SC, Wang DJ, et al. Measurement of cerebral white matter perfusion using pseudocontinuous arterial spin labeling 3T magnetic resonance imaging: an experimental and theoretical investigation of feasibility. *PLoS One* 2013;8:e82679 [CrossRef](#) [Medline](#)
39. Skurdal MJ, Bjørnerud A, van Osch MJ, et al. Voxel-wise perfusion assessment in cerebral white matter with PCASL at 3T: is it possible and how long does it take? *PLoS One* 2015;10:e0135596 [CrossRef](#) [Medline](#)
40. Hellström P, Edsbacke M, Archer T, et al. The neuropsychology of patients with clinically diagnosed idiopathic normal pressure hydrocephalus. *Neurosurgery* 2007;61:1219–26; discussion 1227–28 [CrossRef](#) [Medline](#)

Prevalence of Intracranial Aneurysms in Patients with Aortic Dissection

W.S. Jung, J.H. Kim, S.J. Ahn, S.-W. Song, B.M. Kim, K.-D. Seo, and S.H. Suh



ABSTRACT

BACKGROUND AND PURPOSE: There is an uncertainty about the association between intracranial aneurysms and aortic dissection. We aimed to determine the prevalence of intracranial aneurysms in patients with aortic dissection and evaluate the independent risk factors for the presence of intracranial aneurysms in these patients.

MATERIALS AND METHODS: Seventy-one patients with a confirmed aortic dissection who underwent additional brain imaging were enrolled as the aortic dissection group, and 2118 healthy individuals with brain imaging, as controls. Demographic data were obtained from their medical records, including age, sex, comorbidities, and arch vessel involvement of aortic dissection. Two readers reviewed all brain images independently regarding the presence, morphology, size, and location of intracranial aneurysms. Baseline characteristics were compared between the aortic dissection group and controls by propensity score matching, and logistic regression analysis was performed for independent risk factors for the presence of intracranial aneurysms.

RESULTS: The prevalence of intracranial aneurysms was 12.96% in the aortic dissection group and 1.85% in controls ($P = .022$). The mean diameter of intracranial aneurysms was significantly larger in the aortic dissection group (5.79 ± 3.26 mm in aortic dissection versus 3.04 ± 1.57 mm in controls; $P = .008$), and intracranial aneurysms of >7 mm were also more common in the aortic dissection group (28.6% in aortic dissection versus 5.3% in controls, $P = .003$). On multivariate analysis, arch vessel involvement of aortic dissection was an independent risk factor for the presence of intracranial aneurysms (odds ratio, 6.246; 95% confidence interval, 1.472–26.50; $P = .013$).

CONCLUSIONS: Patients with aortic dissection have a high prevalence of intracranial aneurysms, and selective screening for brain vessels could be considered in these patients with arch vessel involvement. A further prospective study is needed to demonstrate a substantial prevalence of intracranial aneurysms.

ABBREVIATIONS: AD = aortic dissection; IA = intracranial aneurysm

Intracranial aneurysms (IAs) are found in approximately 3% of the general population,¹ and IA rupture with subarachnoid hemorrhage is a life-threatening event with substantial morbidity and mortality.^{2,3} With the advancement of the imaging modalities, early di-

agnosis of IA is relevant, especially in at-risk patients with selected conditions associated with an increased occurrence of IAs.⁴

IAs and aortic diseases are different disease entities but have a similar pathophysiologic mechanism, which may be caused by excessive hemodynamic stress to the vessel wall or genetic factors for vascular fragility. The guidelines for unruptured IAs⁴ have suggested that there is an increased risk of aneurysm formation in some aortic pathologies such as bicuspid aortic valve and coarctation of the aorta. Recently, some authors^{5–7} have published the link between IA and aortic aneurysm, which showed an IA incidence of 9%–11% in patients with aortic aneurysms. However, there are a limited number of genetic or experimental studies^{8–10} and case reports^{11–13} for the association between IA and aortic dissection (AD).

Therefore, we aimed to demonstrate the prevalence of IA in patients with AD and investigate independent risk factors for the presence of IA in these patients.

Received April 6, 2017; accepted after revision June 23.

From the Departments of Radiology (W.S.J., S.J.A., S.H.S.), Neurology (J.H.K.), and Cardiovascular Surgery (S.-W.S.), Gangnam Severance Hospital, Yonsei University College of Medicine, Seoul, Korea; Department of Radiology (W.S.J.), Ajou University School of Medicine, Suwon, Korea; Department of Radiology (B.M.K.) and Severance Institute of Vascular and Metabolic Research (S.H.S.), Yonsei University College of Medicine, Seoul, Korea; and Department of Neurology (K.-D.S.), Wonkwang University Sanbon Hospital, Seoul, Korea.

This work was supported by a grant of the Korea Health Technology R&D Project through the Korea Health Industry Development Institute, funded by the Ministry of Health & Welfare, Republic of Korea (grant No. H15C1056).

Please address correspondence to Sang Hyun Suh, MD, PhD, Department of Radiology, Gangnam Severance Hospital, Yonsei University College of Medicine, 211 Eonju-ro, Gangnam-gu, Seoul, 06273, Korea; e-mail: suhsh11@yuhs.ac

Indicates open access to non-subscribers at www.ajnr.org

<http://dx.doi.org/10.3174/ajnr.A5359>

MATERIALS AND METHODS

Patients

After approval of the institutional review board (Gangnam Severance Hospital) for this retrospective study, informed consent was waived. Patients with AD were recruited from the medical data base of this tertiary hospital between January 2009 and June 2016. Inclusion criteria for the AD group were as follows: 1) patients with a confirmed AD as the indication for the CT angiography of the aorta; and 2) patients with AD who had undergone additional brain imaging such as brain CTA or MR angiography for the evaluation of any neurologic symptoms and follow-up of known IAs. Exclusion criteria were patients with traumatic AD and known connective tissue diseases such as Marfan, Ehlers-Danlos, and Loeys-Dietz syndromes.

Among healthy individuals at the Health Promotion Center of our tertiary hospital between January 2011 and December 2012, those who paid for their brain imaging at their own expense were consecutively enrolled as a control group. This Health Promotion Center was not advertised, and each examinee voluntarily decided to visit and choose brain imaging for his or her health examination.

We obtained demographic data of all patients from medical records: age, sex, and comorbidities (hypertension, diabetes, hyperlipidemia, and smoking); history of cerebrovascular disease, including intracerebral hemorrhage or cerebral infarction; and arch vessel involvement. Arch vessel involvement was defined as extension of the AD into any cervicobrachial vessels, such as the right brachiocephalic artery, left common carotid artery, or left subclavian artery.

Image Acquisition

Brain CTA was performed with a 128-channel multidetector CT scanner (Somatom Definition AS+; Siemens, Erlangen, Germany) with iopromide (Ultravist 370 mg iodine/mL; Schering Korea, Seoul, Korea). The imaging parameters were as follows: an exposure setting of 120 kV and 140 mA with automatic tube current modulation (CARE Dose4D; Siemens), a collimation of 64×0.6 mm, a section acquisition of 128×0.6 mm, and a pitch of 0.45. The imaging volume ranged from the vertex of the skull to the posterior arch of the C1 vertebra.

Brain MRA was performed with a 3T scanner (Discovery MR750; GE Healthcare, Milwaukee, Wisconsin). 3D time-of-flight MRA protocol parameters were as follows: TR/TE, 23/2.5 ms; flip angle, 20°; FOV, 210×185 mm; 4 slabs (176 sections); section thickness, 1.4 mm; matrix, 416×224 ; and acquisition time, 5 minutes 9 seconds.

All axial source data of CTA and MRA were reconstructed for the maximum intensity projections (axial, sagittal, and coronal) and volume-rendered images of the cerebral arteries.

Image Analysis

Two experienced neuroradiologists (S.H.S., S.J.A.) reviewed the axial brain images independently on the PACS, together with all reconstructed images of the brain vessels. The presence of IAs was determined in a consensus reading, and any clinical information or knowledge about this study was not provided to the readers.

IA was defined as an abnormal focal outpouching of the cerebral artery on brain CTA or MRA.¹⁴ Aneurysm size was measured

by the largest diagonal diameter. Aneurysm locations were classified as the internal carotid artery, anterior cerebral artery including the anterior communicating artery, middle cerebral artery, and vertebrobasilar artery; and the morphology of the aneurysm was categorized as saccular or fusiform.

Statistical Analysis

Differences between the AD group and controls were evaluated with a χ^2 or Fisher exact test for all categorical variables and an independent 2-sample *t* test for all continuous variables. Simple logistic regression analysis was performed to determine independent risk factors for the presence of IA in the AD group. Multiple logistic regression analysis was performed on variables with an unadjusted effect and $P < .05$ on simple logistic regression analysis. $P < .05$ was considered statistically significant. All statistical analyses were performed with SAS, Version 9.2 (SAS Institute, Cary, North Carolina).

Propensity score matching was performed to minimize the intergroup difference in baseline characteristics. The propensity score was developed with multiple logistic regression with respect to age, sex, hypertension, diabetes mellitus, hyperlipidemia, smoking, and a history of cerebrovascular disease. Using the propensity score of each patient, we matched a selected case with controls by a 1:2 matching. The nearest-neighbor-matching algorithm with a “greedy method” was used to match patients. After patient matching, we performed the paired *t* and McNemar tests. Balance between both groups for each variable was evaluated by propensity score distributions, and absolute standardized differences before and after matching were calculated. After patient matching, absolute standardized differences of <0.10 implied good balance between both groups.

RESULTS

Baseline Characteristics

A total of 505 patients with confirmed AD were collected between January 2009 and June 2016 (Fig 1). Patients without brain imaging ($n = 425$), patients with traumatic aortic dissection ($n = 6$), and those with Marfan disease ($n = 3$) were excluded from this study. Of these patients, 71 with brain imaging were enrolled as the AD group. Brain CTA was performed in 27 patients (38%), and brain MRA, in 44 (62%). Among 71 patients, 45 (63.38%) underwent brain imaging for the evaluation of nonspecific neurologic symptoms; 23 (32.39%), for the evaluation of headache; and 3 (4.23%), for the follow-up imaging of surgically clipped IA.

Of potential controls with a health examination, 2118 with brain MRA were enrolled as the controls.

As shown in Table 1, the mean age of the AD group was significantly higher than that of controls (58.6 ± 13.6 years versus 53.9 ± 9.6 years, respectively; $P = .004$). Hypertension (60.6% in AD versus 29.4% in controls, $P < .0001$) and cerebrovascular disease history (21.1% in AD versus 0.94% in controls, $P < .0001$) were significantly associated with the AD group. After a 1:2 matching, there was no significant difference between both groups regarding age, sex, comorbidities, or cerebrovascular disease history.

Among 71 patients with AD, 46 were included in the Stanford type A group (64.8%) and 25 were type B (35.2%). Among 14 patients with AD and IA, 9 were included in the Stanford type A

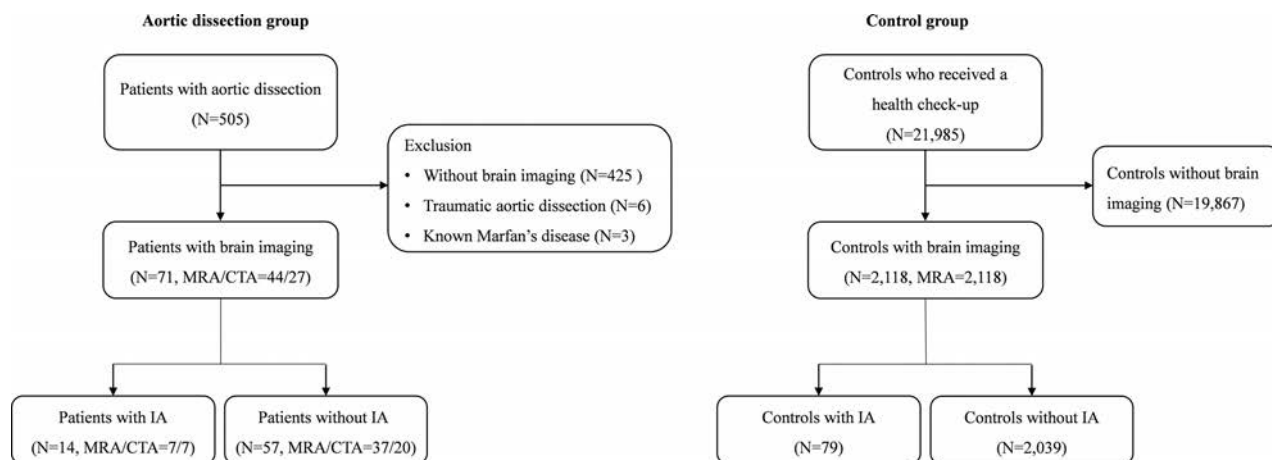


FIG 1. Flowchart of the study population.

Table 1: Comparison of baseline characteristics between the overall and matched study population

Characteristics	Overall ^a				Matched ^b			
	Total (n = 2189)	AD Group (n = 71)	Controls (n = 2118)	P Value	Total (n = 162)	AD Group (n = 54)	Controls (n = 108)	P Value
Presence of IA (No.) (%)	93 (4.25)	14 (19.72)	79 (3.73)	<.0001	9 (5.55)	7 (12.96)	2 (1.85)	.022
Age (mean)	54.03 ± 9.78	58.66 ± 13.6	53.87 ± 9.59	.004	59.20 ± 11.73	58.98 ± 13.09	59.31 ± 11.05	.808
Female sex (No.) (%)	963 (43.99)	33 (46.48)	930 (43.91)	.668	67 (41.36)	24 (44.44)	43 (39.81)	.189
Hypertension (No.) (%)	665 (30.38)	43 (60.56)	622 (29.37)	<.0001	67 (41.36)	24 (44.44)	43 (39.81)	.43
DM (No.) (%)	246 (11.24)	5 (7.04)	241 (11.38)	.255	97 (59.88)	31 (57.41)	66 (61.11)	.436
Hyperlipidemia (No.) (%)	191 (8.73)	2 (2.82)	189 (8.92)	.073	15 (9.26)	4 (7.41)	11 (10.19)	.313
CVD (No.) (%)	35 (1.6)	15 (21.13)	20 (0.94)	<.0001	5 (3.09)	1 (1.85)	4 (3.7)	>.9999
Smoking (No.) (%)	725 (33.12)	15 (21.13)	710 (33.52)	.087	127 (78.39)	43 (79.63)	84 (77.78)	0.732

Note:—DM indicates diabetes mellitus; CVD, cerebrovascular disease.

^a P values before matching were calculated with a χ^2 or independent 2-sample t test.

^b P values after matching were calculated with the McNemar or paired t test.

group (64.2%) and 5 were type B (35.8%). In the AD group, arch vessel involvement was found in 14: 6 of 14 patients with IA (42.8%) and 8 of 57 patients without IA (14%).

Prevalence and Characteristics of IA

IAs were found in 14 of 71 patients with AD (19.72%) versus 79 of 2118 controls (3.73%), which was significantly different ($P < .0001$). After propensity score matching, there were IAs in 7 of 54 patients with AD (12.96%) versus 2 of 108 controls (1.85%), which also showed a significant difference ($P = .022$).

In Table 2, multiple IAs were noted in 11 of 79 controls and not in the AD group. Of these 11 controls, 2 IAs were found in eight; 3 IAs, in 1; and 4 IAs, in 2. All IAs were saccular except 1 fusiform IA in a control. The mean diameter of IAs was significantly larger in the AD group (5.79 ± 3.26 mm in AD versus 3.04 ± 1.57 mm in controls, $P = .008$), and IAs of >7 mm were also more common in the AD group (28.6% in AD versus 5.3% in controls, $P = .003$). In the AD group, IAs were frequently situated in the MCA (35.7% in AD versus 8.4% in controls, $P = .012$) or vertebrobasilar artery (21.4% in AD versus 2.1% in controls, $P = .015$), while ICA aneurysms were more common in the controls (77.9% in controls versus 28.5% in AD, $P < .001$).

Independent Risk Factors for the Presence of IA in the AD Group

Univariate analysis showed that arch vessel involvement (OR, 4.594; 95% CI, 1.257–16.78; $P = .021$) was significantly correlated

Table 2: Characteristics of intracranial aneurysms between the AD group and controls

Characteristics	AD Group (n = 14)	Controls ^a (n = 95)	P Value
Location			
MCA	5 (35.7)	8 (8.4)	.012
ACA	2 (14.3)	11 (11.6)	.673
ICA	4 (28.5)	74 (77.9)	<.0001
VBA	3 (21.4)	2 (2.1)	.015
Aneurysm size			
Mean diameter (mm)	5.79 ± 3.26	3.04 ± 1.57	.008
≥7 mm	4 (28.6)	5 (5.3)	.003
Aneurysm morphology			
Saccular type	14 (100)	94 (98.9)	
Arch vessel involvement	6 (42.8)	0	
Diagnostic imaging modality			
Brain CTA	7 (50)	0	
Brain MRA	7 (50)	95 (100)	

Note:—ACA indicates anterior cerebral artery; VBA, vertebrobasilar artery.

^a Multiple aneurysms in 11 of 79 controls: 2 IAs in 8, three IAs in 1, and 4 IAs in 2.

with the presence of IAs. On multivariate analysis, arch vessel involvement (OR, 6.246; 95% CI, 1.472–26.50; $P = .013$) was also significantly associated with the presence of IAs (Table 3).

Relationship between Arch Vessel Involvement and IAs

Five of 6 patients and AD and arch vessel involvement showed right brachiocephalic artery involvement, and in 4 of these 5 patients, an IA was detected in the ipsilateral ICA, MCA, or VA (Table 4).

Table 3: Independent predictors of intracranial aneurysms in the AD group

Predictors	Univariate		Multivariate	
	OR (95% CI)	P Value	OR (95% CI)	P Value
Female sex	0.833 (0.256–2.71)	.762		
Age	1.028 (0.982–1.077)	.232		
Hypertension	2.865 (0.721–11.38)	.135		
SBP	1.007 (0.987–1.028)	.473		
DBP	1.027 (0.994–1.063)	.113		
Diabetes mellitus	0.576 (0–3.374)	.643		
Hyperlipidemia	0.765 (0.018–33.015)	.889		
CVD	1.673 (0.441–6.345)	.449		
Smoking	0.341 (0.014–8.188)	.507		
Arch vessel involvement	4.594 (1.257–16.78)	.021	6.246 (1.472–26.5)	.013

Note:—SBP indicates systolic blood pressure; DBP, diastolic blood pressure; CVD, cerebrovascular disease.

Table 4: Summary of the association between arch vessel involvement and intracranial aneurysm location in 6 patients with AD

Involved Arch Vessels	IA Location	IA Size (mm)
Right BCA, left SCA	Right VA	11
Right BCA, left CCA	Right MCA bifurcation	4
Right BCA	Right cavernous ICA	9
Right BCA	Right cavernous ICA	9
Left CCA, Left SCA	Right MCA bifurcation	6
Right BCA	Anterior communicating artery	5

Note:—BCA indicates brachiocephalic artery; CCA, common carotid artery; VA, vertebral artery.

DISCUSSION

This study showed a much higher prevalence of IAs in patients with AD than in the control group or general population.¹ In the AD group, IAs of >7 mm in diameter were frequently found, and IAs were located predominantly within the MCA or vertebrobasilar artery. An independent risk factor for the presence of IAs in patients with AD was arch vessel involvement.

After propensity score matching, IA prevalence was estimated at 12.96%, which was 7 times higher than that in the controls and was comparable with that in patients with various aortic diseases.^{5,6,15,16} Compared with the general population,¹ IA prevalence in this study was much higher by 4-fold. Curtis et al¹⁵ described a 10.3% prevalence in patients with coarctation of the aorta, and Schievink et al¹⁶ evaluated 9.8% in the bicuspid aortic valve. Some authors^{5,6} reported >11% of IA concurrence in patients with aortic aneurysm. To our knowledge, this is the first retrospective study to determine IA prevalence in patients with AD.

Although the reason for the high IA prevalence in patients with AD is unclear, recent studies proposed several potential explanations for the association between IAs and AD. Regalado et al¹⁰ suggested the possibility of a genetic link between IA and thoracic aortic aneurysm and dissection in a cohort of 514 families, in which 29 IAs were found. They found an autosomal dominant inheritance between IA and thoracic aortic aneurysm and dissection. In addition, hypertension was a major risk factor of AD and IA.^{4,17} Fukuda et al⁸ demonstrated that both IA and AD were caused by chronic inflammation of the arterial wall in hypertensive rats treated with the prostaglandin receptor antagonist.

In this study, IAs of >7 mm were frequently found in the AD group, and they were located predominantly in the MCA or vertebrobasilar artery. Several large-cohort studies^{14,18} demon-

strated size (>7 mm) and location (posterior cerebral distribution) of the aneurysm as independent predictors of IA rupture. In a pooled analysis of 6 prospective cohort studies,¹⁹ predictors of aneurysm rupture were also aneurysm size (>7 mm), location including the vertebrobasilar artery, and ethnic difference. Although the treatment of unruptured IAs is still controversial, clinicians should consider the likelihood of IA rupture during an aortic operation for such patients because cerebral perfusion pressure may increase temporarily by

clamping or balloon occlusion of the aorta.¹⁵

Our study showed that arch vessel involvement was an independent risk factor for the presence of IA in patients with AD. While its significance is ambiguous, experimental studies²⁰ have shown that vascular fragility may result from abnormal development of neural crest–derived cells, which comprise the tunica media of the aortic arch and its branches; and the neural crest defect has been implicated previously in the association of aortocephalic arterial dissections and congenital bicuspid aortic valves. Inamasu et al¹¹ recently reported a rare case of concurrent IA rupture and acute AD of Stanford type A, in which the right brachiocephalic trunk was involved. Moreover, our study showed right brachiocephalic artery involvement of AD in 5 patients, and IAs were detected along the ipsilateral ICA, MCA, or VA in 4 of 5, which may be induced by altered hemodynamics in the cranial vessels from the involvement of great vessel origins. Therefore, selective screening for brain vessels should be weighed carefully in these patients with arch vessel involvement.

There are several limitations in our study. First, only a small number of patients with brain imaging were retrospectively enrolled, which may be a selection bias; and the possibility of overestimation or underestimation of IA incidence cannot be excluded. Second, the diagnosis of IA was based on brain MRA or CTA, which may make it difficult to diagnose small IAs of <3 mm and to differentiate small aneurysms from junctional dilations.^{21,22} Third, ethnic differences for these 2 diseases should be considered for generalization. In addition, no pedigree or genetic study was available in our retrospective study. Finally, we could not exclude the possibility that the healthy controls might have an asymptomatic aortic pathology. For validation of the link between IA and AD, a further prospective, large-cohort study is needed.

CONCLUSIONS

In our study, patients with AD have a high prevalence of IAs, and selective screening for brain vessels could be considered prudent in case of arch vessel involvement. A further prospective, large-scale cohort study is needed to demonstrate a substantial prevalence of IAs.

ACKNOWLEDGMENTS

All authors appreciate Hye Sun Lee and Sinae Kim for their assistance in the statistics of this study.

REFERENCES

1. Vlak MH, Algra A, Brandenburg R, et al. **Prevalence of unruptured intracranial aneurysms, with emphasis on sex, age, comorbidity, country, and time period: a systematic review and meta-analysis.** *Lancet Neurol* 2011;10:626–36 [CrossRef Medline](#)
2. Brisman JL, Song JK, Newell DW. **Cerebral aneurysms.** *N Engl J Med* 2006;355:928–39 [CrossRef Medline](#)
3. van Gijn J, Kerr RS, Rinkel GJ. **Subarachnoid haemorrhage.** *Lancet* 2007;369:306–18 [CrossRef Medline](#)
4. Thompson BG, Brown RD Jr, Amin-Hanjani S, et al; American Heart Association Stroke Council, Council on Cardiovascular and Stroke Nursing, and Council on Epidemiology and Prevention, American Heart Association, American Stroke Association. **Guidelines for the Management of Patients with Unruptured Intracranial Aneurysms: a Guideline for Healthcare Professionals From the American Heart Association/American Stroke Association.** *Stroke* 2015;46:2368–400 [CrossRef Medline](#)
5. Rouchaud A, Brandt MD, Rydberg AM, et al. **Prevalence of intracranial aneurysms in patients with aortic aneurysms.** *AJNR Am J Neuroradiol* 2016;37:1664–68 [CrossRef Medline](#)
6. Shin YW, Jung KH, Moon J, et al. **Site-specific relationship between intracranial aneurysm and aortic aneurysm.** *Stroke* 2015;46:1993–96 [CrossRef Medline](#)
7. Kuzmik GA, Feldman M, Tranquilli M, et al. **Concurrent intracranial and thoracic aortic aneurysms.** *Am J Cardiol* 2010;105:417–20 [CrossRef Medline](#)
8. Fukuda M, Aoki T, Manabe T, et al. **Exacerbation of intracranial aneurysm and aortic dissection in hypertensive rat treated with the prostaglandin F-receptor antagonist AS604872.** *J Pharmacol Sci* 2014;126:230–42 [CrossRef Medline](#)
9. Regalado ES, Guo DC, Villamizar C, et al. **Exome sequencing identifies SMAD3 mutations as a cause of familial thoracic aortic aneurysm and dissection with intracranial and other arterial aneurysms.** *Circ Res* 2011;109:680–86 [CrossRef Medline](#)
10. Regalado E, Medrek S, Tran-Fadulu V, et al. **Autosomal dominant inheritance of a predisposition to thoracic aortic aneurysms and dissections and intracranial saccular aneurysms.** *Am J Med Genet A* 2011;155A:2125–30 [CrossRef Medline](#)
11. Inamasu J, Suzuki T, Wakako A, et al. **Concurrence of aneurysmal subarachnoid hemorrhage and Stanford type A acute aortic dissection.** *J Stroke Cerebrovasc Dis* 2016;25:e86–88 [CrossRef Medline](#)
12. Sakata N, Hamasaki M, Iwasaki H, et al. **Dissecting aneurysms involving both anterior cerebral artery and aorta.** *Pathol Int* 2007;57:224–28 [CrossRef Medline](#)
13. Inaba S, Iwata S, Kayano T, et al. **Perioperative management of a patient with subarachnoid hemorrhage complicated with descending aortic dissection [in Japanese].** *Masui* 2005;54:680–82 [Medline](#)
14. Morita A, Kirino T, Hashi K, et al; UCAS Japan Investigators. **The natural course of unruptured cerebral aneurysms in a Japanese cohort.** *N Engl J Med* 2012;366:2474–82 [CrossRef Medline](#)
15. Curtis SL, Bradley M, Wilde P, et al. **Results of screening for intracranial aneurysms in patients with coarctation of the aorta.** *AJNR Am J Neuroradiol* 2012;33:1182–86 [CrossRef Medline](#)
16. Schievink WI, Raissi SS, Maya MM, et al. **Screening for intracranial aneurysms in patients with bicuspid aortic valve.** *Neurology* 2010;74:1430–33 [CrossRef Medline](#)
17. Erbel R, Aboyans V, Boileau C, et al; ESC Committee for Practice Guidelines. **2014 ESC Guidelines on the diagnosis and treatment of aortic diseases: document covering acute and chronic aortic diseases of the thoracic and abdominal aorta of the adult—the Task Force for the Diagnosis and Treatment of Aortic Diseases of the European Society of Cardiology (ESC).** *Eur Heart J* 2014;35:2873–926 [CrossRef Medline](#)
18. International Study of Unruptured Intracranial Aneurysms Investigators. **Unruptured intracranial aneurysms: risk of rupture and risks of surgical intervention.** *N Engl J Med* 1998;339:1725–33 [CrossRef Medline](#)
19. Greving JP, Wermer MJ, Brown RD Jr, et al. **Development of the PHASES score for prediction of risk of rupture of intracranial aneurysms: a pooled analysis of six prospective cohort studies.** *Lancet Neurol* 2014;13:59–66 [CrossRef Medline](#)
20. Schievink WI, Mokri B. **Familial aorto-cervicocephalic arterial dissections and congenitally bicuspid aortic valve.** *Stroke* 1995;26:1935–40 [CrossRef Medline](#)
21. Wang H, Li W, He H, et al. **320-detector row CT angiography for detection and evaluation of intracranial aneurysms: comparison with conventional digital subtraction angiography.** *Clin Radiol* 2013;68:e15–20 [CrossRef Medline](#)
22. Sailer AM, Wagemans BA, Nelemans PJ, et al. **Diagnosing intracranial aneurysms with MR angiography: systematic review and meta-analysis.** *Stroke* 2014;45:119–26 [CrossRef Medline](#)

Reaction Time Is Negatively Associated with Corpus Callosum Area in the Early Stages of CADASIL

S. Delorme, F. De Guio, S. Reyes, A. Jabouley, H. Chabriat, and E. Jouvent



ABSTRACT

BACKGROUND AND PURPOSE: Reaction time was recently recognized as a marker of subtle cognitive and behavioral alterations in the early clinical stages of CADASIL, a monogenic cerebral small-vessel disease. In unselected patients with CADASIL, brain atrophy and lacunes are the main imaging correlates of disease severity, but MR imaging correlates of reaction time in mildly affected patients are unknown. We hypothesized that reaction time is independently associated with the corpus callosum area in the early clinical stages of CADASIL.

MATERIALS AND METHODS: Twenty-six patients with CADASIL without dementia (Mini-Mental State Examination score > 24 and no cognitive symptoms) and without disability (modified Rankin Scale score ≤ 1) were compared with 29 age- and sex-matched controls. Corpus callosum area was determined on 3D-T1 MR imaging sequences with validated methodology. Between-group comparisons were performed with t tests or χ^2 tests when appropriate. Relationships between reaction time and corpus callosum area were tested using linear regression modeling.

RESULTS: Reaction time was significantly related to corpus callosum area in patients (estimate = -7.4×10^3 , standard error = 3.3×10^3 , $P = .03$) even after adjustment for age, sex, level of education, and scores of depression and apathy (estimate = -12.2×10^3 , standard error = 3.8×10^3 , $P = .005$). No significant relationship was observed in controls.

CONCLUSIONS: Corpus callosum area, a simple and robust imaging parameter, appears to be an independent correlate of reaction time at the early clinical stages of CADASIL. Further studies will determine whether corpus callosum area can be used as an outcome in future clinical trials in CADASIL or in more prevalent small-vessel diseases.

ABBREVIATIONS: BPF = brain parenchymal fraction; CC_A = corpus callosum area; MB = microbleeds; RT = reaction time; SE = standard error; SVD = small-vessel disease

Cerebral autosomal dominant arteriopathy with subcortical infarcts and leukoencephalopathy (CADASIL) is a monogenic cerebral small-vessel disease (SVD) caused by mutations of the *NOTCH3* gene.¹ In unselected patients, brain atrophy and the volume of lacunes are the main MR imaging markers of disease severity.^{2,3} By contrast, in nondisabled patients without dementia, CADASIL may present without brain atrophy and with few if any lacunes, and MR imaging correlates of disease severity are

unknown. Simple and robust MR imaging markers at these early stages would be of interest because future therapeutic trials will likely include the patients with the least severe diseases.

We recently showed that reaction time (RT) is a marker of subtle cognitive and behavioral alterations observed in nondisabled patients without dementia with CADASIL.⁴ The MR imaging correlates of RT in these patients are undetermined.

Both in healthy aging and in sporadic SVD, the corpus callosum area (CC_A) reflects white matter integrity and is related to various estimates of processing speed.^{5,6} In the present study, we

Received March 1, 2017; accepted after revision June 23.

From the University Paris Diderot (S.D., F.D.G., H.C., E.J.), Sorbonne Paris Cité, UMR-S 1161 INSERM, Paris, France; DHU NeuroVasc Sorbonne Paris Cité (F.D.G., H.C., E.J.), Paris, France; and Department of Neurology (S.R., A.J., H.C., E.J.), AP-HP, Lariboisière Hospital, Paris, France.

This work was funded by a Network of European Funding for Neuroscience Research grant (01EW1207) under the Seventh Framework Programme and the European Research Area Net, with the support of the French-Cerebral Autosomal-Dominant Arteriopathy with Subcortical Infarcts and Leukoencephalopathy Association, the PLANIOL Foundation, the NRJ Foundation, and the Leducq Foundation. The sponsor was Assistance Publique, Hôpitaux de Paris (Département de la Recherche Clinique et du Développement).

Please address correspondence to Eric Jouvent, MD, Service de Neurologie, Hôpital Lariboisière, Two rue Ambroise Paré, 75010 Paris, France; e-mail: eric.jouvent@aphp.fr

Indicates open access to non-subscribers at www.ajnr.org

Indicates article with supplemental on-line appendix.

Indicates article with supplemental on-line photos.

<http://dx.doi.org/10.3174/ajnr.A5378>

aimed to test whether RT is independently related to CC_A in non-disabled patients with CADASIL without dementia.

MATERIALS AND METHODS

Study Participants

Twenty-six patients with genetically confirmed CADASIL followed within a prospective cohort study in the French Referral Centre for Rare Vascular Diseases of the Eye and the Brain (CERVCO, <http://www.cervco.fr>) were included. Within our referral center, about 250 patients with CADASIL are evaluated every 18 months with a comprehensive neuropsychological battery by an experienced neuropsychologist (S.R. or A.J.). Patients were invited to participate in the present study if they presented at the most recent evaluation (within 18 months) without global cognitive alterations as confirmed by the patient and his or her relatives; if neuropsychological testing scores were within the expected range according to the patient's age and level of education with a Mini-Mental State Examination score superior to 24 and did not have significant disability (modified Rankin Scale score of 0 or 1). Patients with overt motor deficits were excluded, but most reported minor poststroke residual symptoms such as gait disturbances or focal sensory deficits. Given the fluctuations of subjective cognitive and behavioral symptoms, particularly regarding fatigue and concentration issues, they are not systematically recorded at each visit and the evaluations reported in the present study are only based on objective measures. The present group of 26 patients included 22 patients for whom relationships between RT and cognitive alterations were reported previously⁴ and 4 additional patients recruited afterward. Twenty-nine age- and sex-matched control subjects were recruited from a local data base of healthy volunteers free of any history of neurologic or psychiatric disorders (except migraine). None of the patients or controls had a history of head trauma or demyelinating disease. An ethics committee validated the study protocol. All patients and controls gave their informed consent for participating in the present study.

Neuropsychological Assessment

All participants underwent a comprehensive neuropsychological evaluation, details of which have been published previously.⁴ RT was measured with a simple computerized task. Subjects were asked to click a mouse button as soon as a white X appeared on the screen for a maximum duration of 2000 ms. Twenty stimuli were presented sequentially during each trial, and 4 trials were performed in a row. During trials 2 and 3, the visual stimulus was primed by an auditory stimulus presented with a random time interval varying between 100 and 1000 ms. RT was recorded in milliseconds for each subject on the basis of the complete results obtained after 4 trials. We used the median RT based on the 4 trials for analyses. The total duration of this simple task was about 5 minutes. The Mini-Mental State Examination was used as a measure of global cognitive performance,⁷ and the presence of depression was defined according to the *Diagnostic and Statistical Manual of Mental Disorders*, 4th ed. Text Revision criteria,⁸ and the Montgomery-Asberg Depression Rating Scale score was obtained for all subjects.⁹ Subjects were considered apathetic if they had a Starkstein Apathy Scale score of ≥ 14 and fulfilled the Starkstein Structured Clinical Interview for Apathy criteria.¹⁰

MR Imaging Acquisition and Processing

The original MR imaging protocol included 3D T1-weighted images obtained at 3T with a Tim Trio scanner (Siemens, Erlangen, Germany) equipped with a 12-channel head coil, with a standard sagittal magnetization-prepared rapid acquisition of gradient echo sequence (in-plane resolution, $1 \times 1 \text{ mm}^2$; section thickness, 1.1 mm; TR, 2300 ms; TE, 2.98 ms; TI, 900 ms; flip angle, 9° ; bandwidth, 238 Hz/pixel; and acquisition time, 7 minutes 45 seconds). FLAIR and T2*-weighted sequences were not part of the present MR imaging protocol, but all patients also underwent a standard MR imaging protocol on a 1.5T scanner (Signa; GE Healthcare, Milwaukee, Wisconsin) within 6 months. The FLAIR sequence was used for the segmentation of white matter hyperintensities of presumed vascular origin, and the T2* sequence, for counting the number of microbleeds (MB), using previously validated methodologies.^{2,11} Brain parenchymal fraction (BPF), defined as the ratio of brain volume to the intracranial cavity volume, and the volume of lacunes were determined from the 3D-T1 sequence in all subjects.¹² Masks of lacunes were obtained manually by a trained rater. Hypointense lesions with a signal identical to that of CSF, sharp delineation, and a diameter of $>2 \text{ mm}$ were selected for this segmentation. Lacunes were distinguished from perivascular spaces by using STandards for ReportIng Vascular changes on nEuroimaging recommendations, including size criterion.¹¹

The 3D-T1 scans were manually registered to the midsagittal plane, with rotation transforms in Multi-image Analysis GUI (Mango; Research Imaging Institute, University of Texas Health Science Center at San Antonio; <http://ric.uthscsa.edu/mango>). Anterior/posterior commissures and the aqueduct of Sylvius were aligned on the interhemispheric plane. Once re-aligned, scans were processed with manual drawing in Anatomist (www.brainvisa.info) to delineate the corpus callosum on noninterpolated images (Fig 1). This approach is generally considered the reference method.¹³ Given the strong links between head size and the area of the corpus callosum,¹⁴⁻¹⁶ CC_A was normalized to the intracranial cavity volume (ICV) while raising the CC_A at the power $3/2$ to obtain a dimensionless value ($CC_A^{3/2}/ICV$). Intra- and interrater reliability were evaluated in a sample including 10 patients and 10 controls selected randomly from the whole sample of 55 subjects. Intraclass correlation coefficients were 0.94 and 0.92, respectively.

To further explore the relationships between CC_A and lacunes, we used a template of the corpus callosum from the ICBM-DTI-81 white matter atlas (http://www.loni.usc.edu/ICBM/Downloads/Downloads_DTI-81.shtml),¹⁷ which was thereafter projected into the native space of each patient to systematically identify lacunes within the central part of the corpus callosum.

Statistical Analysis

Statistical analyses were performed with R statistical and computing software (<http://www.r-project.org>). Between-group comparisons were performed with *t* tests for continuous variables with normal distributions. Wilcoxon tests were used otherwise. For categorical variables and comparisons of proportions, χ^2 tests were used. Multiple linear regression modeling was used to test the relationship between CC_A and MR imaging markers or be-

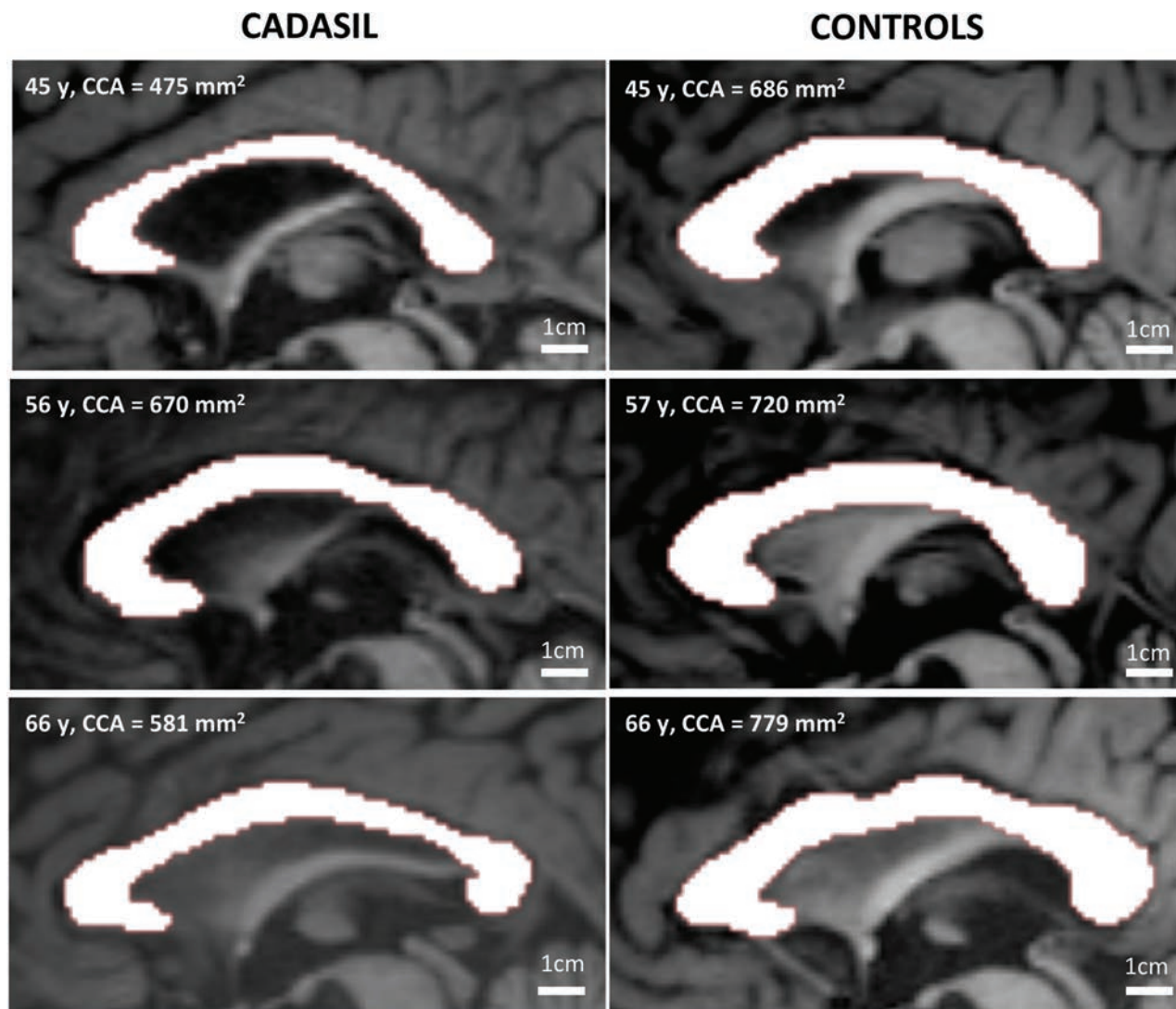


FIG 1. Examples of corpus callosum area delineation in 3 patients with CADASIL and 3 age-matched controls. Reproduction at the same scale of noninterpolated midsagittal T1-weighted images of the corpus callosum in 3 patients (*left column*) compared with 3 age-matched controls (*right column*). Corpus callosum atrophy appears obvious in some cases.

tween RT and CC_A . Analyses were adjusted when necessary for the following variables, based on data from the literature: age, sex, level of education, and scores of depression and apathy. For all analyses, $P < .05$ (2-tailed) was considered significant.

RESULTS

Characteristics of patients and controls are given in the Table. In line with our previous results,⁴ patients had significantly longer RTs than controls (288 ± 56 ms versus 253 ± 43 ms, $P = .02$). Patients also had significantly greater scores of depression (Montgomery-Asberg Depression Rating Scale: 5.9 ± 6.9 versus 1.7 ± 3.0 , $P = .007$) and a significantly lower level of education (11.3 ± 3.7 years versus 13.5 ± 3.5 years, $P = .02$), but the difference in RT between patients and controls remained significant after adjustment for age, sex, level of education, and scores of depression and apathy (estimate = 29.8, standard error [SE] = 14.8, $P = .04$).

CC_A was significantly smaller in patients (estimate = $1.3 \times 10^{-2} \pm 3.0 \times 10^{-3}$ versus $1.6 \times 10^{-2} \pm 3.0 \times 10^{-3}$, $P < .001$), even after adjustment for age and sex (estimate = 3.3×10^{-3} ,

SE = 7.6×10^{-4} , $P < .001$). By contrast, patients showed no brain atrophy (BPF: in patients, 0.84 ± 0.03 , versus controls, 0.84 ± 0.03 ; $P = .77$), even after adjustment for age and sex (estimate = -2.5×10^{-3} , SE = 7.1×10^{-3} , $P = .72$).

In patients, RT was negatively related to CC_A both before (estimate = -7.4×10^3 , SE = 3.3×10^3 , $P = .03$) (Fig 2) and after adjustment for age, sex, level of education, and score of depression and apathy (estimate = -1.2×10^4 , SE = 3.8×10^3 , $P = .005$). Further adjustment for the number of MB, the volume of white matter hyperintensities, volume of lacunes, and BPF did not alter our results (estimate = -1.4×10^4 , SE = 5.3×10^3 , $P = .02$).

In patients, there was no significant association between RT and any of the classic MR imaging markers: number of MB (estimate = -1.05 , SE = 2.07, $P = .62$), volume of white matter hyperintensities (estimate = 1.7×10^{-4} , SE = 1.6×10^{-4} , $P = .30$), volume of lacunes (estimate = -3.3×10^{-2} , SE = 2.5×10^{-2} , $P = .20$) and BPF (estimate = -4.1×10^2 , SE = 4.4×10^2 , $P = .37$).

Characteristics of patients with CADASIL and control subjects

	Patients with CADASIL (n = 26)	Control Subjects (n = 29)	P Value
Demographic characteristics			
Age (mean) (yr)	54.0 ± 10.4	53.9 ± 11.0	.973
Male sex (No.)	13 (50.0%)	15 (51.7%)	.901
Right-handed (No.)	26 (100%)	29 (100%)	NA
Level of education (mean) (yr)	11.3 ± 3.7	13.5 ± 3.5	.022
History of stroke (No.) (%)	20 (77%)	0 (0%)	NA
Neuropsychological tests			
Reaction time (mean) (ms)	288 ± 56	253 ± 43	.02
MMSE score (mean)	28.4 ± 1.8	29.0 ± 1.1	.169
Apathy scale (mean)	8.6 ± 4.6	6.8 ± 3.0	.119
MADRS scale (mean)	5.9 ± 6.9	1.7 ± 3.0	.007
Imaging markers			
Corpus callosum area (mean) (mm ²)	609 ± 93	713 ± 111	<.001, <.001 ^a
Brain parenchymal fraction (mean)	0.84 ± 0.03	0.84 ± 0.03	.766
Volume of white matter (mean) (cm ³)	450.5 ± 66.6	433.9 ± 44.5	.35
Volume of lacunes ^b (mean) (median) (range) (mm ³) (n = 15/26, 57.6%)	529, 303, 14–1975	No control had lacunes ^c	NA
Volume of WMH (mean) (median) (range) (mm ³) (n = 26/26, 100%)	93,638; 74,087; 7249–267,095	No control had significant lesions ^c	NA
No. of MB ^b (mean) (median) (range) (n = 8/26, 30.7%)	6.5, 2.5, 1–32	No control had MB ^c	NA

Note:—MMSE indicates Mini-Mental State Examination; MADRS, Montgomery and Asberg Depression Rating Scale; WMH, white matter hyperintensities; NA, not applicable.

^a Adjusted for age, sex, and intracranial cavity.

^b In patients with such lesions.

^c Visually rated from a concomitant 7T protocol, including high-resolution 3D-T1 and 2D gradient recalled echo T2* sequences.

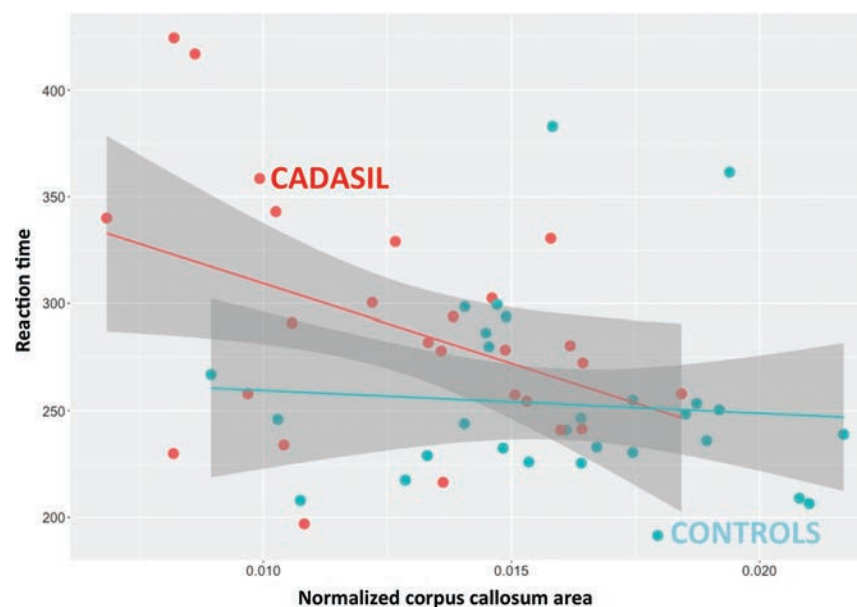


FIG 2. The relationship between reaction time and CC_A in patients with CADASIL and in controls. The mean reaction time appears significantly and negatively associated with the corpus callosum area in patients (estimate = -7.4×10^3 , SE = 3.3×10^3 , $P = .03$), while no association is observed in controls (estimate = -1.1×10^3 , SE = 2.6×10^3 , $P = .69$).

In controls, there was no significant association between RT and CC_A (estimate = -1.1×10^3 , SE = 2.7×10^3 , $P = .69$).

In patients, CC_A was negatively related to the volume of lacunes (estimate = -3.1 , SE = 0.9 , $P = .002$). Results were unchanged when we removed the 3 patients with lacunes within the central part of the corpus callosum (data not shown) from our analysis. Additionally, CC_A was positively related to BPF (estimate = 4.6 , SE = 1.5 , $P = .008$). By contrast, there was no significant association with the volume of white matter hyperintensities

(estimate = -0.4 , SE = 7.6 , $P = .96$) or the number of MB (estimate = -1.2 , SE = 0.8 , $P = .12$).

DISCUSSION

In the present study, we found that CC_A is an independent MR imaging marker of reaction time at the early clinical stages of pure SVD. By contrast, other conventional MR imaging markers were not associated with reaction time. In this sample of patients with CADASIL without disability and without dementia who had no brain atrophy and few if any lacunes, CC_A was lower than in age- and sex-matched controls. The effect of the volume of lacunes on CC_A was not mediated only by the 3 patients having lacunes on its most central part. This suggests that CC_A somehow summarizes the widespread effect of lacunes on its fiber bundles rather than only lacunes close to midline. Altogether, these results support the hypothesis that the accumulation of lacunes along the fibers of the corpus callosum leads to secondary degeneration translating into corpus callosum atrophy and also slows the connections between brain hemispheres, as illustrated by an increase in reaction time. While we did not observe any significant relationships between the volume of white matter hyperintensities or the number of MB and the corpus callosum area, smaller ischemic lesions, not visible with conventional MR imaging such as microinfarcts, might induce similar changes.

Brain atrophy is often considered a final common pathway adding up the various consequences of vascular lesions accumulating within the brain parenchyma.¹⁸ In the present study, patients showed lower CC_A but no brain atrophy compared with age- and sex-matched controls. Because of its very simple shape, detection of subtle alterations of the corpus callosum structure might be technically easier than those of the whole brain. However, given the cross-sectional nature of our study, we could not formally exclude the possibility that patients with CADASIL have innate lower CC_A compared with healthy subjects, but some arguments contradict this hypothesis. First, in the present study, we found that CC_A is independently associated with the volume of lacunes, suggesting that reduction of CC_A might be secondary to degeneration of long-range fibers passing through the altered parenchyma, in line with the description of remote cortex atrophy after subcortical infarcts.¹⁹ Note that we observed, in 10 of 26 patients, imaging aspects compatible with such secondary changes after the occurrence of lacunes in the corpus callosum fibers (Fig 3). Also, in additional analyses, we compared 28 other patients with CADASIL without lacunes from our national cohort study who were age- and sex-matched to the control group of the present study. When considering the difference in field strengths possibly altering CC_A delineation, CC_A in patients with CADASIL was not significantly different from that of age- and sex-matched controls (On-line Appendix and On-line Figs 1–5). Altogether, these results strongly support that CC_A is actually lower in patients as a consequence of the accumulation of vascular lesions throughout the brain parenchyma and, thus, reflects the disease severity.

Given that CC_A was negatively related to the volume of lacunes and positively related to brain atrophy, it might be considered a marker of white matter atrophy. However, several reports have now shown that the presence of lacunes in the white matter is associated with widespread cortical microinfarcts that may themselves explain these relationships independent of direct white matter damage.²⁰ While the results of the present study highlight the potential interest in CC_A as a marker of SVD, the mechanisms leading to a smaller CC_A in patients with CADASIL remain beyond the reach of our methodology.

The mechanisms leading to reaction time slowing remain largely unknown. While it may be tempting to look deeper into the relationships between reaction time and specific brain structure and/or networks, one must keep in mind that even in healthy subjects, the mechanisms underlying reaction time are strongly debated, with some authors considering it a stochastic process unrelated to specific brain areas or networks.²¹ Note that the main assumption underlying our results is that reaction time involves efficient interhemispheric cooperation. Further studies including more advanced methods such as assessment of fiber tracts, as previously performed in CADASIL, will be needed to further understand the mechanisms of reaction time slowing in this disorder.²²

Processing speed has previously been associated with CC_A in sporadic forms of SVD and in other brain disorders.^{5,23–25} Regarding reports of sporadic forms of SVD, the absence of control subjects did not allow formally disentangling the effects of age from those of SVD in these studies. Moreover, study samples were

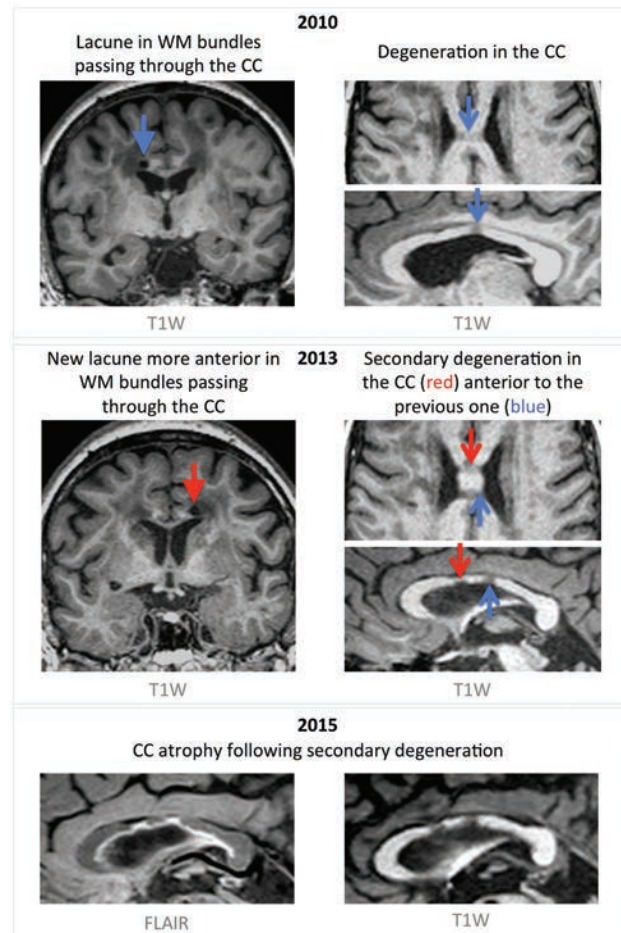


FIG 3. Corpus callosum atrophy through the appearance of lacunes and secondary white matter degeneration. An example of a 56-year-old patient with CADASIL presenting in 2010 with hypointense T1-weighted signal in the corpus callosum (CC), presumably as a consequence of a lacune located in white matter bundles passing through the CC body (*top panel*). In 2013, a new lacune occurred in bundles passing through the CC, localized anterior to the previous one and leading to another hypointense area in the CC (*middle panel*). Images acquired in 2015 show progressive CC atrophy due to degeneration secondary to the appearance of lacunes (*bottom panel*). T1W indicates T1-weighted.

heterogeneous, including older patients, with a significant proportion probably having associated Alzheimer disease (29% of diagnosed dementia on a 3-year follow-up⁶). Here, the significantly larger CC_A in controls, with no relationship with RT, strongly supports our observation of a specific effect of the disease. Further studies relying, for instance, on diffusion tensor imaging may be of interest to locally quantify the effects of the disease on the corpus callosum structure.

Our study has various limitations. First, study samples were small, including only 26 patients. Given the very strict inclusion criteria of the present study, patient recruitment is challenging and prevents studying large cohorts of patients at this stage of the disease. However, despite small sample sizes, we observed significant and coherent results, emphasizing the strength of the observed relationships. The use of several covariates in multiple regression analyses with such sample sizes may lead to overfitting of the data, but the coherence of our results argues against this hypothesis. More elaborate MR imaging markers, requiring inten-

sive postprocessing methods, might also be related to reaction time. However, we chose to restrict our analyses to the corpus callosum area to provide robust and easy-to-obtain markers for therapeutic trials. Finally, given that most patients had strokes before being prospectively followed, we were not able to determine exactly, for each patient, which of the lacunes initially led to stroke symptoms. We were thus unable to explore separately the relationships between CC_A and lacunes that led to stroke and between CC_A and “silent” lacunes.

Our study also has strengths. We tested a clear and unique hypothesis with a straightforward methodology, with the use of a simple MR imaging parameter, easily obtained manually and strongly correlated with volumetric measures obtained with methods requiring postprocessing skills. Our patients represent a homogeneous sample of a pure vascular disorder, including patients of various ages, allowing differentiating the effects of disease from those of age. Additionally, the detection of relationships between reaction time and corpus callosum area in small samples implies a large effect size. In patients, the effect of corpus callosum thinning was roughly twice that of aging in controls regarding an increase of reaction time.

CONCLUSIONS

We have shown that the CC_A is a simple and independent imaging marker of reaction time in the early clinical stages of CADASIL. Given that clinical variability is a well-known characteristic of patients with vascular cognitive impairment, markers such as CC_A can appear of high interest for future therapeutic trials in CADASIL, which will likely be performed in patients with the least severe disease. Additional studies are needed to determine whether our results are translatable in the context of sporadic SVD.








ACKNOWLEDGMENTS

We thank Chantal Ginisty, Séverine Roger, and Séverine Desmidt (Translational and Applicative Neuroimaging Research Unit, NeuroSpin) for performing the MR imaging acquisitions. We also acknowledge Jocelyne Ruffié, Véronique Joly-Testaud, and Laurence Laurier for the recruitment process of patients and controls. *Money paid to the institution.

REFERENCES

- Chabriat H, Joutel A, Dichgans M, et al. CADASIL. *Lancet Neurol* 2009;8:643–53 Medline
- Viswanathan A, Godin O, Jouvent E, et al. Impact of MRI markers in subcortical vascular dementia: a multi-modal analysis in CADASIL. *Neurobiol Aging* 2010;31:1629–36 CrossRef Medline
- Chabriat H, Hervé D, Duering M, et al. Predictors of clinical worsening in cerebral autosomal dominant arteriopathy with subcortical infarcts and leukoencephalopathy: prospective cohort study. *Stroke* 2016;47:4–11 CrossRef Medline
- Jouvent E, Reyes S, De Guio F, et al. Reaction time is a marker of early cognitive and behavioral alterations in pure cerebral small vessel disease. *J Alzheimers Dis* 2015;47:413–19 CrossRef Medline
- Jokinen H, Ryberg C, Kalska H, et al; LADIS group. Corpus callosum atrophy is associated with mental slowing and executive deficits in subjects with age-related white matter hyperintensities: the LADIS Study. *J Neurol Neurosurg Psychiatry* 2007;78:491–96 Medline
- Frederiksen KS, Garde E, Skimminge A, et al. Corpus callosum tissue loss and development of motor and global cognitive impairment: the LADIS study. *Dement Geriatr Cogn Disord* 2011;32:279–86 CrossRef Medline
- Folstein MF, Folstein SE, McHugh PR. “Mini-mental state”: a practical method for grading the cognitive state of patients for the clinician. *J Psychiatric Res* 1975;12:189–98 CrossRef Medline
- American Psychiatric Association. *Diagnostic and Statistical Manual of Mental Disorders*. 4th ed. Text Revision. Arlington: American Psychiatric Association; 2000
- Montgomery SA, Asberg M. A new depression scale designed to be sensitive to change. *Br J Psychiatry* 1979;134:382–89 CrossRef Medline
- Starkstein SE, Ingram L, Garau ML, et al. On the overlap between apathy and depression in dementia. *J Neurol Neurosurg Psychiatry* 2005;76:1070–74 CrossRef Medline
- Wardlaw JM, Smith EE, Biessels GJ, et al; STRIVE v1). Neuroimaging standards for research into small vessel disease and its contribution to ageing and neurodegeneration. *Lancet Neurol* 2013;12:822–38 CrossRef Medline
- Peters N, Holtmannspotter M, Opherck C, et al. Brain volume changes in CADASIL: a serial MRI study in pure subcortical ischemic vascular disease. *Neurology* 2006;66:1517–22 CrossRef Medline
- Herron TJ, Kang X, Woods DL. Automated measurement of the human corpus callosum using MRI. *Front Neuroinform* 2012;6:25 CrossRef Medline
- Häncke L, Staiger JF, Schlaug G, et al. The relationship between corpus callosum size and forebrain volume. *Cereb Cortex* 1997;7:48–56 CrossRef Medline
- Bishop KM, Wahlsten D. Sex differences in the human corpus callosum: myth or reality? *Neurosci Biobehav Rev* 1997;21:581–601 CrossRef Medline
- Sullivan EV, Rosenbloom MJ, Desmond JE, et al. Sex differences in corpus callosum size: relationship to age and intracranial size. *Neurobiol Aging* 2001;22:603–11 CrossRef Medline
- Mori S, Oishi K, Jiang H, et al. Stereotaxic white matter atlas based on diffusion tensor imaging in an ICBM template. *Neuroimage* 2008;40:570–82 CrossRef Medline
- O’Sullivan M, Jouvent E, Saemann PG, et al. Measurement of brain atrophy in subcortical vascular disease: a comparison of different approaches and the impact of ischaemic lesions. *Neuroimage* 2008;43:312–20 CrossRef Medline
- Duering M, Righart R, Wollenweber FA, et al. Acute infarcts cause focal thinning in remote cortex via degeneration of connecting fiber tracts. *Neurology* 2015;84:1685–92 CrossRef Medline
- van Veluw SJ, Hilal S, Kuijf HJ, et al. Cortical microinfarcts on 3T MRI: clinical correlates in memory-clinic patients. *Alzheimers Dement* 2015;11:1500–09 CrossRef Medline
- Siettos CI, Smyrnis N. Reaction time as a stochastic process implemented by functional brain networks. *Cogn Neurosci* 2017;8:133–35 CrossRef Medline
- Mascalchi M, Pantoni L, Giannelli M, et al. Diffusion tensor imaging to map brain microstructural changes in CADASIL. *J Neuroimaging* 2017;27:85–91 CrossRef Medline
- Jokinen H, Lipsanen J, Schmidt R, et al; LADIS Study Group. Brain atrophy accelerates cognitive decline in cerebral small vessel disease: the LADIS study. *Neurology* 2012;78:1785–92 CrossRef Medline
- Karbasforoushan H, Duffy B, Blackford JU, et al. Processing speed impairment in schizophrenia is mediated by white matter integrity. *Psychol Med* 2015;45:109–20 CrossRef Medline
- Bergendal G, Martola J, Stawiarz L, et al. Callosal atrophy in multiple sclerosis is related to cognitive speed. *Acta Neurol Scand* 2013;127:281–89 CrossRef Medline

MR Imaging Features of the Cerebellum in Adult-Onset Neuronal Intranuclear Inclusion Disease: 8 Cases

 A. Sugiyama,  N. Sato,  Y. Kimura,  T. Maekawa,  M. Enokizono,  Y. Saito,  Y. Takahashi,  H. Matsuda, and  S. Kuwabara

ABSTRACT

SUMMARY: Neuronal intranuclear inclusion disease is a neurodegenerative disorder pathologically characterized by eosinophilic hyaline intranuclear inclusions. A high-intensity signal along the corticomedullary junction on DWI has been described as a specific MR imaging finding of the cerebrum in neuronal intranuclear inclusion disease. However, MR imaging findings of the cerebellum in neuronal intranuclear inclusion disease have not been fully evaluated. Here, we review MR imaging findings of the cerebellum in a series of 8 patients with pathologically confirmed neuronal intranuclear inclusion disease. The MR imaging results showed cerebellar atrophy (8/8 patients) and high-intensity signal on FLAIR images in the medial part of the cerebellar hemisphere right beside the vermis (the “paravermal area”) (6/8) and in the middle cerebellar peduncle (4/8). The paravermal abnormal signals had a characteristic distribution, and they could be an indicator of the diagnosis of neuronal intranuclear inclusion disease even when using the results of past MR imaging examinations in which DWI findings were not examined.

ABBREVIATIONS: FAB = Frontal Assessment Battery; FXTAS = fragile X-associated tremor/ataxia syndrome; MMSE = Mini-Mental State Examination; NIID = neuronal intranuclear inclusion disease

Neuronal intranuclear inclusion disease (NIID) is a neurodegenerative disorder pathologically characterized by eosinophilic hyaline intranuclear inclusions in the central and peripheral nervous systems and in the visceral organs.¹ Both sporadic and familial cases of NIID are reported, and NIID is divided into 3 clinical subgroups according to the individual’s age at onset and disease duration: the infantile, juvenile, and adult forms.² The highly variable clinical manifestations of NIID previously made the antemortem diagnosis difficult, but since the usefulness of a skin biopsy for the diagnosis was described in sporadic³ and familial cases of NIID,⁴ the number of NIID diagnoses has increased.

Some researchers also noted that an NIID finding on brain MR imaging (ie, a high-intensity signal along the corticomedullary junction on DWI) is a strong indicator of the antemortem diagnosis of NIID.^{3,5} However, the MR imaging findings of the cerebellum in patients with NIID have not been fully evaluated, to our

knowledge. We recently encountered patients in whom abnormal signals were distributed in characteristic regions of the cerebellum on brain MR images. Herein, we present these MR imaging findings, focusing on the cerebellum in 8 patients with adult-onset NIID.

Case Series

This retrospective study was approved by our institutional review board. The diagnosis of NIID was made histopathologically by skin biopsy in all cases. We reviewed the medical records of the 8 patients including their medical history and neurologic examination findings, Mini-Mental State Examination (MMSE), Frontal Assessment Battery (FAB), and CSF results. A score of 24 was used as the cutoff for the MMSE,⁶ and the published age-matched average was used as the cutoff for the FAB.^{7,8} All MR imaging examinations were performed as routine clinical care with 1.5T in 3 patients and 3T in the other 5 patients. Diffusion-weighted and FLAIR images were available for all patients. The MR imaging data of each patient were retrospectively evaluated separately and then jointly by 2 neuroradiologists (Y.K. and M.E.).

We evaluated the following findings: 1) high-intensity signal along the corticomedullary junction on DWI, 2) diffuse high-intensity signal of cerebral white matter on FLAIR images, 3) atrophy of the cerebellum, 4) high-intensity signal in the medial part of the cerebellar hemisphere right beside the vermis (the “paravermal area”) on FLAIR images (Fig 1), and

Received February 22, 2017; accepted after revision May 20.

From the Departments of Radiology (A.S., N.S., Y.K., T.M., M.E.), Pathology and Laboratory Medicine (Y.S.), Neurology (Y.T.), and Integrative Brain Imaging Center (H.M.), National Center of Neurology and Psychiatry, Tokyo, Japan; and Department of Neurology (A.S., S.K.), Graduate School of Medicine, Chiba University, Chiba, Japan.

Please address correspondence to Noriko Sato, MD, Department of Radiology, National Center of Neurology and Psychiatry, 4-1-1 Ogawa-Higashi, Kodaira, Tokyo 187-0031, Japan; e-mail: snoriko@ncnp.go.jp

<http://dx.doi.org/10.3174/ajnr.A5336>

5) high-intensity signal in the middle cerebellar peduncle on FLAIR images (Fig 1B).

In all 8 cases, NIID was suspected from cerebral DWI findings, and a skin biopsy was performed. Light microscopy showed eosinophilic ubiquitin–positive and p62-positive intranuclear inclusions in the adipocytes, fibroblasts, and sweat gland cells. Electron microscopy was conducted in all patients except patient 6, and it revealed attenuated filament material without a limiting

membrane. The patients' clinical presentations are summarized in Table 1.

Dementia was observed in 3 of the 8 patients (37.5%). Mild ataxia was found in 3 patients (37.5%). In all cases, the deep tendon reflex was reduced or absent. One of the 8 patients showed a decreased MMSE score, and 5 of the 7 patients showed impaired FAB scores.

The CSF examinations showed elevated protein in all cases.

The MR imaging findings of the 8 patients with NIID are summarized in Table 2. MR imaging showed a high-intensity signal along the corticomedullary junction on DWI and diffuse high-intensity signal of cerebral white matter and cerebellar atrophy on FLAIR images in all cases (Fig 2). Six patients (75%) showed abnormal FLAIR high-intensity signal in the paravermal area (Figs 1 and 2). Four patients (50%) showed high-intensity signal in the middle cerebellar peduncle (Figs 1 and 3).

DISCUSSION

We have presented the MR imaging features of the cerebellum in 8 patients with pathologically confirmed adult-onset NIID. We observed abnormal FLAIR high-intensity signal in the paravermal area and middle cerebellar peduncle as characteristic MR imaging findings of

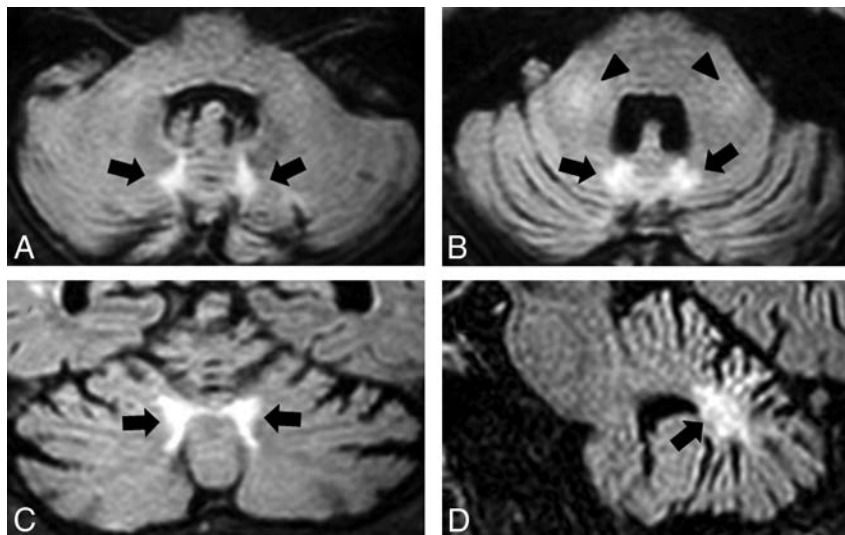


FIG 1. A representative case (patient 1) showing the abnormal signals at the paravermal area and the middle cerebellar peduncle. FLAIR axial images (A and B), a coronal image (C), and a sagittal image (D) show atrophy of the cerebellum and bilateral high signal intensity in the medial part of the cerebellar hemisphere immediately beside the vermis (the paravermal area) (black arrows) and in the middle cerebellar peduncle (black arrowheads).

Table 1: Summary of the clinical features of patients with NIID

	Patient No.							
	1	2	3	4	5	6	7	8
Age at onset (yr)	64	52	62	62	67	67	67	64
Sex	M	F	F	M	F	M	F	M
Disease duration at MRI (yr)	2	9	8	3	5	6	1	5
Clinical manifestations								
Dementia	–	–	–	+	+	–	+	–
Delusion	–	–	+	–	–	–	–	–
Muscle weakness	–	–	–	–	–	–	–	–
Tremor	–	–	Postural	–	Postural	Postural	–	Resting, postural
Rigidity	–	–	–	–	–	–	–	–
Ataxia	–	–	–	+	+	–	–	+
Hyporeflexia or areflexia in DTR	+	+	+	+	+	+	+	+
Sensory disturbance	–	–	–	–	–	–	–	–
Urinary incontinence	–	–	–	+	+	–	–	–
Transient visual field abnormality	+	+	–	–	–	–	–	+
Transient hemiparesis	–	+	–	–	–	–	–	–
Transient abnormal behavior	–	+	–	+	–	+	–	–
Generalized convulsion	–	–	–	–	–	–	–	–
Disturbance of consciousness	–	–	–	–	–	+	+	+
Cognitive screening test								
MMSE	30	29	30	14 ^a	30	28	24	29
Frontal lobe function test								
FAB	13 ^b	16	14 ^b	11 ^b	12 ^b	16	8 ^b	NE
CSF								
Cell (mm ³)	3	2	4	1	1	6	NE	NE
Protein (mg/dL)	66	55	100	47	52	48	NE	NE

Note:—DTR indicates deep tendon reflex; –, absence of the manifestation; +, presence of the manifestation; NE, not examined.

^a Decreased MMSE score below a cutoff score of 24.

^b Decreased FAB score below the published age-matched average.

Table 2: Summary of MRI findings of the 8 patients with NIID

	Patient No.							
	1	2	3	4	5	6	7	8
Cerebrum								
High-intensity signal along the corticomedullary junction on DWI	+	+	+	+	+	+	+	+
Diffuse high-intensity signal of cerebral white matter on FLAIR images	+	+	+	+	+	+	+	+
Cerebellum								
Atrophy	+	+	+	+	+	+	+	+
High-intensity signal in the medial part of cerebellar hemisphere right beside the vermis on FLAIR images	+	—	+	+	+	+	—	+
High-intensity signal in the middle cerebellar peduncle on FLAIR images	+	+	+	—	—	+	—	—

Note: — indicates absence of the finding; +, presence of the finding.

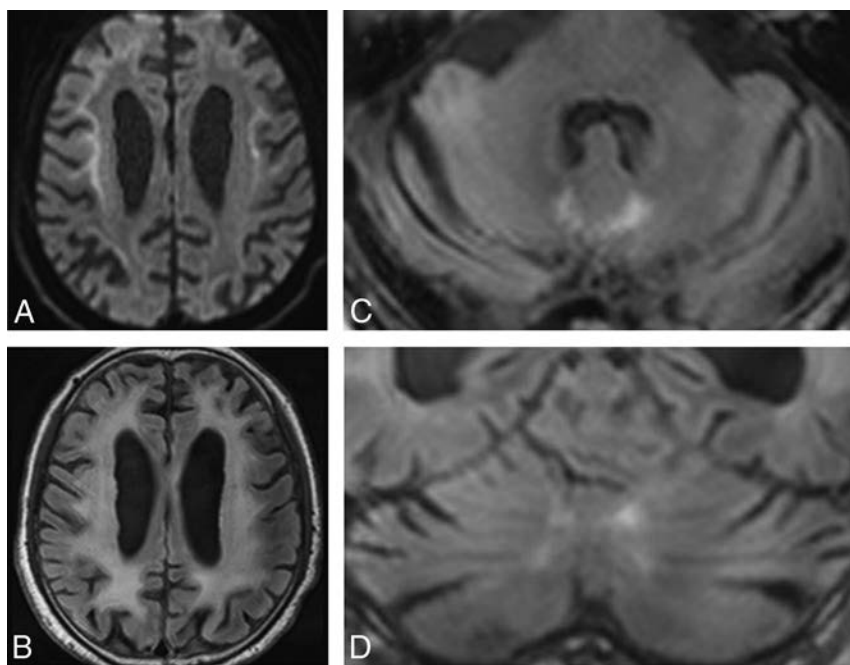


FIG 2. Patient 4. DWI (A) shows high-intensity signal along the corticomedullary junction. A FLAIR axial image (B) shows diffuse high intensity in the bilateral cerebral hemispheres. FLAIR axial (C) and coronal (D) images show atrophy of the cerebellum and high-intensity signal in the medial part of the cerebellar hemisphere right beside the vermis (the paravermal area).

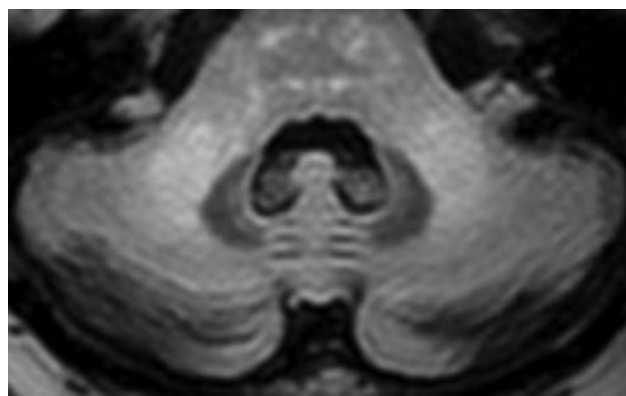


FIG 3. Patient 2. A FLAIR axial image shows bilateral high signal intensities in the middle cerebellar peduncle.

the cerebellum in NIID. Although cerebellar atrophy in NIID has been described in several cases,^{3,9,10} there is no report focusing on the distribution of abnormal signals in the cerebellum.

Previous studies have demonstrated that remarkable diffuse high-intensity signal of the cerebral white matter and DWI high-

intensity signal along the corticomedullary junction are characteristic MR imaging findings of patients with NIID.^{3,5} The DWI finding of high-intensity signal along the corticomedullary junction could thus be a strong indicator of the diagnosis of NIID. According to a study comparing MR imaging and pathologic findings in NIID, DWI high-intensity signal along the corticomedullary junction and FLAIR high-intensity signal in the white matter correlated with pathologic spongiotic changes and diffuse myelin pallor without spongiosis, respectively.¹¹ The spongiotic changes were restricted to the subcortical lesions proximal to the U-fibers, and these changes might induce an inactivation of water diffusion.

That report¹¹ also described a remarkable loss of glial fibrillary acidic protein–positive astrocytes compared with relatively mild axonal loss in the subcortical lesions, and astrocyte dysfunction has been considered a possible cause of white matter damage that ranges

from myelin pallor to spongiotic change. These MR imaging findings extend predominantly into the frontal lobe and are thought to be related to white matter dementia, which is more easily detectable by the FAB than the MMSE.⁵ Consistent with this previously reported finding, most of our patients showed a decreased FAB score. Although it was not observed in our patients, transient focal brain edema with gadolinium enhancement has also been reported in patients with NIID during subacute encephalic episodes.⁵

In accordance with previous reports,^{3,9,10} all 8 of our patients with NIID presented with cerebellar atrophy. In addition, an abnormal signal in the medial part of the cerebellar hemisphere right beside the vermis, which we defined as the paravermal area, was observed at a high frequency in our patient series. The paravermal area is included in the intermediate part of the cerebellar hemisphere that receives somatosensory input from the limbs and projects via the interposed nucleus to the lateral corticospinal and rubrospinal systems.¹² A previous investigation revealed that lesions in this intermediate part induced impaired gait balance control.¹³

In the present study, the relationship between the extent of the lesion and the severity of ataxia could not be assessed, but all 3

patients with ataxia presented with an abnormal signal in the paravermal area. It is possible that the lesions in the paravermal area observed in our patients influence the ataxic gait in NIID. In our patients, the second most frequent abnormal signal in the cerebellum was the middle cerebellar peduncle lesion. Although we could not determine the pathologic background of these abnormal signals in the cerebellum in our patients, in previous reports describing the cerebellar pathology of NIID, a loss of myelin in the white matter of the cerebellum was described.^{9,14,15}

The paravermal abnormal signal observed in our patients might be a specific finding for NIID. Another lesion in the medial part of the cerebellar hemisphere, in the peridentate white matter with and without a middle cerebellar peduncle lesion, has been described in several disorders, such as fragile X-associated tremor/ataxia syndrome (FXTAS),^{16,17} Erdheim-Chester disease,¹⁸ neurofibromatosis,¹⁹ and progressive multifocal leukoencephalopathy.²⁰ However, the distribution of the lesions in the peridentate white matter observed in these disorders is different from that in the lesions in the paravermal area found in our cases. Although the term “paravermal” has been used in a case with brain infarction,²¹ it has never been used to describe a lesion of a neurodegenerative disorder, to our knowledge.

The paravermal abnormal signal observed in our patients has a unique distribution, and it could be an indicator of the diagnosis of NIID, along with the DWI finding of a high-intensity signal along the corticomedullary junction. The middle cerebellar peduncle lesion is also considered a characteristic finding of NIID, though it can be found in other neurodegenerative disorders such as FXTAS, multiple system atrophy, and spinocerebellar ataxia and diseases due to other etiologies (neoplasm, metabolic, cerebrovascular, inflammatory, and demyelinating diseases).²² Like the high-intensity signal along the corticomedullary junction on DWI, this lesion may also help clinicians distinguish between NIID and clinically similar diseases such as gelsolin amyloidosis, which can present with neuropathy, ataxia, and dementia.²³

The limitation of this study was that in no patients was brain pathology obtained. However, in both sporadic and familial cases of NIID, it was reported that nuclear inclusions detected by skin biopsy are morphologically and immunohistochemically identical to those reported for NIID inclusions in neuronal cells.^{3,4} Moreover, in cases of NIID diagnosed by both postmortem dissection and skin biopsy, the histopathologic features of the inclusions in the skin and central nervous system tissues were identical.⁵ We therefore think that the absence of postmortem cases of NIID does not limit the validity of our findings. On the other hand, as in our patients, a skin biopsy has been performed, with the abnormal findings on DWI as a trigger for most cases reported in recent years.⁵ The frequency of an abnormal signal along the corticomedullary junction on DWI may be overestimated in NIID.

Another limitation of our study is that the CGG repeat length of the *FMR1* gene was not analyzed. In FXTAS, which is caused by permutation alleles of the *FMR1* gene, eosinophilic ubiquitin-positive intranuclear inclusions, similar to those reported in NIID, were observed in neurons and glial cells.^{24,25} However, whereas the core clinical features of FXTAS are progressive tremor and gait ataxia, the core clinical feature of adult-onset

NIID in our patients was dementia.^{5,26} There was no family history of symptoms or medical history that suggested FXTAS in any of our patients. In addition, in a study of 27 cases of NIID with the analyzed *FMR1* gene, all cases showed a normal range of CGG repeats.⁵ The possibility that FXTAS was present among our patients thus seems to be extremely low.

CONCLUSIONS

We observed abnormal FLAIR high-intensity signals in the paravermal area and middle cerebellar peduncle other than cerebellar atrophy as characteristic MR imaging findings of the cerebellum in NIID. The paravermal abnormal signal could indicate the diagnosis of NIID, even when using the findings of past MR imaging examinations in which DWI was not performed.

Disclosures: Satoshi Kuwabara—UNRELATED: Board Membership: *Journal of Neurology, Neurosurgery, and Psychiatry*, Comments: I serve as Deputy Editor of the journal; Other: Japanese Agency of Medical Research Development, Comments: grant for intractable neuroimmunologic disease.* *Money paid to the institution.

REFERENCES

- Lindenberg R, Rubinstein LJ, Herman MM, et al. **A light and electron microscopy study of an unusual widespread nuclear inclusion body disease: a possible residuum of an old herpesvirus infection.** *Acta Neuropathol* 1968;10:54–73 [CrossRef Medline](#)
- Takahashi-Fujigasaki J. **Neuronal intranuclear hyaline inclusion disease.** *Neuropathology* 2003;23:351–59 [CrossRef Medline](#)
- Sone J, Kitagawa N, Sugawara E, et al. **Neuronal intranuclear inclusion disease cases with leukoencephalopathy diagnosed via skin biopsy.** *J Neurol Neurosurg Psychiatry* 2014;85:354–56 [CrossRef Medline](#)
- Sone J, Tanaka F, Koike H, et al. **Skin biopsy is useful for the ante-mortem diagnosis of neuronal intranuclear inclusion disease.** *Neurology* 2011;76:1372–76 [CrossRef Medline](#)
- Sone J, Mori K, Inagaki T, et al. **Clinicopathological features of adult-onset neuronal intranuclear inclusion disease.** *Brain* 2016; 139:3170–86 [CrossRef Medline](#)
- Wind AW, Schellevis FG, Van Staveren G, et al. **Limitations of the Mini-Mental State Examination in diagnosing dementia in general practice.** *Int J Geriatr Psychiatry* 1997;12:101–08 [Medline](#)
- Dubois B, Slachevsky A, Litvan I, et al. **The FAB: a Frontal Assessment Battery at bedside.** *Neurology* 2000;55:1621–26 [CrossRef Medline](#)
- Appollonio I, Leone M, Isella V, et al. **The Frontal Assessment Battery (FAB): normative values in an Italian population sample.** *Neurol Sci* 2005;26:108–16 [CrossRef Medline](#)
- Sloane AE, Becker LE, Ang LC, et al. **Neuronal intranuclear hyaline inclusion disease with progressive cerebellar ataxia.** *Pediatr Neurol* 1994;10:61–66 [CrossRef Medline](#)
- Zannolli R, Gilman S, Rossi S, et al. **Hereditary neuronal intranuclear inclusion disease with autonomic failure and cerebellar degeneration.** *Arch Neurol* 2002;59:1319–26 [CrossRef Medline](#)
- Yokoi S, Yasui K, Hasegawa Y, et al. **Pathological background of subcortical hyperintensities on diffusion-weighted images in a case of neuronal intranuclear inclusion disease.** *Clin Neuropathol* 2016; 35:375–80 [CrossRef Medline](#)
- Kandel ER, Schwartz JH, Jessell TM, et al. *Principles of Neural Science*. 5th ed. New York: McGraw-Hill; 2013:960–81
- Ilg W, Giese MA, Gizewski ER, et al. **The influence of focal cerebellar lesions on the control and adaptation of gait.** *Brain* 2008;131: 2913–27 [CrossRef Medline](#)
- Soffer D. **Neuronal intranuclear hyaline inclusion disease presenting as Friedreich's ataxia.** *Acta Neuropathol* 1985;65:322–29 [CrossRef Medline](#)
- Funata N, Maeda Y, Koike M, et al. **Neuronal intranuclear hyaline inclusion disease: report of a case and review of the literature.** *Clin Neuropathol* 1990;9:89–96 [Medline](#)

16. Brunberg JA, Jacquemont S, Hagerman RJ, et al. **Fragile X permutation carriers: characteristic MR imaging findings of adult male patients with progressive cerebellar and cognitive dysfunction.** *AJNR Am J Neuroradiol* 2002;23:1757–66 [Medline](#)
17. Jacquemont S, Hagerman RJ, Leehey M, et al. **Fragile X permutation tremor/ataxia syndrome: molecular, clinical, and neuroimaging correlates.** *Am J Hum Genet* 2003;72:869–78 [CrossRef Medline](#)
18. Weidauer S, von Stuckrad-Barre S, Dettmann E, et al. **Cerebral Erdheim-Chester disease: case report and review of the literature.** *Neuroradiology* 2003;45:241–45 [CrossRef Medline](#)
19. Menor F, Marti-Bonmati L, Arana E, et al. **Neurofibromatosis type 1 in children: MR imaging and follow-up studies of central nervous system findings.** *Eur J Radiol* 1998;26:121–31 [CrossRef Medline](#)
20. Boster A, Hrena S, Berger JR, et al. **Progressive multifocal leukoencephalopathy and relapsing-remitting multiple sclerosis: a comparative study.** *Arch Neurol* 2009;66:593–99 [Medline](#)
21. Amarenco P, Chevrie-Muller C, Roullet E, et al. **Paravermal infarct and isolated cerebellar dysarthria.** *Ann Neurol* 1991;30:211–13 [CrossRef Medline](#)
22. Okamoto K, Tokiguchi S, Furusawa T, et al. **MR features of diseases involving bilateral middle cerebellar peduncles.** *AJNR Am J Neuroradiol* 2003;24:1946–54 [Medline](#)
23. Pihlmaa T, Suominen S, Kiuru-Enari S. **Familial amyloidotic polyneuropathy type IV–gelsolin amyloidosis.** *Amyloid* 2012;19:30–33 [CrossRef Medline](#)
24. Greco CM, Berman RF, Martin RM, et al. **Neuropathology of fragile X-associated tremor/ataxia syndrome (FXTAS).** *Brain* 2006;129:243–55 [Medline](#)
25. Gokden M, Al-Hinti JT, Harik SI. **Peripheral nervous system pathology in fragile X tremor/ataxia syndrome (FXTAS).** *Neuropathology* 2009;29:280–84 [CrossRef Medline](#)
26. Hagerman RJ, Leehey M, Heinrichs W, et al. **Intention tremor, parkinsonism, and generalized brain atrophy in male carriers of fragile X.** *Neurology* 2001;57:127–30 [CrossRef Medline](#)

Differences in Morphologic and Hemodynamic Characteristics for “PHASES-Based” Intracranial Aneurysm Locations

 N. Varble,  H. Rajabzadeh-Oghaz,  J. Wang,  A. Siddiqui,  H. Meng, and  A. Mowla



ABSTRACT

BACKGROUND AND PURPOSE: Several recent prospective studies have found that unruptured intracranial aneurysms at various anatomic locations have different propensities for future rupture. This study aims to uncover the lack of understanding regarding rupture-prone characteristics, such as morphology and hemodynamic factors, associated with different intracranial aneurysm location.

MATERIALS AND METHODS: We investigated the characteristics of 311 unruptured aneurysms at our center. Based on the PHASES study, we separated and compared morphologic and hemodynamic characteristics among 3 aneurysm location groups: 1) internal carotid artery; 2) middle cerebral artery; and 3) anterior communicating, posterior communicating, and posterior circulation arteries.

RESULTS: A mixed model statistical analysis showed that size ratio, low wall shear stress area, and pressure loss coefficient were different between the intracranial aneurysm location groups. In addition, a pair-wise comparison showed that ICA aneurysms had lower size ratios, lower wall shear stress areas, and lower pressure loss coefficients compared with MCA aneurysms and compared with the group of anterior communicating, posterior communicating, and posterior circulation aneurysms. There were no statistical differences between MCA aneurysms and the group of anterior communicating, posterior communicating, and posterior circulation aneurysms for morphologic or hemodynamic characteristics.

CONCLUSIONS: ICA aneurysms may be subjected to less rupture-prone morphologic and hemodynamic characteristics compared with other locations, which could explain the decreased rupture propensity of intracranial aneurysms at this location.

ABBREVIATIONS: AcomA = anterior communicating artery; IA = intracranial aneurysm; LSA = low wall shear stress area; PcomA = posterior communicating artery; PHASES = Population, Hypertension, Age, Size of aneurysm, Earlier SAH from another aneurysm, and Site of aneurysm; PLC = pressure loss coefficient; SR = size ratio; WSS = wall shear stress

Intracranial aneurysms (IAs) occur in approximately 3% of the population.¹ Although the rupture rate is very low,² the consequences of rupture are devastating. With increased detection of incidental IAs, clinicians are routinely faced with the decision of whether to treat. However, because treatment carries substantial

risk,³ the decision is difficult at times. Therefore, objective guidelines are required to assess the aneurysm rupture risk.


Several prospective studies have found that aneurysm size and location may play a significant role in IA rupture propensity and, consequently, are among the most important factors that clinicians consider for IA management.^{2,4} In the landmark International Study of Unruptured Intracranial Aneurysms,⁴ the highest rupture rates at 5-year follow-ups occurred in aneurysms located in the posterior circulation. Later, the PHASES (Population, Hypertension, Age, Size of aneurysm, Earlier SAH from another aneurysm, and Site of aneurysm) study pooled the analyses of 6 prospective cohort studies and found that the patient's geographic region, hypertension status, age, IA size, history of SAH, and IA site were independent predictors of aneurysm rupture.⁴ More specifically, the PHASES study showed that aneurysms in the ICA location had the lowest risk of rupture; aneurysms in the MCA had a medium risk of rupture; and anterior communicating artery (AcomA), posterior communicating artery (PcomA), and posterior circulation artery aneurysms had the highest risk of rupture.⁴

Received February 21, 2017; accepted after revision June 9.

From the Department of Mechanical and Aerospace Engineering (N.V., H.R.-O., H.M.), Toshiba Stroke and Vascular Research Center (N.V., H.R.-O., A.S., H.M.), Departments of Biostatistics (J.W., A.M.), Neurosurgery (A.S., H.M.), Biomedical Engineering (H.M.), and Neurology (A.M.), University at Buffalo, State University of New York, Buffalo, New York.

This work was supported by National Institutes of Health grants (R01 NS091075 and R03 NS090193) and resources from the Center for Computational Research at the University at Buffalo.

Please address correspondence to Ashkan Mowla, MD, FAHA, FAAN, Department of Neurology, Gates Vascular Institute, School of Medicine and Biomedical Sciences, University at Buffalo, State University of New York, 100 High St, Buffalo, NY 14203; e-mail: mowla_a@yahoo.com

 Indicates open access to non-subscribers at www.ajnr.org

<http://dx.doi.org/10.3174/ajnr.A5341>

Table 1: Description of the patient population

	ICA			AcomA/PcomA/Post			
	ICA		MCA	Posterior			Total
	Cavernous	ICA		AcomA	PcomA	Circulation	
Age (years \pm SD)	58 \pm 12	59 \pm 14	60 \pm 10	58 \pm 13	64 \pm 11	61 \pm 13	59 \pm 13
No. of patients							
Hypertension	21	40	18	23	11	25	138
Smoking	22	44	10	25	6	17	124
Earlier SAH	3	1	1	7	0	3	15
IA multiplicity	10	41	6	3	1	4	65
Number of IAs	51	111	41	46	15	47	311
Total No. of patients (% of entire population)	40 (16%)	86 (34%)	31 (12%)	37 (15%)	12 (5%)	45 (18%)	251

Although it is generally accepted that aneurysms in different locations have a different risk of rupture and growth, there remains a lack of understanding regarding the geometric differences and the potentially different hemodynamic forces imposed on aneurysms at different locations. In this study, by using 3D morphologic calculations and hemodynamics parameters from image-based computational fluid dynamics, we investigated differences between IAs at different locations. We consecutively collected 311 unruptured aneurysms from our center and split them into 3 locations according to the perceived risk of rupture based on the PHASES score.⁴ The first group (PHASES risk score of 0) consisted of ICA and ICA cavernous aneurysms; the second group (PHASES risk score of 2) consisted of MCA aneurysms; and the third group (PHASES risk score of 4) consisted of AcomA, PcomA, and posterior circulation aneurysms. Using a mixed model analysis and pair-wise comparisons, we aimed to reveal if these aneurysm locations had different rupture-prone morphologic and hemodynamic characteristics.

MATERIALS AND METHODS

Population

Three hundred eleven (311) saccular IAs from 251 patients were consecutively collected between 2006 and 2013 with institutional review board approval at the Buffalo General Hospital University at Buffalo (Buffalo, New York). This dataset was partially derived from a previously analyzed dataset of 119 IAs⁵ and, later, 204 IAs.^{6,7} Patients who met the selection criteria underwent 3D imaging, had an unruptured IA at the time of imaging, and had sufficient image quality for 3D segmentation. A description of the comorbidities of the patients included in our cohort are summarized in Table 1.

The aneurysms were separated into 3 location-based categories based on the PHASES score.⁴ The first group consisted of aneurysms in the ICA. The second group consisted of MCA aneurysms. The third group consisted of AcomA, PcomA, and posterior circulation aneurysms and is termed the AcomA/PcomA/Post aneurysm group. The IAs of the posterior circulation included the aneurysms from the basilar artery, basilar tip, posterior cerebral artery, cerebellar arteries, and intracranial vertebral artery. There were 162 ICA aneurysms (ICA cavernous, 51; other ICA, 111), 41 MCA aneurysms, and 108 AcomA/PcomA/Post aneurysms (AcomA, 46; PcomA, 15; posterior circulation, 47).

Morphologic Factors

To generate 3D models for morphologic and hemodynamic calculations, angiographic images were segmented in the Vascular Modeling Toolkit (www.vmtk.org).⁸ 3D morphologic calculations were performed in a custom Matlab code (R2014a; MathWorks, Natick, Massachusetts). A detailed description of the calculated parameters can be found in previous literature.^{9,10} Briefly, aneurysm size is the maximum distance from the center of the neck plane to a point in the aneurysm dome, size ratio (SR) is the ratio of the IA size to the parent vessel diameter, aspect ratio is the ratio of the IA size to the neck diameter, undulation index is the degree of surface irregularity, ellipticity index is the deviation of the IA from a perfect hemisphere, and nonsphericity index is the deviation of the IA from a perfect hemisphere while also considering surface undulations.

undulation index is the degree of surface irregularity, ellipticity index is the deviation of the IA from a perfect hemisphere, and nonsphericity index is the deviation of the IA from a perfect hemisphere while also considering surface undulations.

Computational Fluid Dynamics Methods

To simulate blood flow and compute hemodynamic factors for all aneurysm geometries, pulsatile computational fluid dynamics simulations were conducted according to previously detailed methodology.⁵ Based on grid-refinement studies, computational meshes were generated consisting of 300,000–1.5 million volumetric tetrahedral elements. To ensure proper resolution at the wall, 4 refined prism layers were generated with a maximum size equal to one-tenth of the volumetric element size. Meshes were generated by using ICEM CFD (ANSYS, Canonsburg, Pennsylvania). Computational fluid dynamics simulations were run in STAR-CCM+ (CD-adapco, Melville, New York). A rigid wall, no-slip boundary condition, and Newtonian fluid properties were assumed ($\rho = 1056 \text{ kg/m}^3$; $\mu = 3.5 \text{ cP}$). A pulsatile waveform was taken from a transcranial Doppler sonography measurement from a healthy patient and imposed at the vessel inlet,⁵ and the principle of minimum work, or flow split assumption, was applied at the outlet.¹¹ A pressure implicit with splitting of operator algorithm was applied for temporal discretization, and a second-order upwind-differencing scheme was used for spatial discretization to solve the transient incompressible Navier–Stokes equations. To assure numerically stable results, each pulsatile simulation was run for 3 cardiac cycles, and the last cycle was used for analysis. Postprocessing was performed in Tecplot 360 (Tecplot, Bellevue, Washington).

Hemodynamic Factors

The hemodynamic factors analyzed included: normalized time-averaged wall shear stress (WSS), or the average of the frictional or tangential force on the aneurysm wall normalized by parent artery time-averaged WSS; oscillatory shear index (OSI), or the average of the directional change of WSS over 1 cardiac cycle; relative residence time (RRT), or the average relative time that blood spends at the wall; low WSS area (LSA),

Table 2: Statistical comparison of morphologic and hemodynamic factors between aneurysms from the 3 PHASES-based locations^a

Factors	ICA Mean ± SD	MCA Mean ± SD	AcomA/PcomA/Post Mean ± SD	Overall Comparison P Value
Size (mm)	5.11 ± 3.72	4.45 ± 2.39	4.74 ± 3.61	.6236
SR	1.54 ± 1.17	2.35 ± 1.25	2.45 ± 2.22	<.0001 ^b
AR	1.11 ± 0.58	1.26 ± 0.64	1.18 ± 0.71	.3916
UI	0.058 ± 0.050	0.074 ± 0.057	0.066 ± 0.071	.1318
EI	0.119 ± 0.058	0.138 ± 0.062	0.132 ± 0.058	.0719
NSI	0.142 ± 0.069	0.164 ± 0.072	0.152 ± 0.064	.1679
WSS	0.66 ± 0.36	0.53 ± 0.37	0.57 ± 0.52	.0121
OSI	0.005 ± 0.008	0.005 ± 0.011	0.011 ± 0.049	.0413
RRT	2.38 ± 2.97	3.98 ± 6.15	4.09 ± 5.40	.0050
LSA	0.097 ± 0.182	0.206 ± 0.271	0.198 ± 0.271	.0003 ^b
MWSS	4.43 ± 2.12	4.49 ± 5.06	3.98 ± 2.53	.0358
PLc	2.64 ± 3.71	6.06 ± 5.23	5.88 ± 5.71	<.0001 ^b
EL (W/m ³)	6193 ± 11339	6505 ± 8593	7793 ± 12539	.5271

Note:—AR indicates aspect ratio; EI, ellipticity index; EL, energy loss; MWSS, maximum normalized wall shear stress; NSI, nonsphericity index; OSI, oscillatory shear index; Post, posterior circulation; RRT, relative residence time; UI, undulation index.

^a ICA aneurysms, MCA aneurysms, and AcomA, PcomA, and posterior circulation aneurysms were compared by a mixed model approach. An overall *P* value of <.0038 ($\alpha = .05$; number of tests, 13) indicated a statistically significant difference between the 3 IA groups.

^b Indicates statistically significant by mixed model analysis.

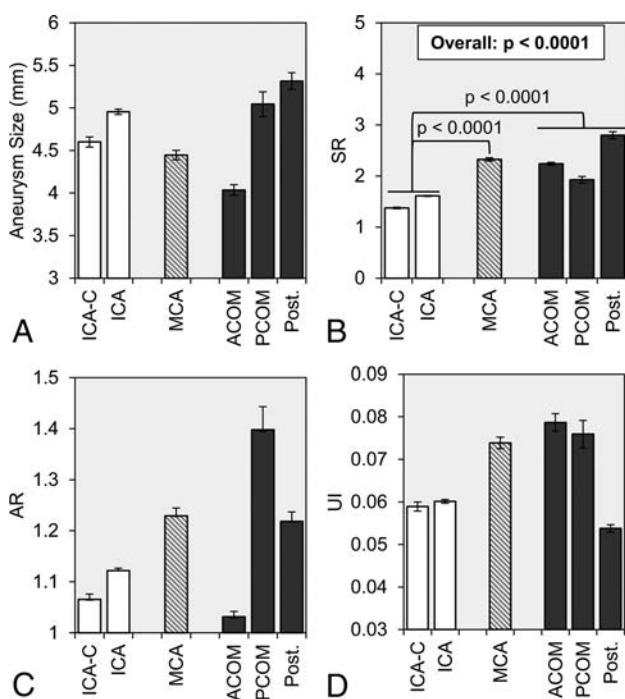


FIG 1. Statistical comparison of morphologic parameters was performed between 3 location groups: ICA (white), MCA (dashed gray lines), and AcomA, PcomA, and posterior circulation aneurysms (dark gray). The group-averaged values of A, aneurysm size, B, SR, C, AR, and D, UI are given with error bars that represent standard error. The overall *P* value is given for SR, for which statistical significance was achieved by a mixed model comparison of the 3 groups. In addition, from pair-wise comparisons, the brackets show statistically significant differences between the ICA, MCA, and AcomA/PcomA/Post groups. AR indicates aspect ratio; ICA-C, cavernous internal carotid artery; Post, posterior circulation; UI, undulation index.

or the percentage of the aneurysm wall exposed to physiologically low WSS; maximum WSS on the aneurysm dome⁵; energy loss (EL), or the energy expenditure caused by viscous friction; and the pressure loss coefficient (PLc), or the pressure loss due to viscous friction.¹²

Statistical Analysis

To assess the differences in the morphologic and hemodynamic parameters between the 3 IA location groups, a mixed model analysis was used. This method was used to consider the potential correlation of morphologic and hemodynamic parameters between IAs from patients with multiple aneurysms and used for comparison between the 3 IA location groups. A Bonferroni correction was used, and each variable was checked for normal distribution. Non-normally distributed data were normalized by taking the square root of the data, and the outliers were identified and removed. A *P* value of <.004 was considered statistically significant ($\alpha = .05$; number of tests, 13) and indicated that a difference between the group means exists.

If the variables were found to be statistically significant by the mixed model analysis, a pair-wise comparison was then performed with an *F* test. For pair-wise comparisons, a *P* value of <.02 was considered statistically significant ($\alpha = .05$; number of tests, 3). Statistical analyses were performed in SAS 9.4 (SAS Institute, Cary, North Carolina).

RESULTS

Table 2 summarizes the comparison of morphologic and hemodynamic parameters between the IA groups. Figs 1 and 2 show the mean and standard error of more discrete subsets of locations within the 3 PHASES-based location groups. As shown in Fig 1, we analyzed the difference in morphologic parameters between the 3 groups. By the mixed model analysis, we found that there was no statistical difference in the IA size between the 3 groups (overall: *P* = .6236). However, as shown in Fig 1B, SR was significantly different between the 3 groups (overall: *P* < .0001). Furthermore, by pair-wise comparison, we found that SR was statistically lower in ICA aneurysms (1.54 ± 1.17) compared with both MCA aneurysms (2.35 ± 1.25 ; *P* < .0001) and AcomA/PcomA/Post aneurysms (2.45 ± 2.22 ; *P* < .0001). However, there was no difference between the group-averaged SR of MCA aneurysms and AcomA/PcomA/Post aneurysms (*P* = .7387).

Fig 2 summarizes the comparison of hemodynamic parameters between different IA groups. By the mixed model analysis, we found that LSA and PLc were statistically different between the 3 location groups (*P* = .0003 and *P* < .0001 for LSA and PLc, respectively). As illustrated by WSS contours in Fig 3, the pair-wise comparison showed that LSA was significantly lower for ICA aneurysms (0.097 ± 0.182) compared with both MCA aneurysms (0.206 ± 0.271 ; *P* = .0084) and AcomA/PcomA/Post aneurysms (0.198 ± 0.271 ; *P* = .0005). Pair-wise comparison also showed that PLc was significantly lower in ICA aneurysms (2.64 ± 3.71) compared with both MCA (6.06 ± 5.23 ; *P* < .0001) and AcomA/PcomA/Post aneurysms (5.88 ± 5.71 ; *P* < .0001). As illustrated by velocity streamlines in Fig 4, ICA aneurysms had more organized

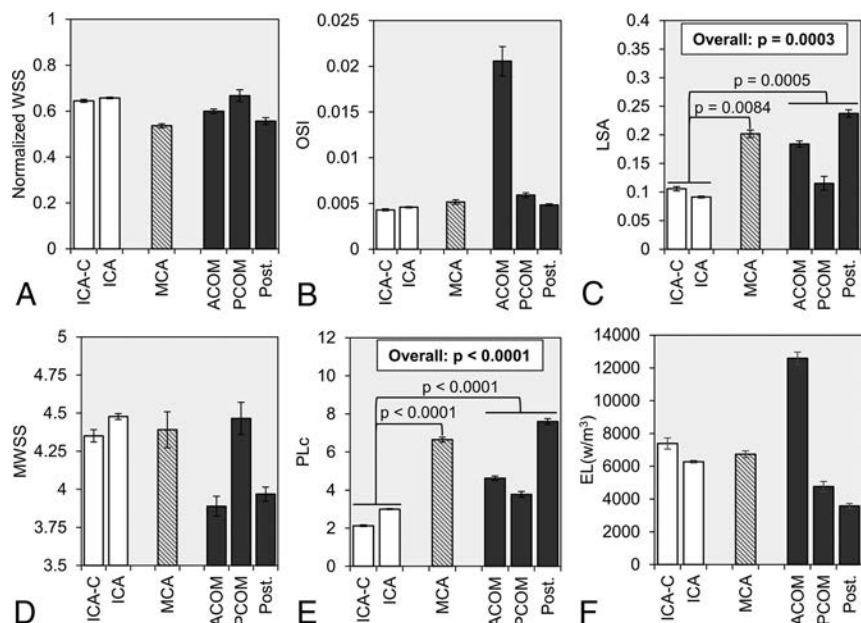


FIG 2. Statistical comparison of hemodynamic parameters was made between 3 location-based groups: ICA (white), MCA (dashed gray lines), and AcomA, PcomA, and posterior circulation aneurysms (dark gray). The group-averaged values of A, normalized WSS, B, OSI, C, LSA, D, MWSS, E, PLc, and F, EL are given with error bars that represent standard error. The overall P value is given from LSA and PLc, for which statistical significance was achieved by a mixed model comparison of the 3 groups. In addition, from pair-wise comparisons, the brackets show statistically significant differences between the ICA, MCA, and AcomA/PcomA/Post groups. EL indicates energy loss; ICA-C, cavernous internal carotid artery; OSI, oscillatory shear index; Post., posterior circulation; MWSS, maximum normalized wall shear stress.

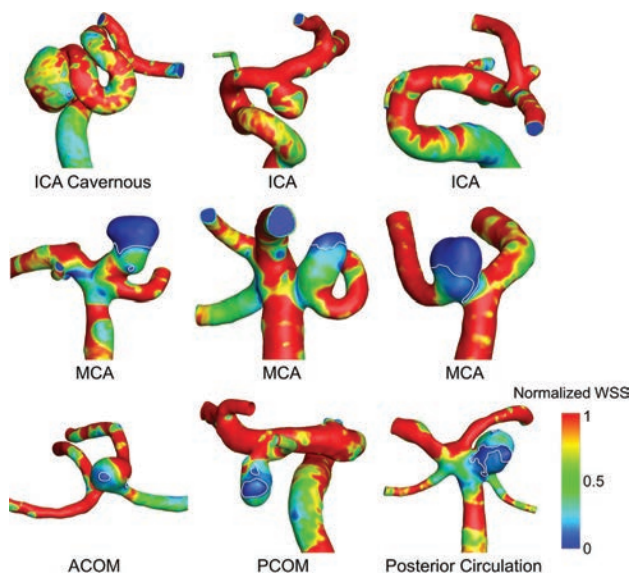


FIG 3. Normalized WSS contour plots for representative aneurysms from each of the 3 location-based groups. The areas of low WSS are outlined in white. ICA aneurysms (top), MCA aneurysms (middle), and AcomA/PcomA/Post aneurysms (bottom) are shown. ICA aneurysms had significantly higher LSA compared with both other groups.

flow patterns compared with MCA aneurysms and the aneurysms from the AcomA/PcomA/Post group. Similar to SR, for both LSA and PLc, the pair-wise comparison showed no statistical difference between MCA and AcomA/PcomA/Post aneurysms ($P = .8262$ and $P = .4325$ for LSA and PLc, respectively).

DISCUSSION

Previous clinical studies have suggested a significant association between IA location and a higher risk of growth and rupture.^{2,4,13} However, there is a lack of understanding regarding the differences in aneurysm location from hemodynamic and morphologic standpoints, which might play a role in the different rupture propensities between IA locations. In this study, by using a consecutively collected aneurysm data base of 311 unruptured aneurysms from our center, we attempt to uncover morphologic and hemodynamic characteristics unique to IA locations.

Following the PHASES study by Greving et al,⁴ we separated the aneurysm cases in our cohort into 3 categories: ICA aneurysms, MCA aneurysms, and AcomA/PcomA/Post aneurysms, consisting of AcomA, PcomA, and posterior circulation aneurysms. We then analyzed the differences in morphologic and hemodynamic characteristics between the 3 groups by focusing on parameters found to be previously associated with rupture risk in cross-sectional

datasets.^{7,12,14,15} Our study finds that ICA aneurysms may have characteristics that make them the least rupture-prone.

SR, or the size of the aneurysm relative to the parent vessel, has been independently associated with rupture risk in both cross-sectional^{5,10,16-19} and prospective studies.²⁰ In this study, we found that SR was significantly smaller in the aneurysms from the ICA location compared with other aneurysms. Consistent with previous longitudinal studies, this suggests that these aneurysms may not be as rupture-prone as aneurysms in other locations. The finding that SR is significantly smaller in ICA aneurysms is not surprising because of the larger diameter of the parent vessel. As previously suggested,⁵ our data support that SR can surrogate the aneurysm location.

High SR, together with pulsatile flow conditions, may result in an adverse hemodynamic environment. Previous computational studies have found that with increasing SR, aneurysm-averaged WSS decreased and the number of vortices increased.²¹ In the present study, we found that MCA aneurysms and AcomA/PcomA/Post aneurysms also had a higher LSA and PLc compared with ICA aneurysms.

Low aneurysmal WSS has been previously associated with IA rupture in location-specific studies.^{22,23} In 24 IAs, Chien et al²³ found that low WSS was associated with IA rupture status in basilar artery and AcomA aneurysms. In addition, in 106 MCA IAs, Miura et al²² found that low aneurysm WSS was independently associated with IA rupture. WSS, the frictional force of blood on the aneurysm wall, has been shown to affect vascular remodeling and degeneration.²⁴ WSS can be sensed by the endothelium, and persistent exposure to nonphysiologic hemodynamics has been

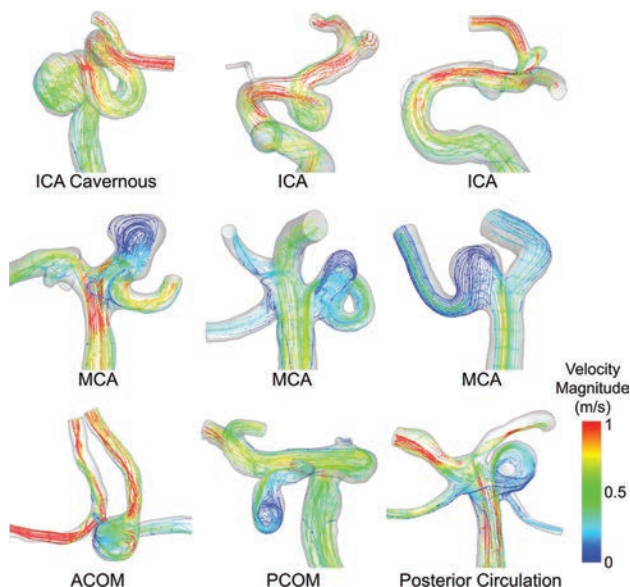


FIG 4. Velocity streamlines for representative cases from each of the 3 location-based groups. ICA aneurysms had more organized flow patterns that resulted in lower PLc.

linked to initiation, growth, and rupture of IAs.²⁴⁻²⁶ Our study suggests that aneurysms in locations other than the ICA are subjected to a low WSS hemodynamic environment that may result in higher rupture rates.

PLc is an indicator of viscous energy loss in the aneurysm because of the inflow and geometry. More complex aneurysm geometries result in complex flow patterns, higher viscous losses, and a higher PLc. Our study found that PLc was significantly different among the unruptured IAs in our cohort and was lowest in ICA aneurysms. Complex flow has been previously associated with IA rupture. A study of 117 ruptured and unruptured bifurcation IAs by Doddasomayajula et al²⁷ showed that complex and oscillatory aneurysmal flow patterns were associated with basilar tip IA rupture, a location with high rupture rates. However, a study of 50 sidewall ICA IAs and 50 bifurcation MCA IAs by Takao et al¹² showed that a lower PLc was independently associated with rupture. This difference may be because of the analysis of only unruptured IAs in our study or the presence of bifurcation and sidewall type IAs at both MCA and ICA locations in our cohort.

We also observed that the mean undulation index (irregular shape) was higher in MCA and AcomA/PcomA/Post aneurysms compared with ICA aneurysms; however, it was not statistically different between the IA location groups. The undulation index quantifies the 3D surface irregularities and may indicate local wall degeneration and thrombosis in the lumen potentially leading to rupture.²⁸ Recently, the radiologic identification of aneurysm irregularities or the presence of daughter aneurysms was independently associated with aneurysm rupture in a Finnish cohort.²⁹ Our objective quantification of surface irregularities is supported by the findings of previous work by our group that found the undulation index was a significant risk factor for rupture in our cross-sectional data base.^{5,7}

In addition, we observed that for some morphologic and hemodynamic parameters where statistical significance was not

found between IA groups, an analysis of more discrete IA locations might be warranted. The aspect ratio has been found in many large studies to be a statistically significant predictor of rupture.^{30,31} Although the aspect ratio is not statistically different among the IA groups in our study, Fig 1C shows that PcomA IAs have a large aspect ratio compared with other IA groups. Similarly, oscillatory shear index and energy loss have been suggested to be associated with IA rupture.^{5,32} As Figs 2B and 2F show, both the mean oscillatory shear index and energy loss are highest in the AcomA group. The complex flow in AcomA IAs is most likely caused by the 2 flow inlets that are present in AcomA aneurysms. This may lead to the collision of the inflow jets, and the directional changes of the WSS and energy losses may be amplified. Larger studies that analyze more discrete IA locations may reveal morphologic and hemodynamic differences between locations such as the AcomA and PcomA locations.

Finally, we recognize that assessing IA rupture potential is not limited to the morphologic and hemodynamic factors or the IA location. Earlier studies of ruptured and unruptured IAs that included IA location, type, and morphologic and hemodynamic parameters showed that hemodynamics did not contribute significantly to rupture discrimination.³³ As suggested by the PHASES score, increased rupture propensity may be related to hypertension, patient age, and history of SAH. However, from additional analysis in our cohort, there was no statistically significant difference between patients with IAs at different locations when considering age over 70 years ($P = .5584$), hypertension ($P = .0227$), or previous SAH ($P = .1939$), where $P < .017$ was considered statistically significant ($\alpha = .05$; number of tests, 3). Therefore, we may assume that our population is matched across IA locations when considering comorbidities relevant to the PHASES score.

Our study has several limitations. First, our data are limited to a single center, and therefore, it is unknown if our findings would apply to other datasets. Second, this study examines cross-sectional data and does not directly identify factors that can lead to future rupture at specific IA locations. Third, because of a lack of patient-specific information, we assumed that blood is non-Newtonian for computational fluid dynamics simulations, we applied a generic patient-specific waveform at the inlet, and we assumed that the vessel walls were rigid.

CONCLUSIONS

Previous studies have suggested a significant association between IA location and risk of rupture. In this study, we analyzed 311 aneurysm cases from our center and compared the differences in morphologic and hemodynamic factors. We found that SR, LSA, and PLc were different between IA groups. In addition, our results showed that ICA aneurysms had lower size ratios, less low WSS areas, and lower pressure loss coefficients compared with aneurysms in other locations. Our results suggest that ICA aneurysms have fewer rupture-prone morphologic characteristics and may be subjected to less adverse hemodynamic environments. Therefore, ICA aneurysms have better long-term outcomes with regard to rupture risk compared with other aneurysm locations.

Disclosures: Nicole Varble—*RELATED: Grants/Grants Pending:* National Institutes of Health, *Comments:* R01NS091075. Adnan Siddiqui—*UNRELATED: Board Membership:* Intersocietal Accreditation Committee; *Consultancy:* Codman & Shurtleff, Medtronic, GuidePoint Global Consulting, Penumbra, Stryker, MicroVention, W.L. Gore & Associates, Three Rivers Medical Center, Corindus Vascular Robotics, Amnis Therapeutics, CereVasc, Pulsar Vascular, The Stroke Project, Cerebrotech Medical Systems, Rapid Medical, Neuravi, Silk Road Medical, Rebound Therapeutics; *Stock/Stock Options:* StimMed, Valor Medical, Neuro Technology Investors, Cardinal Health, Medina Medical Systems, Buffalo Technology Partners, Inc., International Medical Distribution Partners; *Other:* National Steering Committees: Penumbra, 3D Separator Trial, Covidien (Now Medtronic), SWIFT PRIME and SWIFT DIRECT Trials, MicroVention, FRED Trial, MicroVention, CONFIDENCE Study, LARGE Trial, POSITIVE Trial, Penumbra, COMPASS Trial, INVEST Trial. Hui Meng—*RELATED: Grants/Grants Pending:* National Institutes of Health-National Institute of Neurological Disorders, *Comments:* SR01 NS091075*; *UNRELATED: Grants/Grants Pending:* National Institutes of Health Small Business Innovation Research, *Comments:* principal investigator Vince Tutino; *Neurovascular Diagnostics*:* *Patents (Planned, Pending or Issued):* Provisional patent on blood-based diagnostic technology, *Comments:* filed in 9/2016 by University at Buffalo*; *Stock/Stock Options:* Neurovascular Diagnostics, *Comments:* new small company, no monetary activities so far. Ashkan Mowla—*RELATED: Grants/Grants Pending:* National Institutes of Health*; *UNRELATED: Grants/Grants Pending:* National Institutes of Health*. *Money paid to the institution.

REFERENCES

1. Vlak MH, Algra A, Brandenburg R, et al. **Prevalence of unruptured intracranial aneurysms, with emphasis on sex, age, comorbidity, country, and time period: a systematic review and meta-analysis.** *Lancet Neurol* 2011;10:626–36 [CrossRef Medline](#)
2. Wiebers DO. **Unruptured intracranial aneurysms: natural history, clinical outcome, and risks of surgical and endovascular treatment.** *Lancet* 2003;362:103–10 [CrossRef Medline](#)
3. Johnston SC, Higashida RT, Barrow DL, et al. **Recommendations for the endovascular treatment of intracranial aneurysms: a statement for healthcare professionals from the Committee on Cerebrovascular Imaging of the American Heart Association Council on Cardiovascular Radiology.** *Stroke* 2002;33:2536–44 [CrossRef Medline](#)
4. Greving JP, Wermer MJ, Brown RD Jr, et al. **Development of the PHASES score for prediction of risk of rupture of intracranial aneurysms: a pooled analysis of six prospective cohort studies.** *Lancet Neurol* 2014;13:59–66 [CrossRef Medline](#)
5. Xiang J, Natarajan SK, Tremmel M, et al. **Hemodynamic-morphologic discriminants for intracranial aneurysm rupture.** *Stroke* 2011;42:144–52 [CrossRef Medline](#)
6. Xiang J, Yu J, Choi H, et al. **Rupture Resemblance Score (RRS): toward risk stratification of unruptured intracranial aneurysms using hemodynamic-morphological discriminants.** *J Neurointerv Surg* 2015;7:490–95 [CrossRef Medline](#)
7. Xiang J, Yu J, Snyder KV, et al. **Hemodynamic-morphological discriminant models for intracranial aneurysm rupture remain stable with increasing sample size.** *J Neurointerv Surg* 2016;8:104–10 [CrossRef Medline](#)
8. Antiga L, Piccinelli M, Botti L, et al. **An image-based modeling framework for patient-specific computational hemodynamics.** *Med Biol Eng Comput* 2008;46:1097–112 [CrossRef Medline](#)
9. Raghavan ML, Ma B, Harbaugh RE. **Quantified aneurysm shape and rupture risk.** *J Neurosurg* 2005;102:355–62 [CrossRef Medline](#)
10. Dhar S, Tremmel M, Mocco J, et al. **Morphology parameters for intracranial aneurysm rupture risk assessment.** *Neurosurgery* 2008;63:185–96; discussion 196–97 [CrossRef Medline](#)
11. Oka S, Nakai M. **Optimality principle in vascular bifurcation.** *Biorheology* 1987;24:737–51 [Medline](#)
12. Takao H, Murayama Y, Otsuka S, et al. **Hemodynamic differences between unruptured and ruptured intracranial aneurysms during observation.** *Stroke* 2012;43:1436–39 [CrossRef Medline](#)
13. Backes D, Vergouwen MD, Tiel Groenestege AT, et al. **PHASES score for prediction of intracranial aneurysm growth.** *Stroke* 2015;46:1221–26 [CrossRef Medline](#)
14. Meng H, Tutino VM, Xiang J, et al. **High WSS or low WSS? Complex interactions of hemodynamics with intracranial aneurysm initiation, growth, and rupture: toward a unifying hypothesis.** *AJNR Am J Neuroradiol* 2014;35:1254–62 [CrossRef Medline](#)
15. Xiang J, Tutino VM, Snyder KV, et al. **CFD: computational fluid dynamics or confounding factor dissemination? The role of hemodynamics in intracranial aneurysm rupture risk assessment.** *AJNR Am J Neuroradiol* 2014;35:1849–57 [CrossRef Medline](#)
16. Kashiwazaki D, Kuroda S. **Size ratio can highly predict rupture risk in intracranial small (<5 mm) aneurysms.** *Stroke* 2013;44:2169–73 [CrossRef Medline](#)
17. Ma D, Tremmel M, Paluch RA, et al. **Size ratio for clinical assessment of intracranial aneurysm rupture risk.** *Neurol Res* 2010;32:482–86 [CrossRef Medline](#)
18. Lin N, Ho A, Gross BA, et al. **Differences in simple morphological variables in ruptured and unruptured middle cerebral artery aneurysms.** *J Neurosurg* 2012;117:913–19 [CrossRef Medline](#)
19. Ma B, Harbaugh RE, Raghavan ML. **Three-dimensional geometrical characterization of cerebral aneurysms.** *Ann Biomed Eng* 2004;32:264–73 [Medline](#)
20. Rahman M, Smietana J, Hauck E, et al. **Size ratio correlates with intracranial aneurysm rupture status: a prospective study.** *Stroke* 2010;41:916–20 [CrossRef Medline](#)
21. Tremmel M, Dhar S, Levy EI, et al. **Influence of intracranial aneurysm-to-parent vessel size ratio on hemodynamics and implication for rupture: results from a virtual experimental study.** *Neurosurgery* 2009;64:622–30; discussion 630–31 [CrossRef Medline](#)
22. Miura Y, Ishida F, Umeda Y, et al. **Low wall shear stress is independently associated with the rupture status of middle cerebral artery aneurysms.** *Stroke* 2013;44:519–21 [CrossRef Medline](#)
23. Chien A, Castro MA, Tateshima S, et al. **Quantitative hemodynamic analysis of brain aneurysms at different locations.** *AJNR Am J Neuroradiol* 2009;30:1507–12 [CrossRef Medline](#)
24. Meng H, Wang Z, Hoi Y, et al. **Complex hemodynamics at the apex of an arterial bifurcation induces vascular remodeling resembling cerebral aneurysm initiation.** *Stroke* 2007;38:1924–31 [CrossRef Medline](#)
25. Bousset L, Rayz V, McCulloch C, et al. **Aneurysm growth occurs at region of low wall shear stress: patient-specific correlation of hemodynamics and growth in a longitudinal study.** *Stroke* 2008;39:2997–3002 [CrossRef Medline](#)
26. Dolan JM, Kolega J, Meng H. **High wall shear stress and spatial gradients in vascular pathology: a review.** *Ann Biomed Eng* 2013;41:1411–27 [CrossRef Medline](#)
27. Daddasomayajula R, Chung B, Hamzei-Sichani F, et al. **Differences in hemodynamics and rupture rate of aneurysms at the bifurcation of the basilar and internal carotid arteries.** *AJNR Am J Neuroradiol* 2017;38:570–76 [CrossRef Medline](#)
28. Frösen J. **Smooth muscle cells and the formation, degeneration, and rupture of saccular intracranial aneurysm wall—a review of current pathophysiological knowledge.** *Transl Stroke Res* 2014;5:347–56 [CrossRef Medline](#)
29. Lindgren AE, Koivisto T, Björkman J, et al. **Irregular shape of intracranial aneurysm indicates rupture risk irrespective of size in a population-based cohort.** *Stroke* 2016;47:1219–26 [CrossRef Medline](#)
30. Weir B, Amidei C, Kongable G, et al. **The aspect ratio (dome/neck) of ruptured and unruptured aneurysms.** *J Neurosurg* 2003;99:447–51 [CrossRef Medline](#)
31. Backes D, Vergouwen MD, Velthuis BK, et al. **Difference in aneurysm characteristics between ruptured and unruptured aneurysms in patients with multiple intracranial aneurysms.** *Stroke* 2014;45:1299–303 [CrossRef Medline](#)
32. Qian Y, Takao H, Umezumi M, et al. **Risk analysis of unruptured aneurysms using computational fluid dynamics technology: preliminary results.** *AJNR Am J Neuroradiol* 2011;32:1948–55 [CrossRef Medline](#)
33. Schneiders JJ, Marquering HA, van Ooij P, et al. **Additional value of intra-aneurysmal hemodynamics in discriminating ruptured versus unruptured intracranial aneurysms.** *AJNR Am J Neuroradiol* 2015;36:1920–26 [CrossRef Medline](#)

Angioarchitectures and Hemodynamic Characteristics of Posterior Communicating Artery Aneurysms and Their Association with Rupture Status

 B.J. Chung,  R. Doddasomayajula,  F. Mut,  F. Detmer,  M.B. Pritz,  F. Hamzei-Sichani,  W. Brinjikji,  D.F. Kallmes,  C.M. Jimenez,  C.M. Putman, and  J.R. Cebal



ABSTRACT

BACKGROUND AND PURPOSE: Intracranial aneurysms originating at the posterior communicating artery are known to have high rupture risk compared with other locations. We tested the hypothesis that different angioarchitectures (ie, branch point configuration) of posterior communicating artery aneurysms are associated with aneurysm hemodynamics, which in turn predisposes aneurysms to rupture.

MATERIALS AND METHODS: A total of 313 posterior communicating artery aneurysms (145 ruptured, 168 unruptured) were studied with image-based computational fluid dynamics. Aneurysms were classified into different angioarchitecture types depending on the location of the aneurysm with respect to parent artery bifurcation. Hemodynamic characteristics were compared between ruptured and unruptured aneurysms, as well as among aneurysms with different angioarchitectures.

RESULTS: Angioarchitecture was associated with rupture ($P = .003$). Ruptured aneurysms had higher, more concentrated, and more oscillatory wall shear stress distributions (maximum wall shear stress, $P < .001$; shear concentration index, $P < .001$; mean oscillatory shear index, $P < .001$), stronger and more concentrated inflow jets (represented as Q , $P = .01$; inflow concentration index, $P < .001$), and more complex and unstable flow patterns (vortex core length, $P < .001$; proper orthogonal decomposition entropy, $P < .001$) compared with unruptured aneurysms. These adverse conditions were more common in aneurysms with bifurcation-type angioarchitectures compared with those with lateral or sidewall angioarchitectures. Interestingly, ruptured aneurysms also had lower normalized mean wall shear stress ($P = .02$) and minimum wall shear stress ($P = .002$) than unruptured aneurysms.

CONCLUSIONS: High-flow intrasaccular hemodynamic characteristics, commonly found in bifurcation-type angioarchitectures, are associated with the posterior communicating artery aneurysm rupture status. These characteristics include strong and concentrated inflow jets, concentrated regions of elevated wall shear stress, oscillatory wall shear stress, lower normalized wall shear stress, and complex and unstable flow patterns.

ABBREVIATIONS: PCOM = posterior communicating artery; WSS = wall shear stress

On average, the combined risk carried by aneurysm treatment far exceeds the annual risk of aneurysm rupture.^{1–3} As such, the best clinical practice would be to treat only those aneurysms

that are relatively likely to rupture. Today, aneurysm size and location drive most clinical decisions, with consideration also given to surgical accessibility/endovascular feasibility, prior history of subarachnoid hemorrhage, family history, and patient age and general health.⁴ However, small aneurysms clearly are not entirely benign because the mean size of ruptured aneurysms is far smaller than 10 mm, and many are 4 mm or less in diameter.⁵ Understanding the mechanisms that degrade the aneurysm wall and induce progression and eventual rupture or, alternatively, successful remodeling and repair that stabilizes the aneurysm, carries the promise of improving aneurysm evaluation as well as the development of novel therapies that target specific pathways of these mechanisms.


The posterior communicating artery (PCOM) is a common site for aneurysm development. PCOM aneurysms account for approximately 25% of all intracranial aneurysms.⁶ Aneurysms at


Received March 15, 2017; accepted after revision June 9.

From the Bioengineering Department (B.J.C., R.D., F.M., F.D., M.B.P., J.R.C.), George Mason University, Fairfax, Virginia; Department of Neurosurgery (F.H.-S.), Mt. Sinai Medical Center, New York, New York; Department of Radiology (W.B., D.F.K.), Mayo Clinic, Rochester, Minnesota; Neurosurgery Department (C.M.J.), University of Antioquia, Medellin, Colombia; and Interventional Neuroradiology Unit (C.M.P.), Inova Fairfax Hospital, Falls Church, Virginia.

This work was supported by the National Institutes of Health/National Institute of Neurological Disorders and Stroke (NIH-NINDS) grant #R21NS094780.

Please address correspondence to Juan R. Cebal, PhD, Bioengineering Department, Volgenau School of Engineering, George Mason University, 4400 University Dr, MSN 2A1, Fairfax, VA 22030; e-mail: jcebal@gmu.edu

 Indicates open access to non-subscribers at www.ajnr.org

 Indicates article with supplemental on-line photo.

<http://dx.doi.org/10.3174/ajnr.A5358>



FIG 1. A, Distribution of all ruptured and unruptured aneurysms in our data base by aneurysm location, and B, distribution of ruptured and unruptured PCOM aneurysms by size. ACA indicates anterior cerebral artery; ACOM, anterior communicating artery; BA, basilar artery; PCA, posterior cerebral artery; VA, vertebral artery.

this location have larger rupture risk than aneurysms at other locations such as the MCA or other segments of the ICA.^{7,8} As such, clinicians often need to decide whether to treat PCOM aneurysms, but reliable aneurysm-specific parameters to guide and support decision making are lacking. A previous study showed that PCOM aneurysms, along with anterior communicating artery and basilar tip aneurysms, occur more frequently in patients with an anatomic variant or incomplete circle of Willis.⁹ A recent study found that inflow angle and the aneurysm area under low wall shear stress (WSS) were independently associated with rupture.¹⁰ These studies support the idea that hemodynamics are largely influenced by the local geometry of the vessels and aneurysm configurations and that they may play an important role in the development and evolution of intracranial aneurysms at this location.

To further test this hypothesis, the purpose of this study was to analyze the hemodynamic characteristics of ruptured and unruptured PCOM aneurysms and their relationship to the anatomic configuration of the aneurysm with respect to the ICA-PCOM bifurcation (ie, its angioarchitecture). The objective was to identify distinguishing characteristics that could be used to understand the underlying mechanisms of aneurysm evolution and, ultimately, use them to improve current risk assessment of PCOM aneurysms.

MATERIALS AND METHODS

Data Base

We have constructed a data base of intracranial aneurysms that have been imaged with 3D rotational angiography. In addition to the 3D rotational angiography images, the data base contains anonymized patient and aneurysm information such as aneurysm location, size, and rupture status as well as patient sex and age. Currently, the data base contains 2022 aneurysms in 1386 patients collected consecutively. All data have been anonymized, and the study has been approved by the George Mason institutional review board. The distribution of all ruptured and unruptured aneurysms in this data base by location is shown in Fig 1A. In this data base, PCOM aneurysms had the second largest rupture rate (46%) after anterior communicating artery aneurysms (63%) and

were the third most common ($n = 313$) after ICA ($n = 855$) and MCA ($n = 390$) aneurysms. All PCOM aneurysms with known rupture status in this data base were selected for study. This selection resulted in a total of 313 PCOM aneurysms, 145 ruptured and 168 unruptured. The distribution of ruptured and unruptured PCOM aneurysms by size is presented in Fig 1B, showing that many of the ruptured aneurysms are small (<6 mm), and that even medium-sized aneurysms (6–10 mm) have large rupture rates (63%).

Angioarchitectures

To test the hypothesis that different configurations of the ICA and PCOM arteries in relation to the location of the aneurysm can have important effects on intra-aneurysmal hemodynamics and, consequently, on aneurysm rupture, all PCOM aneurysms were classified into a set of angioarchitecture types presented in Fig 2. Aneurysms in type 3 were also classified into 2 subcategories: a) aneurysmal lesion, where the aneurysmal dilation occurs along an axis different from the PCOM axis, and b) infundibula, where the dilation is mainly aligned with the PCOM axis. The classification was done visually by inspection of volume-rendered 3D rotational angiography images by 2 independent observers, and disagreements were resolved by consensus. To verify the invisibility of the PCOM in aneurysms of type 6, the transfer function of the volume rendering was interactively varied to enhance structures of low intensity. Examples of aneurysms in each angioarchitecture type are presented in the On-line Figure.

A posteriori, to simplify the analysis and increase the statistical power, aneurysms of types 2, 5, and 8 were combined into a “bifurcation” group, whereas types 1, 3a, 4, 6, and 7 were combined into a “lateral” group. In the lateral group, the aneurysm orifice is on the ICA (or the PCOM for type 1) and away from the bifurcation, whereas in the bifurcation group, the aneurysm ostium is near the bifurcation, hence their names. Infundibula (type 3b) were not considered for further analysis.

Models

Computational fluid dynamics models of all 313 PCOM aneurysms were created by using the patient-specific vascular ge-

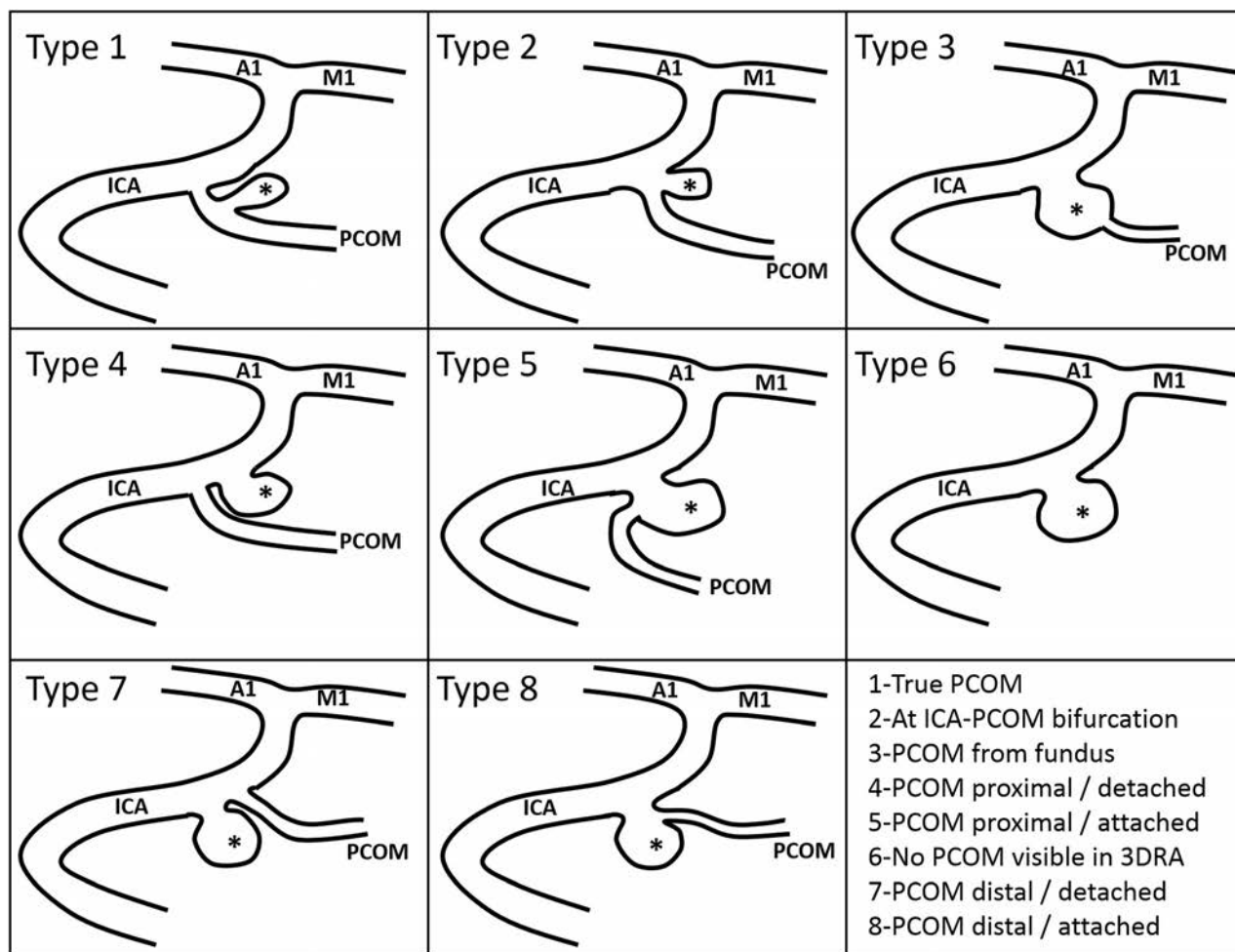


FIG 2. Angioarchitecture types of PCOM aneurysms. A1 indicates proximal segment of anterior cerebral artery; M1, proximal segment of the MCA. The aneurysm is marked with an asterisk.

ometries reconstructed from the corresponding 3D rotational angiography images.¹¹ The models were extended proximally to the cavernous segment of the ICA and distally to the M1 segment of the MCA and the A1 segment of the anterior cerebral artery. It was verified that the reconstructed geometries adequately represented the assigned aneurysm angioarchitectural class. The geometries were meshed with tetrahedral elements with a minimum resolution of 200 μm , resulting in computational grids ranging from 2–5 million elements.

Numeric simulations based on the 3D incompressible Navier-Stokes equations were carried out assuming Newtonian viscosity and neglecting vessel wall compliance. Pulsatile inflow conditions were prescribed at the inlet boundary located at the proximal ICA. A flow waveform derived from phase-contrast MR measurements at the ICA of healthy subjects¹² was scaled with the inlet cross-sectional area.¹³ The Womersley velocity profile was used to prescribe Dirichlet boundary conditions.¹⁴ Outflow boundary conditions were selected to produce flow divisions consistent with Murray's principle of minimal work to avoid unrealistic jumps in the WSS from parent to daughter arterial branches. Simulations were run for 2 cardiac cycles with a time resolution of 10 ms, and the results from the second cycle were used for analysis to discard transients associated with the initialization of the numeric calcu-

lations. All simulations were carried out in parallel on shared memory computers by using an in-house fully implicit finite element solver.¹⁵

To quantitatively characterize the intrasaccular hemodynamic environments of the aneurysms and to compare ruptured and unruptured aneurysms, a set of flow variables (listed in Table 1) defined over the aneurysm region were computed.^{16,17}

Data Analysis

The flow variables in Table 1 were used to test whether ruptured and unruptured PCOM aneurysms have different hemodynamic environments and whether different angioarchitectures are associated with different intra-aneurysmal flow characteristics. Two-sided Wilcoxon rank sum (Mann-Whitney *U*) tests were used to compare the mean values of each continuous variable between the different aneurysm groups (ruptured/unruptured or different angioarchitectures). Differences were considered statistically significant if $P < .05$ (95% confidence). The association between angioarchitecture categories and aneurysm rupture rate was tested by using contingency table analysis (Fisher test for 2×2 tables, χ^2 test for $N \times M$ tables). Statistical analysis was carried out in R software (<http://www.r-project.org/>).¹⁸

RESULTS

Angioarchitecture Associated with Rupture

The numbers of ruptured and unruptured PCOM aneurysms of each angioarchitecture are presented in Fig 3A. It can be seen that the largest proportions of ruptured aneurysms are in types 2 and 5 (bifurcation aneurysms), whereas the largest proportion of unruptured aneurysms is in type 6, where the PCOM is not visible and the aneurysm can be considered a sidewall or lateral aneurysm. Aneurysms with angioarchitectures 1, 4, 7, and 8 were quite uncommon. Angioarchitecture was associated with aneurysm rupture according to contingency table analysis using the χ^2 test ($P = .003$).

Table 1: Flow variables used to characterize different aspects of the hemodynamic environment of ruptured and unruptured PCOM aneurysms^a

Variable	Unruptured	Ruptured	P
Wall shear stress distribution characteristics			
WSSmin, dyne/cm ²	0.64 ± 1.39	0.29 ± 0.74	.002 ^b
WSSmean, dyne/cm ²	22.34 ± 20.16	24.17 ± 23.21	.59
WSSnorm	0.51 ± 0.33	0.43 ± 0.28	.02 ^b
WSSmax, dyne/cm ²	231.54 ± 172.1	341.30 ± 299.9	<.001 ^b
MWSSnorm	5.71 ± 5.05	6.10 ± 3.18	<.001 ^b
OSImax	0.261 ± 0.137	0.336 ± 0.102	<.001 ^b
OSImean	0.013 ± 0.014	0.017 ± 0.015	<.001 ^b
SCI	5.76 ± 8.50	7.04 ± 7.17	<.001 ^b
LSA	52.32 ± 31.91	59.63 ± 30.46	.05
Aneurysm inflow characteristics			
Q, cm ³ /s	0.71 ± 0.85	0.88 ± 0.99	.01 ^b
ICI	0.649 ± 0.785	0.782 ± 0.674	.02 ^b
Intra-aneurysmal flow characteristics			
Vmax, cm/s	67.89 ± 33.84	95.73 ± 59.21	<.001 ^b
VE, cm/s	9.75 ± 7.39	10.71 ± 7.67	.18
VO, 1/s	320.47 ± 274.3	323.66 ± 254.7	.57
SR, 1/s	236.26 ± 201.9	235.06 ± 182.4	.67
CORELEN, cm	1.837 ± 2.484	3.133 ± 2.982	<.001 ^b
PODENT	0.179 ± 0.140	0.206 ± 0.117	<.001 ^b

Note:—CORELEN indicates vortex core length - flow complexity; ICI, inflow concentration index; LSA, low shear area (% of aneurysm sac); MWSSnorm, maximum normalized WSS; OSImax, maximum oscillatory shear index; OSImean, mean oscillatory shear index; PODENT, proper orthogonal decomposition entropy—flow stability; Q, aneurysm inflow rate; SCI, shear concentration index; SR, mean aneurysm shear rate; VE, mean aneurysm velocity; Vmax, maximum aneurysm velocity; VO, mean aneurysm vorticity; WSSmax, maximum WSS; WSSmean, average WSS; WSSmin, minimum WSS; WSSnorm, normalized WSS.

^a Values given are mean ± standard deviation, and *P* values correspond to the Mann-Whitney *U* test.

^b Statistically significant association.

The distributions of ruptured and unruptured aneurysms in the combined bifurcation and lateral angioarchitecture groups are presented in Fig 3B. Fig 3B shows that the bifurcation group has a larger rupture rate than the lateral group (54.6% versus 36.4%). This association is statistically significant according to the Fisher exact test for the 2 × 2 contingency table ($P = .004$).

Hemodynamic Characteristics Associated with Rupture

Results of the association between hemodynamic variables and aneurysm rupture are presented in Table 1. Irrespective of angioarchitecture, compared with unruptured aneurysms, ruptured PCOM aneurysms had larger maximum WSS ($P < .001$; normalized maximum WSS, $P < .001$), more concentrated WSS distributions (shear concentration index, $P < .001$), more oscillatory WSS (maximum oscillatory shear index, $P < .001$; mean oscillatory shear index, $P < .001$), larger inflow rates (represented as *Q*, $P = .01$) and maximum velocity ($P < .001$), more concentrated inflow jets (inflow concentration index, $P < .001$), more complex flows (vortex core length, $P < .001$), and more unstable flow patterns (proper orthogonal decomposition entropy, $P < .001$). Interestingly, ruptured aneurysms also had lower normalized mean WSS ($P = .02$) and minimum WSS ($P = .002$) than unruptured aneurysms.

Hemodynamic Characteristics Associated with Angioarchitectures

Results of the association between hemodynamic variables and rupture of aneurysms of different angioarchitectures are summarized in Table 2. Table 2 indicates which hemodynamic variables were

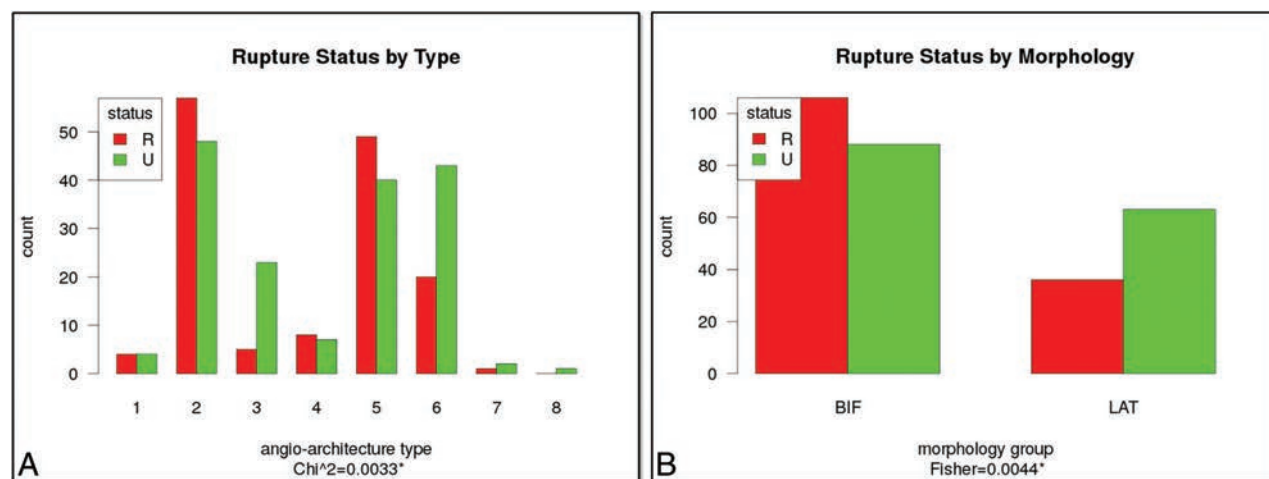


FIG 3. A, Number of ruptured and unruptured PCOM aneurysms in each angioarchitecture type, and B, number of ruptured and unruptured PCOM aneurysms in “bifurcation” (types 2, 5, and 8 combined) and “lateral” (types 1, 3, 4, 6, and 7 combined) angioarchitectures. BIF indicates bifurcation; LAT, lateral.

Table 2: Summary of univariate statistical tests comparing the means between ruptured and unruptured aneurysms considering all aneurysms, subdividing by angioarchitecture types 1–8, and combining angioarchitectures into “bifurcation” and “lateral” configurations^a

Variable	All	Angioarchitecture Type								Combined Angioarchitectures		
		1	2	3	4	5	6	7	8	BIF	LAT	BIF vs LAT
WSSmin	U						U					L
WSSmean												
WSSnorm	U										U	
WSSmax	R		R				R			R	R	
MWSSnorm	R									R		B
OSImax	R						R			R	R	B
OSImean	R						R				R	B
SCI	R						R					B
LSA												
Q	R											B
ICI	R									R		B
Vmax	R		R			R	R			R	R	
VE												
VO												
SR												
CORELEN	R		R			R	R			R	R	B
PODENT	R						R					B

Note:—BIF indicates bifurcation; CORELEN, vortex core length - flow complexity; ICI, inflow concentration index; LAT, lateral; LSA, low shear area (% of aneurysm sac); MWSSnorm, maximum normalized WSS; OSImax, maximum oscillatory shear index; OSImean, mean oscillatory shear index; PODENT, proper orthogonal decomposition entropy—flow stability; Q, aneurysm inflow rate; SCI, shear concentration index; SR, mean aneurysm shear rate; VE, mean aneurysm velocity; Vmax, maximum aneurysm velocity; VO, mean aneurysm vorticity; WSSmax, maximum WSS; WSSmean, average WSS; WSSmin, minimum WSS; WSSnorm, normalized WSS.

^aR indicates mean value significantly larger ($P < 0.05$) in ruptured compared with unruptured aneurysms. U indicates mean value significantly larger ($P < 0.05$) in unruptured compared with ruptured aneurysms. B indicates mean value significantly larger ($P < 0.05$) in BIF compared with LAT aneurysms. L indicates mean value significantly larger ($P < 0.05$) in LAT compared with BIF aneurysms. Empty cells indicate no statistically significant difference.

significantly different between ruptured and unruptured aneurysms of each angioarchitecture type and whether the value was larger in the ruptured or unruptured group or between the combined bifurcation and lateral groups. In general, bifurcation aneurysms had larger maximum normalized WSS ($P < .001$), lower minimum WSS ($P = .001$), more oscillatory WSS ($P = .0033$; mean oscillatory WSS, $P = .01$), more concentrated WSS (shear concentration index, $P < .001$), larger and more concentrated inflow jet (Q, $P = .001$; inflow concentration index, $P < .001$), and more complex and unstable flows (vortex core length, $P = .003$; proper orthogonal decomposition entropy, $P = .01$) than lateral aneurysms.

DISCUSSION

Aneurysm evolution is thought to be governed by the progressive degradation of the wall in response to abnormal hemodynamic and biomechanical stimuli.¹⁹ Previous studies of aneurysms in other locations have found angioarchitectural differences between ruptured and unruptured aneurysms. In basilar tip aneurysms, bifurcation angles between the basilar and posterior cerebral arteries and the diameters of the posterior cerebral arteries were different between ruptured and unruptured aneurysms.²⁰ In aneurysms at the MCA bifurcation²¹ and the anterior communicating complex,²² neck location, flow deviation, and relation of neck/daughter artery were different between ruptured and unruptured aneurysms. Therefore, it is logical to ask whether different angioarchitectures could be associated with different hemodynamic conditions that in turn could predispose the aneurysm to rupture or stabilization.

Our current study found that ruptured PCOM aneurysms had distinct hemodynamic environments compared with unruptured

aneurysms. Specifically, the hemodynamics in ruptured aneurysms were characterized by concentrated elevations of WSS, oscillatory WSS, stronger and more concentrated inflow jets, and more complex and unstable flow patterns than in unruptured aneurysms. Similar trends were observed when subdividing by angioarchitectural types, though in some types, the trends did not reach statistical significance, likely because of small sample sizes. This suggests that hemodynamic environments with these characteristics may be more harmful to the wall, thus increasing the likelihood of rupture. This reasoning is supported by previous studies that found similar hemodynamic characteristics associated with weakened aneurysm walls²³ as well as inflammation and other histologic changes of the wall.²⁴

Interestingly, ruptured aneurysms also had lower normalized WSS and minimum WSS than unruptured aneurysms. Therefore, our results are in agreement with previous studies that pointed to “high WSS” mechanisms as responsible for aneurysm rupture²⁵ as well as with studies that proposed “low WSS” mechanisms.^{10,26,27} This finding suggests that previous results may not be conflicting or contradictory, but rather that the different metrics used in different studies characterize different aspects of the adverse flow environment. Both abnormally high and low WSS have been associated with processes that could degrade the aneurysm wall.²⁸ Our study suggests that aneurysms with high local flow conditions (eg, high maximum WSS, high velocity, and complex and unstable flows) as well as low local flow conditions (eg, low normalized WSS and low minimum WSS) may be more likely to rupture.

Further, the current study showed that the proposed angioarchitecture types are associated with aneurysm rupture. In par-

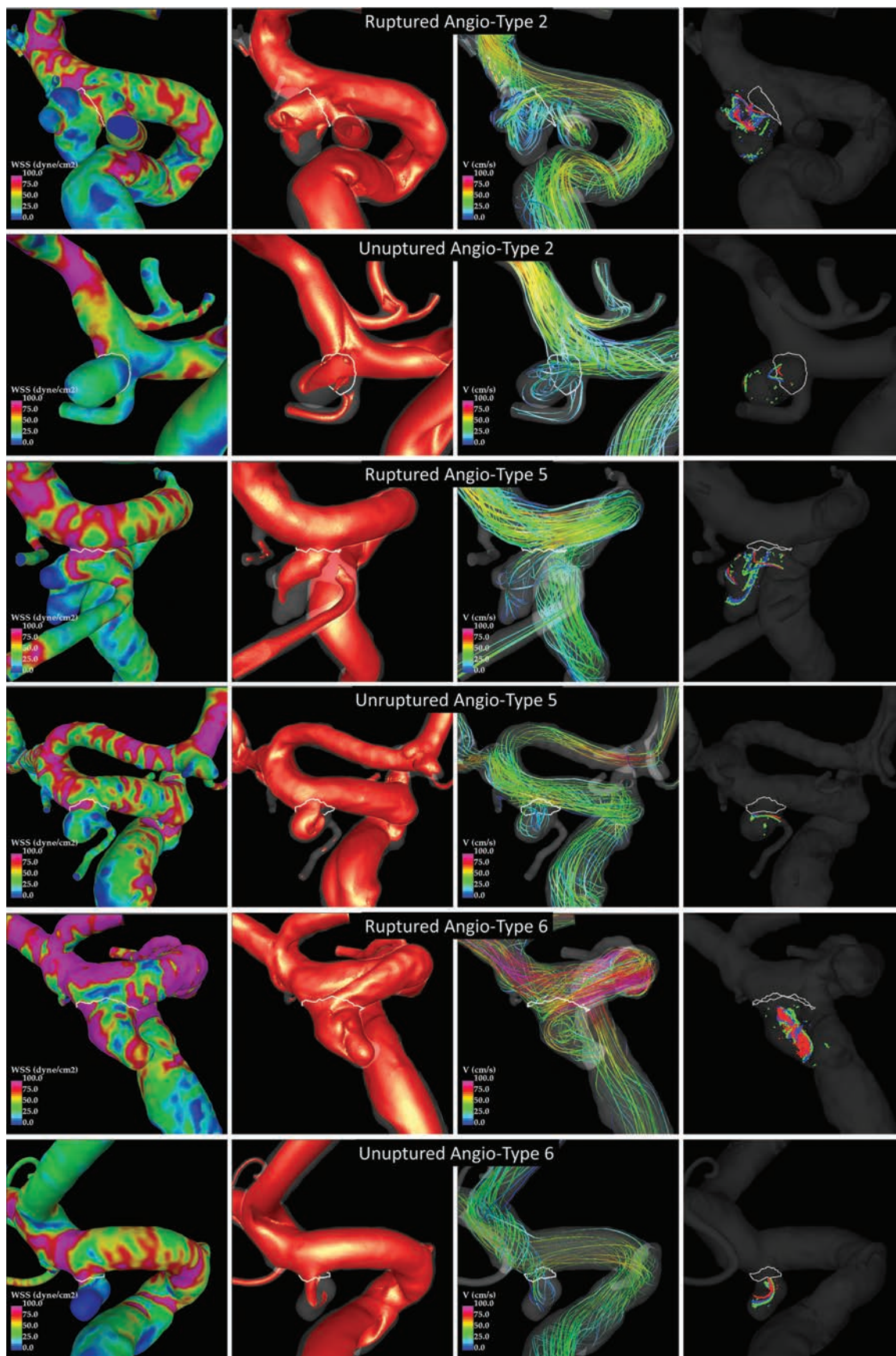


FIG 4. Examples of ruptured and unruptured aneurysms in the most common angioarchitecture classes (types 2, 5, and 6). Columns show, from left to right, respectively: WSS magnitude, inflow jet, flow pattern at peak systole, and vortex cores at 3 instants of the cardiac cycle.

ticular, bifurcation-type aneurysms had significantly higher rupture rates than aneurysms that behave as lateral aneurysms. Furthermore, aneurysms in the bifurcation group had hemodynamic environments characterized by concentrated elevations of WSS, oscillatory WSS, larger and more concentrated inflow jets, and more complex and unstable flow patterns. This suggests that bifurcation angioarchitectures are more likely to generate these adverse intra-aneurysmal hemodynamic conditions that predispose the aneurysms to rupture.

It is conceivable that compared with more lateral or sidewall aneurysm configurations, bifurcation aneurysms are more likely to have stronger inflow jets directed toward the aneurysm fundus that create localized regions of concentrated WSS and spread into complex and unstable flow patterns. To illustrate this point, examples of ruptured and unruptured aneurysms of angioarchitecture types 2, 5, and 6 are presented in Fig 4.

Although the current sample was large enough to obtain statistically significant differences, some limitations in this study should be considered, and the results should be confirmed with data from other populations as well as with longitudinal data. The current study purposely focused only on PCOM aneurysms to eliminate confusion related to aneurysm location. However, the proposed angioarchitecture classification and corresponding hemodynamic analysis could be directly evaluated with aneurysms at other locations, such as the anterior choroidal artery, or extended to other locations, such as the MCA bifurcation or the superior cerebellar artery. The study was performed on a set from a data base of consecutive aneurysms that had undergone angiography and/or embolization over a 10-year period. Selection bias related to referral patterns and indications for treatment may have led to the exclusion of important aneurysms subsets. In addition, a number of assumptions and approximations were made during the modeling process, including the approximations of the vascular geometry, the inflow conditions, the Newtonian rheology, and the rigid walls assumption.

CONCLUSIONS

High-flow intrasaccular hemodynamic characteristics are associated with PCOM aneurysm rupture. High-flow characteristics include strong and concentrated inflow jets, concentrated regions of elevated WSS, oscillatory WSS, and complex and unstable flow patterns. These adverse conditions are more commonly found in aneurysms with bifurcation-type angioarchitectures in contrast to aneurysms that have a hemodynamic behavior similar to sidewall aneurysms. Angioarchitecture and hemodynamic characteristics associated with rupture are useful to further understand the underlying mechanisms of aneurysm evolution and rupture and could potentially be used to refine the clinical evaluation of PCOM aneurysms and plan more specific and personalized therapeutic strategies.

Disclosures: Ravi Daddasomayajula—RELATED: Grants/Grants Pending: National Institutes of Health, Comments: research grant as mentioned in the manuscript*. Fernando Mut—RELATED: Grants/Grants Pending: National Institutes of Health*. Waleed Brinjikji—UNRELATED: Other: Marblehead Medical LLC, Comments: CEO of Marblehead Medical. David F. Kallmes—UNRELATED: Consultancy: Medtronic, Comments: steering committee participation*; Grants/Grants Pending: Microvention, Sequent Medical, NeuroSigma, Medtronic, Comments: preclinical research and clinical trials*. Christopher Putman—UNRELATED: Payment for Lectures (including

service on Speakers Bureaus): Penumbra. Juan R. Cebral—RELATED: Grants/Grants Pending: National Institutes of Health, Comments: research grant*; UNRELATED: Grants/Grants Pending: National Institutes of Health, Comments: research grants*. *Money paid to the institution.

REFERENCES

- Kassell NF, Torner JC, Haley EC Jr, et al. **The International Cooperative Study on the Timing of Aneurysm Surgery. Part 1: overall management results.** *J Neurosurg* 1990;73:18–36 CrossRef Medline
- Nishioka H, Torner JC, Graf CJ, et al. **Cooperative study of intracranial aneurysms and subarachnoid hemorrhage: a long-term prognostic study. II. Ruptured intracranial aneurysms managed conservatively.** *Arch Neurol* 1984;41:1142–46 CrossRef Medline
- White PM, Wardlaw JM. **Unruptured intracranial aneurysms.** *J Neuroradiol* 2003;30:336–50 Medline
- Greving JP, Wermer MJ, Brown RD Jr, et al. **Development of the PHASES score for prediction of risk of rupture of intracranial aneurysms: a pooled analysis of six prospective cohort studies.** *Lancet Neurol* 2014;13:59–66 CrossRef Medline
- Weir B. **Unruptured intracranial aneurysms: a review.** *J Neurosurg* 2002;96:3–42 CrossRef Medline
- Golshani K, Ferrell A, Zomorodi A, et al. **A review of the management of posterior communicating artery aneurysms in the modern era.** *Surg Neurol Int* 2010;1:88 CrossRef Medline
- Cebral JR, Raschi M. **Suggested connections between risk factors of intracranial aneurysms: a review.** *Ann Biomed Eng* 2013;41:1366–83 CrossRef Medline
- Weir B, Disney L, Karrison T. **Sizes of ruptured and unruptured aneurysms in relation to their sites and the ages of patients.** *J Neurosurg* 2002;96:64–70 CrossRef Medline
- Songsang D, Geibprasert S, Willinsky R, et al. **Impact of anatomical variations of the circle of Willis on the incidence of aneurysms and their recurrence rate following endovascular treatment.** *Clin Radiol* 2010;65:895–901 CrossRef Medline
- Lu N, Wang C, Karmonik C, et al. **Morphological and hemodynamic discriminators for rupture status in posterior communicating artery aneurysms.** *PLoS One* 2016;11:e0149906 CrossRef Medline
- Cebral JR, Castro MA, Appanaboyina S, et al. **Efficient pipeline for image-based patient-specific analysis of cerebral aneurysm hemodynamics: technique and sensitivity.** *IEEE Trans Med Imaging* 2005;24:457–67 CrossRef Medline
- Ford MD, Alperin N, Lee SH, et al. **Characterization of volumetric flow rate waveforms in the normal internal carotid and vertebral arteries.** *Physiol Meas* 2005;26:477–88 CrossRef Medline
- Cebral JR, Castro MA, Putman CM, et al. **Flow-area relationship in internal carotid and vertebral arteries.** *Physiol Meas* 2008;29:585–94 CrossRef Medline
- Taylor CA, Hughes TJR, Zarins CK. **Finite element modeling of blood flow in arteries.** *Comp Meth App Mech Eng* 1998;158:155–96 CrossRef
- Mut F, Aubry R, Löhner R, et al. **Fast numerical solutions of patient-specific blood flows in 3D arterial systems.** *Int J Numer Method Biomed Eng* 2010;26:73–85 CrossRef Medline
- Mut F, Löhner R, Chien A, et al. **Computational hemodynamics framework for the analysis of cerebral aneurysms.** *Int J Numer Method Biomed Eng* 2011;27:822–39 CrossRef Medline
- Byrne G, Mut F, Cebral JR. **Quantifying the large-scale hemodynamics of intracranial aneurysms.** *AJNR Am J Neuroradiol* 2014;35:333–38 CrossRef Medline
- R Development Core Team. *R: A Language and Environment for Statistical Computing.* Vienna, Austria: R Foundation for Statistical Computing; 2016
- Sforza DM, Putman CM, Cebral JR. **Hemodynamics of cerebral aneurysms.** *Annu Rev Fluid Mech* 2009;41:91–107 CrossRef Medline
- Ambekar S, Madhugiri V, Bollam P, et al. **Morphological differences between ruptured and unruptured basilar bifurcation aneurysms.** *J Neurol Surg B Skull Base* 2013;74:91–96 CrossRef Medline
- Sadatomo T, Yuki K, Migita K, et al. **Morphological differences between**

- ruptured and unruptured cases in middle cerebral artery aneurysms. *Neurosurgery* 2008;62:602–09; discussion 602–09 [CrossRef Medline](#)
22. Sadatomo T, Yuki K, Migita K, et al. **The characteristics of the anterior communicating artery aneurysm complex by three-dimensional digital subtraction angiography.** *Neurosurg Rev* 2006;29:201–07 [CrossRef Medline](#)
 23. Cebral JR, Duan X, Chung BJ, et al. **Wall mechanical properties and hemodynamics of unruptured intracranial aneurysms.** *AJNR Am J Neuroradiol* 2015;36:1695–703 [CrossRef Medline](#)
 24. Cebral J, Ollikainen E, Chung BJ, et al. **Flow conditions in the intracranial aneurysm lumen are associated with inflammation and degenerative changes of the aneurysm wall.** *AJNR Am J Neuroradiol* 2017;38:119–26 [CrossRef Medline](#)
 25. Cebral JR, Mut F, Weir J, et al. **Quantitative characterization of the hemodynamic environment in ruptured and unruptured brain aneurysms.** *AJNR Am J Neuroradiol* 2011;32:145–51 [CrossRef Medline](#)
 26. Xiang J, Natarajan SK, Tremmel M, et al. **Hemodynamic-morphologic discriminants for intracranial aneurysm rupture.** *Stroke* 2011;42:144–52 [CrossRef Medline](#)
 27. Zhang Y, Jing L, Liu J, et al. **Clinical, morphological, and hemodynamic independent characteristic factors for rupture of posterior communicating artery aneurysms.** *J Neurointerv Surg* 2016;8:808–12 [CrossRef Medline](#)
 28. Meng H, Tutino VM, Xiang J, et al. **High WSS or low WSS? Complex interactions of hemodynamics with intracranial aneurysm initiation, growth, and rupture: toward a unifying hypothesis.** *AJNR Am J Neuroradiol* 2014;35:1254–62 [CrossRef Medline](#)

Patient Outcomes and Cerebral Infarction after Ruptured Anterior Communicating Artery Aneurysm Treatment

J.J. Heit, R.L. Ball, N.A. Telischak, H.M. Do, R.L. Dodd, G.K. Steinberg, S.D. Chang, M. Wintermark, and M.P. Marks



ABSTRACT

BACKGROUND AND PURPOSE: Anterior communicating artery aneurysm rupture and treatment is associated with high rates of dependency, which are more severe after clipping compared with coiling. To determine whether ischemic injury might account for these differences, we characterized cerebral infarction burden, infarction patterns, and patient outcomes after surgical or endovascular treatment of ruptured anterior communicating artery aneurysms.

MATERIALS AND METHODS: We performed a retrospective cohort study of consecutive patients with ruptured anterior communicating artery aneurysms. Patient data and neuroimaging studies were reviewed. A propensity score for outcome measures was calculated to account for the nonrandom assignment to treatment. Primary outcome was the frequency of frontal lobe and striatum ischemic injury. Secondary outcomes were patient mortality and clinical outcome at discharge and at 3 months.

RESULTS: Coiled patients were older (median, 55 versus 50 years; $P = .03$), presented with a worse clinical status (60% with Hunt and Hess Score >2 versus 34% in clipped patients; $P = .02$), had a higher modified Fisher grade ($P = .01$), and were more likely to present with intraventricular hemorrhage (78% versus 56%; $P = .03$). Ischemic frontal lobe infarction (OR, 2.9; 95% CI, 1.1–8.4; $P = .03$) and recurrent artery of Heubner infarction (OR, 20.9; 95% CI, 3.5–403.7; $P < .001$) were more common in clipped patients. Clipped patients were more likely to be functionally dependent at discharge (OR, 3.2; $P = .05$) compared with coiled patients. Mortality and clinical outcome at 3 months were similar between coiled and clipped patients.

CONCLUSIONS: Frontal lobe and recurrent artery of Heubner infarctions are more common after surgical clipping of ruptured anterior communicating artery aneurysms, and are associated with poorer clinical outcomes at discharge.

ABBREVIATIONS: AcomA = anterior communicating artery aneurysm; RAH = recurrent artery of Heubner; HHS = Hunt and Hess Scale

Subarachnoid hemorrhage secondary to rupture of a cerebral aneurysm affects 30,000 people in the United States every year and results in significant morbidity and mortality.¹ Clinical outcomes after aneurysm rupture and treatment are influenced by cumulative cerebral infarction burden.^{2,3} Furthermore, patients who recover from aneurysm rupture are often left with disabling cognitive deficits that may result in the patient's dependency on others, which is reflected by higher mRS scores.^{4,5} The severity of

these cognitive deficits has been correlated to the Hunt and Hess Scale (HHS) grade on admission, older age, aneurysm location, and treatment-related brain injury.^{6–8}


Anterior communicating artery aneurysms (AcomAs) are among the most commonly identified ruptured aneurysms,^{9,10} and AcomA rupture and treatment are more strongly associated with cognitive and behavioral deficits relative to other aneurysm locations.^{5,11–14} The cause of these neuropsychiatric deficits remains uncertain, but prior studies have suggested ischemic injury to the frontal cortex, ventromedial prefrontal (orbitofrontal) cortex, or striatum as a possible etiology.^{15–17}


Ruptured aneurysms may be successfully treated by microsurgical clipping or endovascular coil embolization.^{5,9,18} However, surgical clipping of AcomAs has been associated with more severe cognitive and behavioral deficits and higher rates of patient dependency compared with endovascular coil embolization, which may be caused by retraction injury to the frontal lobe or other causes of cerebral infarction.^{2,5,11,13,14,17,19}

Received March 28, 2017; accepted after revision June 16.

From the Department of Radiology, Neuroimaging and Neurointervention Division (J.J.H., N.A.T., H.M.D., M.W., M.P.M.), Department of Medicine, Quantitative Sciences Unit (R.L.B.), and Department of Neurosurgery (R.L.D., G.K.S., S.D.C.), Stanford University School of Medicine, Stanford, California.

Please address correspondence to Jeremy J. Heit, MD, PhD, 300 Pasteur Dr, Room S-047, Stanford, CA 94305; e-mail: jheit@stanford.edu; @JeremyHeitMDPHD

 Indicates article with supplemental on-line table.

 Indicates article with supplemental on-line photos.

<http://dx.doi.org/10.3174/ajnr.A5355>

Our primary aim was to determine whether there is an increase in frontal lobe or striatum ischemic injury after treatment with surgical clipping compared with coil embolization in patients with ruptured AcomA. Our secondary outcomes were patient mortality and clinical outcome at discharge and at 3 months of follow-up. We therefore characterized patterns of cerebral ischemic injury and patient outcomes after treatment of ruptured AcomA at our neurovascular referral center.

MATERIALS AND METHODS

Patient Information

The study was approved by our institutional review board and complied with the Health Insurance Portability and Accountability Act. We retrospectively reviewed our radiology data base and medical records to identify consecutive patients who presented with SAH caused by AcomA rupture between January 2010 and December 2014. The patient flow in this study is summarized in On-line Fig 1. Patient demographic, treatment, and outcome data were determined by electronic medical record review. A good clinical outcome was defined as an mRS score of 2 or less, and mRS scores were documented in the electronic medical record.

Image Acquisition and Analysis

Head NCCT and CTA were performed in all patients with standard protocols by using a 64-section helical CT scanner (Light-Speed; GE Healthcare, Milwaukee, Wisconsin). Axial NCCT images were obtained with 120 kVp, 170 mA, and 5-mm section thickness reconstruction. MR imaging and MRA were performed in 49 patients on a 1.5T or 3T scanner (Signa; GE Healthcare) by using standard departmental and vendor protocols. DSA was performed in all patients in a biplane neuroangiography suite (Axium Artis; Siemens, Erlangen, Germany). Selective angiography of the bilateral internal carotid arteries and at least 1 vertebral artery was performed. AcomA coiling was performed after femoral artery access with general anesthesia and neurophysiologic monitoring. DSA was not performed before treatment technique decisions in all patients, and treatment decisions were at the discretion of the admitting neurosurgeon.

All CT, MR imaging, and DSA images were independently reviewed in a blinded manner by 3 interventional neuroradiologists with 2, 3, and 30 years of experience. Aneurysm size was determined by 3D rotational angiography when available or by CTA with 3D reformations. Follow-up studies were performed at various time points after endovascular or surgical treatment of the ruptured AcomA and ranged from postoperative day 0–159, with 80% performed within 2 days and 95% performed within 5 days. If follow-up head imaging was not performed because of an excellent clinical status (no symptoms other than a mild headache), the patient was excluded from the subsequent imaging analysis. The presence of SAH, intraparenchymal hemorrhage, and intraventricular hemorrhage was noted on each study. Cerebral infarction was defined as new hypoattenuation on CT, restricted diffusion on MR imaging, or confluent T2 signal abnormality on MR imaging performed after treatment. Cerebral infarction secondary to vasospasm was defined as new hypoattenuation on CT, restricted diffusion on MR imaging, or confluent T2 signal abnormality on MR imaging on subsequent studies when severe vaso-

spasm was identified on an accompanying CTA, MRA, or DSA. Cerebral infarction was considered to be within the recurrent artery of Heubner (RAH) vascular territory if the infarction involved the caudate head with possible extension into the ipsilateral anterior limb of the internal capsule and/or medial lentiform nucleus. Other areas of cerebral infarction were also recorded.

Outcomes

The primary outcome was the frequency of frontal lobe and striatum ischemic infarction before discharge. Patients who did not receive imaging were not included in the primary analysis, but a sensitivity analysis was completed that included these patients (see “Statistical Analysis” section for details). Secondary outcome measures included patient mortality, clinical outcome at discharge, and clinical outcome at 3 months.

Statistical Analysis

Differences in patient demographics, clinical presentation, and aneurysm characteristics between the clipped and coiled groups were assessed with either the 2-sided Wilcoxon rank sum test for continuous characteristics or the 2-sided Fisher exact test for categorical characteristics; significance was assessed at the .05 level. To account for the nonrandom assignment to treatment, propensity scores were calculated with a multivariable logistic regression model with treatment as the response, and explanatory variables included demographic and other characteristics at presentation that were significantly different between treatment groups.²⁰

Differences between treatments in primary and secondary outcomes were tested with the likelihood ratio test, where the restricted model included only the intercept and propensity score and the full model included the intercept, propensity score, and treatment; significance was assessed at the .05 level. Odds ratios were calculated as the odds of the outcome when clipping was applied divided by the odds of the outcome when coiling was applied after correcting for the nonrandom assignment to treatment by the propensity score. Analyses on outcomes were completed on data where the outcome was known, and if outcomes were missing, the number of missing values was noted. Because imaging to evaluate possible infarction was not performed on patients who had excellent clinical status, we completed a sensitivity analysis on the primary outcome of infarction that assumed patients with no imaging had not experienced an infarction. All analyses were completed in the statistical software R (<http://www.r-project.org/>).²¹

RESULTS

A total of 100 consecutive patients with ruptured AcomAs were identified, which coincidentally included 50 patients treated by microsurgical clipping (“clipped” patients) and 50 patients treated by coil embolization (“coiled” patients). Coiled patients were older (median age, 55 years compared with 50 years in the clipped group; $P = .03$), but there were no other significant differences with respect to sex, hypertension, hyperlipidemia, diabetes, coronary artery disease, smoking, illicit drug use, alcohol abuse, or a family history of aneurysms (Table 1). Clipped pa-

Table 1: Patient demographic and presentation information

	Clip	Coil	P Value
No. of patients	50	50	
Median age (IQR), yr	50 (41.00–58.00)	55 (48.00–63.75)	.03
Female sex, no. (%)	26 (52)	31 (62)	.42
Hunt and Hess score, no. (%)			.01
1	6 (12)	2 (4)	
2	27 (54)	18 (36)	
3	14 (28)	16 (32)	
4	3 (6)	14 (28)	
Hypertension, no. (%)	31 (62)	28 (56)	.69
Diabetes mellitus, no. (%)	7 (14)	5 (10)	.76
Hyperlipidemia, no. (%)	12 (24)	16 (32)	.50
Coronary artery disease, no. (%)	3 (6)	5 (10)	.72
Smoking status, no. (%)			.73
Never	28 (56)	31 (62)	
Current	19 (38)	15 (30)	
Prior	3 (6)	4 (8)	
Drug use, no. (%)	5 (10)	5 (10)	1
Alcohol use, no. (%)	4 (8)	2 (4)	.68
Family history of aneurysm, no. (%)	3 (6)	4 (8)	1

Note:—IQR indicates interquartile range.

Table 2: Patient neuroimaging evaluation at presentation

	Clip	Coil	P Value
No. of patients	50	50	
Modified Fisher score, no. (%)			.01
0	1 (2)	0 (0)	
1	2 (4)	0 (0)	
2	6 (12)	4 (8)	
3	29 (58)	19 (38)	
4	12 (24)	27 (54)	
IVH, no. (%)	28 (56)	39 (78)	.03
Frontal lobe IPH, no. (%)	9 (18)	10 (20)	1
Ischemic frontal lobe infarction, no. (%)	0 (0)	1 (2.0)	.50
Median aneurysm size (IQR), mm	5.50 (4.40–7.07)	6.05 (4.03–7.83)	.29
Median aneurysm neck size (IQR), mm	2.50 (2.00–3.00)	3.00 (2.30–4.00)	.02
Median aneurysm ratio (IQR)	2.10 (1.50–2.70)	2.00 (1.70–2.30)	.29

Note:—IPH indicates intraparenchymal hemorrhage; IQR, interquartile range; IVH, intraventricular hemorrhage.

tients presented with a more favorable clinical status as determined by the HHS ($P = .01$).

Head CT upon presentation demonstrated higher modified Fisher grades in patients who subsequently underwent coiling ($P = .01$; Table 2). Intraventricular hemorrhage was present in 67% of all patients and was present more frequently in coiled patients compared with clipped patients (39 patients [78%] versus 28 patients [56%]; $P = .03$). Intraparenchymal hemorrhage was identified on presentation in 19 patients (19%), and there was no difference ($P = 1$) in the frequency of intraparenchymal hemorrhage between those who were clipped (9 patients [18%]) and coiled (10 patients [20%]). A single patient who underwent coil embolization presented with an ischemic infarction in the left superior frontal gyrus, which was secondary to severe anterior cerebral artery vasospasm identified at the time of presentation. No other areas of ischemic infarction were identified on presentation head CT studies or imaging studies obtained before aneurysm treatment. These data are summarized in Table 2.

There was no significant difference in median maximal aneurysm diameter between clipped (5.5 mm) and coiled (6.1 mm) patients ($P = .29$). Aneurysms treated by coiling had a larger median neck diameter of 3.0 mm compared with 2.5 mm in clipped patients ($P = .02$). However, there was no difference in

the median size-to-neck ratio between clipped (2.1) and coiled (2.0) patients ($P = .29$). These data are summarized in Table 2.

For the outcomes analysis, we calculated propensity scores (On-line Fig 2) for all patients by using a logistic regression model with probability of coiling as the response and covariates that included demographic and other characteristics at presentation that were significantly different between the treatment groups. The covariates analyzed included patient age, the HHS, modified Fisher grade, and intraventricular hemorrhage at presentation and aneurysm neck size.

Symptomatic vasospasm requiring endovascular treatment with intra-arterial nicardipine infusion and/or cerebral arterial angioplasty occurred in 25 patients (12 clipped and 13 coiled). After accounting for the propensity score, there was no significant difference ($P = .36$) between treatments in patients requiring endovascular treatment of vasospasm. However, clipped patients (9 of 12 compared with 3 of 13 coiled patients) were more likely to require angioplasty for treatment of severe vasospasm (OR, 17.8; 95% CI, 1.4–819.7; $P = .03$). In a separate logistic regression analysis, endovascular vasospasm treatment was highly predictive of mortality

(OR, 5.6; 95% CI, 1.5–23.9; $P = .01$). All patients who required vasospasm treatment and survived (19 of 25 patients) were dependent (mRS > 2) at discharge ($P = .001$). Seven (of 19) patients who underwent vasospasm treatment improved by 3 months and were independent (mRS ≤ 2), but vasospasm remained highly predictive of a poor outcome (mRS > 2) at 3-months (OR, 4.4; 95% CI, 1.5–13.3; $P = .005$).

Follow-up head CT or MR imaging was performed after AcomA clipping or coiling in 94 patients (94%), including 46 clipped patients (92%) and 48 coiled patients (96%). Follow-up MR imaging was performed in 22 clipped patients (48%) and 27 coiled patients (56%). The 6 patients in whom follow-up imaging was not obtained each had an excellent clinical status and were symptom-free after treatment. On follow-up imaging, intraparenchymal hemorrhage was present in 12 of 46 clipped patients (26%, compared with 9 patients on presentation imaging) and 11 of 48 coiled patients (23%, compared with 10 patients on presentation imaging), but these differences were not significant ($P = .06$). This increased frequency of intraparenchymal hemorrhage was caused by hemorrhage related to extraventricular drain placement, aneurysm rerupture before treatment, or intraprocedural rupture during surgical clipping or endovascular coil embolization. These results are summarized in Table 3.

Table 3: Patient neuroimaging evaluation after aneurysm treatment

	Clip	Coil	OR (95% CI)	P Value
No. of patients	50	50		
Patients without FU imaging, no. (%)	4 (8)	2 (4)		
Frontal lobe IPH after treatment, no. (%) ^a	12 (26.1)	11 (22.9)	3.0 (1.0–10.1)	.06
Nonvasospasm ischemic frontal lobe infarction, no. (%) ^a	12 (26.1)	2 (4.2)	8.5 (1.9–62.3)	.004
Artery of Heubner infarction after treatment, no. (%) ^a	15 (32.6)	1 (2.1)	20.9 (3.5–403.7)	<.001
Embolic infarction after treatment, no. (%) ^a	4 (8.7)	12 (25)	0.3 (0.1–1.1)	.07
Vasospasm-related ischemic infarction, no. (%) ^a	7 (15.2)	8 (16.7)	0.9 (0.3–3.1)	.85
Any ischemic infarction after treatment, no. (%) ^a	33 (71.7)	24 (50)	4.1 (1.5–12.4)	.005

Note:—FU indicates follow-up; IPH, intraparenchymal hemorrhage.

^a Percentages refer to the number of patients with non-missing values (46 clip and 48 coil). P values are from the likelihood ratio test using propensity scores and odds ratios, and resulting 95% CIs are derived from the logistic model that includes both treatment and propensity scores (see “Materials and Methods” section).

Clipped patients had greater odds of experiencing any ischemic cerebral infarction when all types of infarction were considered (OR, 4.1; 95% CI, 1.5–12.4; $P = .005$). RAH territory ischemic infarction was more likely in clipped patients compared with coiled patients (OR, 20.9; 95% CI, 3.5–403.7; $P < .001$) (Fig 1, Table 3). Clipped patients also had greater odds of ischemic frontal lobe infarction (OR, 8.5; 95% CI, 1.9–62.3; $P = .004$). There was a trend toward more frequent punctuate emboli infarctions in coiled patients, but this difference was not significant (OR, 0.3; 95% CI, 0.1–1.1; $P = .07$). A sensitivity analysis that treated missing imaging as indicative of no infarction did not alter these conclusions except that intraparenchymal hemorrhage on follow-up was significantly associated with clipping (OR, 3.1; 95% CI, 1.0–10.7; $P = .05$; On-line Table). To be thorough, we considered a less likely scenario and treated missing imaging as indicative of an infarction, but even this unlikely scenario did not alter the conclusions (On-line Table). There was no difference in the frequency of confluent arterial territorial infarction secondary to known vasospasm between clipped and coiled groups. These results are summarized in Table 3.

Secondary patient outcomes were mortality and, for those who survived to discharge, mRS at discharge and at 3 months (Table 4). There were 10 deaths before discharge, including 3 clipped patients (6%) and 7 coiled patients (14%), and no additional deaths occurred by 3 months. There was no difference in mortality between clipped and coiled patients (OR, 0.5; 95% CI, 0.1–2.0; $P = .31$).

Among all patients at discharge, there were 13 coiled patients and 13 clipped patients with an mRS ≤ 2 . When the propensity score was applied to a logistic regression model including all patients, there was no significant difference between the outcomes of clipped and coiled patients (OR, 3.0; 95% CI, 1.0–10.1; $P = .06$). However, when we considered only patients who survived to discharge, we found that clipped patients were more likely to have a worse clinical outcome (mRS > 2) at discharge compared with coiled patients (OR, 3.4; 95% CI, 1.2–12.3; $P = .04$).

At 3-month follow-up, no additional deaths had occurred, and 16 patients (8 coiled, 8 clipped) were lost to follow-up, which left 74 patients (35 coiled and 39 clipped) for analysis (On-line Fig 1). Of these patients, 28 coiled patients (80%) and 30 clipped patients (77%) had a good clinical outcome (mRS ≤ 2). After baseline differences were accounted for by using a propensity score, we did not find any significant association between treatment choice and 3-month outcomes (OR, 2.1; 95% CI, 0.6–8.0; $P = .24$).

DISCUSSION

Cerebral infarction is common after cerebral aneurysm rupture,^{22,23} and prior studies have correlated the cumulative burden of cerebral infarction to poor clinical outcome and cognitive outcomes.^{2,3} In this study, we questioned whether differences in cerebral infarction pattern and burden after treatment of ruptured AcomAs by clipping compared with coiling might account for differences in clinical outcome.

The frequency of cerebral infarction (61%) in our study is in agreement with prior studies, which have described cerebral infarction rates ranging from 39%–87%.^{2,22,23} Similar to prior studies, we found increased cumulative cerebral infarct burden among patients with ruptured AcomA treated by microsurgical clipping (72% of patients) compared with those treated by endovascular coil embolization (50% of patients).^{2,17} Moreover, the less frequent use of MR imaging in clipped patients may slightly underestimate the frequency of cerebral infarction in this group. The increased frequency of embolic infarction in patients undergoing endovascular coiling is not surprising, given that endovascular procedures are known to result in punctuate infarctions. However, these punctuate infarctions are often clinically silent, and in this study, we found that the difference was not significant.²⁴ These data suggest that the cumulative differences in cerebral infarction between clipped and coiled patients reflect the mode of treatment rather than the natural history of the ruptured AcomA.

We found cerebral infarction in the vascular distribution of the RAH to be significantly more common among patients treated with microsurgical clipping compared with endovascular coil embolization (OR, 20.9; 95% CI, 3.5–403.7). A prior study found RAH territory infarction in 50% of patients with amnesia after AcomA clipping, but patients treated with endovascular coiling were not analyzed.²⁵ Another study found RAH territory infarction in 15% of patients treated for AcomA by clipping compared with 2% for those treated by coiling, though patient outcomes related to these infarctions were not described.¹⁷ RAH infarction causes injury to the medial and basal striatum, especially the caudate head,²⁶ and memory dysfunction and behavioral deficits have been linked to caudate head infarction.^{12,15,16} The reason for this increased frequency of RAH infarction in patients with ruptured AcomAs treated by microsurgical clipping is not clear. The RAH may be stretched or injured in the setting of SAH because of AcomA rupture, the surgical clips may impinge upon the RAH, or vasospasm may be more likely to develop after surgical manipulation, which may result in RAH territory infarction. Postmortem analyses have found the anatomic course of the

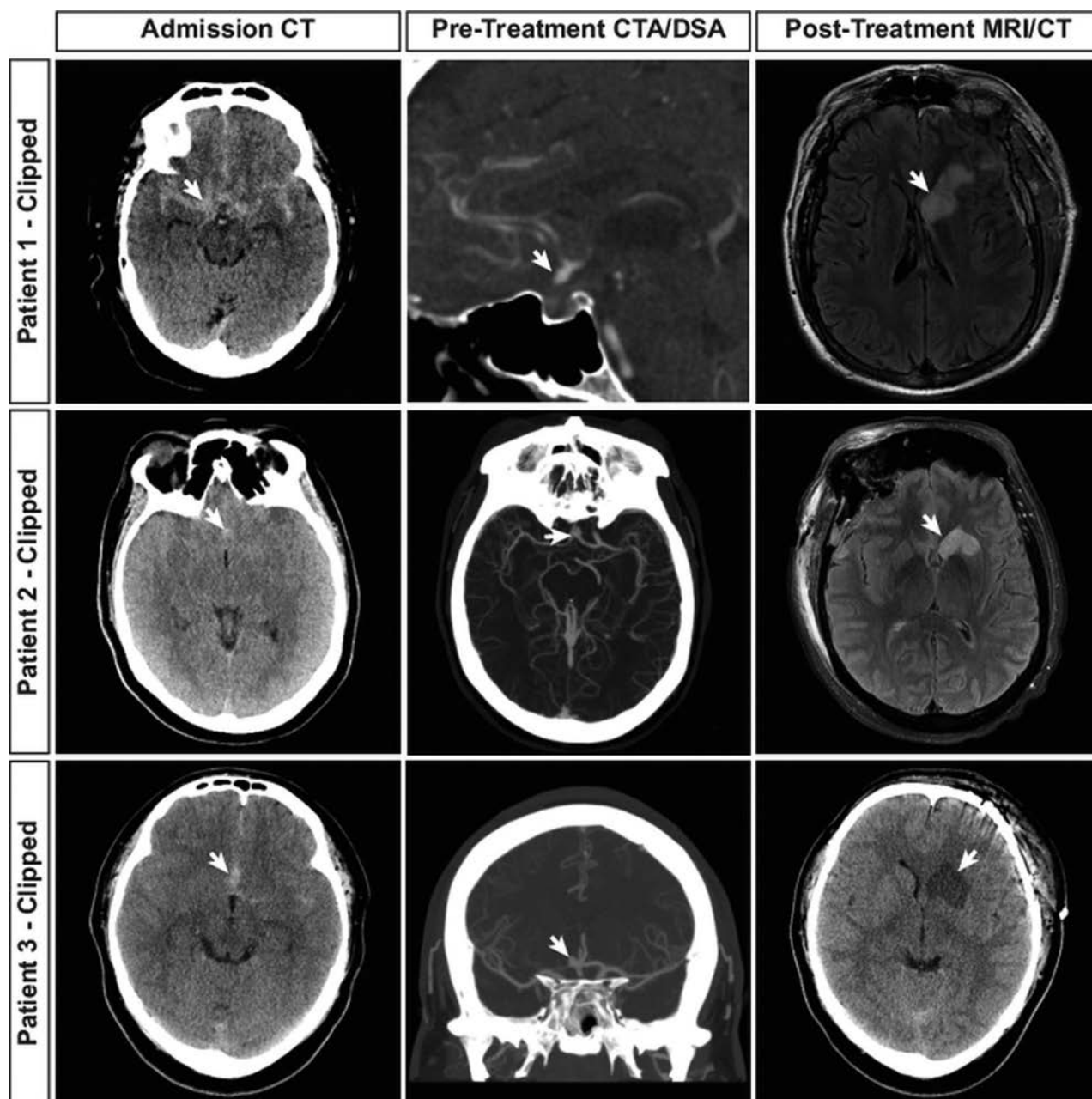


FIG 1. Recurrent artery of Heubner infarction in patients with ruptured AcomA treated by microsurgical clipping. Neuroimaging studies from 3 patients with ruptured AcomA treated by microsurgical clipping are shown. Admission head CT shows SAH (arrows, first column) as hyperattenuated blood in the subarachnoid space. Vascular imaging demonstrates the AcomA (arrows, second column) in each patient by CTA. Postclipping neuroimaging demonstrates cerebral infarction in the RAH territory (arrows, third column) by fluid-attenuated inversion recovery MR imaging (patients 1 and 2) or NCCT (patient 3).

Table 4: Clinical outcome in patients treated by aneurysm clipping versus coiling^a

	All, no. (%)	Clip, no. (%)	Coil, no. (%)	OR (95% CI)	P Value
No. of patients	100 (100)	50 (50)	50 (50)		
Mortality by discharge ($n = 100$; 50 clip, 50 coil)	10 (10)	3 (6.0)	7 (14.0)	0.5 (0.1–2.0)	.31
mRS >2 at discharge ($n = 100$; 50 clip, 50 coil)	74 (74)	37 (74)	37 (74)	3.0 (1.0–10.0)	.06
Survivors' mRS >2 at discharge ($n = 90$; 47 clip, 43 coil)	64 (71.1)	34 (72.3)	30 (69.8)	3.4 (1.2–12.3)	.04
Survivors' mRS >2 at 3 months ($n = 74$; 39 clip, 35 coil)	16 (22)	9 (23.1)	7 (20.0)	2.1 (0.6–8.0)	.24

^a Percentages refer to the number of patients with non-missing values. *P* values are from the likelihood ratio test using propensity scores and odds ratios, and resulting 95% confidence intervals are derived from the logistic model that includes both treatment and propensity scores (see "Materials and Methods" section).

RAH to be variable, which leads to additional challenges in the preservation of this artery during surgery.^{26,27}

Frontal lobe ischemic infarction was also more common in

clipped patients compared with coiled patients in our study (OR, 8.5; 95% CI, 1.9–62.3). Prior studies have shown that cerebral infarction and encephalomalacia in the frontal lobes is more com-

mon after clipping than coiling,^{2,17} which likely reflects a combination of retraction injury and ischemic stroke within the vascular territory of the anterior cerebral arteries and perforators that arise from the anterior communicating artery complex.

Similar to prior studies that have shown better clinical outcomes after endovascular treatment of ruptured aneurysms,^{18,28-30} we found that coiled patients were more likely to be discharged with an independent status (mRS ≤ 2). However, by 3 months of follow-up this difference in functional independence was no longer significantly different. The International Subarachnoid Aneurysm Trial showed that coil embolization of ruptured aneurysms results in higher rates of functional independence that lasts years after treatment,^{5,18} and our discrepant findings at 3 months most likely reflect the relatively small sample size of our cohort. We postulate that the better clinical outcomes among coiled patients in our study reflect the reduced rates of cerebral infarction, particularly within the frontal lobes and striatum.

Cognitive and behavioral deficits that result in poor clinical outcomes and reduced rates of functional independence are more common after AcomA rupture,^{5,11,12} and AcomA treatment by microsurgical clipping is associated with more severe cognitive deficits compared with endovascular coil embolization.^{2,5,11,19} Similarly, surgical treatment of ruptured AcomAs is associated with a greater decline in perioperative Glasgow Coma Scale scores compared with endovascular coiling,³¹ but the reason for these differences remains unclear. Detailed neuropsychological testing after AcomA rupture and treatment is not routinely performed at our institution, which precludes correlating the degree and pattern of cerebral infarction to cognitive outcome in our series. However, many prior studies have now linked memory dysfunction and behavioral deficits to ischemic injury of the striatum, frontal lobe, and ventromedial prefrontal (orbitofrontal) cortex,^{2,3,15,16,32} and our analysis suggests that the higher burden of RAH territory and frontal lobe infarction may account for the worse cognitive outcomes associated with AcomA clipping.^{2,5,11,19} Future multicenter studies that include additional patients, detailed neuropsychologic testing, and neuroimaging studies should be performed to determine whether the higher rate of cerebral infarction in the striatum and frontal lobe after surgical treatment of ruptured AcomA accounts for worse cognitive and behavioral outcomes in these patients.

Limitations

This study is limited by its relatively small size, retrospective design, lack of randomization to clipping/coiling treatment, and single-center patient series, all of which may introduce selection bias. These biases may limit the generalizability of our findings despite our efforts to mitigate these biases with a propensity score in analyzing the outcomes. The posttreatment imaging analysis cannot be blinded to treatment type, given the different imaging appearance of the treatment modalities, which may introduce bias to the results. Moreover, 16% of patients were lost to follow-up at 3 months, which may limit the detection of differences in outcome between clipped and coiled patients at this time point. Neurocognitive testing is not routinely performed at our institution, and our study is limited in its inability to measure neurocog-

nitive deficits that may have resulted from the patterns of infarction identified in this study.

CONCLUSIONS

Frontal lobe infarction and RAH infarction were more common after surgical clipping of ruptured AcomAs. Coiled patients had a better outcome at discharge and were more likely to be functionally independent than clipped patients. However, there were no differences in mortality or clinical outcome at 3 months between coiled and clipped patients. Further neuropsychological studies are warranted to determine whether postsurgical frontal lobe and RAH infarctions contribute to cognitive and behavioral deficits after ruptured AcomA treatment.

Disclosures: Jeremy Heit—UNRELATED: Consultancy: MicroVention, Comments: modest consulting fees with this company for work unrelated to cerebral aneurysm treatment; Employment: Stanford University, Comments: I am a practicing neurointerventionalist radiologist at Stanford, and I treat cerebral aneurysms as a part of my practice. Gary Steinberg—UNRELATED: Consultancy: Peter Latic US Inc, Qool Therapeutics, Neurosave, Comments: serves in an advisory role for Peter Latic US, Qool Therapeutics, and NeuroSave. Max Wintermark—UNRELATED: Board membership: GE NFL advisory board. Michael Marks—UNRELATED: Consultancy: Medtronic.

REFERENCES

- Connolly ES Jr, Rabinstein AA, Carhuapoma JR, et al. **Guidelines for the management of aneurysmal subarachnoid hemorrhage: a guideline for healthcare professionals from the American Heart Association/American Stroke Association.** *Stroke* 2012;43:1711–37 CrossRef Medline
- Hadjivassiliou M, Tooth CL, Romanowski CA, et al. **Aneurysmal SAH: cognitive outcome and structural damage after clipping or coiling.** *Neurology* 2001;56:1672–77 CrossRef Medline
- Wong GK, Nung RC, Sitt JC, et al. **Location, infarct load, and 3-month outcomes of delayed cerebral infarction after aneurysmal subarachnoid hemorrhage.** *Stroke* 2015;46:3099–104 CrossRef Medline
- Mayer SA, Kreiter KT, Copeland D, et al. **Global and domain-specific cognitive impairment and outcome after subarachnoid hemorrhage.** *Neurology* 2002;59:1750–58 CrossRef Medline
- Molyneux AJ, Kerr RS, Yu LM, et al. **International subarachnoid aneurysm trial (ISAT) of neurosurgical clipping versus endovascular coiling in 2143 patients with ruptured intracranial aneurysms: a randomised comparison of effects on survival, dependency, seizures, rebleeding, subgroups, and aneurysm occlusion.** *Lancet* 2005;366:809–17 CrossRef Medline
- Bornstein RA, Weir BK, Petruk KC, et al. **Neuropsychological function in patients after subarachnoid hemorrhage.** *Neurosurgery* 1987; 21:651–54 CrossRef Medline
- Sonesson B, Ljunggren B, Säveland H, et al. **Cognition and adjustment after late and early operation for ruptured aneurysm.** *Neurosurgery* 1987;21:279–87 CrossRef Medline
- Ljunggren B, Sonesson B, Säveland H, et al. **Cognitive impairment and adjustment in patients without neurological deficits after aneurysmal SAH and early operation.** *J Neurosurg* 1985;62:673–79 CrossRef Medline
- Brisman JL, Song JK, Newell DW. **Cerebral aneurysms.** *N Engl J Med* 2006;355:928–39 CrossRef Medline
- Heit JJ, Gonzalez RG, Sabbag D, et al. **Detection and characterization of intracranial aneurysms: a 10-year multidetector CT angiography experience in a large center.** *J Neurointerv Surg* 2016;8:1168–72 CrossRef Medline
- Chan A, Ho S, Poon WS. **Neuropsychological sequelae of patients treated with microsurgical clipping or endovascular embolization for anterior communicating artery aneurysm.** *Eur Neurol* 2002;47: 37–44 CrossRef Medline
- Martinaud O, Perin B, Gérardin E, et al. **Anatomy of executive deficit**

- following ruptured anterior communicating artery aneurysm. *Eur J Neurol* 2009;16:595–601 [CrossRef Medline](#)
13. Fontanella M, Perozzo P, Ursone R, et al. **Neuropsychological assessment after microsurgical clipping or endovascular treatment for anterior communicating artery aneurysm.** *Acta Neurochir (Wien)* 2003;145:867–72; discussion 872 [CrossRef Medline](#)
 14. Proust F, Martinaud O, Gérardin E, et al. **Quality of life and brain damage after microsurgical clip occlusion or endovascular coil embolization for ruptured anterior communicating artery aneurysms: neuropsychological assessment.** *J Neurosurg* 2009;110:19–29 [CrossRef Medline](#)
 15. Mendez MF, Adams NL, Lewandowski KS. **Neurobehavioral changes associated with caudate lesions.** *Neurology* 1989;39:349–54 [CrossRef Medline](#)
 16. Mizuta H, Motomura N. **Memory dysfunction in caudate infarction caused by Heubner's recurring artery occlusion.** *Brain Cogn* 2006;61:133–38 [CrossRef Medline](#)
 17. Mortimer AM, Steinfert B, Faulder K, et al. **Rates of local procedural-related structural injury following clipping or coiling of anterior communicating artery aneurysms.** *J Neurointerv Surg* 2016;8:256–64 [CrossRef Medline](#)
 18. Molyneux A, Kerr R, Stratton I, et al. **International Subarachnoid Aneurysm Trial (ISAT) of neurosurgical clipping versus endovascular coiling in 2143 patients with ruptured intracranial aneurysms: a randomised trial.** *Lancet* 2002;360:1267–74 [CrossRef Medline](#)
 19. Scott RB, Eccles F, Molyneux AJ, et al. **Improved cognitive outcomes with endovascular coiling of ruptured intracranial aneurysms: neuropsychological outcomes from the International Subarachnoid Aneurysm Trial (ISAT).** *Stroke* 2010;41:1743–47 [CrossRef Medline](#)
 20. Austin PC. **An introduction to propensity score methods for reducing the effects of confounding in observational studies.** *Multivariate Behav Res* 2011;46:399–424 [CrossRef Medline](#)
 21. R Development Core Team. *R: A Language and Environment for Statistical Computing.* Version 3.0.1. Vienna, Austria: R Foundation for Statistical Computing; 2013
 22. Vilkki JS, Juvela S, Siironen J, et al. **Relationship of local infarctions to cognitive and psychosocial impairments after aneurysmal subarachnoid hemorrhage.** *Neurosurgery* 2004;55:790–802; discussion 802–03 [CrossRef Medline](#)
 23. Rabinstein AA, Weigand S, Atkinson JL, et al. **Patterns of cerebral infarction in aneurysmal subarachnoid hemorrhage.** *Stroke* 2005;36:992–97 [CrossRef Medline](#)
 24. Krings T, Willmes K, Becker R, et al. **Silent microemboli related to diagnostic cerebral angiography: a matter of operator's experience and patient's disease.** *Neuroradiology* 2006;48:387–93 [CrossRef Medline](#)
 25. Mugikura S, Kikuchi H, Fujii T, et al. **MR imaging of subcallosal artery infarct causing amnesia after surgery for anterior communicating artery aneurysm.** *AJNR Am J Neuroradiol* 2014;35:2293–301 [CrossRef Medline](#)
 26. Zunon-Kipre Y, Peltier J, Haidara A, et al. **Microsurgical anatomy of distal medial striate artery (recurrent artery of Heubner).** *Surg Radiol Anat* 2012;34:15–20 [CrossRef Medline](#)
 27. Maga P, Tomaszewski KA, Skrzat J, et al. **Microanatomical study of the recurrent artery of Heubner.** *Ann Anat* 2013;195:342–50 [CrossRef Medline](#)
 28. Lanzino G, Murad MH, d'Urso PI, et al. **Coil embolization versus clipping for ruptured intracranial aneurysms: a meta-analysis of prospective controlled published studies.** *AJNR Am J Neuroradiol* 2013;34:1764–68 [CrossRef Medline](#)
 29. Li H, Pan R, Wang H, et al. **Clipping versus coiling for ruptured intracranial aneurysms: a systematic review and meta-analysis.** *Stroke* 2013;44:29–37 [CrossRef Medline](#)
 30. McDougall CG, Spetzler RF, Zabramski JM, et al. **The Barrow Ruptured Aneurysm Trial.** *J Neurosurg* 2012;116:135–44 [CrossRef Medline](#)
 31. Ayling OG, Ibrahim GM, Drake B, et al. **Operative complications and differences in outcome after clipping and coiling of ruptured intracranial aneurysms.** *J Neurosurg* 2015;123:621–28 [CrossRef Medline](#)
 32. Mavaddat N, Kirkpatrick PJ, Rogers RD, et al. **Deficits in decision-making in patients with aneurysms of the anterior communicating artery.** *Brain* 2000;123 (Pt 10):2109–17 [CrossRef Medline](#)

Comparison of Clinical Outcomes of Intracranial Aneurysms: Procedural Rupture versus Spontaneous Rupture

H.H. Choi, E.J. Ha, J.J. Lee, D.H. Yoo, W.-S. Cho, J.E. Kim, Y.D. Cho, M.H. Han, and H.-S. Kang



ABSTRACT

BACKGROUND AND PURPOSE: Procedural rupture of an intracranial aneurysm is a devastating complication in endovascular treatment. The purpose of this study was to evaluate the clinical outcomes of patients with procedural rupture of unruptured saccular intracranial aneurysms compared with those with spontaneously ruptured aneurysms.

MATERIALS AND METHODS: A retrospective review was performed for 1340 patients with 1595 unruptured saccular intracranial aneurysms that underwent endovascular coil embolization between February 2010 and December 2014. The clinical outcomes of patients with procedural rupture of unruptured saccular intracranial aneurysms were compared with those of 198 patients presenting with spontaneously ruptured aneurysms.

RESULTS: In this series, procedural rupture developed in 19 patients (1.4% per patient and 1.2% per aneurysm), and the morbidity related to procedural rupture was 26.3% (95% confidence interval, 8.5%–61.4%) with no mortality. Hunt and Hess scale grades and hospitalization days of patients with procedural rupture were equivalent to those of patients presenting with spontaneous aneurysm rupture. Subsequent treatment procedures after hemorrhage (including lumbar drainage, extraventricular drainage, decompressive craniectomy, and permanent shunt) showed no difference between the 2 groups. The hemorrhage volumes were smaller in the procedural-rupture group ($P = .03$), and the endovascular vasospasm therapies tended to be more frequently required in the spontaneous aneurysm-rupture group ($P = .08$). At postictus 6 months, the proportion of modified Rankin Scale scores of ≥ 2 were lower in the procedural-rupture group (5.3% versus 26.8%, $P = .049$). In multivariate analysis, spontaneous aneurysm rupture was a significant risk factor for worse clinical outcome (OR = 14.9; 95% CI, 1.2–193.1; $P = .039$).

CONCLUSIONS: This study showed better clinical outcomes in the procedural-rupture group. Even though there is a potential chance of aneurysm rupture during treatment, the clinical outcomes after procedural bleeds seem to be more favorable than those of spontaneous rupture.

ABBREVIATIONS: PR = procedural rupture; SR = spontaneous aneurysm rupture; UIA = unruptured saccular intracranial aneurysm

Endovascular coil embolization for intracranial aneurysms is a recent development that is gradually replacing surgical clipping because of attributes that include minimal invasiveness and lower rates of morbidity and mortality.^{1,2} Nevertheless, procedural rupture (PR) of an aneurysm being treated remains a devastating complication in endovascular treatment. Although the incidence, risk factors, and clinical outcome of PR have been pre-

viously reported,^{1,3–9} the clinical prognosis of pure PR remains unclear because the reports included ruptured aneurysms, hindering the assessment of the harmful influence of PR. In addition, there have been various treatment guidelines in unruptured intracranial aneurysms (UIAs),^{10–14} and some argue that no treatment might be cost-effective in some clinical situations.^{10,15,16} In principle, the treatment decision should be made on the basis of treatment benefit and its accompanying risks in comparison with the disease burden. The purpose of this study was to assess the clinical outcomes of patients with PR of UIAs compared with those with spontaneously ruptured aneurysms.

MATERIALS AND METHODS

Patient Characteristics

From February 2010 to December 2014, 2025 aneurysms in 1711 patients were treated with endovascular procedures at a

Received March 28, 2017; accepted after revision June 9.

From the Departments of Neurosurgery (H.H.C.), Dongguk University College of Medicine, Dongguk University Hospital, Ilsan, Korea; and Departments of Neurosurgery (E.J.H., W.-S.C., J.E.K., H.-S.K.) and Radiology (J.J.L., D.H.Y., Y.D.C., M.H.H.), Seoul National University College of Medicine, Seoul National University Hospital, Seoul, Korea.

Please address correspondence to Hyun-Seung Kang, MD, PhD, Department of Neurosurgery, Seoul National University College of Medicine, Seoul National University Hospital, 101 Daehak-ro, Jongno-gu, Seoul 03080, Korea; e-mail: hsk4428@yahoo.com

<http://dx.doi.org/10.3174/ajnr.A5344>

single tertiary care institution (Seoul National University Hospital). Of these, 232 aneurysms were excluded from statistical analysis; they were retreated, dissecting, blisterlike, or false aneurysms. Thus, we intended to analyze the clinical outcomes of PR in saccular aneurysms treated with detachable coil embolization. The study cohort included 1531 patients with 1793 saccular aneurysms treated in 1538 sessions. Among them, 198 patients presented with subarachnoid hemorrhage. There were 455 (29.7%) male and 1076 (70.3%) female patients with a mean age of 55.8 years (median, 59 years; range, 13–89 years) at the time of the procedure. The procedural rupture occurred in 1.2% per aneurysm (19/1595) among patients with unruptured aneurysms. We compared the clinical outcomes of the 19 patients (PR group) with those of 198 patients with spontaneously ruptured aneurysms (SR group). This study was conducted according to the principles outlined in the Declaration of Helsinki and was approved by the institutional review board.

Treatment

The endovascular treatment technique was properly selected under the consensus of the cerebrovascular team in a multidisciplinary decision-making process with consideration of the patient's preference. The coiling of aneurysms was performed mostly with the patient under general anesthesia. For these patients with unruptured aneurysms, preprocedural medication with antiplatelet agents was provided. Systemic administration of heparin was performed after deployment of an arterial introducer sheath in unruptured aneurysms and after placement of the first coil in ruptured aneurysms with a bolus dose of 3000 IU followed by a maintenance dose of 1000 IU per hour with monitoring of the activated clotting time. Several kinds of detachable coils, chosen by the operator, were used. Coil placement proceeded until optimal satisfactory aneurysm obliteration was achieved.

Procedural rupture was diagnosed by the extravasation of contrast and direct visualization of a device outside the aneurysm lumen on cerebral angiography. When PR occurred, protamine sulfate was administered immediately to reverse the effects of heparin and coils were deployed quickly to occlude the aneurysm. After the embolization, a CT scan was performed to evaluate the amount of subarachnoid hemorrhage and the development of hydrocephalus. Depending on the patient's neurologic condition, further intervention ensued, which included lumbar drainage, extraventricular drainage, or decompressive surgery. Endovascular vasospasm therapy was performed when the patients showed neurologic deterioration with angiographic vasospasm during the ensuing days.

Clinical Variables and Outcomes

All the relevant medical records were reviewed, including data regarding patient age, sex, aneurysm location, maximal aneurysm diameter, applied endovascular treatment technique, Hunt and Hess scale grade,¹⁷ modified Fisher grade,¹⁸ hospitalization days, and clinical outcome. The treatment procedural data, including lumbar drainage, extraventricular drainage, decompressive crani-

Table 1: Comparison of patient characteristics

	PR Group (n = 19)	SR Group (n = 198)	P Value
Female	16 (84.2%)	116 (58.6%)	.047 ^a
Mean age (yr)	53.6 ± 1.5	55.8 ± 1.0	.22
Mean aneurysm size (mm)	4.6 ± 0.5	6.5 ± 0.2	.01 ^a
Aneurysm location			.15
Anterior cerebral artery	4 (21.1%)	93 (47.0%)	
Middle cerebral artery	5 (26.3%)	35 (17.7%)	
Internal carotid artery	9 (47.4%)	57 (28.8%)	
Posterior circulation	1 (5.2%)	13 (6.5%)	
Hunt and Hess scale ^b			.82
1	1 (5.3%)	7 (3.5%)	
2	13 (68.4%)	123 (62.1%)	
3	2 (10.5%)	36 (18.2%)	
4	3 (15.8%)	26 (13.1%)	
5	0 (0%)	6 (3.1%)	
Modified Fisher grade			.03 ^a
Small volume (grade 1)	14 (73.7%)	89 (45.0%)	
Large volume (grades 2–4)	5 (26.3%)	109 (55.0%)	

^a Significant.

^b Hunt and Hess scale grades were immediately assessed after the patient recovered from the anesthesia in the PR group and at admission in the SR group without adjustment of comorbidity.

ectomy, endovascular vasospasm therapy, and ventriculoperitoneal shunt, were also collected.

Aneurysm size was measured on the basis of 3D reconstruction angiograms. Follow-up angiographic results were evaluated with the last follow-up digital subtraction angiography and/or MR angiography. The results were divided into 2 categories: stable occlusion and recanalization.

Hunt and Hess scale grades were immediately assessed after recovery from anesthesia in the PR group and were assessed on admission in the SR group. Adjustments were not made for comorbidities. The modified Fisher grades were denoted and then were categorized into 2 groups: small hemorrhage volume (grade 1) and large volume (grades 2–4). Clinical outcome was evaluated with the modified Rankin Scale scores, and poor functional outcome was defined as an mRS score of ≥2 at postictus 6 months.¹⁹ When 6-month mRS scores were not recorded, the score nearest to 6 months was used in the analysis.

Statistical Analysis

Continuous variables were expressed as the mean ± SD (range). χ^2 , Fisher exact, and Student *t* tests were performed as necessary. A binary logistic regression model was used to ensure that procedural or spontaneous aneurysm rupture was independently predictive of clinical outcomes. Log-rank tests were used to compare time to aneurysm recanalization. A 2-tailed *P* value < .05 was considered statistically significant. The data were analyzed with the Statistical Package for the Social Sciences (Version 21; IBM, Armonk, New York) and MedCalc for Windows, Version 14.12.0 (MedCalc Software, Ostend, Belgium).

RESULTS

Enrolled Patients and Aneurysms

The patient characteristics are shown in Table 1. There was a somewhat higher proportion of female patients in the PR group (PR versus SR group, 84.2% versus 58.6%; *P* = .047). Mean aneurysmal size was larger in the SR group (6.5 versus 4.6 mm, *P* =

.01). The most frequent aneurysm location was the internal carotid artery (47.4%) in the PR group and the anterior cerebral artery in the SR group (47.0%).

The distribution of Hunt and Hess scale grades was not significantly different between the 2 groups. The hemorrhage volume, determined by modified Fisher grade, was larger in the SR group ($P = .03$). Most (73.7%) in the PR group showed grade 1 bleeds, while more than half of the patients in the SR group presented with higher than grade 1 bleeds.

Table 2: Comparison of embolization techniques and treatment procedures^a

	PR Group (n = 19)	SR Group (n = 198)	P Value
Technique			<.01 ^b
Single microcatheter	12 (63.2%)	108 (54.6%)	
Double microcatheter	2 (10.4%)	65 (32.8%)	
Balloon remodeling	4 (21.1%)	5 (2.5%)	
Stent-assisted	1 (5.3%)	20 (10.1%)	
Lumbar drainage			.23
Yes	6 (31.6%)	38 (19.2%)	
No	13 (68.4%)	160 (81.2%)	
Extraventricular drainage			.32
Yes	1 (5.3%)	34 (17.2%)	
No	18 (94.7%)	164 (82.8%)	
Decompressive craniectomy			1.00
Yes	0 (0%)	4 (2.0%)	
No	19 (100%)	194 (98.0%)	
Endovascular vasospasm therapy			.08
Yes	0 (0%)	32 (16.2%)	
No	19 (100%)	166 (83.8%)	
Permanent shunt			1.00
Yes	1 (5.3%)	19 (9.6%)	
No	18 (94.7%)	179 (90.4%)	

^a Data are No. (%) unless otherwise indicated.

^b Significant.

Table 3: Comparison of clinical outcome and imaging follow-up

	PR Group (n = 19)	SR Group (n = 198)	P Value
Mean hospitalization (day)	13.7 ± 3.1	18.4 ± 1.2	.25
Compromised outcome ^a (No.)	1 (5.3%)	53 (26.8%)	.049 ^b
Follow-up imaging (No.)			
Recanalization	1 (5.3%)	40 (20.2%)	
Stable	14 (73.6%)	122 (61.7%)	
Absence of follow-up imaging	4 (21.1%)	36 (18.1%)	

^a Modified Rankin Scale scores of ≥2 at postictus 6 months.

^b Significant.

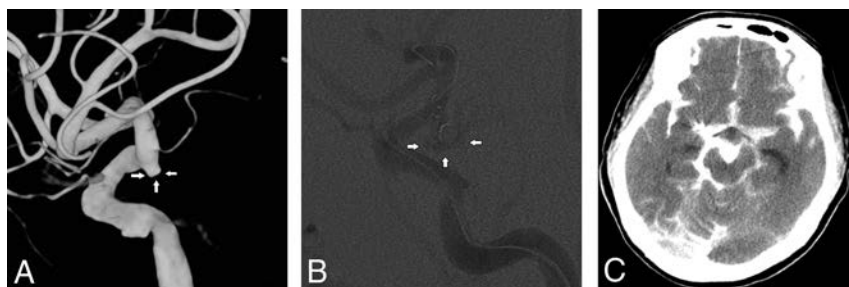


FIG 1. Cerebral angiography demonstrates a right posterior communicating artery aneurysm (A). During coil embolization with balloon remodeling, the aneurysm was ruptured by a coil (B). Despite rapid obliteration of the ruptured aneurysm, the volume of subarachnoid hemorrhage was considerable (modified Fisher grade 3) (C).

Procedural Characteristics

The endovascular procedures and subsequent interventions are presented in Table 2. The embolization techniques were significantly different between the 2 groups ($P < .01$); notably, the balloon-remodeling technique was more frequently used in the PR group (PR group versus SR group, 21.1% versus 2.5%; $P < .01$). The culprit devices causing procedural aneurysmal rupture were coils in most cases ($n = 17$, 89.5%), and the remaining devices were microcatheters ($n = 2$, 10.5%).

The procedures subsequent to the coil embolization were not significantly different between the 2 groups (Table 2), except that more patients tended to require endovascular vasospasm therapy in the SR group (PR group versus SR group, 0% versus 16.2%; $P = .08$). On further analysis, the patients with larger hemorrhage volume required endovascular vasospasm therapy more frequently (modified Fisher grade 1 versus grades 2–4, 8.7% versus 20.2%, $P = .02$).

Clinical Outcomes

All 19 patients in the PR group were asymptomatic before PR. Headache without neurologic symptoms was the most common symptom following PR ($n = 13$, 68.4%), followed by motor weakness ($n = 3$, 15.8%), diplopia ($n = 1$), and altered mentality ($n = 1$). One patient was asymptomatic despite PR. The hospitalization days of the PR group were 13.7 days on average (median, 12 days; range, 3–63 days), which did not differ significantly from those patients in the SR group (mean, 18.4 days; median, 15 days; range, 3–209 days) ($P = .25$) (Table 3).

In the PR group, there were 5 patients with morbidity (26.3%; 95% confidence interval, 8.5%–61.4%) and no mortality. Compromised clinical outcome (defined as an mRS score of ≥2) at the 6-month follow-up evaluation was found in 1 patient (5.3%) in the PR group, whose mRS score was 4 (Fig 1). The other 18 patients did not have any associated symptoms at postictus 6 months. In the SR group, compromised clinical outcomes were found in 53 patients (26.8%), which was a significantly higher rate in comparison with that in the PR group ($P = .049$) (Fig 2). Multivariate analysis indicated that spontaneous aneurysm rupture was one of independent risk factors for poor clinical outcome (OR = 14.9; 95% CI, 1.2–193.1; $P = .039$), along with patient age, Hunt and Hess scale grade, and the amount of bleed as measured by the modified Fisher grade (Table 4).

Follow-up angiographic images were available in 15 patients (78.9%) in the PR group and in 162 (81.8%) in the SR group. One of the 15 patients (6.7%) had recanalization in the PR group, and 40 (20.2%) had recanalization in the SR group ($P = .064$). Kaplan-Meier estimates of the rates of stable aneurysmal occlusion are presented in Fig 3.

DISCUSSION

In our study, 1340 patients with 1595 UIAs were treated with endovascular coil embolization. The risk of PR was low (1.4% per patient and 1.2% per aneurysm), like that in previous studies that reported a 0%–2.2% rate of PR in UIAs.^{1–3,5,7} The PR-re-

lated symptomatic complication rate was 0.1% (1 of 1340) in clinical assessment at 6 months after ictus. The hospitalization days and Hunt and Hess scale grades did not differ significantly between the 2 groups. However, the proportion of patients with small hemorrhage volume (modified Fisher grade 1) was greater, and endovascular vasospasm therapies were less frequently required in the PR group. Accordingly, the clinical outcomes in the patients with PR of UIAs were more favorable compared with those of the patients presenting with spontaneously ruptured aneurysms. Although we cannot choose between spontaneous SAH and intraoperative rupture, physicians may inform patients with UIAs of expected clinical outcomes of PR before decision-making for the treatment.

Many neurointerventionists are concerned about PR. Various factors, including size, location, and morphology of aneurysms and a previous rupture history, have been analyzed to evaluate the risk factors of PR.^{1,3-9} A multicenter study reported increased periprocedural death or disability in 63% of patients with PR compared with 15% without PR,²⁰ and another study reported a 33% risk of death and 5% risk of disability with PR in ruptured aneurysms.²¹ However, the clinical outcome for PR of UIAs is not well-described because of the limited number of cases.^{1,6,22,23} Concerning unruptured aneurysms, Im et al² and Schuette et al⁵ reported 4 cases and 1 case of PR, respectively; there was no mortality or morbidity, but the number of cases was too small to conclude a reliable clinical outcome. Mitchell et al⁷ reported higher rates of 30-day mortality with PR of UIAs (1 of 6, 16.7%) than in patients without PR (2 of 249, 0.8%). In the present study, there were 5 cases of morbidity but no mortality in the 19 PR cases treated for unruptured aneurysms. At 6 months after ictus, only 1 of 1340 patients (0.1%) had poor mRS scores (> 2) related to PR.

The clinical outcome of PR seems to have 1 of 2 extremes: death or recovery.²² Sluzewski et al²² reported 20 deaths and 31 good outcomes in 51 procedure-related ruptures; most patients (97.4%) were treated after rupture. Of the 19 patients with PR in our series, 5 had neurologic symptoms such as weakness or altered mentality, and 14 patients had headache only on the immediate neurologic examina-

tion after PR. In the 5 symptomatic patients, only 1 patient had permanent hemiparesis, and 4 patients fully recovered without neurologic sequelae. Unlike those with ruptured aneurysms, the patients with PR of UIAs had favorable functional outcomes and did not have fatal outcomes. The favorable results in PR of UIAs might be due to the rapid obliteration of the aneurysm to prevent massive hemorrhage when PR occurs during coil embolization. When the PR occurred, additional coils were deployed promptly, sometimes in conjunction with a balloon or a stent to control leakage. Symptomatic vasospasm after aneurysmal SAH occurred in 16.2% of patients with spontaneously ruptured aneurysms, comparable with reported rates of 17%–40%.²⁴ Notably, the patients with PR did not present with symptomatic vasospasm in any case in our series. We believe that the rapid obliteration of PR leads to less hemorrhage volume, no symptomatic vasospasm, and more favorable clinical outcomes.

Stapleton et al⁹ reported an increased risk of symptomatic hydrocephalus requiring temporary or permanent cerebral fluid diversion with rerupture of ruptured intracranial aneurysms. In our study, treatment procedures after rupture were not significantly different between the PR and SR groups, including lumbar drainage, extraventricular drainage, decompressive craniectomy, and permanent ventricular shunt.

In the present study, the balloon remodeling technique was used less often in the SR group than in the PR group. Several multicenter studies reported that balloon-remodeling coil embolization was not

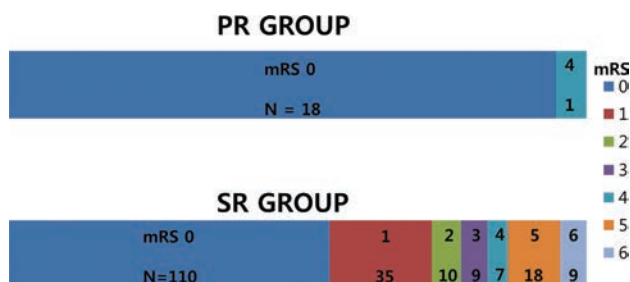


FIG 2. Modified Rankin Scale scores at the 6-month posttreatment period.

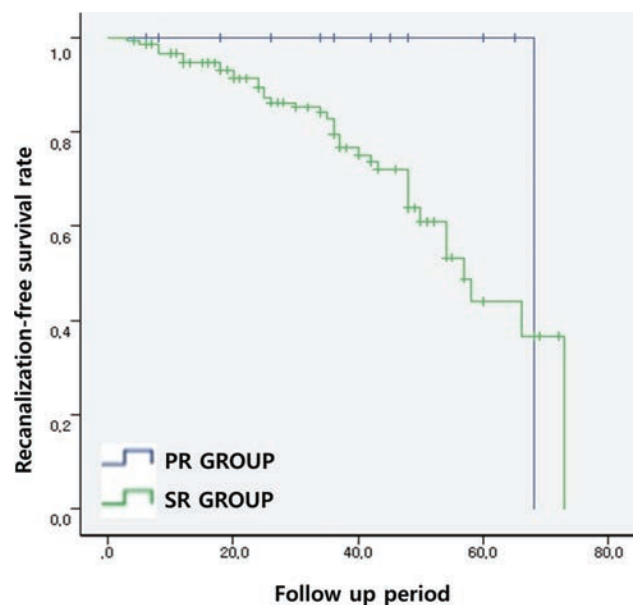


FIG 3. Kaplan-Meier estimates of the rates of stable aneurysmal occlusion: procedural rupture group versus spontaneous rupture group.

Table 4: Logistic regression model assessing risk factors of poor clinical outcome

Variables	Univariate Analysis			Multivariate Analysis		
	Odds Ratio	95% CI	P Value	Odds Ratio	95% CI	P Value
Age	1.051	1.024–1.079	.000 ^a	1.053	1.020–1.087	.001 ^a
Sex	1.016	0.541–1.909	.961	—	—	—
Hunt and Hess scale grade	4.874	3.075–7.725	.000 ^a	4.565	2.608–7.989	.000 ^a
Modified Fisher grade	9.868	4.203–23.167	.000 ^a	2.867	1.053–7.809	.039 ^a
SR	6.579	0.857–50.503	.070 ^a	14.908	1.151–193.054	.039 ^a

Note: — indicates variable was not included in the multivariate analysis.

^a Significant.

related to an increase in PR.^{25,26} In contrast, Sluzewski et al²⁷ reported a high complication rate with balloon-remodeling coil embolization. The increased risk of PR during balloon-remodeling coil embolization is still debated.^{25,28–30}

This study has limitations inherent in a single-institution retrospective study. Therefore, the results should be viewed considering the statistical constraint resulting from the limited number of patients with PR. A multicenter study with a larger number of cases is needed to confirm the results.

CONCLUSIONS

The patients with PR of UIAs had less hemorrhage volume with lower modified Fisher grades and underwent endovascular vasospasm therapy less frequently than those with SR. Accordingly, clinical outcomes of these patients were more favorable. Patients with PR of UIAs can recover well if rapid obliteration of the aneurysm and subsequent appropriate management are undertaken.

Disclosures: Moon Hee Han—UNRELATED: Consultancy: MicroVention*. *Money paid to the institution.

REFERENCES

1. Brisman JL, Niimi Y, Song JK, et al. **Aneurysmal rupture during coiling: low incidence and good outcomes at a single large volume center.** *Neurosurgery* 2005;57:1103–09; discussion 1103–09 CrossRef Medline
2. Im SH, Han MH, Kwon OK, et al. **Endovascular coil embolization of 435 small asymptomatic unruptured intracranial aneurysms: procedural morbidity and patient outcome.** *AJNR Am J Neuroradiol* 2009;30:79–84 Medline
3. Li MH, Gao BL, Fang C, et al. **Prevention and management of intraprocedural rupture of intracranial aneurysm with detachable coils during embolization.** *Neuroradiology* 2006;48:907–15 CrossRef Medline
4. Nguyen TN, Raymond J, Guilbert F, et al. **Association of endovascular therapy of very small ruptured aneurysms with higher rates of procedure-related rupture.** *J Neurosurg* 2008;108:1088–92 CrossRef Medline
5. Schuette AJ, Hui FK, Spiotta AM, et al. **Endovascular therapy of very small aneurysms of the anterior communicating artery: five-fold increased incidence of rupture.** *Neurosurgery* 2011;68:731–37; discussion 737 CrossRef Medline
6. Santillan A, Gobin YP, Greenberg ED, et al. **Intraprocedural aneurysmal rupture during coil embolization of brain aneurysms: role of balloon-assisted coiling.** *AJNR Am J Neuroradiol* 2012;33:2017–21 CrossRef Medline
7. Mitchell PJ, Muthusamy S, Dowling R, et al. **Does small aneurysm size predict intraoperative rupture during coiling in ruptured and unruptured aneurysms?** *J Stroke Cerebrovasc Dis* 2013;22:1298–303 CrossRef Medline
8. Zhang Y, Li G, Cai Y, et al. **Rupture during the endovascular treatment of intracranial aneurysms: outcomes and technical aspects.** *Acta Neurochir (Wien)* 2013;155:569–77 CrossRef Medline
9. Stapleton CJ, Walcott BP, Butler WE, et al. **Neurological outcomes following intraprocedural rupture during coil embolization of ruptured intracranial aneurysms.** *J Neurosurg* 2015;122:128–35 CrossRef Medline
10. Komotar RJ, Mocco J, Solomon RA. **Guidelines for the surgical treatment of unruptured intracranial aneurysms: the first annual J Lawrence Pool memorial research symposium—controversies in the management of cerebral aneurysms.** *Neurosurgery* 2008;62:183–93; discussion 193–94 CrossRef Medline
11. Thompson BG, Brown R Jr, Amin-Hanjani S, et al; American Heart Association Stroke Council, Council on Cardiovascular and Stroke Nursing, and Council on Epidemiology and Prevention, American Heart Association, American Stroke Association. **Guidelines for the Management of Patients with Unruptured Intracranial Aneurysms: A Guideline for Healthcare Professionals from the American Heart Association/American Stroke Association.** *Stroke* 2015;46:2368–400 CrossRef Medline
12. Steiner T, Juvela S, Unterberg A, et al. **European Stroke Organization. European Stroke Organization guidelines for the management of intracranial aneurysms and subarachnoid haemorrhage.** *Cerebrovasc Dis* 2013;35:93–112 CrossRef Medline
13. Burns JD, Brown RD Jr. **Treatment of unruptured intracranial aneurysms: surgery, coiling, or nothing?** *Curr Neurol Neurosci Rep* 2009;9:6–12 CrossRef Medline
14. Raabe A, Seifert V, Schmiedek P, et al; American Heart Association, Section of Vascular Neurosurgery of the German Society of Neurosurgery. **Recommendations for the management of unruptured intracranial aneurysms** [in German]. *Zentralbl Neurochir* 2002;63:70–76 CrossRef Medline
15. Greving JP, Rinkel GJ, Buskens E, et al. **Cost-effectiveness of preventive treatment of intracranial aneurysms: new data and uncertainties.** *Neurology* 2009;73:258–65 CrossRef Medline
16. Brown RD Jr, Broderick JP. **Unruptured intracranial aneurysms: epidemiology, natural history, management options, and familial screening.** *Lancet Neurol* 2014;13:393–404 CrossRef Medline
17. Hunt WE, Hess RM. **Surgical risk as related to time of intervention in the repair of intracranial aneurysms.** *J Neurosurg* 1968;28:14–20 CrossRef Medline
18. Frontera JA, Claassen J, Schmidt JM, et al. **Prediction of symptomatic vasospasm after subarachnoid hemorrhage: the modified Fisher scale.** *Neurosurgery* 2006;59:21–27; discussion 21–27 CrossRef Medline
19. van Swieten JC, Koudstaal PJ, Visser MC, et al. **Interobserver agreement for the assessment of handicap in stroke patients.** *Stroke* 1988;19:604–07 CrossRef Medline
20. Eljovich L, Higashida RT, Lawton MT, et al; Cerebral Aneurysm Rupture After Treatment (CARAT) Investigators. **Predictors and outcomes of intraprocedural rupture in patients treated for ruptured intracranial aneurysms: the CARAT study.** *Stroke* 2008;39:1501–06 CrossRef Medline
21. Cloft HJ, Kallmes DF. **Cerebral aneurysm perforations complicating therapy with Guglielmi detachable coils: a meta-analysis.** *AJNR Am J Neuroradiol* 2002;23:1706–09 Medline
22. Sluzewski M, Bosch JA, van Rooij WJ, et al. **Rupture of intracranial aneurysms during treatment with Guglielmi detachable coils: incidence, outcome, and risk factors.** *J Neurosurg* 2001;94:238–40 CrossRef Medline
23. Tummala RP, Chu RM, Madison MT, et al. **Outcomes after aneurysm rupture during endovascular coil embolization.** *Neurosurgery* 2001;49:1059–66; discussion 1066–67 Medline
24. Charpentier C, Audibert G, Guillemin F, et al. **Multivariate analysis of predictors of cerebral vasospasm occurrence after aneurysmal subarachnoid hemorrhage.** *Stroke* 1999;30:1402–08 CrossRef Medline
25. Pierot L, Cognard C, Anxionnat R, et al. **Remodeling technique for endovascular treatment of ruptured intracranial aneurysms had a higher rate of adequate postoperative occlusion than did conventional coil embolization with comparable safety.** *Radiology* 2011;258:546–53 CrossRef Medline
26. Pierot L, Spelle L, Vitry F. **Immediate clinical outcome of patients harboring unruptured intracranial aneurysms treated by endovascular approach: results of the ATENA study.** *Stroke* 2008;39:2497–504 CrossRef Medline
27. Sluzewski M, van Rooij WJ, Beute GN, et al. **Balloon-assisted coil embolization of intracranial aneurysms: incidence, complications, and angiography results.** *J Neurosurg* 2006;105:396–99 CrossRef Medline
28. Levy E, Koebe CJ, Horowitz MB, et al. **Rupture of intracranial aneurysms during endovascular coiling: management and outcomes.** *Neurosurgery* 2001;49:807–11; discussion 811–13 Medline
29. Pierot L, Spelle L, Leclerc X, et al. **Endovascular treatment of unruptured intracranial aneurysms: comparison of safety of remodeling technique and standard treatment with coils.** *Radiology* 2009;251:846–55 CrossRef Medline
30. Pierot L, Cognard C, Spelle L, et al. **Safety and efficacy of balloon remodeling technique during endovascular treatment of intracranial aneurysms: critical review of the literature.** *AJNR Am J Neuroradiol* 2012;33:12–15 CrossRef Medline

Flow Diversion with Low-Profile Braided Stents for the Treatment of Very Small or Uncoilable Intracranial Aneurysms at or Distal to the Circle of Willis

K. Aydin, M. Barburoglu, S. Sencer, M. Berdikhojayev, B. Coskun, and S. Akpek



ABSTRACT

BACKGROUND AND PURPOSE: The endovascular treatment of aneurysms located at or distal to the circle of Willis and not amenable to coiling remains a challenge. We report our experience with flow-diversion treatment using low-profile braided stents as a stent monotherapy procedure for treating distally located very small or uncoilable aneurysms.

MATERIALS AND METHODS: We retrospectively reviewed our data bases to identify patients with aneurysms located at or distal to the circle of Willis who were treated with stent monotherapy using low-profile braided stents. The immediate and follow-up angiographic findings and clinical status of the patients were assessed.

RESULTS: Twenty aneurysms in 19 patients were included in the study. The mean size of the aneurysms was 4.7 ± 2.4 mm. Patients were treated via telescopic implantation of 2 stents for 11 aneurysms; single-stent placement was used for the remaining aneurysms. The technical success rate was 95%. We observed a technical complication in 1 case (5.3%) and a late ischemic event in another (5.3%). The final angiographies during a mean follow-up of 14.7 months showed complete aneurysm occlusion in 73.7%. The complete occlusion rate of the aneurysms treated with telescopic stent placement was 81.8%. The modified Rankin scale scores of all patients at the last follow-up were between 0 and 2.

CONCLUSIONS: Flow diversion with low-profile braided stents as a stent monotherapy procedure for very small or uncoilable intracranial aneurysms located at or beyond the circle of Willis is a promising, relatively safe, and durable endovascular procedure.

ABBREVIATION: OKM = O'Kelly-Marotta grading scale

In the past decade, several self-expandable stents dedicated to intracranial use have been introduced to treat wide-neck and complex aneurysms previously not amenable to coiling.^{1–4} Stents create a mechanical scaffold, which prevents coil protrusion into the parent artery. In addition to this mechanical scaffolding effect, the implantation of stents also produces hemodynamic and biologic effects in the parent arteries that promote aneurysm occlusion. Stent deployment across the orifice of an aneurysm redirects the blood flow in the parent artery to decrease hemodynamic

stress, which facilitates thrombosis in the aneurysmal sac.⁵ Furthermore, stents induce neointimal proliferation in the parent artery, which eventually leads to healing of the aneurysm neck.⁶ The hemodynamic and biologic effects of stents promote the progressive occlusion of partially coiled aneurysms and impede their recanalization.

On the basis of the hemodynamic and biologic effects of stents, flow-diversion treatment as a stent monotherapy procedure using conventional stents has been proposed for the endovascular treatment of intracranial aneurysms not amenable to coiling or alternative open surgical procedures.⁷ Flow diversion as a stent monotherapy procedure consists of the implantation of a self-expandable stent or stents across the neck of an aneurysm, without coiling the aneurysm sac. A limited number of previous case series reported the application of stent monotherapy with balloon-expandable or conventional self-expandable stents and focused on the treatment of aneurysms located proximal to the circle of Willis.^{7–10}

Low-profile braided stents have been recently introduced to treat aneurysms located at small-sized, distal parent arteries. Low-

Received May 31, 2017; accepted after revision July 3.

From the Department of Radiology (K.A., M.Barburoglu, S.S.), Neuroradiology Division, Istanbul Faculty of Medicine, Istanbul University, Capa, Istanbul, Turkey; Department of Radiology (K.A.), Interventional Radiology Unit, Koç University School of Medicine, Koç University Hospital, Topkapi, Istanbul, Turkey; Department of Neurosurgery (M.Berdikhojayev), JSC Central Clinical Hospital, Almaty City, Kazakhstan; and Department of Radiology (B.C., S.A.), Vehbi Koc Vakfi American Hospital, Nisantasi, Istanbul, Turkey.

Please address correspondence to Kubilay Aydin, MD, Istanbul Medical Faculty, Cerrahi monoblok Kat: Bodrum 1, Nororadyoloji Bilim Dali, Capa, Istanbul, Turkey; e-mail: dr.aydink@gmail.com

Indicates open access to non-subscribers at www.ajnr.org

<http://dx.doi.org/10.3174/ajnr.A5362>

profile intracranial stents can be deployed into arteries with diameters between 1.5 and 3.5 mm, and they can be delivered through microcatheters with an internal diameter of 0.0165 inches, which allows easier navigation in small-sized, delicate vessels.¹¹ In this report, we present our experience with flow-diversion treatment as a stent monotherapy procedure for treating very small or uncoilable intracranial aneurysms located at or beyond the circle of Willis using low-profile braided stents. In this retrospective study, we investigated the feasibility, efficacy, and mid-term durability of the stent monotherapy procedure with LEO Baby stents (Balt, Montmorency, France).

MATERIALS AND METHODS

After approval of the study by the institutional ethics committee, we retrospectively reviewed our data base records to identify patients with intracranial aneurysms located at or distal to the circle of Willis who were treated with the stent monotherapy procedure using low-profile stents. In all cases, the decision regarding the most appropriate method of treatment was made by a multidisciplinary neurovascular team. Flow diversion with low-profile braided stents as a stent monotherapy procedure was performed to treat patients with very small aneurysms (<3 mm) located at or distal to the circle of Willis, distal aneurysms with a complex morphology that impeded the application of the conventional endovascular techniques such as balloon remodeling or stent-assisted coiling, and distal aneurysms from which important branches or perforators arose.

The review of our data base records revealed 19 patients with 28 aneurysms who underwent the stent monotherapy procedure to treat intracranial aneurysms. There were 15 female (79%) and 4 male patients, with a mean age of 46.6 ± 17.9 years (range, 7–71 years). Twenty aneurysms in 19 patients were included in this study. Eight aneurysms treated with other endovascular techniques or clipping were excluded. All except 1 of the aneurysms reported in this study were unruptured. One patient with an anterior cerebral artery aneurysm was referred to our center for endovascular surgery 3 weeks after the rupture of the aneurysm. Another patient with an anterior cerebral artery aneurysm had a history of subarachnoid hemorrhage caused by the rupture of a contralateral middle cerebral artery aneurysm, which was treated by clipping at that time. Two aneurysms had been previously coiled and then became recanalized during the follow-up assessments. Eighteen of the 20 aneurysms had not received prior treatment. The mean dome size of the aneurysms was 4.7 ± 2.4 mm (range, 1.5–9 mm). Five aneurysms were in the A1–2 segments of the anterior cerebral artery, 4 aneurysms were in the posterior-inferior cerebellar artery, 3 aneurysms were in the pericallosal segment of the anterior cerebral artery, 3 aneurysms were in the posterior cerebral artery, 3 aneurysms were in the M1 segment of the MCA, and 2 aneurysms were in the bifurcation of the MCA. Three aneurysms had a complex morphology, and 17 aneurysms were saccular.

The preoperative clinical status of patients was evaluated with the modified Rankin Scale. The preoperative mRS scores of 17 patients were all zero. Two patients with a history of subarachnoid hemorrhage had a preoperative mRS score of 2.

Endovascular Procedure

In all cases, the endovascular procedure consisted of the implantation of a low-profile, self-expandable stent or stents covering the neck of the aneurysm, without coiling of the aneurysm. The patients with unruptured aneurysms received 75 mg of clopidogrel and 300 mg of aspirin daily for at least 5 days before the procedure. In the patient with a recently ruptured aneurysm, antiplatelet therapy was initiated 12 hours before the endovascular procedure with a loading dose of 300 mg of aspirin and 600 mg of clopidogrel. A 6F guiding catheter (Envoy; Codman & Shurtleff, Raynham, Massachusetts) or a 6F guiding sheath (Neuron Max; Penumbra, Alameda, California) was placed into the target artery (the internal carotid artery or the proximal vertebral artery) at the beginning of the procedure. A microcatheter (Echelon 10, Covidien, Irvine, California; or Vasco 10, Balt) for stent delivery was positioned in the parent artery distal to the neck of the aneurysm with the guidance of a 0.014-inch microguidewire (Transend, Stryker, Kalamazoo, Michigan; Traxcess, MicroVention, Tustin, California; Hybrid, Balt). A low-profile braided stent (LEO Baby plus; Balt) was deployed into the parent artery to cover the neck of the aneurysm in all cases.

After the deployment of the stent, control angiography was performed to assess the opening and the apposition of the stent. In some cases, an additional stent was deployed, overlapping the initial stent. In these cases, the stent delivery microcatheter was navigated through the first deployed stent, and the second stent was telescopically deployed inside the initial stent. If there was no sign of any complication on the control angiograms, the stent delivery wire was removed and the procedure was completed. Postprocedural dual antiplatelet treatment, including 75 mg/day of clopidogrel and 300 mg/day of aspirin, was continued for 3–6 months. Thereafter, the dual antiplatelet therapy was switched to aspirin.

All technical and clinical complications were recorded. Complications were defined as periprocedural if they occurred during the procedure or within 48 hours following completion of the procedure. Clinical complications that occurred between 48 hours and 14 days were defined as early postprocedural, while those occurring after 2 weeks were defined as late postprocedural complications. The neurologic status of patients was recorded at discharge from the hospital using the mRS score.

Follow-Up Assessment

An immediate postprocedural control angiography was performed at the end of the procedure to evaluate the patency of the stents, the filling status of the aneurysm, and the patency of side branches and perforators. The filling status of the aneurysms was evaluated with the O'Kelly-Marotta (OKM) grading scale.¹² The degree of aneurysm filling was graded between A and D (A = complete filling, B = incomplete filling, C = entry remnant, D = total occlusion). The degree of stasis in the aneurysm sac was scaled between 1 and 3 (1 = arterial, 2 = capillary, 3 = venous). Follow-up MR angiography was performed at 3–4 months. The first digital subtraction angiography follow-up was performed at 3–6 months. The second examination was performed at 9–12 months. The third follow-up angiography was performed at 24–36 months, depending on the findings of the second follow-up angiography. The neurologic status of patients was assessed with the mRS score at each follow-up.

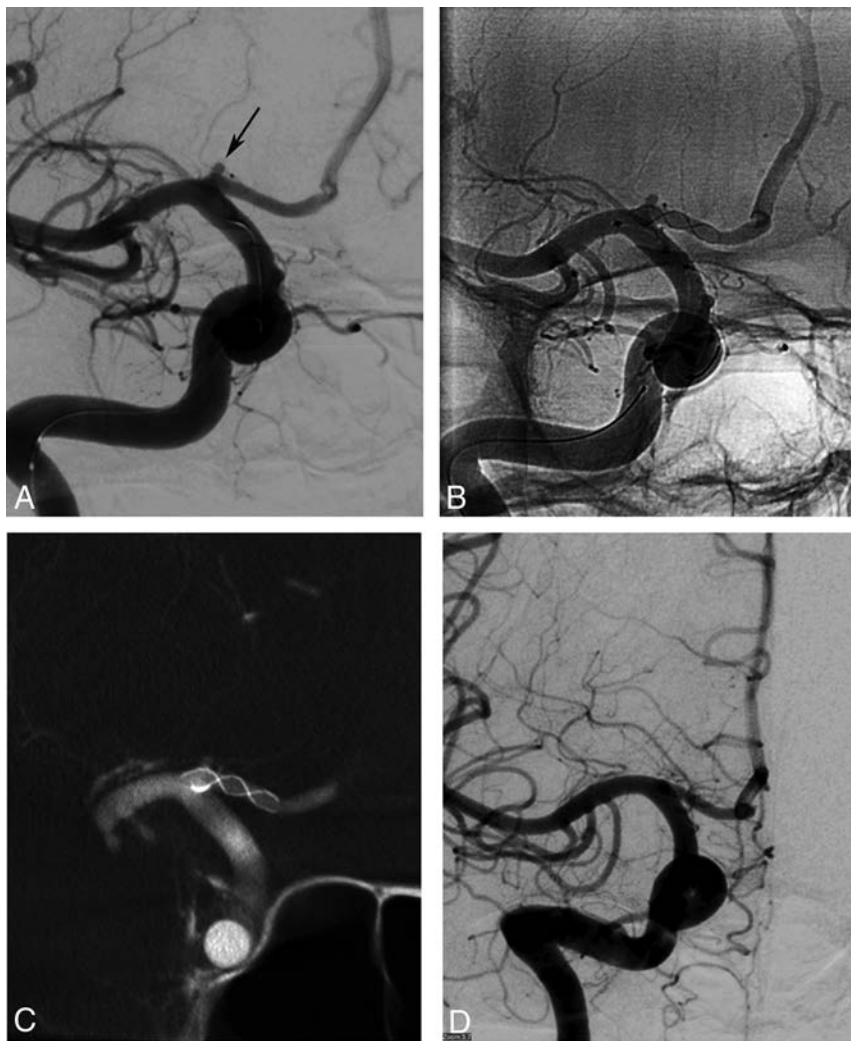


FIG 1. Procedural and follow-up angiograms of a 28-year-old female patient with a history of subarachnoid hemorrhage due to rupture of a contralateral MCA bifurcation aneurysm. *A*, A preprocedural DSA image shows a 1.5-mm saccular aneurysm (arrow) located in the A1 segment of the right anterior cerebral artery. *B*, A nonsubtracted angiography image obtained during the procedure demonstrates the successful implantation of a stent in the A1 segment of the anterior cerebral artery, covering the neck of the aneurysm. This image also shows the filling of the aneurysm (OKM grade A). *C*, A VasoCT image (Philips Healthcare, Best, the Netherlands) obtained immediately after stent deployment reveals the full apposition of the stent to the parent artery walls. *D*, The 10-month follow-up DSA image shows complete occlusion of the aneurysm (OKM grade D).

RESULTS

Thirty-one stents were deployed to treat 20 aneurysms. The telescopic implantation of double stents was performed to treat 11 aneurysms. Single stents were deployed for the remaining 9 aneurysms (Fig 1). The technical success rate of the procedure was 95% (19 of 20 aneurysms) (Fig 2). A technical complication developed in 1 patient with a dissecting/fusiform PICA aneurysm, which resulted in the failure of the procedure. The parent artery (the left PICA) in this patient had stenotic and extremely tortuous segments. After the deployment of the stent, the immediate control angiography revealed an incomplete opening of the stent in the stenotic/tortuous segment and the subsequent development of acute and complete thrombosis of the stent. The thrombosed stent was then retrieved with a microcatheter and microsnare to restore blood flow in the PICA. This patient awoke without any

neurologic deficits. The deployment of stents in all the other patients was uneventful.

The immediate control angiography images revealed complete occlusion of 1 aneurysm (OKM grade D) (5%), stagnated partial filling of 3 aneurysms (OKM grade B2–3) (15%), stagnated filling of 11 aneurysms (OKM grade A2–3) (55%), and complete filling of 5 aneurysms, including the case in which the stent was retrieved due to acute thrombosis (OKM grade A1) (25%) (Fig 3).

Complications

No mortality occurred during this study. Complications, including the asymptomatic technical complication, developed in 2 patients (10.5%). The mRS scores at discharge were equal to the preoperative scores for all patients. We observed a late postprocedural complication in a patient with an MCA aneurysm treated by the telescopic implantation of 2 stents (5.3%). This patient developed monoparesis in his right (contralateral) leg 2 months after the cessation of clopidogrel at the 6-month follow-up. His cranial MR image revealed a small lacunar infarct in the left basal ganglia extending to the genu of the internal capsule. We prolonged the dual antiplatelet treatment in this case, and his symptoms regressed completely within weeks. His final mRS score at the last follow-up was zero.

Follow-Up Assessments

Follow-up imaging was performed for 19 aneurysms in 18 patients (94.7%). The mean duration of follow-up was 14.7 ± 8.5 months (range, 4–36 months).

The follow-up imaging revealed an OKM grade D in 14 of 19 aneurysms (73.7%), OKM C2–3 grade filling in 2 aneurysms (10.5%), OKM B2–3 filling in 2 aneurysms (10.5%), and OKM grade A3 filling in 1 aneurysm (5.3%). None of the aneurysms ruptured during the follow-up period. The last follow-up of 11 aneurysms treated with telescopic stent placement revealed total occlusion (OKM grade D) of 9 aneurysms (81.8%) (Fig 4). The last follow-up angiography assessments of the aneurysms treated with a single stent revealed a total occlusion rate of 62.5%.

We observed in-stent stenosis in the first follow-up angiography examinations of 5 patients (27.8%). In 3 of them, the aneurysms had been treated by the telescopic implantation of double stents. The second follow-up angiography examinations demonstrated regression of the in-stent stenosis in 3 patients. The in-

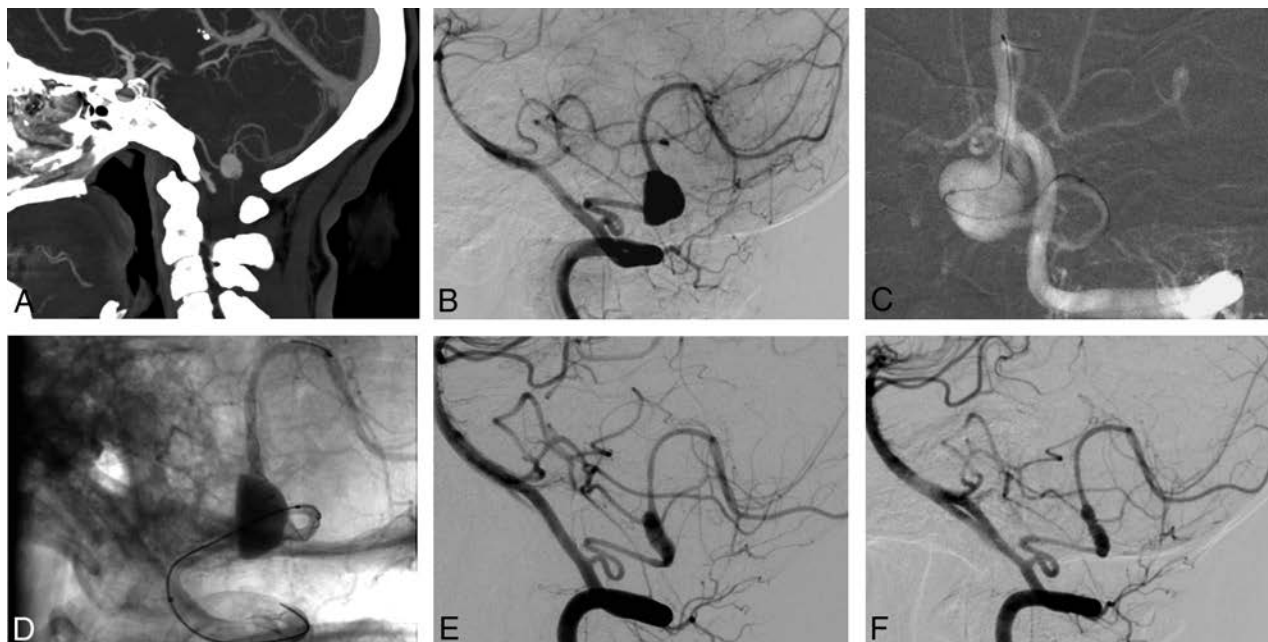


FIG 2. Preprocedural CT and procedural and follow-up angiograms of a 39-year-old female patient with a distal PICA aneurysm. *A*, CT angiography reconstructed on a sagittal projection shows a saccular aneurysm in the PICA. *B*, A preprocedural DSA image depicts a 7-mm saccular aneurysm located in the tonsillomedullary segment of the left PICA. *C*, A roadmap DSA image obtained during the procedure shows the catheterization of the distal PICA for stent placement. This image also demonstrates that the aneurysm has a very complex morphology without a definable neck. *D*, A nonsubtracted angiography image shows the deployment of the stent into the PICA. Please note the compaction and expansion of the stent across the orifice of the aneurysm. *E*, A 12-month follow-up DSA image reveals the reconstruction of the parent artery and no aneurysm filling. *F*, The 24-month follow-up DSA image confirms the stable occlusion of the aneurysm.

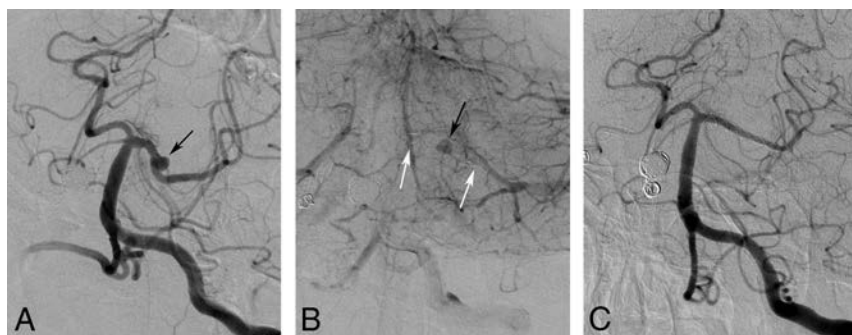


FIG 3. Procedural and follow-up DSA images of a 62-year-old female patient with a small posterior cerebral artery aneurysm. *A*, A preprocedural DSA image obtained in the left anterior oblique projection reveals a 2.5-mm saccular aneurysm (arrow) located in the left posterior cerebral artery. *B*, The venous phase of the DSA image obtained immediately after stent deployment shows the stagnation of injected contrast medium in the aneurysm sac (black arrow) and the deployed stent (white arrows) in the left posterior cerebral artery. *C*, The 7-month follow-up DSA image demonstrates total occlusion of the aneurysm (OKM grade D) and a mild degree of in-stent stenosis.

stent stenosis was mild (<50%) and remained asymptomatic in all cases. Therefore, no intervention was performed to treat the in-stent stenosis.

The mRS score at the last follow-up evaluation was zero in 16 of 18 patients. The mRS scores of 2 patients with preprocedural scores of 2 did not change until their last follow-up.

DISCUSSION

The endovascular treatment of distally located, very small-sized aneurysms is a challenge for interventional neuroradiologists. The risk of intraprocedural rupture is significantly high during the coiling of very small aneurysms.^{13,14} The microcatheteriza-

tion of small aneurysms is very difficult, and microcatheter or microguidewire maneuvers can cause rupture. Furthermore, because of the limited space inside the aneurysm sac, coiling itself can lead to the rupture of a small aneurysm. We performed the stent monotherapy technique with a flow-diversion strategy to treat very small aneurysms located at or distal to the circle of Willis. The stent monotherapy procedure is a safe alternative endovascular method for treating distally located, very small-sized aneurysms. The lack of aneurysm catheterization nearly eliminates the risk of intraprocedural rupture of very small aneurysms during stent monotherapy.

The principle of stent monotherapy for intracranial aneurysms is based on flow diversion and the biologic effects of stents. Aneurysm flow velocity and wall shear stress are important hemodynamic parameters associated with the growth and rupture of intracranial aneurysms.¹⁵⁻¹⁹ The placement of a stent or stents across the neck of an aneurysm redirects the blood flow and decreases intra-aneurysmal flow velocity by disturbing the inflow. The reduced aneurysmal flow induces stasis and consequently thrombosis of the aneurysm.⁵ Tateshima et al¹⁹ investigated the alterations in intra-aneurysmal hemodynamics with the placement of high-porosity open-cell stents across the necks of aneurysms and found that the placement of a single Neuroform stent (Stryker Neurovascular) reduced the intra-aneurys-

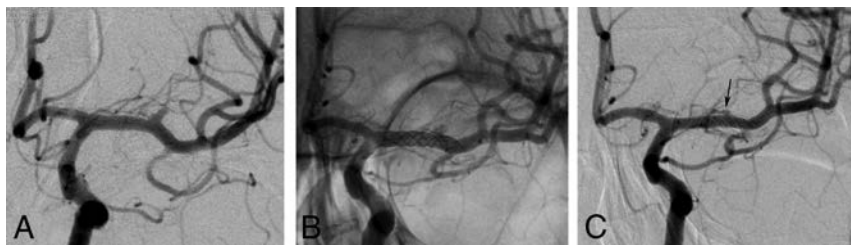


FIG 4. Procedural and follow-up angiograms of a 48-year-old female patient with an MCA aneurysm. *A*, A preprocedural DSA image reveals a 2.5-mm saccular aneurysm located in the M1 segment of the left MCA. This image also shows a lenticulostriate artery arising from the aneurysm. *B*, A nonsubtracted angiogram recorded during the procedure demonstrates the telescopic implantation of 2 low-profile stents into the left M1 segment. *C*, The 14-month follow-up DSA image shows total occlusion of the aneurysm (OKM grade D) and the reconstruction of the lenticulostriate artery (arrow), which previously arose from the aneurysm.

mal flow velocity by 22%–64%. In another study, Wang et al²⁰ assessed the hemodynamic changes inside aneurysms induced by the implantation of conventional stents and found that the velocity of the jet flow entering the aneurysm and wall shear stresses on the aneurysm were significantly reduced by the placement of a stent.²⁰ These authors suggested that the hemodynamic changes induced by stents promote thrombus formation inside the aneurysm and reduce the risk of aneurysm growth and rupture. Blankena et al²¹ studied the correlation between wall shear stress and wall thickness of aneurysms with 7T MR imaging. This group found an inverse correlation between wall shear stress and aneurysm wall thickness. High wall shear stress might be associated with the process of aneurysm wall remodeling, which causes thinning of the aneurysm wall.

The results of previous experimental studies suggest that the hemodynamic changes induced by the placement of stents across the aneurysm neck promote thrombus formation inside the aneurysm, reducing the risks of aneurysm growth and rupture. Fiorella et al⁷ reported the results of 10 patients whose ruptured aneurysms were treated with stent monotherapy by the implantation of open-cell stents. Even though the flow-diversion capacity of high-porosity open-cell stents is relatively low, in their results during a 12-month follow-up period, Fiorella et al observed complete occlusion in 5 (50%) patients and near-total occlusion in 4 (40%). Kim and Ko¹⁰ treated 8 patients with ruptured, small intracranial aneurysms with stent placement alone, without coiling. Follow-up angiographies revealed total aneurysm occlusions in 3 patients (37.5%) and size reduction in 3 patients (37.5%). These investigators did not observe any growth or rupture of the aneurysms during the follow-up periods ranging from 6 to 34 months. Zenteno et al⁹ reported the results of performing the single-stent placement technique to treat posterior circulation aneurysms.

One-year angiographic follow-up examinations revealed a total aneurysm occlusion rate of 80% in this study. The results of our study support the findings of previous experimental and clinical studies. We observed total occlusion in 73.7% of the aneurysms during the mean follow-up of 14.7 months. Furthermore, 21.0% of the aneurysms showed a reduction in size and stasis in the sac during the follow-up period. Additionally, none of the aneurysms showed growth, and we did not observe any aneurysm rupture. Therefore, the results of our study indicate that flow diversion with low-profile braided stents as a stent monotherapy

is an effective endovascular technique for the treatment of very small or uncoilable intracranial aneurysms located at or distal to the circle of Willis.

LEO Baby stents are self-expanding stents that are constructed of braided metal filaments. They have a relatively smaller cell size (approximately 0.9 mm) and a higher metal coverage ratio than other conventional self-expandable stents. The porosity of LEO Baby stents at their nominal diameter is approximately 83%. Bouillot et al²² studied the flow modifications induced by conventional self-expandable and low-porosity

flow-diverter stents and found that conventional, intermediate-porosity braided stents could provide flow-change patterns like those provided by low-porosity flow-diverter stents. The relatively high mesh density of LEO Baby stents provides a relatively high flow-diversion capacity and allows these stents to act as mini flow diverters in appropriate cases. Moreover, it is possible to further decrease the porosity of braided stents during their deployment. When an axial force is applied to braided stents during deployment, the stents can expand along vessel segments with a diameter larger than the nominal diameter of the stent. The expansion of the stent beyond its nominal diameter in unconstrained segments causes a significant reduction in the porosity.²³

Therefore, it is possible to compress braided stents in unconstrained segments to decrease the porosity and increase the flow-reconstruction capacity. We used this feature of LEO Baby stents as a strategy to increase the flow-diversion capacity of the stents deployed to treat the wide-neck or dissecting/fusiform aneurysms. During the deployment of the stents, we attempted to compress the stents by applying an axial force with a delivery microcatheter and a delivery wire. Our second strategy to increase the metal density over the neck of the aneurysm was the telescopic deployment of 2 stents. We performed telescopic stent placement in the treatment of 11 of 20 aneurysms. In an experimental study, Cantón et al²⁴ showed that the sequential placement of multiple stents across the aneurysm neck progressively decreases the hemodynamic stress on the aneurysm. Kim et al²⁵ used a computational fluid dynamics method to quantify the hemodynamic changes achieved by the placement of multiple stents. Kim et al found that the placement of 2 stents caused a significant reduction in wall shear stress and an increase in the turnover time of intraneurysmal flow. Our findings support the results of these experimental studies. In our study, the rate of total occlusion for the aneurysms treated with telescopic stent placement was 81.8%, which is higher than the follow-up results of single-stented aneurysms. This finding indicates that the telescopic implantation of a second stent in appropriate cases would increase the flow-diversion capacity of the stent monotherapy procedure.

Low-porosity stents dedicated to flow diversion have a much higher metal density compared with conventional self-expandable stents. The high metal density of flow-diverter stents might induce faster aneurysm exclusion. However, the risk of side branch or perforator occlusion would also increase with a higher

metal density. The patency of covered side branches and perforators is a major debate in the recent use of flow diverters for the treatment of distally located intracranial aneurysms. Gawlitza et al²⁶ treated 18 aneurysms located beyond the circle of Willis with the implantation of flow-diverter stents, and 17.6% of their patients developed symptomatic ischemic lesions in the territories of the perforators covered by the stents. Furthermore, the follow-up MR imaging examinations revealed asymptomatic lacunar ischemic lesions in 29.4% of the cases. In another study, Pistocchi et al²⁷ treated 30 aneurysms located beyond the circle of Willis with the implantation of flow-diverter stents. These investigators observed the total occlusion of jailed side branches in 38.1% of the cases and restricted flow in 23.8% of the cases.

Because of the potentially high perforator or side branch occlusion risk, we preferred to not use low-porosity flow-diverter stents in our patients. No permanent morbidity was observed in our patients. We observed a symptomatic thromboembolic complication in only 1 patient who developed a lacunar infarction in the territory of the perforators covered by the telescopic stents. The symptoms of this patient regressed completely during the follow-up period. Furthermore, the mRS scores at the last follow-up examinations did not differ from the preprocedural scores for any of the patients.

Another disadvantage of flow-diverter stents in the treatment of distal intracranial aneurysms is the current necessity of catheterizing small-sized intracranial arteries with larger and stiffer microcatheters with internal diameters of 0.021–0.027 inches. The catheterization of distal and small-sized vessels with these large, stiff microcatheters could be technically difficult and traumatic. Low-profile, self-expandable stents are deliverable through low-caliber microcatheters with an internal diameter of 0.0165 inches. Therefore, low-profile stents allow easier catheterization and navigation in small-sized, delicate vessels and enable safer stent placement during the treatment of distal aneurysms. In our patients, some of the aneurysms were in very small-sized and extremely tortuous parent arteries, which could be safely catheterized with low-caliber delivery microcatheters.

In flow-diversion treatment for intracranial aneurysms, the hemodynamic alterations provided by the stent struts initiate the formation of a thrombus inside the aneurysm. However, the final steps necessary to achieve total and durable aneurysm occlusion depend on the cellular processes induced by the stent implantation.²⁸ These cellular events start with the adherence of inflammatory cells to the intersections of the stent struts. Then, endothelialization that begins along the parent artery proceeds over the aneurysm neck. The complete endothelialization of the stent struts over the neck is associated with total occlusion of the aneurysm. Because the endothelial cells that grow over the stent struts are derived from the adjacent parent artery, the full apposition of the stent to the parent artery wall is critical for the achievement of a total aneurysm occlusion.²⁹ LEO Baby stents have a braided, sliding strut design, providing a high degree of conformability and allowing good wall apposition even in tortuous vessels, which may have facilitated the development of total occlusion and the regression of the aneurysms in our study.

The in-stent stenosis incidence at the first follow-up DSAs was relatively high compared with the results of previous studies.^{1,7}

However, most (60%) regressed during follow-up, and all patients remained asymptomatic. The incidence of in-stent stenosis among patients treated with telescopic (27.3%) and single stent placement (28.6%) was similar. Therefore, it seems to be a reversible reaction of endothelium induced by the stent implantation.³⁰ When we consider that the mechanism of aneurysm occlusion following flow-diversion treatment is based on the stent endothelialization, in-stent stenosis may be a consequence of an endothelial healing process that is induced by stent implantation.^{1,28}

There are some limitations to the current study. First, this study was a nonrandomized, retrospective study. Therefore, there was no control group of alternative endovascular or open surgical treatment methods with which to compare the results. The decisions for the most appropriate endovascular method of treatment were made by the neurovascular teams in each patient. Therefore, the effects of patient selection bias cannot be excluded from the results. Finally, the study population was relatively small.

CONCLUSIONS

Flow diversion with low-profile braided stents as a stent monotherapy is a promising, relatively safe, and durable endovascular procedure to treat very small or uncoilable intracranial aneurysms located at or beyond the circle of Willis. Flow diversion with low-profile braided stents may be considered an alternative option to treat distal intracranial aneurysms not amenable to conventional endovascular techniques. Larger series with longer follow-up are necessary to define the long-term durability of this treatment.

REFERENCES

1. Aydin K, Arat A, Sencer S, et al. **Stent-assisted coiling of wide-neck intracranial aneurysms using low-profile LEO Baby stents: initial and midterm results.** *AJNR Am J Neuroradiol* 2015;36:1934–41 [CrossRef Medline](#)
2. Brassel F, Grieb D, Meila D, et al. **Endovascular treatment of complex intracranial aneurysms using Acandis Acclino stents.** *J Neurointerv Surg* 2017;9:854–59 [CrossRef Medline](#)
3. Möhlenbruch M, Herweh C, Behrens L, et al. **The LVIS Jr. microstent to assist coil embolization of wide-neck intracranial aneurysms: clinical study to assess safety and efficacy.** *Neuroradiology* 2014;56:389–95 [CrossRef Medline](#)
4. Pötin M, Blanc R, Spelle L, et al. **Stent-assisted coiling of intracranial aneurysms: clinical and angiographic results in 216 consecutive aneurysms.** *Stroke* 2010;41:110–15 [CrossRef Medline](#)
5. Cantón G, Levy DI, Lasheras JC. **Hemodynamic changes due to stent placement in bifurcating intracranial aneurysms.** *J Neurosurg* 2005;103:146–55 [CrossRef Medline](#)
6. Lopes D, Sani S. **Histological postmortem study of an internal carotid artery aneurysm treated with the Neuroform stent.** *Neurosurgery* 2005;56:E416; discussion E416 [CrossRef Medline](#)
7. Fiorella D, Albuquerque FC, Deshmukh VR, et al. **Endovascular reconstruction with the Neuroform stent as monotherapy for the treatment of uncoilable intradural pseudoaneurysms.** *Neurosurgery* 2006;59:291–300; discussion 291–300 [CrossRef Medline](#)
8. Song J, Oh S, Kim MJ, et al. **Endovascular treatment of ruptured blood blister-like aneurysms with multiple (≥ 3) overlapping Enterprise stents and coiling.** *Acta Neurochir* 2016;158:803–09 [CrossRef Medline](#)
9. Zenteno MA, Santos-Franco JA, Freitas-Modenese JM, et al. **Use of the sole stenting technique for the management of aneurysms in the posterior circulation in a prospective series of 20 patients.** *J Neurosurg* 2008;108:1104–18 [CrossRef Medline](#)

10. Kim YJ, Ko JH. **Sole stenting with large cell stents for very small ruptured intracranial aneurysms.** *Interv Neuroradiol* 2014;20:45–53 [CrossRef Medline](#)
11. Akmangit I, Aydin K, Sencer S, et al. **Dual stenting using low-profile LEO baby stents for the endovascular management of challenging intracranial aneurysms.** *AJNR Am J Neuroradiol* 2015;36:323–29 [CrossRef Medline](#)
12. O’Kelly CJ, Krings T, Fiorella D, et al. **A novel grading scale for the angiographic assessment of intracranial aneurysms treated using flow diverting stents.** *Interv Neuroradiol* 2010;16:133–37 [CrossRef Medline](#)
13. Brinjikji W, Lanzino G, Cloft HJ, et al. **Endovascular treatment of very small (3 mm or smaller) intracranial aneurysms: report of a consecutive series and a meta-analysis.** *Stroke* 2010;41:116–21 [CrossRef Medline](#)
14. Nguyen TN, Raymond J, Guilbert F, et al. **Association of endovascular therapy of very small ruptured aneurysms with higher rates of procedure-related rupture.** *J Neurosurg* 2008;108:1088–92 [CrossRef Medline](#)
15. Cebal JR, Castro MA, Burgess JE, et al. **Characterization of cerebral aneurysms for assessing risk of rupture by using patient-specific computational hemodynamics models.** *AJNR Am J Neuroradiol* 2005;26:2550–59 [Medline](#)
16. Meng H, Tutino VM, Xiang J, et al. **High WSS or low WSS? Complex interactions of hemodynamics with intracranial aneurysm initiation, growth, and rupture: toward a unifying hypothesis.** *AJNR Am J Neuroradiol* 2014;35:1254–62 [CrossRef Medline](#)
17. Meng H, Wang Z, Hoi Y, et al. **Complex hemodynamics at the apex of an arterial bifurcation induces vascular remodeling resembling cerebral aneurysm initiation.** *Stroke* 2007;38:1924–31 [CrossRef Medline](#)
18. Metaxa E, Tremmel M, Natarajan SK, et al. **Characterization of critical hemodynamics contributing to aneurysmal remodeling at the basilar terminus in a rabbit model.** *Stroke* 2010;41:1774–82 [CrossRef Medline](#)
19. Tateshima S, Tanishita K, Hakata Y, et al. **Alteration of intraaneurysmal hemodynamics by placement of a self-expandable stent: laboratory investigation.** *J Neurosurg* 2009;111:22–27 [CrossRef Medline](#)
20. Wang C, Tian Z, Liu J, et al. **Flow diverter effect of LVIS stent on cerebral aneurysm hemodynamics: a comparison with Enterprise stents and the Pipeline device.** *J Transl Med* 2016;14:199 [CrossRef Medline](#)
21. Blankena R, Kleinloog R, Verweij BH, et al. **Thinner regions of intracranial aneurysm wall correlate with regions of higher wall shear stress: a 7T MRI study.** *AJNR Am J Neuroradiol* 2016;37:1310–17 [CrossRef Medline](#)
22. Bouillot P, Brina O, Ouared R, et al. **Particle imaging velocimetry evaluation of intracranial stents in sidewall aneurysm: hemodynamic transition related to the stent design.** *PLoS One* 2014;9:e113762 [CrossRef Medline](#)
23. Makoyeva A, Bing F, Darsaut TE, et al. **The varying porosity of braided self-expanding stents and flow diverters: an experimental study.** *AJNR Am J Neuroradiol* 2013;34:596–602 [CrossRef Medline](#)
24. Cantón G, Levy DI, Lasheras JC, et al. **Flow changes caused by the sequential placement of stents across the neck of sidewall cerebral aneurysms.** *J Neurosurg* 2005;103:891–902 [CrossRef Medline](#)
25. Kim M, Levy EI, Meng H, et al. **Quantification of hemodynamic changes induced by virtual placement of multiple stents across a wide-necked basilar trunk aneurysm.** *Neurosurgery* 2007;61:1305–12; discussion 1312–13 [CrossRef Medline](#)
26. Gawlitza M, Januel AC, Tall P, et al. **Flow diversion treatment of complex bifurcation aneurysms beyond the circle of Willis: a single-center series with special emphasis on covered cortical branches and perforating arteries.** *J Neurointerv Surg* 2016;8:481–87 [CrossRef Medline](#)
27. Pistocchi S, Blanc R, Bartolini B, et al. **Flow diverters at and beyond the level of the circle of Willis for the treatment of intracranial aneurysms.** *Stroke* 2012;43:1032–38 [CrossRef Medline](#)
28. Kadirvel R, Ding YH, Dai D, et al. **Cellular mechanisms of aneurysm occlusion after treatment with a flow diverter.** *Radiology* 2014;270:394–99 [CrossRef Medline](#)
29. Rouchaud A, Ramana C, Brinjikji W, et al. **Wall apposition is a key factor for aneurysm occlusion after flow diversion: a histologic evaluation in 41 rabbits.** *AJNR Am J Neuroradiol* 2016;37:2087–91 [CrossRef Medline](#)
30. Kim YS, Lee SW, Yeom JA, et al. **Angiographic findings of in-stent intimal hyperplasia after stent-assisted coil embolization: are they permanent findings?** *J Neurosurg* 2016;124:328–33 [CrossRef Medline](#)

Anterior Circulation Acute Ischemic Stroke Associated with Atherosclerotic Lesions of the Cervical ICA: A Nosologic Entity Apart

O.F. Eker, P. Panni, C. Dargazanli, G. Marnat, C. Arquizan, P. Machi, I. Mourand, G. Gascou, E. Le Bars, V. Costalat, and A. Bonafé



ABSTRACT

BACKGROUND AND PURPOSE: Mechanical thrombectomy for patients with acute ischemic stroke with tandem occlusions has been shown to present varying reperfusion successes and clinical outcomes. However, the heterogeneity of tandem occlusion etiology has been strongly neglected in previous studies. We retrospectively investigated patients with acute ischemic stroke atherothrombotic tandem occlusion.

MATERIALS AND METHODS: All consecutive patients with acute ischemic stroke with atherothrombotic tandem occlusions treated with mechanical thrombectomy in our center between September 2009 and April 2015 were analyzed. They were compared with patients with acute ischemic stroke with dissection-related tandem occlusion and isolated intracranial occlusion treated during the same period. Comparative univariate and multivariate analyses were conducted, including demographic data, safety, and rates of successful recanalization and good clinical outcome.

RESULTS: Despite comparable baseline severity of neurologic deficits and infarct core extension, patients with atherothrombotic tandem occlusions were older ($P < .001$), were more frequently smokers ($P < .001$), and had globally more cardiovascular risk factors ($P < .001$) than the other 2 groups of patients. The patients with atherothrombotic tandem occlusions had significantly longer procedural times ($P < .001$), lower recanalization rates ($P = .004$), and higher global burden of procedural complications ($P < .001$). In this group, procedural complications ($OR = 0.15$, $P = .02$) and the TICI 2b/3 reperfusion scores ($OR = 17.76$, $P = .002$) were independently predictive factors of favorable clinical outcome.

CONCLUSIONS: Our study suggests that atherothrombotic tandem occlusions represent a peculiar and different nosologic entity compared with dissection-related tandem occlusions. This challenging cause of acute ischemic stroke should be differentiated from other etiologies in patient management in future prospective studies.

ABBREVIATIONS: AIS = acute ischemic stroke; CSA = carotid stent placement and angioplasty; MT = mechanical thrombectomy; sICH = symptomatic intracranial hemorrhage; TO = tandem occlusion

The benefits of mechanical thrombectomy (MT) in reperfusion success, safety, and clinical outcome in patients with acute ischemic stroke (AIS) have been demonstrated by several randomized trials.^{1–5} These trials concerned mostly patients with intracranial large-vessel occlusion in the anterior circulation. However, up to

20% of patients with an intracranial large-vessel occlusion also present with an additional occlusion of the extracranial ICA, mainly due to atherosclerosis or dissection and less frequently to cardioembolism or undetermined etiology.^{6,7} These so-called tandem occlusions (TOs) have poorer prognosis in reperfusion and clinical outcome after IV fibrinolysis,^{7–10} probably because of poor response to fibrinolysis and/or the high clot burden associated with them. They are considered the worst-case scenarios among patients with anterior circulation stroke, leading to severe neurologic morbidity and death in up to 70% and 55% of cases, respectively.^{11–13}

The available data on TOs treated with MT show varying rates of reperfusion success (ranging from 62.5% to 100%) and favorable outcome at 3 months (ranging from 29.2% to 54% of patients with mRS 0–2).^{7,13–15} Many factors may explain these varying results, such as the following: 1) the low incidence of TOs and their systematic exclusion or limited inclusion in most of the main clinical trials of

Received February 16, 2017; accepted after revision June 9.

From the Service de Neuroradiologie (O.F.E., P.P., C.D., P.M., G.G., E.L.B., V.C., A.B.) and Service de Neurologie (C.A.), Hôpital Gui de Chauliac, CHRU de Montpellier, Montpellier, France; Department of Neurosurgery and Radiosurgery (P.P.), San Raffaele University Hospital, Milan, Italy; and Service de Neuroradiologie (G.M., I.M.), Hôpital Pellegrin, CHRU de Bordeaux, Bordeaux, France.

Please address correspondence to O.F. Eker, MD, PhD, Department of Interventional Neuroradiology, Gui de Chauliac Hospital, CHRU de Montpellier, 80 Ave Augustin Fliche, 34295 Montpellier cedex 9, France; e-mail: eker_omer@yahoo.fr



Indicates article with supplemental on-line appendix and tables.



Indicates article with supplemental on-line photo.

<http://dx.doi.org/10.3174/ajnr.A5404>

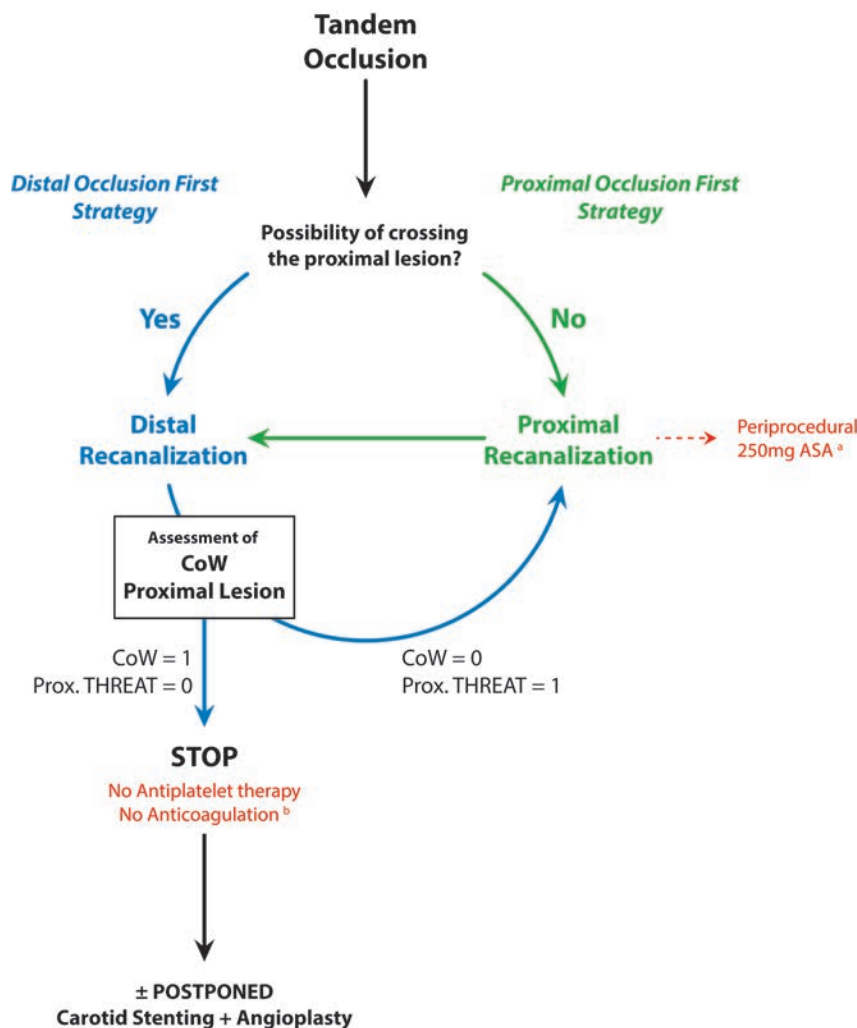


FIG 1. Algorithm of endovascular therapeutic strategies for tandem occlusions. The absence ($n = 0$) or presence ($n = 1$) condition the proximal treatment or not. The algorithm of the therapeutic decisions describes 2 strategies consisting of the treatment of, first, the proximal lesion (proximal occlusion strategy [POF]) or, first, the distal occlusion (distal occlusion first strategy [DOF]). The decision between the POF or DOF strategies is based on the following considerations raised during the endovascular procedure: 1) the ease of crossing the proximal occlusion site (easy crossing? difficult or impossible crossing?); 2) the patency and efficiency of the circle of Willis (efficient CoW or absence of CoW?); and 3) how threatening is the proximal atherosclerotic lesion? (unstable ulcerated plaque? moderate regular plaque?). In thrombus on ulcerated plaque, usually a single thromboaspiration allows easily crossing the proximal occlusion site and treating the distal (ie, intracranial) occlusion. In case of POF (a), the antiplatelet regimen consisted of the periprocedural intravenous administration of a unique loading dose of aspirin (250 mg) until the first imaging follow-up at 24 hours postoperatively. After ruling out any hemorrhagic transformation at 24 hours, a daily dual-antiplatelet therapy (160 mg of aspirin + 75 mg of clopidogrel) was instituted. In case of DOF (b), no anticoagulation or antiplatelet therapies were administered until the first imaging follow-up at 24 hours postoperatively. After we ruled out any hemorrhagic transformation at 24 hours, a daily monoantiplatelet therapy (160 mg of aspirin) was instituted. CoW indicates circle of Willis (efficient = 1; nonefficient or absent = 0); Prox. THREAT indicates any threatening of the proximal lesion (either atherosclerotic or dissecting).

MT for AIS; 2) the limitation of the previously reported data to retrospective small case series with heterogeneous treatment strategies; and 3) the heterogeneity of TO etiologies that has been strongly neglected and may have considerably biased the results. A recent meta-analysis of individualized patient data from the 5 main randomized trials confirmed the benefit of MT for patients with TOs, though the heterogeneity of treatment methods challenges substantially the chances of defining a standardized optimal treatment method.¹⁶

In this work, we evaluated the efficacy and safety of MT for the

treatment of patients with AIS caused by atherothrombotic TO. The results of MT in atherothrombotic TO were secondarily compared to those obtained for patients with dissection-related TO with isolated intracranial occlusion.

MATERIALS AND METHODS

Patient Selection

Data on patients treated with MT for AIS due to atherothrombotic TO between September 2009 and April 2015 were retrospectively extracted from a prospectively maintained data base. The decision for treatment was based on the clinical/radiologic severity mismatch defined as the discrepancy between the NIHSS score and the baseline core infarct size estimated on the DWI-ASPECTS. Age and time after symptom onset were not absolute exclusion criteria. The patient's eligibility for MT was based on the following criteria: mRS 0–2 before the AIS, NIHSS score of ≥ 8 or fluctuating symptoms, intracranial large-vessel occlusion, and DWI-ASPECTS of ≥ 4 . When it was not contraindicated, patients received IV rtPA at the usual dose of 0.9 mg/kg before or concomitantly with MT. The study was approved by the local institutional review board. All patients underwent initial MR imaging with a 1.5T or 3T whole-body scanner (Avanto or Skyra system; Siemens, Erlangen, Germany). The imaging protocol included DWI, FLAIR, gradient-echo T2* imaging, and contrast-enhanced MRA.

Endovascular Procedure and Postintervention Medications

The technical aspects of the endovascular procedure are detailed in the On-line Appendix. A “distal occlusion first treatment strategy” was performed if the proximal cervical lesion could be crossed without problems. After achieving the intracranial reperfusion, we assessed the circle of Willis functionality by opacification of the other supra-aortic trunks. In the case of ineffective circle of Willis supply to the recanalized MCA, a stent was placed across the proximal occlusion. A stent was inserted on a case-by-case basis. In the case of highly stenotic lesions that could not initially be broken through, a “proximal occlusion first” treatment strategy was performed. The proximal lesion was primarily treated by carotid angioplasty and stent placement. Then, intracranial thrombectomy was performed. Figure 1 illustrates the management algorithm for tandem occlusions in our center. All treatments were performed with the patient under general

anesthesia in an operating room with a biplane angiography system (Allura; Philips Healthcare, Best, Netherlands). No heparin was administered before, during, or after the MT. If no hemorrhagic transformation of the infarct was observed at 24 hours, treatment with 160 mg of aspirin daily was initiated. In the case of carotid stent placement and angioplasty (CSA), before the stent placement, patients were given a single IV load of aspirin (250 mg) until the first imaging follow-up (CT or MR imaging) at 24 hours. In the absence of hemorrhagic transformation, a daily dose of 75 mg of aspirin was then maintained in association with 75 mg of clopidogrel for 3 months. Moreover, blood pressure was strictly monitored and pharmacologically controlled to maintain a systolic blood pressure of <140 mm Hg after revascularization because of the risk of hyperperfusion of the ipsilateral hemisphere.

Analyzed Variables

Clinical variables included demographic data, history of hypertension, dyslipidemia, diabetes, cigarette smoking, baseline NIHSS score, and clinical outcome at 3 months assessed by a stroke neurologist not involved in the initial patient management. Imaging data included the ischemic stroke side, DWI-ASPECTS, intracranial occlusion site (intracranial ICA, MCA, M1 or M2 segment, and/or anterior cerebral artery), occurrence of hemorrhagic transformation, and infarct core extension on the 24-hour postprocedure CT or MR imaging scan. Hemorrhagic transformation was categorized according to the European Cooperative Acute Stroke Study criteria (H-1, H-2, PH-1, and PH-2).¹⁷ Symptomatic intracranial hemorrhage (sICH) was defined as a CT- or MR imaging–documented hemorrhage that occurred within 36 hours after treatment onset and was temporally related to a NIHSS worsening of 4 points. Procedural data included the time between symptom onset and reperfusion (onset-to-reperfusion time); the procedural time (ie, from groin puncture to reperfusion); the administration of IV rtPA; the use of stent retrievers for intracranial occlusions and of angioplasty and/or stent placement for extracranial occlusions; recanalization strategy; the final reperfusion outcome (successful reperfusion defined as TICI 2b/3 score),¹⁸ and procedural complications. These included distal embolus defined as an occlusive embolus in a previously uninvolvement territory, vessel dissection, intraparenchymal hemorrhage, device detachment, and severe vasospasm that needed intra-arterial nimodipine administration. Because the study population was limited, only a comparative analysis of the treatment strategies was conducted (ie, proximal occlusion first strategy versus distal occlusion first strategy) rather than a comparison of the different endovascular techniques (eg, percutaneous transarterial angioplasty only versus stent percutaneous transarterial angioplasty).

In addition, we recorded the following data: prior antiplatelet or anticoagulant therapies, stenosis degree on DSA images (graded as 0 = occlusive plaque, 1 = severe stenotic plaque [$>70\%$ of stenosis], 2 = moderate stenotic plaque with occlusive thrombus [$<70\%$ of stenosis], and 3 = nonstenotic but ulcerated plaque with occlusive thrombus), and the occurrence of extracranial intrastent thrombosis during the first week after the treatment.

Statistical Analysis

Continuous values were expressed as medians and interquartile ranges or as means \pm SD, according to their distribution. Categorical variables were expressed as counts and percentages. Differences between categorical variables were analyzed with the Fisher exact or the Kruskal-Wallis rank sum test. Differences among continuous variables were analyzed with the Student *t* or the Mann-Whitney *U* test according to the results of the normality test. To identify factors contributing to the clinical outcome, we analyzed several covariables in the subgroups of patients with mRS 0–2 versus mRS >2 . A *P* value $< .05$ was considered as statistically significant. Variables with *P* values $< .10$ from the univariate analysis were considered candidate predictors of a favorable/unfavorable outcome and were entered in the multivariate analysis that used a logistic regression model. Patients with atherothrombotic TO were compared with patients with dissection-related TO ($n = 20$) and isolated intracranial occlusion ($n = 201$) from the same data base and the same period. Data on the last 2 groups were previously published.¹⁹ The statistical analyses were performed with R Statistical and Computing Software, Version 3.2.1 (<http://www.r-project.org/>).²⁰

RESULTS

Five hundred eighteen consecutive patients with acute intracranial artery occlusion in the anterior circulation were admitted to our institution and treated with MT during the study period. Among these patients, 66 (12.7%) had an additional atherothrombotic lesion of the extracranial ICA. The demographic, procedural, and outcome data in this group as well as the data of dissection-related TO and isolated intracranial occlusion groups are reported in On-line Table 1. In the atherothrombotic TO group, DSA-based evaluation of the atheromatous carotid lesions showed the presence of grade 0 plaque in 39 (59.1%), grade 1 plaque in 17 (25.8%), grade 2 plaque in 4 (6.1%), and grade 3 plaque in 6 (9.1%) patients. The distributions of the stenosis degree among the subgroups “emergent CSA, proximal occlusion first strategy,” “emergent CSA, distal occlusion first strategy,” “postponed CSA,” and “no CSA” were not statistically different ($P = .09$; the results are reported in On-line Table 2).

Recanalization Strategies

MT was performed in 65 patients (98.5%) with stent retrievers. Aspiration thrombectomy alone was performed in only 1 patient (1.5%), and proximal or distal aspiration thrombectomy was performed concomitantly with stent retrieval in 48 patients (72.7%). Two patients (3%) underwent intracranial stent placement. Extracranial acute balloon angioplasty alone was performed in 19 patients (28.9%). Emergent CSA was achieved in 26 (39.4%) patients among whom proximal occlusion first and distal occlusion first strategies were used in 10 (38.5%) and 16 (61.5%) patients, respectively. In the proximal occlusion first group, the cervical plaques were graded as 1 in 7 (70%) and 2 in 3 (30%) patients. In the distal occlusion first group, the cervical plaques were graded as 1 in 9 (56.3%), 2 in 3 (18.7%), 3 in 2 (12.5%), and 4 in 2 (12.5%) patients. Planned (or postponed) CSA was required in 14 patients (21.2%) 1 week later, with stenosis degree graded as 0 in 9 (64.3%) and 1 in 5 (35.7%) patients.

Table 1: Univariate analysis in the atherothrombotic tandem occlusion group

	mRS 0–2 (<i>n</i> = 27) No. (%) or (Mean)	mRS >2 (<i>n</i> = 38) No. (%) or (Mean)	<i>P</i> Value
Age (yr)	27 (64.6 ± 8.1)	38 (69.2 ± 10.6)	.04
Men	27 (0.9 ± 0.3)	38 (0.9 ± 0.3)	.47
Hypertension	21 (77.8)	27 (71.1)	.58
Cigarette smoking	11 (40.7)	21 (55.3)	.32
Dyslipidemia	19 (70.4)	19 (50)	.13
Diabetes	11 (40.7)	14 (36.8)	.80
Other cardiovascular risk factors	2 (7.4)	9 (23.7)	.11
Left side	13 (48.1)	27 (71.1)	.08
Distal ICA occlusion	8 (29.6)	22 (57.9)	.04
Baseline NIHSS score	27 (14.9 ± 6.3)	38 (18.9 ± 5.2)	.005
Baseline DWI-ASPECTS	27 (7.1 ± 1.7)	37 (6.7 ± 1.5)	.22
IV rtPA	16 (59.3)	24 (63.2)	.80
Onset-reperfusion time (min)	24 (377 ± 147.3)	32 (390.4 ± 173.4)	.93
Procedural time (min)	25 (76.6 ± 39.1)	33 (85.8 ± 48.5)	.49
Number of stent retriever passes	27 (1.9 ± 0.9)	37 (2.5 ± 1.2)	.03
Acute stenting	10 (37)	15 (39.5)	1
Procedural complications	5 (18.5)	17 (44.7)	.04
Ischemic extension	2 (7.4)	19 (50)	<.001
Hemorrhagic transformation	8 (29.6)	23 (60.5)	.02
Subarachnoid hemorrhage	1 (3.7)	4 (10.5)	.39
H-1	3 (11.1)	3 (7.9)	.69
H-2	4 (14.8)	7 (18.4)	.75
PH-1	0 (0)	3 (7.9)	.26
PH-2	0 (0)	7 (18.4)	.04
sICH	0 (0)	10 (26.3)	.004
TICI 2b/3	25 (92.6)	16 (42.1)	<.001

Reperfusion and Safety

TICI 2b/3 reperfusion was significantly associated with shorter procedural times ($P = .03$) and higher rates of distal MCA occlusions ($P = .01$). The onset-reperfusion times were longer in patients with TICI 0–2a scores than in those with TICI 2b/3 scores (449 ± 189 minutes versus 356 ± 137 minutes), but this difference was not significant ($P = .06$). Reperfusion failure was significantly associated with higher infarct core extension ($P = .03$) and sICH ($P = .03$) occurrence. Procedural complications occurred in 22 patients (33.3%). They included the following: acute intrastent thrombosis ($n = 1$, 1.5%), distal embolus ($n = 6$, 9.1%), vessel dissection ($n = 4$, 6.1%), intraparenchymal hemorrhage due to vessel perforation ($n = 2$, 3%), stent-retriever rupture ($n = 1$, 1.5%), and severe vasospasm of the cervical or intracranial arteries that required intra-arterial nimodipine infusion ($n = 8$, 12.1%). Day 1 control imaging showed hemorrhagic transformation in 28 patients (42.4%), of whom 10 (15.2%) were symptomatic and were classified as PH-1 or PH-2. sICH was significantly associated with a history of hypertension ($P = .01$), diabetes ($P = .05$), and reperfusion failure ($P = .03$). In the patients who underwent postponed CSA ($n = 14$), 4 patients had an intrastent thrombosis at follow-up imaging (within 1 week or delayed thrombosis), resulting in 5 intrastent thromboses in our series (20% in acute setting and 80% in a delayed manner). In all 5 patients, TICI 2b/3 reperfusion was achieved. In only 2 patients (40%), intrastent thrombosis was associated with clinical worsening at 3-month follow-up (mRS 4 and 6, respectively).

Clinical Outcome

At 7 days, infarct core extension was observed in 21 patients (31.8%). One patient was lost to 3-month follow-up, leaving 65

patients available for the outcome analysis (Table 1). At the 3-month follow-up, 27 patients (41.5%) were mRS 0–2 and 15 (23.1%) were mRS 6, among whom 13 (20%) died before discharge. Favorable outcome at 3 months was significantly associated with younger age ($P = .04$), lower NIHSS score ($P = .005$), and TICI 2b/3 reperfusion ($P < .001$). Poor clinical outcome was associated with intracranial ICA occlusion ($P = .04$), TICI 0–2a reperfusion ($P < .001$), occurrence of procedural complications ($P = .03$), infarct core extension ($P < .001$), and sICH ($P = .004$) at day 1. The baseline NIHSS score was moderately but significantly correlated with the mRS score at 3 months ($R = 0.36$, $P = .003$), whereas the DWI-ASPECTS was not ($P = .21$). The onset-reperfusion and procedural times did not influence the clinical outcome ($P = .93$ and $P = .49$, respectively). The recanalization strategy did not influence the rates of successful reperfusion ($P = 1$) or of favorable clinical outcome at 3 months ($P = .66$). However, proximal occlusion

first was significantly associated with a higher sICH rate ($P = .01$) at day 1 but did not influence the infarct core extension ($P = .33$). Previous antiplatelet or anticoagulation therapies ($n = 15$) and IV rtPA administration ($n = 40$) did not affect the rates of successful reperfusion, sICH, infarct core extension, or favorable clinical outcome at 3 months. However, previous antiplatelet or anticoagulation therapies ($n = 15$) were associated with higher rates of PH-2 hemorrhages at day 1 ($n = 4$, 26.6% versus $n = 3/51$, 5.9% in patients without these treatments; $P = .04$) (On-line Table 3).

Comparison of the Atherothrombotic TO Group with the Dissection-Related TO and Isolated Intracranial Occlusion Groups

Compared with the dissection-related TO group, patients in the atherothrombotic TO group were significantly older ($P < .001$) and more frequently cigarette smokers ($P = .01$). They had significantly higher proportions of intracranial ICA termination occlusion ($P = .001$) and procedural complications ($P = .05$) and a significantly lower proportion of mRS 0–2 at 3 months ($P = .04$) (On-line Table 4). Compared with the isolated intracranial occlusion group, they were more frequently men ($P < .001$) and cigarette smokers ($P < .001$). They had significantly longer onset-reperfusion times ($P = .05$) and procedural times ($P < .001$), lower TICI 2b/3 reperfusion ($P = .002$), higher complication rates ($P < .001$), and higher sICH rates ($P = .01$), and especially PH-2 hemorrhages ($P = .02$). Patients with atherothrombotic TO also had a markedly lower proportion of those with mRS 0–2 and a higher proportion of those with mRS 6, despite the lack of statistical significance (On-line Table 5).

Table 2: Multivariate analysis of good clinical outcome predictors

Groups, Variables	Odds Ratio	95% Lower CI	95% Upper CI	P Value
ATO				
Age	0.93	0.85	1.00	.07
Baseline NIHSS score	0.89	0.79	1.00	.06
Intracranial ICA occlusion	0.39	0.09	1.63	.20
Periprocedural complications	0.15	0.03	0.74	.02
TICI 2b/3	17.76	2.90	108.81	.002
IICO ^a				
Age	0.95	0.93	0.98	<.001
Baseline NIHSS score	0.91	0.85	0.97	.004
Intracranial ICA occlusion	1.33	0.63	2.83	.45
Periprocedural complications	1.36	0.50	3.70	.55
TICI 2b/3	3.57	1.48	8.61	.005

Note:—ATO indicates atherothrombotic tandem occlusion; IICO, isolated intracranial occlusion.

^a Previously published.¹⁹

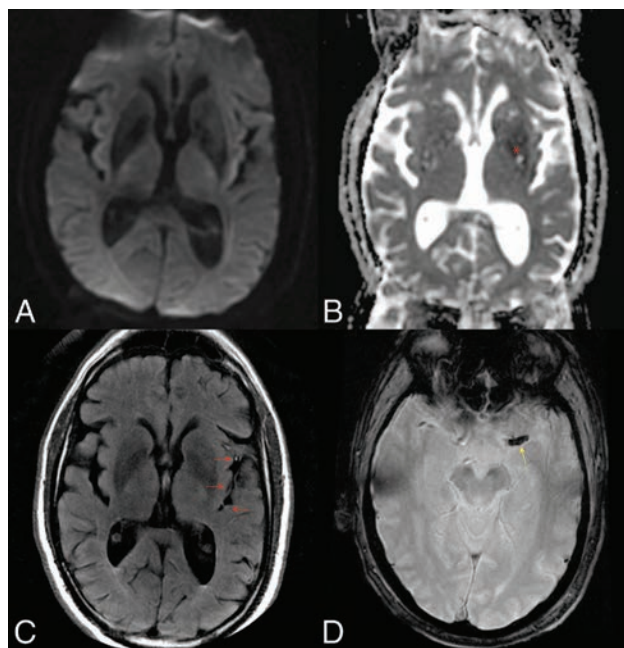


FIG 2. Baseline MR imaging. A 69-year-old patient was admitted for a left middle cerebral artery ischemic stroke, with an NIHSS score of 18 at 3 hours after symptom onset. The DWI and ADC maps (A and B, red asterisk) showed a limited infarct core of the lenticular nucleus, negative findings on FLAIR, and a clot in the M1 segment of the artery with susceptibility artifacts on the T2 echo gradient (D, yellow arrow) acquisition. Some evidence of slow flow was also visible on FLAIR as sulcal hypersignals (C, red arrows).

Due to the small number of patients in the dissection-related TO group, a multivariate logistic regression analysis was performed for only the atherothrombotic TO and isolated intracranial occlusion groups (Table 2). In the atherothrombotic TO group, only procedural complications ($P = .02$) and TICI 2b/3 reperfusion ($P = .002$) were independent predictors of favorable clinical outcome at 3 months. Whereas in the isolated intracranial occlusion group, only younger age ($P < .001$), baseline NIHSS score ($P = .004$), and TICI 2b/3 reperfusion ($P = .005$) were independent predictors of favorable clinical outcome at 3 months.

Figs 2–4 illustrate a case of AIS due to an atherothrombotic TO. In On-line Fig 1, the main results are reported as a flow chart.

DISCUSSION

The available data on TOs treated with MT are limited due to their low incidence, the heterogeneity of TO etiologies, and treatment strategies in the reported case series. In this study, we analyzed a relatively large series of patients with solely atherothrombotic TO treated with MT in terms of reperfusion rate, safety, and clinical outcome as well as the predictors of favorable outcome in this group. Then we compared this group with patients with dissection-related TOs or with isolated intracranial occlusions from the same AIS data base during the same period.

Two important elements emerge from our study. Our results are in good agreement with previously reported findings.^{7,13–16} Despite its retrospective feature, our rigorous methodologic approach strongly supports the previously suggested idea that atherothrombotic TOs represent a peculiar and different nosologic entity of AIS compared with dissection-related TOs and isolated intracranial occlusions. Indeed, despite comparable baseline NIHSS and DWI–ASPECTS distributions, patients with atherothrombotic TO were significantly older and more frequently smokers than patients with dissection-related TOs. They presented globally with more cardiovascular risk factors. Second, atherothrombotic TOs represent an important technical challenge that affects more dramatically the clinical outcome than isolated intracranial occlusions and dissection-related TOs. This is highlighted by the significantly longer procedural times, lower rates of successful reperfusion, and lower rates of favorable clinical outcomes in this group. This might be partly explained by the significantly higher rate of intracranial ICA occlusion and the higher global burden of procedural complications in the atherothrombotic TO group. The first is often associated with bigger clots (ie, technically difficult to retrieve) and an increased probability of collateral circulation impairment due to decreased flow in the anterior cerebral artery. The multivariate analysis supported these results by showing that in patients with atherothrombotic TO, procedural complications ($OR = 0.15$, $P = .02$) and TICI 2b/3 reperfusion ($OR = 17.76$, $P = .002$) were the 2 key elements independently predictive of favorable outcome at the 3-month follow-up.

In our study, the distinction of TOs according to their etiologies revealed a higher rate of complications (33%) compared to that previously reported in large series (from 0% to 21.6%). Whereas in dissection-related TOs group, the complication rate was markedly lower (Table 3).^{7,13–15,21–27} This finding might be due to the design of previous analyses and because we also included severe vasospasms needing the intra-arterial administration of nimodipine. However, in this work, the different patient subgroups were homogeneous, whereas the previously reported studies mostly combined different types of TOs with various ratios of atherothrombotic-/dissection-related TOs. This latter methodologic approach could be confusing and a source of bias in the analysis of populations as well as in the evaluation and devel-

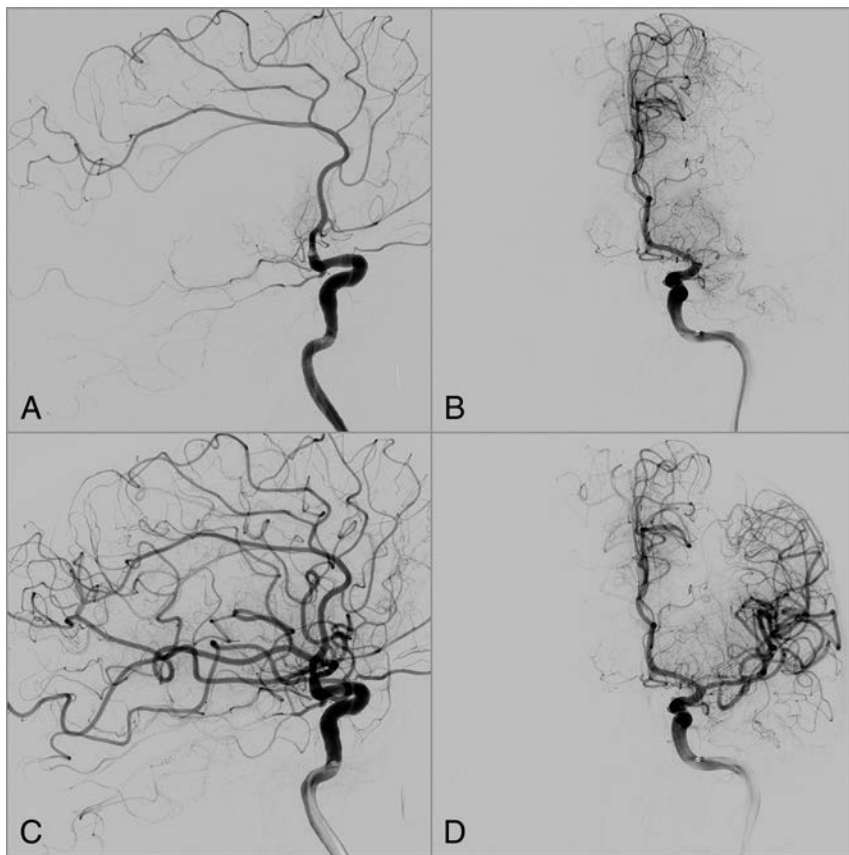


FIG 3. DSA of intracranial reperfusion. The same patient as in Fig 2 underwent mechanical thrombectomy following a distal occlusion first recanalization strategy. The figure shows the angiogram of the intracranial vasculature of left internal carotid artery before and after MT with a stent retriever. Before MT (A and B), the angiogram shows the occlusion of left middle cerebral artery (segment M1) with a TIC1 score of 0 and a poor pial collaterality from the anterior cerebral artery. MT allowed complete reperfusion of the MCA territory with a TIC1 score of 3 (C and D) without any distal emboli.

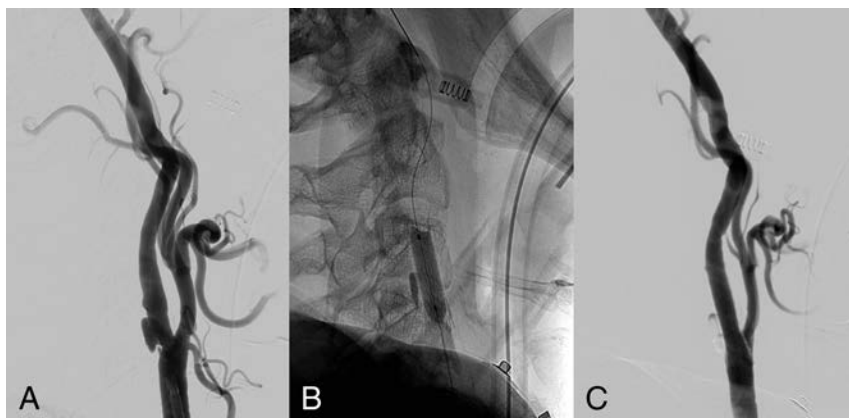


FIG 4. DSA of proximal carotid treatment. After full reperfusion of the intracranial occluded vessel, the patient underwent a stent placement and angioplasty of the extracranial carotid artery. The DSA shows an ulcerated atherosclerotic plaque of the carotid bulb before the treatment (A). After the angioplasty (B), a full recanalization of the vessel was achieved (C).

opment of new management strategies. Indeed, it leads to an inappropriate averaging of the results.

There is no consensus concerning the recanalization sequence strategy for TOs. Both proximal occlusion first and distal occlusion first approaches have their variations, advantages, and shortcomings.^{7,21,26} In our series, the technique was chosen by the

operator on the basis of the proximal lesion and varied with the improvement and availability of new endovascular techniques. Therefore and given the limited number of patients, our work was not able to address this point. However, the proximal occlusion first approach was significantly associated with markedly higher rates of sICH and, less significantly, with infarct core extension at day 1 compared with the distal occlusion first approach. Conversely, both approaches did not differ in the rates of reperfusion and favorable outcome at 3 months.

Atherothrombotic tandem occlusions represent an important technical challenge that affects, more dramatically, the clinical outcome than dissection-related tandem occlusions and isolated intracranial occlusions. This is clearly highlighted by the significantly longer procedural times, lower recanalization rates, and higher global burden of procedural complications in this group. Therefore, alternative therapeutic approaches may be discussed. Few authors proposed emergent endarterectomy for patients with AIS.²⁸ However, their results remain confidential and concerned limited numbers of patients ($n = 6$) with a high risk of fatal hemorrhagic transformation. Similarly, the use of abciximab for intrastent thrombosis has been suggested by other authors.²⁹ We did not use this drug in our patients with intrastent thrombosis because of the high risk of hemorrhagic transformation previously reported.³⁰

Most interesting, in the atherothrombotic TO group, IV rtPA administration did not affect the rate of successful reperfusion and of hemorrhagic transformation or the outcome at 3 months. Although this work does not allow us to draw any conclusions, given the previously mentioned limitations, this observation questions the benefit of IV rtPA in this specific group of patients. Conversely, antiplatelet and/or anticoagulant drugs before AIS significantly

increased the occurrence of PH-2 hemorrhages at day 1 ($P = .04$). These treatments should be considered with caution, especially in the postoperative management of these patients, to prevent the risk of intracranial bleeding.

Our findings are in good agreement with the HERMES collaboration group meta-analysis¹⁶ in term of good clinical outcome at

Table 3: Summary of previously published tandem occlusion series

Authors, Year Published	Patients (No.)	% of TO Etiologies ^a	TICI 2b/3 or TIMI 2–3	mRS ≤2	mRS 6	sICH	Periprocedural Complications
Malik et al, 2011 ²¹	77	100/0/0/0	58.0 (75.3) ^b	32.0 (41.6)	18.0 (23.4)	8.0 (10.4)	NA
Kwak et al, 2013 ²	35	100/0/0/0	26.0 (74.3)	22.0 (62.9)	4.0 (11.4)	1.0 (2.9)	0.0 (0.0)
Stampfl et al, 2014 ²³	24	100/0/0/0	15.0 (62.5)	7.0 (29.2)	4.0 (16.7)	4.0 (16.7)	1.0 (4.2)
Maurer et al, 2015 ²⁴	43	77/7/0/6	33.0 (76.7)	14.0 (32.6)	9.0 (20.9)	5.0 (11.6)	1.0 (2.3)
Cohen et al, 2015 ²⁵	24	100/0/0/0	19.0 (79.2)	13.0 (54.2)	2.0 (8.3)	0.0 (0.0)	0.0 (0.0)
Lockau et al, 2015 ⁷	37	65/35/0/0	27.0 (73.0)	17.0 (45.9)	7.0 (18.9)	4.0 (10.8)	8.0 (21.6)
Spiotta et al, 2015 ²⁶	16	100/0/0/0	16.0 (100.0)	8.0 (50.0)	3.0 (18.8)	2.0 (12.5)	0.0 (0.0)
Lescher et al, 2015 ¹³	39	28/18/54/0	25.0 (64.1)	14.0 (35.9)	4.0 (10.3)	4.0 (10.3)	0.0 (0.0)
Behme et al, 2015 ²⁷	170	100/0/0/0	130.0 (76.5)	62.0 (36.5)	32.0 (18.8)	15.0 (8.8)	NA
Grigoryan et al, 2016 ¹⁵	100	89/11/0/0	88.0 (88.0)	42.0 (42.0)	20.0 (20.0)	NA	NA
Fahed et al, 2016 ¹⁴	70	54/19/19/8	47.0 (67.1)	33.0 (47.1)	9.0 (13.4)	NA	12.0 (17.1)
This series	86	77/23/0/0	56.0 (65.1)	41.0 (48.2)	17.0 (20.0)	11.0 (12.8)	24.0 (27.9)
Atherothrombotic TOs	66		42.0 (63.6)	27.0 (41.5)	15.0 (23.1)	10.0 (15.2)	22.0 (33.3)
Dissecting TOs ¹⁹	20		14.0 (70.0)	14.0 (70.0)	2.0 (10.0)	1.0 (5.0)	2.0 (10.0)

Note:—NA indicates non-available data; TIMI, Thrombolysis in Myocardial Infarction.

^a Distribution of the TO etiologies in percentages: atheromatous/dissection/cardioembolic/other causes.

^b Recanalization assessed with the TIMI score.

3 months (mRS 0–2 = 45.9% in the HERMES analysis versus 41.5% in our cohort). However, our analysis differs from that in the HERMES meta-analysis as well as in previous studies reporting, specifically, experiences in the endovascular management of tandem occlusions in that we compared the atherothrombotic tandem occlusions with dissection-related tandem occlusions and isolated intracranial occlusions. This work provides new knowledge on TO pathology comprehension, which should help in patient management and future study designs. Indeed, the different pathomechanisms of extracranial ICA lesions involved in TOs could call for specific selection criteria and different recanalization strategies according to the TO etiology.

Our work has several limitations. It was a retrospective study with limited number of patients, though data were collected prospectively and consecutively. As a single-center study, our work has an inherent population bias. Therefore, our results cannot be generalized, though this is the largest reported series of atherothrombotic TOs selected by MR imaging, to our knowledge. Moreover, our work does not allow concluding on the safety of emergent carotid angioplasty and stent placement because of the small number of treated patients. However, intrastent thrombosis occurred more frequently in patients stented at the acute setting and was clinically symptomatic in 40% of them with poor clinical outcomes. The grading scale of the proximal ICA stenosis due to atherosclerotic plaque was arbitrary, defined to facilitate the analysis and make the results clearer. However, an underestimation of the grade 2 plaques and an overestimation of the grade 3 plaques cannot be excluded because of the potential iatrogenic ulceration that can be induced during the crossing of the proximal occlusion site.

CONCLUSIONS

Atherothrombotic TOs are a particularly complex and challenging cause of AIS. Compared with dissection-related TOs and isolated intracranial occlusions, they are associated with significantly lower successful reperfusion rates, lower favorable outcomes, and higher rates of procedural complications. Our results support the need to differentiate TOs according to their etiology when designing prospective studies on AIS management. The results of future trials and multicenter studies on specifically this stroke subpopulation are eagerly awaited.

Disclosures: Omer F. Eker—UNRELATED: Consultancy: Stryker; Payment for Educational Presentations: Covidien; Payment for Development of Educational Presentations: Covidien, Medtronic, Stryker. Vincent Costalat—UNRELATED: Grants/Grants Pending: Medtronic; Consultancy: Sequent Medical, Balt, Codman, Stryker; Payment for Lectures (including Service on Speakers Bureaus): Stryker, Balt; Payment for Development of Educational Presentations: Covidien, Stryker, Medtronic. Alain Bonafé—UNRELATED: Consultancy: Medtronic, Stryker, Covidien, ev3; Grants/Grants Pending: Covidien*. *Money paid to the institution.

REFERENCES

- Berkhemer OA, Fransen PS, Beumer D, et al. **A randomized trial of intraarterial treatment for acute ischemic stroke.** *N Engl J Med* 2015; 372:11–20 CrossRef Medline
- Saver JL, Goyal M, Bonafé A, et al; SWIFT PRIME Investigators. **Stent-retriever thrombectomy after intravenous t-PA vs. t-PA alone in stroke.** *N Engl J Med* 2015;372:2285–95 CrossRef Medline
- Goyal M, Demchuk AM, Menon BK, et al; ESCAPE Trial Investigators. **Randomized assessment of rapid endovascular treatment of ischemic stroke.** *N Engl J Med* 2015;372:1019–30 CrossRef Medline
- Campbell BC, Mitchell PJ, Kleinig TJ, et al; EXTEND-IA Investigators. **Endovascular therapy for ischemic stroke with perfusion-imaging selection.** *N Engl J Med* 2015;372:1009–18 CrossRef Medline
- Jovin TG, Chamorro A, Cobo E, et al; REVASCAT Trial Investigators. **Thrombectomy within 8 hours after symptom onset in ischemic stroke.** *N Engl J Med* 2015;372:2296–306 CrossRef Medline
- Adams HP Jr, Bendixen BH, Kappelle LJ, et al. **Classification of subtype of acute ischemic stroke: definitions for use in a multicenter clinical trial—TOAST. Trial of Org 10172 in Acute Stroke Treatment.** *Stroke* 1993;24:35–41 CrossRef Medline
- Lockau H, Liebig T, Henning T, et al. **Mechanical thrombectomy in tandem occlusion: procedural considerations and clinical results.** *Neuroradiology* 2015;57:589–98 CrossRef Medline
- Benninger DH, Georgiadis D, Kremer C, et al. **Mechanism of ischemic infarct in spontaneous carotid dissection.** *Stroke* 2004;35: 482–85 CrossRef Medline
- Kim YS, Garami Z, Mikulik R, et al. **Early recanalization rates and clinical outcomes in patients with tandem internal carotid artery/middle cerebral artery occlusion and isolated middle cerebral artery occlusion.** *Stroke* 2005;36:869–71 CrossRef Medline
- Rubiera M, Ribo M, Delgado-Mederos R, et al. **Tandem internal carotid artery/middle cerebral artery occlusion: an independent predictor of poor outcome after systemic thrombolysis.** *Stroke* 2006;37: 2301–05 CrossRef Medline
- Blinic A, Francis CW. **Transport processes in fibrinolysis and fibrinolytic therapy.** *Thromb Haemost* 1996;76:481–91 Medline
- Molina CA, Montaner J, Arenillas JF, et al. **Differential pattern of tissue plasminogen activator-induced proximal middle cerebral ar-**

- tery recanalization among stroke subtypes. *Stroke* 2004;35:486–90 CrossRef Medline
13. Lescher S, Czeppan K, Porto L, et al. **Acute stroke and obstruction of the extracranial carotid artery combined with intracranial tandem occlusion: results of interventional revascularization.** *Cardiovasc Intervent Radiol* 2015;38:304–13 CrossRef Medline
 14. Fahed R, Redjem H, Blanc R, et al. **Endovascular management of acute ischemic strokes with tandem occlusions.** *Cerebrovasc Dis* 2016;41:298–305 CrossRef Medline
 15. Grigoryan M, Haussen DC, Hassan AE, et al. **Endovascular treatment of acute ischemic stroke due to tandem occlusions: large multicenter series and systematic review.** *Cerebrovasc Dis* 2016;41:306–12 CrossRef Medline
 16. Goyal M, Menon BK, van Zwam WH, et al; HERMES collaborators. **Endovascular thrombectomy after large-vessel ischaemic stroke: a meta-analysis of individual patient data from five randomised trials.** *Lancet* 2016;387:1723–31 CrossRef Medline
 17. Hacke W, Kaste M, Fieschi C, et al. **Intravenous thrombolysis with recombinant tissue plasminogen activator for acute hemispheric stroke: the European Cooperative Acute Stroke Study (ECASS).** *JAMA* 1995;274:1017–25 CrossRef Medline
 18. Zaidat OO, Yoo AJ, Khatri P, et al; Cerebral Angiographic Revascularization Grading (CARG) Collaborators, STIR Revascularization working group, STIR Thrombolysis in Cerebral Infarction (TICI) Task Force. **Recommendations on angiographic revascularization grading standards for acute ischemic stroke: a consensus statement.** *Stroke* 2013;44:2650–63 CrossRef Medline
 19. Marnat G, Mourand I, Eker O, et al. **Endovascular management of tandem occlusion stroke related to internal carotid artery dissection using a distal to proximal approach: insight from the RECOIST study.** *AJNR Am J Neuroradiol* 2016;37:1281–88 CrossRef Medline
 20. Team RC. *R: A Language and Environment for Statistical Computing*. Vienna: R Foundation for Statistical Computing; 2017
 21. Malik AM, Vora NA, Lin R, et al. **Endovascular treatment of tandem extracranial/intracranial anterior circulation occlusions: preliminary single-center experience.** *Stroke* 2011;42:1653–57 CrossRef Medline
 22. Kwak HS, Hwang SB, Jin GY, et al. **Predictors of functional outcome after emergency carotid artery stenting and intra-arterial thrombolysis for treatment of acute stroke associated with obstruction of the proximal internal carotid artery and tandem downstream occlusion.** *AJNR Am J Neuroradiol* 2013;34:841–46 CrossRef Medline
 23. Stampfl S, Ringleb PA, Möhlenbruch M, et al. **Emergency cervical internal carotid artery stenting in combination with intracranial thrombectomy in acute stroke.** *AJNR Am J Neuroradiol* 2014;35:741–46 CrossRef Medline
 24. Maurer CJ, Joachimski F, Berlis A. **Two in one: endovascular treatment of acute tandem occlusions in the anterior circulation.** *Clin Neuroradiol* 2015;25:397–402 CrossRef Medline
 25. Cohen JE, Gomori JM, Rajz G, et al. **Extracranial carotid artery stenting followed by intracranial stent-based thrombectomy for acute tandem occlusive disease.** *J Neurointerv Surg* 2015;7:412–17 CrossRef Medline
 26. Spiotta AM, Lena J, Vargas J, et al. **Proximal to distal approach in the treatment of tandem occlusions causing an acute stroke.** *J Neurointerv Surg* 2015;7:164–69 CrossRef Medline
 27. Behme D, Mpotsaris A, Zeyen P, et al. **Emergency stenting of the extracranial internal carotid artery in combination with anterior circulation thrombectomy in acute ischemic stroke: a retrospective multicenter study.** *AJNR Am J Neuroradiol* 2015;36:2340–45 CrossRef Medline
 28. Sbarigia E, Toni D, Speziale F, et al. **Emergency and early carotid endarterectomy in patients with acute ischemic stroke selected with a predefined protocol: a prospective pilot study.** *Int Angio* 2003;22:426–30 Medline
 29. Abciximab Emergent Stroke Treatment Trial (AbESTT) Investigators. **Emergency administration of abciximab for treatment of patients with acute ischemic stroke: results of a randomized phase 2 trial.** *Stroke* 2005;36:880–90 CrossRef Medline
 30. Heck DV, Brown MD. **Carotid stenting and intracranial thrombectomy for treatment of acute stroke due to tandem occlusions with aggressive antiplatelet therapy may be associated with a high incidence of intracranial hemorrhage.** *J Neurointerv Surg* 2015;7:170–75 CrossRef Medline

Real-Time Motor Cortex Mapping for the Safe Resection of Glioma: An Intraoperative Resting-State fMRI Study

 T.-m. Qiu,  F.-y. Gong,  X. Gong,  J.-s. Wu,  C.-p. Lin,  B.B. Biswal,  D.-x. Zhuang,  C.-j. Yao,  X.-l. Zhang,  J.-f. Lu,  F.-p. Zhu,  Y. Mao, and  L.-f. Zhou



ABSTRACT

BACKGROUND AND PURPOSE: Resting-state functional MR imaging has been used for motor mapping in presurgical planning but never used intraoperatively. This study aimed to investigate the feasibility of applying intraoperative resting-state functional MR imaging for the safe resection of gliomas using real-time motor cortex mapping during an operation.

MATERIALS AND METHODS: Using interventional MR imaging, we conducted preoperative and intraoperative resting-state intrinsic functional connectivity analyses of the motor cortex in 30 patients with brain tumors. Factors that may influence intraoperative imaging quality, including anesthesia type (general or awake anesthesia) and tumor cavity (filled with normal saline or not), were studied to investigate image quality. Additionally, direct cortical stimulation was used to validate the accuracy of intraoperative resting-state fMRI in mapping the motor cortex.

RESULTS: Preoperative and intraoperative resting-state fMRI scans were acquired for all patients. Fourteen patients who successfully completed both sufficient intraoperative resting-state fMRI and direct cortical stimulation were used for further analysis of sensitivity and specificity. Compared with those subjected to direct cortical stimulation, the sensitivity and specificity of intraoperative resting-state fMRI in localizing the motor area were 61.7% and 93.7%, respectively. The image quality of intraoperative resting-state fMRI was better when the tumor cavity was filled with normal saline ($P = .049$). However, no significant difference between the anesthesia types was observed ($P = .102$).

CONCLUSIONS: This study demonstrates the feasibility of using intraoperative resting-state fMRI for real-time localization of functional areas during a neurologic operation. The findings suggest that using intraoperative resting-state fMRI can avoid the risk of intraoperative seizures due to direct cortical stimulation and may provide neurosurgeons with valuable information to facilitate the safe resection of gliomas.

ABBREVIATIONS: BOLD = blood oxygen level–dependent; DCS = direct cortical stimulation; iMRI = intraoperative MR imaging; iR-fMRI = intraoperative resting-state fMRI; pR-fMRI = preoperative resting-state fMRI; R-fMRI = resting-state fMRI

Mapping the motor cortex before and during tumor resection is of great importance to minimize the risks of postoperative neurologic sequelae. Direct cortical stimulation (DCS) is an invasive procedure to locate the function of specific brain regions. Due to its simplicity, DCS is considered the clinical criterion standard for mapping brain function and has demonstrated efficacy

in optimizing glioma resection.^{1,2} However, as an invasive approach, DCS requires a surgical team with rich experience. DCS also has the risk of after discharges, which can induce seizures and result in the inaccurate localization of cortical areas.³

Blood oxygen level–dependent (BOLD) functional MR imaging, a task-based brain functional mapping method, has been


Received February 3, 2017; accepted after revision June 25.


From the Department of Neurological Surgery (T.-m.Q., F.-y.G., X.G., J.-s.W., D.-x.Z., C.-j.Y., X.-l.Z., J.-f.L., F.-p.Z., Y.M., L.-f.Z.), Huashan Hospital, Shanghai Medical College, Fudan University, Shanghai, China; Center for Computational Systems Biology (C.-p.L.), Fudan University, Shanghai, China; and Department of Biomedical Engineering (B.B.B.), New Jersey Institute of Technology, Newark, New Jersey.


Tian-ming Qiu and Fang-yuan Gong contributed equally to this article.

This work was funded by the National Natural Science Foundation of China (grant No. 81401546, 81671308, 81672476), Natural Science Foundation and Major Basic Research Program of Shanghai (grant No. 16JC1420100), and National Key Technology R&D Program of China (grant No. 2014BAI04B05).

Please address correspondence to Liang-fu Zhou, MD, Shanghai Neurosurgical Center, Neurological Surgery Department, Huashan Hospital, Shanghai Medical College, Fudan University, No. 12, Wulumuqi Zhong Rd, Shanghai, 200040, P. R. China; e-mail: lfzhouc@126.com; Dong-xiao Zhuang, MD, PhD, Shanghai Neurosurgical Center, Neurological Surgery Department, Huashan Hospital, Shanghai Medical School, Fudan University, No. 12, Wulumuqi Zhong Rd, Shanghai, 200040, P. R. China; e-mail: ernestzdx@163.com

 Indicates open access to non-subscribers at www.ajnr.org

 Indicates article with supplemental on-line tables.

 Indicates article with supplemental on-line photos.

<http://dx.doi.org/10.3174/ajnr.A5369>

well-established for localizing the brain functional area for pre-surgical planning. BOLD fMRI is of great importance in helping decrease morbidity due to a neurologic operation⁴ and has been integrated into neuronavigation systems to localize the motor area during an operation.⁵ Nonetheless, brain shifting during an operation might reduce the accuracy of preoperative imaging and affect the clinical consequences.⁶

The emergence of intraoperative MR imaging (iMRI) has ushered in a new era in brain tumor neurosurgery.⁷ Real-time structural imaging and diffusion tensor imaging have provided neurosurgeons with valuable information regarding whether and where tumor residues persist after resection and even the relationship between the tumor/tumor cavity and peritumoral tracts.^{8,9} The use of an iMRI navigation system can reliably compensate for the effects of brain shifting.⁶ We have recently reported intraoperative motor mapping with fMRI for the first time; in this procedure, awake intraoperative fMRI was used to localize the sensorimotor areas during awake craniotomy.¹⁰ Cooperation of the patient under specific tasks and complicated surgical procedures is essential for successful mapping. Therefore, task-induced brain mapping cannot be achieved with the patient under general anesthesia.

Resting-state fMRI (R-fMRI) has recently been used to identify the motor cortex without a task stimulus.¹¹ This technique has been used in preoperative motor mapping in patients with brain tumors.¹²⁻¹⁴ Our previous study demonstrated the accuracy of preoperative R-fMRI (pR-fMRI) for motor area localization by DCS before tumor resection.¹³ However, the study was based on pR-fMRI and lacked real-time information regarding the relationship between the tumor cavity/residual and the motor cortex, which might have affected the conclusion of whether further resection is safe.

To our knowledge, functional connectivity based on intraoperative resting-state fMRI (iR-fMRI) has not been applied to real-time motor cortex mapping during an operation. The purpose of this study was to investigate the feasibility and validity of applying iR-fMRI to neurosurgical mapping. The sensitivity and specificity of iR-fMRI in mapping the motor cortex were assessed and compared with those of DCS. The optimum iR-fMRI protocol for better intraoperative imaging quality was also studied.

MATERIALS AND METHODS

General Information

The study examined 30 patients with cerebral tumors involving the motor cortical areas. The patients were recruited and enrolled in this study by the Neurologic Surgery Department at Huashan Hospital, Shanghai. The study was reviewed and approved by the institutional review board of Huashan Hospital.

The patients included 19 men and 11 women 19–70 years of age. The inclusion criteria were as follows: 1) patients with a single lesion and first operation, 2) tumor lesions in the frontal or parietal lobe near (or involving) the precentral gyrus, and 3) no contraindications for MR imaging or intraoperative electrophysiologic monitoring. The exclusion criteria were as follows: 1) recurrent tumors, 2) contraindications to MR imaging or intraoperative electrophysiologic monitoring, 3) preoperative muscle

strength at 0°, and 4) an inability to comply with safety screening requirements during intraoperative MR imaging screening. Each patient's muscle strength was recorded before the operation and within 3 months after it. Muscle function was evaluated and assigned a grade according to the scale of 0–5.

MR Imaging Data Acquisition

Preoperative and intraoperative images were acquired with a 3T interventional MR imaging scanner (Trio; Siemens, Erlangen, Germany) at Huashan Hospital. Preoperative images were obtained 1–2 days before the date of the operation. Enhanced T1-weighted images were acquired to differentiate patients with high- or low-grade gliomas with the following imaging parameters: TR = 1900 ms; TE = 2.93 ms; flip angle = 90°; section number = 176; section thickness = 1 mm; and FOV = 250 × 219 mm. The T2-weighted fluid-attenuated inversion recovery images were acquired with multishot TSE sequences with TR = 9000 ms, TE = 99 ms, TI = 2500 ms, flip angle = 150°, section number = 66, section thickness = 2 mm, and FOV = 240 × 214 mm.

The R-fMRI scans were obtained with a T2-weighted gradient-echo-planar imaging sequence with TR/TE = 2000/35 ms, flip angle = 90°, matrix size = 64 × 64, FOV = 240 × 240/210 × 210 mm (preoperative/intraoperative), 33/25 (preoperative/intraoperative) interleaved axial sections oriented along the anterior/posterior commissure line without intersection gap, and 240 continuous image volumes. The participants were instructed to relax, keep their eyes closed without falling asleep, and not think of anything.

Intraoperative MR Imaging Environment

All the operations were performed in a 3T iMRI-integrated operating room (IMRIS, Winnipeg, Manitoba, Canada) at a constant temperature of 20°–21°C. Because the intraoperative imaging process has been detailed in our previous article, it is only briefly described here.⁹ The patient's head was fixed with an MR imaging-safe head holder before the craniotomy. DCS was used to localize the motor cortex after opening the dura. Sodium valproate was used to prevent seizures. After tumor resection and wound draping, the scanner was moved into the operation room. In the cases that required further resection, the navigational images were updated with iMRI datasets.

To optimize the image quality, we studied factors that may influence intraoperative imaging quality, including anesthesia type and whether the tumor cavity was filled with normal saline during scanning. Twelve of the 30 patients underwent general anesthesia, and the other 18 patients underwent awake anesthesia. General anesthesia was administered intravenously using remifentanyl as an analgesic and propofol as a sedative via endotracheal intubation. The 18 patients who underwent awake anesthesia were administered midazolam for sedation combined with local nerve block anesthesia with remifentanyl as an analgesic and propofol as a sedative. For the tumor cavity process, 12 patients' tumor cavities were filled with normal saline and covered with wet gauze. The tumor cavities of the other 18 patients were only covered with wet gauze without filling.

Intraoperative DCS

DCS was performed by using a Multifunctional Neurologic Workstation (Epoch XP; Axon Systems, Hauppauge, New York) to locate the motor cortex in all 30 patients before tumor resection. The electric current was increased gradually from 2 to 6 mA in 1-mA increments. After discharge, the current was decreased by 0.5–1 mA. During the stimulation process, the compound muscle action potentials were monitored, including those from the abductor pollicis brevis, brachioradialis, triceps, biceps, tibialis anterior, gastrocnemius, and orbicularis oris muscles.

When the compound muscle action potentials or passive movements of the target muscle occurred, the representative area in the cortex corresponding to the movement was identified and noted with a sterile tag. A 10×10 mm area on the exposed cortical surface was considered 1 unit of stimulation. The corresponding motor sites in structural images were then recorded by a navigation system (TRIA i7; Medtronic Navigation, Minneapolis, Minnesota).

R-fMRI Data Processing

The fMRI datasets were preprocessed and analyzed by Data Processing Assistant for Resting-State fMRI, Advanced Edition (Beijing Normal University, Beijing, China),¹⁵ Resting-State fMRI Data Analysis Toolkit (Beijing Normal University),¹⁶ and SPM8 (<http://www.fil.ion.ucl.ac.uk/spm/software/spm12>). The results were visualized with XjView 8 (<http://www.alivelearn.net/xjview>).

pR-fMRI were preprocessed by removal of the first 10 time points. This process was followed by section-timing correction, realignment, registration, smoothing, and detrending to reduce the impact of the magnetic field environment or patient instability on the images. A temporal bandpass filter ($0.01 \text{ Hz} < f < 0.08 \text{ Hz}$) was then applied to remove low-frequency drifts and high-frequency noise. The spurious BOLD variances unlikely to reflect neuronal activity were regressed. These variances included signals from the CSF, white matter, and whole brain, as well as the 6 parameters obtained by rigid-body head motion correction.¹⁷

A 3-mm-diameter seed mask was placed in the hand-knob area of the healthy (nontumor) side,¹⁸ which was identified from high-resolution structural MR imaging and confirmed as a landmark of the precentral gyrus of the brain under normal or disease conditions.¹⁹ Functional connectivity was computed between the selected seed masks, from which time-series signals were averaged and correlated with every voxel in the brain. The threshold and spatial extent of activation corresponding to this threshold were determined by a neuroradiologist. This process was performed by maximizing the functional neuronal activity while minimizing nonspecific noise patterns.¹²

iR-fMRI processing was identical to the pR-fMRI processing. However, because the patient's head was fixed in the holder, motion-induced signal changes were minimal. We required approximately 15 minutes on average to process the data immediately after scanning. During this 15-minute period, we moved the scanner out, redraped the patient, and updated the intraoperative navigation images.

Statistical Analyses

Data analysis was performed by using PASW18.0 statistical software (IBM, Armonk, New York). DCS-positive sites were labeled on iMRI structural images for motor-related tags and were used for comparison. We regarded the following DCS results as “unsatisfactory”: 1) Seizure occurred, and intraoperative mapping was stopped; 2) the intracranial pressure was high after opening the dura; therefore, we only stimulated the cortex corresponding to the potential motor area and did not stimulate all the sites within the exposed cortical surface; and 3) both DCS and R-fMRI had negative results within the exposed cortical surface.

To optimize the imaging quality, we grouped and compared patients with different anesthesia types and tumor cavity fillings. We regarded the following R-fMRI results as showing “unsatisfactory” image quality: 1) A highly correlated functional connectivity map was found in the ventricle, tumor/tumor cavity, or scalp; and 2) obvious irrational motor functional connectivity was found. The Fisher exact test was used to assess differences in image quality by scanning situation. A value of .05 indicated significance.

We chose the cases with satisfactory fMRI and DCS results to calculate the sensitivity and specificity of iR-fMRI. A match was identified when a significant overlap between the 10×10 mm scope around the DCS-positive sites and functional areas was observed on the fMRI. For each patient, a 10×10 mm area on the exposed cortical surface was considered 1 unit for analysis. For each case, with the DCS-positive sites as references, we calculated the number of true-positive, true-negative, false-positive, and false-negative tags. Each cortical site on the DCS map was considered independently. A method for analyzing clustered binary data was used to calculate the sensitivity and specificity of iR-fMRI. This method was developed by Bizzi et al.²⁰ and Roux et al.²¹

RESULTS

All 30 patients underwent preoperative and intraoperative MR imaging and DCS (On-line Table 1). Overall, 27 (of 30) patients had satisfactory pR-fMRI motor mapping, and 21 (of 30) patients had satisfactory iR-fMRI motor mapping. The 9 patients with unsatisfactory iR-fMRI included 3 patients with a highly correlated functional connectivity map found in the tumor/tumor cavity or scalp (cases 4, 11, and 17), 5 patients with obvious irrational motor functional connectivity (cases 10, 13, 15, 16, and 23), and 1 patient with both of the above situations (case 28). Motor mapping with DCS was achieved in 18 cases without high intracranial pressure after craniotomy and no seizures during mapping. Fourteen patients who successfully completed both sufficient iR-fMRI and DCS were used for further analysis to determine the sensitivity and specificity. We listed all the DCS and iR-fMRI results for each site on the exposed cortical surface for each case. On the basis of the clustered binary data above, we constructed a 4-fold table (On-line Table 2) with the sum from true-positives, true-negatives, false-positives, and false-negatives (Table) and then calculated the sensitivity and specificity. The sensitivity and specificity of iR-fMRI were 61.7% (95% CI, 49.02%–72.91%) and 93.7% (95% CI, 88.74%–96.53%), respectively (Table and On-line Table 1).

Comparison of the results from iR-fMRI and DCS for 14 of the 30 patients

No.	Intraoperative R-fMRI			
	TP	TN	FP	FN
2	9	7	0	0
5	3	8	3	0
8	1	22	1	0
12	1	8	1	3
18	0	19	0	1
19	2	19	0	3
20	4	8	0	3
21	1	14	2	0
22	4	3	1	0
25	2	4	0	3
26	3	10	2	1
27	3	12	0	1
29	2	8	0	4
30	2	6	0	4

Note:—TP indicates true-positive; TN, true-negative; FP, false-positive; FN, false-negative.

To identify differences in image quality by scanning situation, we filled the tumor cavities of 12 patients with normal saline and compared the cavities with those of the other 18 patients who did not undergo cavity filling. Our results showed that a tumor cavity filled with normal saline could improve the imaging quality ($P = .049$). In addition, 12 and 18 patients were selected to undergo general and awake anesthesia, respectively. No significant correlation between anesthesia type and imaging quality was found ($P = .102$). Thus, the imaging quality of iR-fMRI was superior when the tumor cavity was filled with normal saline but was not significantly correlated with anesthesia type. We have provided 4 illustrative cases as on-line images, including 2 cases of iR-fMRI without saline in the tumor cavity (On-line Figs 1 and 2), and 2 cases of iR-fMRI with saline (On-line Figs 3 and 4). These raw data showed how image quality changed because of saline in the intraoperative cavity.

Six patients experienced motor deficits (muscle strength decreased) immediately after the operation, with 4 of the 6 recovering to their preoperative condition within 3 months.

Case 1

A 41-year-old woman (case 22 in On-line Table 1) had recurrent seizures for >2 months with normal muscle strength before the operation. MR imaging showed that the lesion was in the right frontal lobe, while the pR-fMRI scan revealed that the motor cortex was located posteriorly (Fig 1A). The patient underwent awake craniotomy and DCS to locate 2 positive sites in the hand area and 2 in the mouth area (Fig 1B). The positive sites were recorded on the MR images and overlaid with the motor cortex displayed on the pR-fMRI. The results agreed with the pR-fMRI findings (Fig 1A). After tumor resection, the navigation was updated by the intraoperative image, while the positive sites located by DCS were recorded by navigation on the iMRI and overlaid with the motor cortex displayed on the iR-fMRI. The results demonstrated that the positive sites still agreed with the iR-fMRI results (Fig 1C). After the operation, the patient had mild loss of muscle strength but recovered to normal after 1 week.

Case 2

A 25-year-old man (case 5 in On-line Table 1) had general seizures for 2 months with normal muscle strength before the operation. The preoperative MR imaging showed that the tumor was in the left frontal lobe, while the R-fMRI revealed that the motor cortex was posterior to the lesion (Fig 2A). The DCS identified 2 positive sites in the hand area, 1 in the foot area, and 2 in the language area corresponding to speech fluency (Fig 2B). After tumor resection, iMRI indicated a small amount of tumor residue close to the deep motor area behind the tumor cavity (Fig 2D), while the iR-fMRI showed some distance between the motor cortex and tumor residue (Fig 2C). Accordingly, another resection was performed, and the subsequent iMRI scan demonstrated that the tumor was completely removed (Fig 2F). The iR-fMRI scan showed that the motor cortex was well-protected (Fig 2E). With iR-fMRI guidance, further resection was safely performed. The patient had transient slow right-limb movement start-up that gradually improved to normal.

DISCUSSION

High-field iMRI is an innovative technique to aid the functional guidance of neurosurgery. It is a challenge for patients to perform tasks during the operation. R-fMRI provides a window for identifying the motor cortex without the patient's cooperation. The combination of iMRI and R-fMRI (ie, iR-fMRI) was applied in this study. Intraoperative mapping of regional brain functions with iR-MR imaging was validated by DCS. This new intraoperative technique is noninvasive compared with DCS. Our results indicated that iR-fMRI might be a promising tool for real-time motor cortex mapping during a glioma operation.

Accumulating evidence has suggested that more extensive surgical resection is associated with a longer life expectancy for patients with gliomas.^{22,23} In addition, surgical morbidities may also affect survival time. Preoperative and intraoperative care should be taken to avoid surgical sequelae in the management of gliomas.^{24,25} Accurate real-time positioning of intraoperative brain function is among the most important issues for neurosurgeons. In recent studies, R-fMRI was found to be well-correlated with the pre- and postoperative clinical condition of patients.²⁶ DCS serves as a reliable method to locate brain function areas, and it has been popularized. However, repeat stimulations may greatly increase the incidence of seizure, reduce surgical safety, and directly affect DCS accuracy.^{3,27} Notably, DCS cannot really be applied after partial tumor removal. Noninvasive iR-fMRI, which was verified by DCS in the current research, may provide neurosurgeons with important information conducive to safe tumor resection, especially for patients who cannot cooperate with DCS and task fMRI. Our results indicated that the fusion of functional and structural findings could clearly reveal the spatial location of the tumor residue and motor cortex, information valuable to neurosurgeons in assessing whether further resection is feasible and safe.

Our results demonstrated that 70% of iR-fMRI quality was satisfactory for neurosurgery reference. However, 30% of the iR-fMRI data did not meet the criteria for acceptance. Our results indicated that the imaging quality was not significantly affected by the anesthesia type. The lack of effect from anesthesia on R-fMRI

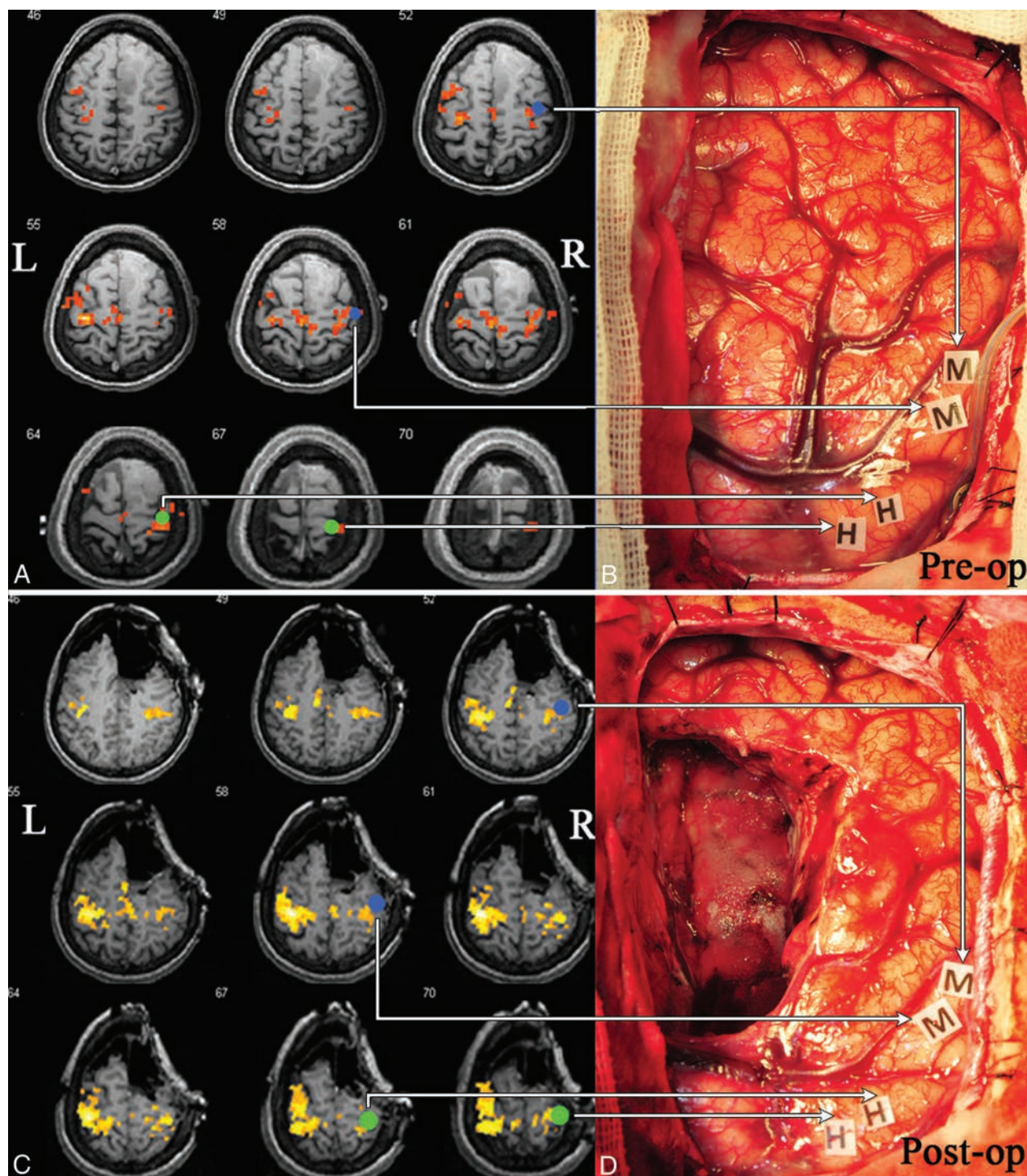


FIG 1. Validation of iR-fMRI with DCS. *A*, The pR-fMRI scan shows the motor cortex located posterior to the tumor. *B*, DCS locates positive sites in the hand area (H) and positive sites in the mouth area (M). The *green and blue dots* in *A* represent the positive sites in the hand and mouth areas, respectively, located by intraoperative DCS. *C*, iR-fMRI reveals that the motor cortex is behind the tumor cavity. *D*, Intact motor cortex after tumor resection. The *green and blue dots* represent the positive sites in the hand and mouth areas, respectively, located by intraoperative DCS. Pre-op indicates preoperative; Post-op, postoperative; L, left; R, right.

signal has also been found in other studies.^{26,28} The image quality, however, could be improved by filling the tumor cavity with normal saline. This improvement might result from the creation of a homogeneous imaging environment, minimizing the susceptibility artifacts during iR-fMRI acquisition. However, not all patients who underwent normal saline filling had satisfactory iR-fMRI

quality. Whether normal saline is the most ideal substance for tumor cavity filling remains questionable.

The iR-fMRI scan was useful for guidance of brain tumor operations but still had several limitations. The BOLD signal, which is observed using the blood oxygen level to reflect brain activation, cannot directly show the electrical activities of neurons, a finding

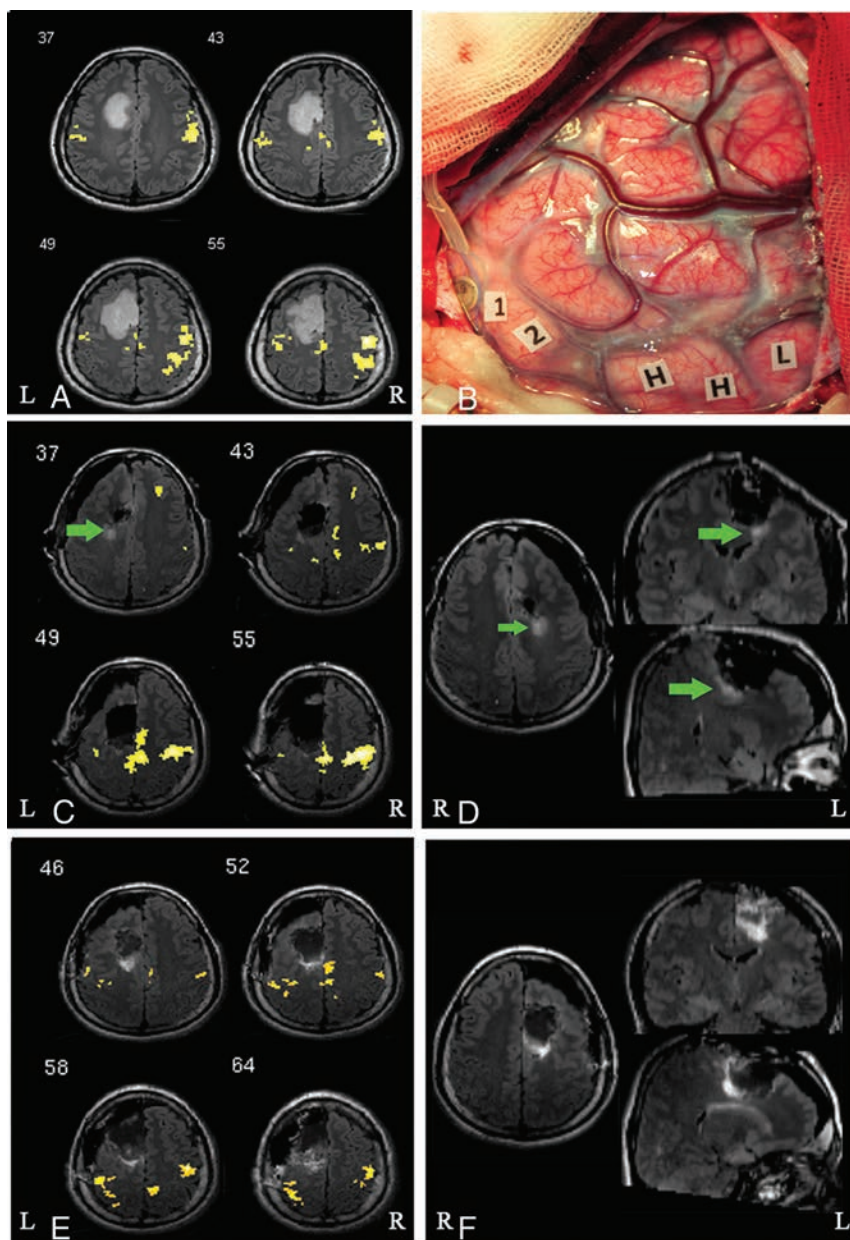


FIG 2. Procedure for iR-fMRI- and DCS-assisted tumor resection. *A*, pR-fMRI scan reveals that the motor cortex is located behind the left frontal lesion. *B*, Direct cortical stimulation locates 2 positive sites in the hand area (H), 1 positive site in the foot area (L), and 2 positive sites in the language area (1 and 2). *C*, The iR-fMRI scan displays the motor cortex behind the tumor cavity at a distance from the tumor residue (green arrow). *D*, Intraoperative MR image suggests a small amount of tumor residue closer to the deep motor area behind the tumor cavity (green arrow). *E*, The final iR-fMRI scan shows that the motor cortex located behind the tumor cavity is well-protected. *F*, The final MR imaging scan reveals complete tumor resection. L indicates left; R, right.

that is different from that in DCS. However, BOLD has irreplaceable significance in localizing functional areas when DCS does not work or a seizure occurs. The results of the seed-based method could be assessed in real-time. Nonetheless, we also found that a prominently decreased ipsilesional BOLD signal was present compared with that in the normal side. We supposed that this finding may be attributed to tumor-induced neurovascular uncoupling.²⁹ Abnormal vasculature due to tumors causes significant hemodynamic responses in the cerebrovascular reactivity that affect the BOLD signal, resulting in false-negative results, which may explain why the overall sensitivity was not very high

in this study. In recent studies, breath-holding fMRI was used to calibrate resting-state fMRI or task-based fMRI to reduce tumor-related neurovascular factors. We have been attempting to use this method to try to obtain better results. Additionally, this is a relatively small sample, which may be responsible for the trend level. We are attempting to collect additional cases and obtain significant results. Further studies are essential to solve these problems to ensure that iR-fMRI becomes a safe and effective tool for clinical applications. We are currently exploring other analysis methods, including amplitude of low frequency fluctuation, regional homogeneity, and independent component analysis,^{12,30} to further optimize the analysis.

CONCLUSIONS

This study investigated the iR-fMRI technique for the intraoperative localization of the motor cortex. Although this research is in its infancy, we demonstrated the feasibility of applying iR-fMRI for real-time functional localization. The areas located by iR-fMRI provided the motor regions that overlapped with the corresponding areas identified by DCS. Therefore, iR-fMRI provides an alternative opportunity for real-time mapping of motor areas and increases the safety of the resection of intra-axial brain tumors.

ACKNOWLEDGMENTS

The authors thank Jian-bing Shi and Zhong Yang for assembling the image data base, Wei-jun Tang for checking the data processing, Gen Xu for providing the direct cortical stimulation, and Yan-yan Song and Chun-xiao Wu for performing the statistical analyses.

REFERENCES

1. Matz PG, Cobbs C, Berger MS. **Intraoperative cortical mapping as a guide to the surgical resection of gliomas.** *J Neurooncol* 1999;42: 233–45 CrossRef Medline
2. Yetkin FZ, Mueller WM, Morris GL, et al. **Functional MR activation correlated with intraoperative cortical mapping.** *AJNR Am J Neuroradiol* 1997;18:1311–15 Medline
3. Trebuchon A, Guye M, Tcherniack V, et al. **Interest of EEG recording during direct electrical stimulation for brain mapping function in surgery** [in French]. *Ann Fr Anesth Reanim* 2012;31:e87–90 CrossRef Medline
4. Vlioger EJ, Majoie CB, Leenstra S, et al. **Functional magnetic reso-** *AJNR Am J Neuroradiol* 38:2146–52 Nov 2017 www.ajnr.org 2151

- nance imaging for neurosurgical planning in neurooncology. *Eur Radiol* 2004;14:1143–53 [CrossRef Medline](#)
5. Krishnan R, Raabe A, Hattingen E, et al. Functional magnetic resonance imaging-integrated neuronavigation: correlation between lesion-to-motor cortex distance and outcome. *Neurosurgery* 2004;55:904–14; discussion 914–15 [Medline](#)
6. Nimsy C, Ganslandt O, Cerny S, et al. Quantification of, visualization of, and compensation for brain shift using intraoperative magnetic resonance imaging. *Neurosurgery* 2000;47:1070–79; discussion 1079–80 [CrossRef Medline](#)
7. Black PM, Moriarty T, Alexander E 3rd, et al. Development and implementation of intraoperative magnetic resonance imaging and its neurosurgical applications. *Neurosurgery* 1997;41:831–42; discussion 842–45 [CrossRef Medline](#)
8. Nimsy C, Ganslandt O, Hastreiter P, et al. Preoperative and intraoperative diffusion tensor imaging-based fiber tracking in glioma surgery. *Neurosurgery* 2007;61:178–85; discussion 186 [Medline](#)
9. Qiu TM, Yao CJ, Wu JS, et al. Clinical experience of 3T intraoperative magnetic resonance imaging integrated neurosurgical suite in Shanghai Huashan Hospital. *Chin Med J (Engl)* 2012;125:4328–33 [Medline](#)
10. Lu JF, Zhang H, Wu JS, et al. “Awake” intraoperative functional MRI (ai-fMRI) for mapping the eloquent cortex: is it possible in awake craniotomy? *Neuroimage Clin* 2012;2:132–42 [CrossRef Medline](#)
11. Biswal B, Yetkin FZ, Haughton VM, et al. Functional connectivity in the motor cortex of resting human brain using echo-planar MRI. *Magn Reson Med* 1995;34:537–41 [CrossRef Medline](#)
12. Shimony JS, Zhang D, Johnston JM, et al. Resting-state spontaneous fluctuations in brain activity: a new paradigm for presurgical planning using fMRI. *Acad Radiol* 2009;16:578–83 [CrossRef Medline](#)
13. Qiu TM, Yan CG, Tang WJ, et al. Localizing hand motor area using resting-state fMRI: validated with direct cortical stimulation. *Acta Neurochir (Wien)* 2014;156:2295–302 [CrossRef Medline](#)
14. Schneider FC, Pailler M, Faillenot I, et al. Presurgical assessment of the sensorimotor cortex using resting-state fMRI. *AJNR Am J Neuroradiol* 2016;37:101–07 [CrossRef Medline](#)
15. Chao-Gan Y, Yu-Feng Z. DPARSF: A MATLAB Toolbox for “Pipeline” data analysis of resting-state fMRI. *Front Syst Neurosci* 2010;4:13 [CrossRef Medline](#)
16. Song XW, Dong ZY, Long XY, et al. REST: a toolkit for resting-state functional magnetic resonance imaging data processing. *PLoS One* 2011;6:e25031 [CrossRef Medline](#)
17. Fox MD, Raichle ME. Spontaneous fluctuations in brain activity observed with functional magnetic resonance imaging. *Nat Rev Neurosci* 2007;8:700–11 [CrossRef Medline](#)
18. Boroojerdi B, Foltys H, Krings T, et al. Localization of the motor hand area using transcranial magnetic stimulation and functional magnetic resonance imaging. *Clin Neurophysiol* 1999;110:699–704 [CrossRef Medline](#)
19. Yousry TA, Schmid UD, Alkadhi H, et al. Localization of the motor hand area to a knob on the precentral gyrus: a new landmark. *Brain* 1997;120(pt 1):141–57 [CrossRef Medline](#)
20. Bizzi A, Blasi V, Falini A, et al. Presurgical functional MR imaging of language and motor functions: validation with intraoperative electrocortical mapping. *Radiology* 2008;248:579–89 [CrossRef Medline](#)
21. Roux FE, Boulanouar K, Lotterie JA, et al. Language functional magnetic resonance imaging in preoperative assessment of language areas: correlation with direct cortical stimulation. *Neurosurgery* 2003;52:1335–45; discussion 1345–47 [CrossRef Medline](#)
22. Smith JS, Chang EF, Lamborn KR, et al. Role of extent of resection in the long-term outcome of low-grade hemispheric gliomas. *J Clin Oncol* 2008;26:1338–45 [CrossRef Medline](#)
23. Sanai N, Berger MS. Glioma extent of resection and its impact on patient outcome. *Neurosurgery* 2008;62:753–64; discussion 764–66 [CrossRef Medline](#)
24. De Witt Hamer PC, Robles SG, Zwinderman AH, et al. Impact of intraoperative stimulation brain mapping on glioma surgery outcome: a meta-analysis. *J Clin Oncol* 2012;30:2559–65 [CrossRef Medline](#)
25. Sanai N, Mirzadeh Z, Berger MS. Functional outcome after language mapping for glioma resection. *N Engl J Med* 2008;358:18–27 [CrossRef Medline](#)
26. Roder C, Charyasz-Leks E, Breikopf M, et al. Resting-state functional MRI in an intraoperative MRI setting: proof of feasibility and correlation to clinical outcome of patients. *J Neurosurg* 2016;125:401–09 [CrossRef Medline](#)
27. Blume WT, Jones DC, Pathak P. Properties of after-discharges from cortical electrical stimulation in focal epilepsies. *Clin Neurophysiol* 2004;115:982–89 [CrossRef Medline](#)
28. Bisdas S, Charyasz-Leks E, Roder C, et al. Evidence of resting-state activity in propofol-anesthetized patients with intracranial tumors. *Acad Radiol* 2016;23:192–99 [CrossRef Medline](#)
29. Agarwal S, Sair HI, Yahyavi-Firouz-Abadi N, et al. Neurovascular uncoupling in resting state fMRI demonstrated in patients with primary brain gliomas. *J Magn Reson Imaging* 2016;43:620–66 [CrossRef Medline](#)
30. Kokkonen SM, Nikkinen J, Remes J, et al. Preoperative localization of the sensorimotor area using independent component analysis of resting-state fMRI. *Magn Reson Imaging* 2009;27:733–40 [CrossRef Medline](#)

Apparent Diffusion Coefficient Histograms of Human Papillomavirus–Positive and Human Papillomavirus–Negative Head and Neck Squamous Cell Carcinoma: Assessment of Tumor Heterogeneity and Comparison with Histopathology

T. de Perrot, V. Lenoir, M. Domingo Ayllón, N. Dulguerov, M. Pusztazeri, and M. Becker



ABSTRACT

BACKGROUND AND PURPOSE: Head and neck squamous cell carcinoma associated with human papillomavirus infection represents a distinct tumor entity. We hypothesized that diffusion phenotypes based on the histogram analysis of ADC values reflect distinct degrees of tumor heterogeneity in human papillomavirus–positive and human papillomavirus–negative head and neck squamous cell carcinomas.

MATERIALS AND METHODS: One hundred five consecutive patients (mean age, 64 years; range, 45–87 years) with primary oropharyngeal ($n = 52$) and oral cavity ($n = 53$) head and neck squamous cell carcinoma underwent MR imaging with anatomic and diffusion-weighted sequences ($b = 0$, $b = 1000$ s/mm², monoexponential ADC calculation). The collected tumor voxels from the contoured ROIs provided histograms from which position, dispersion, and form parameters were computed. Histogram data were correlated with histopathology, p16-immunohistochemistry, and polymerase chain reaction for human papillomavirus DNA.

RESULTS: There were 21 human papillomavirus–positive and 84 human papillomavirus–negative head and neck squamous cell carcinomas. At histopathology, human papillomavirus–positive cancers were more often nonkeratinizing (13/21, 62%) than human papillomavirus–negative cancers (19/84, 23%; $P = .001$), and their mitotic index was higher (71% versus 49%; $P = .005$). ROI-based mean and median ADCs were significantly lower in human papillomavirus–positive ($1014 \pm 178 \times 10^{-6}$ mm²/s and $970 \pm 187 \times 10^{-6}$ mm²/s, respectively) than in human papillomavirus–negative tumors ($1184 \pm 168 \times 10^{-6}$ mm²/s and $1161 \pm 175 \times 10^{-6}$ mm²/s, respectively; $P < .001$), whereas excess kurtosis and skewness were significantly higher in human papillomavirus–positive (1.934 ± 1.386 and 0.923 ± 0.510 , respectively) than in human papillomavirus–negative tumors (0.643 ± 0.982 and 0.399 ± 0.516 , respectively; $P < .001$). Human papillomavirus–negative head and neck squamous cell carcinoma had symmetric normally distributed ADC histograms, which corresponded histologically to heterogeneous tumors with variable cellularity, high stromal component, keratin pearls, and necrosis. Human papillomavirus–positive head and neck squamous cell carcinomas had leptokurtic skewed right histograms, which corresponded to homogeneous tumors with back-to-back densely packed cells, scant stromal component, and scattered comedonecrosis.

CONCLUSIONS: Diffusion phenotypes of human papillomavirus–positive and human papillomavirus–negative head and neck squamous cell carcinomas show significant differences, which reflect their distinct degree of tumor heterogeneity.

ABBREVIATIONS: HNSCC = head and neck squamous cell carcinoma; HPV = human papillomavirus; HPV– = human papillomavirus–negative; HPV+ = human papillomavirus–positive

Infection with certain types of human papillomavirus (HPV), particularly HPV16 and HPV18, is a well-established cause for the development of head and neck squamous cell carcinoma (HNSCC) arising in the oropharynx and, to a lesser extent, also in

other head and neck sites. During the infection process, the viral DNA is incorporated in the cell DNA and induces genetic modifications responsible for carcinogenesis.¹ The HPV oncoprotein E7 binds to and degrades the retinoblastoma protein, which leads to the accumulation and overexpression of p16 protein.² P16 immunohistochemistry appears to be the best stand-alone test for HPV testing of HNSCC because it is widely available, very sensitive (up to 100%), and specific for the presence of transcription-

Received March 31, 2017; accepted after revision July 7.

From the Division of Radiology, Department of Imaging and Medical Informatics (T.d.P., V.L., M.D.A., M.B.), Division of Head and Neck Surgery, Department of Clinical Neurosciences (N.D.), and Division of Clinical Pathology, Department of Genetic and Laboratory Medicine (M.P.), Geneva University Hospitals, Geneva, Switzerland.

Please address correspondence to Minerva Becker, MD, Division of Radiology, Department of Imaging and Medical Informatics, Geneva University Hospitals, Rue Gabrielle-Perret-Gentil 4, 1211 Geneva 14, Switzerland; e-mail: Minerva.Becker@hcuge.ch

Indicates open access to non-subscribers at www.ajnr.org

Indicates article with supplemental on-line tables.

Indicates article with supplemental on-line photo.

<http://dx.doi.org/10.3174/ajnr.A5370>

ally active HPV. Polymerase chain reaction is also very sensitive; however, its specificity is limited because the mere presence of HPV DNA does not convey whether the virus is transcriptionally active or simply a bystander.^{2,3} In the oropharynx, HPV- and/or p16-positive (HPV+) HNSCC has a better prognosis than HPV- and/or p16-negative (HPV-) HNSCC,⁴ whereas in the oral cavity and in other head and neck sites, reported results are contradictory.⁴⁻⁶

Morphologic imaging techniques do not allow distinction between HPV+ and HPV- cancers. Some authors found that HPV+ HNSCCs tend to have cystic nodal metastases and extracapsular spread, whereas others reported that morphologic criteria (size, T stage, and cystic nodal disease) and sociodemographic factors were not reliable predictors of HPV status.^{7,8}

DWI is increasingly used for the pretherapeutic work-up and monitoring of treatment response in HNSCC. On DWI, HNSCC displays restricted diffusivity because of increased cellularity, and mean ADC values are in the range of $900\text{--}1300 \times 10^{-6} \text{ mm}^2/\text{s}$.⁹⁻¹² These reported ADC values are based on a monoexponential fitting model with 2 b-values ($b = 0$ and $b = 800\text{--}1000 \text{ s/mm}^2$).^{9-11,13} Mean ADC values are often calculated based on a single freehand ROI drawn over the largest axial tumor area,¹⁴ or alternatively, they are based on elliptical ROIs drawn over the "most cellular" tumor regions,¹¹ the choice of these cellular regions being made visually. In contrast to simple ROI techniques, pixel-based calculations of ADC maps have the advantage of providing a detailed view of the entire area of interest in the form of parametric maps and histograms offering the possibility to assess tumor heterogeneity in a noninvasive fashion.¹⁵ The assessment of tumor heterogeneity plays a major role in cancer research because it influences treatment outcome and has an impact on the development of targeted therapies. Some authors have reported the added value of ADC histograms as predictors of treatment response, whereas others have noted an association between low pretreatment mean ADC and favorable outcome after radiochemotherapy.^{13,16,17} Because the HPV status was not included in the analysis, it is not known whether ADC characteristics associated with improved outcome could actually be attributed to the HPV status.

HPV+ and HPV- HNSCCs are distinct tumors with different molecular pathogenesis. At histopathology, they diverge in terms of microstructural heterogeneity.^{18,19} We hypothesized that diffusion phenotypes based on a histogram analysis of ADC values reflect different degrees of tumor heterogeneity in HPV+ and HPV- HNSCCs. The purpose of this study was to analyze the relationship between ADC histogram parameters and histopathologic features of HPV+ and HPV- HNSCCs and to provide an understanding of the histologic underpinning of this quantitative tool.

MATERIALS AND METHODS

Patient Selection and Inclusion Criteria

This retrospective study was approved by the Institutional Ethics and Research Committee of the University Hospitals Geneva and was performed in accordance with the guidelines of the Helsinki II declaration. Informed consent was waived. Our institution is a tertiary referral center for head and neck oncology and has a weekly multidisciplinary head and neck oncology tumor board.

The inclusion criteria for the current study were as follows: 1) adult patients seen at the multidisciplinary head and neck tumor board, 2) primary HNSCC of the oropharynx and oral cavity, 3) MR imaging examinations (standard of care for HNSCC in our institution) obtained with morphologic sequences and single-shot spin-echo echo-planar DWI with $b = 0$ and $b = 1000 \text{ s/mm}^2$, 4) unequivocal categorization of the HPV status, and 5) histopathology. We included both the oropharynx and the oral cavity in this series to avoid selection bias because though some tumors were classified as originating from the oral cavity, they showed involvement of both subsites and/or originated at the anatomic limit between the 2 subsites. Moreover, recent data suggest that ectopic tonsillar tissue may actually be the origin of HPV+ HNSCC in nonoropharyngeal sites (eg, the floor of the mouth).^{18,19} In addition, because HPV+ HNSCC tends to arise from the depths of tonsillar crypts and then spread submucosally, emerging at a distant site, the tumors can be misclassified as primary nonoropharyngeal HPV+ HNSCC though they are oropharyngeal in origin.^{18,19} A computerized search of the medical records of the multidisciplinary head and neck tumor board over a period of 3 years yielded a total of 112 consecutive patients meeting the inclusion criteria. Three patients had to be excluded because of poor quality DWI caused by severe motion artifacts and metal implants. Four further patients were excluded because the lesions were not seen on diffusion-weighted MRI (2 in situ lesions, 2 T1 lesions according to the Union for International Cancer Control TNM classification). Therefore, a total of 105 consecutive patients formed the basis of the current study.

MR Imaging Protocol

The MR imaging examinations were performed on 1.5T ($n = 45$) and 3T ($n = 60$) MR imaging scanners provided by 2 different manufacturers. There was no statistically significant difference between the number of patients examined at 1.5T and at 3T ($P = .22$). For both field strengths, our imaging protocols included axial T2, coronal STIR, axial T1 before and after intravenous injection of a gadolinium-based contrast agent, and fat-saturated contrast-enhanced T1 in the axial and coronal plane. A single-shot spin-echo echo-planar DWI sequence was performed in all patients before intravenous contrast material with 2 b-values ($b = 0$ and $b = 1000 \text{ s/mm}^2$) and with similar parameters at 1.5T (TR, 7300 ms; TE, 75 ms) and 3T (TR, 7500 ms; TE, 75 ms), respectively. Fat suppression was used for all DWI sequences (spectral fat saturation or STIR with TI, 170–180 ms at 1.5T and 230 ms at 3T). Depending on patient morphology, the FOV ranged from 220–260 mm with corresponding acquisition matrices of 77–192 voxels in height and 112–208 voxels in width. The section thickness was 3–4 mm in 100 cases and 5 mm in 5 patients. All ADC maps were calculated by monoexponential fitting.⁹⁻¹³

Image Analysis, Data Processing, and Criteria for the Interpretation of Histograms

Two radiologists evaluated the MR imaging examinations independently. They were blinded to clinical data, histopathologic results, and HPV status. OsiriX MD version 3 (<http://www.osirix-viewer.com>) was used for image interpretation and measures. The readers were experienced radiologists with >8 years of expertise

in oncologic head and neck MR imaging. Each tumor was identified by using morphologic MR imaging and DWI. The diagnosis of HNSCC was made according to established criteria (mass lesion with high signal on B1000 and low signal on a gray-scale ADC map).^{10,11} After scrolling through all the images, the 2 largest consecutive cross-sectional tumor areas were selected and contoured manually on axial B1000 and corresponding ADC maps by using freehand ROIs. Because DWI shows spatially nonlinear distortions, we did not contour tumor ROIs on morphologic MR imaging, but directly on DWI to avoid including nontumoral pixels in the analysis. Then, the freehand ROIs were saved individually. Although freehand ROIs of the entire tumor may be more representative of tumor heterogeneity, we deliberately contoured only the 2 largest axial tumor areas because we wanted to be certain about tumor margins. In our experience, the identification of tumor margins on the most cranial and most caudal sections may be fraught with errors (partial volume effect with nontumoral tissues and nonlinear image distortions), especially in smaller lesions. Because we were interested in tumor heterogeneity, we contoured the entire cross-sectional tumor area without excluding necrotic portions. The voxels within the contoured tumor areas were exported in an .xml file by using the OsiriX plugin “Export ROIs,” and they were retrieved by the statistical software R (<http://www.r-project.org/>).²⁰

For each set of voxels belonging to a tumor, the software calculated a histogram. For each tumor, the following histogram-derived ADC parameters were obtained: mean and median values (relevant for the histogram center); minimum; maximum; 25% quartile; 75% quartile; interquartile range (value spread around the center); skewness and kurtosis (histogram symmetry and peakedness). The interpretation of histogram parameters was done in accordance with the literature.¹⁵ Kurtosis in a normal distribution is 3. Excess kurtosis (raw kurtosis minus 3) is 0 for a normal distribution. Positive numbers represent “narrow” leptokurtic histograms, and negative numbers correspond to “wide” platykurtic histograms. Skewness associated with a normal and symmetric distribution is 0. Positive skewness represents a histogram with a right longer tail (skewed right), whereas negative skewness represents a histogram with a left longer tail (skewed left).¹⁵ If skewness is <-1 or $>+1$, the distribution is highly skewed. If skewness is between -1 and -0.5 or between $+0.5$ and $+1$, the distribution is moderately skewed. If skewness is between -0.5 and $+0.5$, the distribution is approximately symmetric.

Standard of Reference

For each patient, the HPV status was determined based on the tissue samples obtained by endoscopic biopsy ($n = 52$) or surgical resection ($n = 53$). A 2-step procedure consisting of p16 immunohistochemistry and polymerase chain reaction was used to differentiate between HPV+ and HPV– HNSCC.²¹ Tumors were considered p16+ in the presence of a strong nuclear and cytoplasmic staining of $\geq 70\%$ of the neoplastic cells.² In the presence of p16 overexpression, polymerase chain reaction for the detection of HPV DNA was carried out. Cases were categorized as HPV+ according to p16 immunohistochemistry and polymerase chain reaction results according to American Joint Committee on Cancer 2017 guidelines.³ A degree of histologic differentiation was not

Table 1: Patient^a and tumor characteristics

Characteristics	HPV– HNSCC (n = 84)	HPV+ HNSCC (n = 21)	P Value ^b
Average age (range), yr	65 (45–87)	61 (45–73)	.15 ^c
Sex, no. (%)			
Women	23 (27)	7 (33)	
Men	61 (73)	14 (67)	.79 ^d
Tumor location, no. (%)			
Oral cavity	50 (60)	3 (14)	
Oropharynx	34 (40)	18 (86)	<.001 ^d
T classification according to AJCC 2017, no. (%) ^f			
T1	5 (6)	1 (5)	
T2	22 (26)	6 (29)	
T3	15 (18)	3 (14)	
T4	42 (50)	11 (52)	1 ^e
N classification according to AJCC 2017, no. (%)			
N0	36 (43)	4 (19)	
N1	13 (15)	6 (29)	
N2	35 (42)	9 (43)	
N3	0 (0)	2 (9)	.012 ^e
M classification according to AJCC 2017, no. (%)			
M0	77 (92)	18 (86)	
M1	1 (1)	1 (5)	
Mx	6 (7)	2 (9)	.47 ^e
Tumor keratinization, no. (%)			
Present	65 (77)	8 (38)	
Absent	19 (23)	13 (62)	.001 ^d
Degree of keratinization, no. (%)			
Keratinizing	48 (57)	3 (14)	
Focally keratinizing	17 (20)	5 (24)	<.001 ^e
Nonkeratinizing, no. (%)	19 (23)	13 (62)	
Histologic differentiation, no. (%)			
Well differentiated	15 (18)	Not assessable ^f	
Moderately differentiated	48 (57)		
Poorly differentiated	21 (25)		
Semiquantitative histologic score, no. (%) ^g			
Score 1 (most heterogeneous)	14 (17)	0 (0)	
Score 2	8 (9)	0 (0)	
Score 3	41 (49)	7 (33)	.002 ^e
Score 4	12 (14)	5 (24)	
Score 5 (most homogeneous)	9 (11)	9 (43)	
Mean proliferation index, MIB-1 (%) ^h	49	71	.005 ^c
Range in %	8–90	30–95	

Note:—AJCC indicates American Joint Committee on Cancer.

^a Total patients, 105.

^b P values are indicated for the comparisons between HPV+ and HPV– HNSCCs.

^c Wilcoxon rank sum test.

^d Pearson χ^2 test.

^e Fisher test.

^f HPV+ HNSCC was not graded according to AJCC 2017 guidelines.³

^g The semiquantitative histologic score is described in On-line Table 1.

^h Available in 95 histologic samples.

assigned to HPV+ HNSCCs based on American Joint Committee on Cancer 2017 recommendations.³ A semiquantitative histologic score (On-line Table 1) was used to facilitate correlation between tumor microarchitecture and ADC histograms. This semiquantitative score took the following features into consideration: shape and size of tumor cells and nuclei, quantitative and qualitative stromal characteristics (ie, desmoplasia, lymphocytic infiltration), intratumoral keratinization, mitotic index estimated by MIB-1 immunohistochemistry, and the size and distribution of necrosis.

Statistical Analysis

All statistical analyses were performed by using the R statistical environment version 3.0.2.²⁰ For all tests, the significance level

Table 2: Quantitative ADC parameters from histogram analysis of tumors in the oropharynx and oral cavity at 1.5T and 3T and for all tumors together irrespective of field strength (pooled data)

Histogram-Based ADC Parameters	1.5T (n = 45)			3T (n = 60)			Pooled Data (n = 105)		
	HPV- (n = 33) (mean ± SD)	HPV+ (n = 12) (mean ± SD)	P Value ^a	HPV- (n = 51) (mean ± SD)	HPV+ (n = 9) (mean ± SD)	P Value ^a	HPV- (n = 84) (mean ± SD)	HPV+ (n = 21) (mean ± SD)	P Value ^a
Mean ADC ($\times 10^{-6}$ mm ² /s)	1158 ± 183	989 ± 188	.004	1201 ± 157	1046 ± 167	.02	1184 ± 168	1014 ± 178	<.001
Median ADC ($\times 10^{-6}$ mm ² /s)	1135 ± 193	936 ± 198	.003	1177 ± 162	1016 ± 170	.03	1161 ± 175	970 ± 187	<.001
Minimum ADC ($\times 10^{-6}$ mm ² /s)	422 ± 251	379 ± 172	.36	441 ± 238	286 ± 207	.10	433 ± 242	339 ± 188	.09
25 Quartile ($\times 10^{-6}$ mm ² /s)	977 ± 162	813 ± 172	.008	1004 ± 151	900 ± 165	.13	993 ± 155	850 ± 171	<.001
75 Quartile ($\times 10^{-6}$ mm ² /s)	1318 ± 216	1115 ± 219	.003	1374 ± 183	1163 ± 180	.005	1352 ± 197	1136 ± 200	<.001
Interquartile range ($\times 10^{-6}$ mm ² /s)	341 ± 111	302 ± 79	.33	371 ± 114	263 ± 68	.003	359 ± 113	285 ± 75	.003
Skewness	0.362 ± 0.647	1.012 ± 0.546	.004	0.424 ± 0.416	0.804 ± 0.461	.02	0.399 ± 0.516	0.923 ± 0.510	<.001
Excess kurtosis	0.841 ± 0.116	1.728 ± 1.250	.03	0.514 ± 0.872	2.207 ± 1.583	.001	0.643 ± 0.982	1.934 ± 1.386	<.001

^aP values (Wilcoxon rank sum test) are indicated for the comparisons between HPV+ and HPV- HNSCCs.

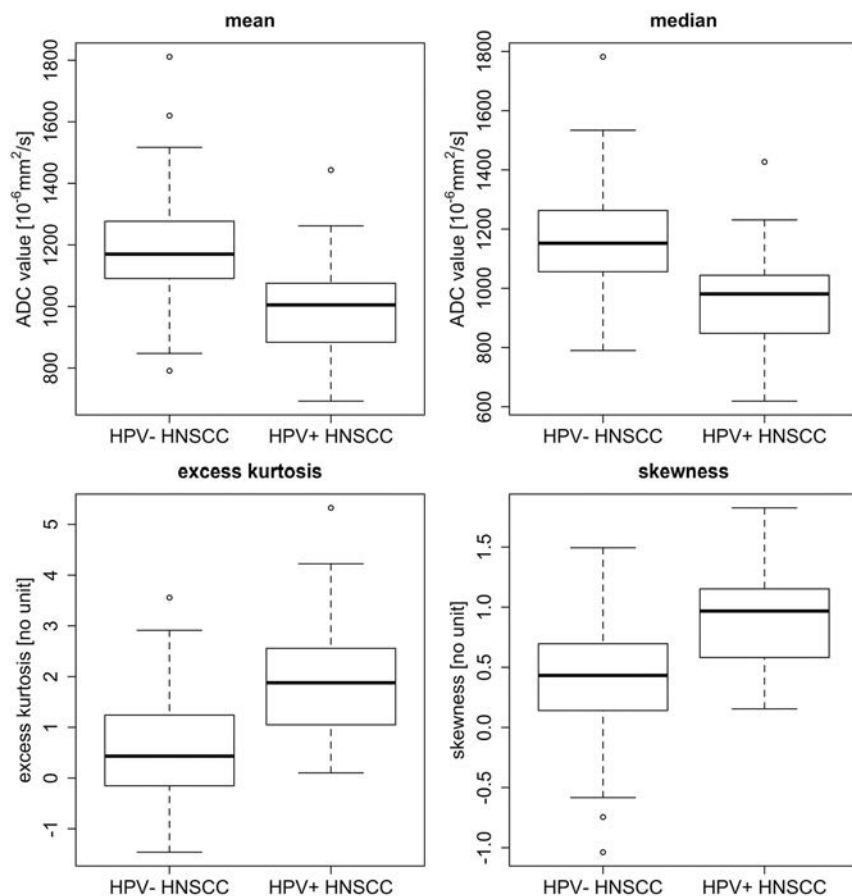


FIG 1. Box plots for mean ADC, median ADC, excess kurtosis, and skewness from ROIs obtained in 105 tumors (84 HPV- HNSCC and 21 HPV+ HNSCC). Horizontal lines indicate median values (black lines). The bottom and the top of the box indicate the first and third quartiles whereas whiskers indicate maximum and minimum values. Outliers are indicated by circles.

was fixed at .05. In the patient characteristics analysis, categorical variables were compared by using the χ^2 test with Yates continuity correction for data grouped in a 2×2 contingency matrix. If the expected frequency in a cell was lower than 5, the Fisher exact test was applied. For continuous variables (eg, patient age), a non-parametric 2-sided unpaired Wilcoxon rank sum test with continuity correction was used. Multivariate logistic regression analysis was obtained to correct for possible confounding factors in the correlation between HPV status and ADC. For quantitative parameters derived from tumor histograms, a comparison between HPV+ and HPV- HNSCCs was performed by using the Wilcoxon rank sum test mentioned above.

RESULTS

Patient and tumor characteristics are summarized in Table 1. The prevalence of HPV+ HNSCCs in the oropharynx (18/52, 35%) was significantly higher ($P < .001$) than in the oral cavity (3/53, 6%). Based on the standard of reference, HPV+ tumors were less often keratinized than HPV- tumors, and the tumor cells were more often basaloid (with limited cytoplasm) or undifferentiated. HPV+ HNSCCs showed a higher mitotic index, a higher proportion of histologic score 4/5, and a higher proportion of nodal metastases than HPV- cancers. These differences were statistically significant (Table 1).

Mean and median (95% CI) ROI size for ADC measurements were 7.7 cm² (range, 2.3–56 cm²) and 5.72 cm² (range, 2.84–10.58 cm²), respectively. Comparison between HPV+ and HPV- HNSCC at both 1.5T and at 3T (Table 2) revealed significant differences between histogram parameters, in particular for mean and median ADC, skewness, and excess kurtosis ($P < .05$). Comparison of histogram parameters of HPV- HNSCCs at 1.5T versus 3T revealed no significant difference between the 2 field strengths ($P > .05$). Similarly, histogram parameters of HPV+ HNSCCs showed no significant difference between 1.5T and 3T, respectively ($P > .05$). The comparison between

HPV+ and HPV- HNSCC for the pooled data irrespective of field strength and subsite is summarized in Table 2 and Fig 1. Comparison between HPV+ HNSCC and HPV- HNSCC in the oropharynx revealed significant differences for all histogram parameters ($P < .05$), whereas in the oral cavity, only a trend was observed because of the small number of HPV+ cases. Comparison between HPV+ HNSCC histograms in the oropharynx versus oral cavity revealed no significant differences ($P > .05$). Multivariate logistic regression analysis showed that the correlation between HPV status and mean ADC was independent of age, sex, tumor site, and T, N, and histologic parameters (On-line Table 2).

Figs 2–4 and the On-line Figure illustrate radiologic, histo-

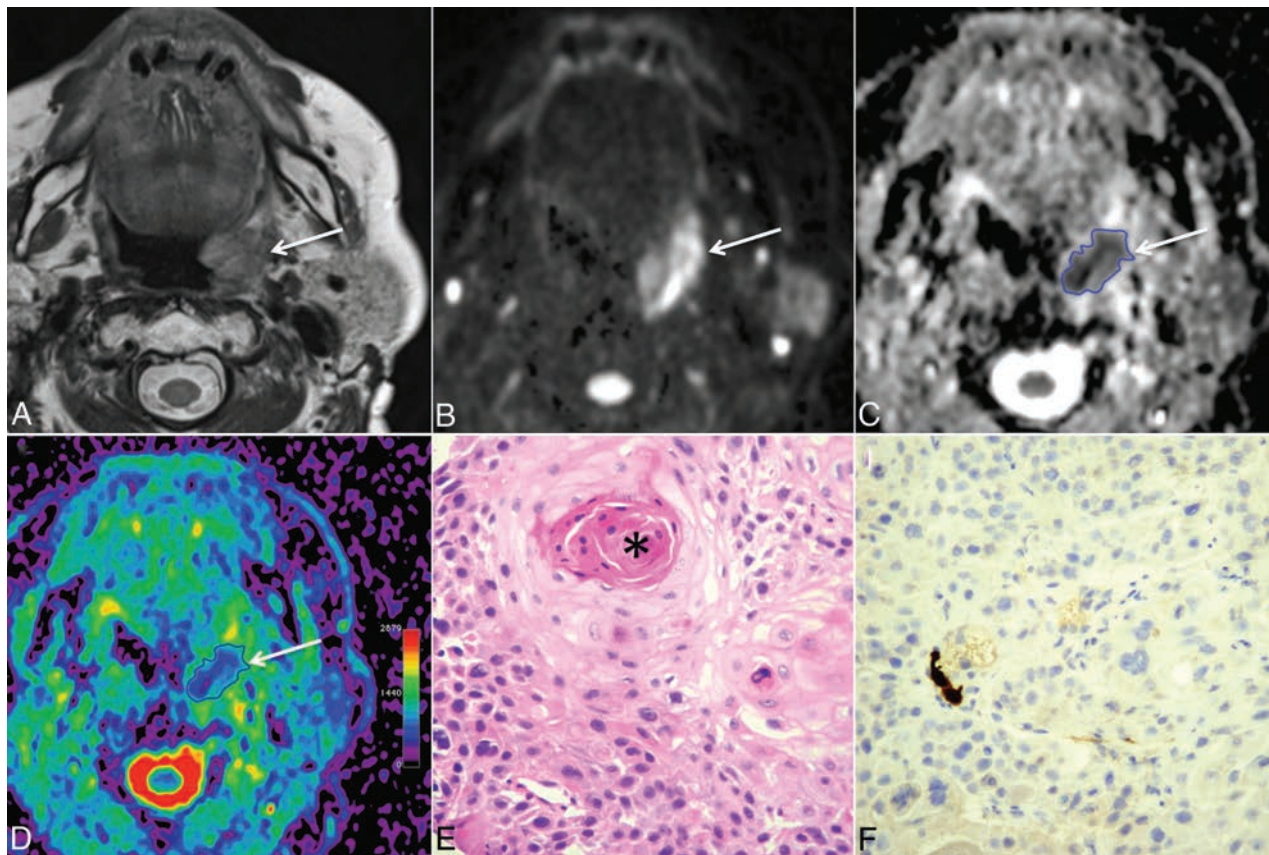


FIG 2. A 59-year-old woman with HPV[−] HNSCC (T2N0M0). *A*, T2-weighted image reveals a left tonsillar tumor (arrow) with intermediate signal intensity. *B*, B1000 and *C*, gray-scale ADC map show restricted tumor diffusion (arrows). The freehand ROI contoured on the ADC map is visible as a blue line. *D*, On the color-coded ADC map (same level as *C*), tumor heterogeneity (purple and various shades of blue-green areas within the tumor) is more easily appreciated than in *C*. *E*, Histology (hematoxylin-eosin; original magnification, 200X) shows heterogeneous tumor matrix with areas of densely packed and loosely packed squamous cells of variable size. Variable amounts of keratin pearls (asterisk) and necrosis were present in this tumor. *F*, Immunohistochemistry for p16 (original magnification, 200X) is negative (ie, most cells show no brownish coloration).

gram, and histologic features of HPV⁺ and HPV[−] HNSCCs. Histopathology revealed that ADC histogram parameters reflected the respective microscopic tumor architecture, in particular, variable tumor heterogeneity. The observed symmetric Gaussian distribution in HPV[−] HNSCC histograms corresponded to heterogeneous tumors with variable cellularity, cell size and shape, keratin pearls, intratumoral necrosis, hemorrhage, and stromal cells (Figs 2 and 4 and the On-line Figure). The observed leptokurtic and skewed right histogram in HPV⁺ HNSCC corresponded histologically to homogeneous tumors with high cellularity, back-to-back homogeneous cell arrangement with little interstitial space, basaloid cells with scant cytoplasm, few to absent keratin pearls, and a higher mitotic index (Figs 3 and 4 and the On-line Figure). These histologic features of HPV⁺ cancers generated a high number of pixels with low ADCs and, therefore, higher kurtosis. The significantly higher positive (right) skewness in HPV⁺ cancers was caused by scattered comedonecrosis, which resulted in a small number of pixels with high ADCs (driving the mean upwards but not affecting the median of the histogram).

DISCUSSION

Although tobacco and alcohol consumption are the most common risk factors for the development of HNSCC, HPV has been recognized as the main etiologic factor in a subgroup of patients.

The incidence of HPV⁺ HNSCC and the proportion of HPV⁺ to HPV[−] HNSCCs depend on tumor localization, geographic and socioeconomic factors, smoking status, and sexual behavior. Most authors currently agree that HPV⁺ HNSCC represents a distinct tumor entity with a more favorable prognosis than alcohol- or tobacco-related HNSCC.

Recent publications have attempted to determine whether mean ADC values calculated by monoexponential fitting could be used to determine the HPV status in HNSCC.^{12,14,22} In contrast to the intravoxel incoherent motion biexponential model, the monoexponential model does not differentiate between molecular movement caused by microperfusion and true diffusion caused by Brownian movement.²³ To obtain a robust fitting, biexponential models require the acquisition of 6–12 b-values, leading to increased examination time and a higher percentage of motion artifacts. Biexponential models are, therefore, not widely used in clinical practice. Publications evaluating the association between mean ADC values with monoexponential fitting and the HPV status in HNSCC have yielded contradictory results; although some authors suggested that mean ADCs at 1.5T are lower in HPV⁺ than in HPV[−] HNSCCs, others found no significant differences.^{12,14,22} In these studies, the methodology of ROI contouring, the type of DWI sequence used, and the range and num-

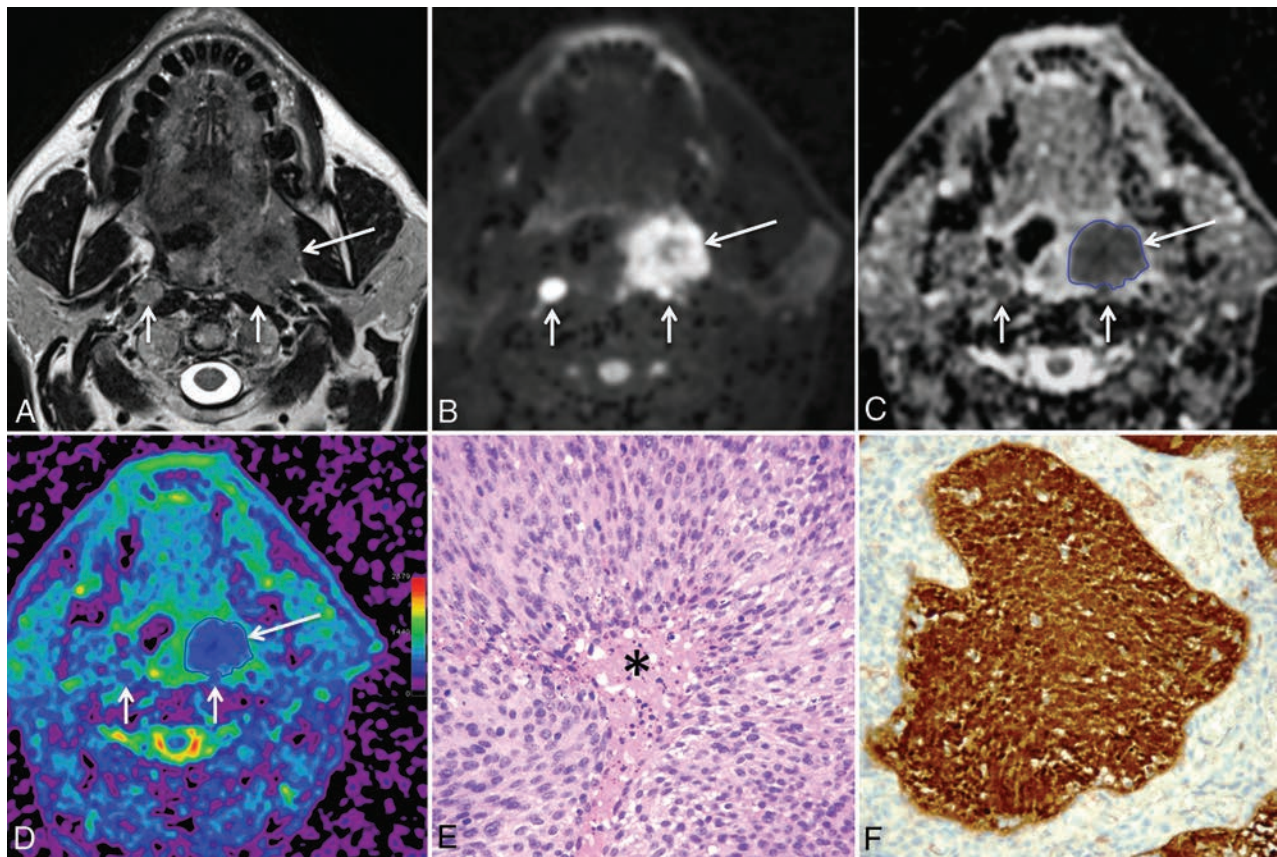


FIG 3. A 60-year-old man with HPV+ HNSCC (T3N2M0). **A**, T2-weighted image reveals a left tonsillar tumor (*long arrow*) with intermediate signal intensity, parapharyngeal space invasion, and bilateral retropharyngeal lymph node metastases (*short arrows*). **B**, B1000 and **C**, gray-scale ADC map show restricted diffusion within the tonsillar tumor (*long arrows*) and within the lymph node metastases (*short arrows*). The freehand ROI contoured on the gray-scale ADC map is visible as a *blue line*. **D**, Color-coded ADC map (same level as **C**). Note that this tumor is less heterogeneous (mainly *blue* areas) than the tumor in Fig 1. **E**, Histology (hematoxylin-eosin; original magnification, 200 \times) shows homogeneous tumor consisting of clusters of densely packed, basaloid cells with scant cytoplasm, and without keratinization. Focal necrosis in the center of the tumor cell clusters (comedonecrosis) is present (*asterisk*). **F**, Immunohistochemistry for p16 is positive; more than 70% of tumor cells show strong cytoplasmic and nuclear staining indicating HPV positivity (original magnification, 200 \times). Polymerase chain reaction for HPV DNA further confirmed HPV positivity.

ber of b-values vary. Nakahira et al¹² contoured the largest axial cross-sectional tumor area on a single section without excluding necrotic portions, Driessen et al²² contoured the entire tumor volume excluding necrotic portions, and Schouten et al¹⁴ contoured the largest cross-sectional area on a single section excluding necrotic portions. In agreement with Nakahira et al¹² and Driessen et al,²² we found that mean ADCs were significantly lower in HPV+ than in HPV- cancers. However, our data are in contradiction to results reported by Schouten et al,¹⁴ who did not find a statistically significant difference between ADCs of both tumor types.¹⁴ A possible explanation is the fact that Schouten et al¹⁴ used a PROPELLER sequence, whereas the other authors, including us, used EPI-based DWI.

Imaging-based first-order histogram analysis of ADC and of dynamic contrast-enhanced MR imaging parameters can be used to measure organ and tumor heterogeneity in a noninvasive fashion.¹⁵ Histogram analysis has been applied for the discrimination between histologic tumor types in renal cell cancers, brain tumors and HNSCC.^{15,16,24,25} Histogram analysis of pretreatment ADCs measured at $b = 2000$ s/mm² was able to distinguish between well, moderately, and poorly differentiated HNSCCs, whereas analysis based on $b = 1000$ s/mm² was not able to do so.²⁵ King et al¹⁶ used

ADC histogram analysis to evaluate the capability of DWI to predict treatment outcome after radiochemotherapy of advanced HNSCC, and Shukla-Dave et al²⁶ used histogram analysis of dynamic contrast-enhanced MRI parameters to predict outcome in HNSCC with nodal metastases.

As suggested by Just, kurtosis and skewness can be regarded as “quantitative surrogate markers of tumor heterogeneity.” Kurtosis reflects distribution peakedness, a narrow distribution being linked to a low voxel value variation and, therefore, to a homogeneous tumor matrix. Skewness measures distribution asymmetry, the meaning of this metric being more difficult to interpret.¹⁵ Data from the current study reveal that ADC histograms of HNSCC reflect the histologic microarchitecture unique to the HPV status. Histologically, in HPV+ tumors, cells are organized in homogeneous clusters with little interstitial space. This finding explains the lower mean and median ADC in HPV+ cancers because the reduced intercellular space restricts diffusion of water molecules. The homogeneous microstructure without major regional variability explains our observation that histograms of HPV+ HNSCCs are more slender (leptokurtic) than histograms with a classic Gaussian distribution (as seen in HPV- cancers). In other terms, higher kurtosis reflects higher tumor matrix homo-

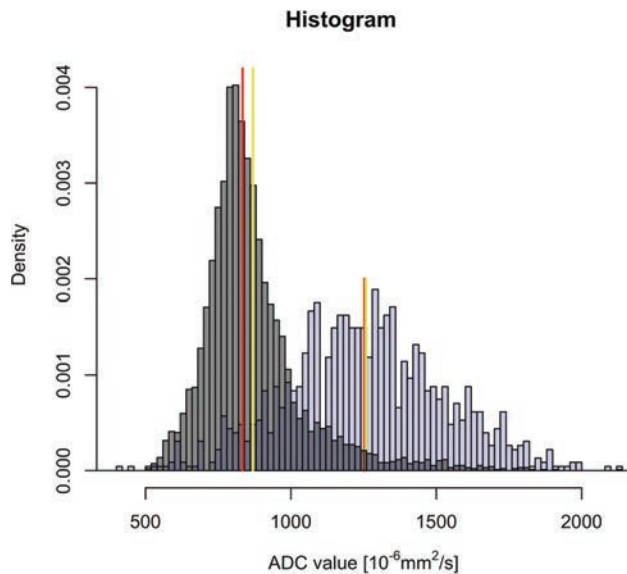


FIG 4. Characteristic histograms obtained in 2 different patients with HNSCC of the base of the tongue. Patient A (T4N2M0) has an HPV+ HNSCC (gray histogram) and patient B (T4N2M0) has an HPV- cancer (blue histogram). Red lines correspond to the median value of each histogram. Yellow lines correspond to the mean value of each histogram. Note that the histogram in the HPV- cancer (blue histogram) is symmetric with widely distributed ADC values around the central line (Gaussian distribution), whereas the histogram in the HPV+ HNSCC (gray histogram) shows asymmetric distribution of ADC values with a right thicker tail (right skew) and an elongated aspect (leptokurtic shape) because a larger proportion of voxel values are located in a narrow band. The mean ADC in HPV+ HNSCC is farther away from the median ADC value (distribution skewed to the right) than in the HPV- histogram.

geneity. The significantly higher positive (right) skewness in HPV+ cancers is caused by a small amount of pixels with high ADCs and a large amount of pixels with low ADCs. This ADC distribution corresponds histologically to large tumor areas with densely packed cells and only minor amounts of scattered comedonecrosis. Kurtosis and skewness thus demonstrate that the ADC distribution in HPV+ cancers tends to be non-Gaussian, whereas HPV- cancers tend to have Gaussian histograms. This difference can be attributed to the higher heterogeneity of HPV- cancers (more scores 1–3 in this series). Data of our study, therefore, support the hypothesis that the distinct histologic microarchitecture of HPV+ and HPV- HNSCCs can be elegantly demonstrated in a noninvasive fashion by ADC histogram analysis. Furthermore, the observed differences between histograms in HPV+ and HPV- cancers were independent of MR imaging field strength and manufacturer.

Commercially available software packages are already able to provide histogram analysis of ROIs contoured during routine image interpretation. ADC histograms could, therefore, be used as a noninvasive triage tool for HPV testing by identifying HPV+ HNSCC located in nonoropharyngeal sites, where p16/polymerase chain reaction testing is not obtained routinely. High kurtosis, positive skewness, and low mean ADC would warrant p16/polymerase chain reaction testing. In addition, ADC histograms could also serve as surrogate indicators of HPV+ HNSCC in cases with insufficient tissue remaining for p16/polymerase chain reaction testing and at the time of intraoperative frozen section evaluation.

HPV+ HNSCC has been linked to a better outcome after radiochemotherapy. Some authors have shown that low mean ADC and/or histograms wherein $>45\%$ of voxels have ADCs $<1.15 \times 10^{-3} \text{ mm}^2/\text{s}$ indicate a favorable response to radiochemotherapy.^{13,16,17} Although the HPV status was not analyzed in these studies, our data suggest that the reported predictive value of ADC histograms and lower mean ADC may in part be related to the HPV status. Therefore, histogram analysis used to monitor treatment response and target new therapeutic approaches should take into consideration the distinct diffusion phenotypes of HPV+ and HPV- HNSCC as revealed by this study.

The current study has limitations inherent to its retrospective study design. Limitations include section thickness variability and the small number of HPV+ HNSCC cases in the oral cavity. Further limitations concern freehand ROI contouring (as opposed to automatic segmentation) and ROI contouring of 2 tumor sections only (as opposed to contouring all tumor sections). Automatic tumor segmentation would in theory produce more robust lesion delineation and require less experienced readers.²⁷ Nevertheless, the method we used is similar to ROI-contouring methods published in other studies.²⁷

CONCLUSIONS

Quantitative ADC histogram analysis reveals significant differences between HPV+ and HPV- HNSCCs irrespective of the MR imaging field strength used. The observed difference in ADC histograms reflects the distinct histopathologic features of these tumors, especially their different degree of microstructural heterogeneity. Because DWI is increasingly used to predict and monitor treatment outcome in HNSCC, diffusion phenotypes of HPV+ and HPV- tumors as demonstrated in this study should be considered in future research protocols.

REFERENCES

- Rampias T, Sasaki C, Psyrri A. **Molecular mechanisms of HPV induced carcinogenesis in head and neck.** *Oral Oncol* 2014;50:356–63 CrossRef Medline
- Bishop JA, Lewis JS Jr, Rocco JW, et al. **HPV-related squamous cell carcinoma of the head and neck: An update on testing in routine pathology practice.** *Semin Diagn Pathol* 2015;32:344–51 CrossRef Medline
- Amin MB, Edge S, Greene F, et al. *AJCC Cancer Staging Manual*, 8th ed. New York: Springer-Verlag; 2017
- Salazar CR, Smith RV, Garg MK, et al. **Human papillomavirus-associated head and neck squamous cell carcinoma survival: a comparison by tumor site and initial treatment.** *Head Neck Pathol* 2014;8:77–87 CrossRef Medline
- Hansson BG, Rosenquist K, Antonsson A, et al. **Strong association between infection with human papillomavirus and oral and oropharyngeal squamous cell carcinoma: a population-based case-control study in southern Sweden.** *Acta Otolaryngol* 2005;125:1337–44 CrossRef Medline
- Duray A, Descamps G, Decaestecker C, et al. **Human papillomavirus DNA strongly correlates with a poorer prognosis in oral cavity carcinoma.** *Laryngoscope* 2012;122:1558–65 CrossRef Medline
- Goldenberg D, Begum S, Westra WH, et al. **Cystic lymph node metastasis in patients with head and neck cancer: An HPV-associated phenomenon.** *Head Neck* 2008;30:898–903 CrossRef Medline
- Byrd JK, Wilhoit CS, Fordham MT, et al. **Predicting HPV status in head and neck cancer: the predictive value of sociodemographic**

- and disease characteristics. *Arch Otolaryngol Head Neck Surg* 2012; 138:1155–59 [CrossRef Medline](#)
9. Varoquaux A, Rager O, Dulguerov P, et al. Diffusion-weighted and PET/MR imaging after radiation therapy for malignant head and neck tumors. *Radiographics* 2015;35:1502–27 [CrossRef Medline](#)
 10. Varoquaux A, Rager O, Lovblad KO, et al. Functional imaging of head and neck squamous cell carcinoma with diffusion-weighted MRI and FDG PET/CT: quantitative analysis of ADC and SUV. *Eur J Nucl Med Mol Imaging* 2013;40:842–52 [CrossRef Medline](#)
 11. Thoeny HC, De Keyser F, King AD. Diffusion-weighted MR imaging in the head and neck. *Radiology* 2012;263:19–32 [CrossRef Medline](#)
 12. Nakahira M, Saito N, Yamaguchi H, et al. Use of quantitative diffusion-weighted magnetic resonance imaging to predict human papilloma virus status in patients with oropharyngeal squamous cell carcinoma. *Eur Arch Otorhinolaryngol* 2014;271:1219–25 [CrossRef Medline](#)
 13. Kim S, Loevner L, Quon H, et al. Diffusion-weighted magnetic resonance imaging for predicting and detecting early response to chemoradiation therapy of squamous cell carcinomas of the head and neck. *Clin Cancer Res* 2009;15:986–94 [CrossRef Medline](#)
 14. Schouten CS, de Graaf P, Bloemena E, et al. Quantitative diffusion-weighted MRI parameters and human papillomavirus status in oropharyngeal squamous cell carcinoma. *AJNR Am J Neuroradiol* 2015;36:763–67 [CrossRef Medline](#)
 15. Just N. Improving tumour heterogeneity MRI assessment with histograms. *Br J Cancer* 2014;111:2205–13 [CrossRef Medline](#)
 16. King AD, Chow KK, Yu KH, et al. Head and neck squamous cell carcinoma: diagnostic performance of diffusion-weighted MR imaging for the prediction of treatment response. *Radiology* 2013;266: 531–38 [CrossRef Medline](#)
 17. Srinivasan A, Chenevert TL, Dwamena BA, et al. Utility of pretreatment mean apparent diffusion coefficient and apparent diffusion coefficient histograms in prediction of outcome to chemoradiation in head and neck squamous cell carcinoma. *J Comput Assist Tomogr* 2012;36:131–37 [CrossRef Medline](#)
 18. Westra WH. The pathology of HPV-related head and neck cancer: implications for the diagnostic pathologist. *Semin Diagn Pathol* 2015;32:42–53 [CrossRef Medline](#)
 19. Chernock RD. Morphologic features of conventional squamous cell carcinoma of the oropharynx: ‘keratinizing’ and ‘nonkeratinizing’ histologic types as the basis for a consistent classification system. *Head Neck Pathol* 2012;6 Suppl 1:S41–47 [CrossRef Medline](#)
 20. R Core Team. R: A Language and Environment for Statistical Computing. The R Foundation for Statistical Computing. 2017. Available at: <https://www.r-project.org/>. Accessed January 24, 2017
 21. Thomas J, Primeaux T. Is p16 immunohistochemistry a more cost-effective method for identification of human papilloma virus-associated head and neck squamous cell carcinoma? *Ann Diagn Pathol* 2012;16:91–99 [CrossRef Medline](#)
 22. Driessen JP, van Bommel AJ, van Kempen PM, et al. Correlation of human papillomavirus status with apparent diffusion coefficient of diffusion-weighted MRI in head and neck squamous cell carcinomas. *Head Neck* 2016;38 Suppl 1:E613–18 [CrossRef Medline](#)
 23. Le Bihan D, Breton E, Lallemand D, et al. Separation of diffusion and perfusion in intravoxel incoherent motion MR imaging. *Radiology* 1988;168:497–505 [CrossRef Medline](#)
 24. Kim H, Choi SH, Kim JH, et al. Gliomas: application of cumulative histogram analysis of normalized cerebral blood volume on 3 T MRI to tumor grading. *PLoS One* 2013;8:e63462 [CrossRef Medline](#)
 25. Ahn SJ, Choi SH, Kim YJ, et al. Histogram analysis of apparent diffusion coefficient map of standard and high B-value diffusion MR imaging in head and neck squamous cell carcinoma: a correlation study with histological grade. *Acad Radiol* 2012;19:1233–40 [CrossRef Medline](#)
 26. Shukla-Dave A, Lee NY, Jansen JF, et al. Dynamic contrast-enhanced magnetic resonance imaging as a predictor of outcome in head-and-neck squamous cell carcinoma patients with nodal metastases. *Int J Radiat Oncol Biol Phys* 2012;82:1837–44 [CrossRef Medline](#)
 27. Porz N, Bauer S, Pica A, et al. Multi-modal glioblastoma segmentation: man versus machine. *PLoS One* 2014;9:e96873 [CrossRef Medline](#)

The Diagnostic Accuracy of Contrast-Enhanced CT of the Neck for the Investigation of Sialolithiasis

Y.M. Purcell, R.G. Kavanagh, A.M. Cahalane, A.G. Carroll, S.G. Khoo, and R.P. Killeen

ABSTRACT

BACKGROUND AND PURPOSE: Sialolithiasis is a common benign pathology affecting the salivary glands but it is unclear if contrast-enhanced CT, which is commonly used for investigation of head and neck pathology, can identify calculi as accurately as noncontrast CT. The aim of this study was to assess the diagnostic accuracy of contrast-enhanced CT of the neck in the diagnosis of sialolithiasis compared with noncontrast CT of the neck used as the criterion standard.

MATERIALS AND METHODS: This was a retrospective, case-control study of 92 consecutive cases in 90 patients who underwent both noncontrast CT of the neck and contrast-enhanced CT of the neck in 2 tertiary referral centers from January 2011 to December 2015 for investigation of sialolithiasis. Axial 3-mm-section images were assessed by a fellowship-trained diagnostic neuroradiologist and diagnostic neuroradiology fellow in consensus. Blinded assessment of the contrast-enhanced CT of the neck was performed first, followed by noncontrast CT of the neck after a 2-week interval. The presence or absence of a stone and stone location and size were documented. Statistical analysis was undertaken to assess the agreement between CT protocols and calculate the sensitivity and specificity of contrast-enhanced CT of the neck.

RESULTS: Fifty calculi were identified on noncontrast CT of the neck in 31 cases; and 48 calculi, in 31 cases on contrast-enhanced CT of the neck. No calculi were identified in the remaining 61 cases. The sensitivity and specificity of contrast-enhanced CT of the neck in the detection of sialolithiasis was 96% (95% CI, 86.3%–99.5%) and 100% (95% CI, 94.1%–100%), respectively. The positive predictive value of contrast-enhanced CT of the neck was 100% (95% CI, 92.6%–100%), and the negative predictive value was 96.8% (95% CI, 89%–99.6%). The accuracy of contrast-enhanced CT of the neck in diagnosing the presence or absence of salivary calculi was 98%.

CONCLUSIONS: Contrast-enhanced CT of the neck is accurate in the detection of sialolithiasis, with no difference in diagnostic accuracy compared with noncontrast CT of the neck.

ABBREVIATIONS: CECTN = contrast-enhanced CT of the neck; NCCTN = noncontrast CT of the neck

Sialolithiasis is defined as the formation of calculi within the salivary glands.¹ It is the most common non-neoplastic condition that affects them. Calculi, which are often multiple, cause partial or complete obstruction of the salivary duct, resulting in obstructive sialadenitis, which may manifest as acute or chronic unilateral gland swelling and pain.^{2–6} Symptoms typically arise during eating because chewing food precipitates salivation.⁷ Sialadenitis can be complicated by bacterial infection and abscess

formation.^{5,8} While calculi in the distal submandibular duct may be readily detectable clinically by bimanual palpation, calculi in the proximal submandibular duct or gland and parotid duct or gland depend on imaging for diagnosis.⁸

Noncontrast CT of the neck (NCCTN) has been recommended for the evaluation of salivary calculi because it is sensitive for the detection of calcifications.⁹ One of the drawbacks of NCCTN is that it provides less detail of duct dilation and intraductal or glandular pathology than contrast-enhanced CT of the neck (CECTN).¹⁰ Traditionally, the use of CECTN in this setting has been in addition to the NCCTN rather than as a stand-alone test.¹¹ Concerns have been raised that on CECTN, blood vessels may simulate small sialoliths and lead to a false-positive diagnosis or reduce diagnostic certainty.^{9,11} CECTN has been used for the evaluation of complicated stone disease in a suspected abscess or an inflammatory process after calculi have been identified on

Received February 16, 2017; accepted after revision June 16.

From the Departments of Radiology (Y.M.P., R.G.K., A.M.C., A.G.C., R.P.K.) and Otolaryngology (S.G.K.), St. Vincent's University Hospital, Elm Park, Dublin, Ireland; and Departments of Otolaryngology (S.G.K.) and Radiology (R.P.K.), Royal Victoria Eye and Ear Hospital, Dublin, Ireland.

Please address correspondence to Yvonne M. Purcell, MD, Radiology Department, St. Vincent's University Hospital, Elm Park, Dublin 4, Ireland; e-mail: yvonne.purcell@gmail.com

<http://dx.doi.org/10.3174/ajnr.A5353>

Patient demographics

Demographics (n = 92)	All (n = 92)	Stone (n = 31)	No Stone (n = 61)	P Value
Mean age (range) (yr)	50 (20–85)	50 (20–79)	49 (20–85)	.76
Sex (M/F) (%)	43:57	48:52	41:59	.52
Referral source (%)				
H&N	79.3% (73/92)	83.9% (26/31)	77% (47/61)	
ED	15.2% (14/92)	12.9% (4/31)	16.4% (10/61)	
Other	5.4% (5/92)	3.2% (1/31)	6.6% (4/61)	
Stone location (n = 50)				
Submandibular system		70% (35/50)		
Gland		38% (19/50)		
Duct		32% (16/50)		
Parotid system		30% (15/50)		
Gland		24% (12/50)		
Duct		6% (3/50)		

Note:—H&N indicates head and neck; ED, emergency department.

NCCTN.^{9,11,12} The use of NCCTN alone gives less detail of glandular and periglandular inflammation.⁹ The addition of CECTN, however, will cause an increase in the patient radiation dose.

The purpose of this study was to determine the accuracy of CECTN alone in the detection of salivary calculi compared with NCCTN alone. A secondary objective was to calculate the patient radiation dose when performing both NCCTN and CECTN.

MATERIALS AND METHODS

Subjects

This retrospective, case-control study was conducted at St. Vincent's University Hospital, a tertiary care, university-affiliated medical center in Dublin, Ireland. The local institutional review board approved this study and waived the requirement for written informed consent.

An electronic search was performed of all consecutive CT neck examinations performed during a 5-year period between January 1, 2011, and December 31, 2015, using the search terms “calculus/calculi,” “stone/stones,” and “sialolith.” Data were collected by electronic query of the hospital Radiology Information System and PACS.

The inclusion criteria were patients older than 16 years of age who had both a NCCTN and CECTN performed during a single visit for the investigation of suspected salivary stones.

CT Image Acquisition

NCCTN and CECTN were acquired on a 64-row multidetector CT scanner (Somatom Sensation 64; Siemens, Erlangen, Germany) in the craniocaudal direction with a collimation of 0.6 mm, gantry rotation of 500 ms, and a pitch of 0.9. Automated dose-control software was used with 120-kV(peak) and reference milliamperes-second (maximum, 200). For the CECTN, 100 mL of nonionic, iodinated low-osmolar contrast medium (Niopam, iopamidol, 340 mg I/mL; Bracco Imaging, Milan, Italy) was injected through a 20-ga or larger cannula, typically sited in the antecubital fossa, at a rate of 2 mL/s with acquisition performed after a delay of 60 seconds. Images for the NCCTN and CECTN were reconstructed with a 512 × 512 matrix and a smooth kernel, with 3-mm axial-section-thickness images set as standard and 3-mm coronal and sagittal reformats. Images were reviewed with syngo Portal Radiologist (Siemens).

Image Analysis

The NCCTN and CECTN were reviewed by both a fellowship-trained diagnostic neuroradiologist and a diagnostic neuroradiology fellow in consensus. The reviewers were blinded to patient details and formal radiology reports. Blinded review of the CECTN was performed first. Following a 2-week interval, a blinded interpretation of the NCCTN was performed. Three-millimeter axial images were inspected, with 3-mm coronal and sagittal reconstructions used for problem-solving. The images were reviewed on soft-tissue neck (center = 50 HU, width = 350 HU), angiographic

lumen (center = 100, width = 700), and bone (center = 500, width = 1500) window settings to optimize detection of calculi. These 3 standard window settings were adjusted manually for every case as the reviewers saw fit. The reviewers recorded the presence or absence of stones, stone location (submandibular or parotid system, gland, or duct; anterior or posterior portion of the duct), stone size, and number of stones. The size of each stone was expressed as the maximal diameter determined on a single axial section. In addition, we recorded the following data: patient demographics (age and sex), the referral source, and the presence of salivary gland masses in the study population.

Statistical Analysis

The accuracy of CECTN in determining the frequency and location of salivary calculi was compared with that of NCCTN used as the criterion standard. Descriptive values were used for patient and stone demographics (actual values, percentages). Statistical analysis was performed by using STATA Statistical Software, Release 12 (StataCorp, College Station, Texas). The sensitivity, specificity, and likelihood ratios were calculated for CECTN in the detection of salivary calculi, with the 95% confidence interval calculated as the measure of variance. The difference in the prevalence of sialolithiasis among different referrers was calculated with the χ^2 test of proportions.

RESULTS

Our search yielded 370 potential cases performed during the 5-year study period. Of these, 92 sets of CT examinations in 90 patients met the inclusion criteria: age older than 16 years and both NCCTN and CECTN performed contemporaneously for the investigation of suspected salivary stones (1 patient had 3 sets of CT examinations) (Table). There were 38 male (42%) and 52 female (58%) patients with a mean age of 50 years (range, 20–85 years). Fifty calculi were identified in 31 patients on NCCTN (the criterion standard), which gives a prevalence of 34%. One patient had 8 calculi, 1 patient had 4 calculi, 1 patient had 3 calculi, 7 patients had 2 calculi, and 21 patients had 1 calculus. Calculi were not present in 59/90 patients (61/92 total cases) on NCCTN.

On CECTN, all patients were correctly categorized as having or not having salivary stones; 48 calculi were identified in 31 patients on CECTN compared with NCCTN as the criterion standard.

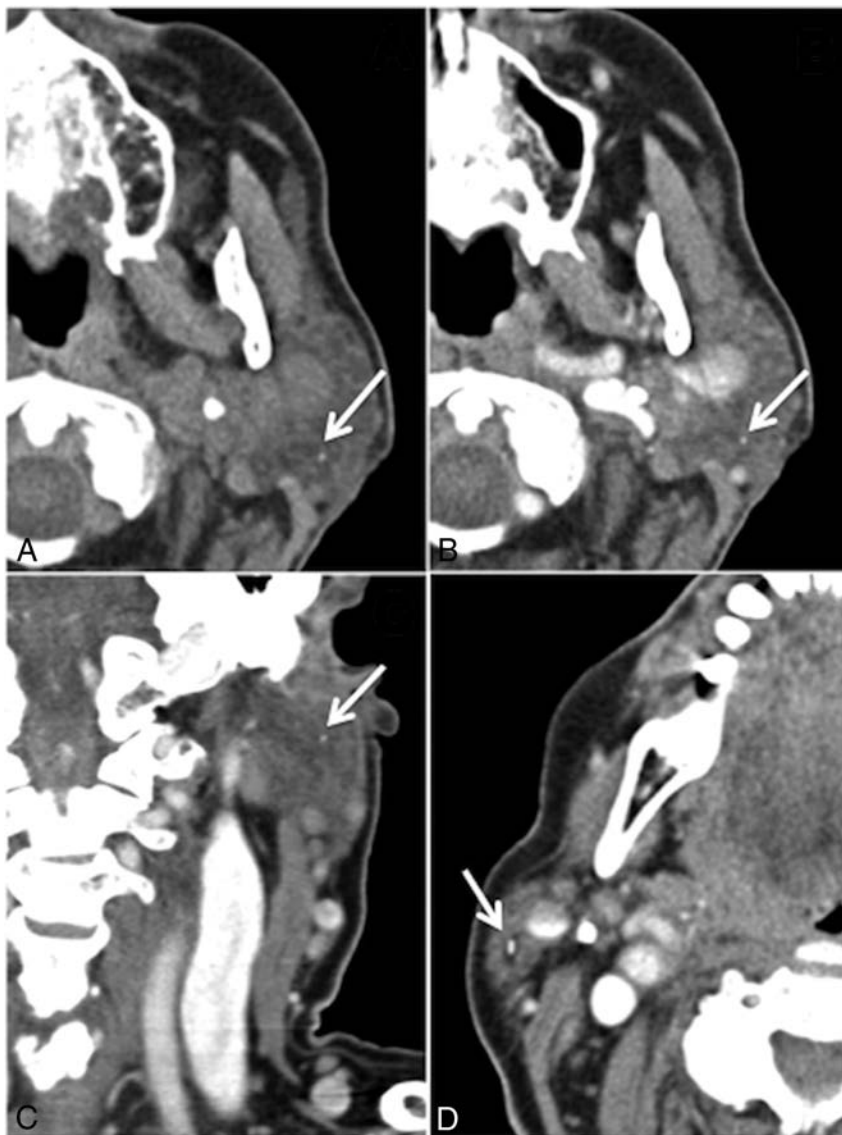


FIG 1. False-negative case. A, Noncontrast CT shows a 1-mm calculus in the superficial lobe of the left parotid gland (arrow), missed on initial review of the CECTN, though it is present on axial (B) and coronal (C, arrows) reconstructions. The distraction is an obstructing 3-mm calculus in the right parotid gland (D, arrow). Note the surrounding intraglandular ductal dilation.

Zero calculi were identified in the remaining 59 patients on CECTN (59/90 patients, 61/92 total cases).

The overall sensitivity of CECTN for the detection of salivary stones was 96% (95% CI, 86.3%–99.5%), and the specificity was 100% (95% CI, 94.1%–100%). The positive predictive value of CECT was 100% (95% CI, 92.6%–100%), and the negative predictive value was 96.8% (95% CI, 89%–99.6%). The positive likelihood ratio was infinity, and the negative likelihood ratio was 0.04 (95% CI, 0.01–0.16). The accuracy of CECTN in diagnosing the presence or absence of salivary stones in our study was 98%.

Two calculi were not identified on CECTN that were identified on the criterion standard NCCTN. Both missed calculi were asymptomatic. The first missed stone was a 1-mm calculus in the left parotid gland in a patient with a symptomatic 3-mm calculus in the right parotid gland (Fig 1A). This was visible on the CECTN in hindsight but was not seen at the time of the review (Fig 1B). It was also visible on the coronal reconstruction (Fig 1C). The sec-

ond missed stone was a 2-mm calculus in the left parotid gland in a patient with multiple bilateral calculi and calcified lymph nodes, which, in retrospect, was visible on the CECTN.

Of the 92 CT studies, 73 (79.3%) referrals came from head and neck surgery; 14 (15.2%), from the emergency department; and 5 (5.4%), from other medical specialties (oncology, cardiology, nephrology, gastroenterology). Of the 73 referrals from head and neck surgery, 26 had calculi, which is a prevalence of 35.6%. Four of the 14 emergency department referrals and 1 of the 5 referrals from other sources had calculi, giving a prevalence of 28.6% and 20%, respectively. The difference in the prevalence of sialolithiasis among different referrers was not statistically significant using the χ^2 test of proportions ($P = .44$) (Table).

The exact locations of the 50 calculi identified are outlined in the Table. Seventy percent of the total calculi (35/50) were in the submandibular system; 38% (19/50), in the submandibular gland and 32% (16/50), in the submandibular duct. Thirty percent (15/50) of the total calculi were in the parotid system; 24% (12/50), in the parotid gland and 6% (3/50), in the parotid duct. The calculi ranged from 1 mm to 2 cm, with a mean diameter of 6 ± 5 mm.

We identified 3 masses: Fine-needle aspiration was performed in 2 cases, and the third case was lost to follow-up. Cytology demonstrated a benign cyst containing inflammatory debris, and the other case was suggestive of an acute inflammatory process with inflammatory

cells and degenerate stromal elements.

The mean total dose-length product of the NCCTN was $290.8 \text{ mGy} \times \text{cm}$, and of the CECTN, it was $366.9 \text{ mGy} \times \text{cm}$. In patients having both CTs, the mean dose-length product was $692.7 \pm 323.5 \text{ mGy} \times \text{cm}$. If the NCCTN had been omitted from each examination, the mean reduction in the effective dose would have been 1.6 mSv, with a standard neck conversion factor of 0.0059, assuming the use of a head CT dose phantom of 16 cm. This is a mean relative dose reduction of 42% per case.

DISCUSSION

Sialolithiasis is the most common benign disorder of the salivary glands.¹ Eighty percent to 90% of calculi are found in the submandibular system, due to the more viscous, alkaline saliva and upward drainage of the duct promoting stasis.^{13,14} Parotid and sublingual calculi account for only 5%–10% and 0%–5% of cases, respectively.¹⁵ In our study, 70% of the total calculi (35/50) were

located in the submandibular system; 38% (19/50), in the submandibular gland and 32% (16/50), in the submandibular duct. This figure is slightly less than rates published in the literature and may be because we only imaged symptomatic patients; those with small calculi may be asymptomatic or those with distal ductal calculi may be clinically managed without imaging. Thirty percent (15/50) of the total calculi were in the parotid system; 24% (12/50), in the parotid gland and 6% (3/50), in the parotid duct. Postmortem studies have indicated that the prevalence of salivary calculi in the population is 1.2%.^{10,16,17} The peak incidence occurs from 30 to 60 years of age.⁵ The mean patient age in our study was 50 years, with a range of 25–85 years and a slight female preponderance of 57% (Table), correlating with that in previously published reports.¹⁸ Clinically symptomatic calculi are less fre-

quent; an incidence of 27–59 cases per million population per year was reported in a review of 15 health regions in England between 1991 and 1995, though a higher incidence rate than previously reported was demonstrated in a nationwide population-based study by Schröder et al,¹⁸ of 14.10 per 100,000 person-years.^{4,19,20} The prevalence of salivary calculi in our study was 34%. There was no significant difference in stone prevalence between patient groups referred by different specialties using the χ^2 test of proportions ($P = .44$).

Imaging techniques available for investigation of salivary calculi include conventional radiography, digital subtraction sialography, sonography, CT, and MR sialography. Conventional radiography is dependent on stone composition, and only about 20% of calculi are radiopaque.²¹ The sensitivity of digital subtraction

sialography ranges from 96% to 100%, and the specificity, from 88% to 91%.²² It is contraindicated in the acute setting due to the potential exacerbation of symptoms associated with infection.⁹ Sonography has been reported to have a sensitivity ranging from 59.1% to 93.7%, and a specificity, from 86.7% to 100%.^{22,23} The sensitivity and specificity of MR imaging sialography have been reported to be 91% and 94%–97%, respectively.¹⁹

CT of the neck with and without contrast is given a rating of 5 by the American College of Radiology, defined as “may be appropriate,” in selected cases if a sialolith is suspected.¹¹ The disadvantage of NCCTN is the lack of detail about potential complications of an obstructing calculus or an alternative diagnosis, such as a salivary tumor.¹² CECTN, while useful for delineation of glandular inflammation or abscess, carries with it the risks associated with intravenous contrast such as allergy, anaphylaxis, extravasation, acute kidney injury, and so forth. Performance of both techniques results in an additional radiation dose to the patient. In our study, a mean reduction in effective dose of 1.6 mSv or a mean relative dose reduction of 42% per case would have been achieved if NCCTN had been omitted from the protocol (using a standard neck conversion factor of 0.0059, assuming use of a head CT dose phantom of 16 cm).

Contrary to previous reports that postulated that contrast may obscure visualization of a calculus,^{9,11} there were no false-positives in our study; calculi can be confidently diagnosed on CECTN. This is the first study, to our knowledge, to directly compare CECTN with

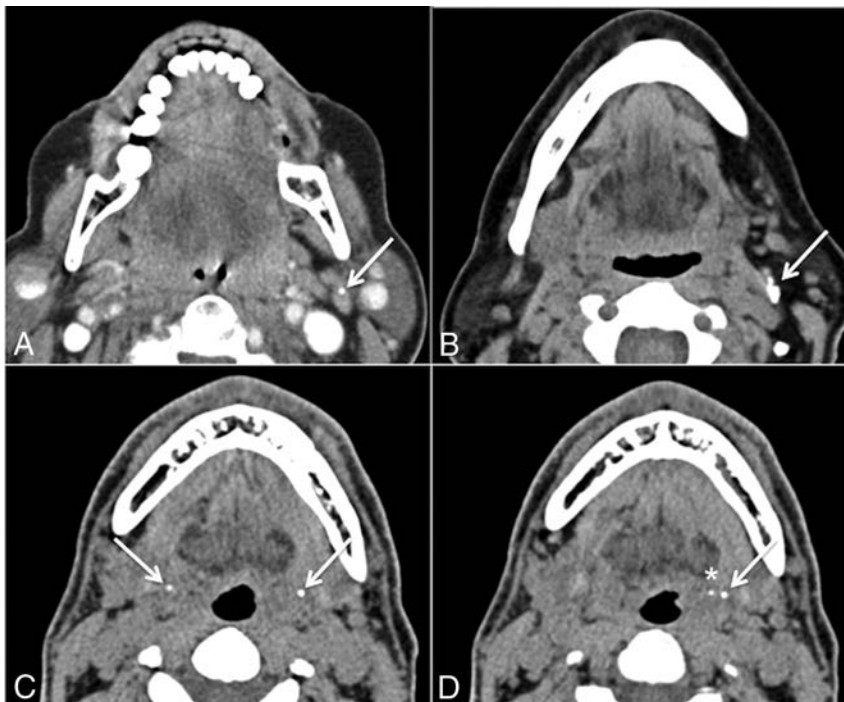


FIG 2. Potential false-positives. A and B, Calcified lymph nodes. C, Bilateral calcification of the stylohyoid ligaments (arrows). D, Calcification of the left stylohyoid ligament (arrow) with an adjacent tonsillolith (asterisk) in the left palatine tonsil.

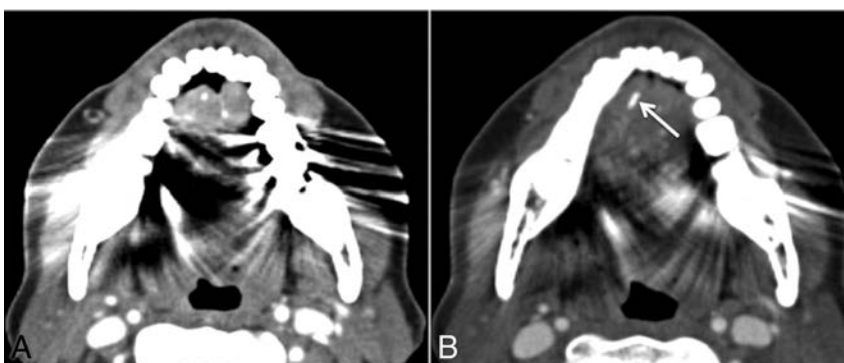


FIG 3. Potential false-negative. A, Axial contrast-enhanced CT. Significant streak artifacts in the floor of the mouth due to dental amalgam. B, Single section inferiorly with windows adjusted manually, revealing an obstructing calculus (arrow) in the right anterior submandibular duct. One should be cautious when analyzing the floor of the mouth because this is a classic location for obstructing submandibular duct calculi and can easily be missed.

NCCTN, used as the criterion standard, for the investigation of suspected salivary calculi.

We report a sensitivity of 96% (95% CI, 86.3%–99.5%) and a specificity of 100% (95% CI, 94.1%–100%) for CECTN in the detection of salivary calculi. In this study, CECTN had an accuracy of 98% for the evaluation of salivary calculi. The diagnoses of the 66% of patients who did not have calculi included acute or chronic sialoadenitis (secondary to infective, granulomatous, or autoimmune etiology), ductal strictures, or cervical lymphadenopathy. We identified 3 masses: Fine-needle aspiration was performed in 2 cases, both benign, and the third case was lost to follow-up.

This study raises the question of the utility of the NCCTN before the CECTN if both studies are being performed, given the accuracy of CECTN in the diagnosis of salivary calculi. The introduction of recent technologic advances such as dual-energy CT may obviate performing both CT examinations. Dual-energy CT acquires images at 2 different energy levels simultaneously and uses the attenuation differences at the different energy levels for deriving additional information. Virtual unenhanced images can be generated from each dataset of a postcontrast CT by extracting the attenuation component attributed to the presence of iodine, thereby removing the need for a separate noncontrast CT and, hence, reducing the dose.^{24,25}

There were no false-positives in our study; all calculi correctly identified on the CECTN were identified on the NCCTN. During this review, we encountered other calcifications in the region of the salivary glands that could be erroneously labeled sialoliths. Entities that radiologists should be aware of that could potentially hamper CT interpretation include calcified lymph nodes (Fig 2A, -B); calcification of the stylohyoid ligament, which can be bilateral (Fig 2C); tonsilloliths (Fig 2D); and phleboliths. Potential false-negatives may be caused by dental amalgam causing metal streak artifacts in the floor of the mouth obscuring a calculus, particularly in the region of the anterior submandibular duct (Fig 3). This is a common location of symptomatic stones that can be easily overlooked if one is not cautious. Radiologists should maximize the basic tools at their disposal, namely manual adjustment of all 3 aforementioned standard window settings. Metal streak artifacts are common and caused by multiple mechanisms (beam-hardening, scatter, noise, undersampling, motion, and conebeam or windmill effects).²⁶ Manufacturers offer an array of techniques to reduce metal streak artifacts, such as filtered back-projection, linear interpolation, selective Algebraic Reconstruction Technique, and the Metal Deletion Technique.²⁷ These techniques were not routinely available at our institution during the study period.

There were 2 false-negatives in our study as previously mentioned; both were asymptomatic intraglandular calculi within the parotid gland.

There are several limitations to this study. It was retrospective and based on radiologic findings only. There was no surgical or pathologic correlation. The clinical outcome of the patients included is not known; therefore, we did not establish which calculi were clinically relevant.

CONCLUSIONS

Contrast-enhanced CT of the neck is accurate in the diagnosis of salivary calculi. If single-phase CECTN instead of dual-phase CT (NCCTN and CECTN) is performed, there is a potential to reduce the effective radiation dose to the patient.

REFERENCES

1. Kiringoda R, Eisele DW, Chang JL. **A comparison of parotid imaging characteristics and sialendoscopic findings in obstructive salivary disorders.** *Laryngoscope* 2014;124:2696–701 CrossRef Medline
2. Marchal F, Dulguerov P, Becker M, et al. **Specificity of parotid sialendoscopy.** *Laryngoscope* 2001;111:264–71 CrossRef Medline
3. Sigismund PE, Zenk J, Koch M, et al. **Nearly 3,000 salivary stones: some clinical and epidemiologic aspects.** *Laryngoscope* 2015;125:1879–82 CrossRef Medline
4. Escudier MP, McGurk M. **Symptomatic sialoadenitis and sialolithiasis in the English population: an estimate of the cost of hospital treatment.** *Br Dent J* 1999;186:463–66 Medline
5. Lustmann J, Regev E, Melamed Y. **Sialolithiasis: a survey on 245 patients and a review of the literature.** *Int J Oral Maxillofac Surg* 1990;19:135–38 CrossRef Medline
6. Marchal F, Dulguerov P, Becker M, et al. **Submandibular diagnostic and interventional sialendoscopy: new procedure for ductal disorders.** *Ann Otol Rhinol Laryngol* 2002;111:27–35 CrossRef Medline
7. Brown JE, Drage NA, Escudier MP, et al. **Minimally invasive radiologically guided intervention for the treatment of salivary calculi.** *Cardiovasc Intervent Radiol* 2002;25:352–55 CrossRef Medline
8. Bialek EJ, Jakubowski W, Zajkowski P, et al. **US of the major salivary glands: anatomy and spatial relationships, pathologic conditions, and pitfalls.** *Radiographics* 2006;26:745–63 CrossRef Medline
9. Yousem DM, Kraut MA, Chalian AA. **Major salivary gland imaging.** *Radiology* 2000;216:19–29 CrossRef Medline
10. Drage NA, Brown JE, Escudier MP, et al. **Interventional radiology in the removal of salivary calculi.** *Radiology* 2000;214:139–42 CrossRef Medline
11. Guideline summary: ACR Appropriateness Criteria neck mass/adenopathy. National Guideline Clearinghouse (NGC) [Web site]. Rockville, Maryland: Agency for Healthcare Research and Quality; 2012. Available: <https://www.guideline.gov>. Accessed July 30, 2017
12. Casselman JW, Mancuso AA. **Major salivary gland masses: comparison of MR imaging and CT.** *Radiology* 1987;165:183–89 CrossRef Medline
13. Escudier MP. **The current status and possible future for lithotripsy of salivary calculi.** *Atlas Oral Maxillofac Surg Clin North Am* 1998;6:117–32 Medline
14. Harrison JD. **Causes, natural history, and incidence of salivary stones and obstructions.** *Otolaryngol Clin North Am* 2009;42:927–47 CrossRef Medline
15. Bodner L. **Salivary gland calculi: diagnostic imaging and surgical management.** *Compendium* 1993;14:572, 574–76, 578 passim; quiz 586 Medline
16. Papadaki ME, McCain JP, Kim K, et al. **Interventional sialoendoscopy: early clinical results.** *J Oral Maxillofac Surg* 2008;66:954–62 CrossRef Medline
17. Williams MF. **Sialolithiasis.** *Otolaryngol Clin North Am* 1999;32:819–34 CrossRef Medline
18. Schröder SA, Andersson M, Wohlfahrt J, et al. **Incidence of sialolithiasis in Denmark: a nationwide population-based register study.** *Eur Arch Otorhinolaryngol* 2017;274:1975–81 CrossRef Medline
19. Becker M, Marchal F, Becker CD, et al. **Sialolithiasis and salivary ductal stenosis: diagnostic accuracy of MR sialography with a three-dimensional extended-phase conjugate-symmetry rapid spin-echo sequence.** *Radiology* 2000;217:347–58 CrossRef Medline
20. Marchal F, Dulguerov P. **Sialolithiasis management: the state of the art.** *Arch Otolaryngol Head Neck Surg* 2003;129:951–56 CrossRef Medline

21. Rauch S, Gorlin RJ. **Disease of the salivary glands.** In: Gorlin RJ, Goldmann HM, eds. *Thomas' Oral Pathology*. St. Louis: Mosby-Year Book; 1970:997–1003
22. Jäger L, Menauer F, Holzknecht N, et al. **Sialolithiasis: MR sialography of the submandibular duct—an alternative to conventional sialography and US?** *Radiology* 2000;216:665–71 [CrossRef Medline](#)
23. Rzymaska-Grala I, Stopa Z, Grala B, et al. **Salivary gland calculi: contemporary methods of imaging.** *Pol J Radiol* 2010;75:25–37 [Medline](#)
24. Aran S, Daftari Besheli L, Karcaaltincaba M, et al. **Applications of dual-energy CT in emergency radiology.** *AJR Am J Roentgenol* 2014; 202:W314–24 [CrossRef Medline](#)
25. Johnson TR. **Dual-energy CT: general principles.** *AJR Am J Roentgenol* 2012;199(5 suppl):S3–8 [CrossRef Medline](#)
26. Barrett JF, Keat N. **Artifacts in CT: recognition and avoidance.** *Radiographics* 2004;24:1679–91 [CrossRef Medline](#)
27. Boas FE, Fleischmann D. **Evaluation of two iterative techniques for reducing metal artifacts in computed tomography.** *Radiology* 2011; 259:894–902 [CrossRef Medline](#)

Prevalence of Internal Auditory Canal Diverticulum and Its Association with Hearing Loss and Otosclerosis

K.J. Pippin, T.J. Muelleman, J. Hill, J. Leever, H. Staecker, and L.N. Ledbetter

ABSTRACT

BACKGROUND AND PURPOSE: Focal low-attenuation outpouching or diverticulum at the anterolateral internal auditory canal is an uncommon finding on CT of the temporal bone. This finding has been described as cavitory otosclerosis in small case reports and histology series. The purpose of this study was to establish the prevalence of internal auditory canal diverticulum and its association with classic imaging findings of otosclerosis and/or hearing loss.

MATERIALS AND METHODS: Temporal bone CT scans of 807 patients, obtained between January 2013 and January 2016, were retrospectively reviewed to identify internal auditory canal diverticula and/or classic imaging findings of otosclerosis. Clinical evaluations for hearing loss were reviewed for patients with internal auditory canal diverticula and/or otosclerosis.

RESULTS: Internal auditory canal diverticula were found in 43 patients (5%); classic otosclerosis, in 39 patients (5%); and both findings, in 7 patients (1%). Most temporal bones with only findings of internal auditory canal diverticula (91%) demonstrated hearing loss, with 63% of this group demonstrating sensorineural hearing loss. The hearing loss classification distribution was significantly different ($P < .01$) from that in the classic otosclerosis group and in the group with both diverticula and otosclerosis.

CONCLUSIONS: Internal auditory canal diverticula are not uncommon on CT examinations of the temporal bone and most commonly occur without classic imaging findings of otosclerosis. These lesions are associated with sensorineural hearing loss, and referral for hearing evaluation may be appropriate when present.

ABBREVIATIONS: CHL = conductive hearing loss; IAC = internal auditory canal; SNHL = sensorineural hearing loss

A focal low-attenuation notch or diverticulum within the temporal bone continuous with the internal auditory canal (IAC) is an unusual finding on imaging studies of the temporal bone. Several histologic and imaging case reports refer to this finding as a form of cavitory otosclerosis¹⁻⁴ and even suggest that the presence is associated with advanced disease.³

Otosclerosis is an osteodystrophic disorder of the otic capsule, resulting in abnormal resorption of endochondral bone and deposition of abnormal vascular bone. Otosclerosis usually appears in the third-to-fifth decades of life, and most commonly affects women. Clinical otosclerosis is present in <1% of the population, though it has been reported in up to 11% of

the population on histology performed at postmortem examination.⁵ On CT of the temporal bone, otosclerosis commonly appears as lucent or hypodense bone surrounding the otic capsule, often limited to the region anterior to the oval window. This process results in either conductive hearing loss (CHL) due to fixation of the stapes footplate or mixed conductive and sensorineural hearing loss (SNHL) due concomitant otic capsule involvement. Otosclerosis presenting with only SNHL in the absence of CHL is rare and is often called “cochlear otosclerosis.”⁵⁻⁹

Establishing the significance of the IAC diverticulum or notch is important for both the radiologist and referring physician in guiding clinical management. Determining the relationship of this lesion to classic imaging findings of otosclerosis could also be helpful in the understanding of otosclerosis and the spectrum of clinical presentations. Therefore, the purpose of this study was the following: 1) to determine the prevalence of IAC diverticula at our institution, and 2) to explore potential associations with otosclerosis and hearing loss in patients identified with an IAC diverticulum.

Received May 1, 2017; accepted after revision July 31.

From the Departments of Radiology (K.J.P., J.H., J.L., L.N.L.) and Otolaryngology (T.J.M., H.S.), University of Kansas Medical Center, Kansas City, Kansas.

Paper previously presented at: Annual Meeting of the American Society of Head and Neck Radiology, September 7–11, 2016; Washington, DC.

Please address correspondence to Luke N. Ledbetter, MD, University of Kansas, Department of Radiology, 3901 Rainbow Blvd, MS 4032, Kansas City, KS 66160; e-mail: lledbetter@kumc.edu; @LNLedbetter

<http://dx.doi.org/10.3174/ajnr.A5399>

Table 1: Demographic characteristics for total study population

Characteristic	Total Population (n = 807)	IAC Diverticulum			Otosclerosis		
		Present (n = 43)	Not Present (n = 764)	P Value	Present (n = 39)	Not Present (n = 768)	P Value
Median age (range) (yr)	52 (18–96)	61 (18–91)	52 (18–96)	<.01 ^a	52 (22–85)	52 (18–96)	.69 ^a
Sex (No.) (%)				.93 ^b			.13 ^b
Male	343 (42.5)	18 (41.9)	325 (42.5)		12 (30.8)	331 (43.1)	
Female	464 (57.5)	25 (58.1)	439 (57.5)		27 (69.2)	437 (56.9)	

^a P value was calculated with the Wilcoxon rank sum test.

^b P value was calculated with the χ^2 test.

MATERIALS AND METHODS

Study Design

This study was approved by the institutional review board and was compliant with the Health Insurance Portability and Accountability Act. A radiology data base was searched for all temporal bone CT examinations performed between January 1, 2013, and January 31, 2016. Exclusion criteria included age younger than 18 years or a prior operation that altered the IAC. Eligible temporal bone CT examinations were retrospectively reviewed by a neuroradiologist (L.N.L.) with 4 years of experience and a Certificate of Added Qualification in neuroradiology. Electronic medical review was performed for patient demographics, otologic history, clinical examination findings, and audiometric evaluation.

Imaging Review

Most imaging examinations were dedicated CTs of the temporal bones performed on a 64-section multidetector CT scanner (LightSpeed VCT; GE Healthcare; Milwaukee, Wisconsin). Protocol parameters included helical acquisition with 120 kV(peak), maximum of 320 mA, and a 0.5 pitch extending from just above the petrous ridge through the skull base. Images of each temporal bone were reformatted at 0.625-mm section thickness without a gap with a 100-mm FOV and 512 × 512 matrix. Standard axial and coronal reformations were reviewed for each temporal bone.

Images were reviewed for the presence of IAC diverticula or classic imaging findings of otosclerosis. An IAC diverticulum was defined as a nonvascular, low-density outpouching from the normal linear contour of the wall of the IAC, identified on both axial and standard coronal reformatted images. No minimum size threshold was used for the diagnosis of diverticulum. Classic imaging otosclerosis was defined as “fenestral” if abnormal lucent bone was anterior to the oval window, “cochlear” if the lucent bone surrounded the cochlea, or a combination of both locations. All findings were described as bilateral or unilateral.

Hearing Review

Association of imaging findings of IAC diverticula and classic imaging otosclerosis with hearing loss was evaluated by review of available clinical and audiometric evaluations. Patients with available clinical data were divided into 4 categories: no hearing loss, conductive hearing loss, sensorineural hearing loss, or mixed hearing loss, based on detailed otolaryngology review. The degree of pure SNHL was determined by the pure tone average, which is the average of the pure tone thresholds in decibels obtained at 4 selected frequencies and is a measure of the severity of hearing loss.¹⁰ The 4-frequency pure tone average in our study was re-

ported with 0.5, 1, 2, and 3 kHz. Audiograms for patients who had undergone prior temporal bone surgery were excluded from hearing analysis to eliminate confounding alterations in hearing loss related to the operation.

Statistical Analysis

The prevalence of findings in the study population and associations between hearing groups were evaluated with Wilcoxon rank sum, Kruskal-Wallis, Fisher exact, and χ^2 analyses performed with SAS software, Version 9.4 (SAS Institute, Cary, North Carolina). A P value of < .05 was used to determine statistical significance.

RESULTS

A total of 810 eligible temporal bone CT examinations were identified during the 3-year study period. Three studies were excluded because of nondiagnostic images due to motion or artifacts. Patient demographics are described in Table 1. Of the 807 patients included in the study, IAC diverticulum was identified in 5% (n = 43) of examinations. The appearance ranged from a small notch to full outpouching, with all diverticula located along the anterior IAC medial to the cochlea (Fig 1). Sixty percent of patients (n = 26) demonstrated bilateral diverticula. Classic imaging findings of otosclerosis were also present in 5% (n = 39) of patients. Sixty-nine percent of patients with classic imaging findings of otosclerosis (n = 27) demonstrated bilateral findings. One percent (n = 7) of all eligible patients demonstrated imaging findings of both otosclerosis and IAC diverticula with 71% (n = 5) of this group demonstrating bilateral otosclerosis and IAC diverticula (Fig 2). Demographics of patients with IAC diverticula, both with and without otosclerosis, are described in Table 2.

Seventy-five of 807 patients (n = 123 temporal bones) demonstrated findings of IAC diverticula, otosclerosis, or both and were further evaluated for hearing loss. These individual temporal bones were divided into 3 groups: IAC diverticulum only, otosclerosis only, and both IAC diverticulum and otosclerosis (Table 3).

In the IAC diverticulum-only group, there were 36 patients with 57 affected temporal bones. Audiogram results were unavailable or excluded due to a prior operation for 14 temporal bones in this group. Of the 43 temporal bones with only an IAC diverticulum and hearing evaluation, 9% (n = 4) demonstrated no hearing loss, 63% (n = 27) demonstrated SNHL, and 28% (n = 12) demonstrated a mixed hearing loss. No temporal bones in this group demonstrated CHL.

In the classic otosclerosis-only group, there were 33 patients with 54 affected temporal bones. Most (81%, n = 44) temporal bones had fenestral otosclerosis only, while 4% (n = 2) had co-

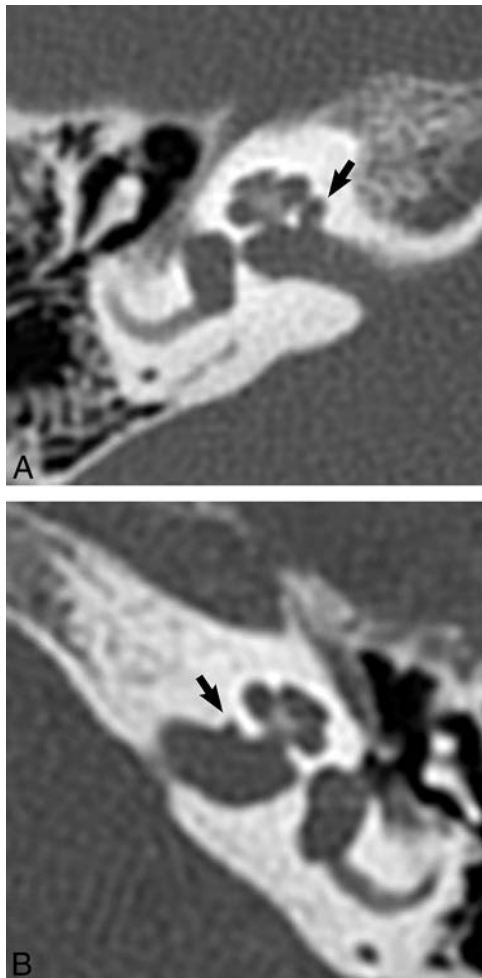


FIG 1. IAC diverticula on temporal bone CT. A, CT of the right temporal bone in a 41-year-old woman with vertigo. A CSF-density saccular outpouching of the anterior IAC medial to the cochlea is compatible with an IAC diverticulum (black arrow). B, CT of the left temporal bone in a 67-year-old woman undergoing evaluation of SNHL. A smaller diverticulum or notch is present along the anterior IAC in a location similar to that of the larger diverticula in A (black arrow).

chlear otosclerosis only and 15% ($n = 8$) had both fenestral and cochlear otosclerosis. Audiogram results were unavailable or excluded for 15 temporal bones in this group. A total of 18% ($n = 7$) demonstrated no hearing loss, 26% ($n = 10$) demonstrated SNHL, 23% ($n = 9$) demonstrated a mixed hearing loss, and 33% ($n = 13$) demonstrated CHL.

In the IAC diverticulum and otosclerosis group, there were 7 patients with 12 affected temporal bones. Fenestral otosclerosis was present in all 12 temporal bones, with 3 temporal bones demonstrating concomitant cochlear otosclerosis. Audiogram results were unavailable or excluded for 5 temporal bones in this group. A total of 14% ($n = 1$) demonstrated no hearing loss, 29% ($n = 2$) demonstrated SNHL, 43% ($n = 3$) demonstrated a mixed hearing loss, and 14% ($n = 1$) demonstrated CHL.

Comparison of the 3 groups demonstrated a statistically significant difference in hearing loss patterns between each group. These findings suggest that SNHL is more commonly associated with IAC diverticulum than with traditional imaging findings of otosclerosis.

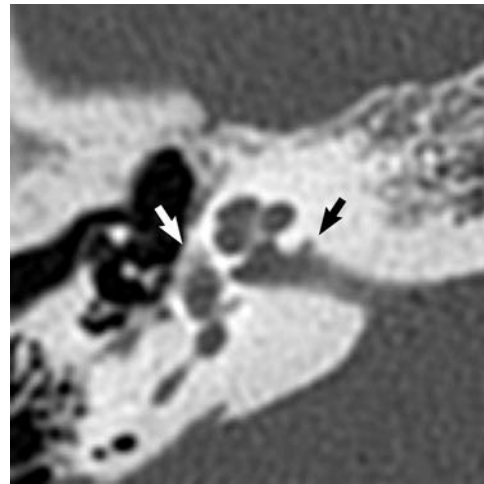


FIG 2. IAC diverticulum with classic imaging findings of otosclerosis on temporal bone CT in a 34-year-old woman evaluated for mixed hearing loss. There is a small IAC diverticulum along the anterior IAC (black arrow) with focal lucency of the otic capsule adjacent to the anterior oval window near the fissula ante fenestram (white arrow).

DISCUSSION

The prevalence and clinical significance of IAC diverticula are not well-established in the current literature. In this large retrospective case review, IAC diverticula were present in 5% of our study population and more frequent ($n = 43$) than classic findings of otosclerosis ($n = 39$). The appearance of diverticula varied from a small notch to a larger outpouching and was always located at the anterior IAC near the medial margin of the dense otic capsule. IAC diverticula were more commonly an isolated finding and rarely occurred with concurrent classic findings of otosclerosis. Compared with patients with isolated otosclerosis (median age, 52 years), patients with IAC diverticula were significantly older at median ages of 62 years with additional findings of otosclerosis and 61 years without additional findings of otosclerosis ($P < .01$).

Most (91%) patients with an isolated IAC diverticulum without additional imaging evidence of otosclerosis had hearing loss with more than half (63%) demonstrating pure SNHL. The pattern of hearing loss in isolated IAC diverticula was also found to be significantly different from hearing loss patterns in the classic imaging appearance of otosclerosis with or without an additional finding of an IAC diverticulum. These findings suggest that IAC diverticula are a clinically important finding on temporal bone CT and have important hearing loss implications.

Audiometric data demonstrated more advanced hearing loss in patients with isolated IAC diverticula than previously reported with presbycusis or age-related hearing loss. Presbycusis or age-related hearing loss is defined as SNHL caused by the aging process without a confounding etiology, such as metabolic disorder, trauma, or noise injury.¹⁰ Presbycusis may play a partial role in SNHL in the diverticula group, given that the median age of the diverticula-only group was 61 years. However, the average pure tone average was 53.5 dB in the 27 temporal bones with isolated IAC diverticula, which is consistent with moderate-to-moderate-severe hearing loss and was greater than expected with presbycusis alone.^{10,11} Moreover, the average pure tone average in the 27 isolated diverticula with SNHL was like that in the 10 temporal bones

Table 2: Demographic characteristics by the presence of IAC or otosclerosis

Characteristic	IAC Diverticulum Only (n = 36)	Otosclerosis Only (n = 32)	IAC Diverticulum + Otosclerosis (n = 7)	None (n = 732)	P Value
Median age (range) (yr)	62 (18–91)	52 (18–91)	61 (30–70)	52 (18–96)	<.01 ^a
Sex (No.) (%)					.47 ^b
Male	15 (41.7)	9 (28.1)	3 (42.9)	316 (43.2)	
Female	21 (58.3)	23 (71.9)	4 (57.1)	416 (56.8)	
Temporal bone involvement (No.) (%)					.02 ^b
Unilateral	9 (20.9)	15 (38.5)	5 (71.4)		
Bilateral	34 (79.1)	24 (61.5)	2 (28.6)		

^a P value was calculated with the Kruskal-Wallis test.

^b P value was calculated with the Fisher exact test.

Table 3: Associations between IAC diverticulum or otosclerosis and hearing loss

Characteristic	IAC Diverticulum Only (n = 43)	Otosclerosis Only (n = 39)	IAC Diverticulum + Otosclerosis (n = 7)	P Value
Hearing loss (No.) (%)				<.01 ^a
None	4 (9%)	7 (18%)	1 (14%)	
SNHL	27 (63%)	10 (26%)	2 (29%)	
PTA (average) (range) (dB)	53.5 (10.6–120)	55.3 (16.9–115)	97.5 (94.4–100.6)	
CHL (No.) (%)	None	13 (33%)	1 (14%)	
Mixed (No.) (%)	12 (28%)	9 (23%)	3 (43%)	

Note:—PTA indicates pure tone average.

^a P value was calculated for comparison of groups with the Fisher exact test.

with isolated imaging findings of otosclerosis presenting with SNHL (55.3 dB). Therefore, the degree of SNHL in temporal bones with diverticula was higher than expected for age-related hearing loss and like that in temporal bones with accepted inner ear pathology.

IAC diverticula are described in small case reports as rare entities reflective of cavitory otosclerosis.^{1–4} Beyond the hearing loss implications of cavitory otosclerosis, Makarem et al² also described the clinical significance of the lesion for potential cochlear implant malpositioning into the diverticulum. The consistent location of all diverticula in this series along the anterior IAC matches that in prior temporal bone histology series descriptions of cavitory otosclerosis.^{12,13} The occurrence of outpouching or notches was like classic CT findings of otosclerosis in this study, both groups representing 5% of all patients. Therefore, the prevalence of IAC diverticula is likely not as rare as previously implied. Moreover, the findings in this series do not support previous reporting of an IAC diverticulum as a manifestation of severe otosclerosis³ due to its high frequency as an isolated finding and the occurrence of the lesion in patients without hearing loss. Previous case reports do not directly address the significance of IAC diverticula as an isolated finding without additional classic CT findings of otosclerosis. This study suggests that isolated IAC diverticula are related to hearing loss in a different pattern than the classic CT presentation of otosclerosis.

Classic otosclerosis invariably involves the anterior stapes footplate near the fissula ante fenestram and presents with a component of CHL.^{5,14} SNHL in otosclerosis is less well-understood and may be due to production of local inflammatory cytokines leading to atrophy and concomitant dysfunction of the spiral ligament.^{15,16} SNHL is usually present with CHL and manifests as a mixed hearing loss classification. Temporal bones in this study that had classic imaging findings of otosclerosis more commonly presented with CHL, and temporal bones with both classic imaging findings of otosclerosis plus diverticula more commonly pre-

sented with mixed hearing loss as expected. No hearing loss was identified in 7 temporal bones with findings of otosclerosis (18% of temporal bones with otosclerosis). These temporal bones had imaging indications for otosclerosis or hearing loss with a unilateral clinical presentation of hearing loss and bilateral imaging findings. Otosclerosis presenting with isolated SNHL without a conductive component is believed to be rare

and not well-understood.^{5,17–19} IAC diverticula may represent an imaging manifestation of otosclerosis with an isolated SNHL, because most patients with diverticula in this study presented with isolated SNHL (63%). A smaller portion of isolated IAC diverticula demonstrated a mixed pattern of hearing loss (28%). These IAC diverticula may result in not only SNHL due to spiral ligament dysfunction but also CHL due to abutment to the scala vestibuli, resulting in a third-window phenomenon.^{2,4,16,20} Another potential explanation of mixed hearing loss with CT findings of isolated diverticula may be otosclerosis involvement of the footplate below the resolution of routine CT temporal bone examinations.

There were several limitations to this study. Its retrospective nature limited the information available for review. Namely, clinical data were not available for all patients with IAC diverticula or classic otosclerosis. Small sample sizes, especially in the combined IAC diverticula and otosclerosis group, limited statistical analysis for comparing grouped populations of CT findings. This study also had a component of selection bias that may have overestimated the prevalence of findings on CT due to referral patterns. MR images of the temporal bone were also not reviewed in this study, despite MR imaging being a frequently ordered examination to evaluate SNHL. With most patients with IAC diverticula demonstrating SNHL, the actual prevalence of IAC diverticula may have been higher on high-resolution MR imaging compared with CT.

The relationship of the anterior internal auditory canal wall to the development of a diverticulum or focal otosclerosis is unclear. The IAC diverticulum may be occasionally present in classic otosclerosis early in the disease process when other changes are too subtle to be detected on imaging. An additional consideration is that the IAC diverticulum represents a variant of cochlear otosclerosis with the nidus for resorption of endochondral bone near the junction of endochondral bone of the medial otic capsule and lamellated bone of the IAC, as opposed to the more common

location of the fissula ante fenestram. In this situation, the diverticula could potentially represent advanced spongiotic bone immediately adjacent to IAC CSF. Hounsfield unit values were not measured to evaluate quantitative density due to the small size of several of the diverticula, limiting accuracy. However, this lesion qualitatively appeared as a low, near-CSF density notch or outpouching in the bone cortex. IAC diverticula are also unlikely to be found in disease processes such as osteoporosis, Paget disease, or osteogenesis imperfecta given their frequency as a small isolated finding. It is also unlikely that an IAC diverticulum reflects a normal anatomic variant, given its association with hearing loss greater than expected for age. While this study cannot determine the etiology of the diverticulum, this lesion does demonstrate a relationship with hearing loss and, most commonly, SNHL.

The results of this study illustrate the clinical importance of identification of IAC diverticula due their association with hearing loss, and radiologists should be aware of this entity. If identified on imaging, otolaryngology consultation and audiometric evaluation should be considered if not previously performed. IAC diverticula can be identified not uncommonly on temporal bone CT and should be mentioned in the radiology report, given their association with hearing loss.

CONCLUSIONS

IAC diverticula are focal CSF attenuation outpouchings at the anterolateral internal auditory canal, present on 5% of CT examinations of the temporal bone in our study population. IAC diverticula are most commonly isolated findings and are associated with a different pattern of hearing loss compared with classic findings of otosclerosis. Identification of this clinically significant finding on CT may warrant audiometric evaluation, given the association with hearing loss, specifically SNHL.

ACKNOWLEDGMENTS

We thank Suzanne Hunt and Yu Wang for assistance with the statistical review of the data.

Disclosures: Hinrich Staecker—UNRELATED: Grants/Grants Pending: National Institute on Deafness and Other Communication Disorders.* Luke N. Ledbetter—UNRELATED: Royalties: Elsevier, Comments: royalties for book chapters in *Diagnostic Imaging: Head and Neck*. 3rd ed. *Money paid to the institution.

REFERENCES

1. Makarem AO, Linthicum FH. **Cavitating otosclerosis.** *Otol Neurotol* 2008;29:730–31 [CrossRef Medline](#)
2. Makarem AO, Hoang TA, Lo WW, et al. **Cavitating otosclerosis: clinical, radiologic, and histopathologic correlations.** *Otol Neurotol* 2010;31:381–84 [CrossRef Medline](#)
3. Hoeberigs M, Postma A, Waterval J, et al. **Prevalence of anterior internal auditory canal “diverticulum” on high resolution CT in patients with otosclerosis.** In: *Proceedings of the Radiological Society of North America 2012 Scientific Assembly and Annual Meeting*, Chicago, Illinois. November 25–30, 2012. <http://archive.rsna.org/2012/12029990.html>. Accessed August 8, 2016
4. Bou-Assaly W, Mukherji S, Srinivasan A. **Bilateral cavitary otosclerosis: a rare presentation of otosclerosis and cause of hearing loss.** *Clin Imaging* 2013;37:1116–18 [CrossRef Medline](#)
5. Chole RA, McKenna M. **Pathophysiology of otosclerosis.** *Otol Neurotol* 2001;22:249–57 [CrossRef Medline](#)
6. Schuknecht HF, Kirchner JC. **Cochlear otosclerosis: fact or fantasy.** *Laryngoscope* 1974;84:766–82 [CrossRef Medline](#)
7. Schuknecht HF. **Cochlear otosclerosis: a continuing fantasy.** *Arch Otorhinolaryngol* 1979;222:79–84 [CrossRef Medline](#)
8. Nelson EG, Hinojosa R. **Questioning the relationship between cochlear otosclerosis and sensorineural hearing loss: a quantitative evaluation of cochlear structures in cases of otosclerosis and review of the literature.** *Laryngoscope* 2004;114:1214–30 [CrossRef Medline](#)
9. Hayashi H, Onerci O, Paparella MM. **Cochlear otosclerosis.** *Otol Neurotol* 2006;27:905–06 [CrossRef Medline](#)
10. Flint PW, Haughey BH, Lund VJ. *Cummings Otolaryngology: Head and Neck Surgery, 3-volume set.* 6th ed. London: Saunders; 2014
11. Wiley TL, Chappell R, Carmichael L, et al. **Changes in hearing thresholds over 10 years in older adults.** *J Am Acad Audiol* 2008;19:281–92; quiz 371 [CrossRef Medline](#)
12. Hueb M, Goycoolea M, Paparella M, et al. **Otosclerosis: the University of Minnesota temporal bone collection.** *Otolaryngol Head Neck Surg* 1991;105:396–405 [CrossRef Medline](#)
13. Schuknecht HF, Barber W. **Histologic variants in otosclerosis.** *Laryngoscope* 1985;95:1307–17 [Medline](#)
14. Rudic M, Keogh I, Wagner R, et al. **The pathophysiology of otosclerosis: review of current research.** *Hearing Res* 2015;330(pt A):51–56 [CrossRef Medline](#)
15. Adams J. **Clinical implications of inflammatory cytokines in the cochlea: a technical note.** *Otol Neurotol* 2002;23:316–22 [CrossRef Medline](#)
16. Merchant S, Nadol J, Schuknecht HF. *Schuknecht's Pathology of the Ear.* 3rd ed. Shelton, Connecticut: McGraw Hill Medical; 2010
17. Young IM, Mikaelian DO, Trocki IM. **Sensorineural hearing level in unilateral otosclerosis.** *Otolaryngol Head Neck Surg* 1979;87:486–90 [CrossRef Medline](#)
18. Virolainen E, Puhakka H, Rahko T. **The cochlear component in operated otosclerosis after a mean period of 16 years: a follow-up study.** *Audiology* 1980;19:101–04 [CrossRef Medline](#)
19. Vincent R, Sperling NM, Oates J, et al. **Surgical findings and long-term hearing results in 3,050 stapedotomies for primary otosclerosis: a prospective study with the otology-neurotology database.** *Otol Neurotol* 2006;27(8 suppl 2):S25–47 [CrossRef Medline](#)
20. Richard C, Linthicum FH Jr. **An unexpected third window in a case of advanced cavitating otosclerosis.** *Otol Neurotol* 2012;33:e47–48 [CrossRef Medline](#)

Clinical and Imaging Characteristics of Arteriopathy Subtypes in Children with Arterial Ischemic Stroke: Results of the VIPS Study

 M. Wintermark,  N.K. Hills,  G.A. DeVeber,  A.J. Barkovich,  T.J. Bernard,  N.R. Friedman,  M.T. Mackay,  A. Kirton,  G. Zhu,  C. Leiva-Salinas,  Q. Hou,  H.J. Fullerton, and the VIPS Investigators



ABSTRACT

BACKGROUND AND PURPOSE: Childhood arteriopathies are rare but heterogeneous, and difficult to diagnose and classify, especially by nonexperts. We quantified clinical and imaging characteristics associated with childhood arteriopathy subtypes to facilitate their diagnosis and classification in research and clinical settings.

MATERIALS AND METHODS: The Vascular Effects of Infection in Pediatric Stroke (VIPS) study prospectively enrolled 355 children with arterial ischemic stroke (2010–2014). A central team of experts reviewed all data to diagnose childhood arteriopathy and classify subtypes, including arterial dissection and focal cerebral arteriopathy–inflammatory type, which includes transient cerebral arteriopathy, Moyamoya disease, and diffuse/multifocal vasculitis. Only children whose stroke etiology could be conclusively diagnosed were included in these analyses. We constructed logistic regression models to identify characteristics associated with each arteriopathy subtype.

RESULTS: Among 127 children with definite arteriopathy, the arteriopathy subtype could not be classified in 18 (14%). Moyamoya disease ($n = 34$) occurred mostly in children younger than 8 years of age; focal cerebral arteriopathy–inflammatory type ($n = 25$), in children 8–15 years of age; and dissection ($n = 26$), at all ages. Vertigo at stroke presentation was common in dissection. Dissection affected the cervical arteries, while Moyamoya disease involved the supraclinoid internal carotid arteries. A banded appearance of the M1 segment of the middle cerebral artery was pathognomonic of focal cerebral arteriopathy–inflammatory type but was present in <25% of patients with focal cerebral arteriopathy–inflammatory type; a small lenticulostriate distribution infarct was a more common predictor of focal cerebral arteriopathy–inflammatory type, present in 76%. It remained difficult to distinguish focal cerebral arteriopathy–inflammatory type from intracranial dissection of the anterior circulation. We observed only secondary forms of diffuse/multifocal vasculitis, mostly due to meningitis.

CONCLUSIONS: Childhood arteriopathy subtypes have some typical features that aid diagnosis. Better imaging methods, including vessel wall imaging, are needed for improved classification of focal cerebral arteriopathy of childhood.

ABBREVIATIONS: FCA = focal cerebral arteriopathy of childhood; FCA-d = focal cerebral arteriopathy–dissection type; FCA-i = focal cerebral arteriopathy–inflammatory type; TCA = transient cerebral arteriopathy; VIPS = Vascular Effects of Infection in Pediatric Stroke

Approximately 2500 children in the United States have an arterial ischemic stroke each year.¹ Childhood arteriopathies are the most common identifiable cause of arterial ischemic stroke (in a previously healthy child, present in up to 64%).^{2–6} They represent a strong predictor of recurrent stroke, with rates

exceeding 30% within 12 months for some arteriopathy subtypes,^{2,7,8} and published guidelines for the prevention of recurrence are specific to type (eg, dissection, Moyamoya disease, transient cerebral arteriopathy, and so forth).⁹ Nonetheless, childhood arteriopathies remain difficult to not only diagnose but classify; they are

Received February 18, 2017; accepted after revision July 6.


From the Department of Radiology (M.W.), Neuroradiology Division, Stanford University, Stanford, California; Departments of Neurology (N.K.H., H.J.F.), Biostatistics and Epidemiology (N.K.H.), Radiology (A.J.B., H.J.F.), and Pediatrics (A.J.B.), University of California, San Francisco, San Francisco, California; Department of Neurology (G.A.D.), Hospital for Sick Children, Toronto, Ontario, Canada; Department of Pediatrics (T.J.B.), University of Colorado, Denver, Colorado; Center for Pediatric Neurology (N.R.F.), Neurological Institute, Cleveland Clinic, Cleveland, Ohio; Children's Stroke Program (M.T.M.), Murdoch Children's Research Institute, Royal Children's Hospital, Melbourne, Victoria, Australia; Departments of Pediatrics and Clinical Neurosciences (A.K.), Alberta Children's Hospital and University of Calgary, Calgary, Alberta, Canada; Department of Neurology (G.Z.), Military General Hospital of Beijing PLA, Beijing, China; Department of Radiology (C.L.-S.), University of Virginia,


Charlottesville, Virginia; and Department of Neurology (Q.H.), Guangdong No.2 Provincial People's Hospital, Guangzhou, China.

This work was supported by National Institutes of Health R01 NS062820 (Principal Investigators H.J. Fullerton, G.A. DeVeber), Bellafilles Foundation, and Marc and Lynne Benioff for statistical support.

See the Appendix for a list of investigators.

Please address correspondence to Max Wintermark, MD, Stanford University, Department of Radiology, Neuroradiology Division, 300 Pasteur Dr, Room S047, Stanford, CA 94305-5105; e-mail: Max.Wintermark@gmail.com; @StanfordNRAD

 Indicates open access to non-subscribers at www.ajnr.org

 Indicates article with supplemental on-line tables.

<http://dx.doi.org/10.3174/ajnr.A5376>

rare but heterogeneous, and MRA imaging, frequently substituted for conventional angiography, is technically limited. Publication of consensus-based definitions of childhood arteriopathy in 2004 (adapted for the Vascular Effects of Infection in Pediatric Stroke [VIPS] study in 2009) and the development of the Interbody Fusion Devices in the Treatment of Cervicobrachial Syndrome (CASCADE)¹⁰ system in 2012 (which provided a novel approach to classifying the “anatomic site of disease” in childhood arterial ischemic stroke) have largely been addressed to pediatric stroke specialists.

These tools are less useful for nonexperts, however, who are frequently responsible for making timely decisions crucial to the prevention of stroke recurrence. It is this gap that in large part, we seek to address. In the prospective, international, National Institutes of Health–funded Vascular Effects of Infection in Pediatric Stroke study, a 4-person team of pediatric stroke experts classified the etiology of 355 cases of pediatric arterial ischemic stroke (based on rigorous central review of neuroimaging and clinical data). With this “expert opinion” as the criterion standard, the goal of the current analysis was to guide the classification of childhood arteriopathies by quantifying the prevalence and odds ratios for clinical and imaging biomarkers that were used in the expert review to do the following: 1) distinguish arteriopathy from cardioembolism, and 2) distinguish among the most common subtypes of childhood arteriopathy. In other words, we aimed to identify and quantify biomarkers that could allow trained neuroradiologists and neurologists who are nonexperts in childhood arteriopathies to generate a reasonable differential diagnosis for a child with stroke.

MATERIALS AND METHODS

Study Design

Ethics committee approvals were obtained at all sites. From 2009 to 2014, the VIPS study enrolled 355 children (29 days to 18 years of age) with arterial ischemic stroke at 37 international sites, collected detailed clinical data (eg, medical history such as cardiac disease and sickle cell anemia, recent exposures such as infection, and head trauma), and performed central review of brain and cerebrovascular imaging (by M.W., H.J.F., G.A.D., and A.J.B.). Details of VIPS methods have been published.¹¹ As a part of the VIPS study, an exhaustive and systematic centralized review of baseline and follow-up vascular imaging and clinical data was performed to first arrive at a diagnosis of arteriopathy and then to classify the arteriopathy subtype.¹² For this study, we included all children with abnormal vascular imaging findings that could be definitively classified as due to arteriopathy or cardioembolism.

Imaging Review

In our review of brain parenchymal imaging, we recorded infarct size (using ABC/2),¹³ laterality, location, acuity, and associated hemorrhage. Vascular imaging findings were first classified as normal or abnormal and then were completely described with respect to type of abnormality (eg, hypoplasia, irregularity, banding, stenosis, occlusion, and so forth), vascular territories and sides affected, number and type of arterial segments affected, and degree of collateral flow. Details of the VIPS imaging review have been published.¹²

Childhood Arteriopathy Classification

Two primary reviewers (M.W., H.J.F.) independently used clinical data and parenchymal and vascular imaging features to determine a diagnosis of either definite, possible, or no arteriopathy (“primary diagnosis”).¹² Disagreements were resolved through consensus discussion by the full review team (M.W., H.J.F., G.A.D., and A.J.B.). We defined arteriopathy as “the imaging appearance of an in situ arterial abnormality (stenosis, irregularity, occlusion, banding, pseudoaneurysm, dissection flap) not attributable to an exogenous thrombus (eg, cardioembolism) and not considered a normal developmental variant.”¹² The imaging finding of an isolated arterial occlusion could be classified as “no arteriopathy” (eg, if the clinical history and/or the parenchymal imaging typified cardioembolism), “possible arteriopathy” (eg, if the differential diagnosis included both cardioembolism and arterial dissection), or “definite arteriopathy” (eg, if the imaging was definitive for Moyamoya disease or dissection). The reviewers then classified the arteriopathies into subtypes (“secondary diagnosis”) using pre-established definitions for childhood arteriopathies^{10,14}: arterial dissection, including unilateral focal cerebral arteriopathy–dissection type (FCA-d, further defined below); unilateral focal cerebral arteriopathy–inflammatory type (FCA-i), which includes transient cerebral arteriopathy (TCA); primary and secondary Moyamoya disease (bilateral cerebral arteriopathy of childhood); genetic or syndromic arteriopathies, such as PHACES (posterior fossa malformations, hemangiomas, arterial anomalies, cardiac defects, eye abnormalities, and sternal or supraumbilical defects), a cutaneous condition characterized by multiple congenital abnormalities^{15,16}; primary and secondary diffuse/multifocal vasculitis; fibromuscular dysplasia¹⁷; iatrogenic; and others. The primary reviewers independently classified the secondary diagnosis; disagreements were resolved through consensus discussion by the full review team. The final conclusion (the expert opinion regarding the stroke etiology of that case) constituted the criterion standard diagnosis. The diagnoses in the children included in this study are shown in Fig 1.

The original definition of focal cerebral arteriopathy of childhood (FCA) consisted of “stenosis [of intracranial arteries] on vascular imaging not otherwise classified as dissection, Moyamoya disease, sickle cell arteriopathy, postvaricella arteriopathy, vasculitis, or other specific diagnoses (such as postirradiation arteriopathy)” and included “unifocal or multifocal, unilateral, or bilateral lesions of the large and/or medium-sized vessels visualized on angiography.”⁷ Use of this term has evolved in the pediatric stroke literature, and in North American pediatric stroke centers, it is typically used to describe a specific angiographic appearance of unilateral stenosis and/or irregularity of the intracranial anterior circulation; it has a differential diagnosis including TCA, intracranial dissection, unilateral Moyamoya disease, and the other diagnoses listed above.¹⁸ Hence, we implemented an updated definition of FCA: unifocal and unilateral stenosis/irregularity of the large intracranial arteries of the anterior circulation (distal internal carotid artery and/or its proximal branches). FCA-dissection type (FCA-d) referred to intracranial arterial dissection of the anterior circulation, typically with trauma.¹⁹ FCA-inflammation type (FCA-i) referred to FCA that is presumed inflammatory (ie, thought to represent a focal vasculitis). This could be

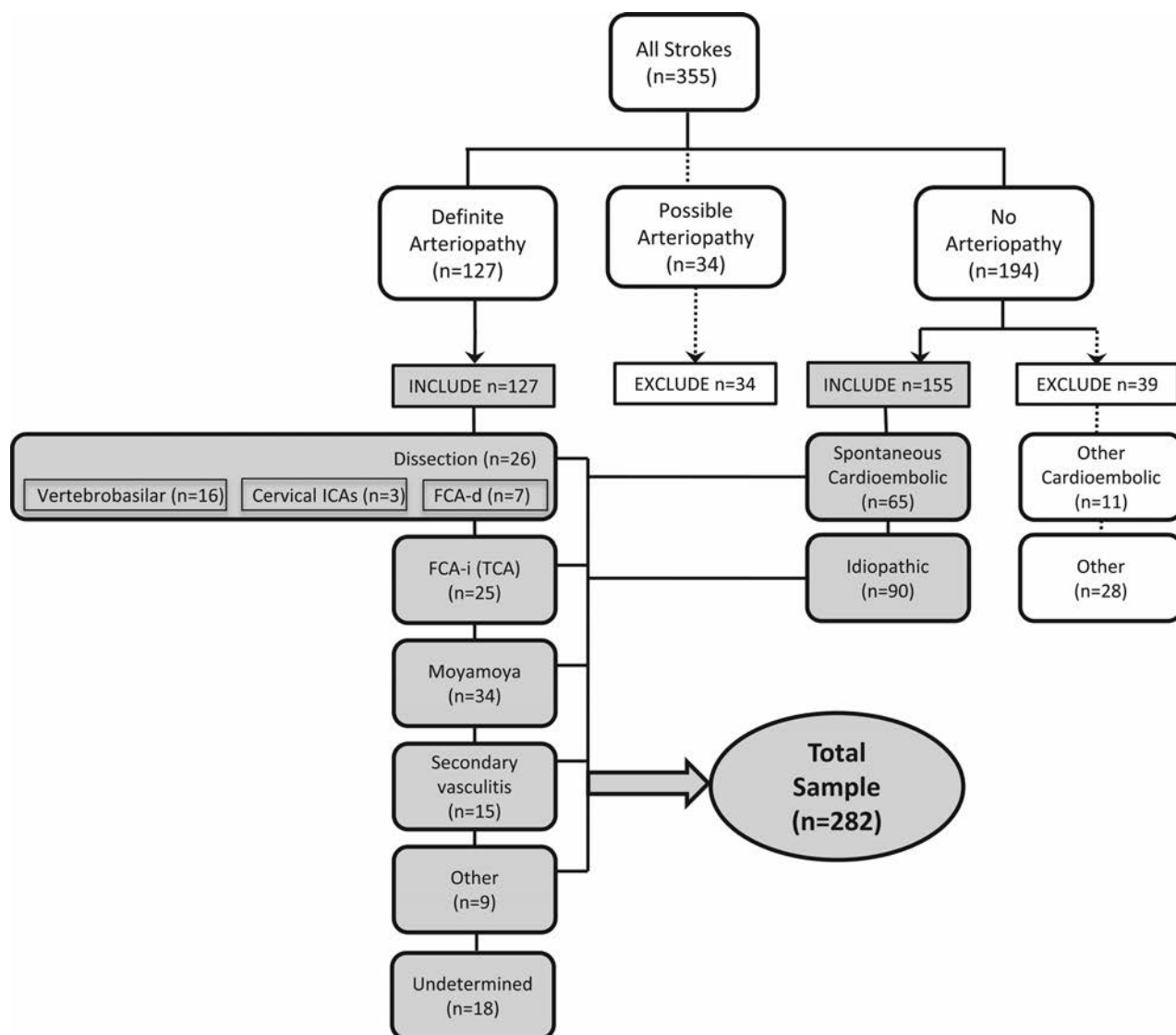


FIG 1. Classification of stroke subtype among 355 children with arterial ischemic stroke enrolled in the VIPS study. The cases used for the current study are highlighted in gray.

diagnosed, for instance, because of marked enhancement of the abnormal arterial segment on vessel wall imaging²⁰ or preceding varicella zoster infection (if considered clinically relevant by the local pediatric stroke neurologist for a diagnosis of postvaricella arteriopathy).^{21,22} FCA-i was also diagnosed when the evolution of the arteriopathy was typical of TCA: a stereotyped, monophasic natural history characterized by frequent early progression (from days to weeks), a plateau with nonprogression by 6 months, and subsequent improvement in some, with complete resolution in a minority.^{14,23} FCA that could not be further classified was considered “undetermined” arteriopathy subtype (in which case the reviewers created a differential diagnosis).

Statistical Analysis

The outcome variables for our analyses were the stroke etiology (primary and secondary diagnoses) as classified by the VIPS team. In children with abnormal vascular imaging findings, arteriopathy must first be distinguished from cardioembolism (primary diagnosis); to this end, we first developed a predictive model for

cardioembolic stroke. We then addressed our primary goal, modeling clinical and imaging biomarkers associated with the most commonly diagnosed arteriopathy subtypes (secondary diagnosis): dissection, FCA-i, Moyamoya disease, and secondary diffuse/multifocal vasculitis. By design, we evaluated as predictors biomarkers that were used by the reviewers in the classification process; though circular, this evaluation allowed the quantification of the prevalence of the biomarker and the strength of its association with a specific subtype.

For our preliminary model (cardioembolic versus arteriopathic stroke), we compared 65 children classified as having spontaneous cardioembolism (excluding strokes attributed to cardiac surgery) with 109 with definite arteriopathy (excluding those with possible arteriopathy, but including those whose definite arteriopathy could not be further classified; Fig 1). We first used univariate logistic regression models to identify clinical and/or parenchymal and/or vascular imaging characteristics associated either positively or negatively with these 2 broad categories. We

Summary results of independent predictors of arteriopathy subtypes

Arteriopathy Subtype	Cardioembolic	Dissection	FCA-i	Moyamoya	Secondary Vasculitis	Other Definite
Demographic characteristics						
Black race vs other				+++		
Clinical characteristics						
Congenital or acquired heart disease	+++					
Down syndrome				+++		
Meningitis					+++	
Sepsis/bacteremia					+++	
Head trauma		+++				
Presentation						
Dysarthria			++			
Nausea/vomiting		+				
Vertigo		+++				
Decreased level of consciousness				—	+++	
Infarct characteristics: location						
Lenticulostriate artery territory			+++			
Infarct characteristics: volume						
Infarct volume (smaller)			++			
Vascular imaging abnormal findings						
Occlusion					—	
Stenosis	—					
Irregularity	—					
Banding			+++			
>1 vascular territory	—			+++		
>1 arterial segment			—			
Affected artery						
Proximal MCA (M1)			+++			
Distal ICA (supracaloid)				+++		+++
Cervical artery		+++				

Note:—Positive association: +++ indicates odds ratio > 20; ++, OR 5–15; +, 1 < OR < 5; $P < .05$ in all. Negative association: —, OR < 1 and $P < .05$.

then constructed a multivariable model by entering all predictors significant at the .10 level in univariate analysis. Backward-selection logistic regression analysis was used to estimate adjusted odds ratios, with a significance level of .05 specified for removal of a variable from the model.

We followed a similar process to create models predictive of each individual arteriopathy subtype. Univariate logistic regression models were first used to identify characteristics associated with each subtype individually. For these models, we compared each subtype with the group of all other subtypes combined (excluding the 18 subjects with definite arteriopathy that could not be further classified). In addition to calculating odds ratios and 95% confidence intervals for each potential predictor, we determined the frequency with which the predictor was observed within the subtype. We then constructed multivariable models for each subtype as described for the preliminary model above. All models were assessed with postestimation techniques, and C-statistics were compared among potential models. Adjustments were made when necessary to improve the model fit before a final model was determined. All analyses were performed with STATA, Version 14 (StataCorp, College Station, Texas).

RESULTS

All 355 patients with VIPs had initial brain vascular imaging—MRA (91%), CTA (24%), and/or conventional angiography (14%); 53% had cervical vascular imaging; and 3.9% had vessel wall imaging. Overall, 41% had at least 1 follow-up brain vascular imaging study; the last follow-up was a median of 277 days (interquartile range, 172–408 days) poststroke. Figure 1 demon-

strates the results of the stroke subtype classification. Characteristics that distinguish cardioembolism from arteriopathic stroke (with a P value < .10 on univariate analysis) are shown in On-line Table 1. Characteristics associated with arteriopathy subtype (with a P value < .10 on univariate analysis) are shown On-line Tables 2–4. All the variables tested are shown in On-line Tables 5–11. Independent predictors are summarized in the Table and shown in detail in On-line Table 11.

Cardioembolic versus Arteriopathic Stroke

In multivariable analysis, characteristics determined to best distinguish cardioembolic from arteriopathic stroke were the presence of congenital heart disease and involvement of multiple vascular territories (both positively associated with cardioembolic stroke); the presence of vascular stenosis or irregularity spoke against the possibility of cardioembolic stroke (Table and On-line Table 11). All cases of cardioembolic stroke had underlying congenital or acquired cardiac disease (On-line Tables 1 and 5). Having multiple or bilateral arterial segments affected unexpectedly decreased the odds of cardioembolism because these features were seen more frequently in arteriopathy. On vascular imaging, the most common abnormality in cardioembolic stroke was arterial occlusion, present in almost half; however, arterial occlusion was a nonspecific finding observed commonly in the arteriopathy group (61.5% of patients with arteriopathy). Arterial irregularities and stenosis reduced the odds of cardioembolism, though each was observed in about 10% of patients with cardioembolic strokes.

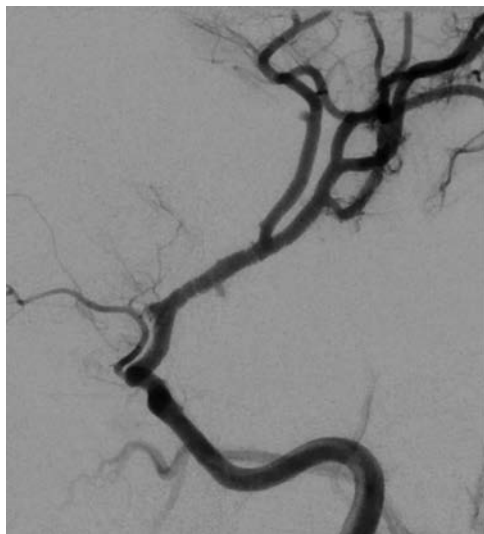


FIG 2. Banding pattern observed in 24% of patients with FCA-i.

Characteristics of Childhood Arteriopathy Subtypes

Our final multivariable model to distinguish arterial dissection (intracranial, which includes FCA dissection, or extracranial) from other arteriopathy subtypes included a history of head trauma and involvement of the cervical arteries (Table and On-line Table 11). Arterial dissection was associated with a history of head trauma in 39% of cases (On-line Tables 2 and 6). Dissections were equally distributed between the anterior and posterior circulation. Dissections tended to present as unilateral occlusions.

Characteristics associated with FCA-i in multivariable analysis included presentation with dysarthria, smaller infarcts in the lentulostriate territory, infarct volume of $<25 \text{ cm}^3$, arterial banding, and isolated involvement of the M1 segment of the middle cerebral artery (Table and On-line Table 11). FCA-i tended to occur more often in children between 8 and 15 years of age (On-line Tables 3 and 7). The banding pattern (Fig 2), while pathognomonic, was uncommon (24% of patients with FCA-i).

Forty-one children met the criteria for FCA: 7 with FCA-d, 25 with FCA-i, and 9 who could not be further classified. Our analysis of characteristics that distinguish FCA-i from FCA-d (On-line Tables 8 and 9) was limited by small sample sizes and the availability of vessel wall imaging in only 8 of the 25 children with FCA-i. The expert review team used a history of head trauma to make a diagnosis of FCA-d; it was present in 5 of the 7 patients with FCA-d (and in none of those with FCA-i). Infarct volumes were larger for FCA-d (median, 88 cm^3 ; interquartile range, $3.3\text{--}20 \text{ cm}^3$) than for FCA-i (median, 14 cm^3 ; interquartile range, $8.6\text{--}99 \text{ cm}^3$; $P = .05$). Arterial occlusion was seen in 86% of subjects with FCA-d versus 40% of those with FCA-i ($P = .06$). Banding was seen in 24% of subjects with FCA-i but in none with FCA-d ($P = .28$). In contrast, all 7 patients with FCA-d had involvement of both the supraclinoid ICA and M1. A coincident cervical artery abnormality was more suggestive of FCA-d (4/7 with FCA-d versus 1/25 with FCA-i, $P = .007$).

Our multivariable model for a Moyamoya disease diagnosis included both primary and secondary forms (Table and On-line Table 11). Of 34 children with Moyamoya disease, 17 were diag-

nosed with primary (idiopathic) Moyamoya disease, and 17, with secondary Moyamoya disease syndrome, most commonly caused by sickle cell anemia ($n = 9$) or Down syndrome ($n = 6$). An association between black race and Moyamoya disease was almost entirely explained by sickle cell anemia; Asian race did not affect the risk of Moyamoya disease in our cohort (On-line Tables 4 and 10). Imaging characteristics included bilateral distal ICA occlusion or stenosis and infarcts involving multiple vascular territories. Involvement of the posterior circulation was present in 21%. Although Moyamoya disease is an intracranial arteriopathy, abnormalities of the cervical arteries were noted in 6 patients (18%) with this condition, likely representing the MRA finding of small cervical internal carotid arteries due to reduced intracranial flow. Patients with Moyamoya disease typically did not present with a decreased level of consciousness, differentiating them from children with secondary vasculitis who had similar distal ICA involvement.

There were no cases of primary diffuse/multifocal vasculitis in VIPs, but there were 15 cases of secondary diffuse/multifocal vasculitis due to meningitis ($n = 11$), other infection (cavernous sinus thrombophlebitis, $n = 1$; mycotic aneurysm, $n = 1$), autoimmune disease ($n = 1$), or other ($n = 1$). Hence, clinical characteristics associated with this diagnosis included meningitis and bacteremia/sepsis and presentation with a decreased level of consciousness (Table and On-line Table 11). Complete occlusion of the affected artery reduced the odds of diffuse/multifocal vasculitis. Diffuse/multifocal vasculitis was seen more frequently in Asian patients: There were 6 cases of stroke due to tubercular meningitis enrolled in the Philippines.

Among 7 children with Down syndrome in our cohort, 6 had Moyamoya disease and 1 had a cardioembolic stroke.

DISCUSSION

The diagnosis of childhood arteriopathy is complex, and pediatric stroke experts have developed their diagnostic acumen across the years through the cumulative exposure to many cases. However, because these diseases are rare, pediatric patients with childhood arteriopathy are often seen by health care professionals who have not developed this expertise. The VIPs study presented a unique opportunity to help nonexperts in not only accurately diagnosing pediatric patients with childhood arteriopathy but also distinguishing among specific types based on objectively defined clinical and imaging parameters. The VIPs study previously demonstrated that arteriopathies can be more accurately classified when clinical data are used than when imaging findings are used alone, and when follow-up vascular imaging is performed.¹¹ The current analysis adds to our prior publication by defining the prevalence and predictive value of the individual characteristics that a pediatric stroke expert uses to diagnose childhood arteriopathy. In addition, it allows identification of patterns (ie, combinations of characteristics that distinguish certain arteriopathies) and assessment of the relative importance of each of these characteristics. This analysis assumes the availability of complete and accurate clinical and imaging data at the time of the arteriopathy classification; in real clinical situations, arteriopathy classification should be revisited as new data become available with time.

As a first step in the approach to vascular imaging abnormal-

ities in a child with arterial ischemic stroke, radiologists and clinicians should consider whether the abnormality represents inherent arterial disease (ie, arteriopathy) versus thrombus from a proximal source (cardioembolism or artery-to-artery embolism). Underlying cardiac disease strongly favors cardioembolism; however, 4 children with congenital heart disease had an arteriopathic stroke (1 with a dissection, 3 with Moyamoya disease), indicating that arteriopathic stroke should be considered even in patients with cardiac disease.

Arterial stenosis or irregularity reduces the odds of cardioembolism but can be seen with a recanalizing thrombus. Complete arterial occlusion appeared to reduce the odds of cardioembolism in our model but only because it is a common feature of arteriopathies like Moyamoya disease and dissection; it was still the most common vascular imaging finding in cardioembolism. Distinguishing arteriopathy from thrombus remains challenging; our expert team could not make the distinction in 34 cases (designated possible arteriopathy, Fig 1), highlighting the need for an echocardiogram as part of the work-up of pediatric patients suspected of having childhood arteriopathy.

The most common childhood arteriopathies in our cohort of children presenting with acute arterial ischemic stroke were Moyamoya disease, arterial dissection (intracranial and extracranial), and FCA-i. This distribution would likely be different in a cohort including all children with cerebral or cervical arteriopathy; primary small-vessel CNS vasculitis, for example, typically presents with only headache or cognitive decline and no focal signs or symptoms. Although atherosclerosis may begin in childhood, it was not seen as a cause of stroke in VIPS, consistent with findings in prior reports.^{3,24}

Age was the one demographic characteristic that helped distinguish among arteriopathy subtypes. FCA-i tended to affect older school-aged children, while Moyamoya disease affected younger children; dissection had no age predilection. Sex and race did not correlate with arteriopathy subtype (after accounting for sickle cell disease). Although primary Moyamoya disease occurs more commonly in Korean and Japanese populations,²⁵ we had no enrolling sites in those countries and saw a broad distribution of ethnicities among our subjects with Moyamoya disease.

A diagnosis of dissection is suggested by the involvement of cervical arteries. On the basis of current definitions, FCA-i does not include arteriopathies affecting the posterior circulation. Moyamoya disease predominantly affects the anterior circulation; posterior circulation involvement, when present, is rarely symptomatic. Hence, dissection is high on the differential in a previously healthy child presenting with a posterior circulation arterial ischemic stroke. In addition, FCA-i, Moyamoya disease, and secondary vasculitis are intracranial arteriopathies; involvement of the cervical arteries is strongly suggestive of dissection.

Distinguishing the etiologies of FCA—focal stenosis or irregularity of the distal ICA or proximal MCA—remains a challenge even to pediatric stroke experts. The differential diagnosis includes FCA-i, FCA-d (intracranial dissection of the anterior circulation), and early, unilateral Moyamoya disease. All typically present with hemiparesis, but headache at the stroke ictus is common in FCA-i and FCA-d, but not in Moyamoya disease. Banding was considered a pathognomonic feature for FCA-i but was pres-

ent in less than one-quarter of cases (being more conspicuous on conventional angiograms compared with CTAs and MRAs); hence, it was useful when present but not a sensitive feature of FCA-i. Infarct location in the lenticulostriate territory and smaller infarct size correlated with FCA-i and were more prevalent biomarkers. However, FCA-i and FCA-d are, in general, difficult to distinguish from each other as shown in postmortem cases.²⁶

An infarct in the superficial middle cerebral artery territories (ie, cerebral convexities) was more suggestive of Moyamoya disease. Chronic deep borderzone infarcts, also common in Moyamoya disease, do not result in focal deficits; because this is a cohort of children with acute arterial ischemic stroke, such infarcts were not included in this analysis. A history of head trauma and/or coincident cervical artery abnormalities suggests dissection. Improved neuroimaging techniques, including vessel wall imaging,²⁷ are needed to distinguish forms of FCA with greater certainty, though vessel wall imaging may not be 100% specific and there may be some overlap, with FCA-d showing minimal enhancement on vessel wall imaging and FCA-i typically presenting with marked enhancement on vessel wall imaging. The distinction between FCA-d and FCA-i is particularly important because their management strategies differ. FCA-i and FCA-d are currently treated with antiplatelet therapy. In addition, life-long restriction of activities (eg, no contact sports) is often recommended after an arterial dissection,²⁸ and clinical trials of corticosteroids for the treatment of FCA-i are under development.

In this article, the definition of FCA-i was restricted to focal disease of the distal ICA and its proximal branches, including but not limited to TCA.^{14,23} However, we anticipate that increased use of vessel wall imaging,²⁷ allowing the delineation of enhancing arterial segments, will necessitate a broader definition of FCA. For example, we observed cases of focal stenosis of the petrous carotid or posterior circulation arteries that we diagnosed as having a definite arteriopathy that could not be further classified. If such cases had vessel wall imaging demonstrating enhancement of the affected vessel, it may be reasonable to expand the definition of FCA-i to include these cases. In addition, we identified 1 case of FCA-i that demonstrated arteriopathy progression after 6 months, contrary to the traditional definition of TCA; this highlights the fact that while FCA-i includes TCA, not all cases FCA-i are TCA.

The main limitation of our study is that there is no true criterion standard for the diagnosis of childhood arteriopathies. Our expert review team was uncertain about the classification in 52 cases: 34 with possible arteriopathy and 18 with a definite arteriopathy that could not be further classified (Fig 1). Even among the arteriopathies that the review team classified with high certainty, there was likely some misclassification that cannot be measured. Because all imaging was performed on a clinical basis, there was variability in both the type and timing of imaging performed. As noted in our prior study, follow-up vascular imaging was helpful for classification, yet it was available in only a minority of patients.¹⁴ The circularity of some analyses—biomarkers used to classify a subtype and then evaluated as predictors of that subtype—must be emphasized; head trauma, for example, was an anticipated predictor of arterial dissection because it was used in the classification process. In such cases, the value of the analysis is

in the prevalence of the predictor, such as noting that a minority of dissection cases had trauma, so an absence of trauma does not rule out this diagnosis.

Last, analyses of arteriopathy subtypes were underpowered (as reflected by large confidence intervals of coefficients in the multivariable models), so they should be interpreted with caution. However, advantages of our study include a prospectively collected cohort, a large sample size relative to most pediatric stroke studies, and rigorous classification methods based on independent, central expert reviews and adjudication. Our study allows the quantification of the prevalence of the predictors, the strength of their correlations with specific diagnoses, and patterns of multiple predictors. These results should provide a guide for clinicians and neuroradiologists to generate a reasonable differential for an arteriopathic stroke in a child and to prioritize diagnoses on that list. The application of these findings will depend, however, on the accurate characterization of the imaging biomarkers by the interpreting neuroradiologist.

CONCLUSIONS

The different types of childhood arteriopathies are associated with typical clinical and parenchymal and vascular imaging features that can help narrow the differential diagnosis in pediatric patients with stroke with vascular anomalies (Table).

APPENDIX

Coauthors within the VIPS Investigators Group

Michael M. Dowling (University of Texas Southwestern Medical Center, Dallas); Susan L. Benedict (Primary Children's Medical Center, Salt Lake City); Timothy J. Bernard (Denver Children's Hospital); Christine K. Fox (University of California, San Francisco); Gabrielle A. DeVeber (The Hospital for Sick Children, Toronto); Neil R. Friedman (Cleveland Clinic Children's Hospital); Warren D. Lo (Ohio State University and Nationwide Children's Hospital, Columbus); Rebecca N. Ichord (Children's Hospital of Philadelphia); Marilyn A. Tan (University of the Philippines–Philippine General Hospital, Manila); Mark T. Mackay (Royal Children's Hospital Melbourne); Adam Kirton (Alberta Children's Hospital and University of Calgary, Calgary, Alberta); Marta I. Hernandez-Chavez (Pontificia Universidad Catolica de Chile, Santiago); Peter Humphreys (Children's Hospital of Eastern Ontario, Ottawa); Lori C. Jordan (Vanderbilt University Medical Center, Nashville); Sally Sultan (Columbia University Medical Center, New York); Michael J. Rivkin (Boston Children's Hospital); Mubeen F. Rafay (Children's Hospital, Winnipeg, University of Manitoba); Luigi Titomanlio (Hôpital Robert Debré-Paris); Gordana S. Kovacevic (Mother and Child Health Care Institute, New Belgrade, Serbia); Jerome Y. Yager (Stollery Children's Hospital, Edmonton); Catherine Amlie-Lefond (Seattle Children's Hospital); Nomazulu Dlamini (Evelina London Children's Hospital); John Condie (Phoenix Children's Hospital); Ann Yeh (Women and Children's Hospital of Buffalo); Rachel Kneen (Alder Hey Children's Hospital, Liverpool); Bruce Bjornson (British Columbia Children's Hospital, Vancouver); Paola Pergami (West Virginia University, Morgantown); Li Ping Zou (Chinese PLA General Hospital, Beijing); Jorina M. Elbers (Stanford Children's Health, Palo Alto); Abdalla Abdalla (Akron

Children's Hospital); Anthony K. Chan (McMaster University, Hamilton); Osman Farooq (Women and Children's Hospital of Buffalo); Mingming J. Lim (Evelina London Children's Hospital); Jessica L. Carpenter (Children's National Medical Center, Washington, DC); Steven Pavlakis (Maimonides Medical Center, Brooklyn); Virginia C. Wong (Queen Mary Hospital, Hong Kong); and Robert Forsyth (Institute of Neuroscience, Newcastle University, Newcastle upon Tyne, UK).

ACKNOWLEDGMENTS

The authors acknowledge the important contributions of the research coordinators at VIPS sites and of the patients and their families.

Disclosures: Max Wintermark—RELATED: Grant: National Institutes of Health*; UNRELATED: Board Membership: GE NFL Advisory Board. Nancy K. Hills—RELATED: Grant: National Institute of Health*, Bellafies Foundation and Marc and Lynne Benioff. Gabrielle A. DeVeber—RELATED: Grant: National Institute of Health*. Anthony J. Barkovich—RELATED: Grant: National Institutes of Health*. Tim J. Bernard—RELATED: Grant: National Institute of Health*. Adam Kirton—RELATED: Grant: National Institute of Health*; UNRELATED: Expert Testimony: medicolegal consults, Comments: multiple expert opinions; Royalties: Elsevier, Comments: small values for editing a textbook on pediatric brain stimulation. Heather J. Fullerton—RELATED: Grant: National Institutes of Health. *Money paid to the institution.

REFERENCES

1. Agrawal N, Johnston SC, Wu YW, et al. **Imaging data reveal a higher pediatric stroke incidence than prior US estimates.** *Stroke* 2009;40:3415–21 CrossRef Medline
2. Fullerton HJ, Wu YW, Sidney S, et al. **Risk of recurrent childhood arterial ischemic stroke in a population-based cohort: the importance of cerebrovascular imaging.** *Pediatrics* 2007;119:495–501 CrossRef Medline
3. Ganesan V, Prengler M, McShane MA, et al. **Investigation of risk factors in children with arterial ischemic stroke.** *Ann Neurol* 2003;53:167–73 CrossRef Medline
4. Sträter R, Becker S, von Eckardstein A, et al. **Prospective assessment of risk factors for recurrent stroke during childhood: a 5-year follow-up study.** *Lancet* 2002;360:1540–45 CrossRef Medline
5. Chabrier S, Husson B, Lasjaunias P, et al. **Stroke in childhood: outcome and recurrence risk by mechanism in 59 patients.** *J Child Neurol* 2000;15:290–94 CrossRef Medline
6. Zimmer JA, Garg BP, Williams LS, et al. **Age-related variation in presenting signs of childhood arterial ischemic stroke.** *Pediatr Neurol* 2007;37:171–75 CrossRef Medline
7. Amlie-Lefond C, Bernard TJ, Sébire G, et al; International Pediatric Stroke Study Group. **Predictors of cerebral arteriopathy in children with arterial ischemic stroke: results of the International Pediatric Stroke Study.** *Circulation* 2009;119:1417–23 CrossRef Medline
8. Danchaivijitr N, Cox TC, Saunders DE, et al. **Evolution of cerebral arteriopathies in childhood arterial ischemic stroke.** *Ann Neurol* 2006;59:620–26 CrossRef Medline
9. Roach ES, Golomb MR, Adams R, et al; American Heart Association Stroke Council, Council on Cardiovascular Disease in the Young. **Management of stroke in infants and children: a scientific statement from a Special Writing Group of the American Heart Association Stroke Council and the Council on Cardiovascular Disease in the Young.** *Stroke* 2008;39:2644–91 CrossRef Medline
10. Bernard TJ, Manco-Johnson MJ, Lo W, et al. **Towards a consensus-based classification of childhood arterial ischemic stroke.** *Stroke* 2012;43:371–77 CrossRef Medline
11. Fullerton HJ, Elkind MS, Barkovich AJ, et al. **The Vascular Effects of Infection in Pediatric Stroke (VIPS) study.** *J Child Neurol* 2011;26:1101–10 CrossRef Medline
12. Wintermark M, Hills NK, deVeber GA, et al; VIPS Investigators. **Arteriopathy diagnosis in childhood arterial ischemic stroke: results**

- of the Vascular Effects of Infection in Pediatric Stroke study. *Stroke* 2014;45:3597–605 [CrossRef Medline](#)
13. Sims JR, Gharai LR, Schaefer PW, et al. **ABC/2 for rapid clinical estimate of infarct, perfusion, and mismatch volumes.** *Neurology* 2009;72:2104–10 [CrossRef Medline](#)
 14. Sébire G, Fullerton H, Riou E, et al. **Toward the definition of cerebral arteriopathies of childhood.** *Curr Opin Pediatr* 2004;16:617–22 [CrossRef Medline](#)
 15. Hess CP, Fullerton HJ, Metry DW, et al. **Cervical and intracranial arterial anomalies in 70 patients with PHACE syndrome.** *AJNR Am J Neuroradiol* 2010;31:1980–86 [CrossRef Medline](#)
 16. Frieden IJ, Reese V, Cohen D. **PHACE syndrome: the association of posterior fossa brain malformations, hemangiomas, arterial anomalies, coarctation of the aorta and cardiac defects, and eye abnormalities.** *Arch Dermatol* 1996;132:307–11 [Medline](#)
 17. Kirton A, Crone M, Benseler S, et al. **Fibromuscular dysplasia and childhood stroke.** *Brain* 2013;136:1846–56 [CrossRef Medline](#)
 18. Tolani AT, Yeom KW, Elbers J. **Focal cerebral arteriopathy: the face with many names.** *Pediatr Neurol* 2015;53:247–52 [CrossRef Medline](#)
 19. Fullerton HJ, Johnston SC, Smith WS. **Arterial dissection and stroke in children.** *Neurology* 2001;57:1155–60 [CrossRef Medline](#)
 20. Swartz R, Bhuta S, Farb R, et al. **Intracranial arterial wall imaging using high-resolution 3-Tesla contrast-enhanced MRI.** *Neurology* 2009;72:627–34 [CrossRef Medline](#)
 21. Lanthier S, Armstrong D, Domi T. **Post-varicella arteriopathy of childhood: natural history of vascular stenosis.** *Neurology* 2005;64:660–63 [CrossRef Medline](#)
 22. Chabrier S, Sébire G, Fluss J. **Transient cerebral arteriopathy, post-varicella arteriopathy, and focal cerebral arteriopathy or the unique susceptibility of the M1 segment in children with stroke.** *Stroke* 2016;47:2439–41 [CrossRef Medline](#)
 23. Chabrier S, Rodesch G, Lasjaunias P, et al. **Transient cerebral arteriopathy: a disorder recognized by serial angiograms in children with stroke.** *J Child Neurol* 1998;13:27–32 [CrossRef Medline](#)
 24. Sträter R, Becker S, von Eckardstein A, et al. **Prospective assessment of risk factors for recurrent stroke during childhood: a 5-year follow-up study.** *Lancet* 2002;360:1540–45 [CrossRef Medline](#)
 25. Kim JS. **Moyamoya disease: epidemiology, clinical features, and diagnosis.** *J Stroke* 2016;18:2–11 [CrossRef Medline](#)
 26. Dlamini N, Freeman JL, Mackay MT, et al. **Intracranial dissection mimicking transient cerebral arteriopathy in childhood arterial ischemic stroke.** *J Child Neurol* 2011;26:1203–06 [CrossRef Medline](#)
 27. Mandell D, Mossa-Basha M, Qiao Y, et al. **Intracranial vessel wall MRI: principles and expert consensus recommendations of the American Society of Neuroradiology.** *AJNR Am J Neuroradiol* 2017;38:218–29 [CrossRef Medline](#)
 28. Bernard TJ, deVeber GA, Benke TA. **Athletic participation after acute ischemic childhood stroke: a survey of pediatric stroke experts.** *J Child Neurol* 2007;22:1050–53 [CrossRef Medline](#)

Brain Temperature Is Increased During the First Days of Life in Asphyxiated Newborns: Developing Brain Injury Despite Hypothermia Treatment

Z.P. Owji, G. Gilbert, C. Saint-Martin, and P. Wintermark



ABSTRACT

BACKGROUND AND PURPOSE: Therapeutic hypothermia is the current treatment for neonates with hypoxic-ischemic encephalopathy. It is believed to work by decreasing the brain temperature and reducing the baseline metabolism and energy demand of the brain. This study aimed to noninvasively assess brain temperature during the first month of life in neonates with hypoxic-ischemic encephalopathy treated with hypothermia.

MATERIALS AND METHODS: Neonates with hypoxic-ischemic encephalopathy treated with hypothermia and healthy neonates were enrolled prospectively. MR imaging was used to identify the presence and extent of brain injury. MR imaging multivoxel spectroscopy was used to derive brain temperatures in the basal ganglia and white matter at different time points during the first month of life. Brain temperature measurements were compared between neonates with hypoxic-ischemic encephalopathy and healthy neonates.

RESULTS: Forty-three term neonates with hypoxic-ischemic encephalopathy treated with hypothermia had a total of 74 spectroscopy scans, and 3 healthy term neonates had a total of 9 spectroscopy scans during the first month of life. Brain temperatures were lower in neonates with hypoxic-ischemic encephalopathy during hypothermia, compared with the healthy neonates (respectively, on day 1 of life: basal ganglia, $38.81^{\circ}\text{C} \pm 2.08^{\circ}\text{C}$, and white matter, $39.11^{\circ}\text{C} \pm 1.99^{\circ}\text{C}$; and on days 2–3 of life: basal ganglia, $38.25^{\circ}\text{C} \pm 0.91^{\circ}\text{C}$, and white matter, $38.54^{\circ}\text{C} \pm 2.79^{\circ}\text{C}$). However, neonates with hypoxic-ischemic encephalopathy who developed brain injury had higher brain temperatures during hypothermia (respectively, on day 1 of life: basal ganglia, $35.55^{\circ}\text{C} \pm 1.31^{\circ}\text{C}$, and white matter, $37.35^{\circ}\text{C} \pm 2.55^{\circ}\text{C}$; and on days 2–3 of life: basal ganglia, $35.20^{\circ}\text{C} \pm 1.15^{\circ}\text{C}$, and white matter, $35.44^{\circ}\text{C} \pm 1.90^{\circ}\text{C}$) compared with neonates who did not develop brain injury (respectively, on day 1 of life: basal ganglia, $34.46^{\circ}\text{C} \pm 1.09^{\circ}\text{C}$, and white matter, $33.97^{\circ}\text{C} \pm 1.42^{\circ}\text{C}$; and on days 2–3 of life: basal ganglia, $33.90^{\circ}\text{C} \pm 1.34^{\circ}\text{C}$, and white matter, $33.07^{\circ}\text{C} \pm 1.71^{\circ}\text{C}$). Also, brain temperatures tended to remain slightly higher in the neonates who developed brain injury around day 10 of life and around 1 month of age.

CONCLUSIONS: Therapeutic hypothermia using current guidelines decreased the brain temperature of neonates with hypoxic-ischemic encephalopathy during the first days of life but did not prevent an early increase of brain temperature in neonates with hypoxic-ischemic encephalopathy who developed brain injury despite this treatment.

Therapeutic hypothermia is the current standard treatment for term neonates with hypoxic-ischemic encephalopathy to try to prevent the development of brain injury.^{1–4} Although this treatment has reduced the rate of death and neurologic impairment in neonates with hypoxic-ischemic encephalopathy at 18

months of age,^{5–7} some neonates still develop brain injury and long-term neurologic sequelae. Induced hypothermia is believed to work by decreasing the brain temperature and thus reducing the baseline metabolism and energy demand of the brain.⁸ Therefore, it would be of great importance to monitor brain temperature for these neonates during and after hypothermia treatment.

In recent years, techniques using MR imaging have been developed to noninvasively measure brain temperature (referenced

Received April 5, 2017; accepted after revision June 12.

From the Department of Pediatrics, Division of Newborn Medicine, Research Institute of the McGill University Health Centre (Z.P.O., P.W.), and Department of Pediatric Radiology (C.S.-M.), Montreal Children's Hospital, McGill University, Montreal, Quebec, Canada; and MR Clinical Science (G.G.), Philips Healthcare, Montreal, Quebec, Canada.

Pia Wintermark receives research grant funding from the Fonds de la recherche en santé du Québec Clinical Research Scholar Career Award Junior 2 (32814) and the New Investigator Research Grant from the SickKids Foundation and the Canadian Institutes of Health Research Institute of Human Development, Child and Youth Health (NII3-049R).

Please address correspondence to Pia Wintermark, MD, McGill University/Montreal Children's Hospital, Division of Newborn Medicine, Research Institute of the McGill University Health Centre, 1001 Blvd. Décarie, Site Glen Block E, EM0.3244, Montréal, Quebec H4A 3J1, Canada; e-mail: pia.wintermark@blueemail.ch; @PiaWintermark

Indicates open access to non-subscribers at www.ajnr.org

<http://dx.doi.org/10.3174/ajnr.A5350>

as “brain thermometry”) even in neonates. One such technique is proton MR spectroscopy (^1H -MR spectroscopy), which can be used to estimate brain temperature by monitoring the chemical shift of water with temperature compared with the resonance frequency of a reference metabolite,⁹ such as *N*-acetyl aspartic acid. MR spectroscopy has been used for brain thermometry in healthy adults,^{10–12} in adults with stroke,^{13,14} and in adults with traumatic brain injury.¹⁵ However, until now, brain thermometry has been used only a few times with neonates,^{16,17} and even more rarely with neonates with hypoxic-ischemic encephalopathy.^{18,19} Bainbridge et al¹⁸ have demonstrated the feasibility of this technique with neonates using single-voxel MR spectroscopy placed in the thalamus and/or white matter to show the correlation between brain and rectal temperatures in healthy neonates; in addition, in their study, only 9 neonates had brain temperature measurements during hypothermia treatment. Wu et al¹⁹ studied 18 neonates with hypoxic-ischemic encephalopathy treated with hypothermia with single-voxel MR spectroscopy placed in the thalamus, basal ganglia, and/or cortical gray matter. They found that the initial degree of encephalopathy seemed to influence brain temperature measurements during and after hypothermia. Neither of these 2 studies correlated their brain temperature measurements with the extent of brain injury.

The present study hypothesized that neonates with hypoxic-ischemic encephalopathy who developed brain injury despite hypothermia treatment will have a higher brain temperature compared with neonates with hypoxic-ischemic encephalopathy who did not develop brain injury during and after treatment. Thus, the present study was designed to noninvasively assess brain temperature during the first month of life in term neonates with hypoxic-ischemic encephalopathy treated with hypothermia.

MATERIALS AND METHODS

Patients

We conducted a prospective cohort study of term neonates with hypoxic-ischemic encephalopathy admitted to our neonatal intensive care unit at the Montreal Children’s Hospital, McGill University, from 2010 to 2015 who met the criteria for induced hypothermia:^{1,3} 1) gestational age of 36 weeks or older and birth weight of ≥ 1800 g; 2) evidence of fetal distress (eg, a history of an acute perinatal event, cord pH ≤ 7.0 , or base deficit ≤ -16 mEq/L); 3) evidence of neonatal distress (eg, an Apgar score of ≤ 5 at 10 minutes, postnatal blood gas pH within the first hour of life of ≤ 7.0 or a base deficit of ≤ -16 mEq/L, or continuous need for ventilation with the initiation at birth and duration for at least 10 minutes); and 4) evidence of moderate or severe encephalopathy obtained by a standardized neurologic examination and/or by an amplitude-integrated electroencephalogram. The initial background pattern of the amplitude-integrated electroencephalogram^{2,20} was assessed on admission and collected to classify the neonates. Eligible neonates received whole-body cooling to an esophageal temperature of 33.5°C , initiated by 6 hours of life and continued for 72 hours. Three additional healthy term neonates were included as controls. The research protocol was approved by the institutional review board, and informed parental consent was obtained in all cases.

Brain MR Imaging

As per standard clinical protocol at our institution, a brain MR imaging was performed for all these neonates after hypothermia treatment was completed, usually around day 10 of life. In addition, since 2010, when possible (ie, when the parents consented for their neonates to have additional MRIs, when the neonates were hemodynamically stable, and when a team of a nurse and a respiratory therapist was available to go to the MR imaging), neonates were enrolled in an MR imaging research study, and MR imaging scans were performed on day 1 of life, on days 2–3 of life, around day 10 of life, and around 1 month of age. These time points were chosen to ensure the absence of antenatal brain injury (day 1 of life), to assess early patterns of injury (days 2–3 of life), and to define the extent of definitive brain injuries (around day 10 of life and around 1 month of life). Neonates receiving hypothermia had the hypothermia therapy maintained during the MR imaging scan without any adverse events.²¹ Any ventilation, pressor support, or sedation was maintained during the MR imaging process, and additional sedation was avoided. The healthy term neonates had normal imaging findings at the same time points; they were kept at regular temperature during the MR imaging.

The MR imaging was performed with a 3T clinical system (Achieva X; Philips Healthcare, Best, the Netherlands). Each MR imaging study included 3D T1-weighted gradient-echo (TR, 24 ms; TE, 4.6 ms; matrix size, 180×180 ; FOV, 180 mm; flip angle, 30° ; sagittal sections, 104; section thickness, 1.0 mm; and multiplanar reformations in axial and coronal planes), TSE high-resolution T2-weighted (TR, 5000 ms; TE, 90 ms; TSE factor, 15; matrix size, 300×300 ; FOV, 150 mm; flip angle, 90° ; axial sections, 27; section thickness, 3.0 mm), and a single-shot echo-planar diffusion-tensor imaging sequence (TR, 5937.8 ms; TE, 69 ms; matrix size, 100×100 ; FOV, 180 mm; sensitivity encoding factor, 2; directions, 32; b-value, 750 s/mm^2 ; axial sections, 64; section thickness, 2.2 mm). In addition, if time allowed and the neonates were still sleeping, neonates enrolled in the MR imaging research study underwent a ^1H -MR spectroscopy with a 2D point-resolved spectroscopy sequence (TR, 2000 ms; TE, 288 ms; FOV, 180×180 mm; bandwidth, 2000 Hz; 1024 points; voxel size, $15 \times 15 \times 15$ mm). The multivoxels were placed over the whole cerebrum at the level of the basal ganglia. Data acquisition was performed at room temperature ($22^\circ\text{C} \pm 1^\circ\text{C}$). This sequence was used to noninvasively measure absolute brain temperature in the neonates.

Pediatric neuroradiologists, who were blinded to the clinical conditions of the infants, interpreted the MR imaging studies of the asphyxiated neonates treated with hypothermia. They reported the presence and extent of brain injury in the cerebrum according to a previously described MR imaging scoring system.²² The MR imaging scores obtained around day 10 of life were used as the reference to determine the extent of the brain injury for each patient.^{23,24}

Temperature Measurements in Neonates

MR spectra data were obtained with the previously mentioned 2D point-resolved spectroscopy sequence. On the basis of the princi-

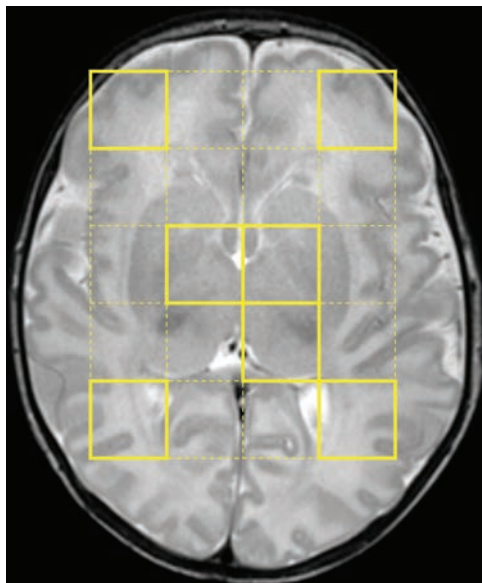


FIG 1. ROIs. T2-weighted image shows where the multivoxels were placed over the whole cerebrum at the level of basal ganglia (yellow dotted lines). In this example, temperature was measured in a total of 7 voxels—that is, in the voxels in the left thalamus, the remaining basal ganglia bilaterally, and the anterior and posterior white matter bilaterally (yellow lines).

ple that temperature affects the hydrogen bonding between water molecules,⁹ which leads to a shift in the spectral position of the water signal relative to a reference metabolite that has less sensitivity to temperature changes—such as *N*-acetyl aspartate—on MR spectroscopy,^{11,17,25,26} brain temperature was derived by analyzing the chemical shift differences (δ ppm) between the water peak and the NAA spectrum.¹⁹ This method has been demonstrated previously to have an accuracy of $\pm 0.5^\circ\text{C}$ and a precision of 0.3°C .^{14,17,26} The chemical shift differences were plotted against the temperature to obtain the calibration line for estimating the brain temperature of the neonates.¹⁹ The software package jMRUI (Version 5.2; www.mrui.uab.es/mrui/mrui_download/)^{27,28} was used to estimate the position of the water peak and NAA in each of these voxels and thus measure the chemical shift differences. A 2D fast Fourier transform was applied to the signals as the preprocessing steps in the software. To remove undesirable resonance frequencies, we used a Hankel Lanczos Singular Value Decomposition²⁹ filter, implemented in jMRUI.

The multivoxels were placed over the whole cerebrum of the neonates at the level of basal ganglia (Fig 1). For each MR multivoxel spectra acquired for the neonate, brain temperature was subsequently measured in the voxels located in the basal ganglia (ie, a voxel in the thalamus and a voxel in the remaining basal ganglia) and the white matter (ie, a voxel in the anterior white matter and a voxel in the posterior white matter) on each side of the brain (Fig 1). Measurements were obtained on the right and left sides of the brain in these different ROIs and then averaged. The voxels containing noisy and poor signals were excluded manually from the data. Then, for each scan, brain temperature was estimated with a previously described calibration equation.³⁰

Statistical Analysis

In healthy neonates, differences of brain temperature in the basal ganglia and white matter across time were assessed for statistical significance with Kruskal-Wallis tests.

For the first comparison of brain temperature measurements between neonates with hypoxic-ischemic encephalopathy treated with hypothermia and healthy neonates, the neonates with hypoxic-ischemic encephalopathy treated with hypothermia were categorized into 2 subgroups according to their initial degree of encephalopathy on an amplitude-integrated electroencephalogram (ie, moderate versus severe). For the second analysis, the same neonates were categorized into 2 subgroups based on the presence or absence of brain injury in the ROI on their conventional MR imaging performed around day 10 of life. We assessed the following differences at each time point for statistical significance with Kruskal-Wallis tests: 1) between neonates with hypoxic-ischemic encephalopathy treated with hypothermia with initial moderate encephalopathy versus those with initial severe encephalopathy versus healthy neonates, and 2) neonates with hypoxic-ischemic encephalopathy treated with hypothermia who developed brain injury versus those without brain injury versus healthy neonates. For multiple comparisons, the Dunn post hoc comparison tests comparing the 3 groups at each time point were applied to adjust the α level as necessary. An overall (2-sided) α level of .05 was used to indicate statistical significance.

RESULTS

Forty-three term neonates with hypoxic-ischemic encephalopathy treated with hypothermia had a total of 74 spectroscopy scans over the first month of life. Fifty-three percent (23/43) of these neonates had an initial moderate encephalopathy by amplitude-integrated electroencephalography. Fifty-two percent (12/23) did not develop brain injury, 13% (3/23) developed basal ganglia injury, 26% (6/23) developed watershed injury, and 9% (2/23) developed near-total injury. Forty-nine percent (21/43) of these neonates had an initial severe encephalopathy by an amplitude-integrated electroencephalogram. Thirty-five percent (7/20) did not develop brain injury, 10% (2/20) developed basal ganglia injury, 5% (1/20) developed watershed injury, and 50% (10/20) developed near-total injury. In addition, 3 healthy term neonates had a total of 9 spectroscopy scans during the first month of life. Seventeen percent (8/46) of the neonates enrolled in the present study had a spectroscopy scan on day 1 of life, 35% (16/46) had a spectroscopy scan on days 2–3 of life, 76% (35/46) had a spectroscopy scan around day 10 of life, and 35% (16/46) had a spectroscopy scan around 1 month of age. Among the 8 voxels where temperature was measured, a mean of 1.30 ± 1.56 voxels per patient was excluded manually from the data because they contained noisy and poor signals.

In healthy neonates, brain temperature remained similar in the basal ganglia (average, $38.50^\circ\text{C} \pm 1.21^\circ\text{C}$; comparison between time points, $P = .89$) and in the white matter (average, $38.88^\circ\text{C} \pm 1.86^\circ\text{C}$; comparison between time points, $P = .76$) during the first month of life (Fig 2). In the same neonates, brain

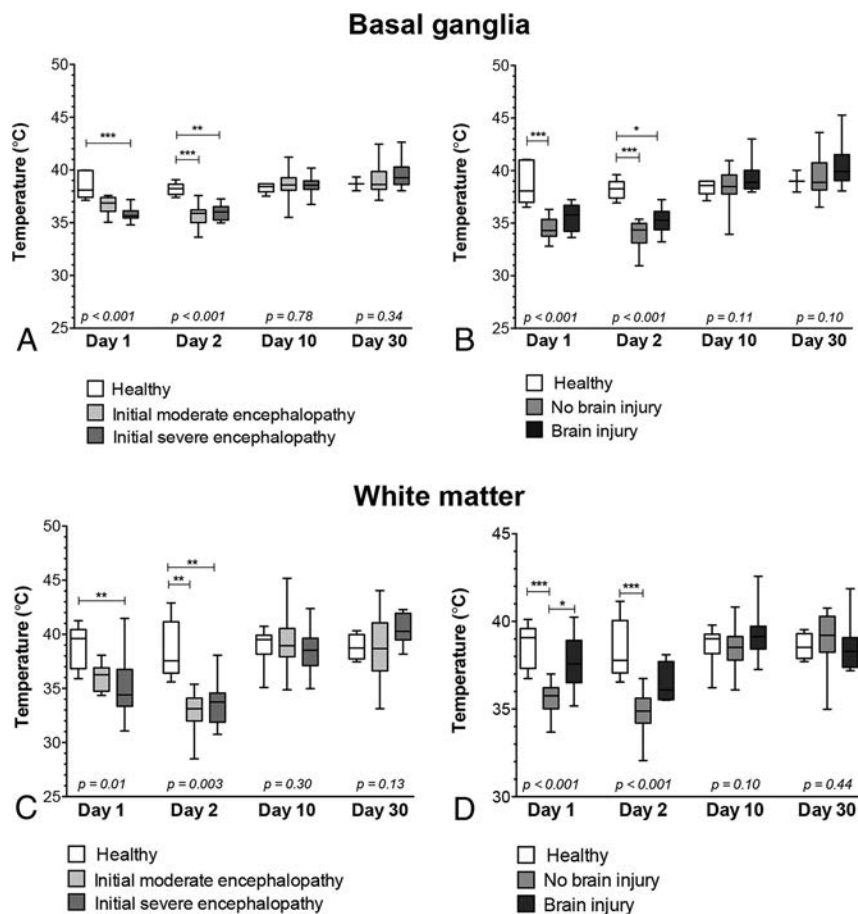


FIG 2. Comparison of brain temperature values in the basal ganglia and white matter according to the initial degree of encephalopathy and the presence of brain injury. Brain temperature values in the basal ganglia according to the initial degree of encephalopathy (A) and according to the presence of brain injury (B). Brain temperature values in white matter according to the initial degree of encephalopathy (C) and the presence of brain injury (D). Box-and-whisker plots (median, minimum, and maximum in degrees Celsius). Significance was derived from Kruskal-Wallis tests, followed by the Dunn post hoc comparison tests for multiple comparisons: The asterisk indicates $P < .05$; 2 asterisks, $P < .01$; 3 asterisks, $P < .001$.

temperature was not different between the basal ganglia and white matter ($P = .23$).

When we compared the brain temperature results of the neonates with hypoxic-ischemic encephalopathy—according to their initial degree of encephalopathy—and the healthy neonates, brain temperatures were significantly different in the 3 groups (moderate encephalopathy, severe encephalopathy, and healthy) on day 1 of life (respectively, basal ganglia, $P < .001$, and white matter, $P = .01$) and on days 2–3 of life (respectively, basal ganglia, $P < .001$, and white matter, $P = .003$) (Fig 2). Neonates with moderate encephalopathy tended to have lower brain temperatures (respectively, basal ganglia, $35.82^{\circ}\text{C} \pm 1.31^{\circ}\text{C}$, and white matter, $36.84^{\circ}\text{C} \pm 0.83^{\circ}\text{C}$) on day 1 of life compared with healthy neonates (respectively, basal ganglia, $38.81^{\circ}\text{C} \pm 2.08^{\circ}\text{C}$, and white matter, $38.76^{\circ}\text{C} \pm 1.25^{\circ}\text{C}$); in addition, the brain temperatures of neonates with moderate encephalopathy were significantly lower on days 2–3 of life (respectively, basal ganglia, $34.07^{\circ}\text{C} \pm 1.52^{\circ}\text{C}$, and white matter, $34.87^{\circ}\text{C} \pm 1.12^{\circ}\text{C}$) compared with healthy neonates (respectively, basal ganglia, $38.2^{\circ}\text{C} \pm 0.91^{\circ}\text{C}$, and white matter, $38.40^{\circ}\text{C} \pm 1.76^{\circ}\text{C}$). Neonates with severe encephalopathy had significantly lower brain temperatures on day 1 of life (respec-

tively, basal ganglia, $34.42^{\circ}\text{C} \pm 1.10^{\circ}\text{C}$, and white matter, $36.22^{\circ}\text{C} \pm 1.81^{\circ}\text{C}$) and on days 2–3 of life (respectively, basal ganglia, $34.77^{\circ}\text{C} \pm 1.12^{\circ}\text{C}$, and white matter, $35.23^{\circ}\text{C} \pm 1.16^{\circ}\text{C}$) compared with healthy neonates. Brain temperatures did not differ between the neonates with moderate encephalopathy and the neonates with severe encephalopathy. Brain temperatures did not differ in the 3 groups around day 10 of life (respectively, basal ganglia, $P = .78$, and white matter, $P = .30$) and around 1 month of life (respectively, basal ganglia, $P = .34$, and white matter, $P = .13$) (Fig 2).

When we compared the brain temperature results of the neonates with hypoxic-ischemic encephalopathy—according to the presence or absence of brain injury—and the healthy neonates, we found that the brain temperatures were significantly different in the 3 groups (neonates with hypoxic-ischemic encephalopathy who did not develop brain injury, neonates with hypoxic-ischemic encephalopathy who developed brain injury, and healthy neonates) on day 1 of life (respectively, basal ganglia, $34.46^{\circ}\text{C} \pm 1.09^{\circ}\text{C}$, and white matter, $33.97^{\circ}\text{C} \pm 1.42^{\circ}\text{C}$) and on days 2–3 of life (respectively, basal ganglia, $33.90^{\circ}\text{C} \pm$

1.34°C , and white matter, $33.07^{\circ}\text{C} \pm 1.71^{\circ}\text{C}$) compared with healthy neonates. Neonates who developed brain injury had higher brain temperatures on day 1 of life (respectively, basal ganglia, $35.55^{\circ}\text{C} \pm 1.31^{\circ}\text{C}$, and white matter, $37.35^{\circ}\text{C} \pm 2.55^{\circ}\text{C}$) and on days 2–3 of life (respectively, basal ganglia, $35.20^{\circ}\text{C} \pm 1.15^{\circ}\text{C}$, and white matter, $35.44^{\circ}\text{C} \pm 1.90^{\circ}\text{C}$) compared with neonates with hypoxic-ischemic encephalopathy who did not develop brain injury; however, the brain temperatures of neonates who developed brain injury were not different compared with those in healthy neonates, except on days 2–3 of life in the basal ganglia.

Brain temperatures did not differ for neonates with hypoxic-ischemic encephalopathy with moderate encephalopathy and neonates with hypoxic-ischemic encephalopathy with severe encephalopathy. For all 3 groups, brain temperatures did not differ around day 10 of life (respectively, basal ganglia, $P = .11$, and white matter, $P = .10$) and around 1 month of life (respectively, basal ganglia, $P = .10$, and white matter, $P = .44$) (Fig 2). However, brain temperatures tended to remain higher around day 10 of life (in the basal ganglia, $39.34^{\circ}\text{C} \pm 1.35^{\circ}\text{C}$, and in the white matter, $40.10^{\circ}\text{C} \pm 2.36^{\circ}\text{C}$) and around 1 month of age (in the basal ganglia, $40.58^{\circ}\text{C} \pm 2.15^{\circ}\text{C}$) in the neonates who developed

brain injury compared with those who did not develop brain injury (in the basal ganglia: day 10 of life, $38.31^{\circ}\text{C} \pm 1.69^{\circ}\text{C}$; 1 month of age, $39.25 \pm 1.78^{\circ}\text{C}$; and in the white matter: day 10 of life, $38.74^{\circ}\text{C} \pm 1.84^{\circ}\text{C}$).

DISCUSSION

In this study, we investigated the evolution of brain temperature during the first month of life in neonates with hypoxic-ischemic encephalopathy treated with hypothermia. To the best of our knowledge, this is the largest cohort of term neonates with hypoxic-ischemic encephalopathy treated with hypothermia for whom brain thermometry has been used. This also is the first time that multivoxel spectroscopy was used to perform brain thermometry of neonates with hypoxic-ischemic encephalopathy treated with hypothermia. Previous studies used single-voxel spectroscopy^{18,19} and had to acquire different spectra in the different ROIs, which increased the duration of the MR imaging scans for these patients who often are critically sick. In addition, brain temperature could potentially vary between the times that the different voxels were scanned. Using multivoxel spectroscopy enabled a simultaneous measurement of brain temperature in different ROIs with the same sequence, without prolonging the scan duration. Most interesting, with multivoxel spectroscopy, we did not find consistent differences between the brain temperature measurements performed on the basal ganglia and white matter, contrary to some other studies.^{18,19} In our study, we averaged the measurements performed on the thalami and the remaining basal ganglia on both sides as “basal ganglia” measurements and the measurements performed on the anterior and posterior white matter on both sides as “white matter” measurements. It also is possible that measurements on the white matter were sometimes “contaminated” to varying degrees by the cortical gray matter because it often was technically challenging to pick a voxel located solely in the white matter.

As expected, hypothermia treatment with current guidelines lowered the brain temperatures of the neonates with hypoxic-ischemic encephalopathy compared with the healthy neonates, as has also been suggested by other studies.¹⁹ However, the decrease of brain temperature during hypothermia treatment was not uniform for all the neonates with hypoxic-ischemic encephalopathy. Therapeutic hypothermia did not prevent an early increase of brain temperature in neonates with hypoxic-ischemic encephalopathy who developed brain injury—despite these neonates being actively cooled to around 33.5°C —compared with those who did not develop brain injury. These results are similar to those found in adults with traumatic brain injury, which showed that brain temperature dissociates from core body temperature and increases when brain injury develops.¹⁰ The increased brain temperatures in the neonates who developed brain injury probably correspond to an increased brain perfusion despite hypothermia treatment, which has been previously reported in these neonates despite hypothermia treatment.^{31–33} The increased brain temperatures in the neonates who developed brain injury may also correspond to the often-described phenomenon of luxury perfusion during which brain perfusion exceeds the metabolic demands, which leads to an increase of cerebral oxygen delivery.^{34–37} Thus, the current hypothermia guidelines did not seem to prevent the

development of brain injury when increased brain temperatures were found during the first days of life. These neonates with increased brain temperatures may be candidates for adjustments in their hypothermia therapy or for adjunctive therapies.^{19,33}

Brain temperatures tended to remain slightly higher in the basal ganglia and in the white matter around day 10 of life, and in the basal ganglia around 1 month of age in the neonates who developed brain injury compared those not who did not. Similar results were found when measuring brain perfusion in these neonates³⁸: Brain perfusion remained somewhat increased in the brain regions with brain injury around day 10 of life and around 1 month of life. It has been hypothesized that these results may be due to increased blood vessels rather than the tone adjustments of the first days of life.³⁸

The analysis of brain temperatures according to the initial degree of encephalopathy did not permit a prediction of the outcome of these neonates because no difference occurred in the brain temperatures of the neonates with initial moderate encephalopathy and those with initial severe encephalopathy recorded on an amplitude-integrated electroencephalogram. These results are consistent with those found when measuring the regional cerebral oxygen saturation in these neonates,³⁵ in which the regional cerebral oxygen saturation did not differ for neonates with initial moderate encephalopathy and those with initial severe encephalopathy. However, our results were different compared with those in a previous study by Wu et al,¹⁹ who studied 18 neonates with hypoxic-ischemic encephalopathy treated with hypothermia (including 14 with initial moderate encephalopathy and 4 with initial severe encephalopathy based on a modified Sarnat score) and found that the initial degree of encephalopathy seemed to influence the brain temperature measurements during and after hypothermia. Unfortunately, they did not report the correlation between the brain temperature measurements and the extent of brain injury in each of their neonates, so it is impossible to know whether all their neonates with initial severe encephalopathy developed brain injury. In our study, only 65% of the neonates with an initial severe encephalopathy developed brain injury. This finding might help explain why our results were different from theirs, in addition to our sample size being larger. Also, most of their scans were performed on days 2–3 of life,¹⁹ and our scans were usually performed on days 1 and 2 of life; similarly, previous studies have shown that the regional cerebral oxygen saturation did not differ for neonates with hypoxic-ischemic encephalopathy with moderate-versus-severe encephalopathy, except on day 3 of life.³⁵

In addition to the brain temperature measurements at different time points during the first month of life, another strength of the present study is that brain temperature measurements at the same time points in healthy neonates were also included as comparisons with those of neonates with hypoxic-ischemic encephalopathy. Most interesting, the brain temperature in the healthy neonates was, on average, above 38°C , which is higher than the normal target core temperature; these results were consistent with previously described results¹⁶ and also with the consensus that brain temperature is typically 0.5°C – 1°C higher than core temperature.^{39–41} Similarly, our brain temperature measurements performed during hypothermia were, on average, at least above

34°C in those neonates who did not develop brain injury, which is higher than the target core temperature (ie, 33.5°C) during the treatment, a finding that was also consistent with previously described results.¹⁹

Of note, neonates with hypoxic-ischemic encephalopathy received whole-body cooling in this study. Brain temperature measurements may yield different results in neonates with hypoxic-ischemic encephalopathy treated with head cooling because it has been previously demonstrated in neonatal swine that head cooling creates a temperature gradient across the brain (ie, cooler periphery and warmer central structures) compared with no temperature gradient in those treated with whole-body cooling.^{42,43}

Instead of just comparing our results with previous studies of brain perfusion and/or regional cerebral oxygen saturation measurements, it would have been interesting to correlate directly the brain temperature measurements of these neonates with the brain perfusion measurements by MR arterial spin-labeling and/or with the measurement of regional cerebral oxygen saturation by near-infrared spectroscopy, to better understand the physiopathology underlying the development of brain injury in these neonates. However, these other measurements were not always consistently performed for the neonates enrolled in this study. Another limitation of our study was that the body temperatures of the neonates at each time point were not collected systematically, especially with respect to the MR imaging performed during the hypothermia treatment, so they could not be correlated with the neonates' body temperatures. Other studies have shown that body and brain temperatures correlate in healthy subjects but that a dissociation exists between the 2 in brain injury.¹⁰ In addition, the sample size, even if it is the largest described so far with respect to neonates with hypoxic-ischemic encephalopathy treated with hypothermia, was not sufficient to study, in more detail, the impact of sedation and antiepileptic medications that were sometimes used with these neonates. The sample size of healthy term neonates was also small; thus, the statistical power of our comparisons and the conclusions that can be drawn were limited. Of note, none of the neonates presented with seizures during the MR imaging studies, and minimal sedation was used for all of them as per the standard of care at our institution.

CONCLUSIONS

Therapeutic hypothermia using current guidelines decreased brain temperature in neonates with hypoxic-ischemic encephalopathy during the first days of life but did not prevent an early increase of brain temperature in neonates with hypoxic-ischemic encephalopathy who developed brain injury. Noninvasive monitoring of brain temperatures may permit a better understanding of the development of brain injury despite hypothermia in neonates with hypoxic-ischemic encephalopathy. Further studies are needed to determine whether noninvasive measuring of brain temperature may permit a selection of the neonates who may be candidates for adjustments in their hypothermia therapy or for adjunctive therapies.

ACKNOWLEDGMENTS

The authors thank the families and their neonates for participating in the study. Special thanks are also expressed to the neonatal

intensive care unit nurses, the neonatal intensive care unit respiratory therapists, and the MR imaging technicians who have made this study possible. The authors also thank Mr Wayne Ross Egers for his professional English correction of the manuscript.

Disclosures: Guillaume Gilbert—UNRELATED: Employment: Philips Healthcare, Comments: clinical scientist who participates in and supports clinical research performed with academic partners. Pia Wintermark—RELATED: Grant: New Investigator Research Grant from the SickKids Foundation and the Canadian Institutes of Health Research Institute of Human Development, Child and Youth Health, Comments: Pia Wintermark receives research grant funding from the Fonds de la recherche en santé du Québec Clinical Research Scholar Career Award Junior 2, and the New Investigator Research Grant from the SickKids Foundation and the Canadian Institutes of Health Research Institute of Human Development, Child and Youth Health.* *Money paid to the institution.

REFERENCES

1. Azzopardi D, Strohm B, Marlow N, et al; TOBY Study Group. **Effects of hypothermia for perinatal asphyxia on childhood outcomes.** *N Engl J Med* 2014;371:140–49 CrossRef Medline
2. Gluckman PD, Wyatt JS, Azzopardi D, et al. **Selective head cooling with mild systemic hypothermia after neonatal encephalopathy: multicentre randomised trial.** *Lancet* 2005;365:663–70 Medline
3. Shankaran S, Pappas A, McDonald SA, et al; Eunice Kennedy Shriver NICHD Neonatal Research Network. **Childhood outcomes after hypothermia for neonatal encephalopathy.** *N Engl J Med* 2012;366:2085–92 CrossRef Medline
4. Simbruner G, Mittal RA, Rohlmann F, et al; neo.nEURO.network Trial Participants. **Systemic hypothermia after neonatal encephalopathy: outcomes of neo.nEURO.network RCT.** *Pediatrics* 2010;126:e771–78 CrossRef Medline
5. Edwards AD, Brocklehurst P, Gunn AJ, et al. **Neurological outcomes at 18 months of age after moderate hypothermia for perinatal hypoxic ischaemic encephalopathy: synthesis and meta-analysis of trial data.** *BMJ* 2010;340:c363 CrossRef Medline
6. Jacobs SE, Berg M, Hunt R, et al. **Cooling for newborns with hypoxic ischaemic encephalopathy.** *Cochrane Database Syst Rev* 2013;CD003311 CrossRef Medline
7. Shah PS. **Hypothermia: a systematic review and meta-analysis of clinical trials.** *Semin Fetal Neonatal Med* 2010;15:238–46 CrossRef Medline
8. Polderman KH. **Induced hypothermia and fever control for prevention and treatment of neurological injuries.** *Lancet* 2008;371:1955–69 CrossRef Medline
9. Hindman JC. **Proton resonance shift of water in the gas and liquid states.** *J Chem Phys* 1966;44:4582 CrossRef
10. Childs C, Hiltunen Y, Vidyasagar R, et al. **Determination of regional brain temperature using proton magnetic resonance spectroscopy to assess brain-body temperature differences in healthy human subjects.** *Magn Reson Med* 2007;57:59–66 CrossRef Medline
11. Corbett R, Laptook A, Weatherall P. **Noninvasive measurements of human brain temperature using volume-localized proton magnetic resonance spectroscopy.** *J Cereb Blood Flow Metab* 1997;17:363–69 CrossRef Medline
12. Covaciu L, Rubertsson S, Ortiz-Nieto F, et al. **Human brain MR spectroscopy thermometry using metabolite aqueous-solution calibrations.** *J Magn Reson Imaging* 2010;31:807–14 CrossRef Medline
13. Karaszewski B, Wardlaw JM, Marshall I, et al. **Measurement of brain temperature with magnetic resonance spectroscopy in acute ischemic stroke.** *Ann Neurol* 2006;60:438–46 CrossRef Medline
14. Marshall I, Karaszewski B, Wardlaw JM, et al. **Measurement of regional brain temperature using proton spectroscopic imaging: validation and application to acute ischemic stroke.** *Magn Reson Imaging* 2006;24:699–706 CrossRef Medline
15. Marino S, Ciurleo R, Bramanti P, et al. **1H-MR spectroscopy in traumatic brain injury.** *Neurocrit Care* 2011;14:127–33 CrossRef Medline
16. Cady EB, D'Souza PC, Penrice J, et al. **The estimation of local brain**

- temperature by in vivo 1H magnetic resonance spectroscopy. *Magn Reson Med* 1995;33:862–67 [CrossRef Medline](#)
17. Cady EB, Penrice J, Robertson NJ. Improved reproducibility of MRS regional brain thermometry by ‘amplitude-weighted combination.’ *NMR Biomed* 2011;24:865–72 [CrossRef Medline](#)
18. Bainbridge A, Kendall GS, De Vita E, et al. Regional neonatal brain absolute thermometry by 1H MRS. *NMR Biomed* 2013;26:416–23 [CrossRef Medline](#)
19. Wu TW, McLean C, Friedlich P, et al. Brain temperature in neonates with hypoxic-ischemic encephalopathy during therapeutic hypothermia. *J Pediatr* 2014;165:1129–34 [CrossRef Medline](#)
20. al Naqeeb N, Edwards AD, Cowan FM, et al. Assessment of neonatal encephalopathy by amplitude-integrated electroencephalography. *Pediatrics* 1999;103:1263–71 [CrossRef Medline](#)
21. Wintermark P, Labrecque M, Warfield SK, et al. Can induced hypothermia be assured during brain MRI in neonates with hypoxic-ischemic encephalopathy? *Pediatr Radiol* 2010;40:1950–54 [CrossRef Medline](#)
22. Barkovich AJ, Hajnal BL, Vigneron D, et al. Prediction of neuromotor outcome in perinatal asphyxia: evaluation of MR scoring systems. *AJNR Am J Neuroradiol* 1998;19:143–49 [Medline](#)
23. Executive summary: neonatal encephalopathy and neurologic outcome, second edition—Report of the American College of Obstetricians and Gynecologists’ Task Force on Neonatal Encephalopathy. *Obstet Gynecol* 2014;123:896–901 [CrossRef Medline](#)
24. Boudes E, Tan X, Saint-Martin C, et al. MRI obtained during versus after hypothermia in asphyxiated newborns. *Arch Dis Child Fetal Neonatal Ed* 2015;100:F238–42 [CrossRef Medline](#)
25. Corbett RJ, Laptook AR, Tollefsbol G, et al. Validation of a noninvasive method to measure brain temperature in vivo using 1H NMR spectroscopy. *J Neurochem* 1995;64:1224–30 [Medline](#)
26. Weis J, Covaciu L, Rubertsson S, et al. Noninvasive monitoring of brain temperature during mild hypothermia. *Magn Reson Imaging* 2009;27:923–32 [CrossRef Medline](#)
27. Naressi A, Couturier C, Castang I, et al. Java-based graphical user interface for MRUI, a software package for quantitation of in vivo/medical magnetic resonance spectroscopy signals. *Comput Biol Med* 2001;31:269–86 [CrossRef Medline](#)
28. Stefan D, Di Cesare F, Andrasescu A, et al. Quantitation of magnetic resonance spectroscopy signals: the jMRUI software package. *Meas Sci Technol* 2009;20:104035 [CrossRef](#)
29. Pijnappel WW, van den Boogaart A, de Beer R, et al. SVD-based quantification of magnetic resonance signals. *J Magn Reson* 1992;97:122–34
30. Kuroda K, Takei N, Mulkern RV, et al. Feasibility of internally referenced brain temperature imaging with a metabolite signal. *Magn Reson Med Sci* 2003;2:17–22 [CrossRef Medline](#)
31. De Vis JB, Hendrikse J, Petersen ET, et al. Arterial spin-labelling perfusion MRI and outcome in neonates with hypoxic-ischemic encephalopathy. *Eur Radiol* 2015;25:113–21 [CrossRef Medline](#)
32. Massaro AN, Bouyssi-Kobar M, Chang T, et al. Brain perfusion in encephalopathic newborns after therapeutic hypothermia. *AJNR Am J Neuroradiol* 2013;34:1649–55 [CrossRef Medline](#)
33. Wintermark P, Hansen A, Gregas MC, et al. Brain perfusion in asphyxiated newborns treated with therapeutic hypothermia. *AJNR Am J Neuroradiol* 2011;32:2023–29 [CrossRef Medline](#)
34. Kusaka T, Ueno M, Miki T, et al. Relationship between cerebral oxygenation and phosphorylation potential during secondary energy failure in hypoxic-ischemic newborn piglets. *Pediatr Res* 2009;65:317–22 [CrossRef Medline](#)
35. Peng S, Boudes E, Tan X, et al. Does near-infrared spectroscopy identify asphyxiated newborns at risk of developing brain injury during hypothermia treatment? *Am J Perinatol* 2015;32:555–64 [CrossRef Medline](#)
36. Tichauer KM, Wong DY, Hadway JA, et al. Assessing the severity of perinatal hypoxia-ischemia in piglets using near-infrared spectroscopy to measure the cerebral metabolic rate of oxygen. *Pediatr Res* 2009;65:301–06 [CrossRef Medline](#)
37. Toet MC, Lemmers PM, van Schelven LJ, et al. Cerebral oxygenation and electrical activity after birth asphyxia: their relation to outcome. *Pediatrics* 2006;117:333–39 [CrossRef Medline](#)
38. Shaikh H, Lechpammer M, Jensen FE, et al. Increased brain perfusion persists over the first month of life in term asphyxiated newborns treated with hypothermia: does it reflect activated angiogenesis? *Transl Stroke Res* 2015;6:224–33 [CrossRef Medline](#)
39. Bertolizio G, Mason L, Bissonnette B. Brain temperature: heat production, elimination and clinical relevance. *Paediatr Anaesth* 2011;21:347–58 [CrossRef Medline](#)
40. Kiyatkin EA. Brain temperature homeostasis: physiological fluctuations and pathological shifts. *Front Biosci (Landmark Ed)* 2010;15:73–92 [Medline](#)
41. Rango M, Arighi A, Bresolin N. Brain temperature: what do we know? *Neuroreport* 2012;23:483–87 [CrossRef Medline](#)
42. Iwata S, Iwata O, Thornton JS, et al. Superficial brain is cooler in small piglets: neonatal hypothermia implications. *Ann Neurol* 2006;60:578–85 [CrossRef Medline](#)
43. Laptook AR, Shalak L, Corbett RJ. Differences in brain temperature and cerebral blood flow during selective head versus whole-body cooling. *Pediatrics* 2001;108:1103–10 [CrossRef Medline](#)

Does the Addition of a “Black Bone” Sequence to a Fast Multisequence Trauma MR Protocol Allow MRI to Replace CT after Traumatic Brain Injury in Children?

M.H.G. Dremmen, M.W. Wagner, T. Bosemani, A. Tekes, D. Agostino, E. Day, B.P. Soares, and T.A.G.M. Huisman

ABSTRACT

BACKGROUND AND PURPOSE: Head CT is the current neuroimaging tool of choice in acute evaluation of pediatric head trauma. The potential cancer risks of CT-related ionizing radiation should limit its use in children. We evaluated the role of MR imaging, including a “black bone” sequence, compared with CT in detecting skull fractures and intracranial hemorrhages in children with acute head trauma.

MATERIALS AND METHODS: We performed a retrospective evaluation of 2D head CT and brain MR imaging studies including the black bone sequence of children with head trauma. Two experienced pediatric neuroradiologists in consensus created the standard of reference. Another pediatric neuroradiologist blinded to the diagnosis evaluated brain MR images and head CT images in 2 separate sessions. The presence of skull fractures and intracranial posttraumatic hemorrhages was evaluated. We calculated the sensitivity and specificity of CT and MR imaging with the black bone sequence in the diagnosis of skull fractures and intracranial hemorrhages.

RESULTS: Twenty-eight children (24 boys; mean age, 4.89 years; range, 0–15.5 years) with head trauma were included. MR imaging with the black bone sequence revealed lower sensitivity (66.7% versus 100%) and specificity (87.5% versus 100%) in identifying skull fractures. Four of 6 incorrectly interpreted black bone MR imaging studies showed cranial sutures being misinterpreted as skull fractures and vice versa.

CONCLUSIONS: Our preliminary results show that brain MR imaging complemented by a black bone sequence is a promising nonionizing alternative to head CT for the assessment of skull fractures in children. However, accuracy in the detection of linear fractures in young children and fractures of aerated bone remains limited.

ABBREVIATIONS: NPV = negative predictive value; PPV = positive predictive value

CT is the initial neuroimaging technique of choice for the acute evaluation of pediatric head trauma due to its wider availability, lower cost, and short acquisition time. In addition, CT identifies most traumatic injuries that require urgent treatment and correlates well with clinical scales and outcome.¹ However, CT-related ionizing radiation involves the potential risk of patients developing cancer and strongly argues in favor of alternative neuroimaging techniques such as MR imaging.² The lifetime cancer mortality risk attributable to the radiation from a single CT scan of the head in a 1-year-old child has been estimated as 0.07%. This

small risk translates into a large population-level risk, especially because head trauma in children from 0 to 14 years of age accounts for nearly half a million emergency department visits in the United States annually.^{3,4}

MR imaging is a nonionizing technique that provides superior contrast resolution and has a higher sensitivity and specificity for parenchymal lesions compared with CT.^{3,4} Especially, advanced MR imaging techniques (DWI, SWI) provide additional information that correlates well with outcome.^{5,6} Nonhemorrhagic shear injuries and subtle microhemorrhages are typically seen with higher sensitivity by MR imaging compared with CT. Nevertheless, the role of MR imaging in the acute diagnostic work-up of head trauma in children is still limited.^{2,7,8} This limitation may be partially explained by longer acquisition times and the subsequent need for sedation as well as the low sensitivity of MR imaging for skull fractures.^{2,8} Recently, black bone MR images have been introduced as a new sequence for the evaluation of structural bony abnormalities such as craniosynostosis.⁹

On the basis of the inherent diagnostic quality of the black bone sequence, we aimed to determine whether a trauma brain

Received September 6, 2016; accepted after revision June 10, 2017.

From the Section of Pediatric Neuroradiology (M.H.G.D., M.W.W., T.B., A.T., D.A., E.D., B.P.S., T.A.G.M.H.), Division of Pediatric Radiology and Pediatric Neuroradiology, Department of Radiology and Radiological Science, Johns Hopkins Hospital, Baltimore, Maryland; Division of Pediatric Radiology (M.H.G.D.), Department of Radiology, Erasmus University Medical Center Rotterdam, Rotterdam, the Netherlands; and Institute of Diagnostic and Interventional Radiology (M.W.W.), University Hospital Zurich, Zurich, Switzerland.

Please address correspondence to Marjolein H.G. Dremmen, MD, Department of Radiology, Erasmus University Medical Center Rotterdam, PO Box 2040, 3000 CA Rotterdam, the Netherlands; e-mail: m.dremmen@erasmusmc.nl

<http://dx.doi.org/10.3174/ajnr.A5405>

MR imaging protocol with an included black bone MR image could be an alternative to head CT in the acute work-up of children with head trauma. To address our goal, we compared the diagnostic accuracy of brain MR imaging including the black bone sequence with CT for the detection of skull fractures after traumatic brain injury in children. Images were also studied for coexisting intracranial lesions.

MATERIALS AND METHODS

This single-center retrospective study was approved by the Johns Hopkins Hospital institutional research ethics board, which waived informed consent.

Study Population

Inclusion criteria were the following: 1) a history of head trauma; 2) the availability of thin-section (≤ 3 mm) 2D head CT data and a brain MR imaging study including a black bone sequence acquired within 7 days of each other, and 3) age at neuroimaging younger than 18 years. The exclusion criteria were the following: 1) susceptibility artifacts on a black bone sequence due to implanted materials, and 2) a brain MR imaging study acquired after craniotomy. Data from eligible children were obtained through an electronic search of our pediatric neuroradiology data base covering the period between January 1, 2015 (date when black bone MR imaging was introduced in our hospital), and November 15, 2015.

Image Acquisition

All CT studies performed at our radiology department were acquired on a commercially available 2×128 detector system (Somatom Definition Flash; Siemens, Erlangen, Germany) using the institutional pediatric head CT protocol, including the following parameters: tube voltage, 120 kV; tube current, 380 reference mA; rotation time, 1.0 second; axial acquisition; 0.75-mm section thickness; FOV, 160×160 to 250×250 mm. No intravenous injection of a contrast agent was performed. The CT studies imported to our neuroradiology data base from outside hospitals and officially reviewed by our pediatric neuroradiologists met the inclusion criteria if the studies were performed with a section thickness of ≤ 3 mm.

The brain MR imaging studies were performed on a 1.5T (Magnetom Aera; Siemens) or 3T (Magnetom Skyra; Siemens) clinical scanner using a standard pediatric 16-channel head coil. The institutional pediatric head trauma MR imaging protocol includes a 3D T1-weighted sequence with a sagittal acquisition, an axial T2-weighted sequence, axial FLAIR, DTI, and SWI. In addition, a black bone sequence was acquired in the axial plane from above the skull vertex to below the mandible, with 2D reconstruction in the coronal and sagittal planes. The black bone sequence is a gradient-echo sequence with short TEs and TRs and an optimal flip angle for the differentiation of bone from soft-tissue contrast (TE, 4.20 ms; TR, 8.60 ms; flip angle, 5° ; FOV, 240 mm; section thickness, 1.00 mm; section spacing, 0.2 mm).¹⁰ Signal from fat and water is suppressed to provide uniform soft-tissue contrast, thereby optimizing the visualization of the bone-soft tissue margin.^{10,11}

Image Analysis

Both the CT and MR imaging datasets were evaluated for the presence of skull fractures and intracranial hemorrhages. Addi-

tionally, the fracture type was classified into linear, depressed, or basilar, and the type of intracranial hemorrhage was subdivided into subdural, epidural, subarachnoid, intraparenchymal, intraventricular, and mixed (> 1 type of intracranial hemorrhage).^{3,4}

The standard of reference for the diagnosis of a skull fracture and/or posttraumatic intracranial hemorrhage was established by consensus interpretation of 2 experienced pediatric neuroradiologists with 14 and 22 years of experience (A.T. and T.A.G.M.H.). The complete CT datasets, including 2D and, if available, 3D images, and the full MR imaging datasets were reviewed to create the standard of reference.

The study reader was a pediatric neuroradiologist with 7 years of experience (T.B.). The reader was blinded to the medical records, clinical examination findings, previous neuroimaging studies, and final diagnosis. In a first reading session, he evaluated the available MR imaging studies of all patients in a random order. The reader first assessed the presence, location, and type of skull fractures using only the black bone sequence. After this initial assessment, the reader could use the other available sequences to identify posttraumatic intracranial lesions. No adjustments were made to the black bone interpretation score after the assessment of the intracranial lesions. In a second independent reading session 30 days after the first session, the 2D-CT studies were evaluated in a different random order. The first author (M.H.G.D.) assisted the study reader by opening only the relevant images for each reading session and entering the results of the evaluation on an anonymized data sheet. The black bone images were reviewed in regular and inverted format. Empirically, the inverted MR imaging window level setting resembles the classic bone CT appearance best.

Statistical Analysis

The independent evaluations of the CT images and MR imaging datasets (including the black bone sequence) from the study reader were compared with the standard of reference to analyze the diagnostic accuracy. To compare the CT and MR imaging data for the presence of skull fractures and intracranial hemorrhages, we used 2×2 contingency tables. The decision to report the presence or absence of skull fractures or intracranial hemorrhages was considered as, respectively, a true-positive or true-negative result when it matched the consensus reading of the standard of reference or as, respectively, a false-positive or a false-negative result when it did not match the reading of the standard of reference. To calculate sensitivity, specificity, positive predictive value (PPV), and negative predictive value (NPV), we correlated the specific decisions (true-positive, false-positive, true-negative, or false-negative) with the total decisions for the study reader. For both 2D head CT and brain MR imaging including the black bone sequence, the sensitivity, specificity, PPV, and NPV were calculated for the detection of skull fractures only, intracranial hemorrhages only, and skull fractures and/or intracranial hemorrhages combined (representing whether the neuroimaging study findings were normal for fractures and hemorrhages). Finally, the sensitivity, specificity, PPV, and NPV of brain MR imaging including the black bone sequence in the detection of skull fractures were calculated for 2 different age groups, children up to 2 years of age (with relatively wide cranial sutures) and older than 2 years of

age, and for children with MR imaging studies performed on 1.5T and 3T MR imaging scanners, respectively.

RESULTS

Study Population

Twenty-eight children (24 boys and 4 girls) with acute head trauma met the inclusion criteria for this study. The mean age of the children at the first neuroimaging study was 4.89 years (range, 6 days to 15.5 years). None of the patients died. Fourteen children (50%) were younger than 2 years of age. The field strength of the MR imaging scanner was 1.5T in 12 children and 3T in 16 children. For 7 children (25%), anesthesia was necessary to perform MR imaging. The mean time interval between the CT and MR imaging was 2 ± 1.43 days (range, 0–6 days).

Imaging Analysis

On the basis of the standard of reference, 12 children had skull fractures (43%) and 22 children (79%) had intracranial hemorrhages. The different types of skull fractures and intracranial hemorrhages are shown in Table 1. Six children with a skull fracture were younger than 2 years of age. Twenty-two of 28 children (79%) had at least a skull fracture and/or an intracranial hemorrhage (all children with a skull fracture had an intracranial hemorrhage).

The sensitivity, specificity, PPV, and NPV for 2D head CT and brain MR imaging including the black bone sequence for detecting skull fractures, intracranial hemorrhages, and skull fractures and/or intracranial hemorrhages combined are shown in Table 2. The 2D head CT had a higher sensitivity, specificity, PPV, and NPV compared with brain MR imaging including the black bone sequence for the detection of skull fractures, while brain MR imaging including the black bone sequence had a higher sensitivity,

specificity, PPV, and NPV compared with 2D head CT for the detection of skull fractures and/or intracranial hemorrhages combined.

The sensitivity, specificity, PPV, and NPV for brain MR imaging including the black bone sequence in detecting skull fractures dependent on the age of the children at neuroimaging and the magnetic field strength of the MR scanner are shown in Table 3. In children younger than 2 years of age, the sensitivity and NPV for brain MR imaging including the black bone sequence in detecting skull fractures were higher and the specificity and PPV were lower compared with children older than 2 years of age. In children with brain MR imaging acquired on a 1.5T MR imaging scanner, the sensitivity, PPV, and NPV for brain MR imaging including the black bone sequence in detecting skull fractures were higher and the specificity was lower compared with children with brain MR imaging acquired on a 3T MR imaging scanner.

DISCUSSION

Skull fractures are relatively common in children with head trauma (up to 30%), particularly in the younger age groups.^{12,13} Morphologically, skull fractures can be described as linear, depressed, or basilar (skull base). Most skull fractures are linear (66%–75%).^{14,15} Although isolated fractures themselves rarely require intervention, a neuroimaging study may be needed to describe the full extent of calvarial and intracranial injuries.¹⁶

Black bone is a novel MR imaging sequence that uses short TEs and TRs as well as an optimal flip angle to minimize soft-tissue contrast and enhance the bone–soft-tissue boundary.^{9–11,17} Signal from fat and water is suppressed to provide uniform soft-tissue contrast, thereby optimizing the visualization of the bone–soft-tissue interface.^{10,11} The short TEs and TRs and the volume acquisition result in short imaging times. Black bone MR imaging has been shown to be useful and accurate in the evaluation of cranial bones and sutures in children with craniosynostosis. This finding reveals a considerable clinical potential in the assessment of osseous abnormalities as a non-ionizing alternative to CT.^{9–11,17}

Our study evaluated the diagnostic accuracy of black bone MR imaging in detecting skull fractures in children with head trauma compared with CT. The black bone MR imaging sequence showed a sensitivity of 66.7% and a specificity of 87.5% in the detection of skull fractures (Fig 1). The specificity is acceptable, while the sensitivity is low. To determine the reasons for the low sensitivity of the black bone MR imaging sequence, we studied the 4 false-negative linear fractures and the 2 false-positive linear fractures. In 2 children younger than 2 years of age, false-negative linear

fractures were misinterpreted as cranial sutures (2 false-negative cases). Furthermore, the 2 false-positive cases were children in the younger age group (younger than 2 years), with cranial sutures being falsely identified as linear fractures. In young children, the presence of open sutures is known to increase the diagnostic uncertainty of skull fractures on 2D images as recently shown by a head CT study.¹⁴ In head CT studies, the addition of 3D reconstructions to the 2D dataset has been shown

Table 1: Number and types of skull fractures and intracranial hemorrhages detected on axial 2D head CT and brain MRI including the black bone sequence in 28 children with head trauma

	No. of Patients	Percentage of Patients
Skull fractures	12	43%
Linear	11	39%
Depressed	1	4%
Intracranial hemorrhage	22	79%
Isolated subdural	4	14%
Isolated epidural	3	11%
Isolated intraparenchymal	3	11%
Mixed	12	43%

Table 2: Diagnostic accuracy of axial 2D head CT compared with brain MRI including the black bone sequence for the detection of skull fractures, intracranial hemorrhages, and skull fractures and/or intracranial hemorrhages combined in 28 children with head trauma

	Skull Fractures	Intracranial Hemorrhages	Skull Fracture and/or Intracranial Hemorrhages	
	MRI + BB (Compared with CT)	Axial CT (Compared with MRI)	Axial CT	MRI + BB
Sensitivity	66.7%	72.7%	81.8%	100%
Specificity	87.5%	83.3%	83.3%	100%
PPV	80.0%	94.1%	94.7%	100%
NPV	77.8%	45.5%	55.6%	100%

Note:—BB indicates black bone MRI sequence.

to increase the reader's confidence for correct differentiation of sutures and other nonfracture-related linear lucencies such as vascular channels versus linear fractures.¹⁴ The addition of 3D reconstruction to the 2D black bone MR images as shown for the study of craniosynostosis⁹ could potentially decrease the misinterpretation as shown for head CT.

The third false-negative case was an older child in whom a linear fracture was misinterpreted as a venous transosseous vascular channel. More familiarity with the black bone sequence and the use of 3D reconstruction could potentially help overcome this problem. The fourth case of a missed linear fracture on black bone MR imaging was a fracture in the mastoid region (Fig 2). This case highlights the main limitation of black bone MR imaging: In anatomic regions where bone abuts air (mastoid, craniofacial sinuses), the distinction between air and bone is difficult because both have low signal intensity on this sequence.¹⁰ The application of black bone MR imaging at air-bone interfaces is challenging

and requires experience with the technique and careful review of the images.

The fractures missed on black bone MR images were linear and nondisplaced and did not require specific treatment. Fractures of the mastoid air cells and temporal bone region are potentially of major clinical concern; in case of suspected CSF leaks, damage to inner/middle ear structures, and vascular injury, CT is needed. Further improvement of the black bone imaging technique is necessary for implementation of this technique to all neurotrauma patients. Isolated, linear, nondisplaced skull fractures are known to have a low clinical significance: They are not associated with neurologic deterioration, affected children can be appropriately managed as outpatients, and neurologic outcome is excellent.^{2,18} A precise and complete diagnosis in children with head trauma is important (eg, for medical legal purposes); therefore for the work-up of nonaccidental trauma or for other carefully selected pediatric patients, an additional head CT study may be necessary if the black bone MR images are negative for identification of skull fractures. In most cases, the missed diagnosis of an isolated, linear skull fracture appears to have low clinical significance and no impact on the management of the affected children.

By using MR imaging including the black bone sequence as a primary screening tool in patients with neurotrauma, the number of CT studies in the pediatric population can be decreased. The identification of intracranial hemorrhages, on the other hand, has important implications for acute management and long-term outcome of children with head trauma.^{3,4,19} Our study reveals a higher sensitivity (100% versus 72.7%) and specificity (100% versus 83.3%) of MR imaging including black bone sequence compared

with head CT in detecting intracranial hemorrhages in children with head trauma (Fig 3). The higher sensitivity and specificity of MR imaging is not surprising: The superior contrast resolution of MR imaging compared with CT results in a higher sensitivity for parenchymal lesions.²⁰ The implementation of SWI as part of the MR imaging protocol for children with head trauma further increases the sensitivity for detection of intracranial hemorrhages. Additionally, a strong correlation has been shown between the number and volume of SWI lesions and the severity of injury (determined by the initial Glasgow Coma Scale score and the duration of the coma) as well as neurologic outcome 6–12 months after the injury.²¹ These results emphasize the importance of MR imaging in the acute work-up of children with head trauma. In our opinion, MR imaging as a nonionizing imaging technique should not only be an important alternative to CT in the acute evaluation of pediatric head trauma but also gradually become the main neuroimaging technique for the evaluation of trauma.

Table 3: Differences in diagnostic accuracy of brain MRI including the black bone sequence for the detection of skull fractures in 28 children with head trauma, depending on the age of the child and MR imaging field strength

	Age at MRI		MRI Field Strength	
	Younger Than 2 yr (n = 14)	2 yr and Older (n = 14)	1.5T (n = 12)	3T (n = 16)
Sensitivity	75.0%	50.0%	83.3%	50.0%
Specificity	66.7%	100%	83.3%	90.0%
PPV	75.0%	100%	83.3%	75.0%
NPV	66.7%	83.3%	83.3%	75.0%

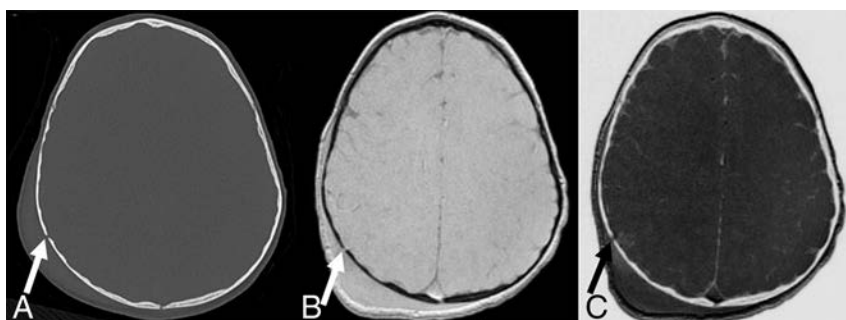


FIG 1. A, Axial CT image shows a nondisplaced linear fracture of the right parietal bone (arrow) with extracranial soft-tissue swelling. Black bone (B) and inverted black bone (C) MR images reveal equivalent visualization of the right parietal fracture (arrows), as well as overlying soft-tissue swelling.

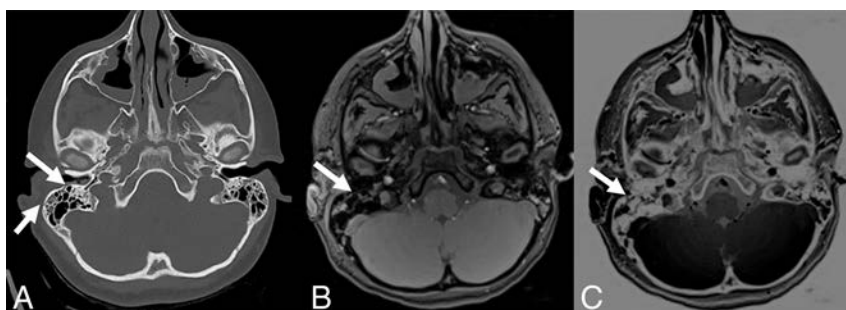


FIG 2. A, Axial CT image shows 2 small nondisplaced linear fractures of the mastoid (arrows). On black bone (B) and inverted black bone (C) MR images, these fractures are barely visible (arrows).

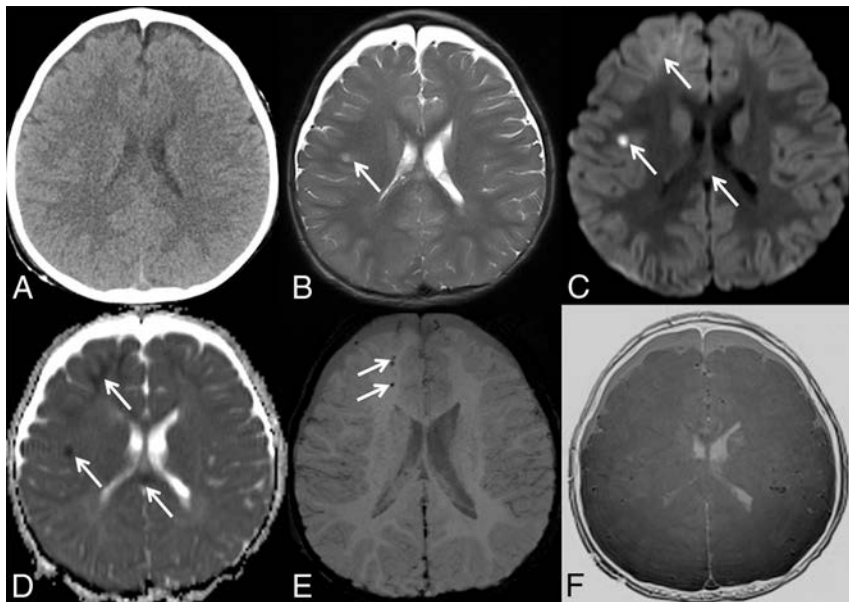


FIG 3. A, Axial CT image does not show intracranial hemorrhage. A matching axial T2-weighted MR image (B), axial trace of diffusion (C), ADC map (D), minimal intensity projection-SWI (E), and inverted black bone MR image (F) reveal areas of T2-hyperintense signal and restricted diffusion within the temporal white matter (arrows in B–D), areas of restricted diffusion within the right frontal lobe and splenium of the corpus callosum (arrows in C and D), and foci of hypointense SWI signal within the right frontal white matter (arrows in E), suggestive of intracranial hemorrhages and diffuse axonal injury not seen on axial CT.

matic skull and brain injury in the pediatric population. Specifically, the combination of highly sensitive MR imaging sequences for identification of intracranial and intra-axial lesions with a relatively sensitive MR image for clinically relevant fractures offers a diagnostically important “one-stop shopping” imaging approach. In our institution, we currently use a fast trauma head MR imaging, which combines the black bone MR image with 3D T1-weighted, axial HASTE T2-weighted, axial DWI, and SWI sequences.

Our results show a negative correlation between the sensitivity of black bone MR imaging and the magnetic field strength of the MR imaging scanner: 83% in 1.5T versus 50% in 3T. The short TE and TR cause the black bone sequence to be a gradient-echo sequence, hence susceptible to artifacts. Movement artifacts, dental braces, and implanted materials (ie, ventriculoperitoneal shunt reservoirs) can potentially degrade image quality and decrease the sensitivity of the study, particularly at 3T due to higher amenability to susceptibility artifacts in 3T datasets. In addition, our study reveals a lower specificity for black bone MR imaging in children younger than 2 years of age compared with older children. This difference is most likely due to the confounding role of open cranial sutures in younger children as shown for head CT data.¹⁴

We acknowledge the limitations of our study, including the small number of patients and its retrospective nature. In addition, the standard of reference was established by experienced pediatric neuroradiologists using all available images (CT and MR imaging), as is typical in daily routine. We had no postmortem studies because all patients survived. Furthermore, head CT and brain MR imaging data were not acquired on the same day in some patients. The optimal study design to compare the diagnostic accuracy of CT and MR imaging datasets would require the acqui-

sition of CT and MR imaging studies on the same day. However, in this retrospective study, this was not feasible due to both practical and ethical reasons. Future prospective research should focus on optimizing the study design to avoid selection bias. For 7 children, anesthesia was necessary to perform brain MR imaging. This was partly because most of the study population was younger than 6 months of age or older than 5 years and the MR imaging examination could be performed with the patient in a vacuum cushion or after preparing and coaching the child and the parents/caregivers, respectively. The increasing availability of child life specialists may further help decrease the need for anesthesia for brain MR imaging in the future. Finally, brain MR imaging examinations were obtained for clinical indications on the basis of the head CT findings or neurologic symptoms not explained by the head CT findings. This choice may have been a potential source of selection bias in our study population. A prospective study

design in which CT and MR imaging studies are performed in all pediatric trauma patients is needed for further evaluation of MR imaging as a primary neuroimaging screening tool in the pediatric population.

CONCLUSIONS

Our preliminary results show that brain MR imaging including the black bone sequence may be a promising alternative to head CT as a primary screening tool for the acute diagnostic work-up of children with head trauma. The higher sensitivity and specificity of MR imaging in detecting intracranial hemorrhages compared with CT highlights the key role of MR imaging for acute management and prognosis of long-term outcome of children with head trauma. The lack of ionizing radiation further supports the use of brain MR imaging as the primary neuroimaging tool for acute head trauma in the pediatric population. Currently, additional head CT studies are indicated for patients without identifiable skull fracture on the black bone sequence because of the possibility of missing certain types of skull fractures. Prospective studies with a larger number of children are needed to further evaluate the diagnostic role of black bone MR imaging in children with acute head trauma. Furthermore, the value of a fast trauma MR imaging protocol should be prospectively evaluated for the wide range of posttraumatic lesions that may be encountered in the brain, including diffuse axonal injury, nonhemorrhagic contusions, and tissue lacerations.

ACKNOWLEDGMENTS

We thank and dedicate this study to our friend and exceptionally gifted and talented colleague Dr Andrea Poretti for providing his insight and expertise. We are immensely grateful for his dedica-

tion to the field of pediatric neuroimaging. He left us too early, and we will miss his sharp intellect, humble character, and relentless effort to advance our understanding of pediatric neurologic diseases.

Disclosures: Marjolein H.G. Dremmen—UNRELATED: Employment: Pediatric Radiologist, Erasmus Medical Center Rotterdam, Comments: 3-month observing fellowship in pediatric neuroradiology, Johns Hopkins Hospital (unpaid). Thangamadhan Bosemani—UNRELATED: Consultancy: Alexion Pharmaceutical. Thierry A.G.M. Huisman—UNRELATED: Board Membership: Editorial Board American Journal of Neuroradiology.

REFERENCES

- Klassen TP, Reed MH, Stiell IG, et al. Variation in utilization of computed tomography scanning for the investigation of minor head trauma in children: a Canadian experience. *Acad Emerg Med* 2000;7:739–44 CrossRef Medline
- Roguski M, Morel B, Sweeney M, et al. Magnetic resonance imaging as an alternative to computed tomography in select patients with traumatic brain injury: a retrospective comparison. *J Neurosurg Pediatr* 2015;15:529–34 CrossRef Medline
- Pinto PS, Poretti A, Meoded A, et al. The unique features of traumatic brain injury in children: review of the characteristics of the pediatric skull and brain, mechanisms of trauma, patterns of injury, complications and their imaging findings—part 1. *J Neuroimaging* 2012;22:e1–17 CrossRef Medline
- Pinto PS, Meoded A, Poretti A, et al. The unique features of traumatic brain injury in children: review of the characteristics of the pediatric skull and brain, mechanisms of trauma, patterns of injury, complications, and their imaging findings—part 2. *J Neuroimaging* 2012;22:e18–41 CrossRef Medline
- Beauchamp MH, Ditchfield M, Babl FE, et al. Detecting traumatic brain lesions in children: CT versus MRI versus susceptibility weighted imaging (SWI). *J Neurotrauma* 2011;28:915–27 CrossRef Medline
- Bosemani T, Poretti A, Huisman TA. Susceptibility-weighted imaging in pediatric neuroimaging. *J Magn Reson Imaging* 2014;40: 530–44 CrossRef Medline
- Schmutz B, Rahmel B, McNamara Z, et al. Magnetic resonance imaging: an accurate, radiation-free, alternative to computed tomography for the primary imaging and three-dimensional reconstruction of the bony orbit. *J Oral Maxillofac Surg* 2014;72:611–18 CrossRef Medline
- Sigmund GA, Tong KA, Nickerson JP, et al. Multimodality comparison of neuroimaging in pediatric traumatic brain injury. *Pediatr Neurol* 2007;36:217–26 CrossRef Medline
- Eley KA, Watt-Smith SR, Sheerin F, et al. “Black bone” MRI: a potential alternative to CT with three-dimensional reconstruction of the craniofacial skeleton in the diagnosis of craniosynostosis. *Eur Radiol* 2014;24:2417–26 CrossRef Medline
- Eley KA, McIntyre AG, Watt-Smith SR, et al. “Black bone” MRI: a partial flip angle technique for radiation reduction in craniofacial imaging. *Br J Radiol* 2012;85:272–78 CrossRef Medline
- Eley KA, Watt-Smith SR, Golding SJ. “Black bone” MRI: a potential alternative to CT when imaging the head and neck: report of eight clinical cases and review of the Oxford experience. *Br J Radiol* 2012; 85:1457–64 CrossRef Medline
- Greenes DS, Schutzman SA. Clinical significance of scalp abnormalities in asymptomatic head-injured infants. *Pediatr Emerg Care* 2001;17:88–92 CrossRef Medline
- Dunning J, Daly JP, Lomas JP, et al; Children’s head injury algorithm for the prediction of important clinical events study group. Derivation of the children’s head injury algorithm for the prediction of important clinical events decision rule for head injury in children. *Arch Dis Child* 2006;91:885–91 CrossRef Medline
- Orman G, Wagner MW, Seeburg D, et al. Pediatric skull fracture diagnosis: should 3D CT reconstructions be added as routine imaging? *J Neurosurg Pediatr* 2015;16:426–31 CrossRef Medline
- Schutzman SA, Greenes DS. Pediatric minor head trauma. *Ann Emerg Med* 2001;37:65–74 Medline
- Bonfield CM, Naran S, Adetayo OA, et al. Pediatric skull fractures: the need for surgical intervention, characteristics, complications, and outcomes. *J Neurosurg Pediatr* 2014;14:205–11 CrossRef Medline
- Eley KA, Watt-Smith SR, Golding SJ. “Black bone” MRI: a potential non-ionizing method for three-dimensional cephalometric analysis—a preliminary feasibility study. *Dentomaxillofac Radiol* 2013;42:20130236 CrossRef Medline
- Powell EC, Atabaki SM, Wootton-Gorges S, et al. Isolated linear skull fractures in children with blunt head trauma. *Pediatrics* 2015;135: e851–57 CrossRef Medline
- Hochstadter E, Stewart TC, Alharfi IM, et al. Subarachnoid hemorrhage prevalence and its association with short-term outcome in pediatric severe traumatic brain injury. *Neurocrit Care* 2014;21: 505–13 CrossRef Medline
- Tang PH, Lim CC. Imaging of accidental paediatric head trauma. *Pediatr Radiol* 2009;39:438–46 CrossRef Medline
- Tong KA, Ashwal S, Holshouser BA, et al. Diffuse axonal injury in children: clinical correlation with hemorrhagic lesions. *Ann Neurol* 2004;56:36–50 CrossRef Medline

Volume of Structures in the Fetal Brain Measured with a New Semiautomated Method

 R. Ber,  D. Hoffman,  C. Hoffman,  A. Polat,  E. Derazne,  A. Mayer, and  E. Katorza



ABSTRACT

BACKGROUND AND PURPOSE: Measuring the volume of fetal brain structures is challenging due to fetal motion, low resolution, and artifacts caused by maternal tissue. Our aim was to introduce a new, simple, Matlab-based semiautomated method to measure the volume of structures in the fetal brain and present normal volumetric curves of the structures measured.

MATERIALS AND METHODS: The volume of the supratentorial brain, left and right hemispheres, cerebellum, and left and right eyeballs was measured retrospectively by the new semiautomated method in MR imaging examinations of 94 healthy fetuses. Four volume ratios were calculated. Interobserver agreement was calculated with the intraclass correlation coefficient, and a Bland-Altman plot was drawn for comparison of manual and semiautomated method measurements of the supratentorial brain.

RESULTS: We present normal volumetric curves and normal percentile values of the structures measured according to gestational age and of the ratios between the cerebellum and the supratentorial brain volume and the total eyeball and the supratentorial brain volume. Interobserver agreement was good or excellent for all structures measured. The Bland-Altman plot between manual and semiautomated measurements showed a maximal relative difference of 7.84%.

CONCLUSIONS: We present a technologically simple, reproducible method that can be applied prospectively and retrospectively on any MR imaging protocol, and we present normal volumetric curves measured. The method shows results like manual measurements while being less time-consuming and user-dependent. By applying this method on different cranial and extracranial structures, anatomic and pathologic, we believe that fetal volumetry can turn from a research tool into a practical clinical one.

ABBREVIATIONS: CV = cerebellar volume; EBV = total eyeball volume; ICC = intraclass correlation coefficient; LEBV = left eyeball volume; LHV = left hemisphere volume; REBV = right eyeball volume; RHV = right hemisphere volume; STV = supratentorial volume

In pediatric and adult populations, 3D volumetric measurement of brain structures is an important tool for the assessment of neurologic patients. Automatic volumetry of the brain is used to diagnose and evaluate different pathologies such as Alzheimer disease, essential tremor, multiple sclerosis, and epilepsy.¹⁻⁴ During the past decade, with the increasing use of MR imaging in prenatal evaluation, attempts to implement brain volumetric

measurements on fetal MR imaging have been made. However, fetal MR imaging presents unique challenges for interpretation and measuring capabilities, such as fetal motion, low resolution, and artifacts due to maternal tissue. Some studies have tried to overcome these difficulties by measuring the volume manually.^{5,6} This method is very time-consuming and interpreter-dependent. Other studies have presented newly developed automatic algorithms to correct the artifacts and align the images affected by fetal motion. However, these methods are costly, not widely applicable, and may require changes in the routine fetal MR imaging protocol.^{2,7-11}


In this study, we introduce a new, Matlab-based (MathWorks, Natick, Massachusetts) semiautomated method for measuring the volume of structures in the fetal brain. We measured 6 structures with this method in a relatively large group and calculated 4 volume ratios. We validated this method by measuring a small control group manually and comparing the results with the measurements of the same group obtained with the new method and assessed its interobserver reliability.


Received March 19, 2017; accepted after revision June 12.

From the Departments of Obstetrics and Gynecology (R.B., D.H., A.P., E.K.) and Diagnostic Imaging (C.H., A.M.), Chaim Sheba Medical Center, Tel Hashomer, affiliated with the Sackler Faculty of Medicine, Tel-Aviv University, Tel-Aviv, Israel; and Sackler Faculty of Medicine (C.H., E.D.), Tel-Aviv University, Tel-Aviv, Israel.

R. Ber and D. Hoffman contributed equally to this work.

Please address correspondence to Roee Ber, BSc, Department of Obstetrics and Gynecology, Chaim Sheba Medical Center, Tel Hashomer, Israel; e-mail: berlerner@gmail.com

 Indicates article with supplemental on-line tables.

 Indicates article with supplemental on-line photos.

<http://dx.doi.org/10.3174/ajnr.A5349>

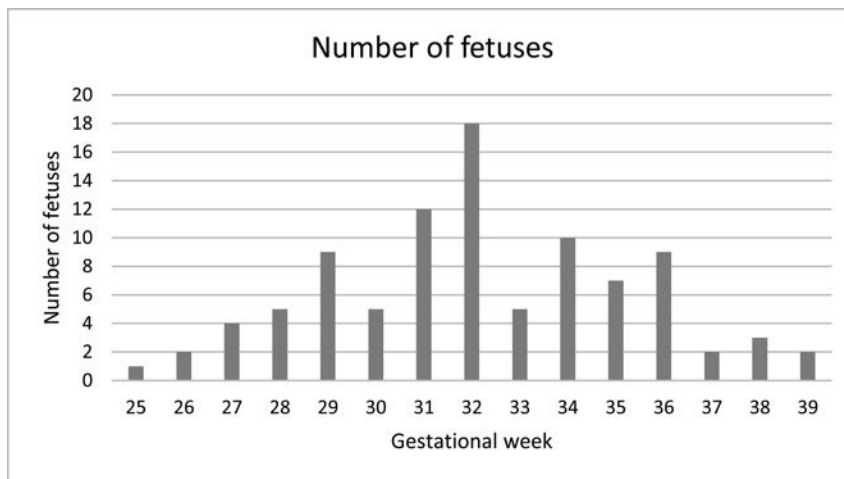


FIG 1. Distribution of the fetuses measured by gestational week.

MATERIALS AND METHODS

Subjects

This is a retrospective review of 94 fetal MR imaging examinations performed in the Chaim Sheba Medical Center between 2011 and 2014. Indications for MR imaging examinations included suspected pathologic findings on ultrasonographic evaluation, extracranial pathologic findings, maternal cytomegalovirus infection, and a family member with an intracranial pathology.

The inclusion criteria were no pathologic findings according to the neuroradiologist's evaluation and normal 2D biometric measurements according to previously reported biometric studies.^{12,13} The distribution of gestational age is presented in Fig 1.

MR Imaging

This study was based on the routine fetal MR imaging procedure performed in our institution. No sedation was used during MR imaging examinations. Fetal brain MR imaging was performed with a 1.5T system (Optima scanner; GE Healthcare, Milwaukee, Wisconsin). Single-shot fast spin-echo T2-weighted sequences in 3 orthogonal planes were performed with the half-Fourier technique (NEX = 0.53) with the following parameters: section thickness of 3 or 4 mm, no gap, flexible coil (8-channel cardiac coil). The FOV was determined by the size of the fetal head with a range of 24 × 24 cm to 30 × 30 cm. Acquisition time was between 40 and 45 seconds; matrix, 320/224; TE, 90 ms; TR, 1298 ms; pixel bandwidth, 122 Hz/pixel. Specific absorption rate values were between 1.1 and 1.7 W/kg.¹⁴

Measurements

We measured 6 structures in 94 fetal brain MR imaging examinations with the semiautomated method. For comparison between manual and semiautomated measurements, we used data of manual measurements of the supratentorial brain volume (STV) previously reported by Polat et al.¹⁴ The coronal plane sequence was used for measurements in both methods. Delineation was made by a semiautomated algorithm or drawn manually. In both methods, the ROI traced created an area that was then multiplied by the section thickness to produce the volume. ROI volumes from successive sections were then summed to yield the full volume of the

desired region. The measuring time was collected for each fetus measured.

The boundaries of the structures measured were defined as follows:

Supratentorial brain volume: the parenchyma of the frontal, parietal, occipital, and temporal lobes, including the third ventricle and excluding the lateral ventricles (measured separately by the semiautomated method and subtracted), the brain stem, the cerebellum, and the fourth ventricle. Anterior, posterior, superior, and lateral boundaries were defined as the outer edge of the cerebral cortex. The inferior border matched the cortex and an imaginary line crossing the brain stem between the edges of the tentorium cerebelli. The left and right hemisphere volumes (LHV

and RHV) were measured separately with the same lateral boundaries with the interhemispheric fissure as a medial boundary.

Cerebellar volume (CV): cerebellar hemispheres were drawn with the cerebellar peduncles and vermis. The brain stem and the fourth ventricle were excluded. A single-section representative image of STV and CV is presented in Fig 2A.

Left and right eyeball volumes (LEBV, REBV): the eyeball was defined as the vitreous body and the lens, excluding the optic nerve. A representative section image of LEBV and REBV is presented in Fig 2B.

We calculated 4 volume ratios: the ratio between right and left hemispheres (RHV/LHV ratio), right and left eyeballs (REBV/LEBV ratio), cerebellum and supratentorial brain (CV/STV ratio), and the 2 eyeballs and the supratentorial brain (total eyeball volume [EBV]/STV).

Manual Measurements

Images were first transformed from DICOM to TIFF format and analyzed with ImageJ software (National Institutes of Health, Bethesda, Maryland). Delineation was drawn manually through cursor-guided freehand traces on individual images in the coronal plane.

Semiautomated Measurement Algorithm

The semiautomated algorithm was implemented in the Matlab computing environment. The 3D segmentation is achieved by a set of N 2D semiautomated segmentations performed on consecutive coronal sections. The 3 main processing steps are the following:

3D Preprocessing. The brain is cropped interactively by a cuboidal box, and bias-correction is performed to compensate for MR imaging radiofrequency-field inhomogeneity.¹⁵ Eventually, an anisotropic diffusion filter (PeronaMalikFilter; <http://reference.wolfram.com/language/ref/PeronaMalikFilter.html>) is applied to each section for edge-preserving smoothing.¹⁶

Midcoronal Section Processing. An initial closed contour is manually drawn inside the brain parenchyma of the midcoronal sec-

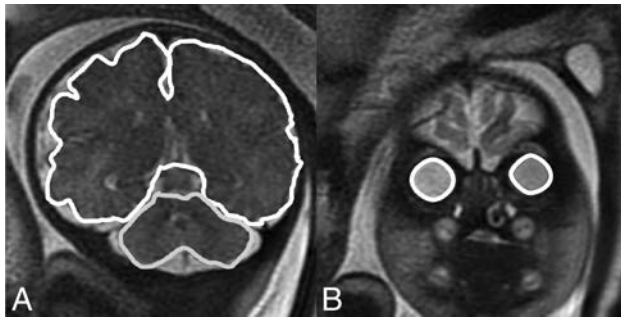


FIG 2. Representative sections of structure boundaries. A, STV and CV. B, REBV and LEBV.

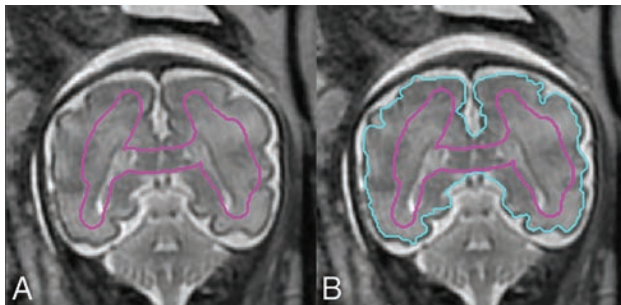


FIG 3. A, The initial contour C_{init} drawn manually on the midcoronal section. B, Contour C_{conv} automatically propagated by a level set-based active contour algorithm.

tion, S_{mid} (Fig 3A). The initial contour, $C_{init}(S_{mid})$, is automatically propagated by a level set-based active contour algorithm until convergence into contour $C_{conv}(S_{mid})$ (Fig 3B).¹⁷ Note that C_{init} does not have to be similar in shape to the targeted brain contour but should contain representative pixels for all the tissues and intensity ranges present in the brain parenchyma, including CSF if present in the considered section.

Forward and Backward Propagation. $C_{conv}(S_{mid})$ is used as an initial contour for the level set in the preceding and successive sections, S_{mid-1} and S_{mid+1} , respectively. The procedure is repeated recursively, with $C_{conv}(S_{mid})$ and $C_{conv}(S_{mid+i})$ serving as the initial contour for S_{mid-1} and S_{mid+i} until the first and last sections of the scan are reached. The propagated contours are downsized from section to section by a fixed quantity determined by the user, to account for the progressive reduction in coronal cross-sections of the brain when departing from the midcoronal section.

Eventually, the resulting set of 2D segmentation contours, $C_{conv}(S_i)$, $i = 1 \dots N$, may be interactively adjusted by dragging contour points in the Matlab GUI (<https://www.mathworks.com/discovery/matlab-gui.html>) with the mouse. The volume is computed as the total number of voxels enclosed by the segmentation contours multiplied by the voxel physical size. Screenshots of the Matlab software GUI are presented in On-line Fig 1.

Statistical Analysis

Statistical analysis was based on a previous study by Ber et al.¹² Analysis was performed by using R statistical and computing software, Version 3.3.1 (<http://www.r-project.org/>). The reference intervals were estimated by using the Generalized Additive Models

for Location, Scale, and Shape model¹⁸ as the World Health Organization suggested method.¹⁹ In our study, the model for centile q at gestational age t is the following: $c_q = \mu_t + \sigma_t Z_q$, where μ_t and σ_t are the mean and SD at age t , measured in days, and Z_q is the q centile of the standard normal distribution. The functions μ_t and σ_t were estimated and smoothed by using the Rigby and Stasinopoulos algorithm¹⁸ with a cubic spline smoothing. The normality assumption was slightly inadequate, but the resulting curves were almost identical to those achieved by assuming the Box-Cox t distribution (with 4 parameters) recommended.¹⁹ In addition, we found the skewness and kurtosis parameters of the Box-Cox t distribution to be nonsignificant for all response variables; this finding supports our decision to simply use the normal distribution without any transformation.

For the ratio variables, we examined the hypothesis $\mu_t = \mu$ to assess the independence of the ratios with the gestational age. The hypothesis was tested with the Generalized Additive Models for Location, Scale, and Shape model. If the ratio was independent of gestational age ($P > .05$), we calculated its mean and SD. If the ratio was dependent on gestational age ($P < .05$), we applied the same analysis used for the structures measured.

The intraclass correlation coefficient (ICC) and limits of agreement were used to study the reliability of measurements across measurers, and 20 subjects were measured by 2 measurers for this purpose. Results were defined as poor for $ICC < 0.6$, satisfactory for $0.6 < ICC < 0.8$, good for $0.8 < ICC < 0.9$, and excellent for $ICC > 0.9$.

For comparing the manual and semiautomated methods, we calculated the maximum relative difference $\left(2 \times \frac{A - M}{A + M}\right) \times 100\%$, where A and M represent the semiautomated and manual absolute measurements, respectively. This analysis was performed by using SPSS, Version 23 (IBM, Armonk, New York).

Ethics Approval

The research was approved by the hospital research ethics board.

RESULTS

Normal curves of STV, RHV, LHV, CV, REBV, and LEBV are presented in Fig 4. Normal percentile reference data for each structure measured by gestational age are presented in On-line Tables 1–6.

The ratio variables RHV/LHV and REBV/LEBV are independent of gestational age ($P = .20$ and $P = .07$, respectively), and their mean value and SD are 1.00 ± 0.04 and 1.01 ± 0.09 , respectively. The ratio variables CV/STV and EBV/STV are dependent on gestational age ($P < 10^{-10}$ for both). Their normal curves are presented in Fig 5, and their normal percentile reference data are presented in On-line Tables 7 and 8.

Measurement results of STV in 19 randomly selected fetuses obtained from the semiautomated and manual methods are presented in a Bland-Altman plot with 95% limits of agreement in On-line Fig 2. The mean difference between the semiautomated and manual methods was $2.11 \pm 9.03 \text{ cm}^3$; 95% limits of agreement, $16.87\text{--}21.09 \text{ cm}^3$; and the maximum relative difference between the 2 methods, 7.84% of the mean. The average measuring

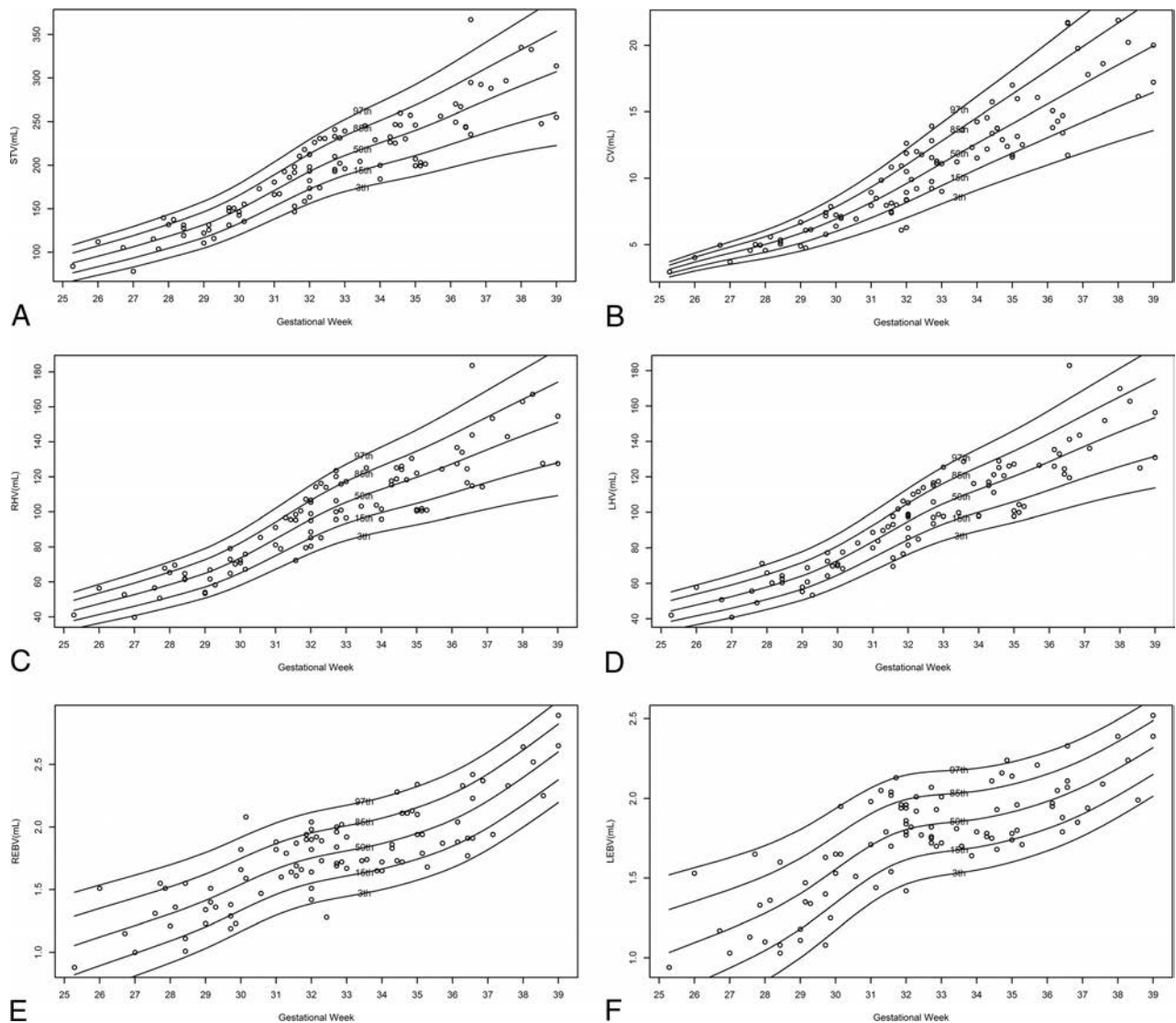


FIG 4. Normal volumetric curves of measured structures according to gestational age. A, STV. B, CV. C, RHV. D, LHV. E, REBV. F, LEBV.

times of STV with the semiautomated and the manual methods were 9.2 ± 1.1 and 22.4 ± 2.1 minutes, respectively.

The interobserver agreement per structure between the 2 measurers is presented in the Table.

DISCUSSION

Fetal volumetry might be the next step in prenatal diagnosis and evaluation of brain pathologies, as it is in pediatric and adult neurologic evaluations. Therefore, it is widely investigated, and many groups are trying to develop an accurate yet practical way to overcome the unique challenges that fetal MR imaging presents. During the past decade, attempts have been made to develop an automated volumetric measurement method that will eliminate user dependence and time consumption presented by manual volumetric measurements. The 2 most challenging obstacles of the automated prenatal volumetric evaluation are the intersection motion of the fetus and the isolation of fetal from maternal tissue. Some studies have introduced new methods to overcome these challenges and developed algorithms for isolation of fetal from maternal tissue and for motion correction. These methods have

promise for future use, but they are either computationally complicated^{7,20} or require a change in the standard prenatal MR imaging protocol¹¹ and, therefore, may be clinically inapplicable for the time being and should be validated.

The new semiautomated method presented in this study is a combination of the simplicity of the manual method and the efficiency of the automated method. This method is not perfect and is rather a compromise: It is still relatively user-dependent; the more the fetus moves during the examination, the more manual corrections need to be performed; therefore, the method may still be time-consuming. However, it is suitable for any kind of protocol used for the examination, can be applied retrospectively, and is fast and easily applicable for most prenatal MR imaging examinations. It is a simple Matlab-based algorithm that can also be adjusted and changed according to the user requirements.

We used the new method to measure 6 structure volumes and 4 ratios and presented the results as normal growth curves and percentile reference data. The previously reported structures measured were STV and CV. Hatab et al²¹ measured CV manually and reported it to be 2.8–5.0 mL at the 28th gestational week,

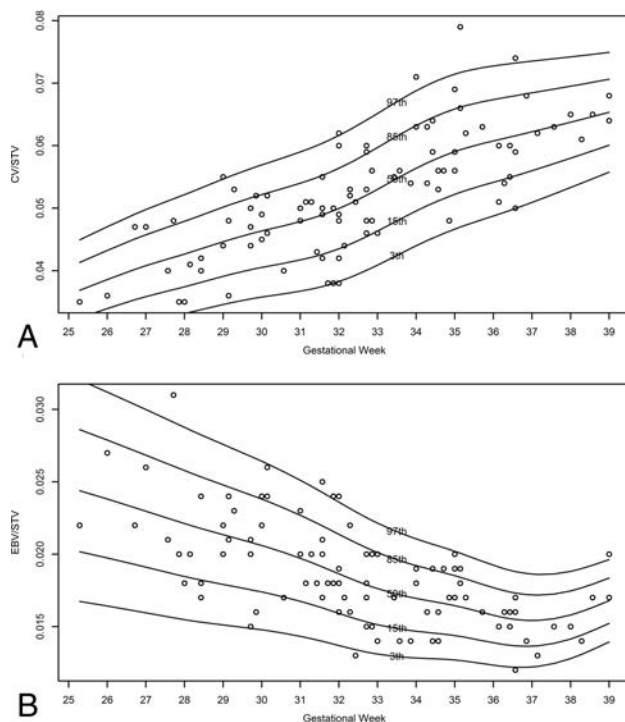


FIG 5. Normal curves of the ratio variable according to gestational age. A, CV/STV ratio. B, EBV/STV ratio.

Intraclass correlation coefficient between 2 observers per structure measured

Structure Measured	ICC	95% Confidence Interval
STV	0.995	(0.987–0.998)
LHV	0.990	(0.974–0.996)
RHV	0.985	(0.920–0.995)
CV	0.977	(0.944–0.991)
REBV	0.946	(0.871–0.978)
LEBV	0.886	(0.735–0.954)

4.6–7.9 mL at the 32nd gestational week, and 6.6–11 mL at the 36th gestational week. This report is consistently smaller than the volumes measured by the new semiautomated method for which we report a CV of 3.9–6 mL at the 28th gestational week, 7.0–12.1 mL at the 32nd gestational week, and 11.0–20.1 mL at the 36th gestational week. However, our results are closer to the results of Clouchoux et al,¹¹ who reported a mean CV of 5.5 mL at the 28th gestational week, 11 mL at the 32nd gestational week, and 16 mL at the 36th gestational week. Mean STVs reported by Clouchoux et al were 135, 190, and 250 mL at the 28th, 32nd, and 36th gestational weeks, respectively, which are like our measurements of 118, 192, and 256 mL at the same gestational weeks, respectively.

In addition to previously reported volumetric measurements of CV and STV, we used the new method to measure smaller and clinically relevant structures such as EBV and presented their reference data. Microphthalmia can be an important marker for congenital infections such as rubella²² and for several rare congenital pathologies, such as congenital glaucoma and persistent hyperplastic primary vitreous.²³ These are sometimes difficult to detect prenatally and require an experienced investigator. A few studies have addressed the issue of eyeball biometry either in ultrasound or in 2D MR imaging.^{24,25} We measured the eyeball

volumes, presented their growth curves according to gestational age, and supplied normal reference data. We also presented the ratio between EBV and STV with gestational age and showed that the EBV change rate is slower than the STV change rate. This information may become an important tool when assessing a suspected rubella infection during the second or third trimester, for example.

In their recent publication, Kasprian et al²⁶ have addressed the issue of fetal brain asymmetry and reported significant asymmetric morphologic and biometric properties, some of them with lateralization patterns. In our study, we confirm the above findings that some volumetric asymmetry exists between the right and left hemispheres and right and left eyeballs. However, we have found no lateralization patterns. The SDs of the right and left ratios presented in the “Results” section may be of clinical significance when evaluating nonstandard volumetric asymmetry.

To systematically validate the method, we compared 19 fetal STVs measured manually with the same volumes measured by the semiautomated method. The relative difference revealed a maximum <8% discrepancy between the volumes measured by the 2 methods. The reproducibility of the new semiautomated method represented by the interobserver agreement was good or excellent for all structures measured, with an interclass correlation coefficient ranging between 0.88 and 0.99. However, for smaller structures, such as LEBV and REBV, the agreement was worse than for larger structures. This finding might be explained by the effect of section thickness on measurements of smaller structures and is a limitation of the new method. We demonstrated another benefit generated by our method, by comparing the time needed for measuring STV by both methods and found that using the new method took less than half the time of measuring it manually.

The semiautomated method we developed makes fetal volumetry accessible for both prospective and retrospective use. On the basis of our experience with this method, we can guardedly say that other structures in the brain can be measured relatively easily and quickly, even in small structures such as EBV. However, there are some limitations to this method. The software requires practice to understand the initial contour S_{init} that gives the best result for each structure. The practice time required is short, and adequate experience is gained within a few measurements of each structure. In addition, as previously mentioned, because the structure measured is smaller, it is more prone to dependence on section thickness, affecting the accuracy and reproducibility of the measurement. Nevertheless, we believe that this method can be easily applied on intracranial structures and perhaps on extracranial structures as well, such as the heart, kidneys, and placenta. It might also be used on large pathologic lesions such as cysts, tumors, and any lesion not isointense on MR imaging.

CONCLUSIONS

We present a new semiautomated method to measure the volume of structures in the fetal brain on MR imaging. This method is technologically simple, easy to learn, and reproducible and can be applied prospectively and retrospectively on any MR imaging protocol. We provide normal growth curves and volumetric reference data measured by this method in a relatively large cohort. We believe that by applying it on different cranial and extracranial

structures, anatomic and pathologic, fetal volumetry can evolve from a research tool to a practical clinical tool.

REFERENCES

- de Flores R, La Joie R, Landeau B, et al. **Effects of age and Alzheimer's disease on hippocampal subfields: comparison between manual and FreeSurfer volumetry.** *Hum Brain Mapp* 2015;36:463–74 [CrossRef Medline](#)
- Jain S, Sima DM, Ribbens A, et al. **Automatic segmentation and volumetry of multiple sclerosis brain lesions from MR images.** *Neuroimage Clin* 2015;8:367–75 [CrossRef Medline](#)
- Shin H, Lee DK, Lee JM, et al. **Atrophy of the cerebellar vermis in essential tremor: segmental volumetric MRI analysis.** *Cerebellum* 2016;15:174–81 [CrossRef Medline](#)
- Farid N, Girard HM, Kemmotsu N, et al. **Temporal lobe epilepsy: quantitative MR volumetry in detection of hippocampal atrophy.** *Radiology* 2012;264:542–50 [CrossRef Medline](#)
- Hoffmann C, Grossman R, Bokov I, et al. **Effect of cytomegalovirus infection on temporal lobe development in utero: quantitative MRI studies.** *Eur Neuropsychopharmacol* 2010;20:848–54 [CrossRef Medline](#)
- Damodaram MS, Story L, Eixarch E, et al. **Foetal volumetry using magnetic resonance imaging in intrauterine growth restriction.** *Early Hum Dev* 2012;88(suppl 1):S35–40 [CrossRef Medline](#)
- Scott JA, Habas PA, Kim K, et al. **Growth trajectories of the human fetal brain tissues estimated from 3D reconstructed in utero MRI.** *Int J Dev Neurosci* 2011;29:529–36 [CrossRef Medline](#)
- Gholipour A, Estroff JA, Barnewolt CE, et al. **Fetal brain volumetry through MRI volumetric reconstruction and segmentation.** *Int J Comput Assist Radiol Surg* 2011;6:329–39 [CrossRef Medline](#)
- Grossman R, Hoffman C, Mardor Y, et al. **Quantitative MRI measurements of human fetal brain development in utero.** *Neuroimage* 2006;33:463–70 [CrossRef Medline](#)
- Pier DB, Levine D, Kataoka ML, et al. **Magnetic resonance volumetric assessments of brains in fetuses with ventriculomegaly correlated to outcomes.** *J Ultrasound Med* 2011;30:595–603 [CrossRef Medline](#)
- Clouchoux C, Guizard N, Evans AC, et al. **Normative fetal brain growth by quantitative in vivo magnetic resonance imaging.** *Am J Obstet Gynecol* 2012;206:173.e1–8 [CrossRef Medline](#)
- Ber R, Bar-Yosef O, Hoffmann C, et al. **Normal fetal posterior fossa in MR imaging: new biometric data and possible clinical significance.** *AJNR Am J Neuroradiol* 2015;36:795–802 [CrossRef Medline](#)
- Ginath S, Lerman-Sagie T, Haratz Kraiden K, et al. **The fetal vermis, pons and brainstem: normal longitudinal development as shown by dedicated neurosonography.** *J Matern Fetal Neonatal Med* 2013;26:757–62 [CrossRef Medline](#)
- Polat A, Barlow S, Ber R, et al. **Volumetric MRI study of the intra-uterine growth restriction fetal brain.** *Eur Radiol* 2017;27:2110–18 [CrossRef Medline](#)
- Ashburner J, Friston KJ. **Unified segmentation.** *Neuroimage* 2005;26:839–51 [CrossRef Medline](#)
- Perona P, Malik J. **Scale-space and edge detection using anisotropic diffusion.** *IEEE Trans Pattern Anal Mach Intell* 1990;12:629–39 [CrossRef](#)
- Li C, Xu C, Gui C, et al. **Distance regularized level set evolution and its application to image segmentation.** *IEEE Trans Image Process* 2010;19:3243–54 [CrossRef Medline](#)
- Rigby RA, Stasinopoulos DM. **Automatic smoothing parameter selection in GAMLSS with an application to centile estimation.** *Stat Methods Med Res* 2014;23:318–32 [CrossRef Medline](#)
- Borghi E, de Onis M, Garza C, et al; WHO Multicentre Growth Reference Study Group. **Construction of the World Health Organization child growth standards: selection of methods for attained growth curves.** *Stat Med* 2006;25:247–65 [CrossRef Medline](#)
- Keraudren K, Kuklisova-Murgasova M, Kyriakopoulou V, et al. **Automated fetal brain segmentation from 2D MRI slices for motion correction.** *Neuroimage* 2014;101:633–43 [CrossRef Medline](#)
- Hatab MR, Kamourieh SW, Twickler DM. **MR volume of the fetal cerebellum in relation to growth.** *J Magn Reson Imaging* 2008;27:8404–05 [CrossRef Medline](#)
- Merdassi A, Limaïem R, Turki F, et al. **Ophthalmologic manifestations of congenital rubella [in French].** *Arch Pediatr* 2011;18:870–73 [CrossRef Medline](#)
- Esmer AC, Sivriköz TS, Gulec EY, et al. **Prenatal diagnosis of persistent hyperplastic primary vitreous: report of 2 cases and review of the literature.** *J Ultrasound Med* 2016;35:2285–91 [CrossRef Medline](#)
- Bojikian KD, de Moura CR, Tavares IM, et al. **Fetal ocular measurements by three-dimensional ultrasound.** *J AAPOS* 2013;17:276–81 [CrossRef Medline](#)
- Paquette LB, Jackson HA, Tavaré CJ, et al. **In utero eye development documented by fetal MR imaging.** *AJNR Am J Neuroradiol* 2009;30:1787–91 [CrossRef Medline](#)
- Kasprian G, Langs G, Brugger PC, et al. **The prenatal origin of hemispheric asymmetry: an in utero neuroimaging study.** *Cereb Cortex* 2011;21:1076–83 [CrossRef Medline](#)

Transient Focal Neurologic Symptoms Correspond to Regional Cerebral Hypoperfusion by MRI: A Stroke Mimic in Children

 L.L. Lehman,  A.R. Danehy,  C.C. Trenor III,  C.F. Calahan,  M.E. Bernson-Leung,  R.L. Robertson, and  M.J. Rivkin

ABSTRACT

SUMMARY: Children who present with acute transient focal neurologic symptoms raise concern for stroke or transient ischemic attack. We present a series of 16 children who presented with transient focal neurologic symptoms that raised concern for acute stroke but who had no evidence of infarction and had unilateral, potentially reversible imaging features on vascular and perfusion-sensitive brain MR imaging. Patients were examined with routine brain MR imaging, MRA, perfusion-sensitive sequences, and DWI. Fourteen (88%) children had lateralized MRA evidence of arterial tree pruning without occlusion, all had negative DWI findings, and all showed evidence of hemispheric hypoperfusion by susceptibility-weighted imaging or arterial spin-labeling perfusion imaging at presentation. These findings normalized following resolution of symptoms in all children who had follow-up imaging (6/16, 38%). The use of MR imaging with perfusion-sensitive sequences, DWI, and MRA can help to rapidly distinguish children with conditions mimicking stroke from those with acute stroke.

Children who present with sudden onset of focal neurologic symptoms raise concern for acute stroke and transient ischemic attack. Yet certain conditions, such as complex migraine, postictal hemiparesis, or conversion disorder, can imitate acute stroke and are considered “stroke mimics.” Patients with stroke mimics present with an acute onset of focal neurologic symptoms but, on further evaluation, do not have an infarction or hemorrhage. Rapid differentiation of a stroke mimic from a cerebrovascular emergency constitutes a critically important diagnostic step before the initiation of time-dependent treatment such as thrombolysis or thrombectomy. Neuroimaging and MR imaging, in particular, provide essential information in the diagnosis of stroke.^{1–3} Diffusion imaging documents irreversible tissue infarction.¹ Arterial spin-labeling and susceptibility-weighted imaging provide information on regional differences in brain perfusion, which can include the core infarct but also encompass tissue beyond it that is hypoperfused but not yet irreversibly infarcted.^{2,4} MRA, which is based on flow-related enhancement, is used for documentation of vascular attenuation or obstruction consistent with both a patient’s clinical symptoms and core infarct location.³

We report a case series of 16 children with transient neurologic symptoms who had unilateral cerebral hypoperfusion and lateralized vascular pruning without associated diffusion abnormalities by MR imaging. The resolution of neurologic symptoms without stroke-specific intervention and the normalization of the initial MR imaging features in patients with follow-up imaging confirm this clinicoradiologic entity as a stroke mimic. Recognition of these imaging patterns may help distinguish true stroke requiring urgent intervention from a stroke mimic condition in children presenting acutely with focal neurologic symptoms.⁵

CASE SERIES

Cases were collected retrospectively as part of a larger, institutional review board–approved review of children with transient neurologic symptoms presenting to a free-standing children’s hospital. A total of 16 children met both the clinical criteria of transient focal neurologic symptoms and the imaging criteria of focal hypoperfusion and/or focal vascular pruning. We collected clinical information on each of the children, including symptoms at presentation, time from presentation to imaging, headache at presentation, and history of migraines. All clinical information was reviewed by a pediatric neurologist.

Clinical Features

Our cohort of 16 children included 6 females (38%). The children ranged from 2 to 16 years of age. Among the 16 children, 13 (81%) had headache at presentation. Only 6 (38%) had a previous diagnosis of migraine (Table 1). Most patients (94%) did not meet the International Classification of Headache Disorders criteria for

Received January 30, 2017; accepted after revision May 9.

From the Stroke and Cerebrovascular Center (L.L.L., A.R.D., C.C.T., C.F.C., M.E.B.-L., M.J.R.), Departments of Neurology (L.L.L., C.F.C., M.E.B.-L., M.J.R.), Psychiatry (M.J.R.), Radiology (A.R.D., R.L.R., M.J.R.), and Division of Hematology/Oncology (C.C.T.), Boston Children’s Hospital, Harvard Medical School, Boston, Massachusetts.

R.L. Robertson and M.J. Rivkin are co-senior authors.

Please address correspondence to Richard Robertson, MD, Boston Children’s Hospital, 300 Longwood Ave, Main 2, Boston, MA 02115; e-mail: richard.robertson@childrens.harvard.edu

<http://dx.doi.org/10.3174/ajnr.A5296>

Table 1: Clinical details of the presentation of the children

Patient No.	Age (yr)	Sex	Headache	History of Migraine Headache	Time from Presentation to Imaging	Clinical Symptoms
1	15	Female	Yes	Yes	4.5 hr	Right face and arm weakness, hypoesthesia, hemianopia, aphasia
2	13	Male	Yes	No	5.5 hr	Left face and hand paresthesia
3	16	Female	Yes	No	6.75 hr	Left hand and foot paresthesia and weakness
4	14	Male	Yes	Yes	4.5 hr	Aphasia, right hemianopia
5	2	Male	No	No	<12 hr	Right hemiparesis and hemianopia
6	12	Female	Yes	Yes	6 hr	Aphasia
7	13	Male	Yes	No	4.25 hr	Aphasia and right face and arm weakness
8	8	Male	Yes	No	11 hr	Aphasia, bilateral blurry vision, left hand paresthesia
9	10	Male	Yes	No	6 hr	Right hand paresthesia, confusion
10	11	Female	No	Yes	<1 hr	Right hand paresthesia
11	5	Male	No	No	4 hr	Right hemiparesis, dysarthria, and confusion
12	13	Female	Yes	No	7.5 hr	Left hand weakness and paresthesia, aphasia
13	8	Male	Yes	Yes	16.25 hr	Left facial weakness, hemiparesis
14	15	Male	Yes	Yes	10.5 hr	Aphasia
15	10	Male	Yes	No	8.5 hr	Aphasia and blurry vision
16	4	Female	Yes	No	<16 hr	Left facial weakness, dysarthria

hemiplegic migraine.⁶ All patients had complete resolution or marked improvement in symptoms by 24 hours after symptom onset. Only 6 (38%) had recurrence of transient neurologic symptoms since the initial presentation; none had stroke at the time of presentation or at follow-up. We had a median follow-up of 0.7 years with a range of 1 day to 3.4 years.

Imaging Approach and Features

MR imaging was performed at a median of 6.4 hours, with all patients imaged within 16.5 hours of presentation. All examinations were performed on a 3T Magnetom Skyra or Trio imaging system (Siemens, Erlangen, Germany) with a 32- or 64-channel head coil. All patients were examined with the standard institutional brain imaging sequences, including the following: sagittal T1 MPRAGE (TR = 1520–2530 ms, TE = 1.63–3.39 ms, section thickness = 0.90–1 mm, echo-train length = 1, matrix = 220–256/220–256, one or 4 excitations); axial fast spin-echo T2 (TR = 4400–14,143 ms, TE = 89–100 ms, section thickness = 2.5 mm, echo-train length = 13–19, matrix = 269–359/512, two-to-three excitations); axial T2 FLAIR (TR = 6800–9000 ms, TE = 135–137 ms, section thickness = 4 mm, echo-train length = 13–16, matrix = 250–320/320, one-to-two excitations); diffusion tensor imaging with 30 or 35 directions, $b=1000$ s/mm² (TR = 5300–13,800 ms, TE = 88–92 ms, section thickness = 2–4 mm, echo-train length = 1, 48, or 51, matrix = 128/128, one excitation); and 3D time-of-flight angiography (TR = 21–22 ms, TE = 3.43–3.88 ms, section thickness = 0.60–0.80 mm, echo-train length = 1, matrix = 230–344/384–512, one excitation). Perfusion-sensitive sequences, including perfusion-weighted pulsed arterial spin-labeling ($n = 11$ patients: TR = 2500–5000 ms, TE = 11–35 ms, section thickness = 3–5 mm, echo-train length = 1–51, matrix = 64–96/64–84, one-to-sixty excitations, TI = 700 ms); velocity-selective arterial spin-labeling ($n = 2$ patients: TR = 3000 ms, TE = 13 ms, section thickness = 5 mm, matrix = 64/64, one excitation, TI₁ = 700 ms, TI_{1,stop} = 1400 ms, and TI₂ = 2000 ms [to the center section]); and axial susceptibility-weighted imaging ($n = 16$ patients: TR = 28 ms, TE = 20 ms, section thickness = 1.25 mm, echo-train length = 1, matrix = 184–336/256–384, one excitation) were also performed.

Images were independently reviewed by 2 pediatric neuroradiologists. The final interpretation was reached by consensus in cases of disagreement between the reviewers. Each MR imaging examination was evaluated for the following imaging abnormalities: linear sulcal signal abnormality on FLAIR imaging, subcortical hypointensity on T2-weighted imaging, localized brain parenchymal signal or diffusion abnormalities, gyral swelling, venous prominence on susceptibility-weighted imaging, perfusion abnormality on arterial spin-labeling, abnormal leptomeningeal and parenchymal enhancement following the administration of intravenous contrast, and evidence of increased/decreased flow-related enhancement or vessel stenosis on 3D TOF MR angiography. Imaging abnormalities were further characterized according to vascular distribution for MRA and lobes of the brain involved in SWI and arterial spin-labeling.

DWI revealed no areas of decreased diffusivity in any patient. None had evidence of gyral swelling. Linear sulcal signal abnormality in the hemodynamically affected region was seen on FLAIR imaging in 2 patients (2/16, 13%). One patient had subcortical hypointensity on T2-weighted imaging (1/16, 6%). All 16 patients had unilateral increased prominence of the cortical or medullary veins in ≥ 1 cerebral lobe on SWI, suggesting elevated venous deoxyhemoglobin, indicative of hypoperfusion. Of the 11 patients evaluated with arterial spin-labeling, decreased perfusion to ≥ 1 lobe of the brain was evident in all. Diminished flow-related enhancement due to decreased hemispheric flow in at least 1 branch vessel of the circle of Willis was evident in 14 patients (14/16, 88%). Multivessel unilateral vascular pruning was present in 9 patients. None of the patients demonstrated hemodynamic change in the posterior fossa structures. Arterial beading on MRA was not demonstrated in any patient. Intravenous contrast was administered in 3 patients (3/16, 19%) with increased leptomeningeal prominence seen in the regions corresponding to those with arterial spin-labeling, SWI, and MRA changes in all 3. No parenchymal enhancement was observed in any of the 3 patients administered contrast. The Figure represents an example of the imaging findings observed in our cohort. Follow-up imaging was performed in 6 patients (6/16, 38%). Resolution of MR imaging changes, including normalization of arterial spin-labeling, SWI, and MRA findings, was observed in all 6 patients who had follow-up imaging (Table 2).

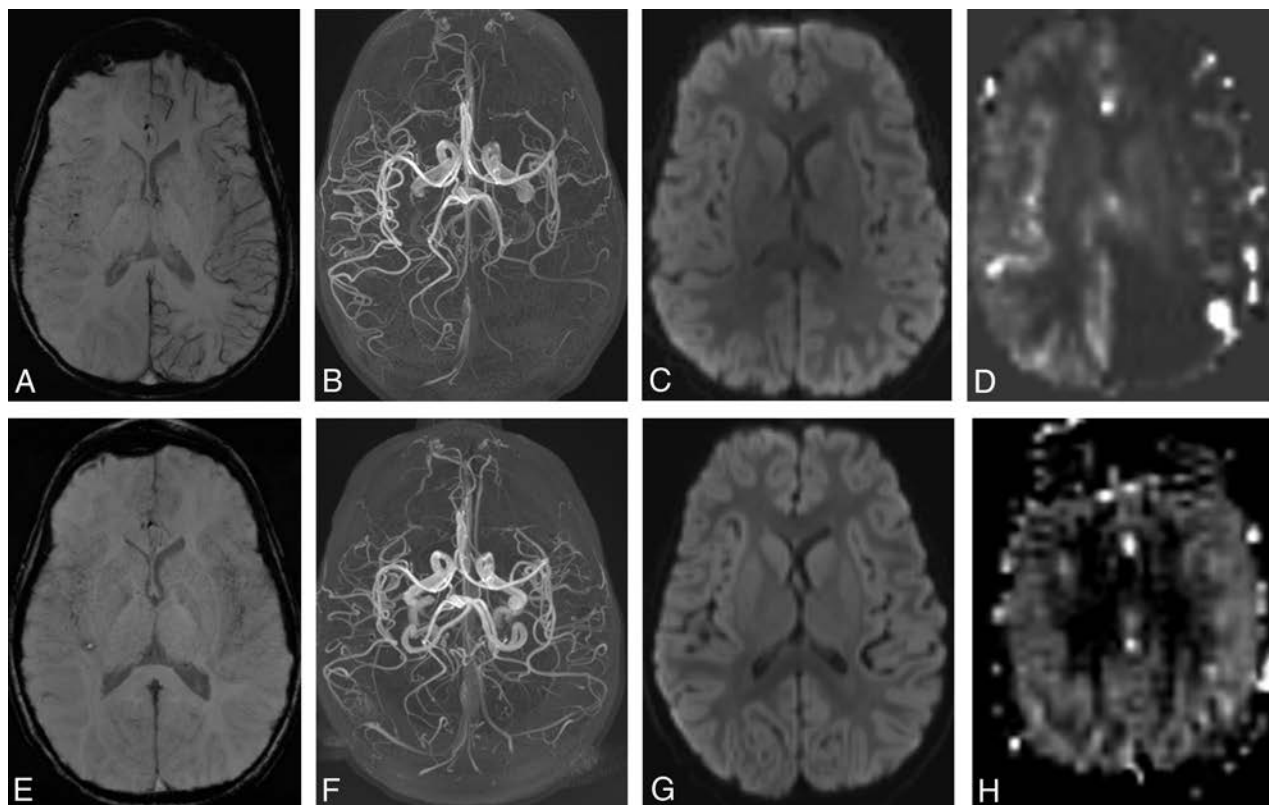


FIGURE. A 5-year-old boy presenting with right-sided weakness. Symptoms were improving at the time of the initial MR imaging performed 3 hours after presentation (A–D). A, Susceptibility-weighted imaging shows increased prominence of the cortical veins throughout the left cerebral hemisphere, indicating increased deoxyhemoglobin on the left. B, Collapsed maximum intensity projection from time-of-flight MR angiography shows reduced flow-related enhancement in the left anterior, middle, and posterior cerebral arteries. C, The average trace of the diffusion tensor image shows no abnormality of diffusion. D, Pulsed arterial spin-labeled perfusion-weighted imaging relative CBF map shows a marked decrease in perfusion throughout the left cerebral hemisphere. Follow-up imaging at 4 days after presentation (E–H). E, SWI shows resolution of venous asymmetry. F, MRA shows normal flow-related enhancement in the left anterior, middle, and posterior cerebral arteries. G, Findings of the average trace image continue to be negative. H, Pulsed arterial spin-labeled relative CBF map shows resolution of perfusion asymmetry.

Table 2: Radiology findings of children with ASL and SWI reported in lobes and MRA in vessels involved

Patient No.	Side	pASL (Decrease)	vASL (Decrease)	SWI (Increase)	MRA (Decrease)	Resolution
1	Left	P/T/O	ND	F/P/T/O	MCA/PCA	ND
2	Left	P/T	ND	P/T	MCA	Yes
3	Right	P	ND	P	MCA	ND
4	Left	P/T/O	ND	P/T/O	None	Yes
5	Left	F/P/T/O	ND	F/P/T/O	ACA/MCA/PCA	Yes
6	Left	F/P/T/O	Left F/P/O/T	F/P/T/O	ACA/MCA/PCA	ND
7	Left	F/T	ND	F/T	MCA	ND
8	Left	P/T	ND	P/T	None	ND
9	Left	F/P/T/O	ND	F/P/T/O	ACA/MCA	ND
10	Left	ND	ND	P/T/O	MCA/PCA	ND
11	Left	F/P/T/O	ND	F/P/T/O	ACA/MCA/PCA	Yes
12	Right	F/P/T/O	ND	F/P/T/O	ACA/MCA/PCA	Yes
13	Right	ND	Right P/O/T	P/T/O	MCA/PCA	Yes
14	Left	ND	ND	F/P/T/O	MCA/PCA	ND
15	Left	ND	ND	F/P	MCA	ND
16	Left	ND	ND	P/T/O	MCA	ND

Note:—pASL indicates pseudocontinuous arterial spin-labeling; vASL, velocity-selective arterial spin-labeling; ND, study not done; F, frontal; P, parietal; T, temporal; O, occipital; ACA, anterior cerebral artery; PCA, posterior cerebral artery.

DISCUSSION

We describe a cohort of children with a specific radiologic presentation that included negative diffusion-weighted imaging findings, evidence of lobar or hemispheric hypoperfusion by susceptibility-weighted imaging, and/or arterial spin-labeled perfusion

imaging associated with transient focal neurologic symptoms. MRA evidence of arterial pruning without occlusion was usually present. In all children who had repeat imaging, the vascular and perfusion findings had normalized and there was no evidence of infarction. Most children had headache at presentation, and only

one-third had recurrence of symptoms. Most interesting, only 1 of the children met the International Classification of Headache Disorders criteria for hemiplegic migraine.^{5,6}

The literature describing the neuroimaging findings in children with transient focal neurologic symptoms is limited. Imaging findings of focal hypoperfusion and vascular pruning have been reported previously in pediatric and adult patients with hemiplegic migraine (genetically proved or clinically diagnosed) in case reports and small case series.^{7–9} Perfusion findings have been reported and are temporally variable in children with acute onset of migraine with an aura. In a case-control study, 10 patients with migraine with an aura were acutely imaged with arterial spin-labeled perfusion imaging and found to have a change in perfusion compared with controls. The children had decreased perfusion if scanned <14 hours from the onset of symptoms, while evidence of increased perfusion was found if imaging was performed at >17 hours from symptom onset.¹⁰ In addition, Safier et al¹¹ reported a series of 8 children with hemiplegic migraine who demonstrated vascular narrowing by MRA. However, in their case series, only the middle cerebral artery was examined.¹¹ The study by Safier et al did not report on the other branch vessels of the circle of Willis. Consequently, it is not certain whether the vascular changes occurred in only the middle cerebral artery in their patients or if other vessels were similarly affected but not evaluated as part of the study. In our patient cohort, several branch vessels were usually affected.

Children who present with the acute onset of focal neurologic symptoms raise concern for stroke. Rapid neuroimaging of these children is extremely important, given the availability of treatment with thrombolysis or endovascular thrombectomy for acute stroke. DWI permits differentiation of a stroke from a stroke mimic.⁵ While negative DWI excludes an infarction requiring acute stroke therapy, the addition of perfusion-sensitive imaging in patients with diffusion-negative transient neurologic deficits can provide additional information regarding the etiology of the neurologic symptoms. Our findings indicate that a subset of children with symptoms mimicking acute stroke lack the anatomic or diagnostic diffusion-related changes of infarction but exhibit perfusion and flow-related vascular changes indicating reduced regional perfusion as a cause of symptoms. All children in our cohort with anatomic- and DWI-negative but perfusion-positive imaging findings demonstrated decreased rather than increased regional perfusion. The decreased perfusion findings in these children help to differentiate symptoms due to an ischemic cause from other conditions that may mimic stroke, such as a postictal state that typically shows increased regional blood flow.^{12–14}

We recognize limitations in our study. Our series is retrospective in nature and small in number. Furthermore, only a portion of the children we report had repeat imaging following resolution of symptoms. Finally, we have only limited outcome information.

CONCLUSIONS

The use of combined MR imaging to include perfusion-sensitive, diffusion-weighted, and angiographic imaging can help to rapidly distinguish children who present with stroke mimics whose symptoms are likely to be transient and who do not require stroke treatment from those with an acute stroke. In our series,






the imaging findings of unilateral, often multilobar, hypoperfusion and arterial vascular pruning without evidence of diffusion restriction in a child presenting with focal neurologic symptoms reflect a benign stroke mimic and confirm a vasoconstrictive basis for the patient's symptoms. Our observations support the routine use of perfusion-sensitive sequences as part of the neuroimaging evaluation of any child presenting with stroke or stroke-like symptoms.

Disclosures: Richard L. Robertson—UNRELATED: Other: GE Healthcare*. *Money paid to the institution.

REFERENCES

- Schellinger PD, Bryan RN, Caplan LR, et al; Therapeutics and Technology Assessment Subcommittee of the American Academy of Neurology. **Evidence-based guideline: the role of diffusion and perfusion MRI for the diagnosis of acute ischemic stroke—report of the Therapeutics and Technology Assessment Subcommittee of the American Academy of Neurology.** *Neurology* 2010;75:177–85 CrossRef Medline
- Haacke EM, Mittal S, Wu Z, et al. **Susceptibility-weighted imaging: technical aspects and clinical applications, part 1.** *AJNR Am J Neuroradiol* 2009;30:19–30 Medline
- Wintermark M, Sanelli PC, Albers GW, et al; American Society of Neuroradiology, American College of Radiology, Society of Neuro-Interventional Surgery. **Imaging recommendations for acute stroke and transient ischemic attack patients: a joint statement by the American Society of Neuroradiology, the American College of Radiology and the Society of NeuroInterventional Surgery.** *J Am Coll Radiol* 2013;10:828–32 CrossRef Medline
- Zaharchuk G, Olivot JM, Fischbein NJ, et al. **Arterial spin labeling imaging findings in transient ischemic attack patients: comparison with diffusion- and bolus perfusion-weighted imaging.** *Cerebrovasc Dis* 2012;34:221–28 CrossRef Medline
- Rivkin MJ, deVeber G, Ichord RN, et al. **Thrombolysis in pediatric stroke study.** *Stroke* 2015;46:880–85 CrossRef Medline
- Headache Classification Committee of the International Headache Society (IHS). **The International Classification of Headache Disorders, 3rd edition (beta version).** *Cephalalgia* 2013;33:629–808 CrossRef Medline
- Bosemani T, Burton VJ, Felling RJ, et al. **Pediatric hemiplegic migraine: role of multiple MRI techniques in evaluation of reversible hypoperfusion.** *Cephalalgia* 2014;34:311–15 CrossRef Medline
- Kim S, Kang M, Choi S. **A case report of sporadic hemiplegic migraine associated cerebral hypoperfusion: comparison of arterial spin labeling and dynamic susceptibility contrast perfusion MR imaging.** *Eur J Pediatr* 2016;175:295–98 CrossRef Medline
- Fedak EM, Zumberge NA, Heyer GL. **The diagnostic role for susceptibility-weighted MRI during sporadic hemiplegic migraine.** *Cephalalgia* 2013;33:1258–63 CrossRef Medline
- Boulouis G, Shotar E, Dangouloff-Ros V, et al. **Magnetic resonance imaging arterial-spin-labelling perfusion alterations in childhood migraine with atypical aura: a case-control study.** *Dev Med Child Neurol* 2016;58:965–69 CrossRef Medline
- Safier R, Cleves-Bayon C, Vaisleib I, et al. **Magnetic resonance angiography evidence of vasospasm in children with suspected acute hemiplegic migraine.** *J Child Neurol* 2014;29:789–92 CrossRef Medline
- Kim BS, Lee ST, Yun TJ, et al. **Capability of arterial spin labeling MR imaging in localizing seizure focus in clinical seizure activity.** *Eur J Radiol* 2016;85:1295–303 CrossRef Medline
- Matsuura K, Maeda M, Okamoto K, et al. **Usefulness of arterial spin-labeling images in periictal state diagnosis of epilepsy.** *J Neurol Sci* 2015;359:424–29 CrossRef Medline
- Verma RK, Abela E, Schindler K, et al. **Focal and generalized patterns of cerebral cortical veins due to non-convulsive status epilepticus or prolonged seizure episode after convulsive status epilepticus: A MRI study using susceptibility-weighted imaging.** *PLoS One* 2016;11:e0160495 CrossRef Medline

MR Neurography of Greater Occipital Nerve Neuropathy: Initial Experience in Patients with Migraine

 L. Hwang,  R. Dessouky,  Y. Xi,  B. Amirlak, and  A. Chhabra

ABSTRACT

BACKGROUND AND PURPOSE: MR imaging of peripheral nerves (MR neurography) allows improved assessment of nerve anatomy and pathology. The objective of this study was to evaluate patients with unilateral occipital neuralgia using MR neurography and to assess the differences in greater occipital nerve signal and size between the symptomatic and asymptomatic sides.

MATERIALS AND METHODS: In this case-control evaluation using MR neurography, bilateral greater occipital nerve caliber, signal intensity, signal-to-noise ratios, and contrast-to-noise ratios were determined by 2 observers.

RESULTS: Among 18 subjects with unilateral occipital migraines, the average greater occipital nerve diameter for the symptomatic side was significantly greater at 1.77 ± 0.4 mm than for the asymptomatic side at 1.29 ± 0.25 mm ($P = .001$). The difference in nerve signal intensity between the symptomatic and asymptomatic sides was statistically significant at 269.06 ± 170.93 and 222.44 ± 170.46 , respectively ($P = .043$). The signal-to-noise ratios on the symptomatic side were higher at 15.79 ± 4.59 compared with the asymptomatic nerve at 14.02 ± 5.23 ($P = .009$). Contrast-to-noise ratios were significantly higher on the symptomatic side than on the asymptomatic side at 2.57 ± 4.89 and -1.26 ± 5.02 , respectively ($P = .004$). Intraobserver performance was good to excellent (intraclass coefficient correlation, $0.68-0.93$), and interobserver performance was fair to excellent (intraclass coefficient correlation, $0.54-0.81$).

CONCLUSIONS: MR neurography can be reliably used for the diagnosis of greater occipital nerve neuropathy in patients with unilateral occipital migraines with a good correlation of imaging findings to the clinical presentation.

ABBREVIATIONS: Botox = onabotulinumtoxin A; CNR = contrast-to-noise ratio; GON = greater occipital nerve; ICC = intraclass correlation coefficient; MRN = MR neurography; PSIF = reversed fast imaging with steady-state precession

Migraine is a common debilitating neurovascular disorder. Thirty-five million Americans, women more than men, have migraines leading to substantial pain and medical costs of \$1 billion yearly.¹⁻⁵ The exact pathogenesis of migraines is debated between a more popular central theory of cortical spreading depression and neuronal hyperexcitability⁶ versus an extracranial pathology with compression and/or irritation of peripheral branches of the trigeminal and occipital nerves. The latter is hypothesized to result in triggered release of inflammatory and nociceptive peptides, which reach the meninges, inducing meningeal nociception and migraine.⁶⁻¹⁰ A number of conservative and

surgical peripheral nerve treatments have been reported for peripheral neuropathy (eg, perineural injections of steroids or onabotulinumtoxin A [Botox], radiofrequency ablation, and surgical decompression).¹¹⁻²⁹ The greater occipital nerve (GON) is a sensory branch that arises from the dorsal ramus of the second cervical spinal nerve,³⁰ and its compression has been proposed as the etiology of clinically manifested occipital migraines.¹⁸ Currently, the diagnosis is established on the basis of a combination of clinical history of posterior head and neck pain, tenderness on physical examination limited to the occipital area, and, in some cases, response to perineural injections.³¹

MR neurography (MRN) is a multiplanar nerve-selective imaging used to evaluate peripheral nerve anatomy and pathology.³² MRN has been successfully used in brachial plexopathies and has been shown to affect clinical diagnosis and management.³³⁻³⁵ In particular, 3D reversed fast imaging with steady-state precession (3D PSIF) has been shown to selectively identify small peripheral nerves around the head and neck region due to suppression of perineural fat and vascular signal.^{36,37} This is an isotropic se-

Received March 15, 2017; accepted after revision June 14.

From the Departments of Plastic Surgery (L.H., B.A.) and Radiology (R.D., Y.X., A.C.), University of Texas Southwestern Medical Center, Dallas, Texas; and Department of Radiology (R.D.), Faculty of Medicine, Zagazig University, Zagazig, Egypt.

Please address correspondence to Avneesh Chhabra, MD, Musculoskeletal Radiology, UT Southwestern Medical Center, 5323 Harry Hines Blvd, Dallas, TX 75390-9178; e-mail: avneesh.chhabra@utsouthwestern.edu

<http://dx.doi.org/10.3174/ajnr.A5354>

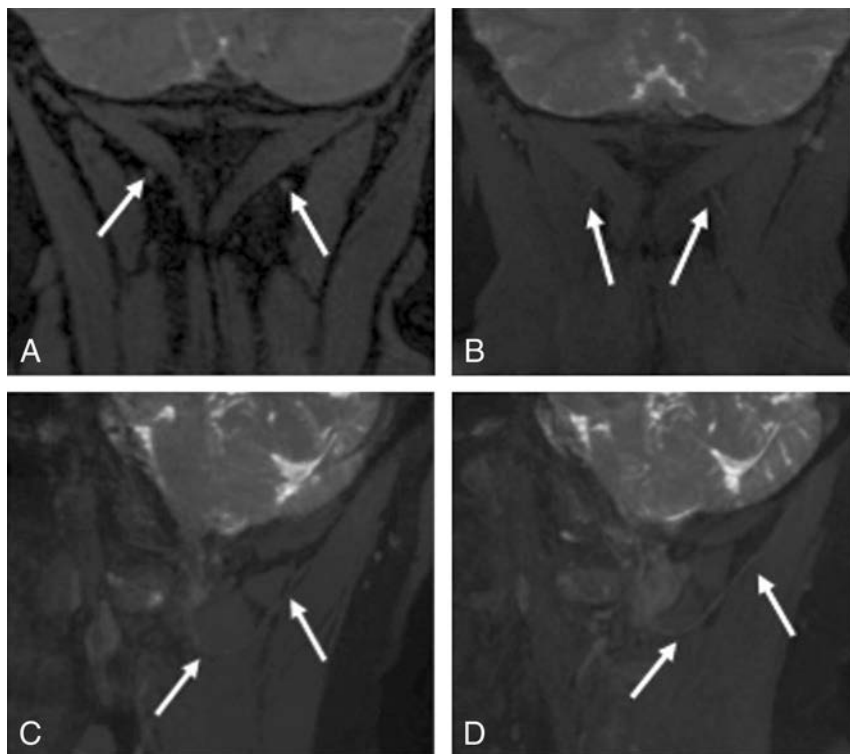


FIG 1. 3T MRN demonstrating a normal GON. A, Coronal 3D PSIF shows bilateral GONs (arrows). B, Eight-millimeter-thick MIP reconstruction in the coronal plane shows the normal GONs (arrows). C and D, Eight-millimeter-thick isotropic MIP reconstruction in the sagittal plane shows right and left GONs (arrows).

quence, which can be obtained in sub-1-mm resolution and provides a high signal-to-noise ratio and soft-tissue contrast. Normal nerves on 3D DWI-PSIF appear isointense to muscle, while nerve entrapment and resultant neuropathy are demonstrated by an increase in size and signal intensity proximal to the entrapment.^{38,39} There have been no reports of quantitative evaluation of the GON signal and contrast characteristics in patients with occipital neuralgia (migraine), to our knowledge. Classically, the SNR has been defined as a measure comparing the level of a desired signal with the level of background noise of the image.^{40,41} The contrast-to-noise ratio (CNR) is defined as the difference in SNR between 2 relevant tissue types⁴² (ie, the nerve in question [GON] and the adjoining muscle [semispinalis capitis]).

The aim of this study was to evaluate patients with clinically suspected unilateral occipital neuralgia with MRN and assess the differences in GON signal and size characteristics between the symptomatic and asymptomatic sides. Our hypothesis was that the symptomatic side GON will be different (brighter and thicker) than the one on the asymptomatic side. In addition, inter- and intraobserver performance was evaluated.

MATERIALS AND METHODS

Patient Population

This is a Health Insurance Portability and Accountability Act-compliant, institutional review board-approved retrospective cross-sectional study. Informed consent was waived. A consecutive series of patients underwent occipital nerve MRN with the primary diagnosis of chronic unilateral occipital neuralgia from 2014 to 2016 at our institution. The patients were referred as a

convenience sample from the plastic surgery clinic. Patient demographic factors were recorded, including age, sex, and clinical characteristics of their migraines, including laterality of pain, frequency, duration, intensity (on a qualitative scale from 1 to 10), subjective triggers, and occipital tenderness on physical examination. Possible predisposing factors to migraines such as family history of migraines, previous head trauma, and comorbidities were recorded. Previous methods of treatment including Botox, nerve block, radiofrequency ablation, and an operation were recorded as well as any previous head and neck imaging for comparison. Patients were excluded from this study if they were unable to localize their pain to one side or unable to quantify the difference in pain between the 2 sides (ie, zero versus reduced pain on the contralateral side). The subsequent treatment and outcomes are the subject of another study and article. This study was limited to evaluating nerve characteristic differences among the symptomatic-versus-asymptomatic GONs.

Image Acquisition and GON Analysis

Occipital MRN from the level of the base of the skull to the C5–6 area was performed, encompassing bilateral GONs in all 18 patients who met the criteria for possible GON compression based on history and physical examination, as described above. 3D coronal PSIF imaging was performed in all cases on high-field MR imaging scanners (Avanto, 1.5T, Siemens, Erlangen, Germany; and Achieva, 3T, Philips Healthcare, Best, the Netherlands). The parameters included TR = 12 ms, TE = 3 ms, voxel size = 0.9 mm, isotropic, fat suppression = water-selective. Eight-millimeter-thick-slab maximum intensity projections were obtained, which displayed the nerve in multiple planes (Fig 1 shows the normal nerve from an asymptomatic subject for comparison). The GON was visualized in all cases on both sides exiting from the cervical spine and coursing toward and lateral to the occipital protuberance. Two trained, experienced radiologists measured the signal and transverse diameter of the GON and semispinalis capitis, regardless of the affected side and blinded to the laterality of symptoms (Figs 2 and 3). The first observer (reader 1) had 7 years of experience interpreting MRN scans, while the second observer (reader 2) had 1 year of experience. The time between the first and second data collections of reader 1 spanned approximately 4 months. The GON signal and size were measured on the coronal image, midway between the spinal foramen and the point where it courses under the semispinalis capitis muscle. The largest diameter or most hyperintense T2 signal persisting on at least two 0.9-mm sections was measured. The freehand ROI tool on Intelispace PACS (Isite; Philips Healthcare) was used to include the

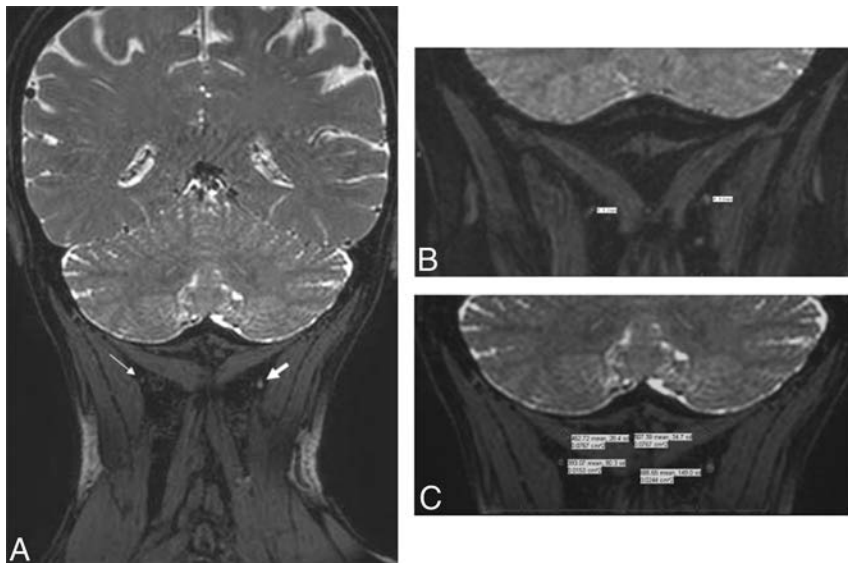


FIG 2. 3D Coronal PSIF images at 3T. *A*, Enlarged, hyperintense left greater occipital nerve (in comparison with the right). *B*, Caliber measurements show a larger left occipital nerve (1.6 mm) compared with the right (1.2 mm). *C*, Signal intensity measurements for both greater occipital nerves and semispinalis capitis muscles.

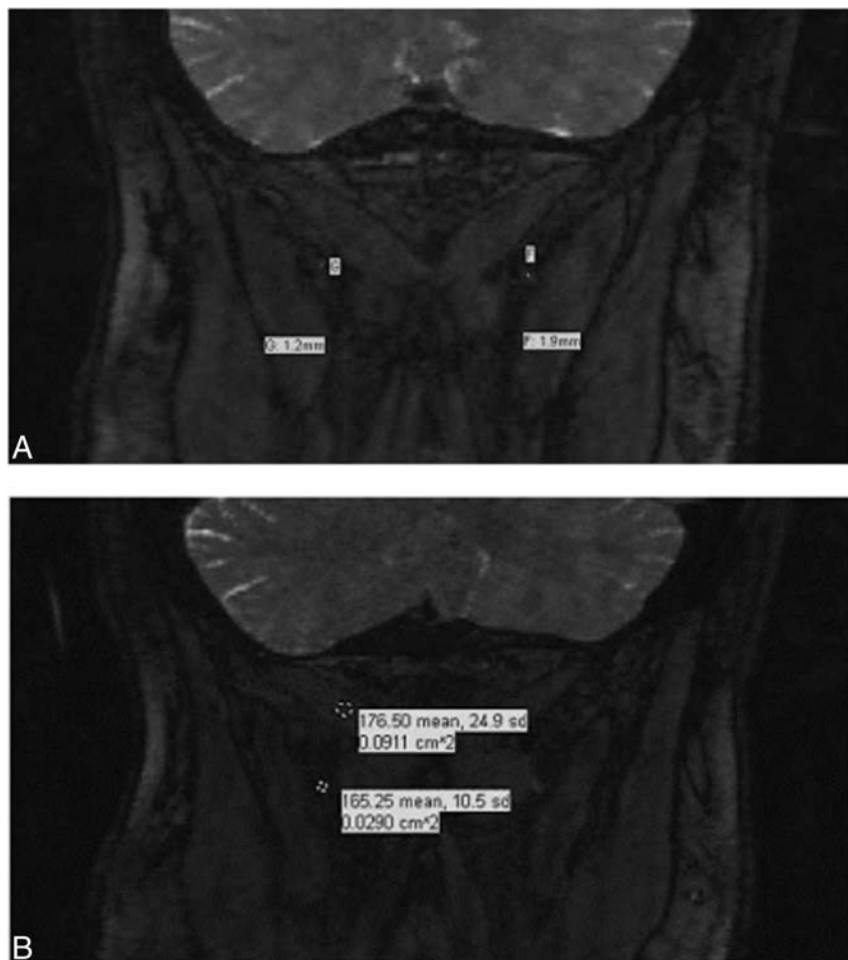


FIG 3. Coronal 3D PSIF images at 1.5T. *A*, Caliber measurements for the right and left GONs. *B*, Signal intensity measurements for the right GONs and semispinalis capitis muscles.

GON while excluding any extraneous soft tissues, such as fat or muscle. A 10-mm circular ROI was used for muscle signal measurement.

For each case, the control group consisted of nerve measurements obtained from the asymptomatic side, whereas the subject group included nerve measurements from the symptomatic side. After we obtained nerve diameter and signal intensity for both symptomatic and asymptomatic GONs, the T2 signal-to-noise ratio [$SNR = SI_{\text{nerve}} / (SI_{\text{nerve}})^{1/2}$] and the contrast-to-noise ratio [$CNR = (SI_{\text{nerve}} - SI_{\text{muscle}}) / (SI_{\text{nerve}})^{1/2}$] were calculated for each nerve in both groups. All data points, measurements, and calculations were recorded on an Excel spreadsheet (Microsoft, Redmond, Washington) for data analysis.

Statistical Analysis

Descriptive statistics were used for GON diameter, signal intensity, SNR, and CNR measurements on MRN. Differences in subject-versus-control groups were tested with a paired *t* test at .05. Interobserver performance was assessed with intraclass correlation coefficients (ICCs). Agreement was classified as excellent (0.75–1.0), good (0.60–0.74), fair (0.40–0.59), and poor (<0.40).⁴³ Furthermore, to evaluate whether a correlation existed between the duration of migraine symptoms from onset to MR imaging acquisition and MRN findings such as GON caliber and signal, we determined the Spearman rank correlation coefficients. A confidence interval of 95% was used throughout this study. R statistical and computing software, Version 3.3.2 (<http://www.r-project.org>) and SAS 9.4 (SAS Institute, Cary, North Carolina) were used for statistical analysis.

RESULTS

There were 18 patients with persistent chronic unilateral occipital migraine histories (Table 1) who underwent a broad spectrum of treatment options (Table 2) before MRN acquisition. Seven (39%) patients were imaged on a 3T MRN scanner versus 11 (61%) patients imaged on a 1.5T MRN scanner. None of the patients had a known central brain, neck, or spinal mass lesion. Prior outside imaging (performed in 6 of 18 patients) included CT/MR imag-

Table 1: Patient demographic factors (n = 18) and migraine histories prior to MR neurography

Age (yr)		Sex		Migraine Frequency ^a		Migraine Laterality		Positive Family History		Previous Head Trauma	
Younger than 40	Older than 40	Male	Female	<15 per mo	>15 per mo	Left	Right	Yes	No	Yes	No
6 (33%)	12 (67%)	3 (17%)	15 (83%)	5 (38%)	8 (62%)	10 (56%)	8 (44%)	3 (17%)	15 (83%)	5 (28%)	13 (72%)

^a Five patients were not reported.

Table 2: Migraine diagnostic and treatment modalities prior to acquisition of MR neurography

Botox		Nerve Block		Radiofrequency Ablation		Previous Operation ^a		Previous Head/Neck Imaging ^b	
Yes	No	Yes	No	Yes	No	Yes	No	Yes	No
13 (72%)	5 (28%)	15 (83%)	3 (17%)	5 (28%)	13 (72%)	6 (33%)	12 (67%)	6 (33%)	12 (67%)

^a Previous migraine operations included occipital nerve neurectomies or neurolysis.

^b All previous imaging was either standard 1.5T of the brain or cervical spine MRI or CT and evaluated as negative for pathology related to migraine symptoms.

Table 3: Statistical analysis of differences in GON diameter, signal intensity, calculated SNR, and calculated CNR comparing the symptomatic (subject group) versus asymptomatic (control group) side using a paired t test in patients with unilateral occipital migraines^a

MRN Characteristic	Subject Group	Control Group	P Value
Diameter	1.77 ± 0.4	1.29 ± 0.25	.001
Signal	269.06 ± 170.93	222.44 ± 170.46	.043
SNR	15.79 ± 4.59	14.02 ± 5.23	.009
CNR	2.57 ± 4.89	-1.26 ± 5.02	.004

^a All values are mean ± SD.

ing of the brain or cervical spine, and findings were unremarkable with respect to migraine etiology.

On the quantitative analysis of reader 1, the mean GON diameter for the symptomatic side was significantly greater (1.77 mm) than that on the asymptomatic side (1.29 mm) ($P = .001$; Table 3 and Figs 4 and 5). In addition, the difference of GON signal intensity between the symptomatic and asymptomatic sides was statistically significant at 269.06 versus 222.44, respectively ($P = .043$; Table 3). The calculated SNRs of the GON on the symptomatic side were notably higher at 15.79 compared with those on the asymptomatic side at 14.02 ($P = .009$; Table 3). Furthermore, the calculated CNRs of the GON relative to the ipsilateral semispinalis capitis muscle were significantly higher and more positive on the symptomatic side than on the asymptomatic side at 2.57 and -1.26 ($P = .004$; Table 3).

Intra- and interobserver statistical analysis with the intraclass correlation coefficient demonstrated fair-to-excellent interobserver and intraobserver performance ($ICC > 0.54$) in all 4 parameters (nerve diameter, nerve signal, SNR, and CNR), including excellent performance when analyzing the nerve diameter ($ICC, 0.81-0.93$; Table 4). Furthermore, no statistically significant correlation was found between the duration of migraine symptoms (defined as the length of time between onset and MRN acquisition) and the GON diameter (Spearman rank correlation coefficient, 0.21; $P = .4$), and only a moderate negative correlation was found between the duration of symptoms and the GON signal (Spearman rank correlation coefficient, -0.499; $P = .351$) (Fig 6). The mean duration of migraine symptoms in this cohort of 18 patients was 3415 ± 3127 days (approximately 9 years).

DISCUSSION

Migraine headaches present a challenge to health care providers because they have a spectrum of symptoms and are often difficult to manage. While new evidence emerges about the etiology and pathophysiology of chronic migraines, many uncertainties remain. Currently, the diagnostic strategy is limited and is based on clinical findings and blinded or targeted perineural injections.³¹ This study establishes that a noninvasive technique, MRN, can be used to evaluate the greater occipital nerve in such cases.

Among our cohort of 18 patients, a statistically significant difference was observed with respect to the GON diameter and signal intensity alterations, both being higher on the symptomatic side and thus consistent with the previous literature citing qualitative differences.^{35,36} Furthermore, the SNR of the GON was significantly higher on the symptomatic side, suggesting greater resolution of the nerve versus surrounding noise and the ability to detect differences in normal peripheral nerve anatomy versus pathology. The CNR, the difference in SNR between 2 relevant tissue types, was significantly higher and a more positive value on the symptomatic side than the asymptomatic side. This finding suggests more signal activation from the nerve than from background noise of muscle on the symptomatic side.⁴² In most cases, when there was a discrepancy between MRN findings and the clinical laterality of pain, confounding factors such as pathology on the other side may have produced discrepant results. The CNR showed a relatively lower ICC. Thus, SNR seems to be the more useful parameter in predicting the symptomatic side in these subjects with complex migraines. The variability may have resulted from different locations of ROIs in the muscle, while neural abnormality was more apparent on 3D imaging.

As medical innovation and technology continue to evolve,³⁹ the potential use of MRN in the future as a targeted approach to treatment planning in patients with migraine seems promising. An objective demonstration of neural abnormality has the potential to guide treatment and improve outcomes. The current standard of care is based on clinical history, physical examination including point tenderness of the GON, and response to nerve block and Botox in that location. However, if patients do not respond to injections, documentation of a normal or pathologic GON by MRN can help the treating physician choose the most suitable treatment plan for that individual. MRN is also useful in depicting the nerve abnormality proximal to the entrapment

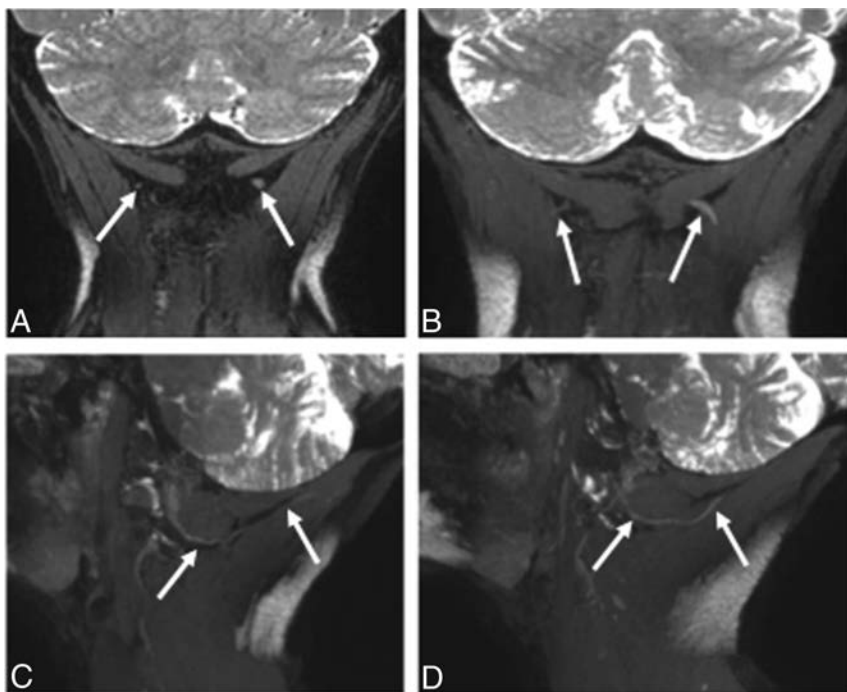


FIG 4. 3T MRN demonstrating left GON neuropathy in a 62-year-old woman with left occipital neuralgia. A and B, Coronal 3D PSIF and 8-mm-thick MIP reconstruction show an asymmetrically thickened and hyperintense left GON (arrows). C and D, Eight-millimeter-thick isotropic MIP reconstruction in the sagittal planes. Note the normal right GON (arrows in C) and abnormal left GON (arrows in D) with increasing thickening proximal to the muscle entrapment site.

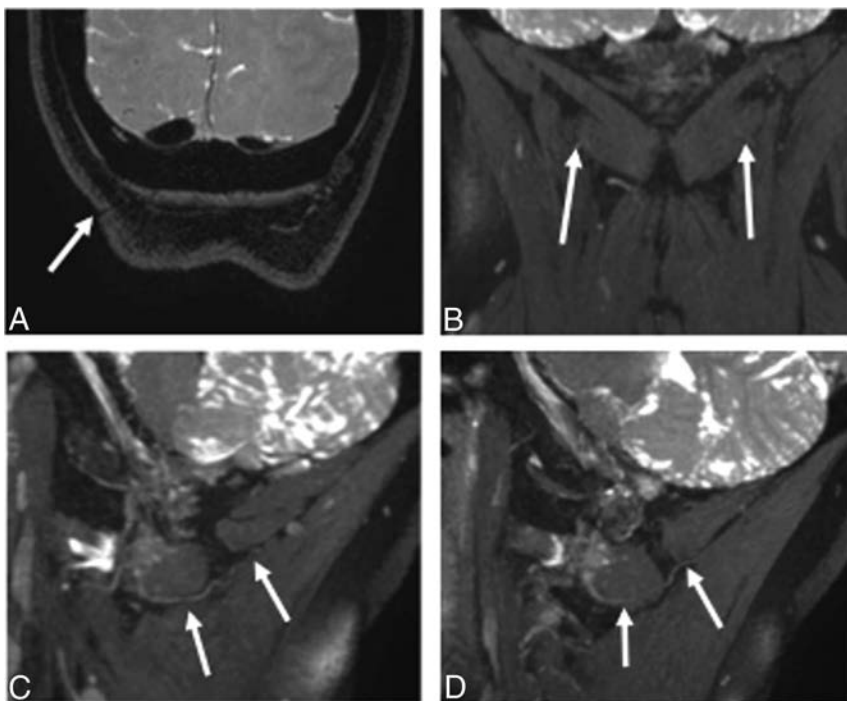


FIG 5. 3T MRN demonstrating persistent right GON neuropathy in a 55-year-old woman with prior right occipital neurolysis and persistent right occipital neuralgia. A, Coronal 3D PSIF shows the surgical scar site (arrow). B, A more anterior coronal image shows minimal hyperintensity of the right GON (arrows). C and D, Eight-millimeter-thick isotropic MIP reconstruction in the sagittal planes. Note the normal persistently hyperintense right GON (arrows in C) and normal left GON (arrows in D).

site. Therefore, the technique could show persistent abnormality, despite prior neurolysis (Fig 5).

The limitations of our study include the small sample size. However, the radiologists were blinded to the laterality of symptoms, and each of these patients served as his or her own control, given unilateral GON migraine symptoms, making these initial observations valuable. This value is reflected by fair-to-excellent ICCs. We have also considered that previous perineural injection and Botox injections, radiofrequency ablation, and surgical procedures could impact the appearance of the nerve on imaging. Our chart review revealed limited documentation of specific previous treatments performed by other health care providers before presenting to our institution, including frequency, dates, method, and location. However, the patients were imaged for persistent symptoms of unilateral occipital neuralgia. We did not evaluate other imaging sequences performed as part of an occipital neuralgia protocol because they were used to rule out any central lesion at the base of the brain or incidental spinal or neck lesion that could contribute to symptoms.

Further limitations of this study are due to restrictions in current medical technology. The strength of the magnetic field used in this study varied, with 7 (39%) patients undergoing the newer 3T MR imaging versus 11 (61%) patients undergoing 1.5T MR imaging. While the difference in 1.5T and 3T MRN can be significant and may make data nonhomogeneous and thus more difficult to analyze and compare, our investigation is nevertheless a pilot study, validating the use of multiple scanners. On 3T MR imaging technology, the SNR is usually superior, with improved resolution of images. Thus, in addition to the SNR, nerve diameter and CNR were also evaluated. Finally, both sides were compared in all cases to mitigate the effects of individual scans because symptomatic GON measurements were compared with the contralateral asymptomatic GON measurements within the same MRN image and not compared with measurements obtained among different images.

In the future, we hope to both increase the study sample and expand the

Table 4: Intra- and interobserver statistical analysis showing inter- and intraobserver performance among all 4 parameters using ICCs

	ICC
Reader 1 (initial) versus reader 1 (4 mo later)	
Nerve diameter (mm)	0.93
Nerve signal	0.79
SNR	0.74
CNR	0.68
Reader 1 versus reader 2	
Nerve diameter (mm)	0.81
Nerve signal	0.71
SNR	0.67
CNR	0.54

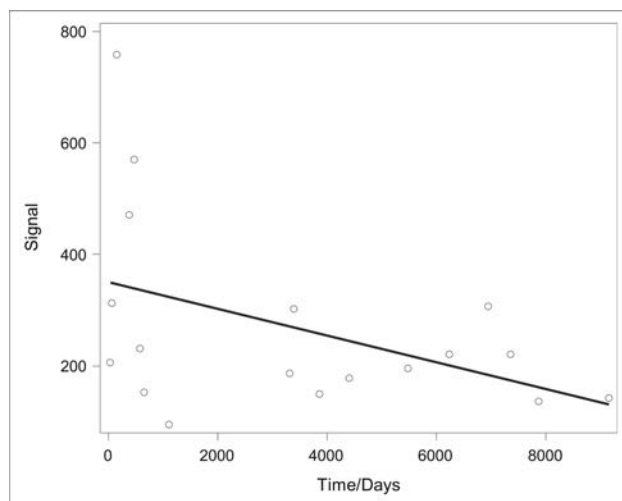


FIG 6. Evaluation of the correlation between the duration of migraine symptoms (defined as length of “time” in days from symptom onset to MRN acquisition) and the GON signal yielded a Spearman rank correlation coefficient of -0.499 with $P = .351$. When we compared the duration of symptoms and the GON diameter using the same statistical methodology, no significant correlation was found (Spearman rank correlation, 0.21 ; $P = .4$). The mean duration of migraine symptoms in this cohort of 18 patients was 3415 ± 3127 days (approximately 9 years).

scope of this study to include previously nontreated patients and other migraine trigger sites, including the frontal, temporal, and nasoseptal regions. As diagnostic imaging continues to evolve and methodologies of image acquisition are improved, we hope that MRN will help provide individualized care to patients with migraines.

CONCLUSIONS

In patients with unilateral clinical signs of GON compression, quantitative evaluation of the GON on MRN reveals different imaging appearances of the affected-versus-unaaffected nerves. In the future, the study can be expanded to include larger cohorts and other peripheral nerve disorders.

Disclosures: Avneesh Chhabra—UNRELATED: Consultancy: Icon Medical; Royalties: Jaypee Wolters.

REFERENCES

- Stewart WF, Simon D, Shechter A, et al. **Population variation in migraine prevalence: a meta-analysis.** *J Clin Epidemiol* 1995;48:269–80 CrossRef Medline
- Merikangas KR. **Contributions of epidemiology to our understanding of migraine.** *Headache* 2013;53:230–46 CrossRef Medline
- Edmeads J, Mackell JA. **The economic impact of migraine: an analysis of direct and indirect costs.** *Headache* 2002;42:501–09 CrossRef Medline
- Lipton RR, Stewart WF, Diamond S, et al. **Prevalence and burden of migraine in the United States: data from the American Migraine Study II.** *Headache* 2001;41:646–57 CrossRef Medline
- Leonardi M, Steiner TJ, Scher AT, et al. **The global burden of migraine: measuring disability in headache disorders with WHO’s Classification of Functioning, Disability and Health (ICF).** *J Headache Pain* 2005;6:429–40 CrossRef Medline
- Moskowitz MA, Nozaki K, Kraig RP. **Neocortical spreading depression provokes the expression of c-fos protein-like immunoreactivity within trigeminal nucleus caudalis via trigeminovascular mechanisms.** *J Neurosci* 1993;13:1167–77 Medline
- Bolay H, Reuter U, Dunn AK, et al. **Intrinsic brain activity triggers trigeminal meningeal afferents in a migraine model.** *Nat Med* 2002;8:136–42 CrossRef Medline
- Ambrosini A, D’Alessio C, Magis D, et al. **Targeting pericranial nerve branches to treat migraine: current approaches and perspectives.** *Cephalalgia* 2015;35:1308–22 CrossRef Medline
- Schueler M, Messlinger K, Dux M, et al. **Extracranial projections of meningeal afferents and their impact on meningeal nociception and headache.** *Pain* 2013;154:1622–31 CrossRef Medline
- Schueler M, Neuhuber WL, De Col R, et al. **Innervation of rat and human dura mater and pericranial tissues in the parieto-temporal region by meningeal afferents.** *Headache* 2014;54:996–1009 CrossRef Medline
- Guyuron B, Varghai A, Michelow BJ, et al. **Corrugator supercilii muscle resection and migraine headaches.** *Plast Reconstr Surg* 2000;106:429–34; discussion 435–37 CrossRef Medline
- Guyuron B, Tucker T, Davis J. **Surgical treatment of migraine headaches.** *Plast Reconstr Surg* 2002;109:2183–89 CrossRef Medline
- Dirnberger F, Becker K. **Surgical treatment of migraine headaches by corrugator muscle resection.** *Plast Reconstr Surg* 2004;114:652–57; discussion 658–59 CrossRef Medline
- Guyuron B, Kriegler JS, Davis J, et al. **Comprehensive surgical treatment of migraine headaches.** *Plast Reconstr Surg* 2005;115:1–9 Medline
- Poggi JT, Grizzell BE, Helmer SD. **Confirmation of surgical decompression to relieve migraine headaches.** *Plast Reconstr Surg* 2008;122:115–22; discussion 123–24 CrossRef Medline
- Guyuron B, Reed D, Kriegler JS, et al. **A placebo-controlled surgical trial of the treatment of migraine headaches.** *Plast Reconstr Surg* 2009;124:461–68 CrossRef Medline
- Guyuron B, Kriegler JS, Davis J, et al. **Five-year outcome of surgical treatment of migraine headaches.** *Plast Reconstr Surg* 2011;127:603–08 CrossRef Medline
- Janis JE, Barker JC, Javadi C, et al. **A review of current evidence in the surgical treatment of migraine headaches.** *Plast Reconstr Surg* 2014;134(4 suppl 2):131S–41S CrossRef Medline
- Ducic I, Hartmann EC, Larson EE. **Indications and outcomes for surgical treatment of patients with chronic migraine headaches caused by occipital neuralgia.** *Plast Reconstr Surg* 2009;123:1453–61 CrossRef Medline
- Caputi CA, Firetto V. **Therapeutic blockade of greater occipital and supraorbital nerves in migraine patients.** *Headache* 1997;37:174–79 CrossRef Medline
- Dach F, Éckeli AL, Ferreira Kdos S, et al. **Nerve block for the treatment of headaches and cranial neuralgias: a practical approach.** *Headache* 2015;55(suppl 1):59–71 CrossRef Medline
- Dilli E, Halker R, Vargas B, et al. **Occipital nerve block for the short-term preventive treatment of migraine: a randomized, double-blinded, placebo-controlled study.** *Cephalalgia* 2015;35:959–68 CrossRef Medline
- Singh M, Rios Diaz AJ, Gobble R, et al. **Causal relation between nerve compression and migraine symptoms and the therapeutic role of**

- surgical decompression.** *Plast Reconstr Surg Glob Open* 2015;3:e395 CrossRef Medline
24. Palamar D, Uluduz D, Saip S, et al. **Ultrasound-guided greater occipital nerve block: an efficient technique in chronic refractory migraine without aura?** *Pain Physician* 2015;18:153–62 Medline
 25. Inan LE, Inan N, Karadaş, et al. **Greater occipital nerve blockade for the treatment of chronic migraine: a randomized, multicenter, double-blind, and placebo-controlled study.** *Acta Neurol Scan* 2015; 132:270–77 CrossRef Medline
 26. Becker D, Amirlak B. **Beyond beauty: onobotulinumtoxin A (Botox®) and the management of migraine headaches.** *Anesthes Pain Med* 2012;2:5–11 CrossRef Medline
 27. Janis JE, Dhanik A, Howard JH. **Validation of the peripheral trigger point theory of migraine headaches: single-surgeon experience using botulinum toxin and surgical decompression.** *Plast Reconstr Surg* 2011;128:123–31 CrossRef Medline
 28. Sannic K, Borsting E, Amirlak B. **Decompression-avulsion of the auriculotemporal nerve for treatment of migraines and chronic headaches.** *Plast Reconstr Surg Glob Open* 2016;4:e678 CrossRef Medline
 29. Amirlak B, Sannic K, Pezeshk R, et al. **Anatomical Regional Targeted (ART) Botox injection technique: a novel paradigm for migraines and chronic headaches.** *Plast Reconstr Surg Glob Open* 2016; 4:e1194 CrossRef Medline
 30. Mosser SW, Guyuron B, Janis JE, et al. **The anatomy of the greater occipital nerve: implications for the etiology of migraine headaches.** *Plast Reconstr Surg* 2004;113:693–97; discussion 698–700 CrossRef Medline
 31. VanderHoek MD, Hoang HT, Goff B. **Ultrasound-guided greater occipital nerve blocks and pulsed radiofrequency ablation for diagnosis and treatment of occipital neuralgia.** *Anesthes Pain Med* 2013; 3:256–59 CrossRef Medline
 32. Grant GA, Goodkin R, Maravilla KR, et al. **MR neurography: diagnostic utility in the surgical treatment of peripheral nerve disorders.** *Neuroimaging Clin N Am* 2004;14:115–33 CrossRef Medline
 33. Fisher S, Wadhwa V, Manthuruthil C, et al. **Clinical impact of magnetic resonance neurography in patients with brachial plexus neuropathies.** *Br J Radiol* 2016;89:20160503 CrossRef Medline
 34. Vargis MI, Viallon M, Nguyen D, et al. **New approaches in imaging of the brachial plexus.** *Eur J Radiol* 2010;74:403–10 CrossRef Medline
 35. Wang X, Harrison C, Mariappan YK, et al. **MR neurography of brachial plexus at 3.0 T with robust fat and blood suppression.** *Radiology* 2017;283:538–46 CrossRef Medline
 36. Chhabra A, Subhawong TK, Bizzell C, et al. **3T MR neurography using three-dimensional diffusion-weighted PSIF: technical issues and advantages.** *Skeletal Radiol* 2011;40:1355–60 CrossRef Medline
 37. Zhang Z, Meng Q, Chen Y, et al. **3-T imaging of the cranial nerves using three-dimensional reversed FISP with diffusion-weighted MR sequence.** *J Magn Reson Imaging* 2008;27:454–58 CrossRef Medline
 38. Cox B, Zuniga JR, Panchal N, et al. **Magnetic resonance neurography in the management of peripheral trigeminal neuropathy: experience in a tertiary care centre.** *Eur Radiol* 2016;26:3392–400 CrossRef Medline
 39. Zhang Z, Song L, Meng Q, et al. **Morphological analysis in patients with sciatica: a magnetic resonance imaging study using three-dimensional high-resolution diffusion-weighted magnetic resonance neurography techniques.** *Spine* 2009;34:E245–50 CrossRef Medline
 40. Parrish TB, Gitelman DR, LaBar KS, et al. **Impact of signal-to-noise on functional MRI.** *Magn Reson Med* 2000;44:925–32 Medline
 41. Redpath T. **Signal-to-noise ratio in MRI.** *Br J Radiol* 1998;71:704–07 CrossRef Medline
 42. Welvaert M, Rosseel Y. **On the definition of signal-to-noise ratio and contrast-to-noise ratio for fMRI data.** *PLoS One* 2013;8:e77089 CrossRef Medline
 43. Hallgren K. **Computing inter-rater reliability for observational data: an overview and tutorial.** *Tutor Quant Methods Psychol* 2012;8: 23–34 CrossRef Medline

T1-Weighted Dynamic Contrast-Enhanced MR Perfusion Imaging Characterizes Tumor Response to Radiation Therapy in Chordoma

P. Santos, K.K. Peck, J. Arevalo-Perez, S. Karimi, E. Lis, Y. Yamada, A.I. Holodny, and J. Lyo



ABSTRACT

BACKGROUND AND PURPOSE: Chordomas notoriously demonstrate a paucity of changes following radiation therapy on conventional MR imaging. We hypothesized that dynamic contrast-enhanced MR perfusion imaging parameters of chordomas would change significantly following radiation therapy.

MATERIALS AND METHODS: Eleven patients with pathology-proved chordoma who completed dynamic contrast-enhanced MR perfusion imaging pre- and postradiation therapy were enrolled. Quantitative tumor measurements were obtained by 2 attending neuroradiologists. ROIs were used to calculate vascular permeability and plasma volume and generate dynamic contrast-enhancement curves. Quantitative analysis was performed to determine mean and maximum plasma volume and vascular permeability values, while semiquantitative analysis on averaged concentration curves was used to determine the area under the curve. A Mann-Whitney *U* test at a significance level of $P < .05$ was used to assess differences of the above parameters between pre- and postradiation therapy.

RESULTS: Plasma volume mean (pretreatment mean = 0.82; posttreatment mean = 0.42), plasma volume maximum (pretreatment mean = 3.56; posttreatment mean = 2.27), and vascular permeability mean (pretreatment mean = 0.046; posttreatment mean = 0.028) in the ROIs significantly decreased after radiation therapy ($P < .05$); this change thereby demonstrated the potential for assessing tumor response. Area under the curve values also demonstrated significant differences ($P < .05$).

CONCLUSIONS: Plasma volume and vascular permeability decreased after radiation therapy, suggesting that these dynamic contrast-enhanced MR perfusion parameters may be useful for monitoring chordoma growth and response to radiation therapy. Additionally, the characteristic dynamic MR signal intensity–time curve of chordoma may provide a radiographic means of distinguishing chordoma from other spinal lesions.

ABBREVIATIONS: AUC = area under the curve; DCE = dynamic contrast-enhanced; K^{trans} = vascular permeability; max = maximum; RT = radiation treatment; V_p = plasma volume

Chordoma is a rare cancer of persistent or ectopic notochord remnants, commonly found in the clivus, spine, and sacrum.¹ Chordomas account for only 1%–4% of all bone cancers, with an annual incidence of 1 per 1,000,000 and a prevalence of >1 per 100,000.^{2,3} Although having a low grade in histology,

chordomas are locally invasive, aggressive, and prone to recurrence.¹ Thus, patients are faced with a dismal prognosis and clinical progression mirroring that of malignant neoplasms. The median survival of patients with chordoma is currently 6.29 years, with survival rates dropping from 67.6% at 5 years to 39.9% at 10 years.⁴

The diagnosis of chordoma is challenging. Currently, conventional MR imaging is the criterion standard for the primary assessment of chordoma because it allows discrimination of tumor soft tissue from normal architecture, as well as the surveillance of spinal metastases.^{5–7} Classically, chordomas appear isointense or hypointense on T1-weighted MR imaging and hyperintense on T2-weighted MR imaging.⁸ Most lesions exhibit minimum-to-moderate heterogeneous enhancement with gadolinium, mirroring their heterogeneous histology.⁹ Not surprising, conventional MR imaging is limited in its capacity to discriminate chordoma and other spinal cancers.¹⁰

Received April 19, 2017; accepted after revision June 15.

From the Departments of Radiology (P.S., K.K.P., J.A.-P., S.K., E.L., A.I.H., J.L.), Medical Physics (K.K.P.), and Radiation Oncology (Y.Y.), Memorial Sloan Kettering Cancer Center, New York, New York.

This work was funded, in part, through the National Institutes of Health/National Cancer Institute Cancer Center support grant P30 CA008748.

Please address correspondence to Kyung K. Peck, PhD, Department of Medical Physics and Radiology, Memorial Sloan Kettering Cancer Center, 1275 York Ave, New York, NY 10065; e-mail: peckk@mskcc.org

Indicates open access to non-subscribers at www.ajnr.org

Indicates article with supplemental on-line tables.

<http://dx.doi.org/10.3174/ajnr.A5383>

Current treatment guidelines recommend en bloc surgical resection for primary chordoma lesions, followed by adjuvant radiation therapy to eliminate residual disease.^{1,10} Resection quality is largely predictive of postsurgical outcomes: Patients who underwent more aggressive, radical resection exhibited remission lasting nearly 3.5 times longer than those who had only undergone subtotal resection.¹¹ Thus, local recurrence despite resection and adjuvant radiation is considered a marker of treatment failure. However, en bloc excision is not universally feasible for all patients with chordoma. Surgical resection of chordoma is often complicated by local invasion of adjacent vessels and impingement of surrounding structures. In these advanced cases, alternative approaches such as subtotal resection, high-dose radiation therapy, and systemic biologic therapies may be indicated. Determining the need for such therapies requires careful monitoring of tumor response to therapy postresection.

However, monitoring tumor progression with conventional MR imaging is complicated by the indolent nature of chordoma: Its lesions are largely clinically silent until later stages of disease, at which point they are resistant to most traditional chemoradiation regimens.¹ As a result, chordoma lesions typically do not exhibit significant changes in tumor volume in response to therapy, once again limiting the utility of conventional MR imaging in evaluating treatment efficacy and subsequent patient prognosis.

Unlike conventional MR imaging, dynamic contrast-enhanced MR perfusion imaging (DCE-MR imaging) provides insight into the physiologic and hemodynamic characteristics of neoplastic lesions by evaluating tumor vascularity. DCE-MR imaging involves assessing changes in signal intensity with time, before and after contrast injection.¹² Previous studies have shown that DCE-MR imaging is useful for monitoring the response to therapy in spinal bone metastases,¹³ and for discriminating the hypo- and hypervascular spinal lesions of prostate carcinoma and renal cell carcinoma, respectively.¹⁴ More recently, DCE-MR imaging has shown clinical utility in chordoma diagnosis, effectively discriminating between chordoma and giant cell tumors of the axial skeleton.¹⁵

The purpose of this study was to determine whether DCE parameters, plasma volume (V_p) and vascular permeability (K^{trans}), can be used to monitor tumor response to radiation treatment (RT). We hypothesized that DCE-MR imaging parameters obtained via quantitative and semiquantitative methods can be used to characterize tumor response to RT, detecting subsequent changes in chordoma vasculature, which may later predict parallel changes in tumor volume as detected by conventional MR imaging.

MATERIALS AND METHODS

Subjects

We analyzed retrospective radiographic data from patients with pathology-proved chordoma of the sacrum, spine, or clivus. Eleven patients (mean age, 61 years) with DCE-MR perfusion imaging before and after RT were enrolled. Our institutional review board granted a waiver of authorization and consent for this study.

Data Acquisition

MR imaging sequences were acquired with a 1.5T scanner (HDxt 16.0; GE Healthcare, Milwaukee, Wisconsin), equipped with an 8-channel cervical-thoracic-lumbar surface coil. Patients underwent routine MR imaging, including sagittal T1 (FOV, 32–36 cm; section thickness, 3 mm; TR, 400–650 ms; flip angle, 90°) and T2 (FOV, 32–36 cm; section thickness, 3 mm; TR, 3500–4000 ms; flip angle, 90°), axial T1 (FOV, 18 cm; section thickness, 8 mm; flip angle, 90°) and T2 (FOV, 18 cm; section thickness, 8 mm; TR, 3000–4000 ms; flip angle, 90°), and sagittal STIR imaging (FOV, 32–36 cm; section thickness, 3 mm; TR, 3500–6000 ms; flip angle, 90°).

DCE-MR imaging of the spine was acquired on completion of routine MR imaging. A power injector was used to administer a bolus of gadolinium-diethylenetriamine penta-acetic acid at a dose of 0.1 mmol/kg and rate of 2–3 mL/s. The kinetic enhancement of tissue before and after contrast injection was obtained by using a 3D T1-weighted fast-spoiled gradient-echo sequence (TR, 4–5 ms; TE, 1–2 ms; section thickness, 5 mm; flip angle, 25°; FOV, 32 cm; matrix, 256 × 128; temporal resolution, 6–7 seconds) and consisted of 10–12 images in the sagittal plane. Ten phases for preinjection time delay and 30 phases for postinjection were obtained. Sagittal and axial T1-weighted postinjection MR images were additionally acquired after DCE-MR imaging.

Data Analysis

Data processing and analysis were performed with dynamic image processing software (NordicICE, version 2.3.14; NordicNeuroLab, Bergen, Norway). Preprocessing steps included removal of background noise, spatial and temporal smoothing, and detection of the arterial input function from the aorta. The arterial input function was individually calculated in each acquisition. Pixels with a large change in signal intensity, with a rapid change immediately after bolus injection, and with an early peak in intensity were chosen for the arterial input function. Linear assumption was made between the change in signal intensity and gadolinium concentration to convert the signal intensity curve to a concentration-time curve.

Anatomic images that matched the DCE-MR images were used in ROI placements. Voxel-by-voxel estimates of quantitative perfusion parameters, including vascular permeability and plasma volume, were determined with a Tofts 2-compartment pharmacokinetic model¹⁶ analysis. The area under the curve (AUC) was obtained from semiquantitative analysis to assess its potential as a discriminator of tumor histology.

ROIs were drawn to encompass the entirety of the chordoma by 2 attending neuroradiologists who were blinded to biopsy results and other clinical data, including age and sex, with careful consideration to avoid lesion margins, normal-appearing marrow, endplates, spondylotic changes, and vessels (including the basivertebral venous plexus). ROI values were determined for each section. Radiologists placing ROIs were blinded to additional clinical information and additional imaging.

Dynamic Concentration-Time Curves

Dynamic concentration-time curves illustrate changes in MR imaging signal intensity as a function of time. As a semiquantitative

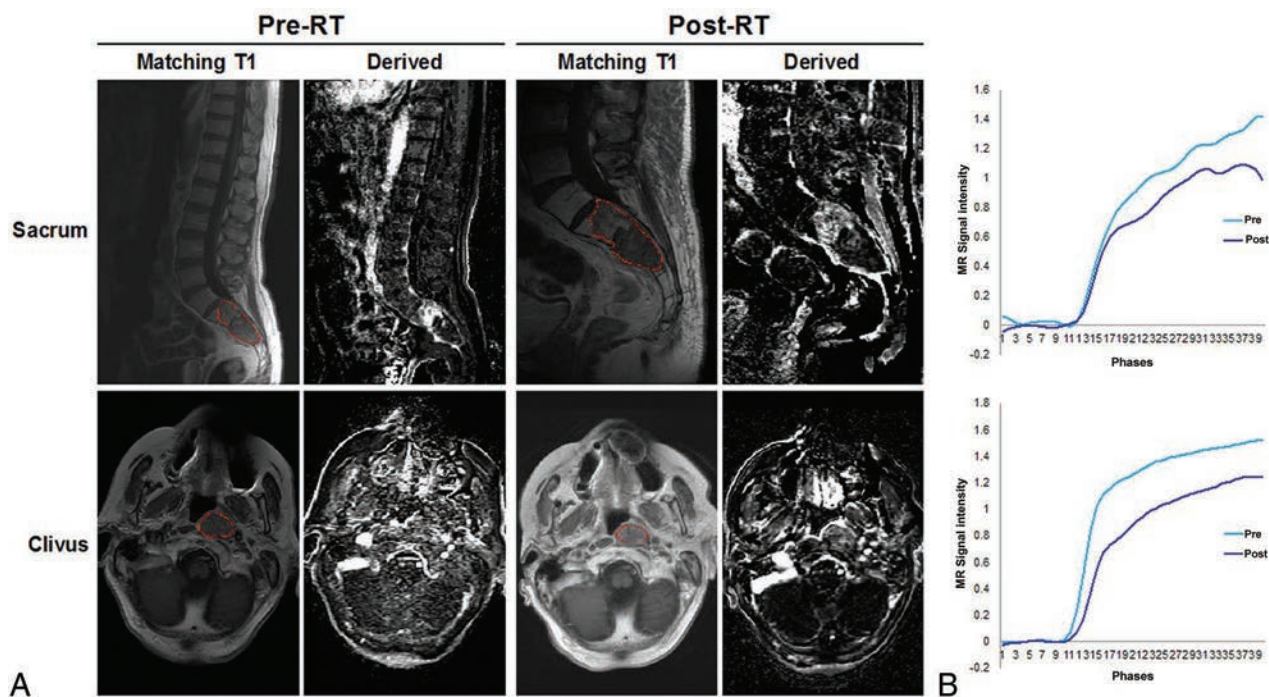


FIG 1. MR signal intensity is diminished in response to radiation therapy in DCE-MR imaging. **A**, Representative sagittal and axial T1-weighted MR images and dynamic derived images from DCE-MR imaging, illustrating a chordoma of the sacrum and clivus, pre- and postradiation therapy. **B**, Individual dynamic MR signal intensity–time curves pre-RT (blue) and post-RT (purple), obtained from corresponding ROIs (red).

analysis, AUCs in the dynamic concentration–time curves were generated from the same ROIs. Two curves for before and after RT were obtained for each patient. Only MR imaging signal intensities corresponding to the phases of the postinjection period were included for the calculation.

Statistical Analysis

A Wilcoxon ranked sign test at a significance of $P \leq .05$ was conducted to assess the difference between the V_p and K^{trans} maximum (max) and mean values pre- and post-RT. A Mann-Whitney U test at a significance of $P \leq .05$ was conducted to assess the difference between the dynamic curves pre- and post-RT.

DCE-MR Imaging Intervals

There was variability with respect to the number of both pre- and posttreatment DCE-MR imaging perfusion scans provided for each patient. In this study, we selected scans on the basis of the proximity to the time of radiation therapy as measured by pretreatment and posttreatment intervals. The pretreatment interval was measured as the number of days between the most proximal pretreatment DCE-MR imaging study and the first day of radiation therapy; the posttreatment interval was measured as the number of days between the last day of radiation therapy and the most proximal posttreatment DCE-MR imaging study.

Therapeutic Response

All subsequent posttreatment surveillance MR images and corresponding reports were reviewed. Time to recurrence was measured as the number of days between the last day of radiation therapy to the first radiology report that noted increasing tumor size/signal enhancement concerning for progression. Corresponding radiation oncology notes were reviewed to confirm that

the patient's clinical presentation aligned with radiologic findings. For 5 of 11 patients, progression-free survival was measured as the number of days from the last day of radiation therapy until the first surveillance MR imaging that reported possible progression. For the remaining 6 of 11 patients with no concerning radiologic findings, progression-free survival was measured from the last day of radiation therapy until their most recent MR imaging.

RESULTS

Patient Demographics and Tumor Characteristics

Six patients had spinal lesions, 4 had sacral lesions, and 1 had a clival lesion. Of the 11 lesions analyzed, 7 were localized and 4 were metastatic. Five lesions were recurrent (On-line Table 1). The average bidimensional size for readers 1 and 2 was 22.9×40.0 cm² and 22.7×40.0 cm² pretreatment, respectively, and 23.6×42.2 cm² and 23.8×40.8 cm² posttreatment, respectively. The average percentage change post-RT was 4.3% for reader 1 and 3.4% for reader 2. There was good interreader reliability across tumor measurements ($R^2 = 1.0$, On-line Table 1).

Vascular Permeability and Plasma Volume

T1-weighted and corresponding DCE perfusion images are presented in Fig 1A, illustrating 2 representative chordoma cases of the sacrum and clivus, pre- and posttreatment. The averaged dynamic concentration time curves in the ROI are presented in Fig 1B.

As expected, chordoma lesions were hypointense or isointense on T1 and hyperintense on T2 (Fig 1A). The overall amplitude of the dynamic concentration time curves is lower at posttreatment. On evaluation of perfusion images, we found that before treat-

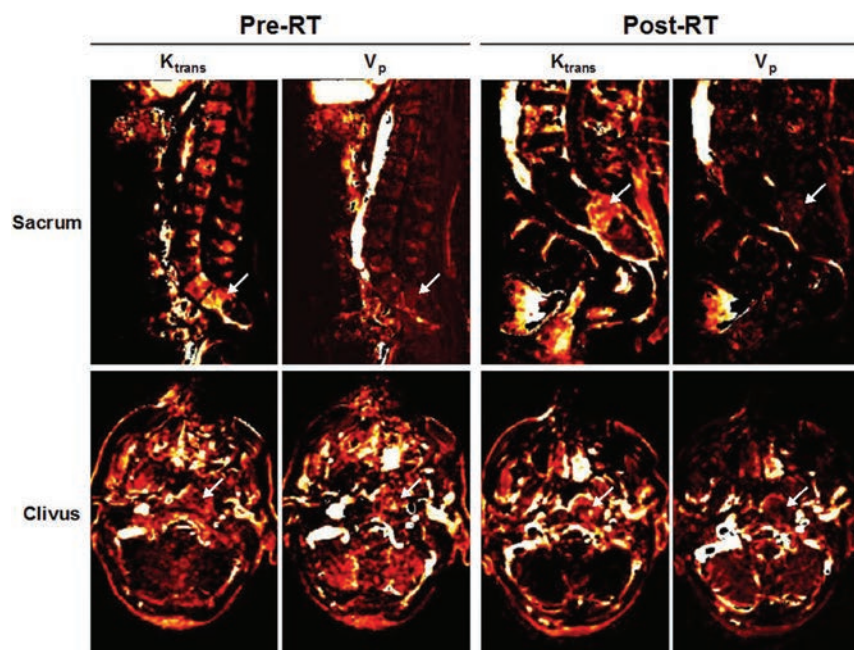


FIG 2. Perfusion maps of K^{trans} and V_p pre- and post-radiation therapy. K^{trans} and V_p maps corresponding to the representative sacrum and clivus cases in Fig 1. Regions of enhancement are indicated by white arrows, both pre-RT and post-RT.

ment, 7 lesions exhibited moderate-to-high enhancement, while the remaining 4 lesions showed little-to-no enhancement. These findings were confirmed by corresponding V_p and K^{trans} maps, which also demonstrated similar enhancement patterns before RT (Fig 2).

Posttreatment, there was decreased enhancement across dynamic images (Fig 1A), as well as V_p and K^{trans} maps (Fig 2). Box-and-whisker representations illustrated significant differences in the perfusion parameters of chordoma lesions treated with RT (Fig 3). Of the 4 quantitative perfusion parameters, V_p mean values showed the most significant difference ($P = .02$) before (mean = 0.82) and after (mean = 0.42) treatment, followed by V_p max (pre-RT mean = 3.56; post-RT mean = 2.27) and K^{trans} mean values (pre-RT mean = 0.046; post-RT mean = 0.028), which also were significant with P values of .04 and .03, respectively (Fig 3). However, K^{trans} max values showed no significant difference with RT (Fig 3).

Dynamic Concentration-Time Curves

Of the 11 time curves generated, 7 exhibited a persistent enhancement pattern pretreatment, while the remaining 4 curves exhibited a plateau pattern of enhancement (Fig 4B). Time curves following rapid contrast injection showed decreased signal intensity posttreatment in 9 of 11 cases (Fig 4B). Thereafter, individual curves were used to generate average time curves pre- and post-treatment (Fig 4A). Semiquantitative AUC analysis of the aggregate pre- and posttreatment curves showed a significant difference ($P = .03$) in MR signal, decreasing from mean = 21.03 pretreatment to mean = 14.52 posttreatment (Fig 4A).

Perfusion and Long-Term Outcomes

Several interesting clinical patterns emerged. First, all tumors imaged exhibited changes in at least 3 of the 5 quantitative (V_p max,

V_p mean, K^{trans} max, K^{trans} mean, AUC) parameters. In contrast, only 4 irradiated tumors exhibited changes in quantitative size measurements on posttreatment conventional MR imaging. On average, the pretreatment DCE-MR imaging interval was 94.27 days before radiation and the posttreatment DCE-MR imaging interval was 153.81 days after radiation. In the 5 patients who later presented with local recurrence/tumor progression, concerning radiographic findings were detected on conventional MR imaging 346 days posttreatment on average. In comparison, significant changes in DCE-MR imaging were detectable 119.57 days posttreatment.

Second, 6 patients who received a shorter, more aggressive course of RT (24 Gy in 1 fraction) exhibited larger percentage changes in V_p mean (mean = -41.93), V_p max (mean = -50.89), K^{trans} mean (mean = -49.45), and K^{trans} max (mean = -24.71) in comparison with patients who received

longer, less aggressive courses of treatment (V_p mean = -9.36, V_p max mean = -9.74, K^{trans} mean = 5.01, and K^{trans} max mean = 36.66) (On-line Table 2).

Third, 7 patients with localized tumors had larger percentage decreases in V_p mean (mean = -52.07) and V_p maximum (mean = -46.48) values in comparison with 4 patients with metastatic disease (V_p mean = 53.33, V_p maximum mean = 17.36), suggesting that localized tumors exhibited marked decreases in vascularity and thus were more responsive to RT. Likewise, 6 never-treated tumors had larger percentage decreases in V_p mean (mean = -55.02), V_p max (mean = -49.74), and K^{trans} mean (mean = -31.56) in comparison with 5 previously treated tumors, supporting previous findings that treatment-naïve tumors are more likely to respond to radiation therapy (V_p mean = 6.34, V_p max mean = -11.12, and K^{trans} mean = -16.47) (On-line Table 2).

DISCUSSION

Conventional MR imaging of chordomas treated with RT typically exhibits little change. Our results suggest that DCE-MR imaging perfusion parameters obtained through quantitative (V_p and K^{trans}) and semiquantitative (AUC) analysis significantly changed following RT and may serve as a more sensitive indicator for monitoring tumor responsiveness to RT than conventional MR imaging.

Major Findings

Of the 3 parameters studied, V_p was the most significant measure of tumor response. Differences in V_p mean and V_p maximum values pre- and posttreatment were significant. On average, V_p max values were approximately 1.6 times greater before treatment, which is concordant with previous work demonstrating the significantly higher vascularization of chordoma in comparison

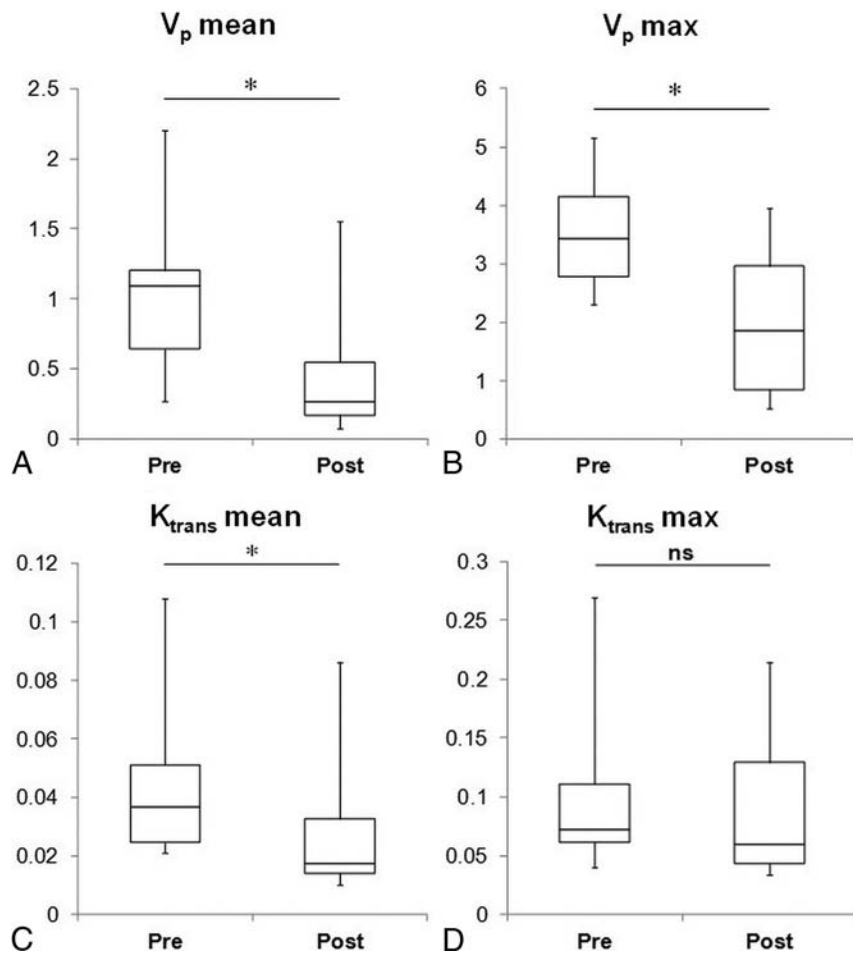


FIG 3. Tumor plasma volume and permeability decreased after radiation therapy. Box-and-whisker plots illustrating a five-number summary for DCE-MR imaging perfusion parameters: A, V_p mean. B, V_p max. C, K^{trans} mean. D, K^{trans} max ($n = 12$). Significant differences were observed pre-RT and post-RT in 3 of 4 parameters: V_p mean (pre-RT mean = 0.82, post-RT mean = 0.42, asterisk indicates $P = .02$), V_p max (pre-RT mean = 3.56, post-RT mean = 2.27, asterisk indicates $P = .04$), and K^{trans} mean (pre-RT mean = 0.046, post-RT mean = 0.028, asterisk indicates $P = .03$). Differences in K^{trans} max values pre-RT (mean = 0.11) and post-RT (mean = 0.092) were not significant ($P = .47$).

with that of adjacent normal tissues.¹⁷ Chordoma has been shown to express elevated vascular endothelial growth factor and matrix metalloproteinase-9, which may work in concert to increase angiogenesis and invasiveness and promote recurrence of chordoma and other bone cancers.^{18–20}

K^{trans} was also a positive indicator of tumor response to therapy. A measure of vascular permeability, K^{trans} represents the rate at which blood is transferred from the vascular compartment to the extravascular extracellular space. Therefore, unlike V_p , K^{trans} is a marker of tumor leakiness rather than actual tumor vascularity. On receiving RT, chordoma lesions exhibited a significant difference in K^{trans} mean values ($P = .03$). In contrast, there was no significant difference between K^{trans} maximum values pre- and posttreatment. However, a downward trend in K^{trans} max values suggests that future analyses of larger patient cohorts may also achieve significance, providing further evidence that tumor leakiness is increased in irradiated chordoma lesions.

Chordoma presented with unusual kinetic patterns on DCE-MR imaging. Typically, malignant tumors carry DCE-MR imaging time–signal intensity curve signatures characterized by rapid early enhancement, followed by fast washout, as demonstrated by the average time–signal intensity curves of renal cell carcinoma and prostate carcinoma (Fig 4C). In contrast, 8 of 11 patients with chordoma presented with “persistently en-

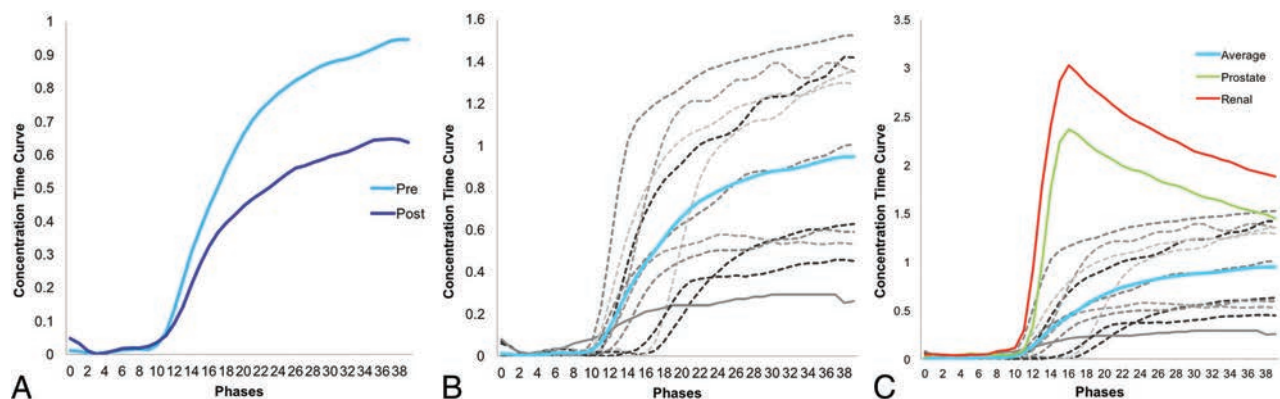


FIG 4. Chordoma is distinguished by its unique signature on DCE-MR signal intensity–time curves. A, Averaged dynamic MR signal intensity curves for patients with chordoma ($n = 12$) pre-RT (blue) and post-RT (purple). Significant differences in areas under the curve pre-RT and post-RT were observed ($P = .03$). B, Individual dynamic MR signal intensity–time curves from 12 patients (gray) were used to generate an average curve (blue). C, Unlike hypervascular renal cell carcinomas (red) and hypovascular prostate carcinomas (green) spinal metastases,¹⁴ chordoma presents with a signal intensity–time curve characterized by slow contrast uptake and lack of peak enhancement, likely due to a slow washout phase. For all graphs, each phase = 1 second.

hancing” time–signal intensity curves before treatment (Fig 4B, -C), a pattern of enhancement generally associated with more benign lesions.²¹ However, this pattern of contrast uptake is also consistent with low-grade tumors, such as chordomas.²² The remaining 3 of 11 patients with chordomas had pretreatment time–signal intensity curves that “plateaued” (Fig 4B, -C). Such curves are more suspicious for malignancy, but not definitive.²² While the pattern of enhancement remained the same for most patients, 2 patients exhibited changes in enhancement dynamics. It remains unclear whether enhancement dynamics offer a predictive value of treatment response.

Additionally, the persisting and plateauing kinetic patterns of enhancement on DCE-MR imaging are not unique to chordoma. Other osseous tumors of the spine, particularly chondrosarcoma and giant cell tumors, also exhibit similar patterns.²³ Furthermore, factors such as the heterogeneous composition of a chordoma and the shape of the ROI may also account for the variation in kinetic patterns observed.⁹ Despite these uncertainties, semiquantitative AUC analysis of aggregate dynamic time–signal intensity curves demonstrated that RT was still associated with a significant decrease ($P = .03$) in signal intensity posttreatment (Fig 4A), suggesting that AUC might be another parameter for characterizing chordoma response to RT.

Our findings are consistent with previous DCE studies that show that physiologic changes in tumor vascularity present earlier than corresponding morphologic changes.^{24,25} A representative case is patient 7. Although the initial posttreatment conventional MR imaging scan suggested that the tumor had responded to radiation therapy (ie, subjectively better), subsequent surveillance scans showed evidence of tumor progression, which was associated with clinical worsening as denoted by the corresponding radiation oncology progress notes. These findings provide evidence supporting DCE-MR perfusion imaging as an intriguing alternate to conventional MR imaging because decreases in detection time are crucial for rapid decision-making, particularly for patients with chordoma who may benefit from prompt treatment modifications. Our findings are also consistent with previous findings demonstrating that single-dose fractions of >10 Gy cause severe vascular damage, resulting in alterations of the tumor microenvironment and triggering tumor cell apoptosis.²² The cytotoxic effects of ionizing RT are well-established, with increasing doses leading to an increased risk of vascular pathologies.²⁶ DCE-MR imaging can detect evidence of vascular damage via decreased V_p and increased K^{trans} . Tumor staging and recurrence may have an influence on both prognostication and posttreatment DCE changes because both our study and previous studies²⁷ have shown that tumor progression is associated with higher V_p and K^{trans} values.

There are several limitations to our study. First, larger sample sizes will permit ROC analysis and more estimation of the predictive value of perfusion parameters. Due to the exceedingly low incidence and prevalence of chordoma, our study was limited by the size of the available patient population. The sample size was further limited to patients with chordoma who received radiation therapy, pre- and posttreatment DCE perfusion scans, and no complicating operations. However, some clinical patterns did emerge that are worth investigating in future studies. Second, as a

retrospective study, there was significant variability in the timing of the posttreatment DCE-MR images. Much of this variability could be attributed to numerous factors, including scheduling constraints of the patient and provider and technical errors resulting in suboptimal DCE-MR images that were excluded from the study. Notably, patients 7 and 11 had posttreatment DCE-MR images obtained after tumor progression was already detected on conventional MR imaging. Additionally, these patients presented with aggressive, widely metastatic disease that had already been previously irradiated. Collectively, these factors limit the predictive value of DCE-MR imaging in these 2 cases; thus, they were not included in the analysis of clinical outcomes.

Third, both the precontrast T1 value and arterial input function must be accurately measured to apply a pharmacokinetic model for quantitative analysis. In the design of DCE-MR imaging studies, competing demands for high spatial resolution, coverage, and signal-to-noise often resulted in inadequate temporal resolution for reliable measurement of the arterial input function. Fourth, the precise mechanism leading to the perfusion differences before and after RT has not been elucidated, and it is probable that the perfusion changes reflect a combination of radiation- and therapy-induced changes, healing bone, and reconstitution of hematopoietic marrow. However, given that successfully treated chordomas could be differentiated by the perfusion changes by a statistically significant margin in our patient population, the results are meaningful regardless of the precise mechanism.

CONCLUSIONS

DCE-MR imaging presents a novel alternative to conventional MR imaging for tumor monitoring in patients with chordoma, providing insight into the physiologic and hemodynamic processes within a particular lesion. Quantitative and semiquantitative DCE parameters such as V_p , K^{trans} , and AUC are significantly decreased posttreatment; this change reflects the extent of vascular damage induced by radiation therapy. Collectively, these findings demonstrate the capacity of DCE-MR imaging to accurately reflect underlying tumor physiology in response to therapy.

Disclosures: Eric Lis—UNRELATED: Payment for Lectures Including Service on Speakers Bureaus: Medtronic. Yoshiya Yamada—UNRELATED: Board Membership: Chordoma Foundation Medical Advisory Board member, Comments: no financial remuneration; Payment for Lectures Including Service on Speakers Bureaus: BrainLab, Comments: Speakers Bureau. Andrei I. Holodny—UNRELATED: Grants/Grants Pending: National Institutes of Health, Comments: Multiple Principal Investigator on National Institutes of Health–National Institute of Biomedical Imaging and Bioengineering 1R01EB022720-01, Principal Investigator on a subaward for National Institutes of Health–National Institute of Biomedical Imaging and Bioengineering 1R01EB022720-01, Principal Investigator on National Institutes of Health–National Cancer Institute R21 CA220144-01*; Other: President of fMRI Consultants, Comments: This is a purely educational company. *Money paid to the institution.

REFERENCES

1. Walcott BP, Nahed BV, Mohyeldin A, et al. **Chordoma: current concepts, management, and future directions.** *Lancet Oncol* 2012;13:e69–76 CrossRef Medline
2. Healey JH, Lane JM. **Chordoma: a critical review of diagnosis and treatment.** *Orthop Clin North Am* 1989;20:417–26 Medline
3. Stiller CA, Trama A, Serraino D, et al; RARECARE Working Group. **Descriptive epidemiology of sarcomas in Europe: report from the RARECARE project.** *Eur J Cancer* 2013;49:684–95 CrossRef Medline
4. McMaster ML, Goldstein AM, Bromley CM, et al. **Chordoma: inci-**

- dence and survival patterns in the United States, 1973–1995. *Cancer Causes Control* 2001;12:1–11 [CrossRef Medline](#)
5. Sung MS, Lee GK, Kang HS, et al. **Sacroccygeal chordoma: MR imaging in 30 patients.** *Skeletal Radiol* 2005;34:87–94 [CrossRef Medline](#)
 6. Smolders D, Wang X, Drevelengas A, et al. **Value of MRI in the diagnosis of non-clival, non-sacral chordoma.** *Skeletal Radiol* 2003;32:343–50 [CrossRef Medline](#)
 7. Rodallec MH, Feydy A, Larousserie F, et al. **Diagnostic imaging of solitary tumors of the spine: what to do and say.** *Radiographics* 2008;28:1019–41 [CrossRef Medline](#)
 8. Llauger J, Palmer J, Amores S, et al. **Primary tumors of the sacrum: diagnostic imaging.** *AJR Am J Roentgenol* 2000;174:417–24 [CrossRef Medline](#)
 9. Chugh R, Tawbi H, Lucas DR, et al. **Chordoma: the nonsarcoma primary bone tumor.** *Oncologist* 2007;12:1344–50 [CrossRef Medline](#)
 10. Stacchiotti S, Sommer J. **Building a global consensus approach to chordoma: a position paper from the medical and patient community.** *Lancet Oncol* 2015;16:e71–83 [CrossRef Medline](#)
 11. Fuchs B, Dickey ID, Yaszemski MJ, et al. **Operative management of sacral chordoma.** *J Bone Joint Surg Am* 2005;87:2211–16 [Medline](#)
 12. Parker G, Buckley D. **Tracer kinetic modeling for T1-weighted DCE-MRI.** In: Jackson A, Buckley D, Parker G. *Dynamic Contrast-Enhanced Magnetic Resonance Imaging in Oncology*. Berlin: Springer; 2005:81–91
 13. Chu S, Karimi S, Peck KK, et al. **Measurement of blood perfusion in spinal metastases with dynamic contrast-enhanced magnetic resonance imaging: evaluation of tumor response to radiation therapy.** *Spine* 2013;38:E1418–24 [CrossRef Medline](#)
 14. Saha A, Peck KK, Lis E, et al. **Magnetic resonance perfusion characteristics of hypervascular renal and hypovascular prostate spinal metastases: clinical utilities and implications.** *Spine* 2014;39:E1433–40 [CrossRef Medline](#)
 15. Lang N, Su MY, Xing X, et al. **Morphological and dynamic contrast enhanced MR imaging features for the differentiation of chordoma and giant cell tumors in the axial skeleton.** *J Magn Reson Imaging* 2017;45:1068–75 [CrossRef Medline](#)
 16. Tofts PS, Brix G, Buckley DL, et al. **Estimating kinetic parameters from dynamic contrast-enhanced T(1)-weighted MRI of a diffusible tracer: standardized quantities and symbols.** *J Magn Reson Imaging* 1999;10:223–32 [Medline](#)
 17. Chen KW, Yang HL, Lu J, et al. **Expression of vascular endothelial growth factor and matrix metalloproteinase-9 in sacral chordoma.** *J Neurooncol* 2011;101:357–63 [CrossRef Medline](#)
 18. Kawashima A, Okada Y, Nakanishi I, et al. **Immunolocalization of matrix metalloproteinases and tissue inhibitors of metalloproteinases in human chondrosarcomas.** *Gen Diagn Pathol* 1997;142:129–37 [Medline](#)
 19. Kumta SM, Huang L, Cheng YY, et al. **Expression of VEGF and MMP-9 in giant cell tumor of bone and other osteolytic lesions.** *Life Sci* 2003;73:1427–36 [CrossRef Medline](#)
 20. Kaya M, Wada T, Kawaguchi S, et al. **Increased pre-therapeutic serum vascular endothelial growth factor in patients with early clinical relapse of osteosarcoma.** *Br J Cancer* 2002;86:864–69 [CrossRef Medline](#)
 21. Johnson LM, Turkbey B, Figg WD, et al. **Multiparametric MRI in prostate cancer management.** *Nature Rev Clin Oncol* 2014;11:346–53 [CrossRef](#)
 22. Park HJ, Griffin RJ, Hui S, et al. **Radiation-induced vascular damage in tumors: implications of vascular damage in ablative hypofractionated radiotherapy (SBRT and SRS).** *Radiat Res* 2012;177:311–27 [CrossRef Medline](#)
 23. De Coninck T, Jans L, Sys G, et al. **Dynamic contrast-enhanced MR imaging for differentiation between enchondroma and chondrosarcoma.** *Eur Radiol* 2013;23:3140–52 [CrossRef Medline](#)
 24. Røe K, Kakar M, Seierstad T, et al. **Early prediction of response to radiotherapy and androgen-deprivation therapy in prostate cancer by repeated functional MRI: a preclinical study.** *Radiat Oncol* 2011;6:65 [CrossRef Medline](#)
 25. Cao Y. **The promise of dynamic contrast-enhanced imaging in radiation therapy.** *Semin Radiat Oncol* 2011;21:147–56 [CrossRef Medline](#)
 26. Grabham P, Sharma P. **The effects of radiation on angiogenesis.** *Vasc Cell* 2013;5:1 [CrossRef Medline](#)
 27. Thomas AA, Arevalo-Perez J, Kaley T, et al. **Dynamic contrast enhanced T1 MRI perfusion differentiates pseudoprogression from recurrent glioblastoma.** *J Neurooncol* 2015;125:183–90 [CrossRef Medline](#)

Celebrating 35 Years of the AJNR

November 1982 edition

Digital Subtraction Cerebral Angiography by Intraarterial Injection: Comparison with Conventional Angiography

Michael Brant-Zawadzki^{1,2}
Robert Gould²
David Norman²
Thomas H. Newton²
Barton Lane¹

For 4 months, a prototype digital subtraction system was used to obtain images of the cerebral vasculature after intraarterial contrast injections. In 12 intraarterial injections were recorded with both a digital subtraction unit and a conventional direct magnification film-screen system. The digital subtraction and conventional film subtraction images were compared and graded for quality and information by three skilled observers. In addition, quantitative measurements of contrast performance and spatial resolution were obtained on both the digital system and the conventional film-screen system. In a clinical setting, both the digital subtraction and conventional film-screen systems provided similar quality images and angiographic information. Contrast-detail curves demonstrated that digital subtraction angiography formed conventional film technique for low-contrast objects. Digital subtraction angiography also reduced the time required to obtain the angiogram, markedly reduced film cost, and lowered the contrast agent burden.

Digital subtraction imaging of the extra- and intracranial cerebral vasculature after intravenous injections of contrast material is becoming an established screening procedure [1-3]. Patient motion, superimposition of multiple contrast agent burden, and suboptimal resolution [4] restrict the diagnostic value of this method. Early work has suggested, however, that digital subtraction imaging of intraarterial contrast injections can provide images of superior diagnostic quality to obviate conventional film-screen angiography, thus reduce film cost, and possibly decreasing time required for the examination [5]. For 4 months, we have evaluated intraarterial cerebral digital subtraction angiography (DSA). In selected instances, a comparison of digital and film-screen angiography was made in the same patient. In addition, quantitative measurements of resolution and contrast sensitivity were obtained for both the digital and film-screen systems.

This article appears in the November/December 1982 issue of *AJNR* and the February 1983 issue of *AJNR*.

Received April 27, 1982; accepted after revision July 9, 1982.

Presented at the XI Symposium Neuroangiography, Washington, D.C., October 1982.

¹ Department of Radiology, San Francisco General Hospital, 1001 Poiner Ave., San Francisco, CA 94110. Address reprint requests to M. Brant-Zawadzki.

² Department of Radiology, University of California Medical Center, San Francisco, CA 94143.

³ Department of Radiology, Mt. Zion Hospital, San Francisco, CA 94110.

AJNR 3:593-598, November/December 1982

0195-6108/82/0306-0593\$02.00

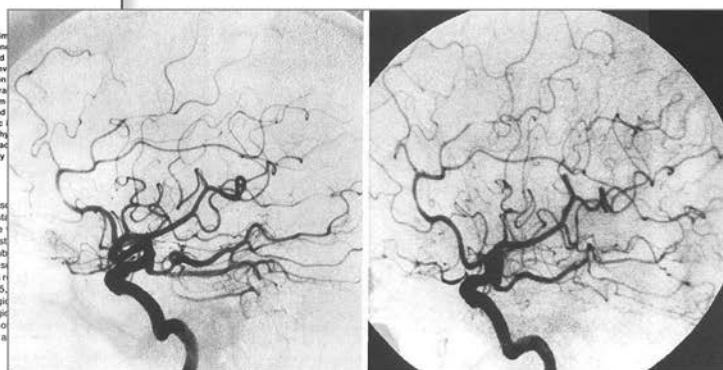
© American Roentgen Ray Society

Subjects and Methods

Equipment

The DSA unit (DF 100, DSA) which included a progressive interlaced with a 9-inch (23 cm) fluoroscopy unit (G.E. Medical Systems) x-ray tube (Maxi 100, G.E. Medical Systems) 0.013-0.030 sec. M. camera (Matrix Instruments).

Conventional 1.8-2.0 x mag and Cronex 4 film (DuPont, N. 125, G.E. Medical Systems).



Falx and Interhemispheric Fissure on Axial CT: II. Recognition and Differentiation of Interhemispheric Subarachnoid and Subdural Hemorrhage

Robert D. Zimmerman¹
Eric J. Russell²
Emily Yurberg³
Norman E. Leeds⁴

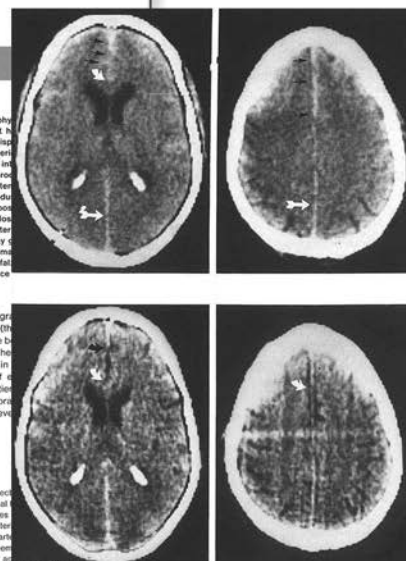
Interhemispheric hyperdensity on unenhanced computed tomography (CT) is considered a sign of subarachnoid hemorrhage, the "falx sign." It has been identified as a normal feature and has also been seen with interhemispheric hemorrhage. To determine the differential features of interhemispheric subarachnoid hemorrhage and 32 patients with interhemispheric subdural hematomas were reviewed. Subarachnoid hemorrhage produced interhemispheric hyperdensity only, with a zigzag contour and external calvarium to the rostrum of the corpus callosum. Interhemispheric subdural hematomas produced crescentic hyperdensities that are largest in the posterior part of the fissure, behind and above the splenium of the corpus callosum. Interhemispheric hyperdensity in children is more complex. Because the anterior fissure is narrow in younger patients, subarachnoid hemorrhage may be overlooked. Likewise, interhemispheric subdural hematomas in children are difficult to recognize. They produce asymmetric thickening of the falx extension over the tentorium. They are, however, of great significance generally seen in abused patients and carry a poor prognosis.

Interhemispheric hyperdensity on unenhanced computed tomography (CT) originally described as a sign of subarachnoid hemorrhage [1-4] (the "falx sign"), but other causes of interhemispheric hyperdensity have since been identified including the normal falx [5-7] and interhemispheric subdural hematomas. We have also noted transient interhemispheric hyperdensity in cerebral edema. To determine the differential CT features of these conditions, 50 patients with subarachnoid hemorrhage, 32 patients with interhemispheric subdural hematomas, and three children with cerebral edema were reviewed. On the basis of this material, criteria have been developed to differentiate these processes from the normal falx.

Materials and Methods

Subarachnoid Hemorrhage

CT scans of 50 patients with subarachnoid hemorrhage were retrospectively reviewed. Criteria for selection were: (1) initial scan within 3 days of injury; (2) spinal fluid evidence of blood within subarachnoid spaces (interhemispheric fissure). In addition, at least one of the following criteria was required: evidence of a source of hemorrhage (e.g., aneurysm or arteriovenous malformation [AVM]) or (2) surgical and/or postmortem confirmation of hemorrhage. The patients were 23 males and 27 females, varying from 3 months to 81 years of age. Findings in this group were compared with those in 200 normal patients (see part 1 of this article [5]).



Received December 16, 1981; accepted after revision June 4, 1982.

Presented at the annual meetings of the American Society of Neuroradiology, Los Angeles, March 1982, and the American Roentgen Ray Society, Las Vegas, April 1982.

¹ Department of Radiology, Montefiore Hospital and Medical Center, 111 E. 210th St., Bronx, NY 10467. Address reprint requests to R. D. Zimmerman.

² Department of Radiology, Rush Presbyterian-St. Luke's Medical Center, Chicago, IL 60612.

AJNR 3:635-642, November/December 1982

0195-6108/82/0306-0635\$02.00

© American Roentgen Ray Society

Emergency Department MR Imaging Scanner: Supportive Data

We read with personal interest the article in the May 2017 *American Journal of Neuroradiology* by M. Buller and J.P. Karis entitled “Introduction of a Dedicated Emergency Department MR Imaging Scanner at the Barrow Neurological Institute.” The authors described the challenges of placing an MR scanner in the emergency department (ED) setting in 2015 and referred to the impact on workflow. They also speculated on the impact this may have on patient care and decision-making. Our analyses on these issues regarding the installation of our ED MR scanner in 2012 have recently been published or are in press. The issues of length of stay (LOS) in the ED versus hospital LOS are areas of appropriate investigation, which we have explored in the settings of stroke^{1,2} and multiple sclerosis.^{3,4} We also have analyzed the impact of MR imaging on the decisions to admit patients, which may decrease unnecessary admissions, another downstream impact.^{1–4}

One important issue that we learned when we installed our ED CT scanner in 1999 is to have an agreed upon list of indications for emergent versus nonemergent but appropriate imaging requests.⁵ For the MR scanner installation, we met with the ED, neurosurgery, neurology, trauma surgery, and otorhinolaryngology departments and came up with a consensus list of ED MR imaging indications. This has led to satisfaction by all parties and less “drift” to inappropriate imaging.

Disclosures: David Yousem—UNRELATED: Expert Testimony: consultant for Expert Witness testimony, Comments: self-employed; Payment for Lectures (including service on Speakers Bureaus): ACR Education Center*; Royalties: Elsevier, Comments: for 5 books. *Money paid to the institution.

REFERENCES

1. Redd V, Levin S, Toerper M, et al. **Effects of fully accessible magnetic resonance imaging in the emergency department.** *Acad Emerg Med* 2015;22:741–49 CrossRef Medline
2. Honig SE, Honig EL, Mirbagheri S, et al. **The impact of installing an MR scanner in the emergency department for patients presenting with acute stroke-like symptoms.** *Clin Imaging* 2017;45:65–70 CrossRef Medline
3. Pakpoor J, Saylor D, Izbudak I, et al. **Follow-up of emergency department MRI scans suggesting new diagnosis of CNS demyelination.** *AJR Am J Roentgenol* 2017;209:171–75 CrossRef Medline
4. Pakpoor J, Saylor D, Izbudak I, et al. **Emergency department MRI scanning of patients with multiple sclerosis: worthwhile or wasteful?** *AJNR Am J Neuroradiol* 2017;38:12–17 CrossRef Medline
5. Oguz KK, Yousem DM, Deluca T, et al. **Effect of emergency department CT on neuroimaging case volume and positive scan rates.** *Acad Radiol* 2002;9:1018–24 CrossRef Medline

● D.M. Yousem

● J. Pakpoor

● L. Babiarz

● S. Honig

Department of Radiology
Johns Hopkins Medical Institution
Baltimore, Maryland

<http://dx.doi.org/10.3174/ajnr.A5315>

REPLY:

We appreciate the interest of Yousem et al in our recent article, "Introduction of a Dedicated MR Imaging Scanner at the Barrow Neurological Institute."¹ The transition to accessible emergency department (ED) MR imaging at the Barrow Neurological Institute is relatively recent, and our article focused on some important factors to consider when implementing a new ED MR imaging program and workflow, as well as associated changes that might be expected in scan volumes and distribution. We thank Yousem et al for bringing to our attention the important works on outcomes following ED MR imaging installation that have been completed at Johns Hopkins. It is encouraging to know that accessible ED MR imaging can have a positive impact on patient admission rates and admission lengths.²⁻⁵

We also agree with the importance of open communication with clinical services; consultation with emergency, neurology, and neurosurgery colleagues before, during, and after installation of an ED MR scanner is crucial to program success and plays an important role in shaping new ED ordering guidelines and protocols.

We hope that our experience, taken in conjunction with work from other centers, may provide support and insight to colleagues

considering the transition to accessible ED MR imaging in the future.

REFERENCES

1. Buller M, Karis JP. **Introduction of a dedicated emergency department MR imaging scanner at the Barrow Neurological Institute.** *AJNR Am J Neuroradiol* 2017 May 11. [Epub ahead of print] [CrossRef Medline](#)
2. Redd V, Levin S, Toerper M, et al. **Effects of fully accessible magnetic resonance imaging in the emergency department.** *Acad Emerg Med* 2015;22:741–49 [CrossRef Medline](#)
3. Honig SE, Babiarz LS, Honig EL, et al. **The impact of installing an MR scanner in the emergency department for patients presenting with acute stroke-like symptoms.** *Clin Imaging* 2017;45:65–70 [CrossRef Medline](#)
4. Pakpoor J, Saylor D, Izbudak I, et al. **Follow-up of emergency department MRI scans suggesting new diagnosis of CNS demyelination.** *AJR Am J Roentgenol* 2017;209:171–75 [CrossRef Medline](#)
5. Pakpoor J, Saylor D, Izbudak I, et al. **Emergency department MRI scanning of patients with multiple sclerosis: worthwhile or wasteful?** *AJNR Am J Neuroradiol* 2017;38:12–17 [CrossRef Medline](#)

● M. Buller

● J.P. Karis

Department of Neuroradiology
Barrow Neurological Institute
Phoenix, Arizona

<http://dx.doi.org/10.3174/ajnr.A5325>

Cerebral Microbleeds: A Call for Standardized Advanced Neuroimaging

In recent years, cerebral microbleeds have received considerable attention, in part due to the widespread availability of advanced neuroimaging methods for their detection.^{1,2} The prevalence of microbleeds has been well-studied in various diseases and in healthy controls. Their significance, however, is still poorly understood. In stroke and transient ischemic attack, for instance, the key question is whether microbleeds are a marker of increased risk of bleeding due to anticoagulants. Clinical opinion leaders have recently advocated for worldwide collaboration in microbleed research^{1,2} and have recognized the need for standardized imaging-acquisition sequences.

Here, we would like to further argue for the use of advanced imaging methods. In a recent meta-analysis, we have shown that the prevalence of microbleeds is influenced by the imaging technique and field strength.³ In Alzheimer disease, for example, the prevalence of microbleeds is twice as high with SWI than with conventional gradient-echo MR imaging. Multisite trials and international consortia are going to face a trade-off between standardization and the use of advanced imaging techniques. The maximization of the number of participating sites needs to be weighed against the ability to acquire and analyze SWI data. However, SWI is increasingly adopted as a new standard in many imaging sites. Furthermore, it may be useful to store the unprocessed images of the SWI scans so that they can be processed into quantitative susceptibility maps.⁴ Most important, future advanced processing does not preclude the conventional evaluation of SWI.

Finally, we support the suggestion that microbleeds be recorded electronically with standardized tools. Ideally, the output of such tools should be logfiles that contain microbleed location and certain attributes, as well as images that record the location and size of the microbleeds. These images and logfiles can be easily analyzed across numerous sites; this feature may result in further insight, such as microbleed location in various disease subtypes. Moreover, a low-cost by-product of this approach will be valuable data about the change in the number and size of microbleeds with time. If these imaging data are shared in conjunction with clinical, genetic, or biochemical data, their analysis will provide much

more insight than meta-analyses of aggregate data in the published literature.

In summary, members of the international consortia on microbleeds who will agree on which imaging techniques to use and how to best analyze and share the data may want to consider more advanced data-acquisition techniques and the high likelihood of future progress in quantitative image analysis. The relatively simple gradient-echo imaging can be used on all scanners, but it precludes further quantitative analysis of magnetic susceptibility, with a high false-negative rate. SWI detects much smaller microbleeds than gradient-echo imaging and has the advantage of allowing advanced quantitative analyses to be performed in the future without compromising standardization in the present.

ACKNOWLEDGMENTS

Alexander Rauscher is funded by Canada Research Chairs. Amir A. Sepehry was funded by the Alzheimer Society of Canada/Canadian Consortium on Neurodegeneration in Aging (ASC/CCNA). G.-Y. Robin Hsiung is funded by the Ralph Fisher and Alzheimer Society of BC professorship in Alzheimer Disease Research.

Disclosures: G.-Y. Robin Hsiung—*UNRELATED*: Research grants from Brain Canada, and Canadian Institutes of Health Research; support for travel to the DIAN study and ADNI study investigators meeting; and other funds from Eli Lilly, Biogen, and Astra-Zeneca for conduction of clinical trials as a site investigator*. *Money paid to the institution.

REFERENCES

1. Charidimou A, Soo Y, Heo JH, et al; META-MICROBLEEDS Consortium. **A call for researchers to join the META-MICROBLEEDS Consortium.** *Lancet Neurol* 2016;15:900 [CrossRef Medline](#)
2. Microbleeds International Collaborative Network. **Worldwide collaboration in the Microbleeds International Collaborative Network.** *Lancet Neurol* 2016;15:1113–14 [CrossRef Medline](#)
3. Sepehry AA, Lang D, Hsiung GY, et al. **Prevalence of brain microbleeds in Alzheimer disease: a systematic review and meta-analysis on the influence of neuroimaging techniques.** *AJNR Am J Neuroradiol* 2016;37:215–22 [CrossRef Medline](#)
4. Schweser F, Deistung A, Lehr BW, et al. **Quantitative imaging of intrinsic magnetic tissue properties using MRI signal phase: an ap-**

proach to in vivo brain iron metabolism? *Neuroimage* 2011;54:2789–807 [CrossRef](#) [Medline](#)

 **A. Rauscher**

Department of Paediatrics, Division of Neurology

 **G.-Y.R. Hsiung**

 **A.A. Sepehry**

Department of Medicine, Division of Neurology

University of British Columbia

Vancouver, British Columbia, Canada

Radiomics Approach Fails to Outperform Null Classifier on Test Data

It is with great pleasure that I read the recent article, the accompanying commentary, wide popular press, and lively ongoing discussion in the community regarding “Computer-Extracted Texture Features to Distinguish Cerebral Radionecrosis from Recurrent Brain Tumors on Multiparametric MRI: A Feasibility Study” by Tiwari et al.¹

With increasingly ubiquitous, cheap, computing infrastructure and the commoditization of high-quality machine-learning algorithms, multivoxel and multimodal pattern classification techniques, so-called “radiomics,” are increasingly being used to incorporate subtle but useful imaging features into our routine clinical decision-making as radiologists. To this end, I commend the authors on their well-thought-out design and implementation of a machine-learning classifier for differentiating tumor recurrence versus radiation necrosis in treated primary and metastatic human brain tumors.

The authors used a state-of-the-art but straightforward method incorporating the following: 1) image texture-based feature extraction, 2) feature selection/reduction via minimum redundancy maximum relevance, 3) generalization performance estimation of a support vector machine classifier, and most important, 4) an external layer of cross-validation to ensure that the feature selection and performance estimation steps were unbiased (ie, not overfit).

The authors widely acknowledged that this is, indeed, an early feasibility study, using limited retrospective data at hand, and this point has already been further explored by other commenters.² Additionally, however, there was no discussion of base rate effects or inclusion of a null classifier. A discussion here will hopefully be useful in both understanding the authors’ specific results and generalizing to the future because we aim to target the specific clinical scenarios where these advanced techniques may have their greatest clinical utility.

Diagnostic testing can be framed in the Bayesian sense of a pretest (prior) probability, which is updated by some new evidence, to yield a posttest (posterior) probability.³ The pretest probability is often informed by some general knowledge about the background prevalence (ie, base rate) in the community. The

new evidence typically takes the form of a test result for the individual. Consider the fringe cases: On the one hand, we can imagine a clinical scenario where the base rate is 50%. Under this regimen, similar to the authors’ training data, incorporation of individual data—even of marginal reliability—will nudge us in favor of 1 group and improve clinical diagnostic accuracy. On the other hand, as the base rate approaches 0% or 100%, even the best diagnostic tests will be useless in practice. For example, consider the challenge of identifying an uncommon disease in a hypothetical healthy population of 1000 individuals. If we examined the whole population, given a supposed baseline prevalence of 0.001 (1 in a 1000), even a terrific “rule out” screening diagnostic test with 100% sensitivity and 95% specificity will result in 1 true-positive test result and 49.95 false-positive test results, for an overall positive predictive value of only approximately 2%.

The crux of the issue then lies in the middle gray zone: As the base rate slides more in favor of 1 group, the bar rises for any additional candidate predictors/features to be “worth it” in terms of the marginal discriminating information they provide with respect to their inherent variability and accompanying measurement error. In the present feasibility study, tumor recurrence was only slightly more prevalent than radiation necrosis among the primary brain tumor training data (12 of 22 cases, or 55%). Therefore, a null classifier incorporating only this information would perform with 55% accuracy on average (the null information rate) and would be beaten handily by the authors’ imaging-based classifier, which achieved 75% estimated generalization accuracy via cross-validation-based resampling on the training data. This 75% number is the benchmark we would like to compare against human performance; however, such an analysis was not performed in the present study.

In the holdout test sample, however, the recurrence group was much more enriched. Therefore, while it may seem impressive that the imaging-based classifier attained 91% accuracy (10/11 cases) and this was the main headline widely publicized in the popular press, we would, in fact, have attained the exact same diagnostic accuracy by ignoring all the machine-learning algorithms, relying solely on our general knowledge of the base rate that tumor recurrence is more common and assigning every holdout test case to the “recurrence” class label without looking at a single image.

This leads to several important discussion points: Because there are so many subtle ways for classification experiments to be methodologically invalidated, there is a strong intuitive desire to see the methods tested on a truly independent test set, held out from the get-go, as was done here. This approach does have the desired effect of making us feel more comfortable with the methods; however, it also has negative effects. Not only does it make less data available for training, thereby decreasing the quality of the classifier, but, as we see here, the test set itself may be biased due to small sample size or other effects. This then provides yet another argument in favor of data-sharing and “reproducible research” in neuroimaging,⁴ whereby the community could easily validate the authors’ methods, confirm their cross-validated results, and obviate a separate holdout test.

It is also worth revisiting the uncomfortable fact that humans are useful but flawed statistical machines (and hence clinical decision-makers), subject to a variety of cognitive biases that have been explored in the literature on the psychology of decision-making during the past half-century.⁵ We underestimate the value of base rate information compared with individual information, overestimate the generalizability of our talents, overestimate the confidence/precision of our estimates, and are able to be systematically nudged by a variety of factors, including the arbitrary sequence in which cases are presented. In particular, as the validity of a task decreases (ie, the signal gets smaller, subtler, or more complex) or accompanying uncertainty increases, the consistency of our approach to intuitive reasoning suffers, and the net effects of these underlying biases may dominate.⁶ Although it was not investigated here, we may speculate that some (or all) of these effects may help explain why the “experts” performed even more poorly than would be expected on the test data. On the bright side, ample data do suggest that the performance of expert intuitive reasoning under this regimen can be successfully augmented by the introduction of even simple algorithms,⁷ as evidenced in our field by the success of the Breast Imaging Reporting and Data

System, the Liver Imaging Reporting and Data System, and so forth.

In summary, while widely publicized, the presented radiomics approach fails to outperform a null classifier on the given test set. Conversely, we are unable to compare the classifier cross-validated performance estimates on the training set with human performance because this analysis was not performed. If one looks forward, this interesting article describes a state-of-the-art radiomics classifier, though it highlights the importance of base rate effects and other cognitive bias when evaluating the usefulness of such a classifier and again argues in favor of both enhanced data-sharing in neuroimaging and enhanced incorporation of our expert intuitive reasoning into more structured frameworks for clinical decision-making.

REFERENCES

1. Tiwari P, Prasanna P, Wolansky L, et al. **Computer-extracted texture features to distinguish cerebral radionecrosis from recurrent brain tumors on multiparametric MRI: a feasibility study.** *AJNR Am J Neuroradiol* 2016;37:2231–36 [CrossRef Medline](#)
2. Schweitzer AD, Chiang GC, Ivanidze J, et al. **Regarding “Computer-Extracted Texture Features to Distinguish Cerebral Radionecrosis from Recurrent Brain Tumors on Multiparametric MRI: A Feasibility Study.”** *AJNR Am J Neuroradiol* 2017;38:E18–19 [CrossRef Medline](#)
3. Elstein AS, Schwartz A, Schwarz A. **Clinical problem solving and diagnostic decision making: selective review of the cognitive literature.** *BMJ* 2002;324:729–32 [Medline](#)
4. Poldrack RA, Baker CI, Durnez J, et al. **Scanning the horizon: towards transparent and reproducible neuroimaging research.** *Nat Rev Neurosci* 2017;18:115–26 [CrossRef Medline](#)
5. Tversky A, Kahneman D. **Judgment under uncertainty: heuristics and biases.** *Science* 1974;185:1124–31 [CrossRef Medline](#)
6. Kahneman D, Klein G. **Conditions for intuitive expertise: a failure to disagree.** *Am Psychol* 2009;64:515–26 [CrossRef Medline](#)
7. Grove WM, Zald DH, Lebow BS, et al. **Clinical versus mechanical prediction: a meta-analysis.** *Psychol Assess* 2000;12:19–30 [Medline](#)

 J.B. Colby

Department of Radiology and Biomedical Imaging
University of California, San Francisco
San Francisco, California

REPLY:

We thank Dr Colby for his interest in our article “Computer-Extracted Texture Features to Distinguish Cerebral Radionecrosis from Recurrent Brain Tumors on Multiparametric MRI: A Feasibility Study.”

We are replying to Dr Colby’s specific comment, “Therefore, while it may seem impressive that the imaging-based classifier attained 91% accuracy (10/11 cases) ... we would, in fact, have attained the exact same diagnostic accuracy by ignoring all the machine-learning algorithms, relying solely on our general knowledge of the base rate that tumor recurrence is more common and assigning every holdout test case to the ‘recurrence’ class label without looking at a single image.”

While we appreciate Dr Colby’s viewpoint, we respectfully disagree with his argument for at least a few reasons.

First, the test set was curated on the basis of the availability of studies that had pathologic confirmation (via multiple biopsies or surgical resections), which, in this case, happened to consist predominantly of recurrence cases. It was not compiled to be representative of the “true” distribution of tumor recurrence and necrosis cases. However, the image-based classifier during testing did not have this information a priori. Similarly, the readers were

blinded to the class distribution of cases in the test set. It is certainly conceivable that readers, when reviewing cases in clinical practice, tend to factor in the a priori distribution of recurrence and necrosis cases into their diagnosis, but there is no suggestion that this information was explicitly taken into account by the readers during the course of this study.

Second, the null classifier alluded to by Dr Colby is more of an abstract, theoretic idea. It so happens that for the number of cases ($n = 11$ with 10 cancer recurrences and 1 necrosis) considered in the test set, applying the “null classifier,” which involves labeling every case as cancer recurrence, would yield the same accuracy as the machine classifier. However, one could argue that if we were to create a subset of studies that had just 1 radiation necrosis case in it, the null classifier would have an accuracy of 0% and the machine classifier would have a 100% accuracy; the machine classifier in the test was able to correctly identify the necrosis case. While the discussion of the performance of the null classifier is certainly interesting from a theoretic perspective, clearly neither the human readers nor the machine classifier in our study invoked this null classifier approach.

 **P. Tiwari**

 **A. Madabhushi**

Department of Biomedical Engineering
Case Western Reserve University
Cleveland, Ohio

<http://dx.doi.org/10.3174/ajnr.A5366>

Imaging Findings of Benign Enhancing Foramen Magnum Lesions

We are grateful to McGuinness et al for their interesting and clinically applicable article “Benign Enhancing Foramen Magnum Lesions: Clinical Report of a Newly Recognized Entity.”¹ In a series of 14 patients, the authors documented the stereotypical appearance of 16 small, enhancing lesions posterior to and separate from the proximal intracranial vertebral artery. In all patients with available imaging, longitudinal follow-up confirmed stability. The authors noted 9 cases in which the enhancing focus was continuous with a presumed bridging vein extending from the internal vertebral venous plexus to the anterior condylar venous confluence. Thus, they suggested that the process might reflect a venous finding, such as a varix, with a small nerve root ganglion/pseudoganglion as a differential consideration.

We recently observed this same finding in a 67-year-old man undergoing a radiation treatment-planning brain MR imaging for a right caudate melanoma metastasis (Fig 1A). The presence of a small (2-mm), enhancing left foramen magnum lesion (Fig 1B) initially generated concern for a second metastasis. However, after we retrieved the patient’s prior MR imaging (Fig 1C), our concern was mitigated by 18-month stability. We were further reassured after noting its appearance was identical to that of the patients of McGuinness et al, supporting the benign nature of the process, despite metastatic disease elsewhere.

The imaging in our patient illustrates several additional notable features. First, he had a prior contrasted soft-tissue neck CT (Fig 1D), on which the process was evident as a small enhancing focus with an attenuation measurement of approximately 90 Hounsfield units. This was less than surrounding arterial vascular structures (for instance, 175 HU in the adjacent vertebral artery) and lower than the intracranial dural venous sinuses (for instance, 190 HU in the transverse sinus). However, its attenuation was similar to that in the upper cervical epidural plexus, suggesting a related venous etiology. Second, while the authors noted that they were unable to visualize the relationship of the process to the

spinal accessory or upper cervical nerve roots, our patient’s thin-section postcontrast imaging reveals its proximity to the latter (Fig 1E). While this could suggest a neural or perineural origin, we likewise referenced the findings of prior anatomic studies, in which small bridging veins approximate nerve roots as they course to and through the surrounding dura.^{2–4} Thus, the spatial relationship between the lesion and the upper cervical nerve roots does not preclude a venous etiology of the process. Last, our patient had a large developmental venous anomaly in the left cerebellum (Fig 1F), superior to the foramen magnum finding, but we suspect this may be coincidental in nature.

Regardless of its specific etiology, we hope that our case illustrates complementary features that can assist radiologic interpretation. Whether observed on CT or MR imaging, the stereotypical imaging characteristics are reassuring, and their recognition can optimize resource allocations by obviating extensive follow-up imaging, even when assessing intracranial metastatic disease.

Disclosures: M. Vittoria Spampinato—UNRELATED: Grants/Grants Pending: Bracco*. *Money paid to the institution.

REFERENCES

1. McGuinness BJ, Morrison JP, Brew SK, et al. **Benign enhancing foramen magnum lesions: clinical report of a newly recognized entity.** *AJNR Am J Neuroradiol* 2017;38:721–25 CrossRef Medline
2. Krings T, Geibprasert S. **Spinal dural arteriovenous fistulas.** *AJNR Am J Neuroradiol* 2009;30:639–48 CrossRef Medline
3. Krings T, Mull M, Bostroem A, et al. **Spinal epidural arteriovenous fistula with perimedullary drainage: case report and pathomechanical considerations.** *J Neurosurg Spine* 2006;5:353–58 CrossRef Medline
4. Thron A, Krings T, Otto J, et al. **The transdural course of radicular spinal cord veins: a microangiographical and microscopical study.** *Clin Neuroradiol* 2015;25:361–69 CrossRef Medline

● M.U. Antonucci

● M.V. Spampinato

Department of Radiology and Radiological Science
Medical University of South Carolina
Charleston, South Carolina

<http://dx.doi.org/10.3174/ajnr.A5330>

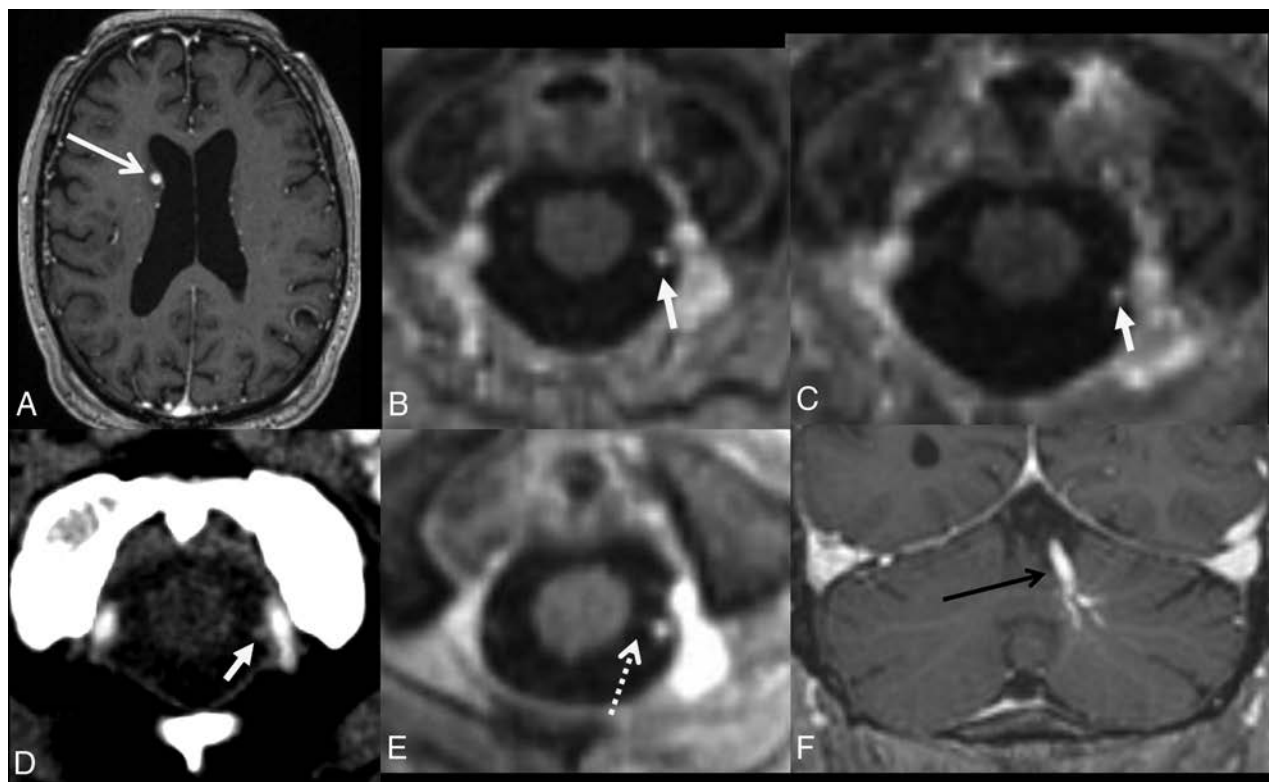


FIG 1. Axial T1 postcontrast volumetric imaging from a radiation-planning MR imaging for a metastatic melanoma lesion (A, *arrow*) demonstrates a 2-mm enhancing focus posterior to the left vertebral artery in the foramen magnum (B, *arrow*). This was unchanged from a study 18 months earlier (C, *arrow*) and was seen on a venous phase soft-tissue neck CT (D, *arrow*). Thin-section postcontrast imaging reveals its close proximity to a barely perceptible upper cervical nerve root (E, *dashed arrow*). A presumably coincidental developmental venous anomaly is seen in the left cerebellar hemisphere (F, *black arrow*).

Selective Poststent Balloon Angioplasty for Carotid Stenting

We read with interest the recent article¹ on the selective use of poststent dilation for carotid atherosclerosis. It confirms our published findings that the omission of routine poststent balloon angioplasty does not affect the angiographic and clinical outcomes in most patients undergoing carotid stent placement procedures.² We find it surprising that the authors have omitted from this recent review our series of 181 patients, in which both routine pre- and poststenting balloon angioplasties were not routinely performed and were only used selectively when required.³ We found that CT angiographic plaque morphology was quite accurate in predicting which patients would require balloon angioplasty to achieve a satisfactory angiographic outcome. Our approach, which we have termed “primary carotid stent” placement, results in less hemodynamic instability than standard techniques⁴ and has a similarly low incidence of periprocedural complications. We

believe that our data would have been a useful addition to this meta-analysis.

REFERENCES

1. Petr O, Brinjikji W, Murad MH, et al. **Selective-versus-standard post-stent dilation for carotid artery disease: a systematic review and meta-analysis.** *AJNR Am J Neuroradiol* 2017;38:999–1005 CrossRef Medline
2. Bussière M, Pelz DM, Kalapos P, et al. **Results using a self-expanding stent alone in the treatment of severe symptomatic carotid bifurcation stenosis.** *J Neurosurg* 2008;109:454–60 CrossRef Medline
3. Pelz DM, Lownie SP, Lee DH, et al. **Plaque morphology (the PLAC Scale) on CT angiography: predicting long-term anatomical success of primary carotid stenting.** *J Neurosurg* 2015;123:856–61 CrossRef Medline
4. Bussière M, Lownie SP, Lee D, et al. **Hemodynamic instability during carotid artery stenting: the relative contribution of stent deployment versus balloon dilation.** *J Neurosurg* 2009;110:905–12 CrossRef Medline

● D.M. Pelz

● S.P. Lownie

Departments of Medical Imaging and Clinical Neurological Sciences
Schulich School of Medicine and Dentistry
Western University
London, Ontario, Canada

<http://dx.doi.org/10.3174/ajnr.A5346>

REPLY:

We would like to thank Drs Pelz and Lownie for their interest in our article.¹ The literature search for this study was designed to include all studies published through January 2015, before the publication of their article titled "Plaque Morphology (the PLAC Scale) on CT Angiography: Predicting Long-Term Anatomical Success of Primary Carotid Stenting."² We have read with interest their article and believe it is a valuable read for those involved in carotid stent placement procedures. In their article, the authors reported that stent placement, without angioplasty, of soft plaques (ie, those with no or minimal calcification) can result in good long-term anatomic outcomes. On the other hand, carotid plaques that are heavily calcified require angioplasty and stent placement or carotid endarterectomy for good anatomic results. We thank the authors for their valuable contribution to the literature and look forward to seeing more of their work.

REFERENCES

1. Petr O, Brinjikji W, Murad MH, et al. **Selective-versus-standard poststent dilation for carotid artery disease: a systematic review**

<http://dx.doi.org/10.3174/ajnr.A5435>

and meta-analysis. *AJNR Am J Neuroradiol* 2017;38:999–1005
[CrossRef Medline](#)

2. Pelz DM, Lownie SP, Lee DH, Boulton M. **Plaque morphology (the PLAC Scale) on CT angiography: predicting long-term anatomical success of primary carotid stenting.** *J Neurosurg* 2015;123:856–61
[CrossRef Medline](#)

 **O. Petr**

Department of Neurologic Surgery
Mayo Clinic
Rochester, Minnesota
Department of Neurosurgery
Medical University Innsbruck
Innsbruck, Austria

 **W. Brinjikji**

Department of Radiology
Mayo Clinic
Rochester, Minnesota

 **M.H. Murad**

Division of Preventive Medicine
Mayo Clinic
Rochester, Minnesota

 **B. Glodny**

Department of Radiology
Medical University Innsbruck
Innsbruck, Austria

 **G. Lanzino**

Departments of Neurologic Surgery and Radiology
Mayo Clinic
Rochester, Minnesota

Open Globe Injury: Ultrasound First!

We read with much interest the article by Dr. Bodanapally and colleagues¹ in the March 2017 issue of *AJNR* regarding the interest of facial CT findings as prognostic predictors of visual outcome in open globe injury. They reported 4 variables associated with poor outcome on a regression model and showed that a grade III posterior segment hemorrhage had a strong positive predictive value of 100% for profound vision loss. Although these results are interesting and innovative, we believe that the interest in CT as a prognostic tool for visual outcome in open globe injury remains limited.

The exploration of the eyeball is still difficult with CT, even more so in case of injury. That is why the authors chose to refer to posterior eyeball injuries collectively as posterior segment hemorrhage. However, CT is only a mere surrogate for major ocular injuries such as retinal (RD) or choroidal detachments, which are reported to be the most important factors influencing final visual acuity in clinical and surgical studies.² Although vitreous hemorrhage may predict RD, it is not associated with poor visual outcome on its own. From a clinical and practical viewpoint, an emergency surgery is often performed on patients with open globe injuries to explore the eyeball, state the injuries, and perform a vitrectomy in the case of intravitreal hemorrhage. The demonstration of an RD or choroidal detachment profoundly changes the management of patients because prompt intervention and repair of these injuries significantly improve visual outcomes.² Thus, distinguishing attenuated vitreous membranes from RD is essential. It is, unfortunately, not directly possible with CT.

Moreover, the quantification of posterior segment hemorrhage is difficult with CT because of heterogeneous and varying blood densities in the eyes depending on the location of the hemorrhage, the presence of RD or choroidal detachment, the presence of a hematoma, or the delay between the injury and the CT. The absence of blood visualization on CT is also not reliable because of a lack of sensitivity.

The most appropriate imaging tool to assess prognostic predictors of visual outcome in open globe injury would be sonography. Its role in the detection of RD in eyes with opaque media has

been established clearly in the past. At present, there is no other method to reliably ascertain the anatomic position of the retina when direct examination is impossible. It allows a direct visualization of the main eyeball injuries, such as RD, globe rupture, perforating injury, or endophthalmitis.² These items are used in the main predictive models that have been developed for clinical decision-making, such as the Ocular Trauma Score,³ which can predict profound vision loss with a sensitivity of 100% and specificity of 91%. Sonography has 100% accuracy in the diagnosis of RD and can distinguish RD from choroidal detachments.² It is reported to be more accurate than CT in the diagnosis of vitreous hemorrhages,⁴ to provide an accurate quantification, and to detect even a small amount of blood that is not visible on CT. It may depict hyphema, lens dislocations, and intraocular foreign bodies. It can provide the exact location of the injuries and can differentiate vitreous from subretinal hemorrhage. It can even indicate some rare injuries that are often inoperable, such as closed-funnel RDs.

Sonography is simple to perform and interpret, easily accessible even at the patient's bedside or in a military setting. It is inexpensive and does not expose patients to ionizing radiation, as opposed to CT. It can be associated with a Doppler measurement of the central retinal artery, which reflects the intraocular hemodynamic, and is also a prognostic predictor for visual outcome. Finally, it is easy to perform sequential sonography during follow-up, which is crucial because one-quarter of patients with an open globe injury will develop an RD or a retinal tear after surgical repair.²

In conclusion, although interesting in the context of emergency, especially for the detection of ocular foreign bodies, we believe that CT has limited value in immediate clinical decision-making and as a prognostic predictor of visual outcome, and we believe that sonography could be a valuable and effective tool to predict outcomes.

REFERENCES

1. Bodanapally UK, Addis H, Dreizin D, et al. **Prognostic predictors of visual outcome in open globe injury: emphasis on facial CT findings.** *AJNR Am J Neuroradiol* 2017;38:1013–18 [CrossRef Medline](#)
2. Andreoli MT, Yiu G, Hart L, et al. **B-scan ultrasonography following open globe repair.** *Eye* 2014;28:381–85 [CrossRef Medline](#)

3. Kuhn F, Maisiak R, Mann L, et al. **The Ocular Trauma Score (OTS).** *Ophthalmol Clin North Am* 2002;15:163–65, vi [CrossRef Medline](#)
4. Bäuerle J, Gross NJ, Egger K, et al. **Terson's Syndrome: diagnostic comparison of ocular sonography and CT.** *J Neuroimaging* 2016;26:247–52 [CrossRef Medline](#)

● **A. Lecler**

Department of Radiology

● **A. Pinel**

Department of Ophthalmology

● **P. Koskas**

Department of Radiology

Fondation Ophtalmologique Adolphe de Rothschild

Paris, France

REPLY:

We thank Lecler et al for their insightful comments and for sharing their opinion on the use of sonography in patients with open globe injuries. Many valid points have been raised about the limitations of CT, with which we agree.

CT has evolved as the imaging technique of choice for evaluating patients with polytrauma in the United States. This imaging technique is widely used in emergency departments and trauma centers.

CT of the face detects not only globe injuries and radiopaque foreign bodies but also intraorbital soft-tissue injuries and orbito-facial fractures, which have major treatment implications. The chaotic environment of the trauma resuscitation units dealing with patients with various forms of blunt and penetrating trauma makes it impractical for ophthalmic sonography to be performed in all emergency settings. The procedure requires both specialized ophthalmic sonography equipment and expertise in its interpretation, which are not available around the clock in many trauma centers. In an emergent situation, CT and clinical examination provide ample information to decide whether a globe injury requires exploration. Our study shows that this information alone also provides prognostic information.

There is still not enough evidence to show that sonography can be performed without inducing pressure on the globe. Pressure on the globe risks the extrusion of intraocular contents and potentiates endophthalmitis or suprachoroidal hemorrhage, all of which could further damage the already injured globe. Hence, the experts at the University of Maryland Shock Trauma center avoid

sonography in patients with suspected globe injury in the acute setting.

Ophthalmic sonography does have a role in select cases to answer specific questions regarding ocular surgical planning and follow-up after globe repair. There is evidence to show that sonography has a major role in detecting complex pathologies that develop after globe repair, specifically differentiating a retinal detachment from a choroidal detachment. The findings from sonography provide useful information for planning management and predicting visual outcome. Andreoli et al¹ reported all these important factors in patients after globe repair. Our study differs in that it mainly deals with patients before globe repair and uses the limited preoperative clinical data available in the acute trauma setting.

In summary, the authors have made a compelling argument for sonography to determine prognostic information after globe repair. The safety of ophthalmic sonography should be established before using it in patients prior to globe repair. Ultimately, ophthalmic sonography is an effective tool in the follow-up of patients after globe repair to identify various traumatic pathologies, plan surgical repair, and predict patient outcomes.

REFERENCE

1. Andreoli MT, Yiu G, Hart L, et al. **B-scan ultrasonography following open globe repair.** *Eye (Lond)* 2014;28:381–85 [CrossRef Medline](#)

 **U.K. Bodanapally**

Department of Radiology

 **O. Saeedi**

Department of Ophthalmology and Visual Sciences

R Adams Cowley Shock Trauma Center

University of Maryland School of Medicine

Baltimore, Maryland

<http://dx.doi.org/10.3174/ajnr.A5379>